Revista Mexicana de Ingeniería Química

Academia Mexicana de Investigación y Docencia en Ingeniería Química, A.C.

Volumen 24, Número 2, Mayo-Agosto 2025

ISSN 1665-2738

Revista Mexicana de Ingeniería Química

Publicación de la Academia Mexicana de Investigación y Docencia en Ingeniería Química, A.C.

La Revista Mexicana de Ingeniería Química publica artículos de investigación originales, con el fin de promover la rápida divulgación de investigaciones significantes en las varias disciplinas que abarca la Ingeniería Química y sus interfaces con otras disciplinas de la Ingeniería. Los temas incluidos son: Termodinámica, Catálisis y Reactores, Control, Simulación, Seguridad, Diseño de Procesos, Biotecnología, Tecnología de Alimentos, Ingeniería Ambiental, Cinética de Materiales, Matemáticas Aplicadas, y Educación.

Revista Mexicana de Ingeniería Química

CONTENIDO

Volumen (Volume) 24, número (number) 2, 2025

IA25520 Heterogeneous photo-Fenton treatment in the degradation of indigo carmine (IC) by using ZeoSonFe as a catalyst through an experimental design

I. Cosme-Torres, F.J. Illescas-Martinez

IE25411 Numerical and experimental study of air heating solar collector constructed of aluminum tube pipes

A. López-López, I.A. García-Montalvo, S. Sandoval-Torres, E. Hernández-Bautista

IE25556 Synergetic Control of Cascade-Configured Anaerobic Digestion Bioreactors for Enhanced Hydrogen Production

O. Messili, S. Semcheddine, A. Chaabna

IE25513 Effect of absorber plate material on the performance of flat plate solar air heater under free convection

R.C. Salmorán-Salgado, F. J. Moreno-García, J.E. Botello-Álvarez, B. Ríos-Fuentes, M. Calderón-Ramirez, M.C. Pérez-Pérez, J.M. Gutiérrez-Villalobos, L. Fausto-Castro

Mat25443 Characterization and efficiency of Luffa cylindrica as bioadsorbent in Cr (VI) remotion from synthetic wastewater

J.G. Moreno-Rubio, N.R. Osornio-Rubio, H. Jiménez-Islas, E. Barrera-Calva, A.Y. Ramírez-Yañez, G.M. Martínez-González

Mat25444 Molecular dynamics of SDS-coated gold nanoparticles in aqueous medium with Coarse-grained model and MARTINI force field

D.E. Altamirano-Bulnes, E.D. Estrada-López

Mat25518 3D printing of microchannels with MSLA technology for microfluidic devices: From design to manufacturing

E.G. Rivera-Medellin, I. Pereyra-Laguna, L.E. Lugo-Uribe, M.A. González-López, J. Mayen-Chaires

Mat25509 Synthesis of zinc ferrite (ZnFe2O4) by mechanical grinding and calcination with a magnetite/maghemite precursor obtained by coprecipitation, its influence on crystalline, morphological and thermal properties, for its potential use at high temperatures

E. M. Garcia-Rosales, M. G. Rosales-Sosa, I. A. Facundo-Arzola, M. García-Yregoi, C. V. Reyes-Guzmán, Y.M. Rangel-Hernández, B. I. Rosales-Sosa

Proc25524 Evaluation of the presence of metallic cations (Cu^{2+}, Zn^{2+}, Fe^{2+}, Pb^{2+}) in silver sulfide leaching with thiosulfate: Thermodynamic and experimental study

G. Cisneros-Flores, J.C. Juárez-Tapia, I.A. Reyes-Domínguez, N. Toro, G. Urbano-Reyes, E.J. Muñoz-Hernández, J.I. Martínez-Soto, A. M. Teja-Ruíz

Sim25480 Numerical analysis of ilmenite particle diameter on thermal and fluid dynamic behavior in a chemical looping combustion system

F. A. Ocampo-Vaca, C. A. Hernández-Bocanegra, R. Maya-Yescas, J. A. Ramos-Banderas

Indizado en/Indexed in:

- **Chemical Abstracts;**
- **Thomson Reuters (*Science Citation Index Expanded, also known as SciSearch®; Chemistry Citation Index®; Journal Citation Reports, Science Edition*);**
- **Periódica;**

- **Latindex;**
- **Redalyc;**
- **Scopus**

RMIQ pertenece al Índice de Revistas Mexicanas de Investigación Científica y Tecnológica del CONACyT
RMIQ belongs to the Mexican Journals Index of Scientific and Technological Research of CONACyT

Vol. 24, No. 2 (2025)

Suscripciones
Envíe giro postal o cheque a nombre de la Academia Mexicana de Investigación y Docencia en Ingeniería Química, A.C. a:

Dr. Tomás Viveros García
Universidad Autónoma Metropolitana-Iztapalapa
Depto. de I. P. H., Area de Ing. Química
Edificio T-160, Av. San Rafael Atlixco No. 186, Vicentina. Tel. (55) 58044600
e-mail: tvig@xanum.uam.mx

Suscripción anual / Annual subscription

Personal	$160 USD
Estudiantes / Students	$80 USD
Institucional / Institutional	$540 USD

El envío de la revista se efectúa por correo ordinario
(Shipping is made by standard mail)

Portada: Purple flowers
Autora de la portada: Cindy García
Año: 2024.
Medidas: 1200x1600 pixeles (31.8 x 42.3 cm aproximado)
Técnica: fotografía digital

Indizado en/ Indexed in: Chemical Abstracts; Thomson Reuters (*Science Citation Index Expanded, also known as SciSearch®; Chemistry Citation Index®; Journal Citation Reports / Science Edition*); **Periódica; Latindex; Scopus; Redalyc**.

RMIQ pertenece al Índice de Revistas Mexicanas de Investigación Científica y Tecnológica del CONACYT

REVISTA MEXICANA DE INGENIERIA QUIMICA, Volumen 24, Número 2, Año 2025, mayo-agosto de 2025, es una publicación cuatrimestral editada por la Universidad Autónoma Metropolitana a través de la Unidad Iztapalapa, División de Ciencias Básicas e Ingeniería, Departamento de Ingeniería de Procesos e Hidráulica. Prolongación Canal de Miramontes, número 3855, colonia Rancho Los Colorines, alcaldía Tlalpan, código postal 14386, Ciudad de México y Av. San Rafael Atlixco No. 186. Col. La Vicentina, Iztapalapa. C.P. 09340. México, D.F. Tel. 58044600. Página electrónica de la revista: www.rmiq.org; dirección electrónica: amidiq@xanum.uam.mx. Editor Responsable: Dr. Tomás Viveros García. Certificado de Reserva de Derechos al Uso Exclusivo de Título No. 04-2012-101810590800-102, ISSN 1665-2738, ambos otorgados por el Instituto Nacional del Derecho de Autor. Certificado de Licitud de Título número 12238 y Certificado de Licitud de Contenido número 8891, ambos otorgados por la Comisión Calificadora de Publicaciones y Revistas Ilustradas de la Secretaría de Gobernación. Impresa por Impresos América, Avenida Hidalgo Número 46, Col. San Vicente Chicoloapan, Municipio de Chicoloapan, Estado de México, C.P. 56370, teléfono 0445522814012. Este número se terminó de imprimir en México, D.F. el 1 de agosto de 2024, con un tiraje de 500 ejemplares.

Vol. 24, No. 2(2025) Alim25472
Revista Mexicana de Ingeniería Química

Assessment on the extrusion parameters, physical and functional properties of a Blue Corn/Red Chief Lentil extrudates added with starch rich amylose and dietary fiber

Evaluación de los parámetros de extrusión, propiedades físicas y funcionales de extruidos de maíz azul y lentejas rojas adicionadas con almidón rico en amilosa y fibra dietética

E.A. Beltran-Medina[1], G.E. Jacques-Fajardo[1], J.J. Berrios[3], A. Suárez-Jacobo[2], R.I. Corona-González[4], E. Arriola-Guevara[4], G.M. Guatemala-Morales[1]*

[1]Tecnología Alimentaria, Centro de Investigación y Asistencia en Tecnología y Diseño del Estado de Jalisco (CIATEJ), Av. Normalistas 800, C.P.44270 Guadalajara, Jalisco, México.

[2]Tecnología Alimentaria, Centro de Investigación y Asistencia en Tecnología y Diseño del Estado de Jalisco (CIATEJ), Cam. Arenero 1227, El Bajío, C.P.45019 Zapopan, Jalisco, México.

[3]Healthy Processed Foods Research, Food Technology, USDA, ARS, PWA, WRRC-PFR, 800 Buchanan Street, Albany, CA 94710

[4]Departamento de Ingeniería Química, Centro Universitario de Ciencias Exactas e Ingenierías, Universidad de Guadalajara, Blvd. Marcelino García Barragán #1421, esq. Calzada Olímpica, C.P.44430 Guadalajara, Jalisco, México

Received: November 19, 2024; Accepted: March 25, 2025

Abstract

The aim of this work was to evaluate the effect of adding commercial un-modified food starch, based on high amylose corn (HylonV®), and soluble prebiotic dietary fiber (FiberSol®-2) in extrudates samples of a mixing base of Blue Corn (BC) and Red Chief Lentil (RL). Extruded samples with varying formulation were produced in a co-rotating twin-screw extruder and physical and functional properties of the expanded extrudates and extrusion parameters were evaluated. In addition, an acceptability test was performed with untrained judges. PCA was employed to analyze correlation amongst variables. The results obtained showed that the first component from PCA was more related to starch content effect per se and the second component to the effect of the FiberSol®-2 content in the food matrix during the extrusion process. In conclusion, based on the desirability function, the optimal formulation for extrusion cooking was 69.93 g/100 g wb BC:RL-mixture, 20.08 g/100 g wb HylonV® and 10.0 g/100 g wb FiberSol®-2 with adequate physical and functional properties of extrudates. The acceptability test showed that untrained judges preferred more expanded extrudates with higher FiberSol®-2 and BC:RL-mixture content and lower HylonV® content.

Keywords: extrusion cooking; mixture design; physical properties; functional properties; principal component analysis.

Resumen

El objetivo fue evaluar el efecto de la adición de almidón comercial no modificado, a base de maíz de alta amilosa (HylonV®), y fibra dietética prebiótica soluble (FiberSol®-2) en extruidos con una base de mezcla de Maíz Azul (BC) y Lenteja Roja (RL). Las muestras extruidas con diferentes formulaciones se elaboraron en un extrusor de doble husillo co-rotativo y se evaluaron las propiedades físicas y funcionales de los extruidos expandidos y los parámetros de extrusión. Además, fue realizada una prueba de aceptabilidad con jueces no entrenados. Se empleó PCA para analizar la correlación entre las variables. Los resultados mostraron que el primer componente estaba relacionado con el efecto del contenido de almidón per se, y el segundo componente al efecto del contenido de FiberSol®-2 en la matriz alimenticia durante el proceso de extrusión. En conclusión, con base en la función de deseabilidad, la formulación óptima fue 69.93 g/100g_{bs} mezcla BC:RL, 20.08 g/100g_{bs} HylonV® y 10.0 g/100g_{bs} FiberSol®-2 con propiedades físicas y funcionales adecuadas de los extruidos. La prueba de aceptabilidad mostró que los jueces no entrenados prefirieron extruidos más expandidos, con mayor contenido de FiberSol®-2 y mezcla BC:RL, y menor contenido de HylonV®.

Palabras clave: cocción por extrusión; diseño de mezclas; propiedades físicas; análisis de componentes principales.

* *Corresponding author. E-mail*: guadisga@msn.com ;
https://doi.org/10.24275/rmiq/Alim25472
ISSN:1665-2738, *issn-e*: 2395-8472

1 Introduction

Nowadays, there has been a trend among consumers to purchase low-calorie foods that have health benefits (Altan *et al.,* 2008; Aguilera & Lillford, 2008). Because of this trend, many research work studies have been incorporated novel ingredients that are potentially beneficial to health into new food products (López-Fernández *et al.*, 2021; Flores-Silva *et al.,* 2021). It has been reported that the addition of legumes to cereal-based products allows for an increase in both the protein content and quality (da Silva *et al.*, 2014). On the other hand, the extrusion process, and in particular of raw materials from food sources, deals with the process of mixing, cooking and transformation of the flours, which with the help of the shear energy exerted by a screw (of different configurations), and together with the supply of an additional heat flow in the compartment containing it, the food material is heated to its melting point, or plasticization point. This process occurs under controlled conditions to form a new material or extruded product, with physicochemical, functional, and sensory properties, very different from the raw materials used (Fellows, 2000). So, extruded legumes have been observed to have good expansion, and are therefore considered highly feasible for the development of high nutritional value, low calorie snacks (da Silva *et al.*, 2014). Extrusion is a widely used technology in chemical and food industry, ranging from processing in a 3D Printing (Wang *et al.,* 2019) to the use by-products from the food industry to obtain functional foods (Beltrán-Medina *et al.,* 2020; Medina-Rendon *et al.,* 2021). Extrusion cooking offers an excellent alternative of processing, extruders are very versatile equipment as they can process a wide variety of powdered ingredients including wholemeal flours and are very effective in the production of low-fat foods (Frame, 1994; Guy *et al.,* 2001).

Different cereals have been used to make expanded extrudates, such as white corn, which has a considerable amount of starch, allowing for the production of ready-to-eat expanded foods. A healthy alternative is the use of blue corn, which has a similar composition to white corn with the benefit of containing phenolic compounds and anthocyanins. The consumption of blue corn has been linked to the prevention of degenerative and chronic diseases, such as cataracts, cancer, and cardiovascular diseases (Camacho-Hernández *et al.,* 2014; Sánchez-Nuño *et al.,* 2024). Pulses (such as red chief lentil) are a good source of dietary fiber, protein, starch, minerals, folate and isoflavones, and are low in fat (they do not contain cholesterol) and sodium. Their components have been associated with beneficial health effects, such as hypocholesterolemic effects (proteins), prevention of some cancers and osteoporosis (isoflavones) (Nayak *et al.,* 2011; Madar & Stark 2002). Lentil polyphenols were reported to have antioxidant, antidiabetic, anticancer and cardioprotective activities. The phenolic compounds in lentils (flavanols) are good enzyme inhibitors of α-glucosidase and lipase, enzymes related to the digestion of glucose and lipids, respectively (Mustafa *et al.,* 2022). The most abundant amino acids in lentils are glutamic acid, aspartic acid, arginine, leucine, and lysine (which is in adequate levels). Lysine is the main limiting amino acid in cereals, so lentils are ideal complementary foods to cereals, which are relatively good sources of the sulfur-containing essential amino acids but low in lysine (Dhull *et al.,* 2023). Extrusion generally does not affect the protein content of extrudates, although a small reduction in certain essential amino acids has been reported due to their interaction with sugars during Maillard reactions. However, it is important to note that adding pulses to extrudates, increases the protein and essential amino acids content compared to cereal-based extrudates such as corn. It has also been shown that the extrusion process increases in vitro protein digestibility when comparing extrudates with raw doughs (García-Cordero *et al.,* 2024).

HylonV® (HyV) food starch is unmodified, based on high amylose corn and contains approximately 55% amylose. As dietary fiber source is use FiberSol®-2 (FS), that is a water-soluble, non-viscous and highly digestion-resistant maltodextrin, with a meal stimulated production of satiety hormones (Ye *et al.,* 2015). However, the incorporation of new ingredients in extrusion-cooking causes wide ranging changes of the morphological and molecular structure of starch granules because of mechanical and thermal energy dissipation (Brümmer *et al.,* 2002; Masatcioglu *et al.,* 2017). As far as these changes are related to the variables (parameters) of the extrusion cooking process it is necessary to differentiate between the effect of the specific mechanical energy input (SME) and that of the product temperature (PDT) on the extruded starch (Brümmer *et al.,* 2002).

Food formulation is a complicated process that requires sophistication, dedication, and a thorough background, both theoretical and practical in formulation chemistry, and could culminates in the introduction of a new product (Stauffer, 2004). The novelty of this work was to formulate an extruded food from a novel ingredient (blue corn) enriched with protein (Red Chief Lentil), also added with ingredients such as commercial corn starch (HyV) and dietary fiber (FS), where, the advantages they offer are taken, primary for its composition and standardized characteristics and secondly, for the benefits that they offer to the finished product (HyV is a biopolymer that provides characteristics of a resistant starch, and FS that allows the study of the addition of dietary

fiber). Therefore, the objectives of this work were to develop an extruded food product through an extreme vertices mixture design by adding Blue Corn and Red Chief Lentil (70:30), commercial corn starch (HyV) and dietary fiber (FS), and to evaluate the effect of the extrudates samples on the operation parameters [specific mechanical energy (SME), product temperature (PDT) and die pressure (DP)] and the physical [porosity (X), sectional expansion index (SEI), bulk density (BD), brittleness (B) and hardness (H)], and functional [water solubility index (WSI), water absorption index (WAI), cold viscosity (CV), pasting temperature (PT), raw peak viscosity (RPV), final viscosity (FV), antioxidant activity (AA), total phenolic content (TPC) and *in vitro* protein digestibility (IVPD)] properties of the food product.

2 Materials and methods

2.1 Materials

Sunny state blue corn (BC) and decorticated red chief lentils (RL) (Lens culinaris Medik) were acquired from a local distributor (California, USA) and kept at room temperature before milling process was carried out. Lentil and corn were ground to a coarse flour and then ground to a fine flour (< 1 mm) in a pin-mill, Alpine 160Z (Hosokawa Alpine AG, Augsburg, Germany). FS was purchased from Archer Daniels Midland/Matsutani LLC (Decatur, IL, USA) and HyV (55 g/100 g wb amylose) from National Starch and Chemical Company (Bridge-water, NJ, USA).

2.2 Blend preparation

Formulations were blended 10 minutes in a mixer, Hobart V-1401 (The Hobart Mfg. Co., Troy, OH, USA), set to the lowest speed, to obtain a uniform batch. Formulations were prepared using a Blue Corn and Red Lentil blend base (BC:RL-mixture, 70:30 p/p wb), following the extreme vertices mixture design, and stored in 4-gallon HDPE airtight buckets until extrusion.

2.3 Extruder and processing conditions

A twin-screw extruder, EVOL HT32-H (Clextral Inc., Tampa, FL, USA) with co-rotating and closely intermeshing screws was used. The D/L ratio was 24 and the extruder was provided with six-barrel sections, BS (each 128 mm long). The process conditions were set as: a screw speed of 500 rpm; a temperature profile BS1 to BS6 of 5, 80, 100, 100, 120, 140 ± 1 °C; a die temperature of 140 ± 1 °C.

Formulations were fed at a rate of 12.41 kg/h (wb), using a gravimetric loss-in-weight feeder, LWFD5-20 (K-Tron Corp., Pitman, NJ, USA). Water was supplied to the extruder to achieve a final moisture content of 20 g/100 g wb, using a triplex variable stroke piston pump, VE-P33 (Bran and Luebbe, Wheeling, IL, USA). The exit diameter of the two circular dies was 3.0 mm each. The pressure in the die was monitored during the extrusion runs, using a PT412-5M pressure transducer (Dynisco Instruments, Sharon, MA, USA). Extruder parameter data were collected at 1 s intervals by Intouch software (FITSYS PLUS ver. 1.23) when operating conditions (torque and pressure) reached steady state (Morales *et al*., 2015).

2.4 Extrusion parameters

Specific mechanical energy (SME), product temperature (PDT) and die pressure (DP) were obtained directly from the extruder software.

2.5 Physical properties

2.5.1 Sectional expansion index

Sectional expansion index (SEI) of the extrudates was evaluated according to the method described by Patil *et al*. (2007). The diameters of 30 samples were measured with a digital caliper, with measurements taken at five randomly chosen locations on the extrudates, each about 4 cm long. The sectional expansion index was calculated as the ratio of the average sectional area of the expanded extrudates to the area of the extruder die (3.0 mm).

2.5.2 Texture

A TA-XT2i Texture Analyzer (Texture Technologies Corp., Scarsdale, NY, USA) was used to measure the peak force as an indication of hardness (H), using 3-point bend test with a pasta blade. The test speed and the distance between two supports were 2 mm/s and 22 mm, respectively. Texture Exponent 32 software (version 5.0) was employed to record and analyze the curve. Brittleness (B) was assessed as the distance (mm) at which a product breaks and was measured from the force–distance curve (Altan *et al.,* 2008). Thirty measurements were performed on each formulation.

2.5.3 Bulk density, true density and porosity

Bulk density (BD) of each formulation was determined based on a method explained by Hwang & Yakawa (1980). The volumetric displacement method used glass beads with a diameter range of 1.00 to 1.18 mm as a displacement medium. Values were the average of three measurements of five grams each. Real density was obtained with a pycnometer, AccuPyc II 1340 (Micromeritics Instrument Corp., USA) and helium was used as

displacement gas. Five values of true density for samples with higher and lower expansion were measured. All the measurements were taken place after leaving the sample for at least 48 h at 25 °C on desiccators. Porosity (X) was calculated according to the equation (1):

$$X = \frac{(\rho t - \rho b)}{\rho b} \quad (1)$$

where: ρt = true density; ρb = bulk density (BD).

2.6 Functional properties

2.6.1 Water absorption index and water solubility index

Water Absorption Index (WAI) and Water Solubility Index (WSI) were analyzed as techno-functional properties. Data is expressed in percentage of change from the original value. Values could be positive if they increased and negative if they decreased.

The methodology described by Anderson et al. (1970) was followed to determine WAI and WSI. One gram of ground sample was added to 10 mL of distilled water in a centrifuge tube and shaken vigorously until completely dispersed on a vortex mixer. Then, it was placed on a rotary shaker at 25°C for 30 minutes. The suspension was centrifugated at 6000 g. WAI was expressed as the weight of the hydrated sample per gram of original sample. Determinations were performed in triplicate.

2.6.2 Pasting properties

The Rapid Visco Analyzer, RVA-4500 (Newport Scientific, Warriewood, Australia) was used to evaluate the pasting properties. 3 g milled sample and 25 mL HPLC grade water were mixed in an RVA-canister prior to analysis. Measurements were performed in triplicate at a constant shear rate of 160 rpm. The temperature program started at 298.15 K and the samples were held for 2 min, then heated to 368.15 K at 14 K/min, held for 3 min, and finally cooled at 17.5 K/min and held at 298.15 K for 1 min. Parameters recorded were cold viscosity (CV), raw peak viscosity (RPV), pasting temperature (PT) and final viscosity (FV) (Crosbie & Ross, 2007).

2.6.3 Antioxidant Activity (AA) and Total Phenolic Content (TPC)

Anthocyanins and soluble phenolic compounds in ground materials were extracted and quantified according to the following protocol: (a) one gram of each sample was mixed with 20 mL of acidic methanol (HCl):water solution (50:50 v/v, pH 2) per triplicate; (b) samples were kept for 1 h at room temperature with constant horizontal shaking in capped centrifuge tubes; (c) samples were centrifuged at 3000 g, 15 min at 4ºC; (d) pellets obtained before were extracted again with 20 mL acetone:water 70:30 v/v; (e) samples were kept for 1 hour at room temperature with constant horizontal shaking; (f) samples were centrifuged at 3000 g, 15 min at 4ºC; and (g) both supernatants of each sample were put together and used for AA by DPPH (Swain & Hillis, 1959) and TPC determination (Brand-Williams *et al.,* 1995).

2.7 Acceptability test

The acceptability test was divided in two steps. Twenty-two people from the western regional research center (Albany, CA) volunteered as untrained judge for the first step. Untrained judges were asked to try separately two codified sets of 6 extruded samples to rate texture acceptability from strongly dislike (2) to strongly like (10) in five levels, where the first and second sets included formulations from 1 to 6, and from 7 to 11 plus formulation 2, respectively. Both sets results were analyzed together by Fisher's least-significant difference (LSD) test and the top five liked formulations were identified. For the second step forty-two volunteers were requested to rank the top five formulations from strongly dislike (1) to strongly like (5). Fisher's least-significant difference (LSD) test was employed for analyzing data (Meilgaard *et al.,* 1999). Three-digit random numbers were used to code the samples and were served in the order of the formulation number. Water and unsalted crackers were provided to judges to cleanse their palates between samples and expectoration cups if they did not wish to swallow the samples.

2.8 Protein digestibility

In vitro protein digestibility (IVPD) was evaluated according to the method of Hsu & Vavak (1977), in samples selected by untrained judges in the acceptability test plus 100 g/100 g wb BC:RL-mixture (as a control), using a multienzyme system (trypsin, chymotrypsin and peptidase). The pH drop after 10 min incubation period was recorded and the percent protein digestibility (Y) was calculated from the equation (2):

$$Y = 210.469 - 18.10X \quad (2)$$

where (X) is the pH change after 10 minutes.

2.9 Experimental design and statistical

For the correlation between extrusion parameters, physical and functional properties, principal components analysis (PCA) was employed (Statgraphics Centurion XV).

Extrusion formulations were established and analyzed with an extreme vertices mixture design

Table 1. Three component extreme vertices mixture design.

Formulation	BC:RL-mixture[1,3]	HylonV®[3]	FiberSol®-2[3]
1	100	0	0
2	90	0	10
3	60	40	0
4	50	40	10
5	95	0	5
6	80	20	0
7	55	40	5
8	70	20	10
9	75	20	5
10	82.5	10	7.5
11	62.5	30	7.5
12[2]	55	40	5
13[2]	62.5	30	7.5

[1] BC:RL-blend: Blue Corn:Red Chief Lentil (70:30). [2] Repeats. [3] g/100 g wb.

(Table 1) with the following variables and levels: BC:RL-mixture (100-50 g/100 g wb), HyV (0-40 g/100 g wb) and FS (0-10 g/100 g wb) (Altan *et al.,* 2008; Caltinoglu *et al.,* 2014). For design and analysis of the extreme vertices mixture, the STATGRAPHICS Centurion XV package was used. Statistically significant differences between values were determined with a p-value < 0.05. A simultaneous optimization was performed to find the best combination of components using the desirability function method, considering the response variables whose models meet the traditional assumptions and that the coefficient of determination (R^2_{adj}) of each model was at least 70%. (Gutiérrez & de la Vara, 2012). The results were expressed as mean values ± standard errors of three separate determinations.

3 Results and discussion

The experimental design formulations for the extrusion process allowed us to obtain extrudates based on blue corn, red chief lentil, HyV starch and FS. Various physical properties were studied on the extruded products; Table 2 summarized them together with extrusion parameters and their standard deviations.

Data for pasting properties due to the extrusion process, antioxidant activity and total phenolic content are shown in Table 3.

3.1 ANOVA for mixture design

Analysis of variance for extrusion parameters, physical and functional properties showed that all but SEI (p=0.07), B (p=0.069), WAI (p=0.28), CV (p=0.137), RPV (p=0.141) and FV (p=0.105), were significantly affected (p<0.05) by BC:RL-mixture, HyV and FS content. Models fitting data were lineal for H (p=0.0224), DP (p=0.0071), AA (p=0.0000) and TPC (p=0.0000); quadratic for BD (p=0.0292) and X (p=0.0376); and cubic for PDT (p=0.0390), SME (p=0.0072), WSI (p=0.0468) and PT (p=0.0036).

Table 2. Measured physical properties of the extruded products from de mixture design and extrusion parameters.

Formulation	SEI	BD (g/cm^3)	H (N)	B (mm)	X	PDT (ºC)	SME (kJ/kg)	DP (kPa)
1	3.57±0.01	0.50±0.00	5.89±1.03	0.14±0.02	0.66±0.00	171.84±8.45	566.50±17.20	7427±187
2	3.68±0.01	0.44±0.00	5.29±1.05	0.16±0.02	0.69±0.00	174.76±8.79	504.65±13.98	6170±107
3	5.89±0.02	0.33±0.00	6.09±1.01	0.20±0.02	0.78±0.00	182.81±8.31	856.06±18.20	7391±283
4	2.88±0.02	0.56±0.04	3.36±0.73	0.11±0.02	0.62±0.04	184.36±8.42	584.68±17.57	7173±172
5	3.62±0.03	0.50±0.01	4.28±0.81	0.14±0.02	0.66±0.01	180.48±10.83	531.93±19.72	7059±236
6	3.27±0.01	0.52±0.01	5.52±0.99	0.14±0.02	0.65±0.01	180.21±4.00	642.16±35.44	8101±339
7	3.28±0.01	0.52±0.02	3.29±0.62	0.11±0.02	0.65±0.02	173.25±8.96	637.52±21.72	8429±157
8	3.58±0.02	0.53±0.00	3.78±0.55	0.11±0.02	0.64±0.00	183.77±3.54	548.56±21.98	6626±100
9	3.48±0.01	0.59±0.02	4.67±0.98	0.14±0.02	0.60±0.02	177.34±6.87	575.65±8.36	7017±154
10	3.74±0.01	0.48±0.01	4.03±0.77	0.13±0.02	0.67±0.01	174.18±8.24	469.82±11.55	6718±118
11	3.26±0.01	0.52±0.03	4.51±1.12	0.13±0.02	0.65±0.02	180.06±9.12	655.05±23.12	7459±195
12	3.23±0.01	0.45±0.05	3.87±0.72	0.14±0.02	0.70±0.05	172.62±6.94	665.32±12.47	8271±119
13	3.12±0.02	0.63±0.02	4.79±0.96	0.14±0.02	0.57±0.02	177.71±7.33	621.53±15.7	6844±159

SEI: Sectional expansion index; BD: Bulk density; H: Hardness; B: Brittleness; X: Porosity; PDT: Product temperature; SME: Specific mechanical energy; DP: Die pressure.

Table 3. Results of functional properties.

Formulation	WSI[1,4] [%]	WAI[1,5] [g gel/g sample]	CV[1,6] [cP]	PT[1,7] [ºC]	RPV[1,8] [cP]	FV[1,9] [cP]	Antioxidant activity[2] Extrudates	Antioxidant activity[2] Raw formulation	Total phenolic content[3] Extrudates	Total phenolic content[3] Raw formulation
1	15.94±0.13	3.38±0.04	139.00±4.58	60.30±0.00	1211.00±32.14	2744.33±24.75	4.33±0.14	4.43±0.28	1.29±0.08	1.28±0.09
2	20.55±0.05	3.30±0.06	75.50±3.44	61.75±0.14	849.00±9.90	2268.00±22.63	4.20±0.32	4.00±0.26	1.29±0.07	1.15±0.09
3	15.14±0.03	3.68±0.00	190.50±2.12	60.20±0.07	544.50±2.12	1082.50±2.12	3.11±0.03	3.27±0.21	0.85±0.06	0.83±0.06
4	18.88±0.01	3.17±0.03	33.00±1.73	62.18±1.48	360.33±2.52	717.00±7.21	3.07±0.30	2.84±0.18	0.81±0.09	0.70±0.06
5	17.70±0.04	3.15±0.01	76.33±5.51	60.30±0.09	1035.00±8.19	2493.67±9.50	4.37±0.48	4.21±0.27	1.26±0.12	1.22±0.09
6	13.91±0.02	3.65±0.06	91.50±3.54	60.40±0.07	855.00±11.31	2039.00±11.31	3.96±0.21	3.85±0.24	1.07±0.06	1.05±0.08
7	16.07±0.14	3.36±0.00	44.50±0.71	60.45±0.07	626.00±1.41	1451.50±9.19	3.35±0.06	3.05±0.20	0.95±0.07	0.76±0.06
8	20.26±0.11	3.12±0.15	54.33±1.15	61.05±0.77	616.33±2.08	1472.00±26.85	3.96±0.15	3.42±0.22	1.10±0.07	0.92±0.07
9	16.97±0.06	3.61±0.01	88.50±2.12	60.30±0.14	701.00±1.41	1613.00±4.24	3.74±0.12	3.63±0.23	1.07±0.02	0.99±0.07
10	19.61±0.03	3.27±0.01	87.33±0.58	60.28±0.06	791.67±40.20	1820.33±13.87	4.04±0.15	3.82±0.24	1.15±0.09	1.07±0.08
11	18.16±0.04	3.42±0.01	54.50±0.71	60.28±0.11	481.00±2.83	1005.00±0.00	3.13±0.26	3.24±0.21	0.91±0.07	0.84±0.06
12	15.06±0.03	3.45±0.00	40.50±0.71	60.30±0.07	485.50±0.71	966.00±1.41	3.31±0.24	3.05±0.20	0.87±0.06	0.76±0.06
13	18.13±0.04	3.44±0.04	54.33±1.53	60.60±0.35	540.00±5.00	1239.33±25.58	3.66±0.27	3.24±0.21	0.99±0.08	0.84±0.06

[1]Mean ±SD; [2]mg TROLOX/g sample wb; [3]mg Gallic Acid/g sample wb;[4]Water Solubility Index (WSI);[5]Water Absorption Index (WAI); [6]ColdViscosity (CV); [7]Pasting Temperature (PT);[8]Raw Peak Viscosity (RPV); [9]Final Viscosity (FV)

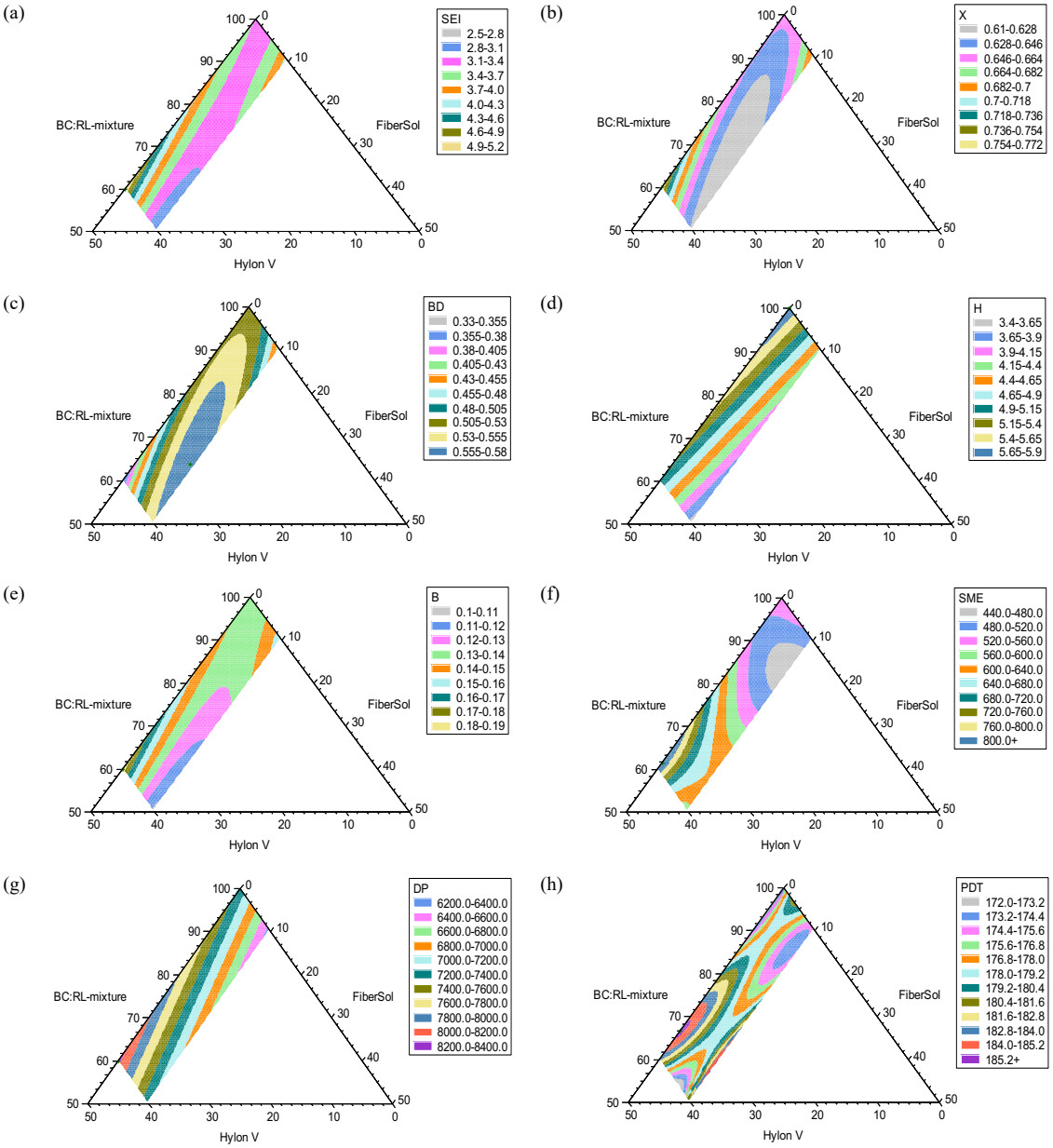

Figure 1. Mixture contour plots for: (a) Sectional expansion index [SEI]; (b) Porosity [X]; (c) Bulk density [BD]; (d) Hardness [H]; (e) Brittleness [B]; (f) Specific mechanical energy [SME]; (g) Die pressure [DP]; and (h) Product temperature [PDT]. BC:RL-mixture, HylonV® and FiberSol®-2 expressed in g/100 g wb.

3.2 Physical properties

The SEI, BD, and X values of expanded extrudates prepared from different formulations containing varying BC:RL-mixture, FS and HyV contents are shown in Table 2. The SEI of extrudates was in the range of 3.12 and 5.89, similarly to another study (Meng *et al.,* 2010), indicating that BC:RL-based extruded products can be obtained with a desirable expansion. Greater expansions were observed in extrudates made from mixtures without FS, being the 40 g/100 g wb HyV mixture the one with the greatest SEI (Figure 1a). This could be due to the fact that by increasing the starch content (HyV) and reducing the protein content (BC:RL-mixture) and without the addition of fiber (FS), the starch will have a greater amount of available water, increasing its gelation capacity and therefore its expansion (García-Cordero *et al.,* 2024). The X values ranged from 0.57 to 0.78, alike to Yağci & Göğüş (2008). A similar behavior to SEI´s was depicted for X, having the maximum value at 40 g/100 g wb HyV and the greatest values when FS content was zero (Figure 1b). BD maximum value (0.63 g/cm^3) was obtained when extrudates were made from mixtures with the highest FS content (SEI, 3.12; X, 0.57). What is in accordance with different studies (Altan *et al.,* 2008; Yağci & Göğüş, 2008; Vanier *et al.,* 2016), they found expansion positively correlated to porosity and both negatively related to BD. Figure 1c shows that as higher the FS content was, higher the BD, this behavior was countered by increasing HyV concentration. Maskan & Altan (2012) explained that the presence of fiber particles tended to break the cell walls before the gas bubbles had expanded to their maximum potential. Thus, the increase in bulk density may be due to the increase in fiber content of the feed material.

3.2.1 Textural properties

The H measurements that were taken for the expanded extrudates ranged from 3.29 to 6.09 N are shown in Table 2 and represented graphically in Figure 1d. Where can be seen that increasing HyV content while keeping FS constant produced a decrease in H values due to higher expansion. Additionally, H was inversely related to FS content for both cases, keeping either BC:RL-mixture content constant or HyV content constant, thus, lower H values were got at maximum FS content (10 g/100 g wb). What would be also related to the matrix disruption (Altan *et al.,* 2008).

As it was reported, physical properties are related to the amount and the type of starch added to the formulation (Vanier *et al.,* 2016). FS particles compete with starch molecules for water, what would prevent mixture matrix to melt, thus producing softer extrudates (Maskan & Altan, 2012). B represented the distance to break the extrudates, with the shortest distance being the most brittle product (Altan *et al*., 2008). Measurements for extrudates ranged from 0.11 to 0.20 mm. It is noticeable that, B values got reduced when FS increased, either keeping constant HyV or BC:RL-mixture content (Figure 1e). B values are in line with H behavior in this work, hence, FS content interfering effect on the matrix from fiber molecules would produce less expanded and more brittle extrudates.

3.2.2 Extrusion parameters

Table 2 depicts behavior for DP, SME, and PDT. Maximum value for SEM was obtained when FS and HyV contents were 0 and 40 g/100 g wb, respectively (Figure 1f), what matches with maximum values found for SEI and X. Higher starch concentrations would increase matrix viscosity while extruding, increasing this way SME values due to stronger gels. Meng *et al*. (2010) explained that higher SME values produced larger expansions due to the starch disruption generated through shear stress, inducing gelatinization and consequently expansion. Therefore, higher viscous dissipation was got, increasing PDT over DP value (Table 2). The highest DP values were obtained when HyV content was maximum (Figure 1g), thus, its behavior would be due to the stronger gel formed and to the water overheating inside the bubbles in the matrix before exiting. High HyV and low FS contents would increase PDT (Figure 1h) due to viscous dissipation.

3.3 Functional properties

3.3.1 AA and TPC

Data are presented in Table 3. Values for extrudates ranged from 3.07 to 4.37 mg TROLOX/g sample wb and from 0.81 to 1.29 mg Gallic Acid/g sample wb, AA and TPC, respectively. These values are like the ones reported by Mora-Rochin *et al*. (2010) for blue corn extrudates. There was not statistically significant difference (NSSD) between extruded and raw formulations for each sample, neither for AA nor for TPC. This might indicate either that the conditions were soft enough to maintain AA or a protective effect from the matrix occurred, preventing phenolic compounds from reacting and losing their structure and/or antioxidant capacity. Thus, phenolic compounds retention with AA after extrusion could be an important finding because contrary to this study, Camacho-Hernandez *et al*. (2014) and Brennan *et al*. (2011) reported anthocyanin content reduction after extrusion. Also, Castro-Montoya *et al*. (2024) reported that a high moisture content or some compound present in the food matrix could cause a lubricating effect during the extrusion process, causing

less thermomechanical damage to the phenolic compounds, avoiding their losses during the extrusion process.

The optimization of the formulation using the desirability function (Gutiérrez & de la Vara, 2012) in the indicated region, maximizing PDT (R^2_{adj}=87.75%), SME (R^2_{adj}=96.13%), AA (R^2_{adj}=86.75%) and TPC (R^2_{adj}=94.23%), and minimizing WSI (R^2_{adj}=86.08%) and PT (R^2_{adj}=97.56%), showed that the optimal values for the studied components were 69.93 g/100 g wb BC:RL-mixture, 20.08 g/100 g wb HyV and 10.0 g/100 g wb FS. The overall desirability was 0.5953. The predicted response values with the desirability function were 183.134°C (PDT), 553.253 kJ/kg (SME), 14.158% (WSI), 60.449°C (PT), 3.7353 mg TROLOX/g sample wb (AA) and 1.0645 mg GA/g sample wb (TPC).

3.4 Correlation amongst formulations, extrusion parameters, physical and functional properties

Twenty-three pairs of variables were found to have a strong correlation ($p<0.05$) in Spearman's rank correlation analysis. Therefore, a principal component analysis (PCA) was performed to better understand the phenomena occurring during extrusion cooking process and the relationship amongst formulation, physical and functional properties. Five components were necessary to explain 89.054% of the variability in the original data. First component explains 33.959% of the variability of the data, the second 25.029%, the third 13.165%, the fourth 10.134% and the fifth 6.767%. Figure 2 depicts the correlation amongst independent variables, extrusion parameters, physical and functional properties of products. It is noteworthy that the first component can be observed by looking at the horizontal axis where the behavior of the variables is mainly explained by the HyV/BC:RL-mixture ratio. This was more related to starch content effect per se. A higher starch concentration would increase matrix viscosity, inducing higher SME values and therefore higher PDT due to viscous dissipation. DP resulted to be strongly correlated to HyV, this correlation might be due to a strongest gel structure formed at higher starch contents, being capable to retain vapor before explosion (Korkerd *et al.,* 2016; Yu *et al.*, 2012). Thus, at constant moisture and extrusion conditions, response variables were mainly controlled by the starch concentration in the matrix. WAI is related to the amount of water absorbed by starch granules after swelling in excess water, being an index of degree of gelatinization (Rodriguez-Miranda *et al.,* 2012). BC:RL-mixture was directly related to WAI, a higher starch concentration might increase matrix gel strength and viscosity. The use

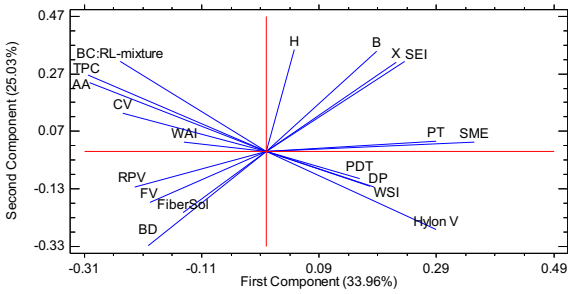

Figure 2. Principal component analysis: loading plot of first two principal components describing the variation and correlation amongst the different ingredients, extrudates properties and system parameters. Two close lines indicate two properties that are highly correlated.

of starch as a stabilizer and thickener has been widely studied (Moscicki, 2011; Manrique-Quevedo *et al.,* 2007; Saha & Bhattacharya, 2010). WAI was positively correlated to RPV. Blanche & Sun (2004) explained that RPV is a measure of the degree of starch transformation (cooking) and Braşoveanu & Nemţanu (2020) stated that RPV indicate the capacity and ability of water absorption of granules. Thus, higher RPV and WAI values indicate cooked extrudates. PT provides an indication of the minimum temperature required to cook the starch (Wang *et al.,* 2014) and was positively correlated to HyV content. After heating starch above the gelatinization temperature, the process of viscosity development in starch pasting occurs (Braşoveanu & Nemţanu, 2020). Furthermore, less cooked extrudates agreed with higher BC:RL-mixture content, AA and TPC, showing a positive strong correlation amongst them, indicating that AA and TPC on extrudates were directly related to initial formulation. Hu & Xu (2011) and Sarawong *et al.* (2014) also reported correlation coefficients between AA (determined by DPPH assay) and TPC higher than 0.90 for soluble compounds.

The second component explains the variables behavior which could be observed along the vertical axis and are mainly explained by the FS effect (Figure 2). FS content was positively related to BD and negatively related to H, B, X and SEI. This could be due to a dilution effect, because an increase in FS content in raw mixtures will produce less starch availability and would also interfere in gelatinized matrix formation during extrusion process. Thus, inducing production of denser, less expanded, softer, and more brittle extrudates. Yağci & Göğüş (2008) explained that after certain concentration fiber molecules disrupt the continuous structure of the melt in extruder, preventing elastic deformation during extrusion. The appearance of FV variability in the middle way of both components indicates the positive effect of BC:RL-mixture and FS on it. Lower fiber contents would let the matrix to

strengthen, increasing viscosity, shearing stress, starch granules disruption, expansion (SEI) and finally break down starch molecules (CV) and starch dextrinization (WSI) if shearing is high enough. This could explain the negative correlation of FS with SEI, WSI and CV. Similarly to Wani & Kumar (2016), Stojceska *et al*. (2009) and Yağci & Göğüş (2008) findings. BC:RL-mixture appears in the middle way of both components, indicating that a higher BC:RL-mixture concentration would increase H due to an increase of the fiber and protein content in the mixture. Some authors found that denser and less expanded extrudates can be obtained increasing protein and fiber content in raw mixtures (Korkerd *et al*., 2016; Yu *et al*., 2012).

3.5 Acceptability test

The acceptability test was carried out to select the samples that would be evaluated in the protein digestibility test, using the formulations with the greatest acceptance by untrained judges. The first panel consisted mainly of males, being mostly Asian and Caucasian between 30 and 59 years old. Besides, the second panel was formed by the same number of men as women, mostly Asian and Caucasian between 18 and 39 years old. The mean scores of both texture evaluations are shown in Figure 3, it is noticeable that in general, untrained judges preferred more expanded extrudates, as can be seen in Table 2 (SEI). Analysis of the surface representing the effect of formulation on texture acceptability behavior showed that untrained judges preferred extrudates with lower content of HyV, higher content of FS and BC:RL-mixture. It has been described that in terms of overall acceptability, formulations with moderate proportions (15 to 35%) of pulses have been better rated by the panelists (García-Cordero *et al.,* 2024), which coincides with this work, since the RL content in formulation 2 was 27%, in 3 it was 18% and in 10 it was 24.75%.

3.6 Protein digestibility

Table 4 shows that IVPD of extrudates increased significantly by extrusion process. The IVPD results agree with those of Rathod & Annapure (2016) on pulses, where the IVPD greatly varied from raw samples. A more significant improvement of IVPD by extrusion cooking was produced in extrudates with less amount of HyV, what might indicate a protective effect from starch over the protein structure. Rathod & Annapure (2016) found that the increase in digestibility was greater in starch than in protein produced by the extrusion processing.

As Stauffer (2004) states, successful food formulation culminates in the introduction of a new product that is tasty, nutritious, economical, convenient, and safe and that consumers react positively to by increasing their purchases of the item. Thus, this study allows us to direct efforts to the development of a functional food, which has the advantage of being ready to eat. The study of the effect of changes in composition by monitoring simple parameters to measure, allows explaining how it affects the structure of the product and could finish in a future in a new healthy product.

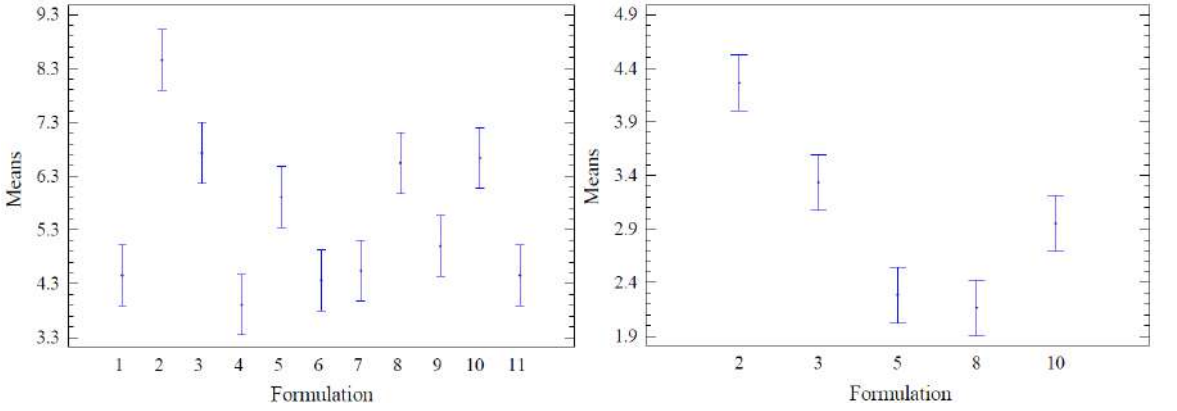

Figure 3. Formulation means' graphs; 95% Fisher's LSD.

Table 4. Protein digestibility.

Formulation	BC:RL- mixture[2,3]	HylonV®[3]	FS[3,5]	Protein digestibility[4]	
				Extrudates[1]	Raw formulations[1]
1	100	0	0	83.56±0.18	78.13±0.00
2	90	0	10	84.23±0.69	78.66±0.51
3	60	40	0	82.93±0.13	78.76±0.13
10	82.5	10	7.5	83.56±0.18	78.31±0.26

[1]Mean±SD; [2]BC:RL-mixture: BlueCorn:RedChiefLentil (70:30); [3]g/100 g wb; [4]%; [5]FS: FiberSol®-2.

Conclusions

It is concluded that directly expanded extrudates can be obtained from a mixture of blue corn and red chief lentil, without any additives or extra ingredient. However, addition of HylonV® increased extrudates expansion indirectly. FiberSol®-2 had a great effect on extrudates physical properties, decreasing sectional expansion index, porosity and hardness. The optimal formulation for extrusion cooking of extrudates with adequate physical properties was 69.93 g/100 g wb BC:RL-mixture, 20.08 g/100 g wb HylonV® and 10.0 g/100 g wb FiberSol®-2.

During extrusion-cooking, new structures of products are formed due to starch, protein and fiber damage. WAI and pasting properties of extruded products were influenced by the ingredient's concentration. It was found a strong correlation amongst antioxidant activity and total phenolic content for soluble compounds, moreover, not statistically significant difference was found amongst extruded and raw formulations. The analysis of acceptability showed that untrained judges preferred more expanded extrudates that contained FiberSol®-2 and lower HylonV® content. Amongst the samples selected by untrained judges, the lowest protein digestibility was obtained in the formulation with the highest HylonV® content.

Acknowledgements

Authors express their gratefulness for the financial support provided by the Consejo Nacional de Humanidades, Ciencia y Tecnología (CONAHCYT), for scholarship number 344813; the Centro de Investigación y Asistencia en Tecnología y Diseño del Estado de Jalisco, A.C. (CIATEJ); the Universidad de Guadalajara; the Healthy Processed Foods Research, Food Technology, USDA, ARS, PWA, WRRC-PFR; and Dr. R. Prado Jímenez.

References

Aguilera, J. M. and Lillford, P. J. (2008). *Food Materials Science: Principles and Practice*, Ed. Springer-Verlag New York, New York.

Altan, A., McCarthy, K.L. and Maskan, M. (2008). Twin-screw extrusion of barley–grape pomace blends: Extrudate characteristics and determination of optimum processing conditions. *Journal of Food Engineering* 89, 24–32. https://doi.org/10.1016/j.jfoodeng.2008.03.025

Anderson, R.A., Conway, H.F. and Peplinski, A.J. (1970). Gelatinization of corn grits by roll cooking, extrusion cooking and steaming. *Starch* 22, 130-135.

Beltrán-Medina, E.A., Guatemala-Morales, G.M., Padilla-Camberos, E., Corona-González, R.I., Mondragón-Cortez, P.M. and Arriola-Guevara, E. (2020). Evaluation of the use of a coffee industry by-product in a cereal-based extruded food product. *Foods* 9, 1008. https://doi.org/10.3390/foods9081008

Blanche, S. and Sun, X. (2004). Physical characterization of starch extrudates as a function of melting transitions and extrusion conditions. *Advances in Polymer Technology* 23, 277-290.

Brand-Williams, W., Cuvelier, M.E. and Berset, C. (1995). Use of a free radical method to evaluate antioxidant activity. *LWT-Food Science and Technology* 28, 25-30.

Braşoveanu, M. and Nemţanu, M.R. (2020). Pasting properties modeling and comparative analysis of starch exposed to ionizing radiation. *Radiation Physics and Chemistry* 168, 108492. https://doi.org/10.1016/j.radphyschem.2019.108492

Brennan, C., Brennan, M., Derbyshire, E. and Tiwari, B.K. (2011). Effects of extrusion on the polyphenols, vitamins and antioxidant activity of foods. *Trends in Food Science and Technology* 22, 570-575.

Brümmer, T., Meuser, F., van Lengerich, B. and Niemann, C. (2002). Expansion and functional properties of corn starch extrudates related to their molecular degradation, product temperature and water content. *Starch - Stärke* 54(1), 9–15. https://doi.org/10.1002/1521-379X(200201)54:1%3c9::AID-STAR9%3e3.0.CO;2-E

Caltinoglu, C., Tonyali, B. and Sensoy, I. (2014). Effects of tomato pulp addition on the extrudate quality parameters and effects of extrusion on the functional parameters of the extrudates. *International Journal of Food Science & Technology* 49(2), 587–594. https://doi.org/10.1111/ijfs.12341

Camacho-Hernández, I.L., Zazueta-Morales, J.J., Gallegos-Infante, J.A., Aguilar-Palazuelos, E., Rocha-Guzmán, N.E., Navarro-Cortez, R.O., Jacobo-Valenzuela, N. and Gómez-Aldapa, C.A. (2014). Effect of extrusion conditions on physicochemical characteristics

and anthocyanin content of blue corn third-generation snacks. *CyTA - Journal of Food* 12(4), 320–330. DOI: https://doi.org/10.1080/19476337.2013.861517

Castro-Montoya, Y.A., Jacobo-Valenzuela, N., Delgado-Nieblas, C.I., Ruiz-Armenta, X.A., Heredia, J.B., Delgado-Murillo, S.A., Calderón-Castro, A. and Zazueta-Morales, J.J. (2024). Effect of the extrusion process on phytochemical, antioxidant, and cooking properties of gluten-free pasta made from broken rice and nopal. *Revista Mexicana de Ingeniería Química* 23(1), 1-15. https://doi.org/10.24275/rmiq/Alim24149

Crosbie, G.B. and Ross, A.S. (2007). *The RVA Handbook*. Ed. AACC International, USA.

da Silva, E.M.M., Ramírez Ascheri, J.L., Piler de Carvalho, C.W., Takeiti, C.Y. and Berrios, J.D.J. (2014). Physical characteristics of extrudates from corn flour and dehulled carioca bean flour blend. *LWT - Food Science and Technology* 58(2), 620–626. https://doi.org/10.1016/j.lwt.2014.03.031

Dhull, S.B., Uebersax, M.A., Kinabo, J. and Siddiq, M. (2023). Nutritional profile, bioactive compounds, and health benefits of lentils. In: *Lentils: Production, processing technologies, products, and nutritional profile*, (Ahmed, J., Siddiq, M., Uebersax, M.A., eds.), Pp. 311-336. John Wiley & Sons Ltd. Published, New York.

Fellows, P. (2000). *Food processing technology. Principles and practice*, Ed. CRC Press LLC, Boca Raton, FL.

Flores-Silva, R.C., Martínez-Yañez, M.E., Rodriguez-Huezo. A. and Alvarez-Ramirez, J. (2021). Nutritional protein quality and digestibility changes during food processing. *Revista Mexicana de Ingeniería Química* 21(1). https://doi.org/10.24275/rmiq/Alim2748

Frame, N.D. (1994). *The technology of extrusion cooking*, Ed. Springer US, New York, NY.

García-Cordero, A.L., Jiménez-Alvarado, R., Bautista, M., Díaz-Sánchez, F., Ibarra, I.S., Sánchez-Ortega, I. and Santos, E.M. (2024). Improvement of corn extruded snacks properties by incorporation of pulses. *Revista Mexicana de Ingeniería Química* 23(3). https://doi.org/10.24275/rmiq/Alim24279

Gutiérrez, H. and de la Vara, R. (2012). Optimización simultánea de varias respuestas. Diseño de experimentos con mezclas. In: *Análisis y diseño de experimentos*, (Toledo, M.A., Roig, P.E., Rocha, M.I., Delgado, A.L., García, Z., eds.), Pp. 385-396, 439-455. McGraw Hill, México.

Guy, R., Riaz, M.N., Mottaz, J., Sellahewa, J., Camire, M.E., Bouvier, J.M. and Kazemzadeh, M. (2001). *Extrusion cooking. Technologies and applications*, Ed. CRC Press, Boca Raton, FL.

Hsu, H. and Vavak, D. (1977). A multienzyme technique for estimating protein digestibility. *Journal of Food Science* 45, 1269-1273.

Hu, Q.P. and Xu, J.G. (2011). Profiles of carotenoids, anthocyanins, phenolics, and antioxidant activity of selected color waxy corn grains during maturation. *Journal of Agricultural and Food Chemistry* 59, 2026-2033.

Hwang M.P. and Yakawa, K.-I.H.A. (1980). Bulk densities of cookies undergoing commercial baking processes. *Journal of Food Science* 45(5), 1400–1402. https://doi.org/10.1111/j.1365-2621.1980.tb06563.x

Korkerd, S., Wanlapa, S., Puttanlek, C., Uttapap, D. and Rungsardthong, V. (2016). Expansion and functional properties of extruded snacks enriched with nutrition sources from food processing by-products. *Journal of Food Science and Technology* 53(1), 561–570. https://doi.org/10.1007/s13197-015-2039-1

López-Fernández, M., Méndez-Montealvo, G., Velazquez, G., Perales-Torres, A., Santiago-Adame, R. and Castillo-Ruíz, O. (2021). Effect of adding pineapple (Ananas comosus) flour on the sensory and textural properties of wheat flour (Triticum aestivum) cookies. *Revista Mexicana de Ingeniería Química* 20(3). https://doi.org/10.24275/rmiq/Alim2406

Madar, Z. and Stark, A. H. (2002). New legume sources as therapeutic agents. *British Journal of Nutrition*, 88(S3), 287. https://doi.org/10.1079/bjn2002719

Manrique-Quevedo, N., González-Soto, R.A., Othman-Abu-Hardan, M., García-Suarez, F.J. and Bello-Pérez, L.A. (2007). Caracterización de mezclas de almidones de mango y plátano pregelatinizados mediante diferentes condiciones de extrusión. *Agrociencia* 41, 637-645.

Masatcioglu, T.M., Sumer, Z. and Koksel, H. (2017). An innovative approach for significantly increasing enzyme resistant starch type 3 content in high amylose starches by using extrusion cooking. *Journal of Cereal Science*

74, 95–102. https://doi.org/10.1016/j.jcs.2017.01.015

Maskan, M. and Altan, A. (2012). *Advances in food extrusion technology*. Ed. CRC Press, Boca Raton, FL.

Medina-Rendon, E.A., Guatemala-Morales, G.M., Padilla-Camberos, E., Corona-González, R.I., Arriola-Guevara, E. and García-Fajardo, J.A. (2021). Production of extrudate food with mango by-products (Mangifera indica): Analysis of physical, chemical, and sensorial properties. *Processes* 9, 1660. https://doi.org/10.3390/pr9091660

Meilgaard, M., Civille, G.V. and Carr, T. (1999). *Sensory evaluation techniques*. Ed. CRC Press, USA.

Meng, X., Threinen, D., Hansen, M. and Driedger, D. (2010). Effects of extrusion conditions on system parameters and physical properties of a chickpea flour-based snack. *Food Research International* 43(2), 650–658. https://doi.org/10.1016/j.foodres.2009.07.016

Mora-Rochin, S., Gutiérrez-Uribe, J.A., Serna-Saldivar, S.O., Sánchez-Peña, P., Reyes-Moreno, C. and Milán-Carrillo, J. (2010). Phenolic content and antioxidant activity of tortillas produced from pigmented maize processed by conventional nixtamalization or extrusion cooking. *Journal of Cereal Science* 52, 502-508.

Morales, P., Berrios, J.J., Varela, A., Burbano, C., Cuadrado, C., Muzquiz, M. and Pedrosa, M.M. (2015). Novel fiber-rich lentil flours as snack-type functional foods: an extrusion cooking effect on bioactive compounds. *Food & Function* 6, 3135. https://doi.org/10.1039/c5fo00729a

Moscicki, L. (2011). *Extrusion-cooking techniques: Applications, theory and sustainability*. Ed. Wiley-VCH, Germany.

Mustafa, A.M., Abouelenein, D., Acquaticci, L., Alessandroni, L., Angeloni, S., Borsetta, G., Caprioli, G., Nzekoue, F.K., Sagratini, G. and Vittori, S. (2022). Polyphenols, saponins and phytosterols in lentils and their health benefits: An overview. *Pharmaceuticals* 15, 1225. https://doi.org/10.3390/ph15101225

Nayak, B., Berrios, J.D.J., Powers, J.R. and Tang, J. (2011). Effect of extrusion on the antioxidant capacity and color attributes of expanded extrudates prepared from purple potato and yellow pea flour mixes. *Journal of Food Science* 76(6), C874–C883. https://doi.org/10.1111/j.1750-3841.2011.02279.x

Patil, R.T., Berrios, J.D.J., Tang, J. and Swanson, B.G. (2007). Evaluation of methods for expansion properties of legume extrudates. *Applied Engineering in Agriculture* 23(6), 777–783. https://doi.org/10.13031/2013.24044

Rathod, R.P. and Annapure, U.S. (2016). Effect of extrusion process on antinutritional factors and protein and starch digestibility of lentil splits. *LWT-Food Science and Technology* 66, 114-123.

Rodriguez-Miranda, J., Delgado-Licon, E., Hernandez-Santos, B., Reyes-Jaquez, D., Aguilar-Palazuelos, E., Medrano-Roldan, H., Navarro-Cortez, R.O., Castro-Rosas, J. and Gomez-Aldapa, C.A. (2012). The effect of pregelatinized potato starch on the functional properties of an extruded aquafeed. *Journal of Animal Production Advances* 2, 335-344.

Saha, D. and Bhattacharya, S. (2010). Hydrocolloids as thickening and gelling agents in food: A critical review. *Journal of Food Science and Technology* 47, 587-597.

Sánchez-Nuño, Y.A., Zermeño-Ruiz, M., Vázquez-Paulino, O.D., Nuño, K. and Villarruel-López, A. (2024). Bioactive compounds from pigmented corn (Zea mays L.) and their effect on health. *Biomolecules* 14, 338. https://doi.org/10.3390/biom14030338

Sarawong, C., Schoenlechner, R., Sekiguchi, K., Berghofer, E. and Ng, P.K.W. (2014). Effect of extrusion cooking on the physicochemical properties, resistant starch, phenolic content and antioxidant capacities of green banana flour. *Food Chemistry* 143, 33-39.

Stauffer, J.E. (2004). Challenges in food formulation. *Cereal Foods World* 49(6), 380-381.

Stojceska, V., Ainsworth, P., Plunkett, A. and Ibanoğlu, Ş. (2009). The effect of extrusion cooking using different water feed rates on the quality of ready-to-eat snacks made from food by-products. *Food Chemistry* 114, 226-232.

Swain, T. and Hillis, W.E. (1959). The phenolic constituents of Prunus domestica. The quantitative analysis of phenolic constituents. *Journal of the Science of Food and Agriculture* 10, 63-68.

Vanier, N.L., Vamadevan, V., Bruni, G.P., Ferreira, C.D., Pinto, V.Z., Seetharaman, K., Zavareze, E.D., Elias, M.C. and Berrios, J.J. (2016).

Extrusion of rice, bean and corn starches: Extrudate structure and molecular changes in amylose and amylopectin. *Journal of Food Science* 81(12), E2932–E2938. https://doi.org/10.1111/1750-3841.13545

Wang, K., Li, S., Rao, Y., Wu, Y., Peng, Y., Yao, S., Zhang, H. and Ahzi, S. (2019). Flexure behaviors of ABS-based composites containing carbon and kevlar fibers by material extrusion 3D printing. *Polymers* 11, 1878. https://doi.org/10.3390/polym11111878

Wang, N., Warkentin, T.D., Vanderberg, B. and Bing, D.J. (2014). Physicochemical properties of starches from various pea and lentil varieties, and characteristics of their noodles prepared by high temperature extrusion. *Food Research International* 55, 119-127.

Wani, S.A. and Kumar, P. (2016). Development and parameter optimization of health promising extrudate based on fenugreek oat and pea. *Food Bioscience* 14, 34-40.

Yağci, S. and Göğüş, F. (2008). Response surface methodology for evaluation of physical and functional properties of extruded snack foods developed from food-by-products. *Journal of Food Engineering* 86, 122–132. https://doi.org/10.1016/j.jfoodeng.2007.09.018

Ye, Z., Arumugam, V., Haugabrooks, E., Williamson, P. and Hendrich, S. (2015). Soluble dietary fiber (Fibersol-2) decreased hunger and increased satiety hormones in humans when ingested with a meal. *Nutrition Research* 35(5), 393–400. https://doi.org/10.1016/j.nutres.2015.03.004

Yu, L., Ramaswamy, H.S. and Boye, J. (2012). Twin-screw extrusion of corn flour and soy protein isolate (SPI) blends: A response surface analysis. *Food and Bioprocess Technology* 5(2), 485–497. https://doi.org/10.1007/s11947-009-0294-8

Vol. 24, No. 2(2025) Alim25498
Revista Mexicana de Ingeniería Química

Evaluation of a chitosan and sodium benzoate-based coating to preserve the postharvest quality of jackfruit (*Artocarpus heterophyllus* L.)

Evaluación de un recubrimiento a base de quitosano y benzoato de sodio para conservar la calidad postcosecha del fruto de yaca (*Artocarpus heterophyllus* L.)

L.D. Coronado-Partida[1,2*], M. O. Estrada-Virgen[1], O. J. Cambero-Campos[1]
[1] *Unidad Académica de Agricultura, Universidad Autónoma de Nayarit. Carretera Tepic-Compostela Km. 9. Xalisco, Nayarit, México.*
[2] *Estancias Posdoctorales- Secretaría de Ciencia, Humanidades, Tecnología e Innovación, Coordinación de Apoyos a Becarios e Investigadores. Dirección de Posgrado, Ciudad de México.*
Received: January 9, 2025; Accepted: May 13, 2025

Abstract
The conservation of jackfruit (*Artocarpus heterophyllus* L.) is essential for its successful commercialization due to its high perishability and susceptibility to postharvest diseases, particularly those caused by *Rhizopus stolonifer*. This study evaluated the effectiveness of a chitosan and sodium benzoate-based coating, classified as Generally Recognized as Safe (GRAS), in extending the fruit's shelf life. A two-stage storage regime (10 °C for 5 days, followed by 25 °C) was implemented, and physicochemical parameters, respiration rate (CO_2 production), and ethylene emission were monitored. The results demonstrated that the coating inhibited *R. stolonifer* development, maintained fruit firmness, and extended shelf life to 17 days. Additionally, the treatment enhanced peroxidase (POD) activity, a key enzyme in the fruit's defense mechanism. These findings highlight the coating's potential as a sustainable postharvest conservation strategy for jackfruit.
Keywords: Climacteric fruit, Defense mechanisms, GRAS substances, Peroxidase activity, Refrigeration.

Resumen
La conservación de la yaca (*Artocarpus heterophyllus* L.) es esencial para su comercialización exitosa debido a su alta perecibilidad y susceptibilidad a enfermedades postcosecha, particularmente aquellas causadas por *Rhizopus stolonifer*. Este estudio evaluó la efectividad de un recubrimiento a base de quitosano y benzoato de sodio, clasificado como Generalmente Reconocido como Seguro (GRAS, por sus siglas en inglés), para extender la vida útil de la fruta. Se implementó un régimen de almacenamiento de dos etapas (10 °C durante 5 días, seguido de 25 °C), y se monitorearon los parámetros fisicoquímicos, la tasa de respiración (producción de CO_2) y la emisión de etileno. Los resultados demostraron que el recubrimiento inhibió el desarrollo de *R. stolonifer*, mantuvo la firmeza de la fruta y extendió la vida útil a 17 días. Además, el tratamiento mejoró la actividad de la peroxidasa (POD), enzima clave en el mecanismo de defensa de la fruta. Estos hallazgos resaltan el potencial del recubrimiento como una estrategia de conservación postcosecha sustentable para la yaca.
Palabras clave: Fruto climatérico, Mecanismos de defensa, Sustancias GRAS, Actividad de la peroxidasa, Refrigeración.

* *Corresponding author. E-mail*: leonardo.coronado@uan.edu.mx ;
https://doi.org/10.24275/rmiq/Alim25498
ISSN:1665-2738, *issn-e*: 2395-8472

1 Introduction

Jackfruit (*Artocarpus heterophyllus* L.) is a climacteric tropical fruit with high postharvest perishability, primarily due to ethylene-induced ripening and susceptibility to fungal infections such as those caused by *Rhizopus stolonifer* (Coronado-Partida *et al*., 2021). In Mexico, Nayarit is the leading producer, with an annual output of approximately 29,375 tons, of which 80% is exported to the United States (SIAP, 2023). Given the fruit's economic importance, technologies that enhance its shelf life and preserve quality are critical for minimizing losses. Conventional postharvest treatments, such as hot water immersion and chemical fungicides, have shown limited success, with the latter raising regulatory and consumer concerns due to potential residues (FDA, 2022). Consequently, bioactive compounds such as chitosan and sodium benzoate have emerged as promising alternatives for postharvest preservation. These compounds combine antimicrobial activity with the ability to form semipermeable coatings that modulate gas exchange, thereby decelerating ripening processes. Chitosan (a cationic biopolymer derived from chitin) exhibits broad-spectrum antimicrobial properties and forms cohesive, semipermeable films that act as physical barriers. When applied as an edible coating, chitosan creates a modified microenvironment around the fruit surface, attenuating respiratory activity by restricting O_2 influx and CO_2 efflux. Given the oxygen-dependent nature of ethylene biosynthesis, this localized hypoxia downregulates ethylene production, effectively extending postharvest shelf life (Gutiérrez-Martínez *et al*., 2018; Martínez-Batista *et al*., 2024). This mechanism is particularly relevant for climacteric fruits like jackfruit, which exhibit a pronounced surge in ethylene and CO_2 production during the climacteric phase. This metabolic shift triggers coordinated physiological changes, including cell wall degradation (mediated by polygalacturonase and pectin methylesterase activity), tissue softening, and biosynthesis of volatile aromatic compounds and pigments (Singh *et al*., 2018). Unmitigated, these processes (driven by elevated respiration rates) accelerate quality deterioration through enzymatic and oxidative spoilage pathways.

Technologies like controlled atmospheres and edible coatings have proven useful for regulating these gases, thereby extending the fruit's shelf life (Jha *et al*., 2012). Sodium benzoate, classified as GRAS by the FDA, has emerged as a viable alternative to conventional fungicides. This compound offers advantages such as high solubility, low cost, and ease of application in packaging facilities (Palou *et al*., 2018). Furthermore, it has been shown to be effective in combination with chitosan for controlling *R. stolonifer*, inhibiting mycelial growth and reducing spore production (Coronado-Partida *et al*., 2023). Its use as an edible coating helps maintain firmness, color, and the fruit's nutritional properties during storage (Mahmood *et al*., 2022).

Refrigeration is one of the most effective strategies for postharvest fruit preservation (Inestroza-Lizardo *et al*., 2016). By lowering the temperature, metabolic processes such as respiration and ethylene production slow down, delaying ripening and deterioration. However, it must be tailored to the specific characteristics of each fruit to avoid chilling injuries, such as cuticle blemishes or firmness loss (Wang *et al*., 2013). Combining refrigeration with edible coatings and controlled atmospheres can enhance the benefits of these techniques (Mahajan and Goswami, 2004). This study evaluated the effect of a chitosan and sodium benzoate-based coating on the preservation of jackfruit stored at temperatures of 10 °C and 25 °C. Physicochemical properties, physiological activity, and peroxidase (POD) enzyme activity associated with plant defense were characterized. This approach aims to contribute to the development of more sustainable and effective strategies for the postharvest conservation of jackfruit.

2 Materials and methods

2.1 Plant material

Jackfruit (*Artocarpus heterophyllus* L.) at physiological maturity, free from mechanical damage and with uniform appearance, were obtained from the municipality of San Blas, Nayarit, Mexico. The fruits were transported to the Agricultural Parasitology Laboratory at the Universidad Autónoma de Nayarit.

2.2 Treatment

A low molecular weight chitosan (Chi) solution (Sigma-Aldrich, MO, USA) at a concentration of 3% (w/v) was prepared in 2% (v/v) acetic acid (EMSURE-USA). The solutions were stirred for 24 hours, and the pH was adjusted to 5.6 using 1N NaOH. Subsequently, 0.1 mL of Tween 80 (Sigma-Aldrich, MO, USA) was added as a surfactant. A sodium benzoate (SB) solution (Deiman, Mexico) at a concentration of 2.5% (w/v) in sterile distilled water was also prepared (Coronado-Partida *et al*., 2023).

The treatments were divided into eight groups: Treatment I: Fruits kept at standard room temperature (25 ±2 °C) without inoculation or additional treatments. Treatment II: Fruits maintained at 25 ±2 °C after inoculation. Treatment III: Fruits initially stored at low temperature (10 ±2 °C) for 5 days and

then transferred to 25 ±2 °C. Treatment IV: Inoculated fruits stored at 10 ± 2 °C for 5 days and then transferred to 25 ±2 °C. Treatment V: Fruits treated with Chi-BS and stored at 25 ±2 °C. Treatment VI: Fruits treated with Chi-BS, initially stored at 10 ±2 °C for 5 days, and then maintained at 25 ±2 °C. Treatment VII: Inoculated fruits treated with Chi-BS and stored at 25 ±2 °C. Treatment VIII: Inoculated fruits treated with Chi-BS, stored at 10 ±2 °C for 5 days, and then transferred to 25 ±2 °C.

2.2.1 *Artificial inoculation*

The fruits designated for inoculation were first washed with a 2% (v/v) sodium hypochlorite solution for two minutes to disinfect the surface. They were then rinsed with potable water and left to air dry at room temperature. After disinfection, five wounds were carefully made on the fruit surface using a sterile needle. Each wound was inoculated with 20 μL of a *R. stolonifer* spore suspension (previously isolated and identified) at a concentration of 10^6 conidia mL^{-1}.

2.3 *Physicochemical parameters*

2.3.1 *Physiological weight loss*

Weight loss was determined as a percentage using the equation [(A-B) / A] x 100 (Northover and Zhou, 2002), where A represents the initial weight of the jackfruit before treatment, and B represents the weight of the fruit every 24 hours.

2.3.2 *Firmness*

Firmness was measured using a penetrometer (Shimpo, FGE-100X) equipped with a 10 mm diameter probe. Penetration tests were conducted at five points along the fruit (ends and middle) with the peel intact. The resistance force to penetration was recorded and expressed in Newtons (N).

2.3.3 *Total soluble solids (TSS)*

The jackfruit pulp was homogenized and filtered through a Whatman No. 1 filter paper. Soluble solids were determined using a digital refractometer (Abbé HI 96801), and the results were reported in °Brix (AOAC, 2005).

2.3.4 *Titratable acidity*

A 5 g fruit sample was titrated with 0.1 M NaOH, using 0.1% phenolphthalein as an indicator. Results were calculated and expressed as the percentage of malic acid per 100 g of fresh weight (Ali *et al*., 2011).

2.4 *Physiological parameters*

Respiration rate: Respiration rate was measured daily until the fruit reached senescence using a portable ethylene and CO_2 analyzer (F-900, CID Bio Science, Inc.). Ethylene production was expressed in μL kg^{-1} h^{-1}, and CO_2 production was expressed in mL CO_2 kg^{-1} h^{-1}.

2.5 *Enzymatic activity*

Enzymatic activity was evaluated every 24 hours after applying the Chi-SB treatment to the jackfruit. The enzyme extract was obtained from the fruit's cuticle using the methodology described by Chen *et al*., (2000). POD activity: The expression of peroxidase (POD) activity was assessed using the method proposed by Chance and Maehly (1955) with minor modifications. Briefly, 0.5 mL of crude extract (supernatant) was mixed with 2 mL of guaiacol buffer solution and incubated for 5 minutes at 30 ±2 ºC. Then, 1 mL of H_2O_2 was added, and absorbance was measured at 460 nm every 5 seconds for 90 seconds using a UV/visible spectrophotometer (VE-6000T-VELAB). Enzyme activity was expressed as U mg^{-1} of protein. Protein content was determined using the Bradford method (1976).

2.6 *Statistical analysis*

A multifactorial design with completely randomized blocks was used. One factor was the coating treatment, another was the storage temperature, and the blocks were the storage days. Data were analyzed using analysis of variance (ANOVA), and mean comparisons were performed with Tukey's test ($p \leq 0.05$) using IBM SPSS Statistics software.

3 Results and discussion

3.1 *Physicochemical parameters*

Table 1 shows that fruits treated solely with the coating achieved a shelf life of 14 days, compared to the control group, which lasted only 7 days. Fruits in the control group exhibited lower firmness, reduced titratable acidity, and a more advanced ripening stage, making them more susceptible to *R. stolonifer* infection. In this group, fruits inoculated, on the fifth day displayed pathogen growth. In contrast, fruits that were inoculated and treated with the coating achieved a shelf life of up to 9 days, demonstrating the antifungal efficacy of the treatment.

Table 1. Evaluation of TSS, titratable acidity and firmness during storage of jackfruit treated with Chi-SB with and without *R. stolonifer* inoculation stored at 25 ±2 °C.

Treatment	Days	TSS (°Brix)	Titratable acidity (%)	Firmness (N)
Control	0	5.12 ± 0.22 a	0.95 ± 0.10 a	330 ± 1.24 a
	7	38.95± 0.98 b	0.56 ± 0.08 b	179 ± 1.33 b
Control (inoculated)	0	7.65± 0.54 a	1.06 ± 0.06 a	308 ± 3.11 a
	5	37.7± 0.58 b	0.74 ± 0.11 b	12 ± 2.58 b
Chi-SB	0	5.55± 0.55 a	1.14 ± 0.09 a	287 ± 1.91 a
	14	25.7± 1.05 b	0.68 ± 0.01 b	244 ± 1.96 b
Chi-BS (inoculated)	0	4.99± 0.46 a	1.01 ± 0.05 a	320 ± 1.84 a
	9	24.55± 0.56 b	0.54 ± 0.02 b	220 ± 1.28 b

The values are the means of three replicates. Different letters within a column indicate significant differences between treatments ($p \leq 0.05$).

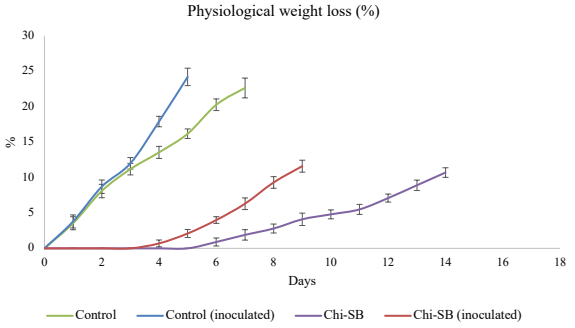

Figure 1. Physiological weight loss of jackfruit stored at 25 ±2 °C.

Figure 1 presents data on the physiological weight loss (PWL) of the analyzed fruits. Control fruits, both inoculated and non-inoculated, exhibited significant weight loss, with reductions of 24% and 22%, respectively, in less than five days. In contrast, fruits treated with the coating maintained their weight over a longer period, recording only a 10% loss by day 14. PWL is directly associated with metabolic processes such as cellular respiration, which induce physiological and structural changes in fruit tissues. According to Vieira *et al*. (2016), coatings made with chitosan and essential oils have proven effective in mitigating weight loss in fruits. For the treated jackfruit, the reduced PWL is attributed to the properties of chitosan, whose hydrophobic structure and polymeric matrix strengthen the cell wall, increase mechanical resistance, and form a barrier that limits water loss (Tokatli and Demirdöven, 2020). Furthermore, sodium benzoate, a widely used antimicrobial compound in the food industry, plays a critical role in preserving fruit quality. This compound inhibits the growth of microorganisms responsible for the degradation of plant tissue, helping maintain cell integrity and reducing transpiration and weight loss during storage. Previous studies have demonstrated the efficacy of sodium benzoate in reducing microbial activity and preserving physical properties such as firmness and weight in food matrices (Montesinos-Herrero *et al*., 2016). Therefore, the inclusion of sodium benzoate in postharvest treatments is proposed as an effective strategy to optimize the conservation of fresh fruits, minimizing losses associated with handling and prolonged storage.

In fruits refrigerated for 5 days at 10 °C, a deceleration in the ripening process was observed, highlighting the positive impact of low temperatures on fruit preservation. Control fruits, both inoculated and non-inoculated, exhibited faster ripening indices compared to treated fruits. This difference was reflected in the total soluble solids (TSS) values, where treated fruits had up to 50% less TSS compared to the control group on the fifth day of storage (Table 2). Firmness values also confirmed these differences, demonstrating better preservation in the treated fruits. Subsequently, after 5 days of storage at 10 °C, the fruits were transferred to 25 °C. Fruits treated with the Chi-SB coating achieved a shelf life of 17 days, while those treated and inoculated with *R. stolonifer* maintained a shelf life of 12 days. These results demonstrate that combining an initial storage period at 10 °C with postharvest treatment, followed by storage at 25 °C, is an effective strategy for preserving jackfruit. Similarly, Ramos-Bell *et al*., (2024) reported that the application of chitosan and salicylic acid in blueberries preserved quality during postharvest storage. At 4 °C, treated fruits exhibited less firmness degradation compared to the control group, while at room temperature (25 °C), the combined treatment significantly reduced weight loss, achieving 11% in treated fruits versus 22% in the control. During refrigeration, weight loss ranged from 5.25% to 6.45%, with no significant differences between treated and control groups. Furthermore, the treatment decreased the rate of changes in soluble solids, pH, and titratable acidity, contributing to maintaining an optimal balance in the sensory quality of the fruit.

Table 2. Evaluation of TSS, titratable acidity and firmness during storage of jackfruit treated with Chi-SB with and without inoculation stored at 10 °C for 5 days and subsequently at 25 ±2 °C with *R. stolonifer*.

Treatment	Days	TSS (°Brix)	Titratable acidity (%)	Firmness (N)
Control	0	6.2 ± 1.08 a	1.01 ± 0.07 a	317 ± 2.54 a
	5	18.05 ± 0.64 b	0.89 ± 0.02 b	280 ± 1.11 b
	10	31.3 ± 0.85 c	0.68 ± 0.06 c	209 ± 1.58 c
Control (inoculated)	0	7.45 ± 0.72 a	0.953 ± 0.06 a	280 ± 1.24 a
	5	25.88 ± 0.89 b	0.78 ± 0.01 b	241 ± 1.26 b
	9	35.44 ± 0.58 c	0.56± 0.02 c	9 ± 0.96 c
Chi-SB	0	5.75 ± 0.63 a	1.02± 0.07 a	325 ± 0.82 a
	5	10.3 ± 0.83 b	0.89 ± 0.01 b	290 ± 1.31 b
	17	26.2 ± 0.78 c	0.68 ± 0.06 c	254 ± 0.73 c
Chi-SB (inoculated)	0	4.9 ± 0.61 a	0.95 ± 0.07 a	309 ± 0.97 a
	5	10.45 ± 0.43 b	0.78 ± 0.03 b	270 ± 1.11 b
	12	28 ± 0.47 c	0.56 ± 0.01 c	235 ± 1.22 c

The values are the means of three replicates. Different letters within a column indicate significant differences between treatments ($p \leq 0.05$).

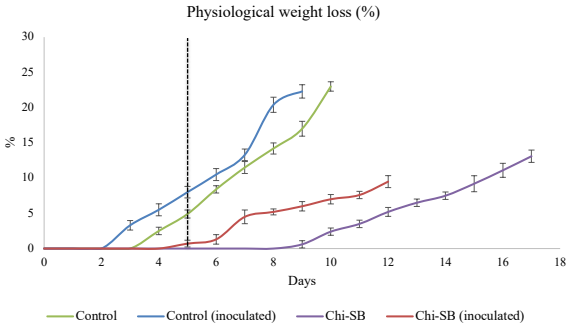

Figure 2. Physiological weight loss of jackfruit stored at 10 °C for 5 days and then stored at 25 °C.

Fruits stored at 10 °C for 5 days and treated with the coating did not show significant weight loss until they were transferred to storage at 25 °C, where the ripening process began. These results, shown in Figure 2, indicate that the treatment extended the fruit's shelf life up to 17 days. In contrast, control fruits stored at 10 °C experienced weight loss even during refrigeration, and after being transferred to 25 °C, they exhibited a 23% weight loss by day 9. Herrera-González *et al*., (2022) demonstrated that a 1.5% chitosan coating significantly reduced physiological weight loss ($p \leq 0.05$) in 'Hass' avocados compared to untreated fruit. This effect was linked to chitosan's formation of a semipermeable film, which mitigates the water potential gradient between the fruit and its environment, thereby suppressing transpiration and evaporative water loss. Similarly, Costantini *et al*., (2018) observed that chitosan nanoparticles reduced weight loss and improved firmness retention in strawberries stored both at 5 °C and room temperature, relative to controls. Both studies attribute these outcomes to chitosan's barrier properties, which restrict gas exchange and transpiration, thus slowing postharvest metabolic activity.

3.2 *Physiological parameters*

The respiration rate of jackfruit treated with the Chi-SB formulation was evaluated. Control fruits artificially inoculated with *R. stolonifer* and stored at 25 °C exhibited a climacteric peak on day 3, followed by a decrease in respiration rate accompanied by signs of soft rot. In contrast, uninoculated control fruits reached their climacteric peak on day 5, with a maximum value of 149.6 mL CO_2 kg^{-1} h^{-1}, after which a progressive decline associated with fruit senescence was observed. Mata-Montes de Oca *et al*., (2007) reported similar behavior in jackfruit stored at 20 °C, with the climacteric peak occurring on day 7 and a maximum CO_2 production of 98.7 mL CO_2 $kg^{-1}h^{-1}$. Fruits treated with Chi-SB and inoculated with the pathogen reached their maximum CO_2 production on day 6, with values of 110 mL CO_2 $kg^{-1}h^{-1}$. In fruits treated solely with the formulation, the climacteric peak occurred on day 8, with a maximum production of 155.8 mL CO_2 $kg^{-1}h^{-1}$ (Fig. 3). These results indicate that the Chi-SB treatment alters the respiratory dynamics of the fruits by delaying the climacteric peak, contributing to an extended shelf life, particularly in the absence of pathogen infection. In previous studies, Nolasco-González *et al*., (2021) evaluated the effect of commercial coatings on jackfruit, observing a significant reduction in ethylene production and respiration rate (CO_2). This effect was attributed to the barrier properties of the coating, which limit gas exchange and modify the fruit's internal atmosphere, slowing metabolism and the ripening process. Additionally, it was highlighted that refrigeration at 8 °C has a considerable impact on reducing respiration and ethylene production, reinforcing the effectiveness of postharvest treatments in preserving fruit quality.

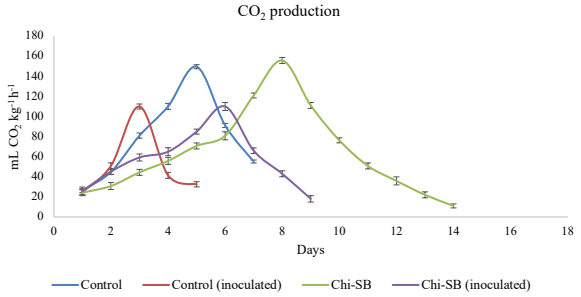

Figure 3. CO_2 production rate in control and Chi-SB-treated jackfruit with and without *R. stolonifer* inoculation stored at 25 ±2 °C.

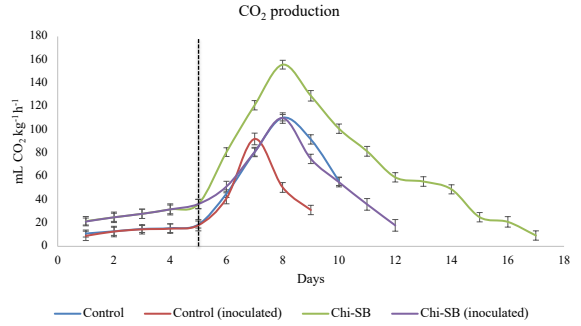

Figure 4. CO_2 production rate in control and Chi-SB-treated jackfruit with and without *R. stolonifer* inoculation stored at 10 °C for 5 days and then stored at 25 ±2 °C.

In fruits stored at 10 °C for the first five days (Fig. 4), the rate of CO_2 production remained controlled, demonstrating that refrigeration regulates this physiological process. Upon transferring the fruits to storage conditions at 25 °C, control fruits inoculated with the pathogen reached a climacteric peak on day 4, with a CO_2 production of 44.2 mL CO_2 $kg^{-1}h^{-1}$. Uninoculated control fruits exhibited their peak on day 5, with a production of 45 mL CO_2 $kg^{-1}h^{-1}$.

In contrast, fruits treated solely with the coating showed controlled CO_2 production, reaching their climacteric peak on day 8 with a maximum value of 155.8 mL CO_2 $kg^{-1}h^{-1}$, followed by a progressive decline to 9.3 mL CO_2 $kg^{-1}h^{-1}$ on day 17. Similarly, fruits treated with the coating and inoculated with the pathogen exhibited a climacteric peak on day 8 (three days after being stored at 25 °C), with CO_2 production of 110 mL CO_2 $kg^{-1}h^{-1}$, followed by a rapid decline in CO_2 production. These results indicate that artificial inoculation with the fungus affects the ripening process, accelerating respiration and associated metabolism. The action of the Chi-SB formulation on the respiratory rate can be explained by its influence on the ethylene biosynthetic pathway. The formulation creates a modified atmosphere that suppresses ethylene production by inhibiting the expression of the enzymes 1-aminocyclopropane-1-carboxylate synthase (ACC synthase) and 1-aminocyclopropane-1-carboxylate oxidase (ACC oxidase). The latter is oxygen-dependent, limiting ethylene synthesis and thus reducing both O_2 consumption and CO_2 production (do Nascimento Sousa *et al*., 2020).

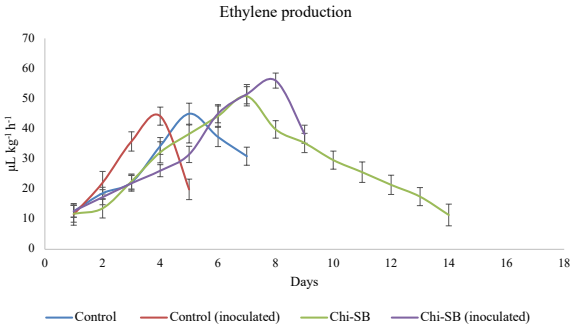

Figure 5. Ethylene production rate in control and Chi-SB-treated jackfruit with and without *R. stolonifer* inoculation stored at 25 ±2 °C.

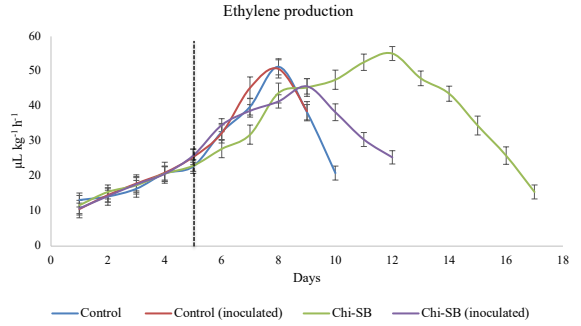

Figure 6. Ethylene production rate in control and Chi-SB-treated jackfruit with and without *R. stolonifer* inoculation stored at 10 °C for 5 days and then stored at 25 ±2 °C.

The production of ethylene in fruits under different treatment and storage conditions was evaluated (Figs. 5 and 6). In control fruits artificially inoculated with *R. stolonifer*, the highest ethylene production was recorded on day 4, reaching 19.9 μL kg^{-1} h^{-1}. In contrast, uninoculated control fruits exhibited peak ethylene production on day 6, with a value of 45 μL kg^{-1} h^{-1}. Mata-Montes de Oca *et al*., (2007) reported that jackfruit stored at 20 °C reached 63.7 μL kg^{-1} h^{-1} on day 4. Fruits treated with Chi-SB and inoculated with the pathogen exhibited a climacteric ethylene production peak on day 8, reaching 56 μL kg^{-1} h^{-1}. Meanwhile, fruits treated solely with the formulation achieved maximum ethylene production on day 7, recording 51.5 μL kg^{-1} h^{-1} before entering senescence and becoming susceptible to fungal invasion. Ramos-Guerrero *et al*., (2019) reported that the application of edible coatings composed of chitosan controlled the respiration rate in soursop fruits by forming a physical barrier, which regulated this process and reduced ethylene production. In fruits stored at 10 °C, the ethylene production rate remained steady during refrigeration. However, after transferring to 25 °C, fruits treated solely with Chi-SB reached

maximum ethylene production on day 12 (55.1 μL kg^{-1} h^{-1}), followed by a decline. Similarly, coated fruits inoculated with *R. stolonifer* exhibited a production peak of 45.7 μL kg^{-1} h^{-1} on day 9, which was followed by a decrease and the appearance of infection signs.

These metabolic changes are associated with the presence of compounds such as chitosan and sodium benzoate on the fruit surface, which modify the internal atmosphere, alter ethylene production, and prolong the fruit's shelf life. Chitosan-based coatings have proven to be an effective strategy for controlling ethylene in postharvest fruits, contributing to extended shelf life and quality preservation. Chitosan, a natural polysaccharide with antimicrobial and antioxidant properties, acts as a physical barrier that limits the diffusion of gases like ethylene, slowing the ripening and senescence processes. Additionally, chitosan has been reported to interact with reactive oxygen species (ROS) and ethylene metabolism, promoting antioxidant enzyme activity and reducing endogenous ethylene production (Hernández-Muñoz *et al*., 2008; Xing *et al*., 2020). This is particularly beneficial for climacteric fruits, where ethylene plays a central role in regulating ripening. Recent studies highlight that chitosan coatings applied to fruits such as bananas and tomatoes can significantly delay their decomposition, maintaining firmness, color, and nutritional value during storage (Ali *et al*., 2021). Jackfruit, being a climacteric fruit, is characterized by a high ethylene production rate, making it highly perishable and susceptible to pathogen invasion during storage.

3.3 Enzymatic activity

Figure 7 illustrates the effect of the Chi-BS treatment on peroxidase (POD) activity. Fruits treated and inoculated with *R. stolonifer* exhibited significantly higher POD activity compared to controls ($p \leq 0.05$). An increase in enzymatic activity was observed in fruits treated solely with Chi-BS on day 4, while fruits treated and artificially inoculated with the pathogen reached maximum POD activity on day 8. In contrast, the control group showed an increase in enzymatic activity up to day 6, followed by a decline associated with the onset of senescence, indicating a lower concentration of POD. Plant peroxidases, also referred to as Class III peroxidases, are monomeric enzymes essential to various physiological processes. Their functions include lignification, auxin metabolism, and protein assembly in the cell wall. Furthermore, these enzymes play a critical role in the plant antioxidant system, contributing to recognition and defense against abiotic stressors such as drought and tolerance to high salt concentrations (Shah *et al*., 2021).

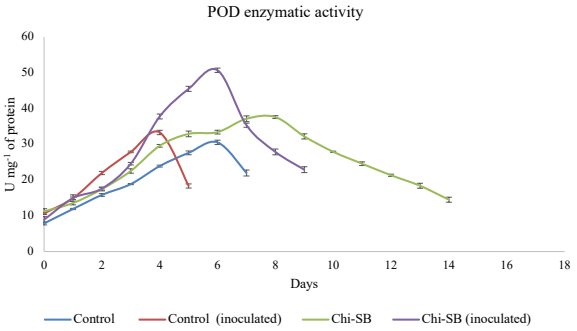

Figure 7. Effect of Chi-SB treatment on POD activity in *R. stolonifer*-inoculated and non-inoculated jackfruit stored at 25 ±2 °C.

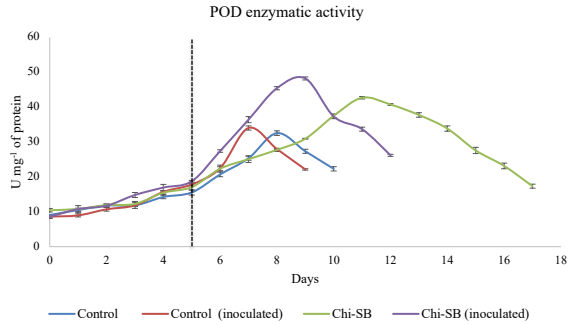

Figure 8. Effect of Chi-SB treatment on POD activity in jackfruit inoculated and non-inoculated with *R. stolonifer* stored at 10 °C for 5 days and then stored at 25 ±2 °C.

Figure 8 shows POD enzyme activity in fruits stored at 10 °C for the first five days, during which no significant differences in activity were observed. However, after transferring the fruits to storage conditions at 25 °C, a progressive increase in POD activity was noted in coated fruits, reaching its peak on day 9 for treated and inoculated fruits and on day 11 for fruits treated only with the coating. In contrast, control fruits exhibited their highest enzymatic activity on day 7 for inoculated fruits and day 8 for uninoculated fruits. These results suggest that the applied treatment, combined with changes in storage conditions, facilitated an adaptive response in treated fruits, prolonging POD activity compared to the control fruits. The increase in POD activity in fruits exposed to biotic stress suggests a response induced by pathogen invasion. This stress activates the synthesis of reactive oxygen species (ROS), such as superoxide radicals (O_2^-) and hydrogen peroxide (H_2O_2). According to Lo'ay *et al*., (2019), fungal infection stimulates POD activity, promoting H_2O_2 production. This compound catalyzes the polymerization of phenolic compounds to form lignin and suberin in the cell wall, creating a structural barrier that restricts pathogen spread in the fruit tissues. Ackah *et al*., (2022) reported that POD activity in wounded fruit treated with chitosan increased by 99% compared to the wounded control fruit on

day 3, concluding that chitosan effectively regulates the formation and elimination of ROS, preventing oxidative stress while maintaining fruit quality under wound-induced stress. H_2O_2 generated by POD can serve as a substrate for other peroxidases, act as an antimicrobial agent, or trigger hypersensitivity reactions that activate defense mechanisms in the fruit (Nie *et al*., 2020). Additionally, H_2O_2 can diffuse intracellularly and activate defense-related genes, leading to programmed cell death (Davison *et al*., 2002).

Conclusions

This study demonstrates that the combined use of a chitosan-sodium benzoate coating and a two-stage storage regime effectively extends the postharvest shelf life of jackfruit. The treatment not only inhibited the development of *Rhizopus stolonifer* but also preserved critical quality parameters such as firmness and weight. Additionally, the coating enhanced peroxidase activity, highlighting its role in the fruit's defense mechanisms. These findings present a sustainable and practical solution for reducing postharvest losses, thereby improving the marketability and economic value of jackfruit.

Acknowledgements

Acknowledgment to the Secretaría de Ciencia, Humanidades, Tecnología e Innovación (SECIHTI) for the postdoctoral fellowship awarded to the corresponding author, and to the Universidad Autónoma de Nayarit (UAN) for the support provided to carry out this study.

References

Ackah, S., Bi, Y., Xue, S., Yakubu, S., Han, Y., Zong, Y., Atuna, R. A. and Prusky, D. (2022). Post-harvest chitosan treatment suppresses oxidative stress by regulating reactive oxygen species metabolism in wounded apples. *Frontiers in Plant Science, 13,* 959762. https://doi.org/10.3389/fpls.2022.959762

Ali, A., Maqbool, M., Ramachandran, S. and Alderson, P. G. (2021). Postharvest chitosan treatment of papaya: Effect on shelf life, fruit quality, and gas exchange. *Journal of Food Science and Technology, 58(3),* 1234–1241.

Ali, A., Muhammad, M. T. M., Sijam, K. and Siddiqui, Y. (2011). Effect of chitosan coatings on the physicochemical characteristics of Eksotika II papaya (*Carica papaya* L.) fruit during cold storage. *Food Chemistry, 124(2),* 620–626.

AOAC (2005) Official method of Analysis. 18th Edition, Association of Officiating Analytical Chemists, Washington, D. C.

Bradford, M. M. (1976). A rapid and sensitive method for the quantitation of microgram quantities of protein utilizing the principle of protein-dye binding. *Analytical Biochemistry, 72,* 248–254.

Chance, B. and Maehly, A. C. (1955). Assay of catalase and peroxidase. *Methods in Enzymology, 2,* 764–775. https://doi.org/10.1016/S0076-6879(55)02300-8

Chen, C., Belanger, R. R., Benhamou, N. and Paulitz, T. C. (2000). Defense enzymes induced in cucumber roots by treatment with plant growth-promoting rhizobacteria (PGPR) and *Pythium aphanidermatum*. *Physiological and Molecular Plant Pathology, 56(1),* 13–23.

Coronado-Partida, L. D., Serrano, M., Romanazzi, G., González-Estrada, R. R., & Gutiérrez-Martínez, P. (2021). Aplicación de compuestos GRAS para el control de la pudrición blanda en frutos de jaca (*Artocarpus heterophyllus* L.) causado por *Rhizopus stolonifer*. *TIP Revista Especializada en Ciencias Químico-Biológicas, 24,* e327.

Coronado-Partida, L., Patrón-Soberano, A., Rodríguez-González, V. and Gutiérrez-Martínez, P. (2023). Antifungal potential of eco-friendly chitosan-sodium benzoate to inhibit the development of *Rhizopus stolonifer* isolated from jackfruit. *Journal of Plant Diseases and Protection, 130,* 905–913. https://doi.org/10.1007/s41348-023-00746-4

Costantini, R., Ventura-Aguilar, R. I., Hernández-López, M., Bautista-Baños, S. and Barrera-Necha, L. L. (2018). Potencial antifúngico de nanopartículas de quitosano y extracto de arándano sobre *Colletotrichum fragariae* en fresa. *Revista Iberoamericana de Tecnología Postcosecha, 19(1).*

Davison, P. A., Hunter, C. N. and Horton, P. (2002). Overexpression of β-carotene hydroxylase enhances stress tolerance in *Arabidopsis*. *Nature, 418(6894),* 203–206. https://doi.org/10.1038/nature00861

do Nascimento Sousa, S. D., Santiago, R. G., Soares Maia, D. A., de Oliveira Silva, E., Vieira, R. S. and Bastos-Neto, M. (2020). Ethylene adsorption on chitosan/zeolite composite films for packaging applications. *Food Packaging and Shelf Life, 26,* 100584. https://doi.org/10.1016/j.fpsl.2020.100584

FDA-Food and Drug Administration. (2022). Import alert 258. https://www.accessdata.fda.gov/cms_ia/importalert_258.html Accessed: December 10, 2024.

Gutiérrez-Martínez, P., Ledezma-Morales, A., Romero-Islas, L. d. L., Ramos-Guerrero, A., Romero-Islas, J., Rodríguez-Pereida, C., Casas-Junco, P., Coronado-Partida, L. and González-Estrada, R. (2018). Antifungal activity of chitosan against postharvest fungi of tropical and subtropical fruits. In R. S. Dongre (Ed.), Chitin-Chitosan: Myriad Functionalities in Science and Technology. IntechOpen. https://doi.org/10.5772/intechopen.76095

Hernández-Muñoz, P., Almenar, E., Del Valle, V., Velez, D. and Gavara, R. (2008). Effect of chitosan coating combined with postharvest calcium treatment on strawberry (Fragaria xananassa) quality during refrigerated storage. *Food Chemistry, 110(2),* 428–435.

Herrera-González, J., Hernández-Sánchez, D., Bueno-Rojas, D., Ramos-Bell, S., Velázquez-Estrada, R., Bautista-Rosales, P. and Gutiérrez-Martínez, P. (2022). Effect of commercial chitosan on in vitro inhibition of *Colletotrichum siamense*, fruit quality and elicitor effect on postharvest avocado fruit. *Revista Mexicana de Ingeniería Química, 21,* Bio2706. https://doi.org/10.24275/rmiq/Bio2706

Inestroza-Lizardo, C., Voigt, V., Muniz, A. C. and Gomez-Gomez, H. (2016). Métodos de enfriamiento aplicables a frutas y hortalizas enteras y mínimamente procesadas. *Revista Iberoamericana de Tecnología Postcosecha, 17(2),* 149–161.

Jha, S. N., Kingsly, A. R. P. and Chopra, S. (2012). Physical and mechanical properties of jackfruit fruit, seed, and spongy tissue. *Journal of Food Engineering, 82(4),* 437–444.

Lo'ay, A. A., Taha, N. A. and El-Khateeb, Y. A. (2019). Storability of 'Thompson Seedless' grapes: Using biopolymer coating chitosan and polyvinyl alcohol blending with salicylic acid and antioxidant enzymes activities during cold storage. *Scientia Horticulturae, 249,* 314–321.

Mahajan, P. V. and Goswami, T. K. (2004). Shelf-life extension of fresh fruits and vegetables by modified atmosphere packaging: A review. *Journal of Food Science and Technology, 41(3),* 1–9.

Mahmood, T., Anwar, F. and Abbas, M. (2022). Sodium benzoate as an effective postharvest treatment to enhance shelf-life and maintain quality attributes of perishable fruits. *Journal of Food Preservation, 46(5),* e15678.

Martínez-Batista, E., González-Arias, C. A., Velázquez-Estrada, R. M., Herrera-González, J. A. and Gutiérrez-Martínez, P. (2024). *In vitro* and *in vivo* antifungal activity of chitosan and identification of potentially toxigenic fungi in stored maize of Nayarit, Mexico. *Revista Mexicana de Ingeniería Química, 23(2) Bio24223*. https://doi.org/10.24275/rmiq/Bio24223

Mata-Montes, M., de Oca, L., Osuna-García, J., Hernández-Estrada, A., Ochoa-Villarreal, M. and Tovar-Gómez, B. (2007). Efecto del 1-metilciclopropeno (1-MCP) sobre la fisiología y calidad de frutos de jaca (*Artocarpus heterophyllus* Lam.). *Revista Chapingo Serie Horticultura, 13*. https://doi.org/10.5154/r.rchsh.2007.02.012

Montesinos-Herrero, C., Moscoso-Ramírez, P. A. and Palou, L. (2016). Evaluation of sodium benzoate and other food additives for the control of citrus postharvest green and blue molds. *Postharvest Biology and Technology, 115,* 72–80.

Nie, Z., Huang, Q., Chen, C., Wan, C. and Chen, J. (2020). Chitosan coating alleviates postharvest juice sac granulation by mitigating ROS accumulation in harvested pummelo (*Citrus grandis* L. Osbeck) during room temperature storage. *Postharvest Biology and Technology, 169,* 111309.

Nolasco-González, Y., Montalvo-González, E., García-Magaña, M. de L., Medellín-Bautista, C. M., Hernández-Fuentes, L. M. and González Hernández, H. (2021). Efecto de recubrimientos en la maduración de yaca almacenada en condición simulada de mercadeo. *Revista Mexicana De Ciencias Agrícolas, 12(2)*, 219–234. https://doi.org/10.29312/remexca.v12i2.2319

Northover, J. and Zhou, T. (2002). Control of *Rhizopus* rot of peaches with postharvest treatments of tebuconazole, fludioxonil, and *Pseudomonas syringae*. *Canadian*

Journal of Plant Pathology, 24(2), 144–153. https://doi.org/10.1080/07060660309506989

Palou, L., Moscoso-Ramírez, P. A. and Montesinos-Herrero, C. (2018). Assessment of optimal postharvest treatment conditions to control green mold of oranges with sodium benzoate. *Acta Horticulturae, 1194,* 221–226.

Ramos-Bell, S., Diaz-Cayetano, G., Hernández-Montiel, L. G., Velázquez-Estrada, R. M., Montalvo-González, E. and Gutiérrez-Martínez, P. (2024). Conservación fisicoquímica de arándanos tratados con quitosano y ácido salicílico en poscosecha. *Revista Mexicana de Ciencias Agrícolas, 15(5),* e3391. https://doi.org/10.29312/remexca.v15i5.3391

Ramos-Guerrero, A., González-Estrada, R., Montalvo-González, E., Miranda-Castro, P. and Gutiérrez-Martínez, P. (2019). Effect of the application of inducers on soursop fruit (*Annona muricata* L.): Postharvest disease control, physiological behaviour and activation of defense systems. *Emirates Journal of Food and Agriculture, 30(12),* 1019–1025. https://doi.org/10.9755/ejfa.2018.v30.i12.1883

Shah, S., Hashmi, M. S., Qazi, I. M., Durrani, Y., Sarkhosh, A., Hussain, I. and Brecht, J. K. (2021). Pre-storage chitosan-thyme oil coating control anthracnose in mango fruit. *Scientia Horticulturae, 284*, 110139.

SIAP. (2023). Anuario Estadístico de la Producción Agrícola. Servicio de Información Agroalimentaria y Pesquera. https://nube.siap.gob.mx/cierreagricola/ Accessed: January 8, 2025.

Singh, S., Gupta, R. and Kumar, A. (2018). Postharvest physiology and quality management of jackfruit (*Artocarpus heterophyllus* Lam.): A review. *Journal of Food Science and Technology, 55(7),* 2547–2558.

Tokatli, K. and Demirdöven, A. (2020). Effects of chitosan edible film coatings on the physicochemical and microbiological qualities of sweet cherry (*Prunus avium* L.). *Scientia Horticulturae, 259*. https://doi.org/10.1016/j.scienta.2019.108656

Vieira, J. M., Flores-López, M. L., de Rodríguez, D. J., Sousa, M. C., Vicente, A. A. and Martins, J. T. (2016). Effect of chitosan-Aloe vera coating on postharvest quality of blueberry (*Vaccinium corymbosum*) fruit. *Postharvest Biology and Technology, 116,* 88–97.

Wang, C. Y. and Buta, J. G. (2013). Maintaining postharvest quality of tropical and subtropical fruits. *Acta Horticulturae, 694,* 73-77.

Xing, Y., He, X., Cao, D., Liu, Q. and Li, X. (2020). Effect of chitosan coating enriched with cinnamon essential oil on postharvest quality of mango fruit. *Food Chemistry, 128(4),* 1056–1062.

Vol. 24, No. 2(2025) Alim25547
Revista Mexicana de Ingeniería Química

Obtention of amaranth resistant starch through succinylation and phosphorylation reaction

Obtención de almidón resistente de amaranto mediante reacción de succinatación y fosforilación

M.A. Robles-Arias[1], H.B. Escalona-Buendía[2], M.A.G. Ramírez-Romero[2], A.E. Cruz-Guerrero[2*]
[1] CONAHCYT-Universidad Autónoma Metropolitana-Iztapalapa, Av. San Rafael Atlixco 186, Col. Vicentina, Ciudad de México, 09340, México.
[2] Departamento de Biotecnología, Universidad Autónoma Metropolitana-Iztapalapa, Av. San Rafael Atlixco 186, Col. Vicentina, Ciudad de México, 09340, México
Received: March 8, 2025; Accepted: May 23, 2025

Abstract
Starch is the human diet's primary energy source and is naturally found as a polysaccharide in grains. Starches from familiar sources such as corn, potato, and rice have been widely studied. However, starch extraction from pseudocereals such as the amaranth seed has also been studied due to their functional characteristics.

Starch is the principal component of the amaranth raw seed (50%-60%), and 0.5% of it corresponds to resistant starch (RS). RS is a fraction of starch not hydrolyzed in the small intestine within 120 min of consumption but can be fermented in the colon. This work studied the use of amaranth starch as a byproduct of protein and lipid extraction to produce RS. The starch was subjected to acid hydrolysis with HCl and modified with octenyl succinic anhydride (OSA) and sodium tripolyphosphate (STPP), obtaining a resistant starch yield of 47% and 56.7%, respectively. Nevertheless, the amaranth starch granules extract could be damaged either during their obtention or in the acid hydrolysis reaction, since water's low absorption and solubilization capacity was recorded. However, amaranth RS could display a low glycemic index and modulate metabolism, acting as dietary fiber.
Keywords: Amaranthus hypochondriacus, starch, resistant starch, succinylation and phosphorylation reaction.

Resumen
El almidón es la principal fuente de energía de la dieta humana y se encuentra de forma natural como polisacárido en los cereales. Los almidones de fuentes comunes como el maíz, la patata y el arroz han sido ampliamente estudiados. Sin embargo, la extracción de almidón de pseudocereales como la semilla de amaranto también se ha estudiado debido a sus características funcionales.

El almidón es el componente principal de la semilla cruda de amaranto (50%-60%), y un 0,5% corresponde a almidón resistente (AR). El AR es una fracción del almidón que no se hidroliza en el intestino delgado en los 120 minutos posteriores al consumo, pero que puede fermentar en el colon. Este trabajo estudió el uso del almidón de amaranto como subproducto de la extracción de proteínas y lípidos para producir AR. El almidón se sometió a hidrólisis ácida con HCl y se modificó con anhídrido octenil succínico (OSA) y tripolifosfato de sodio (STPP), obteniendo un rendimiento de almidón resistente del 47% y el 56,7%, respectivamente. Sin embargo, el extracto de gránulos de almidón de amaranto podría dañarse durante su obtención o en la reacción de hidrólisis ácida, debido a la baja capacidad de absorción y solubilización del agua. No obstante, el AR de amaranto podría presentar un bajo índice glucémico y modular el metabolismo, actuando como fibra dietética.
Palabras clave: *Amaranthus hypochondriacus*, almidón, almidón resistente, reacción de fosfatación, reacción de succinatación.

* *Corresponding author. E-mail*: aec@xanum.uam.mx ;
https://doi.org/10.24275/rmiq/Alim25547
ISSN:1665-2738, *issn-e*: 2395-8472

1 Introduction

Amaranth belongs to the *Amaranthaceae* family and is widely spread in North America, Central America, and South America (Singh & Punia, 2020). Nevertheless, amaranth crops have been introduced to Africa, Asia, and Australia due to the ability to grow in extreme conditions (Assad *et al*., 2017). There is no stipulated number of *Amaranthus* genus; however, it is estimated to be between 60 and 75 (Ward *et al*., 2013). Being *A. hypochondriacus*, *A. cruentus,* and *A. caudatus*, those with the most significant food potential (Sarangi *et al*., 2021).

Amaranth seed contains a higher concentration of protein (13-19%) and is a good source of fat (5-13%). Nevertheless, the principal component of amaranth seed is the starch (50-60%) stored inside the perisperm (Montoya-Rodríguez *et al*., 2015). Amaranth starch granule diameter ranges from 0.8-2.5 μm, which are very small compared to other granules such as rice (3-8 μm) or potato starch (10-15 μm). Additionally, it is low in amylose concentration (1%), conferring low viscosity, high solubility, and low temperature gelatinization compared to other starch sources such as corn starch (Capriles *et al*., 2008; Arendt & Zannini, 2013). Recent studies report the use of amaranth starch as a thickener replacer, which can be used in the production of low-calorie food (Kierulf *et al*., 2024).

A fraction of starch is not hydrolyzed by amylases in the small intestine and passes to the colon, where the microbiota ferments it. This fraction is called resistant starch (RS; Birt *et al*., 2013). Amaranth has only 0.5% resistant starch in raw seed and increases to 1.36% when it is subjected to expansion with hot air (Gamel *et al*., 2005). RS has important advantages over conventional starches such as: improved solubility and adhesion, less tendency to retrogradation and stability at high temperatures (Bhosale & Singhal, 2006; Guerra-DellaValle *et al*., 2008) also compared to traditional fibers, RS has the advantage of not negatively affecting the acceptability of the product, in addition to providing improvements in appearance, texture and mouthfeel compared to fiber (Fuentes-Zaragoza *et al*., 2010).

RS's are divided into 4 categories depending on their nature: physically inaccessible such as some grains and seeds (RS1), resistant granules (RS2), retrograded starches (RS3) and chemically modified starches (RS4) such as starch esters, starch ethers and cross-linked starches (Gutierrez & Tovar, 2021).

Phosphorylated starch consists of introducing phosphate groups into the starch chains, which creates a repulsion between the phosphate groups on adjacent chains. Different reagents such as STMP (sodium trimetaphosphate), STPP (sodium tripolyphosphate), or a mixture of STMP-STTPP have been used to obtain phosphorylated starch, which has been classified as an RS4 (Malik *et al*., 2023). This chemical modification increases hydration and changes the physicochemical properties of the starch, such as gelling agent, thickener, colloidal stabilizer and water retention agent. Therefore, it has been used in the food industry such as additives in yogurt to decrease the syneresis, in bakery to increase the extensibility and viscoelasticity of the dough; stabilizer in frozen food; foam retention in foaming systems and improve roasting properties (Liu *et al*., 2022; Ramadan & Sitohy., 2020).

Chemically modified starches with octenyl succinic anhydride (OSA) are one of the chemically modified starches obtained by substitution modification by chemical groups (Bai *et al*., 2014). The Food and Drug Administration (FDA) restricts food grade succinate starches to a maximum incorporation of 3% OSA based on the weight of starch (Bhosale & Singhal, 2007). Succinate starches, unlike typical surfactants, form strong films at the oil-water interface, resulting in emulsions that are resistant to re-agglomeration, so they can be used to stabilize the flavor of emulsified beverages, oils in salad dressings, and to encapsulate flavors and fragrances (Altuna *et al*., 2018; Bhosale & Singhal, 2006). OSA starches display hydrophilic and hydrophobic character. Therefore, it has been used in the production of sauces, puddings, and baby foods (Bajaj *et al*., 2019). Nevertheless, OSA starches are used mostly in bakery, as they increase water absorption and resistance to deformation, enhancing the bread volume and texture (Korus *et al*., 2021).

This work aimed to obtain succinate and phosphate amaranth starch with a high resistant starch content and evaluate its physicochemical characteristics.

2 Materials and methods

2.1 Material

Acetic acid, boric acid, bromocresol green, chlorohydric acid, copper sulfate pentahydrate, hexanol, methyl red, phenol, potassium sulfate, selenium dioxide, sodium acetate anhydrous, sodium hydroxide, and sulfuric acid were purchased from J. T. Baker (Mexico State, Mexico).

2-Octen-1, succinyl anhydride (mixture of cis and trans 97%), sodium triphosphate pentabasic (purity ≥98%), Tris-hydroxymethyl aminomethane), were all purchased from Sigma Aldrich (St. Lois MO, USA)

Protease from *Bacillus licheninforomis,* (E.C. 3.4.21.62) at ≥2.4 U/g solid, α-amylase thermostable from *Bacillus licheninformis* (E.C. 3.2.1.1) at 1 U/mL, amyloglucosidase from *Aspergillus niger* (E.C. 3.2.1.3) at 30-60 U/mg of protein, pepsin from porcine gastric mucosa (E.C. 3.4.23.1) at ≥250 U/mg solid and

porcine pancreatic amylase type VI-B (E.C. 3.2.1.) at ≥ 10 U/mg were purchased from Sigma Aldrich (St. Lois MO, USA).

Glucose-SL (glucose-oxidase-peroxidase) was purchased from Sekisui Diagnostics (Burlington, Massachusetts, USA).

2.2 Physicochemical characterization of the amaranth starch

Bromatological analysis of the amaranth flour and amaranth starch was performed according to the Official Methods of Analysis (AOAC), which include lipids (920.30), proteins (920.10), crude fiber (978.10), soluble fiber (991.43) and starch concentration by the determination of total carbohydrates, which were quantified by the Dubois *et al*. (1956) technique.

2.3 Starch obtention

Amaranth popped seed flour (*A. hypochondriacus*) was obtained from a local producer of Santiago Tulyehualco (Mexico). An Amaranth:Water suspension (1:4) was made. To deactivate native enzymes in amaranth flour, the suspension was boiled for 10 min and then cooled to 50 °C. Later, 0.036 U/g of *Bacillus licheninformis* protease was added (E.C. 3.4.21.62. ≥2.4 U/g, Sigma Aldrich), and it was incubated in a thermoregulated bath at 50 °C with horizontal stirring at 100 rpm for 4 h (LabTech LSB-015S, Beijing, China). The suspension was brought to 90 °C for 10 min to deactivate the protease and centrifuged at 6000 rpm for 40 min (Avanti J-E, Beckman Coulter, Indianapolis, Indiana, USA). The supernatant containing lipids and proteins was separated, and the pellet consisting of a mix of starch-fiber was dried in a convection oven for 24 h at 45 °C (Felisa FE-291AD, Jalisco, México). Then it was milled and sieved, passed through a 250 μm mesh.

2.4 Starch quantification

Starch content was quantified as described by Soto-Azurduy (2010). This method allows the determination of the total starch content in a sample, ensuring complete availability of the starch for enzymatic degradation. In this procedure, the gelatinization and liquefaction steps were performed simultaneously.

A total of 100 mg of the sample was mixed with 6 mL of distilled water and 0.05 U of α-amylase. The suspension was incubated in a 97 °C water bath for 15 minutes, with gentle shaking every 5 minutes. After incubation, the tube was allowed to cool to room temperature while shaking was continued. Once cooled, the mixture was transferred to a 25 mL volumetric flask and diluted to volume with distilled water.

Next, 1 mL of this solution was transferred to a centrifuge tube, followed by the addition of 2 mL of sodium acetate buffer (0.1 M, pH 4.75). Then, 2.25 U of *Aspergillus niger* amyloglucosidase was added, and the sample was incubated at 60 °C for 30 min (Combi-SV12 FINE PCR), with gentle mixing every 5 minutes.

After incubation, the sample was centrifuged at 6000 rpm using an Eppendorf 5804R centrifuge. The supernatant was transferred to a 100 mL volumetric flask, the tube was rinsed with distilled water, and the rinsate was added to the flask, which was then filled to the mark with distilled water.

For glucose quantification, 20 μL of the resulting solution was mixed with 20 μL of distilled water and 2 mL of glucose quantifier reactive (Glucose-SL, Sekisui Diagnostics) in a centrifuge tube. Absorbance was measured at 500 nm using a spectrophotometer (Shimadzu UV-160A, Japan), interpolating the absorbance in a glucose anhydride calibration curve. Total starch quantification was performed according to *Equation 1*:

$$Total\ starch\ (\%) = \frac{Glucose\ (mg) x25 x100 x0.9}{Sample\ (mg)} x100(\%) \quad (1)$$

2.5 Modified starch obtention

2.5.1 Hydrolyzed starch

Starch suspension at 40% solids was prepared in a hydrochloric acid solution at 3.4% (concerning starch solids). Hydrolysis was performed at 50 °C in a thermoregulated bath with horizontal stirring at 100 rpm for 4 h. The suspension was centrifuged at 6000 rpm for 10 min. The supernatant was discarded, and the pellet was washed twice with distilled water. The sediment was dried at 45 °C for 24 h, ground, and sieved through a 250 μm mesh. The degree of hydrolysis (%) was calculated as the percentage ratio of the hydrolyzed starch solids based on the starch sample's previous hydrolysis, expressed as *Equation 2:*

$$Hydrolysis\ (\%) = \frac{Hydolyzed\ starch\ solids}{Initial\ starch\ solids} \quad (2)$$

2.5.2 Succinate starch

Succinate starch was prepared according to Bhosale & Singhal (2006) with slight modifications to optimize the reaction. A suspension of hydrolyzed starch: water (1:3.8) was prepared. An aliquot of 10 mL was taken and 3 mL of OSA was added and kept at 30 °C for 2 h under constant horizontal stirring at 100 rpm. Different reaction times (3, 4, 5, 6, and 7 h) and pH's

(6, 6.5, 7.5, and 8) were tested by adjusting the pH with NaOH (3%). At the end of the reaction, the pH was adjusted to 6.5 and centrifuged at 6000 rpm for 10 min. The sediment was washed twice with distilled water to remove reagent residues. The succinate starch was dried at 40 °C for 24 h, ground and sieved through a 250 μm mesh.

2.5.3 *Phosphate starch*

The phosphorylation of amaranth starch was performed according to Paschall (1964) with slight modifications. The hydrolyzed starch was dissolved in a 4% sodium tripolyphosphate solution (pent basic sodium triphosphate ≥98%; Sigma Aldrich) in a 1:5 ratio, and the pH was adjusted to 6 with 10% NaOH. Different temperatures (30, 40, 50, and 60 °C) and reaction times (1, 2, 3, 4, and 5 h) were tested. The suspension was heated at 25 °C in a thermoregulated bath with horizontal stirring at 100 rpm. At the end of the reaction, the suspension was centrifuged at 5000 rpm for 5 min. The supernatant was discarded, and the residue was washed with distilled water and centrifuged at 5,000 rpm for 5 minutes, repeating the procedure twice. The residue was dried at 40 °C for 48 h, ground, sieved through a 250 μm mesh, stored in cellophane bags, and subjected to dialysis in water at 4 °C for 4 days, changing the water daily. The phosphate starch was dried at 30 °C for 12 h.

2.6 *Degree of substitution quantification*

The degree of substitution (DS) of the OSA and phosphate modified starch were determined by a titration method. In brief, 1 g (dry basis) of the starch sample was combined with 10 mL of distilled water containing two drops of 1% (w/w) phenolphthalein in a flask. The suspension was then treated with 0.1 N NaOH until a pink coloration appeared. Subsequently, 25 mL of 0.5 N NaOH was added, and the mixture was stirred at 27 ± 2 °C for 40 minutes. The solution was then titrated with 0.5 N HCl to pH 7, indicated by the disappearance of the phenolphthalein color. A blank titration was performed using native starch for comparison.

The DS value of the succinylated starch was calculated according to *Equations 3* and *4*:

$$OSA\ sustitution\ (\%) = \frac{\left(V_{blank} - V_{sample}\right) x 0.1 N x 100\%}{Sample\ (g)} \tag{3}$$

$$DS = \frac{162\ x\ OSA\ sustituion\ (\%)}{21{,}000 - (209(OSA\ sustitution\ (\%))} \tag{4}$$

Where V is the volume of HCl used either in blank or sample titration.

The DS value of the phosphate starch was calculated according to *Equations 5* and 6.

$$A\ (\%) = \frac{\left(V_{blank} - V_{sample}\right) x 0.5 N x 158 x 100\%}{Sample\ (g)} \tag{5}$$

$$DS = \frac{162A}{15800 - 156A} \tag{6}$$

Where A is the content of esterified carboxyl groups (%), V is the volume of HCl used either in blank or sample titration.

2.7 *Resistant starch quantification*

Conversion degree from amaranth native starch to resistant starch by succinate or phosphate was calculated according to Goñi *et al*. (1996). 100 mg of the sample was dissolved in 10 mL of KCl-HCl buffer (pH 1.5) and homogenized. Later, 60 UE of pepsin from porcine gastric mucosa (345 UE/mg solid) was added and incubated at 40 °C for 60 min with orbital agitation at 100 rpm (Combi-SV12, FinePCR, Gyeonggi-do, Korea) and allowed to cool at room temperature. Then, 9 mL of Tris-maleate buffer (0.1 M, pH 6.9) was added to the previous solution, mixed with 200 UE of α-amylase (10 UE/mg), and incubated at 37 °C for 16 h with orbital agitation. The samples were centrifuged for 15 min at 7000 rpm. Supernatants were discarded, and the pellet was resuspended in 3 mL of distilled water and 4 mL of KOH (4 M) and agitated for 30 min at room temperature. Then, 5.5 mL of HCl (2M) and 3 mL of acetate buffer (0.4 M, pH 4.75) were added to the previous solution to reach a pH of 6.9. Later 8 UE of amyloglucosidase from *Aspergillus niger* was added. The samples were centrifuged at 6,000 rpm for 15 min. Supernatants were collected. The pellets were washed with 10 mL of distilled water and centrifuged under the same conditions. The supernatants were mixed, and distilled water was added to reach a final volume of 25 mL. The glucose released was quantified using the glucose oxidase-peroxidase method. Briefly, 20 μL of the last sample was added to 2 mL of the glucose quantifier reactive (Glucose-SL, Sekisui Diagnostics), vortexed and incubated at 37 °C for 30 min. Glucose was spectrophotometrically quantified at a wavelength of 340 nm (Shimadzu UV 160-A, Japan), interpolating the absorbance in a glucose anhydride calibration curve. The resistant starch of the test sample was calculated according to *Equation 7*:

$$RS\ (\%) = \frac{Glucose\ concentration\ (mg)\ x\ 0.9}{Sample\ (mg)} x 100 \tag{7}$$

2.8 *Water absorption index (WAI) and water solubility index (WSI)*

Both indexes were calculated according to Anderson (1969). Briefly, 0.25 mg of the starch samples were resuspended in 3 mL of distilled water. The samples were incubated at 30 °C with orbital agitation at 200 rpm for 30 min and then centrifuged at 6,000 rpm for 10 min. The supernatant was dried until constant weight at 80 °C, and then, both the weight of the evaporated sample and the sedimented dried gel (pellet of the fermentation) were registered. WAI were calculated as indicated in *Equation 8* and WSI according to *Equation 9*:

$$WAI = \frac{Sedimented\ gel\ (g)}{Dry\ weigh\ of\ the\ sample\ (g) - Weight\ of\ the\ evaporated\ sample\ (g)} \tag{8}$$

$$WSI = \frac{Weigh\ of\ the\ evaporated\ sample\ (g)}{Dry\ weigh\ of\ the\ sample\ (g)} \tag{9}$$

2.9 *Scanning electron microscope (SEM)*

The starch samples were visualized in a scanning electron microscope and secondary emission with control of variable vacuum ranges of variable pressure (JEOL JSM-5900 LV), with a coupled EDS spectrometer (Oxford). The samples were mounted on aluminum SEM stubs with carbon adhesive tape and coated with gold (Dentum Vaccum Desk III). The conditions were: gold deposition for 60 seconds until 4 minutes of deposition were completed under vacuum conditions of 50 mTorr. The samples were kept in a sealed Petri dish and dried for 24 h. The samples were visualized under vacuum conditions using an acceleration voltage of 10 kV.

2.10 *Statistical analysis*

All experiments were performed in triplicate, and the results are reported as the mean value ± standard deviation. The statistical analysis was carried out with the IBM SPSS Statistic version 25.0 for Windows (IBM, New York, USA) software. A one-way analysis of variance (ANOVA) was performed to compare all pairs of groups, followed by Tukey's test. A p-value of 0.05 was considered statistically significant.

3 Results and discussion

3.1 *Physicochemical analysis*

Amaranth flour had 54±1.8% of starch, 15.41±1.6% of protein and 9.6±1% of lipids. Khan & Duta (2018) analyzed the popped amaranth flour from *A. hybridus*. The authors reported a carbohydrate concentration of 60.57%±0.06, protein of 11.59%±0.18, and lipids of 7.97±0.15, which differ from the concentrations in this work. Calva-Cruz *et al.* (2023) reported a proximal composition of popped amaranth (*A. hypochondriacus*) of protein: 15.8%±0.6, lipids: 6.7%±1.4 and carbohydrates: 63.4%±3.9. This can be attributed to the difference in the amaranth variety and the cultivation conditions (Venskutonis & Kraujalis, 2013; Shevkani *et al*., 2014).

The RS concentration was determined at 6.9±0.7% which is higher than the data reported by Capriles *et al*. (2008). Authors stated a concentration of RS of 0.50±0.02% for pooped amaranth seed (*A. caudatus*), differences can be related to the amaranth variety.

The method proposed in this work allows obtaining a starch extraction yield of 63.3% with high purity (95%±3.4), with a low protein (5%±0.4) and without lipids. Additionally, the fraction of soluble dietary fiber in the starch extract is 40%±0.4 and 3.0%±0.03 of crude fiber.

These results are similar to those reported by Resio *et al*. (2009), who obtained 67.7% by wet milling using sulfite solutions. Additionally, compared to Villarreal *et al*. (2013), they obtained a yield of 46.18% by wet grinding with prior protease and alkaline hydrolysis. The resistant starch content in amaranth seed (6.9%) was lower than in the starch extract (18%). Shoenlechner *et al*. (2008) reported a soluble dietary fiber in amaranth starch of 33.1 to 49.3 % for *A. hypochondriacus, whereas the crude fiber is reported in the range from 3-8%, depending on the extraction method and amaranth species* (Písaříková *et al*., 2009).

During the process of starch obtention, the high temperature and the prolonged reaction times could cause the gelatinization of the starch, resulting in the formation of RS3. This agrees with Hung *et al*. (2016), who reported an increase in slowly digestible starch and RS after subjecting rice starch to heat-humidity treatments.

3.2 *Acid hydrolysis*

Acid hydrolysis (also known as lintnerization) is one of the most used chemical methods to change the starch structure into a crystalline structure, which is resistant to enzymatic hydrolysis (Aparicio-Saguilán *et al*., 2014). The starch extract obtained was subjected to acid treatment, presenting a hydrolysis yield of 39.27%±1.35, which is lower than the data reported

by García *et al*. (2016). The authors stated a yield of 57.12% hydrolysis for gelatinized corn starch using 100 mL of HCl (1M) per gram of starch and a reaction condition of 50 °C for 2 h. The previous gelatinization of starch could influence the higher hydrolysis yield. Additionally, the small granule size of the amaranth starch contributes to a faster acid hydrolysis compared to bigger starch size granules (such as taro), as well as their amylose content, which is related to the hydrolysis rate; at a higher concentration of amylose, a lower rate of hydrolysis is registered. Furthermore, hydrolysis occurs faster in starch, with few amorphous zones (like amaranth starch). Nevertheless, crystalline regions are also hydrolyzed, indicating an alteration in all the zones of the starch granules. These zones are removed during acid hydrolysis (Bertoft, 2004; Chen *et al*., 2024).

3.3 Resistant starch and DS quantification by succinylation reaction

During succinylation, the hydroxyl groups of the starch molecules are substituted with carbonyl groups of the octenyl succinic anhydride (OSA). When modified OSA, naturally hydrophilic starch acquires hydrophobic properties due to the incorporation of octenyl groups. This modification results in amphiphilic starch molecules, which exhibit both hydrophilic and hydrophobic characteristics (Sweedman *et al*., 21013).

Fig. 1a shows an increment in the RS along with pH in the range 6-7.5, reaching the highest concentration at pH 7.5 (47.92 %) and the highest DS (0.02±0) in 6 h reaction time. Nevertheless, at higher pHs, the concentration decreased. Therefore, a pH of 7.5 was selected for further studies. Additionally, no change was detected in the RS content in the amaranth starch subjected to the same pH conditions but without the OSA reactive. The concentration of RS (47.92%) obtained in this work is higher than that reported by Bai *et al*. (2014) at a pH of 7.5. They recorded a yield of RS of 26.7% in waxy corn starch by using 3% of OSA and a reaction time of 30 min. Under slightly basic conditions, the reduction of hydrogen bonding between starch chains is promoted through the formation of alkoxide groups from starch hydroxyl (–OH) groups, while at pH higher than 8, the hydroxyl groups of starch are not sufficiently activated for the nucleophilic attack of the OSA residues to occur. This disruption of intermolecular bonds enhances the swelling of starch granules and facilitates the diffusion of OSA molecules into the expanded starch matrix (Bhosale & Singhal, 2006; Sweedman *et al*., 2013).

When working at a pH of 7.5, the RS starch in the reaction with OSA increased over time (Fig. 1b). The highest conversion to RS was recorded at 6 h (46.69%). Nevertheless, no significant changes were detected in the control starch (no OSA reagent). Furthermore, the maximum DS (0.02±0) was obtained at 6 h reaction time. Similar results have been reported by Bhosale and Singhal (2006). The authors evaluated the degree of OSA substitution in starch from *A. paniculatus* and reaction conditions of pH 8 and 30 °C and 6 to 30 h reaction times. The higher substitution degree was obtained at 6 h. When increasing the reaction time, the degree of OSA substitution decreased. Nevertheless, when working with waxy corn starch under the same reaction conditions, the higher degree of substitution was recorded when increasing the reaction time to 24 h.

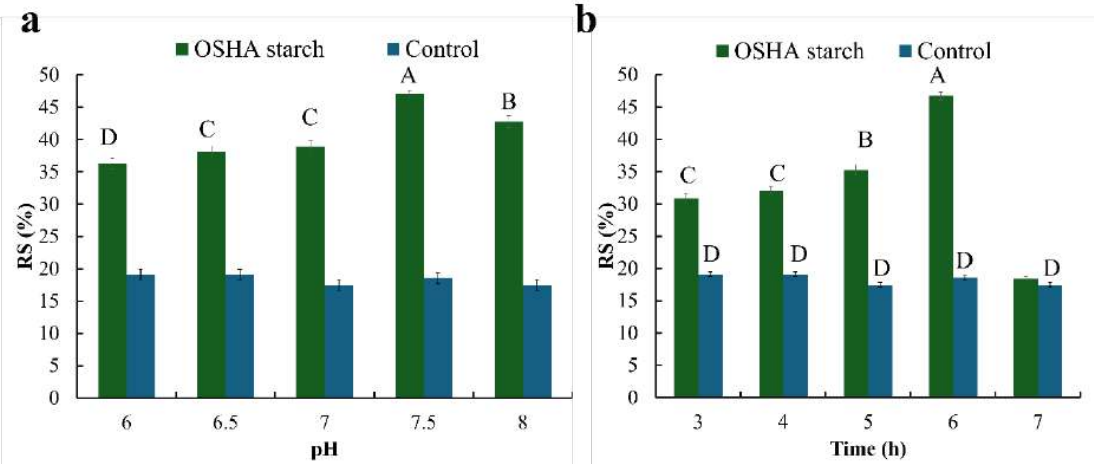

Fig. 1 Resistant starch concentration in the amaranth starch for the succinylation reaction a) Effect of pH, b) Effect of time. Error bars represent the standard deviation of the mean of triplicates.

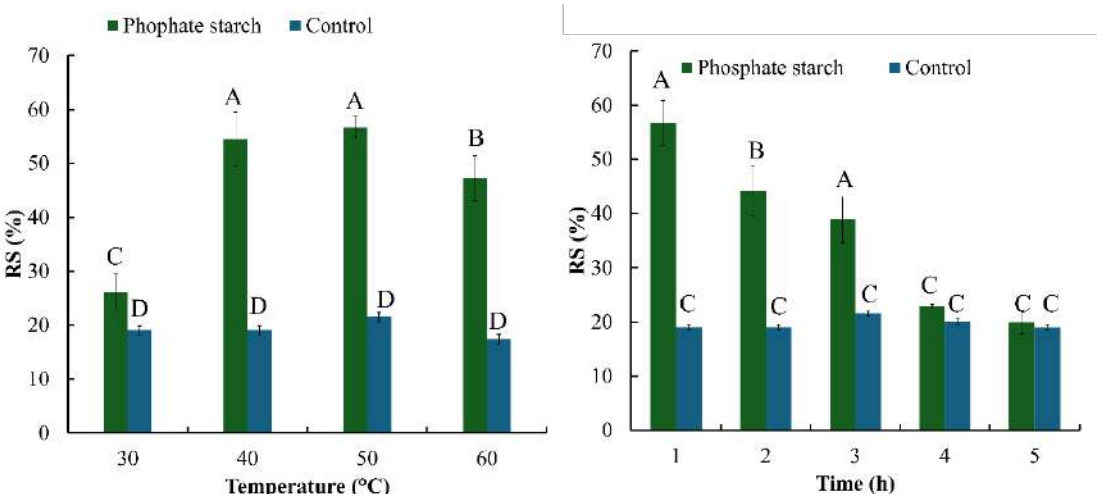

Fig. 2 Resistant starch concentration (RS) in the amaranth starch for the phosphorylation reaction a) Effect of temperature, b) Effect of time. Error bars represent the standard deviation of the mean of triplicates.

Additionally, by Fourier-transform infrared spectroscopy (FTIR), a strech in the 1245 cm^{-1} bands was observed in the fingerprint region between 1500-500 cm^{-1} of modified starches but absent in native starch (Suárez-Castillo *et al*., 2024). Furthermore, a marked band between 1450 cm^{-1} and 1300 cm^{-1} is observed, which is a torsion of the C-H bond of the aldehyde group as a result of the introduction of the OSA molecule into the starch structure (Sánchez de la Concha *et al*., 2020). Unfortunately, FTIR analysis is reliable only if the degree of substitution (DS) is ≥0.3, when OSA DS starches for food-grade products must be ~0.02 (Sweedman *et al*., 2013).

The improvement of the yield of RS during the succinylation reaction due to increasing the time is a direct consequence of the favorable effect of the diffusion and adsorption of the reagents and the starch molecule. A decrease follows the gradual increase in conversion to resistant starch because the OSA monomer is depleted as the succinate reaction proceeds. Furthermore, the reactive sites of starch decrease due to structural modification in the starch backbone (Murúa-Pagola *et al*., 2009). Additionally, the modification of the starch is related to the botanical and morphological origin of the starch granules.

3.4 Resistant starch and DS quantification by phosphorylation reaction

Phosphorylated starch, a chemically modified starch, is produced in large quantities and widely used. The incorporation of phosphate groups into starch chains creates repulsion between adjacent chains and enhances hydration. As a result, even at a low DS, increasing the phosphorylation degree can significantly alter the starch's physicochemical properties, such as rheological, thermal, and nutritional properties by increasing the ion-exchange, gel-forming, and intrinsic biological potential (such as prebiotic), respectively (Liu *et al*., 2022; Polnaya *et al*., 2013). The phosphorylation with STPP allows obtaining a monostich phosphate by an esterification reaction in which one phosphate is transferred into one hydroxyl group of a glucose unit (Ramadan & Sitohy, 2020).

During phosphorylation reaction at 40 and 50 °C, one hour and pH 6 (Fig. 2a), the highest conversion from native to resistant starch is obtained with no significant difference between temperatures (54.47±5.0 and 56.71±2.03, respectively). Additionally, the DS recorded was 0.03±0.001 and 0.03±0.001 for 40 and 50 °C, respectively. 1 Nevertheless, the concentration of RS is lower than the one reported by Sang *et al*. (2010) for wheat starch. The authors stated a 68% RS at reaction conditions of 40°C, pH 12, and a phosphate solution (sodium monophosphate, sodium sulfate, and sodium tripolyphosphate). The difference between the yields could be due to the starch's botanical origin, the reagent's type and concentration.

Fig. 2b shows that at 50 °C and one hour of reaction using STPP as a phosphating agent, the highest conversion to resistant starch was obtained compared to the succinylation reaction. As the reaction time increases, the conversion yield decreases. This could be because the amaranth starch begins to gelatinize at this temperature, and the long reaction time can cause the granules to swell, decreasing their reactivity to the chemical groups. Malik *et al*. (2023) stated the highest phosphorylation degree (51.71 %) at pH 9.5 and 70 °C in the phosphorylation reaction of mandua starch with a mix of STPP and Sodium STMP.

Additionally, FTIR studies showed a particular peak at 1417 $cm^{-1,}$ which is characteristic of the P=O stretching vibration (Liu *et al*., 2022). Esterified amaranth starch (such as phosphorylated) enhanced

their fat replacer characteristics. Therefore, they can be used to partially replace fat in fat-rich products, which can help to minimize health effects associated with the consumption of fatty foods (Fusuan *et al*., 2018).

3.5 Determination of WAI and WSI of the modified starch

The WAI of starch is an indicator of its application in the food industry and a parameter of the starch-polymer's stability against water, as well as an indicator of the starch degree gelatinization, since starch does not absorb water at room temperature (Seker *et al*., 2006; García-Cordero *et al*., 2024). The amaranth flour showed a WAI of 10.93±1.11 (Fig. 3). The WAI recorded in his work is higher than the data reported by Lux *et al*. (2022) for popped amaranth flour from *A. caudatus*. Authors stated a WAI of 6.77±0.21 at 80 °C and a soaking time of 1 h. The difference in WAI could be due to the amaranth variety. The highest WAI in the popped amaranth flour is a result of the gelatinization of the starch and denaturation of the proteins by the heat, resulting in a rapid and strong water absorption (Burgos & Armada, 2021; Gamel *et al*., 2005). Additionally, the WAI in the amaranth flour was higher compared to the starch; similar results have been reported by Zamudio-Flores *et al*. (2015). Authors recorded a higher WAI in oat flour compared to their starch extracts.

On the other hand, in the extract starch modified by acid hydrolysis, the WAI decreased (3.74 ±0.98). The treatment with HCl hydrolyzed the starch into small chains, decreasing its capacity to retain water molecules (Hung *et al*., 2016). After the succinylation and phosphorylation reaction, the WAI increased with no statistical difference between treatments ($p > 0.05$). Nevertheless, the WAI is still lower for all the modified starches than for the amaranth flour. Different results have been reported by Ashwar *et al*. (2017), the authors recorded a 2-2.8-fold increment in the WAI of the phosphorylated rice starch with STMP/STTP. Furthermore, the increase in the WAI of the starch from hybrid maize after the succinylation reaction with succinic anhydride was reported by Lawal (2004) compared to the native starch.

The WSI of starch refers to measuring how much of a starch sample can dissolve in water as a relation of the percentage of soluble polysaccharides released from the starch granules (Rojas-Molina *et al*., 2020). The starch extract has a lower WSI, this may be mainly due to two reasons: the first is that the amaranth seed used in this experiment was popped, a process that causes degradation in the starch polymers, reducing their solubility in water (Lara & Ruales, 1999). The second reason could be related to the starch obtention process that includes the action of protease,

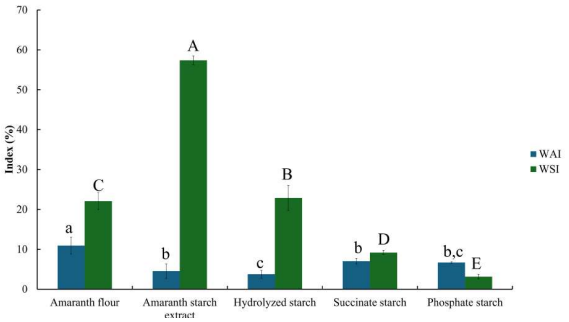

Fig. 3 Effect of the starch treatments in WAI and WSI. Error bars represent the standard deviation of the means of triplicate samples.

possibly attacking the protein matrix that protects the starch granules, causing damage to them. The nature of the granules is the factor that provides the hydration and solubilization capacity of starch in water (Contreras *et al*., 2013), regardless of the inclusion of chemical groups. Some authors have reported that as the RS content increases, there is a decrease in solubility values, which is attributed to the formation of crystalline zones; starches with a higher proportion of crystalline zones tend to have a lower capacity to solubilize in water (Neder-Suárez *et al*., 2016).

3.6 Granule morphology of the treated amaranth starches

Figure 4a shows the morphology of the popped amaranth flour; irregular patterns can be observed in the flour particles. Alonso-Miravalles *et al*. (2020) recorded irregular asymmetrical particles in pseudocereals such as amaranth. Figure 4b shows that the amaranth starch aggregates are more rounded and spaced apart from each other, which differs from that reported by other authors, where its morphology is described as polygonal grouped granules without fissures on the surface (Paredes, *et al*., 1989; Shindu & Singh, 2016). There could be two reasons for this. The first is that the amaranth used in this work was subjected to an expansion process that causes a change in the morphology of the starch granule. And the second is by the process of obtaining starch since conventional processes are carried out with a sodium hydroxide solution at low temperatures, which allows obtaining starch granules with minor changes in the physical, chemical, and rheological properties (Perez *et al*., 1993). In this research, the removal of protein and lipids from the starch granules influenced the final morphology of the granule, since these two constituents are considered to be responsible for the agglomeration of starch molecules (Qian & Kuhn, 1999).

When the amaranth starch extract is subjected to acid hydrolysis, a notable change in its morphology is observed.

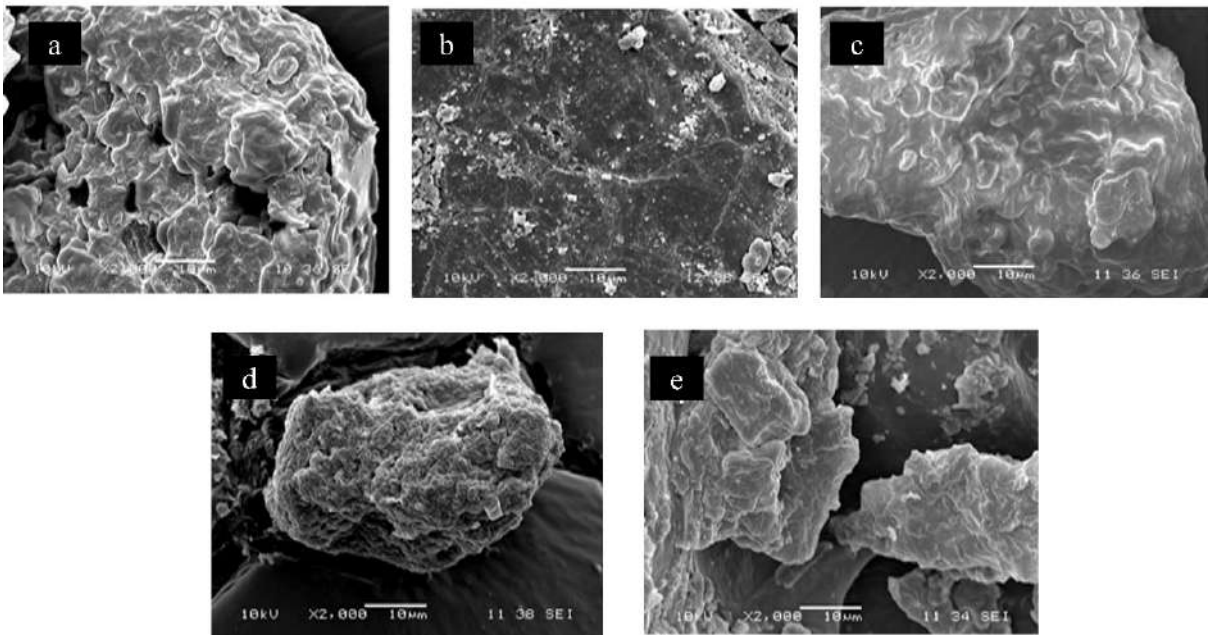

Fig. 4 SEM images of the a) amaranth flour, b) amaranth starch extract, c) hydrolyzed amaranth, d) phosphorylated amaranth starch, e) succinylated amaranth starch.

The rounded shape is lost, and a rougher, aggregate shape is now seen (Figure 4c). Martín & López (2009) stated changes in the external area of the cassava starch, modifying its smooth surface for slightly rougher regions. Additionally, the smaller granules hydrolyze quickly because of the more excellent available surface (Sanguanpong *et al*., 2003), likewise this starch presents a wrinkled surface, probably due to the contraction of the starch agglomerate caused by the high temperatures of the process of both obtaining the starch and its acid hydrolysis (Altay & Gunasekaran, 2006). In Fig. 4d and 4e, when chemical groups were introduced into the molecule, the size of the starch agglomerates increased. In general, these increases are due to the inclusion of phosphate and succinate groups within the starch agglomerates, which create specific repulsive forces that could increase the inter- and intra-molecular spaces, allowing the inclusion of a more significant number of water molecules (Liu *et al*., 2022). In Fig. 4e, it is observed that the succinate starch presents a rough surface, where some small particles are attached to the surface of the starch. This happens as the degree of substitution increases, its characteristic structure is replaced by a fiber-like structure (Xu, Miladino & Hanna, 2004). Liu *et al*. (2022) reported a rough surface and aggregation in the chestnut starch granules. The authors stated this morphological change to the gelatinization of the starch during the acetic anhydride addition. Additionally, Bajaj *et al*. (2019) reported that OSA modified starches from different sources, such as corn, potato, and rice, displayed rough surfaces, loss of the starch edges, development of superficial pores, and pronounced depression on the surface.

Conclusions

The methodology proposed in this work allowed the obtaining of 63.6% of starch from popped amaranth seed. Through the succinylation and phosphorylation reaction, a concentration of resistant starch of 47.92% and 56.7%, respectively, was obtained. Therefore, it could be added to food formulas granting health benefits such as low glycemic index, modulating metabolism, and increasing post-meal satiety.

Acknowledgements

We gratefully acknowledge Secretariat of Science, Humanities, Technology and Innovation (SECIHTI) of Mexico for the postdoctoral scholarship (CVU 621321). Besides, the Autonomous University Metropolitan will provide financial support.

References

Altay, F. and Gunasekaran, S. (2006). Influence of drying temperature, water content, and heating rate on gelatinization of corn starches. *Journal of Agricultural and Food Chemistry 54*(12), 4235-4245. https://doi.org/10.1021/jf0527089

Altuna, L., Herrera, M. L. and Foresti, M. L. (2018). Synthesis and characterization of octenyl succinic anhydride modified starches for food

applications. A review of recent literature. *Food Hydrocolloids 80*, 97-110. https://doi.org/10.1016/j.foodhyd.2018.01.032

Aparicio-Saguilán, A., Valera-Zaragoza, M., Perucini-Avendaño, M., Páramo-Calderón, D. E., Aguirre-Cruz, A., Ramírez-Hernández, A. and Bello-Pérez, L. A. (2015). Lintnerization of banana starch isolated from underutilized variety: morphological, thermal, functional properties, and digestibility. *CyTA-Journal of Food 13*(1), 3-9. https://doi.org/10.1080/19476337.2014.902864

Arendt, E. K. and Zannini, E. (2013). Amaranth. In: *Cereal Grains for the Food and Beverage Industries,* Pp. 439–473. Woodhead Publishing, Cambridge. https://doi.org/10.1533/9780857098924.439

Ashwar, B. A., Gani, A., Shah, A. and Masoodi, F. A. (2017). Physicochemical properties, in-vitro digestibility and structural elucidation of RS4 from rice starch. *International Journal of Biological Macromolecules*, *105*, 471-477. https://doi.org/10.1016/j.ijbiomac.2017.07.057

Anderson, R. (1969). Water Absorption and solubility and amylograph characteristics of roll-cooked small grain products. *Cereal Chemistry 59*(4), 265–269.

Alonso-Miravalles, L., Zannini, E., Bez, J., Arendt, E. K. and O'Mahony, J. A. (2020). Physical and flow properties of pseudocereal-based protein-rich ingredient powders. *Journal of Food Engineering 281*, 109973. https://doi.org/10.1016/j.jfoodeng.2020.109973

Assad, R., Reshi, Z. A., Jan, S. and Rashid, I. (2017). Biology of amaranths. *The Botanical Review 83*, 382-436. https://doi.org/10.1007/s12229-017-9194-1

Bai, Y., Kaufman, R. C., Wilson, J. D. and Shi, Y. C. (2014). Position of modifying groups on starch chains of octenylsuccinic anhydride-modified waxy maize starch. *Food Chemistry 153*, 193–199. http://doi.org/10.1016/j.foodchem.2013.12.012

Bajaj, R., Singh, N. and Kaur, A. (2019). Properties of octenyl succinic anhydride (OSA) modified starches and their application in low fat mayonnaise. *International Journal of Biological Macromolecules 131*, 147-157.

Bertoft, E. (2004). Lintnerization of two amylose-free starches of A-and B-crystalline types, respectively. *Starch-Stärke 56*(5) 167-180. https://doi.org/10.1002/star.200300255

Bhosale, R. and Singhal, R. (2007). Effect of octenylsuccinylation on physicochemical and functional properties of waxy maize and amaranth starches. *Carbohydrate Polymers* 68(3), 447–456. http://doi.org/10.1016/j.carbpol.2006.11.011

Bhosale, R. and Singhal, R. (2006). Process optimization for the synthesis of octenyl succinyl derivative of waxy corn and amaranth starches. *Carbohydrate Polymers 66*(4), 521–527. http://doi.org/10.1016/j.carbpol.2006.04.007

Birt, D., Boylston, T., Hendrich, S., Jane, J., Hollis, J., Li, L. and Whitley, E. (2013). Resistant Starch: Promise for Improving Human Health. *American Society for Nutrition 4,* 587–601. https://doi.org/10.3945/an.113.004325

Burgos, V. E. and Armada, M. (2021). Microstructure and storage stability of precooked kiwicha products. *Journal of Food Processing and Preservation 45*(11), e15911. https://doi.org/10.1111/jfpp.15911

Calva-Cruz, O. D. J., Ovando-Vázquez, C., De León-Rodríguez, A., Veana, F., Espitia-Rangel, E., Treviño, S. and Barba-de la Rosa, A. P. (2023). Dietary supplementation with popped amaranth modulates the gut microbiota in low height-for-age children: a nonrandomized pilot trial. *Foods 12*(14), 2760. https://doi.org/10.3390/foods12142760

Capriles, V. D., Coelho, K. D., Guerra-Matias, A. C. and Arêas, J. A. G. (2008). Effects of processing methods on amaranth starch digestibility and predicted glycemic index. *Journal of Food Science 73*(7). http://doi.org/10.1111/j.1750-3841.2008.00869.x

Chen, C., Huang, Y. and Zhu, F. (2024). Molecular Basis of the Granular Characteristics of Small-Granule Starch: A Comparative Study. *Journal of Agricultural and Food Chemistry 72*(22), 12762-12774.

Contreras-Lozano, K. P., Salcedo-Mendoza, J. G. and Estrada-Garrido, F. (2013). Functional characterization of cationic starch of cassava (*Manihot esculenta*). *Revista ION 26*(2), 31-38.

DuBois, M., Gillies K. E., Hamilton, J. K., Rebers, P. A. and Smith, F. (2002). Calorimetric Dubois Method for Determination of Sugar and Related

Substances. *Analytical Chemistry 28*, 350-356. http://doi.org/10.1021/ac60111a017

Fasuan, T. O., Gbadamosi, S. O. and Akanbi, C. T. (2018). Modification of amaranth (*Amaranthus viridis*) starch, identification of functional groups, and its potentials as fat replacer. *Journal of Food Biochemistry 42*(5), e12537.

Fuentes-Zaragoza, E., Riquelme-Navarrete, M. J., Sánchez-Zapata, E. and Pérez-Álvarez, J. a. (2010). Resistant starch as functional ingredient: A review. *Food Research International 43*(4), 931–942. http://doi.org/10.1016/j.foodres.2010.02.004

Goñi, I., García-Díaz, L., Mañas, E. and Saura-Calixto, F. (1996). Analysis of resistant starch: a method for foods and food products. *Food Chemistry 56*, 445–449. https://doi.org/10.1016/0308-8146(95)00222-7

Gamel, T. H., Linssen, J. P., Mesallem, A. S., Damir, A. A. and Shekib, L. A. (2005). Effect of seed treatments on the chemical composition and properties of two amaranth species: Starch and protein. *Journal of the Science of Food and Agriculture 85*(2), 319–327. http://doi.org/10.1002/jsfa.1988

García-Cordero, A. L., Jiménez-Alvarado, R., Bautista, M., Díaz-Sánchez, F., Ibarra, I. S., Sánchez-Ortega, I. and Santos, E. M. (2024). Improvement of corn extruded snacks properties by incorporation of pulses. *Revista Mexicana de Ingeniería Química 23* (3). https://doi.org/10.24275/rmiq/Alim24279

García-Diaz, S., Hernández-Jaimes, C., Escalona-Buendía, H. B., Bello-Pérez, L. A., Vernon-Carter, E. J. and Álvarez-Ramírez, J. (2016). Effects of $CaCO_3$ treatment on the morphology, crystallinity, rheology and hydrolysis of gelatinized maize starch dispersions. *Food Chemistry 207*, 139–147. https://doi.org/10.1016/j.foodchem.2016.03.095

Guerra-DellaValle, D., Bello-Pérez, L. A., González-Soto, R. A., Solorza-Feria, J. and Arámbula-Villa, G. (2008). Efecto del tiempo de reacción en la acetilación de almidón de plátano. *Revista Mexicana de Ingeniería Química 7*(3), 283-291.

Gutiérrez, T. J. and Tovar, J. (2021). Update of the concept of type 5 resistant starch (RS5): Self-assembled starch V-type complexes. *Trends in Food Science and Technology 109*, 711-724. https://doi.org/10.1016/j.tifs.2021.01.078

Hung, P. Van, Vien, N. L. and Lan Phi, N. T. (2016). Resistant starch improvement of rice starches under a combination of acid and heat-moisture treatments. *Food Chemistry* 191, 67–73. http://doi.org/10.1016/j.foodchem.2015.02.002

Khan, R. and Dutta, A. (2018). Effect of popping on physico-chemical and nutritional parameters of amaranth grain. *Journal of Pharmacognosy and Phytochemistry 7*(3), 954-958.

Kierulf, A., Mosleh, I., Li, J., Li, P., Zarei, A., Khazdooz, L., Smooth, J. and Abbaspourrad, A. (2024). Food LEGO: Building hollow cage and sheet superstructures from starch. *Science Advances 10*(7), eadi7069.

Korus, J., Ziobro, R., Witczak, T., Kapusniak, K., & Juszczak, L. (2021). Effect of octenyl succinic anhydride (OSA) modified starches on the rheological properties of dough and characteristic of the gluten-free bread. *Molecules 26*(8), 2197.

Lara N. and Ruales J. (2002). Popping of amaranth grain (*Amaranthus caudatus*) and its effect on the functional, nutritional and sensory properties, *Journal of the Science of Food and Agriculture 82*(8) 797–805. https://doi.org/10.1002/jsfa.1069.

Lawal, O. S. (2004). Succinyl and acetyl starch derivatives of a hybrid maize: Physicochemical characteristics and retrogradation properties monitored by differential scanning calorimetry. *Carbohydrate Research 339*(16), 2673-2682. https://doi.org/10.1016/j.carres.2004.08.015

Liu, C., Yan, H., Liu, S. and Chang, X. (2022). Influence of phosphorylation and acetylation on structural, physicochemical and functional properties of chestnut starch. *Polymers 14*(1), 172. https://doi.org/10.3390/polym14010172

Lux, T., Kardell, M., Reimold, F., Erdoes, A. and Floeter, E. (2022). Functional, rheological, and microstructural properties of hydrothermal puffed and raw amaranth flour suspensions. *Food Science and Nutrition 10*(11), 3724-3735. https://doi.org/10.1002/fsn3.2970

Malik, M. K., Kumar, V., Singh, J., Bhatt, P., Dixit, R. and Kumar, S. (2023). Phosphorylation of alkali extracted mandua starch by STPP/STMP for improving digestion resistibility. *ACS Omega 8* (13): 11750–67. https://doi.org/10.1021/acsomega.2c05783

Martín, J. C. and López, E. (2009). Physical modification of cassava starch and evaluation of susceptibility to enzyme hydrolysis by alpha amylase. *Revista Colombiana de Química 38*(3), 395-408.

Montoya-Rodríguez, A., Gómez-Favela, M. A., Reyes-Moreno, C. and Milan-Carrillo, J. (2015). Identification of Bioactive Peptide Sequences from Amaranth (*Amaranthus hypochondriacus*) Seed Proteins and Their Potential Role in the Prevention of Chronic Diseases. *Comprehensive Review in Food Science and Food Safety 14*(2), 139-158. https://doi.org/10.1111/1541-4337.12125

Murúa-Pagola, B., Beristain-Guevara, C. I. and Martínez-Bustos, F. (2009). Preparation of starch derivatives using reactive extrusion and evaluation of modified starches as shell materials for encapsulation of flavoring agents by spray drying. *Journal of Food Engineering 91*(3), 380-386. https://doi.org/10.1016/j.jfoodeng.2008.09.035

Neder Suárez, D., Quintero Ramos, A. and Amaya Guerra, C. A. (2016). Efecto de la extrusión-cocción en la formación de almidón resistente. *Investigación y Desarrollo en Ciencia y Tecnología de Alimentos 1*(1), 36-41.

Official Methods of Analysis of AOAC (1997). International, 19th Ed., AOAC International, Gaithers.

Paredes-López, O., Schevenin, M. L., Hernández-López, D. and Cárabez-Trejo, A. (1989). Amaranth Starch - Isolation and Partial Characterization. *Starch - Stärke 41*(6), 205–207. http://doi.org/10.1002/star.19890410602

Paschall, E. 1964. "Phosphatation with Inorganic Phosphate Salts." In: *Methods in Carbohydrate Chemestry:Starch*, Pp. 294-296. Academic Press, New York.

Písařík̆ová, B., Peterka, J., Trčková, M., Moudrý, J., Zralý, Z. and Herzig, I. (2007). The content of insoluble fibre and crude protein value of the aboveground biomass of *Amaranthus cruentus* and *A. hypochondriacus*. *Czech Journal of Animal Science 10*, 348-353

Polnaya, F. J., Marseno, D. W. and Cahyanto, M. N. (2013). Effects of phosphorylation and cross-linking on the pasting properties and molecular structure of sago starch. *International Food Research Journal 20*(4), 1609-1615.

Perez, E., Bahnassey, Y. A. and Breene, W. M. (1993). A simple laboratory scale method for isolation of amaranth starch. *Starch-Stärke 45*(6), 211-214. https://doi.org/10.1002/star.19930450605

Qian, J. and Kuhn, M. (1999). Characterization of *Amaranthus cruentus* and *Chenopodium quinoa starch*. *Starch-Stärke 51*(4), 116-120. https://doi.org/10.1002/(SICI)1521-379X(199904)51:4-116::AID-STAR116>3.0.CO;2-R

Ramadan, M. F. and Sitohy, M. Z. (2020). Phosphorylated starches: Preparation, properties, functionality, and techno-applications. *Starch-Stärke 72*(5-6), 1900302. https://doi.org/10.1002/star.201900302

Resio, A. N. C., Tolaba, M. P. and Suárez, C. (2009). Correlations between wet-milling characteristics of amaranth grain. *Journal of Food Engineering 92*(3), 275-279. https://doi.org/10.1016/j.jfoodeng.2008.11.005

Rojas-Molina, I., Mendoza-Avila, M., Cornejo-Villegas, M. D. L. Á., Real-López, A. D., Rivera-Muñoz, E., Rodríguez-García, M. and Gutiérrez-Cortez, E. (2020). Physicochemical properties and resistant starch content of corn tortilla flours refrigerated at different storage times. *Foods 9*(4), 469. https://doi.org/10.3390/foods9040469

Sang, Y., Seib, P. A., Herrera, A. I., Prakash, O. and Shi, Y. (2010). Effects of alkaline treatment on the structure of phosphorylated wheat starch and its digestibility. *Food Chemistry 118*(2), 323–327. http://doi.org/10.1016/j.foodchem.2009.04.121

Sanguanpong, V., Chotineeranat, S., Piyachomkwan, K., Oates, C. G., Chinachoti, P. and Sriroth, K. (2003). Hydration and physicochemical properties of small-particle cassava starch. *Journal of the Science of Food and Agriculture 83*(2), 123-132. https://doi.org/10.1002/jsfa.1285

Sánchez de la Concha, B. B., Agama-Acevedo, E., Aguirre-Cruz, A., Bello-Pérez, L. A. and Alvarez-Ramírez, J. (2020). OSA esterification of amaranth and maize starch nanocrystals and their use in "Pickering" emulsions. *Starch-Stärke 72*(7-8), 1900271.

Sarangi, D., Jhala, A. J., Govindasamy, P. and Brusa, A. (2021). Amaranthus spp. In: *Biology and Management of Problematic Crop Weed*

Species, (Ed. Chauhan, B.S.) Pp. 21-42. Academic Press, New York.

Sindhu, R. and Khatkar, B. S. (2016). Morphological, pasting and thermal properties of common buckwheat (*Fagopyrum esculentum Moench*) flour and starch. *International Journal of Innovate Research and Advanced Studies 3*(7), 160-164.

Seker, M. and Hanna, M. A. (2006). Sodium hydroxide and trimetaphosphate levels affect properties of starch extrudates. *Industrial Crops and Products 23*(3), 249-255. https://doi.org/10.1016/j.indcrop.2005.08.002

Shevkani, K., Singh, N., Kaur, A. and Rana, J. C. (2014). Physicochemical, pasting, and functional properties of amaranth seed flours: effects of lipids removal. *Journal of food science 79*(7), C1271-C1277. https://doi.org/10.1111/1750-3841.12493

Singh, A. and Punia, D. (2020). Characterization and nutritive values of amaranth seeds. *Current Journal of Applied Science and Technology 39*(3), 27-33. https://doi.org/10.9734/cjast/2020/v39i330511

Soto-Azurduy. (2010). Cuantificación de almidón total y de almidón resistente en harina de plátano verde (*Musa Cavendishii*) y banana verde (*Musa Paradisíaca*). *Revista Boliviana de Química 27*(2), 94–99.

Suárez-Castillo, G. M., Salcedo-Guadalupe, J. G., Contreras-Lozano, K. P., Rangel-Pérez, M. G. and Cervera-Ricardo, J. A. (2024). Increase in the degree of substitution of cassava starches by dual modification processes. *Revista Mexicana de Ingeniería Química 23*(3). https://doi.org/10.24275/rmiq/Poly24303

Sweedman, M. C., Tizzotti, M. J., Schäfer, C. and Gilbert, R. G. (2013). Structure and physicochemical properties of octenyl succinic anhydride modified starches: A review. *Carbohydrate Polymers 92*(1), 905-920.

Venskutonis, P. R. and Kraujalis, P. (2013). Nutritional components of amaranth seeds and vegetables: a review on composition, properties, and uses. *Comprehensive Reviews in Food Science and Food Safety 12*(4), 381-412. https://doi.org/10.1111/1541-4337.12021

Villarreal, M. E. Ribotta, P. D. and Iturriaga, L. B. (2013). Comparing methods for extracting amaranthus starch and the properties of the isolated starches. *LWT - Food Science and Technology 51*(2), 441–447. http://doi.org/10.1016/j.lwt.2012.11.009

Ward, S. M., Webster, T. M. and Steckel, L. E. (2013). Palmer amaranth (*Amaranthus palmeri*): a review. *Weed Technology 27*(1), 12-27. https://doi.org/10.1614/WT-D-12-00113.1

Xu, Y., Miladinov, V. and Hanna, M. A. (2004). Synthesis and characterization of starch acetates with high substitution. *Cereal Chemistry 81*(6), 735-740. https://doi.org/10.1094/CCHEM.2004.81.6.735

Zamudio-Flores, P. B., Tirado-Gallegos, J. M., Monter-Miranda, J. G., Aparicio-Saguilán, A., Torruco-Uco, J. G., Salgado-Delgado, R. and Bello-Pérez, L. A. (2015). Digestibilidad *in vitro* y propiedades térmicas, morfológicas y funcionales de harinas y almidones de avenas de diferentes variedades. *Revista Mexicana de Ingeniería Química 14*(1), 81-97.

Vol. 24, No. 2(2025) Bio25497
Revista Mexicana de Ingeniería Química

Bio-saccharification and fermentation process of a non-conventional starchy material with isolates of autochthonous strains

Bio-sacarificación y fermentación de una materia prima no convencional rica en almidón utilizando microorganismos autóctonos

C.L. Garza-Garza[1], E. Olguin-Maciel[1], R. Valdez-Ojeda[1], E. Huchin-Poot[1], T. Toledano-Thompson[1], K.J. Azcorra-May[1], L. Alzate-Gaviria[1], J. Dominguez-Maldonado[1], P. Lappe-Oliveras[2*] and R. Tapia-Tussell[1*]
[1]Renewable Energy Unit, Yucatan Scientific Research Center, Merida, Yucatan, México.
[2] Mycology Laboratory, Biology Institute, National Autonomous University of Mexico, Mexico, Mexico.
Received: January 8, 2025; Accepted: April 25, 2025

Abstract
Consolidated bio-saccharification (CBS) is a promising technique for converting complex materials like starchy biomass into ethanol through simultaneous liquefaction and saccharification, leading to a more sustainable process. This study developed sequential bio-saccharification and fermentation of *Brosimum alicastrum* seed flour (BSF) in a single reactor using native microorganisms from *B. alicastrum* fruits. The native yeasts were identified through molecular techniques and their amylolytic capacity, growth rate at different temperatures, and ethanol tolerance were assessed, along with the basidiomycete *Trametes hirsuta* RT-1. The identified yeasts were *Candida tropicalis* (PL-1), *Pichia kudriavzevii* (TL-2), *Hanseniaspora guilliermondii* (TL-3), and *Meyerozyma caribbica* (RSL-4). *C. tropicalis* (PL-1) showed cell growth up to 42°C, 8% v/v ethanol tolerance, and partial BSF degradation, while *T. hirsuta* RT-1 showed 3% v/v ethanol tolerance and produced the enzymes α-amylase (49.77 ± 7.54 U/mL) and laccase (8,920 ± 1,236 U/mL). The highest ethanol production (18.93 ± 1.78 g/L) was achieved after 11 days of CBS using both *C. tropicalis* (PL-1) and *T. hirsuta* RT-1. This strategy represents a novel approach for bioethanol production using CBS from an available non-conventional and inexpensive material, without the use of commercial enzymes or microorganisms.
Keywords: *Trametes hirsuta*; *Candida tropicalis*, Amylase, *Brosimum alicastrum*.

Resumen
La bio-sacarificación consolidada (CBS) es una técnica prometedora para producir etanol de manera más sostenible a partir de materiales complejos con alto contenido de almidón que requieren licuefacción y sacarificación simultáneas. Este estudio desarrolló una sacarificación y fermentación simultánea de harina de semillas de *Brosimum alicastrum* (BSF) en un solo reactor utilizando microorganismos nativos de frutas de *B. alicastrum*. Estos microorganismos fueron identificados molecularmente y se evaluó su capacidad amilolítica, tasa de crecimiento a diferentes temperaturas y tolerancia al etanol. Las levaduras identificadas fueron *Candida tropicalis* (PL-1), *Pichia kudriavzevii* (TL-2), *Hanseniaspora guilliermondii* (TL-3) y *Meyerozyma caribbica* (RSL-4). *C. tropicalis* (PL-1) mostró crecimiento hasta 42°C, tolerancia al etanol del 8% v/v y degradación parcial de BSF, mientras que *T. hirsuta* RT-1 presentó tolerancia al etanol del 3% v/v y producción de α-amilasa (49.77 ± 7.54 U/mL) y lacasa (8,920 ± 1,236 U/mL). La mayor producción de etanol fue de 18.93 ± 1.78 g/L y se obtuvo tras 11 días de CBS utilizando *C. tropicalis* (PL-1) y *T. hirsuta* RT-1. Esta estrategia representa un enfoque innovador para la producción de bioetanol utilizando un material disponible en la región, económico y no convencional mediante CBS sin necesidad de enzimas o microorganismos comerciales.
Palabras clave: *Trametes hirsuta*; *Candida tropicalis*, Amilasa, *Brosimum alicastrum*.

*Corresponding author. *E-mail*: rtapia@cicy.mx and lappe@ib.unam.mx ;
https://doi.org/10.24275/rmiq/Bio25497
ISSN:1665-2738, *issn-e*: 2395-8472

1 Introduction

Bioethanol can be produced from competing food crops, lignocellulosic materials, or algal biomass. Bioethanol is classified as first, second, or third generation depending on the substrate from which it is produced (Ferreira *et al*., 2019). The main disadvantage of first-generation bioethanol is the ethical dilemma "food versus fuel". However, the technological infrastructure required for its synthesis is well understood and has proven to be a significant asset. This technological knowledge reduces ambiguity surrounding essential raw materials, the processing thereof, and market dynamics (Lennartsson *et al*., 2014). The raw materials employed in the production of first-generation bioethanol include crops which contain starch, with corn constituting the predominant source. Starch, the second most abundant biopolymer in higher plants after cellulose, plays a primary role in energy storage.

Starchy materials are mainly destined for fresh consumption, and a low percentage of the total available is processed into flours and starches (Suárez-Castillo *et al*., 2024). The use of non-edible starchy sources could be an interesting alternative for bioethanol production since it is a cheap and non-toxic renewable carbon source (Bušić *et al*., 2018; Satyanarayana, 2009). Despite the advantages of the use of starch biomass, process technologies must be applied to improve its functional properties in order to make it suitable for extensive use in various industries (Ramos-Villacob *et al*., 2024).

For bioethanol production from starchy biomass, two primary stages are involved: liquefaction and saccharification, in which, the use of amylases, such as α-amylase and glucoamylase, are essential to breakdown the starch into fermentable sugars. Subsequent to these stages, a fermentation step is initiated, wherein a yeast strain, usually Saccharomyces cerevisiae, is added to convert these sugars into ethanol (Zabed *et al*., 2017).

The use of commercial amylases in the starch-to-ethanol process has been identified as a significant factor in increasing the costs of saccharification, making this step one of the most expensive in the entire process (Favaro *et al*., 2019). Achieving economic viability is imperative for the sustainable production of biofuels, in considering of which several bioconversion strategies have been studied with a view to improving the cost-effectiveness of the saccharification. Consolidated biosaccharification (CBS) and consolidated bioprocess (CBP) are promising technologies for the effective conversion of biomass into bioethanol. CBP involves three simultaneous processes in a single reactor, which are enzyme production, saccharification, and fermentation. As previously mentioned, enzyme production is one of the most expensive steps in bioethanol production. Therefore, CBP could help to make this process profitable compared to conventional technologies by reducing the cost of enzyme procurement. Other advantage of this approach is the use of a single reactor, which can result in lower maintenance and operating costs. However, the main disadvantage is that the processes have different operating conditions, making optimization complicated.

In contrast, consolidating biosaccharification (CBS) involves the use of microorganisms that can produce enzyme cocktails, which catalyze the conversion of biomass and the hydrolysis of simple carbohydrates (Jahangeer *et al*., 2024). This technology entails in the production of enzymes and their subsequent application for saccharification within the same reactor, but the use of native strains can enhance the bioconversion of starch into fermentable sugars and facilitate the fermentation process. This approach has the potential to reduce the cost of bioethanol.

Yeasts currently employed for fermentation have not been carefully selected for the feedstock, but rather, have been used due their historical background (Steensels *et al*., 2014; Umeh *et al*., 2017). The use of native microorganisms has the potential to enhance the cost-effectiveness of bioethanol production, given that native microorganisms are inherently adapted to the local conditions in which they have evolved although they are rarely used in current industrial processes. Several autochthonous yeasts isolated from dates, fruits, sugarcane, and beet molasses crops have demonstrated the potential to enhance bioethanol yields compared to commercial strains (Kechkar et al., 2019). Our research group has identified and studied a native basidiomycete strain, *Trametes hirsuta* Bm-2, which has amylolytic and fermentative capabilities that allow its use in a consolidated bioprocess using a starchy substrate (Olguin-Maciel *et al*., 2019). The pursuit of hyper-productive strains capable of improving hydrolysis and fermentation processes has gained significant prominence, highlighting the necessity to identify novel microorganisms for bioconversion processes.

In this study, the use of *Brosimum alicastrum* Sw. (ramon tree) seed flour is proposed for the production of bioethanol, since it is not currently regarded as a food crop. This tree is native to the Mesoamerican and Caribbean regions; it grows naturally in several Mexican states, including the Yucatan Peninsula; and it also exhibits a remarkable ability to grow in soils with limited nutrients, a trait that contributes to its resilience in different climates. Ramon seeds contain proteins, lipids, calcium, vitamins (A, B, C), fiber, and most importantly a high carbohydrate content (75%),

with approximately 63% of this carbohydrate being starch, which can be transformed into bioethanol. In addition, phenolic compounds, such as gallic, vanillic, caffeic, *p*-coumaric, hydroxybenzoic and chlorogenic acids, have also been identified. These compounds can act as natural redox mediators for enzymes or as substrates for laccase production, thereby facilitating a sustainable exploitation of the material within a biorefinery approach (Meiners *et al*., 2009; Olguin-Maciel *et al*., 2017). The annual seed production per tree is estimated to be 95 kilograms, and this estimate indicates an annual production of 28.6 tons in a plantation with 300 trees per hectare, or 19.7 tons in a plantation with 200 trees per hectare (Hernández-González *et al*., 2014).

The tree also provides important environmental benefits, including the protection of soil, bodies of water, and biodiversity, thus making it a promising species for restoration. Additionally, its slow growth rate contributes to its role as a carbon sink, making it a suitable option for carbon capture programs to combat global warming (Meiners *et al*., 2009). Historical studies suggest that this species was cultivated by the Maya civilization and other Mesoamerican peoples as a staple food and for medicinal purposes. However, BSF is currently an underexploited resource and is rarely used for human consumption in the Yucatan Peninsula (Losoya-Sifuentes *et al*., 2023; Ozer 2017; Pérez-Pacheco et al., 2014). Consequently, the exploitation of the ramon tree is an opportunity to preserve and utilize it for the benefit of ecosystems and rural development, and for the sustainable production of biofuels and value-added compounds, such as phenolic compounds and valuable enzymes (laccase and amylase).

The aim of this study was to develop a sequential bio-saccharification and fermentation process in a single reactor for the bioconversion of *Brosimum* seed flour (BSF) using autochthonous microorganisms: a fungus for liquefaction and saccharification and isolated yeasts from the ramon fruit that were identified through a polyphasic approach for fermentation.

2 Materials and methods

2.1 Raw material

Seeds of *B. alicastrum* were collected from Caucel, Yucatan, Mexico (21°00'53"N 89°42'25"W). The husked seeds were dried in a convection oven (Binder, Fed model 115 ®, Tuttlingen, Germany) at 70°C for 72 h and stored in a desiccator until milling to obtain BSF as previously described by Pérez-Pacheco *et al*., (2014). The BSF used in this work contained 75% carbohydrates of which 63% was starch and 12.24 % were total proteins (Olguin-Maciel *et al*., 2020).

2.2 Identification of yeast cultures and fungal strain

The four native yeasts used in the present study were isolated from the pericarp (P), coat (T) or seed (S) of ramon fruits (Huchin Poot, 2015) and conserved in YPD (Yeast Extract Peptone Dextrose) media for further analysis. They were morphologically identified as *Candida tropicalis* (PL-1), *Pichia kudriavzevii* (TL-2), *Hanseniaspora guilliermondii* (TL-3) and *Meyerozyma caribbica* (RSL-4), using a taxonomy analysis following Kurtzman *et al*. (1990) and Barnett *et al* (2011).

Besides the taxonomical analysis a molecular identification was carried out, and the total genomic DNA was extracted using the methodology proposed by Tapia-Tussell *et al*. (2006). DNA concentration and purity were determined in a NanoDrop ND-1000 spectrophotometer (NanoDrop Technologies, Seattle, WA, USA); then, D1/D2 Domain LSU 26S rDNA was amplified by PCR using the universal primers NL1 (5´-GCA TAT CAA TAA GCG GAG GAA-3´) and NL4 (5´-GGT CCG TGT TTC AAG ACG G-3´) (Libkind *et al*., 2003). Sequences were obtained by Macrogen Inc, Korea, processed with BioEdit Program v 7.0.5 (Hall, 1999), and analyzed using Molecular Evolutionary Genetic Analysis (MEGA) software version 5.0 (Kumar *et al*., 2018). A tree was built using the neighbor-joining method and the unweighted pair group method with arithmetic mean (UPGMA). The relative support of clustering was evaluated by bootstrap analysis (1000 resamples) using *Kluyveromyces maxianus* as the out-group.

Meanwhile, the native fungal strain isolate was obtained from the endemic plant *Accalypha gaumeri* in Tinum, Yucatan, Mexico (20°42´00´´N, 88°29´00´´W). It was identified at species level as *Trametes hirsuta*, by the amplification of the 5.8S-ITS regions using the universal primers ITS1 and ITS4 (White *et al*., 1990). The sequence of the fungus was registered at GenBank with accession number OM732416.1.

2.2.1 Yeast conservation

The yeasts were preserved in distilled water suspensions and in 25% glycerol-YPD broth at -80°C in the Laboratory of Micromycetes C006, Institute of Biology, National Autonomous University of Mexico (UNAM) and were registered in the Fungal Collection of the Herbario Nacional (MEXU-UNAM) with codes MEXU 30461 for *C. tropicalis* PL-1, MEXU 30662 for *P. kudriavzevii* TL-2, MEXU 30463 for *H. guilliermondii* (TL-3) and MEXU 30464 for *M. caribbica* (RSL-4).

2.3 Inoculum preparation and assays

An inoculum of each native isolate was prepared to evaluate their amylolytic capacity, thermotolerance and tolerance to different concentrations of ethanol. This evaluation was used to select the most suitable isolate for the hydrolysis, saccharification and fermentation process. The inoculums were prepared by transferring colonies from YPD cultures with 24 h of incubation, into 10 mL sterile distilled water. The inoculums were incubated at 32 ± 2°C until the standard McFarland turbidity pattern (bioMerieux, Lyon, France) reached a value of 3.

Meanwhile, plugs of 1 cm diameter from a 5-days old PDA (BD Difco Potato-dextrose agar, Becton-Dickinson & Co., Sparks, MD, USA) culture with *T. hirsuta* (RT-1) were added into a 5% (w/v) solution of RSF, and where then it was incubated at 32 ± 2°C for 7 days. α-amylase and laccase activity were determined from the fungal inoculum.

2.3.1 Amylolytic capacity

The amylolytic capacities of the native isolates were tested into 16 mm tubes containing 4.5 mL soluble starch solution (0.5% (w/v) Sigma-Aldrich) with the addition of 0.5 mL of BD Difco Nitrogen Base solution (6.7g DNB/100 mL distilled water) (Wickerham, 1951). The tubes were inoculated with 0.1 mL of the inoculum, and incubated for two weeks at 32 ± 2°C. Subsequently, two drops of Lugol solution were added to each tube to evaluate starch hydrolysis according to the color change of the reagent; from dark violet to: a) to pale yellow, meaning complete hydrolysis; b) to light violet or reddish tones, meaning partial hydrolysis; and c) without color change, indicating there was no hydrolysis.

Meanwhile, *T. hirsuta* RT-1 amylolytic capacity was tested following the same procedure described above. The tubes were inoculated with a 6 mm plug from a 5-day old PDA culture and incubated for seven days at 32 ± 2°C. Starch hydrolysis was evaluated with Lugol´s solution as described above.

2.3.2 Temperature tolerance

Yeast isolates thermotolerance was evaluated in YPD broth incubated at 32, 37, 40, 42, and 45°C, as describe by Kurtzman *et al* (2011). Growth was evaluated by turbidity.

For the *T. hirsuta* RT-1 thermotolerance assay, a 1 cm diameter plug (obtained from a 5-day PDA culture incubated at 32 ± 2°C), was inoculated in the center of RSF agar plates (15 g RSF; 20 g of agar for one liter of the medium) and incubated at 32, 35, 38 and 41°C for seven days. Growth was assessed by measuring the diameter (crosswise) of the colony with a digital vernier.

2.3.3 Ethanol tolerance

The yeast ethanol tolerance was determined in accordance with Lachance (1995), using a liquid medium. Aliquots of cell suspension of each isolate yeast (0.5 mL) were inoculated in 5 mL YM broth (BD Difco) supplemented with glucose at 8% (w/v) and absolute ethanol (3-12% (v/v) with serial increments of 1%. Then they were incubated at 30°C for 24 h. The growth was determined by turbidity.

T. hisuta RT-1 ethanol tolerance was tested as described above but on YM agar plates, instead of YM broth, supplemented with 8% (w/v) glucose. Warm ethanol at 3% (v/v) was added to the agar plate and then a plug of 1 cm diameter of a 5-day old PDA culture with the fungus was inoculated and incubated at 32 ± 2°C for 9 days. The procedure was repeated with subsequent 1% serial ethanol concentration increments, until no mycelial growth was observed.

2.4 Kinetics of direct reducing sugars release by T. hirsuta RT-1

A suspension of RSF at 14% (w/v) was prepared in a sterilized Erlenmeyer flask, then it was inoculated with two plugs of 1 cm diameter from a 5-day old PDA with *T. hirsuta* RT-1 culture. The flask was incubated for 14 days at 32 ± 2º C. An aliquot of 1 mL was sampled every two days from day 0 to day 14, to evaluate starch hydrolysis by quantifying the glucose released using the reducing sugar method proposed by Miller (1959). The samples were also used to quantify the α-amylase and laccase activity.

2.4.1 α- amylase activity of T. hirsuta RT-1

α-amylase activity was evaluated following the methodology in Ahmed et al (2018), with modifications. The analysis was conducted by mixing soluble starch at 1% (w/v) and the sample obtained from section 2.4 in a proportion of 1:1. The mix was diluted using a sodium acetate buffer (0.1 M, pH 5.0). The mix solution was incubated at 40°C for 20 min, then, it was cooled down to 4°C to stop the reaction. Enzyme activity was quantified by measuring the total reducing sugars released from starch hydrolysis with the Miller DNS procedure (1959). The increment in reducing sugar content indicates that the starch was hydrolyzed by *T. hirsuta* RT-1.

2.4.2 Laccase activity of T. hirsuta RT-1

Laccase activity was evaluated using the method described by Johannes and Majcherczyk (2000). The oxidation of ABTS was measured at 420 nm absorbance. The amount of enzyme was expressed as U/mL, one enzyme unit (U) being defined as the

amount of enzyme required to oxidize 1μmol of ABTS per min under assay conditions.

2.5 *Bio-saccharification and fermentation strategy*

Bio-saccharification procedure was performed in 250 mL Erlenmeyer flasks containing 100 mL of RSF sterile suspension at 14% (w/v) inoculated with two 1 cm-diameter plugs obtained from a 5-day old PDA with *T. hirsuta* RT-1 culture. The flasks were incubated in static conditions at 32 ± 2°C for 8 days. Then the fungal mycelium was removed manually, and the flasks were subsequently shaken at 150 rpm for 24 h in a Scorpion Scientific incubator (Model A52101A0, Mexico). A 1 mL sample was taken to determine glucose concentration by HPLC analysis.

Fermentation was induced by adding 1 mL of the *C. tropiclais* PL-1 inoculum (1 x 10^6 cells/mL) to each flask. The assessment of cell viability was conducted by measuring the quantity of cells using a Neubauer chamber, while discrimination between living and dead cells was facilitated using methyl blue. The flasks with the sample and the yeast inoculum were incubated under static semi-anaerobic conditions, at 32 ± 2°C for six days. Throughout the process, aliquots were taken daily to determine glucose consumption by HPLC analysis (described in analytical methods). The fermentation product was centrifuged at 4000 rpm for 20 min to remove solids, then 25 mL of the supernatant was diluted with 25 mL of water and distilled at 100°C until 25 mL of distillate were recovered. Ethanol concentration was quantified using a Gas Chromatograph (described below).

2.6 *Analytical methods*

Glucose analysis by HPLC (Agilent 1260 Infinity II Manual Injector, Santa Clara, USA), was performed using a Zorbax carbohydrate column 4.6 x 250 mm x 5μ (Agilent). The mobile phase was composed of acetonitrile and water (in a ratio of 75:25), and the flow rate was 2 mL/min at 40°C. The detector (RI) was at 35 °C. The injection volume was 20 μL. Glucose standard (CAS 50-99-7, Chem Service Inc., West Chester, PA, USA), was employed to perform a calibration curve.

Ethanol concentration was analyzed using Gas Chromatography (Perkin Elmer Clarus 500 model, Waltham, MA, USA) with a flame ionization detector (FID) and an EC-WAX 30 m x 32 mm x 0.25 μm column (Alltech Grace, Columbia, MA, USA). The carrier gas was nitrogen (N_2) at 7 psi and a 20 mL/min split; the injection temperature was of 120°C and 200°C for FID; and sample volume was of 2 μL.

2.7 *Fermentation conversion yield*

Theoretically 1 g starch equals 1.11 g glucose. Considering 0.511 as the conversion factor of glucose to ethanol, the theoretical yield of ethanol (Gronchi *et al*., 2019) is calculated as follows:

$$Theoretical\ ethanol\ yield\ (g) = \frac{(g\ starch \times 1.11\ glucose)}{1\ g\ starch} \times 0.511 \quad (1)$$

Fermentation efficiency was calculated following this equation:

$$Fermentation\ efficiency\ \% = \frac{ethanol\ produced\ (\frac{g}{l})}{theoretical\ ethanol\ yield\ (g/l)} \times 100 \quad (2)$$

3 Results and discussion

3.1 *Physiological characterization, molecular identification and phylogenetic analysis of the yeast isolate*

The identification of the four native yeasts, *C. tropicalis* PL-1, *P. kudriavzevii* TL-1, *H. guilliermondii* TL-2 and *M. caribbica* RSL-3, was corroborated by base pair sequence analysis of the D1/D2 Domain LSU 26S rDNA. The consensus sequences were aligned against the GenBank database and registered with accession numbers OM743847 (PL-1), OM743848 (TL-1), OM743849 (TL-2), and OM743850 (RSL-3). The native fungal strain RT-1 was identified as *Trametes hirsuta* by sequence of the ITS-5.8S region, and its GenBank accession number is OM732416.

Based on the D1/D2 Domain LSU 26S rDNA sequences of the native yeasts, their phylogenetic relationships were inferred by constructing a tree using the Neighbor-joining method (Figure 1). The four yeasts isolates are grouped into three clades (I, II and III) depending on their genetic relations.

Isolate PL-1 clustered with *Candida tropicalis* sequences; RSL-4 grouped with *Meyerozyma caribbica*; TL-2 with *Pichia kudriavzevii* and finally TL-3 with registered sequences in the GeneBank of *Hanseniaspora guillermondii*. It is worth mentioning that the isolates PL-1 and RSL-4 are the closest in terms of genetics, since they share clade I, which in turn is divided into two subclades (Ia and Ib) with 100% branch support. On the other hand, *P. kudriavzevii* (TL-2), is grouped far from the yeasts previously mentioned, and from *H. guilliermondii* (TL-3), in clade III. This last one is very distant genetically from the rest of the yeasts analyzed. The high support of each clade mentioned confirms their genetic relations.

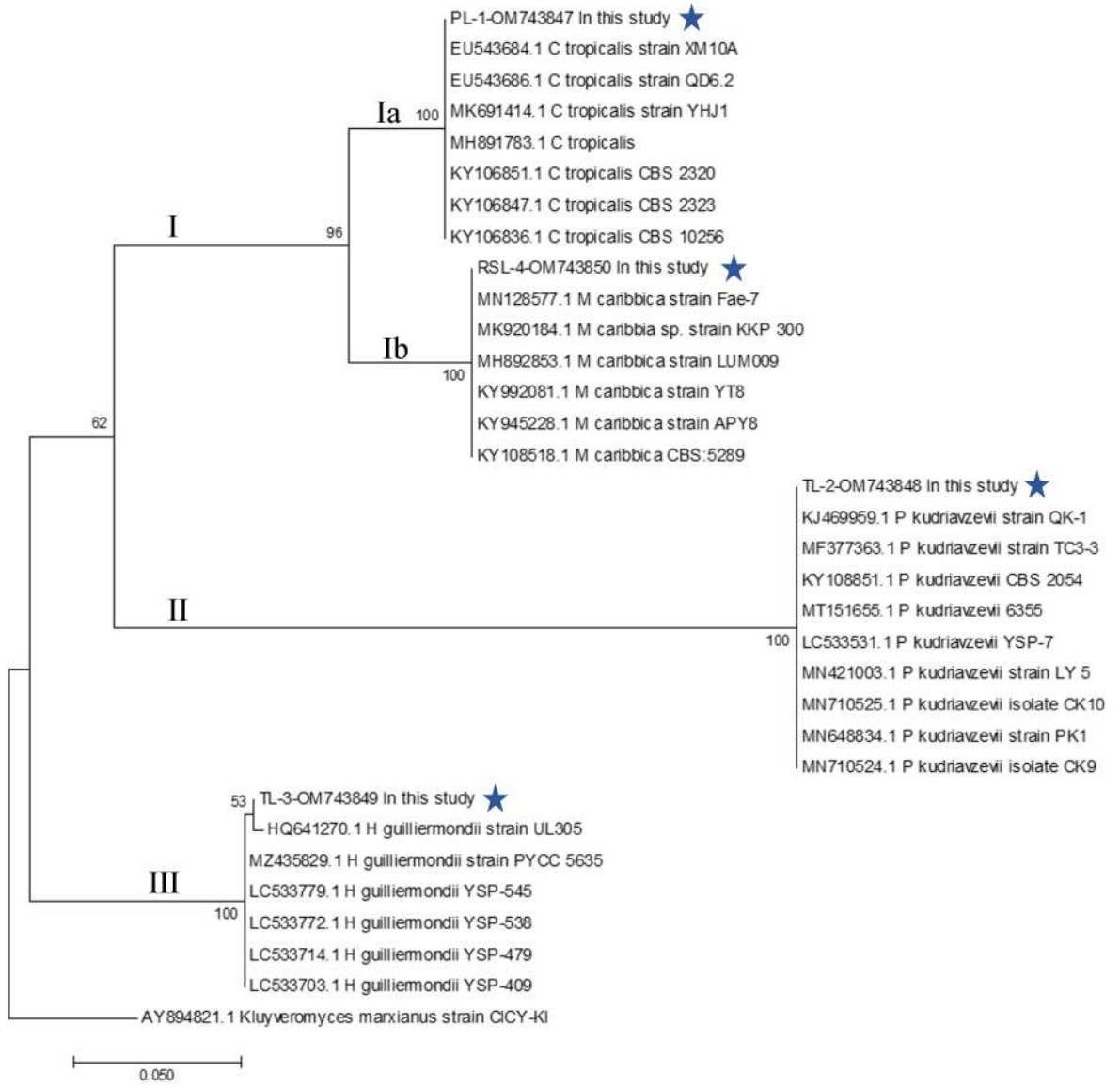

Fig. 1 Phylogenetic tree based on Neighbor Joining method analysis of the 26S rDNA D1/D2 domain of all yeast strains studied. GenBank accession numbers are indicated. The number in each node indicates the boostrap support. *Kluyveromyces maxianus* was the out-group.

Although all yeasts were isolated from ramon fruit, great genetic diversity can be observed among them. For example, *P. kudriavzevii* is a typical endophytic yeast associated with fruits (Matos *et al*., 2021). It has been associated with blossom and ripened apples, pears, and plums in southwest Slovakia (Vadkertiová *et al*., 2012). It is also have been isolated from a variety of niches such as soil samples from fruit gardens, agricultural farms and sugarcane factories (Phong *et al*., 2019). It is known as a typically thermal and furfural-tolerant yeast (Kurtzman *et al*., 2011).

Candida spp. is an indigenous yeast that is commonly found in natural or deliberate alcoholic fermentation. It has the ability to tolerate high concentrations of alcohol (Koulougliotis & Eriotou, 2016). *Candida tropicalis* has been isolated from different sources, including the primary juices of a distillery in Cuba, soil samples from a zoo's gardens in India (Mattam *et al*., 2016), and Moroccan olive-mill wastewater and traditional bread dough (Jamai *et al*., 2001).

Meyerozyma caribbica, was described as *Pichia caribbica*, to distinguish from *P. guilliermondii* (Vaughan-Martini *et al*., 2005). The yeasts isolated from sugar cane in Cuba, was named *Caribbica*. Further analysis repositioned it in a new genus, currently named *Meyerozyma* (Kurtzman & Suzuki, 2010). *M. caribbica* was also reported as a prevalent species in the natural wet fermentation of coffee fruits and beans in Brazil (Evangelista *et al*., 2015) and

Table 1. GeneBank accession numbers for the yeast isolates from *B. alicastrum*.

Isolate code	Accession numbers GeneBank	Species	Closed relative by BLAST	Sequence similarity similarity
PL-1	OM743847.1	*Candida tropicalis*	KY106836.1*(C. tropicalis)*	100 %
TL-2	OM743848.1	*Pichia kudriavzevii*	KY108851.1 *(P. kudriavzevii)*	100 %
TL-3	OM743849.1	*Hanseniaspora guilliermondii*	HQ641270.1*(H. guilliermondii)*	99 %
RSL-4	OM743850.1	*Meyerozyma caribbica*	KY108518.1*(M. caribbica)*	100 %

in *Mangifera indica* in Mexico (Bautista-Rosales *et al*., 2011). This species is therefore found worldwide and in cosmopolitan habit (Matos *et al*., 2021). Additionally, *M. caribbica* is known as a non-toxic yeast that has been used to produce the alcoholic beverage tequila in Mexico (Saucedo-Luna *et al*., 2011).

H. guilliermondii has been isolated from Douro grape musts (Albergaria *et al*., 2003). In other study, grape must, beer wort, grapes skin, and water-cured olives were processed to isolate *H. guillermondii*, a yeast specie which is added to enhance the aromatic profile of beer in mixed-culture fermentation with *Saccharomyces cerevisiae* (Bourbon-Melo *et al*., 2021).

The GenBank accession numbers of each sequence are listed in Table 1. These rDNA sequences constitute the first record of yeasts isolated from the fruit of the *Brosimun alicastrum* tree with the ability to hydrolyze starch.

3.2 Amylolytic capacity

The amylolytic capacity evaluated showed that all yeasts reacted as the control, and only the test tube containing *Candida tropicalis* (PL-1) exhibited a violet color indicating partial breakdown of starch (Figure 2). This confirms that *C. tropicalis* PL-1 has the capacity to synthesize glucoamylase in order to hydrolyze starch. Jamai *et al*. (2007) reported that *C. tropicalis* is a potentially useful organism for the commercial production of ethanol as it is capable of fermenting starch at a low rate (Cholis & Chanson, 2019). In this respect, *Candida* has been reported among the best producers of glucoamylases (α-1, 4-glucan glucohydrolase E.C. (3.2.1.3)), an enzyme that hydrolyzes α-1,4 glycosidic bonds from the non-reducing ends of starch, resulting in the production of glucose which can be further fermented to ethanol (Hostinová & Gašperík, 2010).

Filamentous fungi have been used as the source of glucoamylases for industrial purposes (Hostinová & Gašperík, 2010). In particular, basidiomycete fungi, such as *T. hirsuta*, synthetize α-amylase and glucoamylase (Jamai *et al*., 2007). Thus, it can directly ferment starch, wheat bran and rice straw to ethanol without acid or enzymatic hydrolysis (Okamoto *et al*., 2011). Olguin-Maciel *et al*. (2019), reported *T. hirsuta* (Bm-2) use in production of bioethanol in a consolidated bioprocess. In this study *T. hirsuta* RT-1 showed amylolytic activity through changes in coloration during the time of analysis (Figure 3), which went from a blue-purple color to light purple on the 4th day. However, by the 7th day the coloration had disappeared, confirming the saccharification capacity of starch. This color variation is a consequence of a reduction in the starch chain length related with α-amylase action (Visvanathan *et al*., 2020).

The color of the starch-iodine complex depends on the size of the amylose chain, and is colorless with less than 20 glucose units, red-violet (DP 30-38), blue-violet (DP 39-46) or blue (DP $\geq$ 47) (Visvanathan *et al*., 2020). These results are in accordance with other reports on the amylolytic capacity of *T. hirsuta* Bm-2 (Carrillo-Nieves *et al*., 2020; Olguin-Maciel *et al*., 2019; Zhang *et al*., 2020).

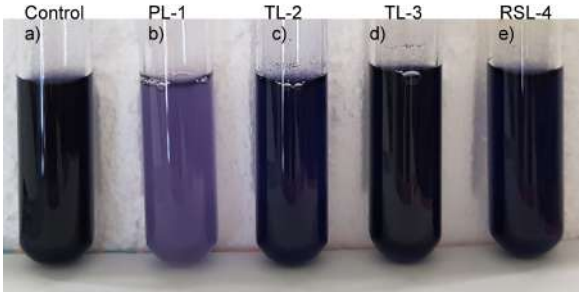

Fig. 2 Soluble starch hydrolysis of native yeasts strains: a) control; b) *Candida tropicalis* PL-1, c) *Pichia kudriavzevii* TL-2, d) *Hanseniaspora guilliermondii* TL-3 y e) *Meyerozyma caribbica* RSL-4.

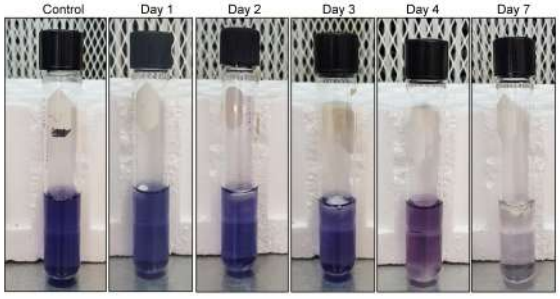

Fig. 3 Soluble starch hydrolysis of *T. hirsuta* RT-1.

3.3 Temperature tolerance

Use of thermotolerant yeasts to obtain ethanol offers several advantages, such as, high yields in

Table 2. Termotolerance of yeast strains to grow at different temperatures.

Yeast strains	32 °C	37 °C	40 °C	42 °C	45 °C
C. tropicalis PL-1	+ + +	+ + +	+ + +	+ + +	-
Pichia kudriavzevii TL-2	+ + +	+ + +	+ +	++	-
Hanseniaspora guilliermondii TL-3	+ + +	+ + +	+ +	-	-
Meyerozyma caribbica RSL-4	+ + +	+ +	-	-	-

+++good growth; ++ moderate growth; + weak growth; - no growth.

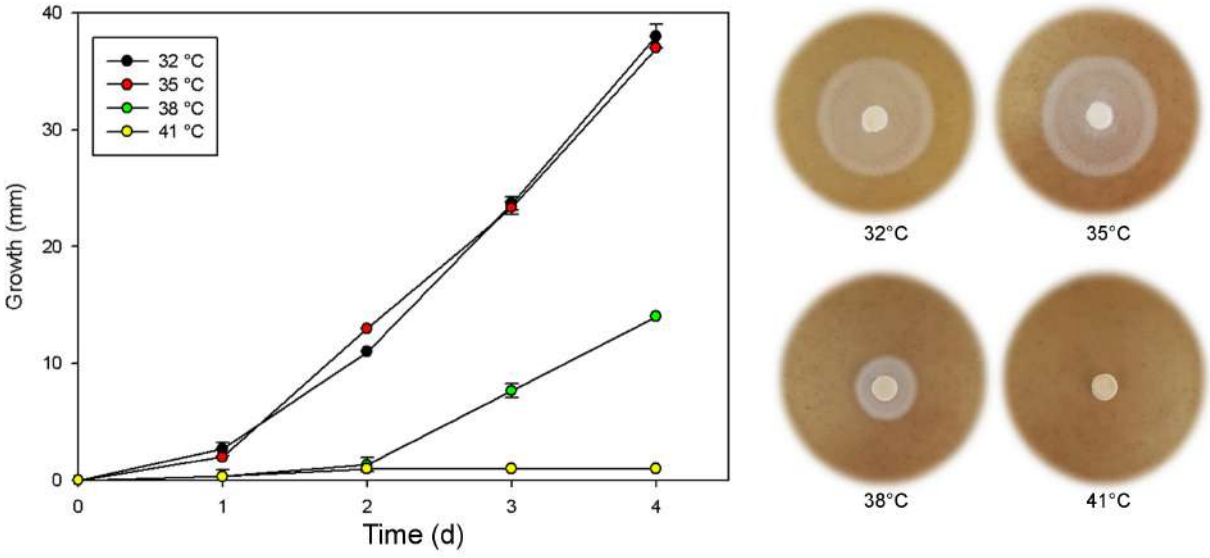

Fig. 4 *T. hirsuta* RT-1 strains tolerance to grow at different temperatures.

saccharification and fermentation products, decreased energy requirement for product recovery and a reduction in cooling costs (Arora *et al*., 2015). Therefore, the screening of yeasts that can sustain growth under a variety of inhibitory conditions e.g., high osmolality, high ethanol concentration, and/or elevated temperatures (>40°C) (Caspeta & Nielsen, 2015), is a priority. In this study, the isolates evaluated showed good growth at 32°C, although as temperature increased yeast resistance diminished. This is the case of *H. guilliermondii* TL-3 and *M. caribbica* RSL-4. *C. tropicalis* PL-1 and *Pichia kudriavzevii* TL-2 displayed good and moderate growth from 32°C up to 42°C (Table 2).

Candida species are considered strong candidates for heat and ethanol tolerance (Kadam & Schmidt, 1997). *C. tropicalis* in particular is useful for ethanol production from starch and lignocellulosic biomass through its cellulase activity (Cholis & Chanson, 2019; Tolieng *et al*., 2018). This species exhibits a lower glycolytic flux and higher oxygen consumption i.e. a Crabtree negative effect, compared with *S. cerevisiae* (Jamai *et al*., 2007). *C. tropicalis* tolerance to 42°C, has not been reported before. This tolerance is well-suited for simultaneous saccharification and fermentation of hemicellulose that occur at a temperature higher than 40°C (Jamai *et al*., 2001). On the other hand, *P. kudriavzevii* is well-known thermotolerant yeast specie that showed good growth at 42° C. Although the highest yields at temperatures over 40°C and low yield of ethanol at 28°C have been reported (Matos *et al*., 2021). In particular, the CM4.2 strain of *P. kudriavzevii* produced the highest ethanol concentration, volumetric ethanol productivity, and ethanol yield with a relatively high fermentation efficiency at 37, 40, and 45°C compared to *Saccharomyces cerevisiae* (Phong *et al*., 2019). *M. caribbica* RSL-4 does not tolerate high temperatures. However, others such as CC003 of *M. caribbica* is a promissing fermenter for alcoholic beverages. Although not tolerant to high temperatures, it is osmotolerant and exhibits high ethanol yield (Matos *et al*., 2021). MJTm3 of *M. caribbica* demonstrated remarkable stress tolerance and fermentative activity in sugarcane molasses at 45°C (Hawaz *et al*., 2023). As for *H. guillermondi*, there was not reported tolerance to heat.

In a consolidated bioprocess, thermophilic enzymes and yeasts are often added at the same time to ensure simultaneous saccharification and fermentation of cellulosic biomass to ethanol. Reducing the use of saccharifying enzymes is essential to lowering the process costs. (Tanimura *et al*., 2015).

Table 3. Yeast isolates growing at different ethanol concentrations.

Yeast	Ethanol concentrations (%)					
	3-4	5-6	7-8	9	10-11	12
Candida tropicalis PL-1	+ + +	+ +	+	-	-	-
Pichia kudriavzevii TL-2	+ + +	+ +	+ +	+ +	+	-
Hanseniaspora guilliermondii TL-3	+ + +	+ +	+ +	+ +	+	-
Meyerozyma caribbica RSL-4	+ + +	+ +	+ +	+ +	+	-

+++good growth; ++ moderate growth; + weak growth; - no growth.

Similarly, the fungus was evaluated to determinate its thermotolerance. *Trametes hirsuta*, produces laccase, a multicopper enzyme with different biological functions and biotechnological applications (Zapata-Castillo *et al*., 2015). The temperature of incubation (around 35-40°C) plays a key role in laccase, lignin peroxidase and Mn-peroxidase production (Krumova *et al*., 2018).

Specifically, *T. hirsuta* grows as temperature is increased. Although it has been reported that it can grow from 12-42°C, its maximum biomass production was achieved at 35°C (Krumova *et al*., 2018). In this study *T. hirsuta* RT-1 showed an optimum growth at 32°C. Temperatures higher than this cause mycelium development to start to diminish and disappear as temperatures increase (Figure 4). Different species from the *Trametes* genus have shown optimal growth at temperatures between 30 and 40°C (Magan, 2008). That is why the optimum temperature for *T. hirsuta* RT-1 growth was chosen to carry out further experiments and the sequential saccharification and fermentation.

3.4 Ethanol tolerance

Ethanol accumulation in the culture broth could affect yeast performance. The yeasts species tolerance to growth in different ethanol concentrations indicated all yeasts enjoy good growth at 3-4 % (v/v) of ethanol (Table 3). However, as ethanol concentration increased, the growth began to diminish.

As mentioned above, all the native yeasts isolated in this study showed good growth at 3-4% ethanol (v/v). However, as ethanol concentrations increased the growth began to diminish from moderate, to weak, and then negative.

In the case of PL-1 isolates, growth ceased at concentrations of 7-8 % (v/v) of ethanol. For the rest of the yeasts, growth ceased at concentrations of 10-11% of ethanol (v/v).

Each yeast species has a different capacity to tolerate, grow in and/or survive in the presence of ethanol (Snoek *et al*., 2016). It has been reported that *C. tropicalis* KPC isolated from sugarcane field soil in Thailand, and *C. tropicalis* KKU-105, isolated from northern Thailand, can tolerate ethanol concentrations up to 20% and 10% (v/v), respectively (Pongcharoen & Kawano-Kawada, 2018), which contrast with the 8% (v/v) tolerated by *C. tropicalis* PL-1.

The yeast isolates *P. kudriavzevii* TL-2, *M. caribbica* RSL-4 and *H. guilliermondii* TL-3 tolerated 11% (v/v) ethanol. However, there are reports in the literature of several strains of the above-mentioned species with a higher ethanol tolerance. In 2017, Techaparin *et al*. (2017) reported that the strains KKUTH33 and KKUTH43 isolated from the northeastern region in Thailand tolerated up to 13% (v/v) ethanol, the same tolerance was reported by Pongcharoen (2022).

The fungus *T. hirsuta* RT-1 was expected to have a similar ethanol tolerance to that reported by Olguin-Maciel *et al*. (2019) for *T. hirsuta* Bm-2, which exhibited a vigorous growth at 10% (v/v) ethanol and fermentative capacity, due to the capacity of some basidiomycetes to synthesize the alcohol dehydrogenase enzyme. However, the RT- 1 strain presented a low ethanol tolerance as the mycelium growth was minimal at 3% (v/v). For this reason no further experiments were done. A similar behavior was seen by Paschos (2015), who observed that biomass and growth rate of *F. oxysporum* in aerobic conditions diminished in the presence of ethanol (1-6% w/v). The results of this experiment implied that the RT-1 isolate will only take part in the saccharification process of the RSF and that the fermentation would be carried out by the PL-1 isolate, which was chosen through the tests of characterization, principally the amylolytic capacity and ethanol tolerance.

3.5 Direct reducing sugars release kinetics, α- amylase and laccase activity of T. hirsuta RT-1

The amylolytic capacity of *T. hirsuta* RT-1 was measured and is shown in Figure 5; the highest concentration of reducing sugars (RS) was 28.95 ± 2.17 g/L and was recorded on day 9. This result is comparable to the one reported by Olguín *et al*. (2019) with *T. hirsuta* Bm-2 strain, which was 30 g/L on day 8. The α-amylase activity was already detectable before inoculating *T. hirsuta* RT-1 as seeds have enzymes like α or β–amylases. After the addition of fungus the activity increased due to the induction of the enzyme by starch or its hydrolytic products such as maltose, which are present in the RSF (Gupta *et al*., 2003; Saranraj & Stella, 2013).

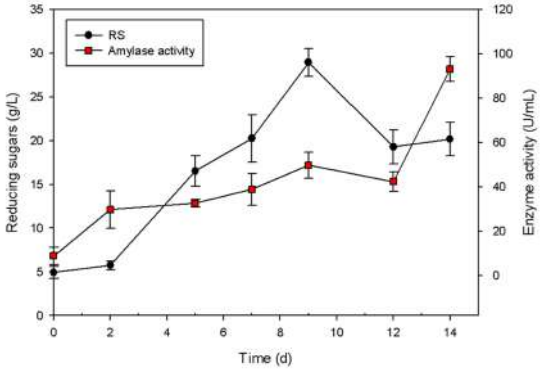

Fig. 5 Direct reducing sugars release kinetics and α-amylase activity of *T. hirsuta* RT-1 strain.

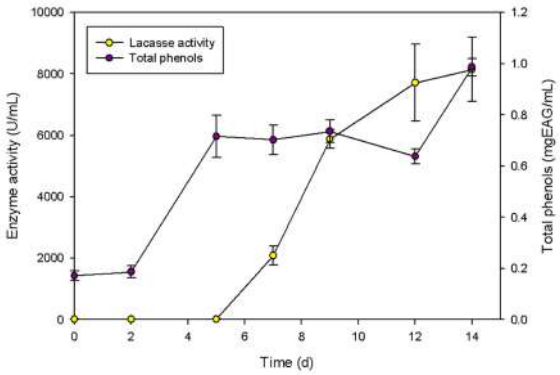

Fig. 6. Lacasse activity of *T. hirsuta* RT-1 and total phenols concentration.

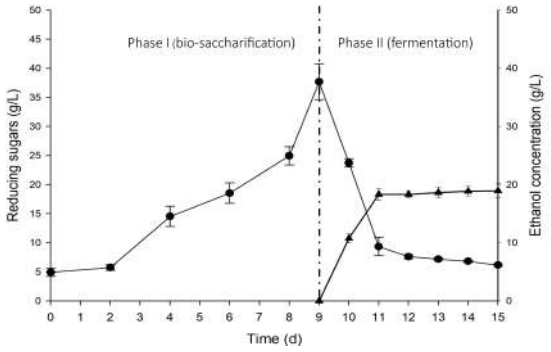

Fig. 7 Consolidated bio-saccharification and fermentation of ramon seed flour (RSF) by *T. hirsuta* RT-1 and *C. tropiccalis* (PL-1) strains.

The production of α-amylase agrees with Pervez *et al*. (2014), who mentioned that amylase from fungal sources was normally produced after 3 to7 days of incubation. The first major activity of the enzyme was on day 9, with 49.77 ± 7.54 U/mL. The increase in reducing sugars (RS) was simultaneous. After that, the activity dropped, probably due to the glucose concentration, because it functions as a catabolic repressor for the enzyme synthesis and once the fungus had consumed the glucose, the enzyme activity increased up to 93.15 ± 6.35 U/mL. In comparison to the result of 135 U/mL reported by Olguin *et al*. (2019) for Bm-2 isolate in the same substrate, RT-1 displayed less enzyme activity, establishing a metabolic difference within the same species. This contrast between the strains occurs as a result of variations in the production and specificity of the enzymes towards the starch, amylose and amylopectin of each microorganism, even among the same genera and species of isolate origin (Gopinath *et al*., 2017; Gupta *et al*., 2003).

The laccase enzyme is a multicopper oxidases which plays an important role in the degradation of lignin (Shraddha *et al*., 2011), and thus it can participate in saccharification by depolymerization of lignin or fibroproteic matrix, making starch granules of RSF susceptible to α-amylase. The maximum laccase activity of 8,920 ± 1,236 U/mL was achieved on day 14th (Figure 6) and was associated with diminishing total phenols. The phenolic compounds in RSF are found as gallic acid, ρ-hydroxybenzoic acid, vanillic and caffeic acid, ρ-coumaric acid and chlorogenic acid. Similary to RT-1, *T. hirsuta* Bm-2 laccase enzyme activity was induced in the presence of vanillic acid (Tapia-Tussell *et al*., 2015). To explain the laccase action, it was assumed that hydrolytic enzymes of proteins, lipids and carbohydrates produced by *T. hirsuta* RT-1 release the phenolic compounds since they are also associated with simple or complex carbohydrates, lipids and fiber (Quirós-Sauceda *et al*., 2014).

3.6 Bio-saccharification and fermentation strategy

As shown in figure 7, the biosaccharification and fermentation process of RSF results in an increase in reducing sugars content (35 ± 3.32 g/L) until the 9th day; additionally, the reduction in the viscosity of the biomass was observed. This is a strong indicator of that *T. hirsuta* RT-1 was producing a mixture of α-amylase (EC 3.2.1.1) and glucoamylase (EC 3.2.1.3), two enzymes responsible for hydrolysis of starch into glucose units (Cripwell *et al*., 2020).

It is worth mentioning that the glucose concentration increased from 24.89 ± 0.81 g/L under static conditions to 37.78 ± 1.24 g/L after agitation. This increment is probably due to hydrolysis of RSF by *T. hirsuta* RT-1. This effect on glucose concentration might be due to the low agitation speed, which allowed the production and activity of amylases that improved enzyme homogenization, substrate-enzyme interactions, and distribution of nutrients and oxygen within the bioreactor (Henshaw & Wakil, 2019; Roldan-Cruz *et al*., 2021). This increment in glucose concentration after agitation had already been reported by Farid *et al*. (2002). At 200-300 rpm the greatest quantity of glucose was produced, and at 150-200 rpm, α-amylase and glucoamylase enzymes. The

effects of mechanical agitation on α-amylase enzyme activity, are not fully understood. It has already been reported that agitation at high speed denaturalizes the enzyme structure, affecting its activity (Henshaw & Wakil, 2019; Roldan-Cruz *et al*., 2021; Rousset & Schlich, 1989; Sivaramakrishnan *et al*., 2006). Another factor to consider is that optimum fungal growth conditions must be similar to those of amylase production, in order to obtain the maximum yield (Rousset & Schlich, 1989).

At the end of saccharification by *T. hirsuta* RT-1, *C. tropicalis* PL-1 was added to the same flask for the start-up of the fermentation phase, with a glucose concentration of 39 ± 3.27 g/L. The sugar intake and ethanol production (Figure 7, phase II), indicated that *C. tropicalis* PL-1, consumed 93% of glucose and produced 18.93 ± 1.78 g/L of ethanol. Thus, the fermentation efficiency was of 95 %. The initial and final pH were 5.45 and 4.60, respectively.

It was observed that the highest glucose consumption occured during the first two days, and the highest ethanol production was also detected at the same time. On the 3rd day, glucose consumption and ethanol production reached a plateau.

In this context, the ideal fermentation time is between 48 and 72 h, since the ethanol production decreases as the fermentation time increases from 72 h to 96 h (Zabed *et al*., 2017).

It is possible that the viability of *T. hirsuta* RT-1, was affected by its low ethanol tolerance. Although more studies are needed to determinate its effect on fungus during the fermentation process, the mycelium it is a suitable source of nutrients (proteins and polysaccharides) for yeast. Romano *et al*. (2006) reported that some species of *Candida* presented proteolytic, glycosidic and pectinolytic activity, which should be evaluated in *C. tropicalis* PL-1.

In the sequential biosaccharification and fermentation strategy, 18.93 ± 1.78 g/L of ethanol was produced, which is less than the 37.76g/L that was reported by Olguin *et al*. (2019) for RSF using a separate hydrolysis and fermentation with *C. tropicalis* PL-1. However, the ethanol production in this study was higher than the ethanol concentration reported by the same authors (13g/L) in a consolidated bioprocess (CBP) with the same raw material and the native isolate *T. hirsuta* Bm-2.

The simultaneous biosaccharification and fermentation process is a suitable solution for CBP drawbacks, by finding the optimal conditions within a single reactor for hydrolytic enzyme secretion, saccharification, and fermentation. The low biosaccharification rate may affected the sequential process for ethanol production, and improvements in fermentation will be required, considering that it can be affected due multiple factors, such as heat and ethanol stress, nutrient deficiency, sugar concentration, and viscosity in the medium, among others.

Some benefits of this strategy are the direct production of amylase enzymes by the fungus RT-1, which allows for hydrolysis without using commercial enzymes. This leads to a reduction in the ethanol production costs, as well as a reduction in the probability of contamination, since the entire process is carried out in a single reactor. On the other hand, as part of the search for a sustainable process, a value-added compound is obtained, namely a fungal biomass with high protein content, that can be used as a food supplement for animals.

Conclusions

The identification of native microorganisms with biotechnological potential can help in the production of second-generation biofuels from starchy biomass due to their natural adaptation to the raw material, which could improve the yields of liquefaction, hydrolysis and fermentation, thus making the process more profitable. Their genetic and biochemical identification allowed for the proper selection of the most suitable biological specimens for bio saccharification and sequential fermentation. The organisms selected for the CBS were the basidiomycete *T. hirsuta* RT-1 and the yeast *C. tropicalis* PL-1. The fungus displayed low ethanol tolerance, which restricted its role to the bio saccharification phase. While PL- 1 was used for fermentation, reaching a conversion of 95% of the fermentable sugars into bioethanol, bioethanol production in the CBS was 18.93 ± 1.78 g/L. It is important to point out that the process was carried out in a single reactor and no reagents or commercial enzymes were used, which could make bioethanol production more sustainable. Further studies can be focused on the enhancement of saccharification and fermentation, on the identification of extracellular enzymes, and on the interaction of the fungus (*T. hirsuta* RT-1) with the yeast (*C. tropicalis* PL-1). During the CBS, in addition to amylase production, starch hydrolysis and fermentation, a laccase enzyme was obtained that can help in the bioconversion of lignocellulosic biomass, making the entire process a novel opportunity to develop a biorefinery approach for the exploitation of ramon seed and other feedstocks.

Acknowledgements

This work was supported by fellowship 714326 from the National Council for Humanity Science and Technology (CONAHCYT) of Mexico.

References

Ahmed, S. A., Mostafa, F. A., & Ouis, M. A. (2018). Enhancement stability and catalytic activity of immobilized α-amylase using bioactive phospho-silicate glass as a novel inorganic support. *International Journal of Biological Macromolecules*, 112, 371–382.

Albergaria, H., Torrão, A. R., Hogg, T., & Gírio, F. M. (2003). Physiological behaviour of *Hanseniaspora guilliermondii* in aerobic glucose-limited continuous cultures. *FEMS Yeast Research*, 3(2), 211–216.

Arora, R., Behera, S., & Kumar, S. (2015). Bioprospecting thermophilic/thermotolerant microbes for production of lignocellulosic ethanol: a future perspective. *Renewable and Sustainable Energy Reviews*, 51, 699–717.

Barnett, J. A., Payne, R. W., & Yarrow, D. (1990). Yeasts: characteristics and identification.

Bautista-Rosales, P. U., Servín-Villegas, R., Calderón-Santoyo, M., & Ragazzo-Sánchez, J. A. (2011). Control biológico de *Colletotrichum* sp. utilizando levaduras antagonistas nativas del mango. *3er Congreso Internacional de Biología, Química y Agronomía. Universidad Autónoma de Guadalajara*, AC, Zapopan, Jalisco, México, 1–10.

Bourbon-Melo, N., Palma, M., Rocha, M. P., Ferreira, A., Bronze, M. R., Elias, H., & Sá-Correia, I. (2021). Use of *Hanseniaspora guilliermondii* and *Hanseniaspora opuntiae* to enhance the aromatic profile of beer in mixed-culture fermentation with *Saccharomyces cerevisiae*. *Food Microbiology*, 95, 103678.

Bušić, A., Mardetko, N., Kundas, S., Morzak, G., Belskaya, H., Ivčanić šantek, M., Komes, D., Novak, S., & šantek, B. (2018). Bioethanol production from renewable raw materials and its separation and purification: a review. *Food Technology and Biotechnology*, 56(3), 289–311.

Carrillo-Nieves, D., Saldarriaga-Hernandez, S., Gutiérrez-Soto, G., Rostro-Alanis, M., Hernández-Luna, C., Alvarez, A. J., Iqbal, H. M. N., & Parra-Saldívar, R. (2020). Biotransformation of agro-industrial waste to produce lignocellulolytic enzymes and bioethanol with a zero waste. *Biomass Conversion and Biorefinery*, 1–12.

Caspeta, L., & Nielsen, J. (2015). Thermotolerant yeast strains adapted by laboratory evolution show trade-off at ancestral temperatures and preadaptation to other stresses. *MBio*, 6(4), 10–1128.

Cholis, M., & Chanson, C. (2019). Molecular identification and potential ethanol production of long-term thermo-tolerant yeast *Candida Tropicalis*. *IOP Conference Series: Earth and Environmental Science*, 239(1), 12004.

Cripwell, R. A., Favaro, L., Viljoen-Bloom, M., & van Zyl, W. H. (2020). Consolidated bioprocessing of raw starch to ethanol by *Saccharomyces cerevisiae*: Achievements and challenges. *Biotechnology Advances*, 42, 107579.

Evangelista, S. R., Miguel, M. G. da C. P., Silva, C. F., Pinheiro, A. C. M., & Schwan, R. F. (2015). Microbiological diversity associated with the spontaneous wet method of coffee fermentation. *International Journal of Food Microbiology*, 210, 102–112.

Farid, M. A., El-Enshasy, H. A., & Noor El-Deen, A. M. (2002). Alcohol production from starch by mixed cultures of *Aspergillus awamori* and immobilized *Saccharomyces cerevisiae* at different agitation speeds. *Journal of Basic Microbiology: An International Journal on Biochemistry, Physiology, Genetics, Morphology, and Ecology of Microorganisms*, 42(3), 162–171.

Favaro, L., Jansen, T., & van Zyl, W. H. (2019). Exploring industrial and natural *Saccharomyces cerevisiae* strains for the bio-based economy from biomass: the case of bioethanol. *Critical Reviews in Biotechnology*, 39(6), 800–816.

Ferreira, J. A., Agnihotri, S., & Taherzadeh, M. J. (2019). Waste biorefinery. In *Sustainable resource recovery and zero waste approaches* (pp. 35–52). Elsevier.

Gopinath, S. C. B., Anbu, P., Arshad, M. K. M., Lakshmipriya, T., Voon, C. H., Hashim, U., & Chinni, S. V. (2017). Biotechnological processes in microbial amylase production. *BioMed Research International*, 2017(1), 1272193.

Gronchi, N., Favaro, L., Cagnin, L., Brojanigo, S., Pizzocchero, V., Basaglia, M., & Casella, S. (2019). Novel yeast strains for the efficient saccharification and fermentation of starchy by-products to bioethanol. *Energies*, 12(4), 714.

Gupta, R., Gigras, P., Mohapatra, H., Goswami, V. K., & Chauhan, B. (2003). Microbial α-amylases: a biotechnological perspective. *Process Biochemistry*, 38(11), 1599–1616.

Hall, T. A. (1999). BioEdit: a user-friendly biological sequence alignment editor and analysis program for Windows 95/98/NT. *Nucleic Acids Symposium Series*, 41(41), 95–98.

Hawaz, E., Tafesse, M., Tesfaye, A., Kiros, S., Beyene, D., Kebede, G., Boekhout, T., Groenwald, M., Theelen, B., & Degefe, A. (2023). Optimization of bioethanol production from sugarcane molasses by the response surface methodology using *Meyerozyma caribbica* isolate MJTm3. *Annals of Microbiology*, 73(1), 2.

Henshaw, E., & Wakil, S. M. (2019). Effect of agitation speed and incubation time on amylase production by *Bacillus* species isolated from malted and fermented Maize (*Zea mays*). *Microbiology Research Journal International*, 27(3), 1–7.

Hernández-González, O., Vergara-Yoisura, S., & Larqué-Saavedra, A. (2014). Studies on the productivity of *Brosimum alicastrum* a tropical tree used for animal feed in the Yucatan Peninsula. *Bothalia Journal*, 44(6), 70–81.

Hostinová, E., & Gašperík, J. (2010). Yeast glucoamylases: molecular-genetic and structural characterization. *Biologia*, 65, 559–568.

Huchin Poot, E. G. (2015). Aislamiento de la microbiota del fruto de *Brosimum alicastrum* swartz para su uso en la producción de bioetanol [Tesis de maestría, Centro de Investigación Científica de Yucatán]. Repositorio académico CICY.

Jahangeer, M., Rehman, M. U., Nelofer, R., Nadeem, M., Munir, B., Smułek, W., Jesionowski, T., & Qamar, S. A. (2024). Biotransformation of lignocellulosic biomass to value-added bioproducts: Insights into bio-saccharification strategies and potential concerns. *Topics in catalysis*, 1-22.

Jamai, L., Ettayebi, K., El Yamani, J., & Ettayebi, M. (2007). Production of ethanol from starch by free and immobilized *Candida tropicalis* in the presence of α-amylase. *Bioresource Technology*, 98(14), 2765–2770.

Jamai, L., Sendide, K., Ettayebi, K., Errachidi, F., Hamdouni-Alami, O., Tahri-Jouti, M. A., McDermott, T., & Ettayebi, M. (2001). Physiological difference during ethanol fermentation between calcium alginate-immobilized *Candida tropicalis* and *Saccharomyces cerevisiae*. *FEMS Microbiology Letters*, 204(2), 375–379.

Johannes, C., & Majcherczyk, A. (2000). Laccase activity tests and laccase inhibitors. *Journal of Biotechnology*, 78(2), 193–199.

Kadam, K. L., & Schmidt, S. L. (1997). Evaluation of *Candida acidothermophilum* in ethanol production from lignocellulosic biomass. *Applied Microbiology and Biotechnology*, 48, 709–713.

Kechkar, M., Sayed, W., Cabrol, A., Aziza, M., Ahmed Zaid, T., Amrane, A., & Djelal, H. (2019). Isolation and identification of yeast strains from sugarcane molasses, dates and figs for ethanol production under conditions simulating algal hydrolysate. *Brazilian Journal of Chemical Engineering*, 36(1), 157–169.

Koulougliotis, D., & Eriotou, E. (2016). Isolation and Identification of Endogenous Yeast Strains in Grapes and Must Solids of *Mavrodafni Kefalonias* and Antioxidant Activity of the Produced Red Wine. *Fermentation technology*, 5(1), 1-9.

Krumova, E., Kostadinova, N., Miteva-Staleva, J., Stoyancheva, G., Spassova, B., Abrashev, R., & Angelova, M. (2018). Potential of ligninolytic enzymatic complex produced by white-rot fungi from genus *Trametes* isolated from Bulgarian forest soil. *Engineering in Life Sciences*, 18(9), 692–701.

Kumar, S., Stecher, G., Li, M., Knyaz, C., & Tamura, K. (2018). MEGA X: molecular evolutionary genetics analysis across computing platforms. *Molecular Biology and Evolution*, 35(6), 1547–1549.

Kurtzman, C., Fell, J. W., & Boekhout, T. (2011). The yeasts: a taxonomic study. Elsevier.

Kurtzman, C. P., & Suzuki, M. (2010). Phylogenetic analysis of ascomycete yeasts that form coenzyme Q-9 and the proposal of the new genera *Babjeviella*, *Meyerozyma*, *Millerozyma*, *Priceomyces*, and *Scheffersomyces*. *Mycoscience*, 51(1), 2–14.

Lachance, M.-A. (1995). Yeast communities in a natural tequila fermentation. Antonie Van Leeuwenhoek, 68, 151–160.

Lennartsson, P. R., Erlandsson, P., & Taherzadeh, M. J. (2014). Integration of the first and second generation bioethanol processes and the importance of by-products. *Bioresource Technology*, 165, 3–8.

Losoya-Sifuentes, C., Pinto-Jimenez, K., Cruz, M., Rodriguez-Jasso, R. M., Ruiz, H. A., Loredo-Treviño, A., ... & Belmares, R. (2023). Determination of nutritional and antioxidant properties of Maya Nut flour (*Brosimum alicastrum*) for development of functional foods. *Foods*, 12(7), 1398.

Magan, N. (2008). Ecophysiology: impact of environment on growth, synthesis of compatible solutes and enzyme production. *British Mycological Society Symposia Series*, 28, 63–78.

Matos, Í. T. S. R., de Souza, V. A., D'Angelo, G. do R., Astolfi Filho, S., do Carmo, E. J., & Vital, M. J. S. (2021). Yeasts with Fermentative Potential Associated with Fruits of Camu-Camu (*Myrciaria dubia*, Kunth) from North of Brazilian Amazon. *The Scientific World Journal*, 2021(1), 9929059.

Mattam, A. J., Kuila, A., Suralikerimath, N., Choudary, N., Rao, P. V. C., & Velankar, H. R. (2016). Cellulolytic enzyme expression and simultaneous conversion of lignocellulosic sugars into ethanol and xylitol by a new *Candida tropicalis* strain. *Biotechnology for Biofuels*, 9, 1–12.

Meiners, M., Sánchez-Garduño, C., & De Blois, S. (2009). El ramón: Fruto de nuestra cultura y raíz para la conservación. *Biodiversitas*, 87, 7–10.

Miller, G. L. (1959). Modified DNS method for reducing sugars. *Analytical Chemistry*, 31(3), 426–428.

Okamoto, K., Nitta, Y., Maekawa, N., & Yanase, H. (2011). Direct ethanol production from starch, wheat bran and rice straw by the white rot fungus *Trametes hirsuta*. *Enzyme and Microbial Technology*, 48(3), 273–277.

Olguin-Maciel, E., Larqué-Saavedra, A., Lappe-Oliveras, P., Barahona-Pérez, L., Alzate-Gaviria, L., Chablé-Villacis, R., Domínguez-Maldonado, J., Pacheco-Catalán, D., Ruíz, H., & Tapia-Tussell, R. (2019). Consolidated Bioprocess for Bioethanol Production from Raw Flour of *Brosimum alicastrum* Seeds Using the Native Strain of *Trametes hirsuta* Bm-2. *Microorganism*, 7(483).

Olguin-Maciel, E., Larqué-Saavedra, A., Pérez-Brito, D., Barahona-Pérez, L. F., Alzate-Gaviria, L., Toledano-Thompson, T., Lappe-Oliveras, P. E., Huchin-Poot, E. G., & Tapia-Tussell, R. (2017). *Brosimum alicastrum* as a novel starch source for bioethanol production. *Energies*, 10(10), 1574.

Olguin-Maciel, E., Singh, A., Chable-Villacis, R., Tapia-Tussell, R., & Ruiz, H. A. (2020). Consolidated bioprocessing, an innovative strategy towards sustainability for biofuels production from crop residues: an overview. *Agronomy*, 10(11), 1834.

Ozer, H. K. (2017). Phenolic compositions and antioxidant activities of Maya nut (*Brosimum alicastrum*): Comparison with commercial nuts. *International Journal of Food Properties*, 20(11), 2772-2781.

Paschos, T., Xiros, C., & Christakopoulos, P. (2015). Ethanol effect on metabolic activity of the ethalogenic fungus *Fusarium oxysporum*. *BMC Biotechnology*, 15, 1–12.

Phong, H. X., Klanrit, P., Dung, N. T. P., Yamada, M., & Thanonkeo, P. (2019). Isolation and characterization of thermotolerant yeasts for the production of second-generation bioethanol. *Annals of Microbiology*, 69, 765–776.

Pongcharoen, P. (2022). The ability of *Pichia kudriavzevii* to tolerate multiple stresses makes it promising for developing improved bioethanol production processes. *Letters in Applied Microbiology*, 75(1), 36–44.

Pongcharoen, P., & Kawano-Kawada, M. (2018). Identification and characterization of *Candida tropicalis* isolated from soil of sugarcane plantation in Thailand for ethanol production. *Asia-Pacific Journal of Science Technology*, 23.

Quirós-Sauceda, A. E., Palafox-Carlos, H., Sáyago-Ayerdi, S. G., Ayala-Zavala, J. F., Bello-Perez, L. A., Alvarez-Parrilla, E., De La Rosa, L. A., González-Córdova, A. F., & González-Aguilar, G. A. (2014). Dietary fiber and phenolic compounds as functional ingredients: interaction and possible effect after ingestion. *Food & Function*, 5(6), 1063–1072.

Ramos-Villacob, V., Figueroa-Flórez, J. A., Salcedo-Mendoza, J. G., Hernandez-Ruydíaz, J. E., & Romero-Verbel, L. A. (2024) Development of modified cassava starches by ultrasound-assisted amylose/lauric acid complex formation. *Revista Mexicana de Ingeniería Química*, 23(1), 1-15.

Roldan-Cruz, C., Garcia-Hernandez, A., Alvarez-Ramirez, J., & Vernon-Carter, E. J. (2021). Effect of the stirring speed in the in vitro activity of α-amylase. *Food Hydrocolloids*, 110, 106127.

Romano, P., Capece, A., & Jespersen, L. (2006). Taxonomic and ecological diversity of food and

beverage yeasts. *In Yeasts in food and beverages* (pp. 13–53). Springer.

Rousset, S., & Schlich, P. (1989). Amylase production in submerged culture using principal component analysis. *Journal of Fermentation and Bioengineering*, 68(5), 339–343.

Saranraj, P., & Stella, D. (2013). Fungal amylase—a review. *International Journal of Microbiological Research*, 4(2), 203–211.

Satyanarayana, T. (2009). Yeast biotechnology: diversity and applications. Springer.

Saucedo-Luna, J., Castro-Montoya, A. J., Martinez-Pacheco, M. M., Sosa-Aguirre, C. R., & Campos-Garcia, J. (2011). Efficient chemical and enzymatic saccharification of the lignocellulosic residue from *Agave tequilana* bagasse to produce ethanol by *Pichia caribbica*. *Journal of Industrial Microbiology and Biotechnology*, 38(6), 725–732.

Shraddha, Shekher, R., Sehgal, S., Kamthania, M., & Kumar, A. (2011). Laccase: microbial sources, production, purification, and potential biotechnological applications. *Enzyme Research*, 2011(1), 217861.

Sivaramakrishnan, S., Gangadharan, D., Nampoothiri, K. M., Soccol, C. R., & Pandey, A. (2006). α-Amylases from Microbial Sources--An Overview on Recent Developments. *Food Technology & Biotechnology*, 44(2).

Snoek, T., Verstrepen, K. J., & Voordeckers, K. (2016). How do yeast cells become tolerant to high ethanol concentrations? *Current Genetics*, 62(3), 475–480.

Steensels, J., Snoek, T., Meersman, E., Nicolino, M. P., Voordeckers, K., & Verstrepen, K. J. (2014). Improving industrial yeast strains: exploiting natural and artificial diversity. *FEMS Microbiology Reviews*, 38(5), 947–995.

Suárez-Castillo, G.M., Salcedo-Guadalupe, J.G., Contreras-Lozano, K.P., Rangel-Pérez, M.G., Cervera-Ricardo, M.A., & Figueroa-Flórez, J.A. (2024). Increase in the degree of substitution of cassava starches by dual modification processes. *Revista Mexicana de Ingeniería Química*, 23(3), 1-15.

Tanimura, A., Kikukawa, M., Yamaguchi, S., Kishino, S., Ogawa, J., & Shima, J. (2015). Direct ethanol production from starch using a natural isolate, *Scheffersomyces shehatae*: toward consolidated bioprocessing. *Scientific Reports*, 5(1), 1–7.

Tapia-Tussell, R., Lappe, P., Ulloa, M., Quijano-Ramayo, A., Cáceres-Farfán, M., Larqué-Saavedra, A., & Perez-Brito, D. (2006). A rapid and simple method for DNA extraction from yeasts and fungi isolated from *Agave fourcroydes*. *Molecular Biotechnology*, 33, 67–70.

Tapia-Tussell, R., Pérez-Brito, D., Torres-Calzada, C., Cortés-Velázquez, A., Alzate-Gaviria, L., Chablé-Villacís, R., & Solís-Pereira, S. (2015). Laccase gene expression and vinasse biodegradation by *Trametes hirsuta* strain Bm-2. *Molecules*, 20(8), 15147–15157.

Techaparin, A., Thanonkeo, P., & Klanrit, P. (2017). High-temperature ethanol production using thermotolerant yeast newly isolated from Greater Mekong Subregion. *Brazilian Journal of Microbiology*, 48(3), 461–475.

Tolieng, V., Kunthiphun, S., Savarajara, A., & Tanasupawat, S. (2018). Diversity of yeasts and their ethanol production at high temperature. *Journal of Applied Pharmaceutical Science*, 8(2), 136–142.

Umeh, S. O., Agwuna, L. C., & Okafor, U. C. (2017). Yeasts from local sources: an alternative to the conventional brewer's yeast. *World Wide Journal of Multidisciplinary Research and Development,* 30, 191–195.

Vadkertiová, R., Molnárová, J., Vránová, D., & Sláviková, E. (2012). Yeasts and yeast-like organisms associated with fruits and blossoms of different fruit trees. *Canadian Journal of Microbiology*, 58(12), 1344–1352.

Vaughan-Martini, A., Kurtzman, C. P., Meyer, S. A., & O'Neill, E. B. (2005). Two new species in the *Pichia guilliermondii* clade: *Pichia caribbica* sp. nov., the ascosporic state of *Candida fermentati*, and *Candida carpophila* comb. nov. *FEMS Yeast Research*, 5(4–5), 463–469.

Visvanathan, R., Qader, M., Jayathilake, C., Jayawardana, B. C., Liyanage, R., & Sivakanesan, R. (2020). Critical review on conventional spectroscopic α-amylase activity detection methods: merits, demerits, and future prospects. *Journal of the Science of Food and Agriculture*, 100(7), 2836–2847.

Wickerham, L. J. (1951). Taxonomy of yeasts (No. 1029). US Department of Agriculture.

White, T. J., Bruns, T., Lee, S., & Taylor, J. (1990). Amplification and direct sequencing of fungal ribosomal RNA genes for phylogenetics. *PCR Protocols: A Guide to Methods and Applications*, 18(1), 315–322.

Zabed, H., Sahu, J. N., Suely, A., Boyce, A. N., & Faruq, G. (2017). Bioethanol production from renewable sources: Current perspectives and technological progress. *Renewable and Sustainable Energy Reviews*, 71, 475–501.

Zapata-Castillo, P., Villalonga-Santana, L., Islas-Flores, I., Rivera-Muñoz, G., Ancona-Escalante, W., & Solís-Pereira, S. (2015). Synergistic action of laccases from *Trametes hirsuta* Bm2 improves decolourization of indigo carmine. *Letters in Applied Microbiology*, 61(3), 252–258.

Zhang, J., Ke, W., & Chen, H. (2020). Enhancing laccase production by white-rot fungus *Trametes hirsuta* SSM-3 in co-culture with yeast *sporidiobolus pararoseus* SSM-8. *Preparative Biochemistry & Biotechnology*, 50(1), 10–17.

Vol. 24, No. 2(2025) Bio25511
Revista Mexicana de Ingeniería Química

Construction of a hydrolysis reactor to obtain monosaccharides from a lignocellulosic residue

Construcción de un reactor de hidrólisis para obtener monosacáridos de un residuo lignocelulósico

J.C. Gómora-Hernández[2], F. Cuellar-Robles[1], N. Flores-Alamo[1], M.C. Carreño-de-León[1]*
[1]*División de Estudios de Posgrado e Investigación, Tecnológico Nacional de México/Instituto Tecnológico de Toluca, Av. Tecnológico s/n. Colonia Agrícola Bellavista, Metepec, Estado de México, C.P. 52149, México.*
[2]*División de Ingeniería Ambiental, Tecnológico Nacional de México/Tecnológico de Estudios Superiores de Tianguistenco, Km. 22, Carretera Tenango-La Marquesa Santiago Tilapa, Santiago Tianguistenco, C.P. 52650, México.*

Received: January 22, 2025; Accepted: March 21, 2025

Abstract

The present work shows the design prototype of a pilot scale full mixing reactor made of stainless steel and which was tested in a dilute acid hydrolysis process. Computational Fluid Dynamics (LS Dyna software) was used to study the geometric configuration and hydrodynamic profile in preliminary tests (at a temperature of 120°C) to obtain reducing sugars from a lignocellulosic waste (pineapple waste), obtaining a maximum production of 45.5 g of sugars per 100 g of residual material at a time of 140 min. The concentration results obtained in the kinetics were adjusted to the Saeman kinetic model, obtaining a production constant k_1 of 0.0168 min^{-1} and a degradation constant k_2 equal to 0.0028 min^{-1} which showed that the production was greater than the degradation. of the sugars obtained.

Keywords: chemical reactor, design, Dyna software, kinetics, hydrolysis.

Resumen

En el presente trabajo se muestra el prototipo de diseño de un reactor de mezcla completa escala piloto fabricado en acero inoxidable y que fue probado en un proceso de hidrólisis ácida diluida. Se utilizó Dinámica de Fluidos Computacional (LS Dyna software) para estudiar la configuración geométrica y perfil hidrodinámico en pruebas preliminares (a una temperatura de 120°C) para la obtención de azúcares reductores a partir de un residuo lignocelulósico (residuo de piña), obteniéndose una producción máxima de 45.5 g de azúcares por cada 100 g de material residual a un tiempo de 140 min. Los resultados de concentración obtenidos en la cinética fueron ajustados al modelo cinético de Saeman, obteniéndose una constante de producción k_1 de 0.0168 min^{-1} y una constante de degradación k_2 igual a 0.0028 min^{-1} lo cual mostro que fue mayor la producción sobre la degradación de los azúcares obtenidos.

Palabras clave: reactor químico, diseño, Dyna software, cinética, hidrólisis.

* *Corresponding author. E-mail*: mcarrenod@toluca.tecnm.mx ;
https://doi.org/10.24275/rmiq/Bio25511
ISSN:1665-2738, *issn-e*: 2395-8472

1 Introduction

Acid hydrolysis is a widely used chemical treatment to revalorize lignocellulosic biomass into valuable products. The main focus of acid hydrolysis is to increase the total surface area of the material, partially removing lignin external layer, reducing crystallinity index and polymerization degree to purify cellulose biopolymer (Rezania et al., 2020). From this, in literature it has reported either diluted or concentrated acid hydrolysis, and their employment depends on the physicochemical changes target on raw biomass. Concentrated acid hydrolysis is also known as swelling or de-crystallization process which aims on disrupting the recalcitrant nature of lignocellulosic matrix, solubilizing hemicellulose and cellulose fractions and breaking down lignin structure. Usually, this process performs at high acid loadings; >25 %w, moderate temperatures; < 60 °C and high solid-liquid ratios; > 1:2.5 (Wolfaardt *et al*., 2021), however, due to the concentrated acid expensive reactors and resistant materials are needed, and thus, this becomes un-practicability and un-sustainability for large scale application.

Diluted acid hydrolysis is most preferable due to low acid loading and lower toxicity compared to concentrated acid, this process usually performs at high temperatures coupled to low acid concentrations and long reaction times and aimed to transform hemicellulose and amorphous cellulose fraction into monomeric sugars that serves as carbon source for the subsequent fermentation stages. The main disadvantage of this hydrolysis treatment is the low lignin removal (only acid-soluble lignin) and the formation of aldehydes like furfural and 5-Hydroxi methyl furfural (HMF), which are inhibitory for microorganisms growing (Gómora-Hernández *et al*., 2020). In several papers, acid hydrolysis has been considered as critical step during lignocellulose revalorization, and thus, most of them have focused on operational conditions optimization from a wide range of biomass, the employment of either organic or inorganic acids as wells as the use of acid hydrolysis treatment as preliminary step for saccharification-fermentation processes to biofuels and bio-based materials production (Selvakumar et al., 2022; Solarte-Toro *et al*., 2019). Despite the interest of this technology in the last decades, there is only a few of papers reporting scaling up strategies for improve acid hydrolysis toward large scale application. As any chemical process, scaling up is a challenge stage, since it depends on several techno-economic and chemical factors. Due to the heterogeneous nature of acid hydrolysis of lignocelluloses, the scaling up of a hydrolysis batch reactor involves not only chemical features but also mass-transfer limitations which could dominate the overall process; however, some authors suggest that using particles lesser than 840 μm diffusion contributions could be avoided (Gómora-Hernández *et al*., 2022). Mass transfer depends on different factors like the physical characteristics of biomass; density, tortuosity, porosity, mechanical resistance, particles volume as well as the nature of acid solution; viscosity, density, concentration, protons diffusion and among others (Chen *et al*., 2015).

Since batch reactor serves as homogeneous stirring tank, the geometrical considerations reported by Mc Cabe *et al*. (2007) can be used for its design. These considerations are not limited to stirring rod, deflectors and reactor body (height and width). In addition to geometrical reactor design, modelling by computational tools is an interesting alternative to depict processes behaviour before its real operation. The understanding of the behaviour of any process prior its large-scale implementation allows eliminating operational stages, reducing costs and thus, the cost-benefit balance and the performance are better.

Computational Fluid Dynamics (CFD) is a novel computational tool based on finite-element method commonly employed to solve differential equations and provides numerical approximation of physics phenomena (Zawawi *et al*., 2018). For fluid dynamics, CFD performs dynamic simulations through 3D structures, which provides flow distribution, hydrodynamic – thermal profiles, velocity and pressure gradients and the hydrodynamic behaviour inside container (Llano-Serna *et al*., 2019). Recently, this powerful tool has been used in a wide range of applications including electromagnetism, heat and mass transfer (Sabliov *et al*., 2006), vehicles design (Sarkar *et al*., 2019) and chemical reactions engineering (Khanghah and Jafari, 2022).

In this work, geometrical configuration design of a hydrolysis batch reactor, hydrodynamic profiles given by CFD analysis as well as the preliminary hydrolysis tests for sugar extraction from a lignocellulose source is reported and discussed. The main focus of the paper is reporting the geometrical design and construction of batch reactor on a homogeneous stirred-tank basis configuration and analysing by finite element method the hydrodynamics profile for proper fluid distribution through 3D structure. Preliminary hydrolysis assay and the kinetic behaviour for sugars extraction was also analysed and compared with some data reported in literature before.

2 Materials and methods

2.1 Raw material

Pineapple crowns were selected as model raw material to evaluate sugar extraction in a batch hydrolysis reactor. They were obtained from local markets and transported to Technological Institute of Toluca for further conditioning and study. Pineapple crowns were washed with distilled water to remove impurities like ground, sand and plastics sliced into small pieces of around 3 cm^2 and dried at 55 °C for 72 hours. After that, they were pulverized and meshed, and the particles lesser than 250 μm were recovered, characterized and used for hydrolysis assays. The content of holocellulose, lignin, moisture and extractives were determined according to a previous paper (Gómora-Hernández *et al*., 2020).

2.2 Geometrical configuration of hydrolysis batch reactor

Geometrical configuration of batch reactor was based on the similar mathematical relationships (Figure 1) reported by Mc Cabe (2007), which allow estimating the width of deflectors, dimensions of blades and propels and the width of batch reactor. For geometrical design, a total volume of 2 L was considered as calculus basis. It is important to note, that the geometrical dimensions are limited to a homogeneous stirred tank, so, other limitations like mass transfer and chemical factors are avoided. The consideration proposed in this paper is based on the nature of sugar extraction reaction during acid hydrolysis which has been considered as pseudo-homogenous reaction when solid particles are lesser than 840 μm, i.e. chemical reaction is carried out in homogeneous liquid phase (Arslan *et al*., 2012).

2.3 CFD analysis of batch reactor and assembly

The second part of hydrolysis batch reactor construction was the instrumentation and validation of stirring profile. For this, each component of batch reactor and a "U" thermal resistance was designed and draw employing CAD software. After that, individual drawings were export to V971_R8 LS Dyna Software, which was used as CFD tool to determine flow profile through batch reactor. Reactor body, stirring rod and thermal resistance were discretized by 1 mm hexahedrons. Since reactor configuration considers a headspace of around 30 % of the total height, air and liquid solution layers were considered for stirring profile.

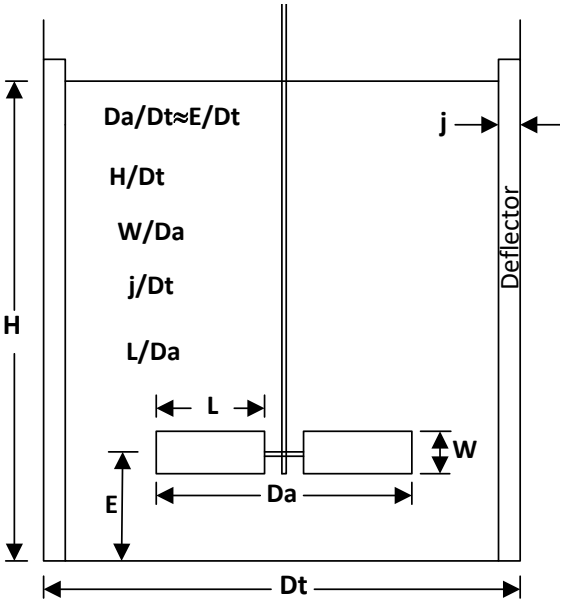

Figure 1. Geometrical configuration of homogeneous stirred tank.

Prior simulation, physicochemical parameters for liquid phase like density and viscosity as well as heat capacities of air and water was feed to the software. Density and viscosity of the mixed was determined by using a conventional glass densitometer and Ostwald viscometer, respectively. The mixed was comprised by 1 g of milled and dried pineapple crown with 20 mL of acid solution; this solid-liquid ratio was proposed based on a previous report (Gutiérrez-López *et al*., 2022).

After geometrical design and CFD study, steel-based reactor was constructed. The body and the down of the reactor were comprised by an only steel piece, while a flange was used as cover. Batch reactor was placed on a metal base and conditioning with mechanical and electronic systems. Stirring rod was connected to the mechanical rotor through bearing system, while thermal components were coupled to an electronic device; electronic control, thermal resistance and temperature dipstick, which maintains operational temperature within the desired range. Finally, reactor body was cover with glass wool to avoid thermal losses. To validate heating system, reactor was charged with distilled water and heating until up 100 °C. Samples were taken from purge valve at different times; temperature was measured using conventional mercury thermometer and compared to that registered by electronic device. Temperature was raised until 120 °C to verify the absence of steam leaks between reactor body and its cover and over mobile parts. Since hydrolysis reaction could be performed at long times, a pigtail pressure gauge was installed to monitor pressure changes attributed to high temperature. Pre-operational tests were performed to validate heating rates, fluid flow inside reactor and heat losses.

2.4 Preliminary acid hydrolysis assays

Acid hydrolysis of pineapple crown particles was carried out by triplicate at 110 °C using a solid-liquid ratio of 1:20. Sulphuric acid solution (1 M) was used as catalyst. Reaction was performed at a constant stirring of 250 rpm and the liquid samples were taken every 20 minutes until 240 minutes. Each sample was air cooled, centrifuged to eliminate suspended solids and the total amount of reducing sugars was quantified by Dinitro salicylic acid method (DNS) as was reported previously (Gómora-Hernández *et al*. 2022).

Kinetics for sugar extraction on batch reactor was studied by Saeman model. This model has extensively been used for acid hydrolysis of lignocelluloses and considers that hydrolysis acts as pseudo-homogeneous first order reaction in which chemical interaction performs in the homogeneous liquid phase, so, Saeman model does not consider limitations due to mass transfer and diffusion through solid porous material (Abril-González *et al*., 2023; Arslan *et al*., 2012). This model considers that acid hydrolysis involves 2 sequential first order reactions; the first related to monomeric sugars production from hemicellulose and amorphous fraction of cellulose, while the second is associated to thermal decomposition of the extracted saccharides into furfural (For C5 sugars) and HMF (For C6 sugars) (Ebikade *et al*., 2018). The mathematical expression of Saeman model is shown in Eq. 1.

$$M = \frac{P_o\, k_1}{k_2 - k_1}\left[e^{-k_1\, t} - e^{-k_2\, t}\right] \tag{1}$$

Where M and P_o are the amount of reducing sugars and holocellulose, respectively, both given in g/ 100 g of raw pineapple crown, k_1 and k_2 are the kinetic constants (min^{-1}) for production and decomposition of sugars, respectively and t the reaction time in minutes. Sugar production yield was calculated according to the following equation:

$$M = \frac{v * C}{1000} * 100 \tag{2}$$

Where v is the volume of hydrolysate recovered after acid hydrolysis, C the concentration of sugars in g/L, 1000 a conversion factor for volume and 100 the calculus basis for mass. In addition, the maximum sugar production and the optimum time at which this production is yielded were determined employing the following equations:

$$Sug_{\max} = P_o\left[\frac{k_2}{k_1}\right]^{\frac{k_2}{k_1 - k_2}} \tag{3}$$

$$t_{opt} = \frac{[\ln(k_2) - \ln(k_1)]}{k_2 - k_1} \tag{4}$$

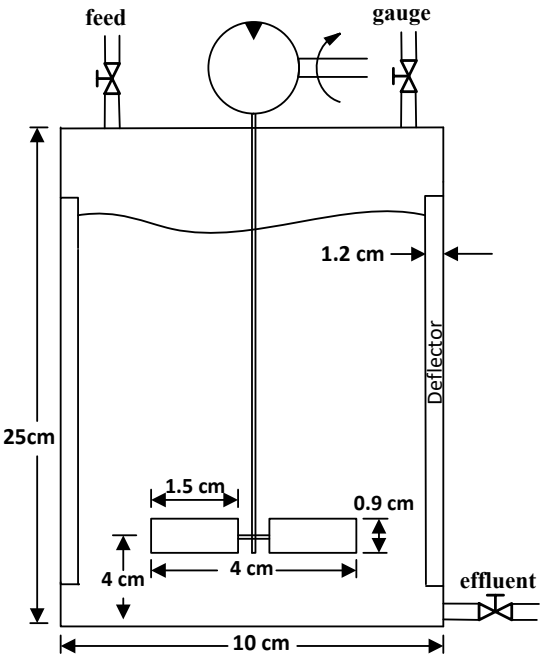

Figure 2. Dimensioning of hydrolysis batch reactor.

3 Results and discussion

3.1 Geometrical configuration and construction of batch reactor

Geometrical dimensions of hydrolysis batch reactor were defined employing Mc Cabe mathematical relationships as was described in a previous section. The use of these relationships allows estimating not only the dimensions (height and width) of reactor body and the stirring rod but also the deflector thickness. During batch reactor dimensioning the following considerations were assumed; cylindrical geometry of reactor body, 4 deflectors through transversal periphery as a larger number would create poor mixing zones, 30% volume for headspace considering the formation of steam due to the temperature change, total volume of 2 L, an effluent valve at the bottom for draining and the presence of inlet valve for raw material loading and bearing accessories in the cover of reactor.

From figure 2, it can appreciate that the height and width of reactor body corresponds to 25 and 10 cm, respectively, with a 20 cm of liquid height. The thickness of each deflector was 1.2 cm and the width of agitator blade was defined as 0.9 cm. For stirring rod, design consideration comprises 2 blades per propel.

Reactor body was made with 10 mm thickness stainless steel. At the bottom, ½ in valve was adapted as effluent conduct. The cover of reactor was made with a stainless-steel blind flange, which was interconnected to reactor body by using screws

Figure 3. Stainless steel-based hydrolysis batch reactor.

and nuts. To avoid steam leaks at high temperatures, neoprene packing was placed between reactor body and its cover. Figure 3 shows the ensembled hydrolysis batch reactor.

3.2 Conditioning of batch reactor and CFD analysis of stirring system

After batch reactor construction, the following stage before its operation for sugars extraction consisted on implementing stirring and heating systems, constructing a metal base to support reactor body and validating the proper distribution of flow inside reactor, so, each component of hydrolysis reactor was drawn using 3D CAD tools (Figure 4).

Drawings were then exported to LS Dyna software to simulate fluid flow profile inside reactor body. The parameters employed for dynamic simulation was: density, 1.004 g / mL; viscosity, 5 centipoise; air heat capacity, 1000 J / kg °C; water heat capacity, 4186 J / kg °C; stirring velocity, 250 rpm; pressure of 1.3 atm. According to the velocity profile shown in Figure 5, the distribution of velocity (mm / s) was not neither homogeneous nor stable, and this can be due to the geometry of thermal resistance which inhibits mass transfer over its surface area. Despite this, there is a semi-homogeneous zone far from resistance where solution was well mixed (Intense blue). The zone appreciated in green colour suggests that mixing process does not well performed, considerably diminishing the linear velocity of solution, however, as can be seen in Figure 5 (left picture), most of the fluid distribution is homogeneous. The use of "U" thermal resistance generates 2 disadvantages: a) reduces mass transfer inside reactor promoting concentration gradient and reducing the overall reaction yield, and b) promotes overheating on resistance surface which can promote an impregnation and burning of solid particles, and the subsequent external resistance damage. To avoid these problems, a new thermal resistance was designed. The new design comprised of a vertical thermal rod with a height of 17 cm and a thickness of 1 cm, coupled to a 1.8 cm thread (Figure 6 (left)), which was adapted to an electronic device that controls reaction temperature and connected into batch reactor. The rod thermal resistance was constructed on stainless steel material and installed from the bottom of the batch reactor.

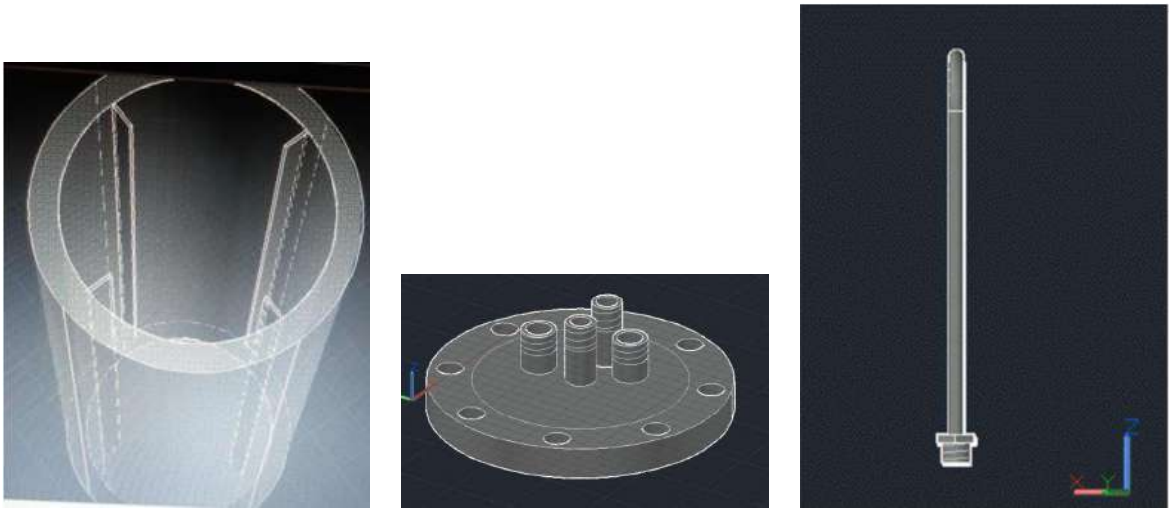

Figure 4. 3D CAD drawings of hydrolysis batch reactor components (From left to right; reactor body, reactor cover and thermometer rod).

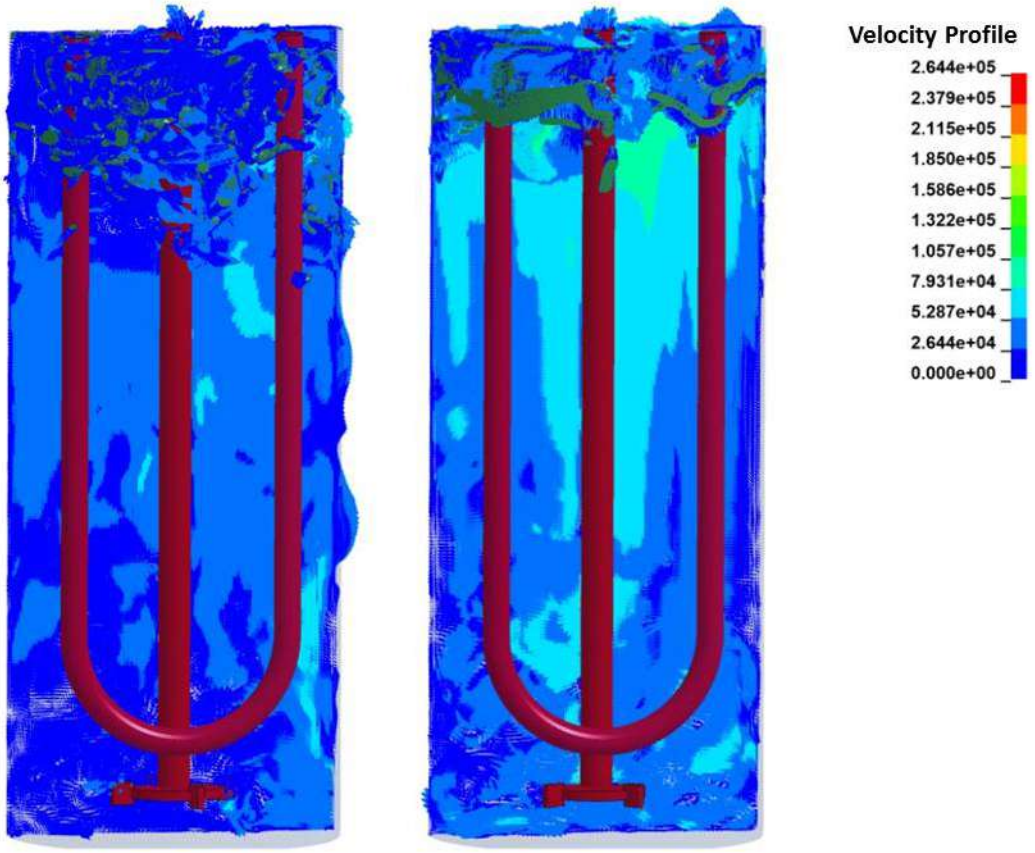

Figure 5. Velocity profile for hydrolysis batch reactor.

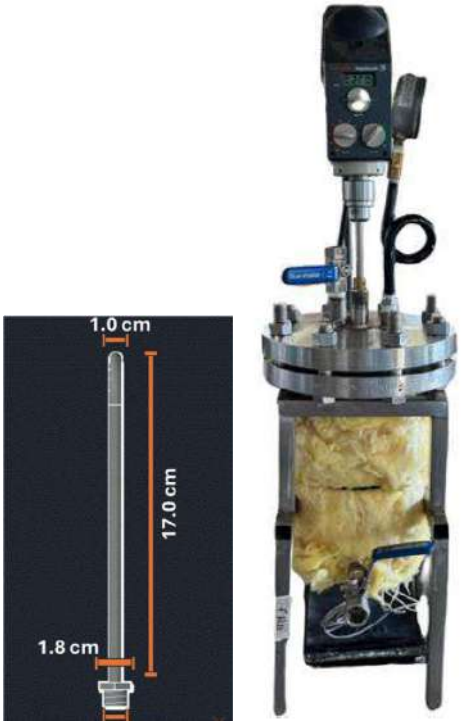

Figure 6. 3D CAD drawing of thermal resistance and the assembled hydrolysis batch reactor.

The assembled hydrolysis batch reactor is presented in Figure 6 (right), as can be seen thermal heating rod was placed at the bottom of the reactor and connected to an electronic device, while stirring system composed by mechanical rotor is placed on reactor cover. The pigtail pressure gauge was adapted near to mechanical rotor, it is expected that hydrolysis reaction operates between 1 and 1.3 atm as internal pressure; this factor will be conditioned on the desired reaction temperature (80 – 130 °C). Since batch reactor was made on stainless steel material, a glass wool cover is necessary to maintain internal temperature by avoiding thermal losses.

The batch reactor has been used for lignocellulose hydrolysis assays employing either direct acid hydrolysis (Rodrigues *et al*., 2010) or enzymatic saccharification (de Godoy *et al*., 2019), producing high sugar yield. The design and construction of heterogeneous batch reactor for hydrolysis purposes date back long years ago, and from this conventional configuration several modifications like plug-flow, percolation, twin gear and shrinking-bed reactors have been proposed in the last decades (Zhou *et al*., 2021). It is well known that batch mode reactor has several advantages; high xylose recovery, easy to operate and maintain as well as simple

design and low cost, however, its main disadvantage is the discharge of hydrolysate at the end of the chemical reaction that promotes sugar thermal cracking diminishing saccharides yield. Plug-flow and percolation reactors avoid this trouble and are able to increase sugar recovery; however, they require high energy demand and large water volumes, which make them nowadays un-practicable for industrial purposes (Torget *et al*., 2000). Most recently, twin gear (Ahmed *et al*., 2020) and twin-screw extrusion reactors (Wang *et al*., 2020) have been used to revalorize lignocellulose, the distinctive characteristic of these technologies are the fibrillation and shortening of the biomass fibers by frictional and shearing forces while chemical reagents are added, so, lignocellulose biomass is simultaneously altered by mechanical and chemical interactions. The complexity of this process involves challenges which must be solving like high capital requirement and energy consumption. The abovementioned makes evident the search of economical and feasible reactor configurations that not only need low capital cost but also achieved high sugar recovery.

The hydrolysis batch reactor reported here aims to diminish the construction cost and the operation complexity, since it uses an electronic device to maintain the desired temperature inside reactor and a conventional stirring system comprised by mechanical rotor and stirring rod. Other researchers have studied acid hydrolysis in more complex reactor systems, as example, Rodrigues *et al*. (2010), employed thermal oil as heating source during sugarcane bagasse hydrolysis with sulfuric acid, reaching a xylose yield of 74 %. Similar yield (77 %) was obtained in a semi-pilot batch reactor hydrolyzing rice straw in sulfuric acid solution catalyst (Roberto *et al*., 2003). The achieved sugar yields coupled to low construction cost and simplicity of the process make batch mode the most suitable option for large-scale and industrial applications. However, in accordance with Wright *et al*. (1987), there are some suggestions that could be considered to increase hydrolysis reaction performance: presoaking process to facilitate phases contact and promote protons diffusion inside lignocellulose material, preliminary stage to increase material porosity and the subsequent mass transport and the use of small particles to avoiding mass transfer limitations. In addition, the use of batch reactors allows determining the kinetic behavior of hydrolysis reaction by using simple kinetic equations like conventional Saeman and biphasic models which assume hydrolysis as pseudo-homogeneous reaction with-no mass transfer limitations. Finally, compared with commercial batch reactors, metal-based options are more expensive than reported here. The construction cost of the steel metal-based reactor provided here is quite similar to commercial glass-based reactors which cannot be used at high pressures or dense solid loadings. In addition, commercial reactors employ steam as a heating source depending on the reactor volume, this implies auxiliary services and high energy demand for boiler employment.

3.3 Pineapple crowns acid hydrolysis

The composition of pineapple crown particles employed for hydrolysis reaction was: moisture, 6.88 ± 0.11 %; extractives, 10.19 ± 0.10 %; holocellulose, 63.66 ± 1.61; lignin, 19.28 ± 0.13 %, which is similar to that determined before by Flores-Álamo *et al*. (2024), 69.36 % and 17.85 % for holocellulose and lignin, respectively. In contrast, the holocellulose content of Brazilian pineapple crowns determined by Fernandes Pereira *et al*. (2021) was quite lesser (36.5 %) with similar lignin percentage (24.3 %). High holocellulose content (84.2 %) coupled to low lignin mass fraction (7.4 %) was reported by Johny et al. (2023) working with Indian pineapple wastes. The variety on pineapple crowns composition can be attributed to difference on environmental properties like moisture, soil features and solar radiation, among others. From the high holocellulose content reported here, it is expected that Mexican pineapple crowns generate high sugars yield as shown in Figure 7. The maximum sugar production was 45.50 g / 100 g raw material, observed at 140 minutes, after this time, sugar concentration diminished because of thermal cracking of sugars into aldehydes reaching 35.88 g / 100 g at the end of the experiment. The sugars decomposition after 140 minutes (Figure 7) has also been observed in other works studying dilute sulphuric acid hydrolysis of corn cob (Gutiérrez-López *et al*., 2022) and oat bagasse (Gómora-Hernández *et al*., 2022) at moderate temperatures. In both papers, furfural concentration increased as temperature rises. In literature it has reported that sugars decomposition can be due to the combined impact of acid loading plus operational temperature, however, this last one is the most prominent variable promoting sugars transition into inhibitory aldehydes. In fact, high temperatures (150 – 240 °C) favoured aldehydes production (Yong *et al*., 2022), i.e. monomeric sugars are slowly degraded under 140 °C and short reaction times. Moreover, high severity processes raise sugars dehydration and thus, aldehydes concentration increases (Luo *et al*., 2019). From the abovementioned, is suggested that hydrolysis batch reactor must operate at moderate conditions; low temperature (< 140 °C), short reaction times (180 minutes) and low acid loading (<5 %v) to improve sugars extraction.

Sugar production data was well fitted to Saeman model obtaining the following regression parameters: k_1= 0.0168 min^{-1}, k_2= 0.0028 min^{-1} and R^2=0.997. The high value of k_1 rate constant is associated to

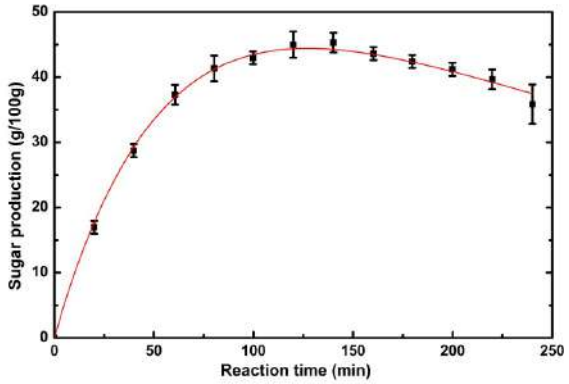

Figure 7. Sugar production data fitted to Saeman kinetic model.

the rapid sugar concentration increase in the first times (t < 140 min). The low value of k_2 is related to the low decomposition of sugars detected after 140 minutes. Previous papers have reported the same kinetic constants trend and related to high sugar yield, i.e. if $k_1 > k_2$, sugar production reaction is favoured (Abril-González *et al*., 2023; Rafiqul and Sakinah, 2012).

The main idea of construct a hydrolysis batch reactor is to increase the amount of lignocelluloses treated to produce more monomeric saccharides. Recently, our research team has made efforts on improving sugars extraction from different sources, as example, pineapple crowns hydrolysis with sulphuric acid was reported at similar operational conditions to that employed here. In this research, the maximum sugar production yielded at lab-scale was 40.27 g / 100 g at 105 °C (Gutiérrez-López *et al*., 2022); this value was lower to that obtained here. The difference can be due to the low temperature difference as well as to the improving on solution stirring in the batch reactor. Results are promising for further sugar extraction improving; however, major details on the hydrodynamic behaviour inside reactor are needed to reduce mass transfer limitations.

Conclusions

The reactor design using CFD showed good agitation using 4 baffles with a width of 12 mm, in addition to a 2-blade stirrer with a length of 1.5 cm. A homogeneous velocity profile was not obtained due to the installed thermal resistance that acted as an obstacle. It was assumed that thermal resistance causes good mass transfer to not be achieved, so a new heating method that does not limit stirring will be required. It was possible to operate with a pressure of 1.3 atm and a temperature of 120 °C, in addition to a stirring speed of 250 rpm.

In the hydrolysis kinetics, the maximum production time of reducing sugars was 140 minutes, obtaining 45.5g/100g. The test was carried out for a time of 250 min, at which time the sugar concentration was reduced to 35.88g/g. The production and degradation constants showed that production was maintained over their degradation.

Acknowledgements

Authors thank Tecnológico Nacional de México/Instituto Tecnológico de Toluca for finnancial support (project 19308.24-P).

References

Abril-González, M., Vele-Salto, A., Pinos-Vélez, V. 2023. Kinetic study of acid hydrolysis of the glucose obtained from banana plant. *ChemEngineering.* 7, 39.

Ahmed, M. A., Mushtaq, A., Terán-Hilares, R., Rehman, M. S. U., Iqbal, J., Raja, A. A., Weon, C. J., Han, J. I. 2020. Dilute acid hydrolysis of sugar canebagasse using a laboratory twin gear reactor. *Renewable Energy.* 153, 61-66.

Arslan, Y., Takac, S., Eken-Saracoglu, N. 2012. Kinetic study of hemicellulosic sugar production from hazelnut shells. *Chemical Engineering Journal.* 185-186, 23-28.

Chen, L., Zhang, H., Li, J., Lu, M., Guo, X., Han, L. 2015. A novel diffusion-biphasic hydrolysis coupled to kinetic model for dilute sulfuric acid pretreatment of corn stover. *Bioresource Technology.* 177, 8-16.

De Godoy, C. M., Machado, D. L., Da Costa, A. C. 2019. Batch and fed-batch enzymatic hydrolysis of pretreated sugarcane bagasse. Assays and modeling. *Fuel.* 253, 392-399.

Ebikade, E., Lym, J., Wittreich, G., Saha, B., Vlachos, D. G. 2018. Kinetic studies of acid hydrolysis of food waste-derived saccharides. *Industrial & Engineering Chemistry Research.* 57, 17365-17374.

Fernandes Pereira, P. H., Ornaghi J., H. L., Arantes, V., Cioffi, M. O. H. 2021. Effect of chemical treatment of pineapple Crown fiber in the production, chemical composition, crystalline structure, thermal stability and thermal degradation kinetic properties of cellulosic materials. *Carbohydrate Research.* 499, 108227.

Flores-Álamo, N., Gutiérrez-López, D., Solache-Ríos, M. J., Cuellar-Robles, F., Carreño-de-León, M. del C. 2024. Production of reducing sugars from leaves crown of pineapple, corn stalk and rose stalk using phosphoric acid: Kinetics and thermodynamics. *Revista Mexicana de Ingeniería Química.* 23, IA24159.

Gómora-Hernández, J.C., Carreño-de-León, M. del C., Flores-Álamo, N., Hernández-Berriel, M. del C., Fernández-Valverde, S. M. 2020. Kinetic and thermodynamic study of corncob hydrolysis in phosphoric acid with a low yield of bacterial inhibitors. *Biomass and Bioenergy*. 143, 105830.

Gómora-Hernández, J. C., Carreño-de-León, M. del C., Cuellar-Robles, F., Flores-Álamo, N. 2022. Sugar production by dilute acid hydrolysis of oat bagasse with three different acids: Kinetics and thermodynamics. *Revista Mexicana de Ingeniería Química.* 21, IA2822.

Gutiérrez-López, D., Carreño-de-León, M. del C., Solache-Ríos, M. J., Gómora-Hernández, J. C., Ventura-Cruz, S., Flores-Álamo, N. 2022. Kinetic and thermodynamic study on acid hydrolysis of corn cob, rose stem and pineapple Crown. *Chemical Engineering Communications*. 210, 1581-1592.

Johny, V., Mani, A. K., Palanisamy, S., Rajan, V. K., Palaniappan, M., Santulli, C. 2023. Extraction and physico-chemical characterization of pineapple crown leaf fibers (PCFL). *Fibers.* 2023. 11, 5.

Khanghah, M. A., Jafari, A. 2022. Kinetic modeling and CFD simulation of catalytic upgrading reactions: From batch to continuous reactors. *Journal of the Taiwan Institute of Chemical Engineers.* 134, 104254.

Llano-Serna, C. E., Coral-Portillo, J. A., Fontalvo, J., Prado-Rubio, O. A. 2019. CFD assisted analysis and design of hydraulic flocculators. *Revista Mexicana de Ingeniería Química.* 18, 995-1015.

Luo, Y., Li, Z., Li, X., Liu, X., Fan, J., Clark, J. H., Hu, C. 2019. The production of furfural directly from hemicellulose in lignocellulosic biomass: A review. *Catalysis today.* 319, 14-24

McCabe, Warren L., Julian C. Smith, and Peter Harriott. 2007. Unit operations of chemical engineering. McGraw-hill.

Rafiqul, I. S. M., Sakinah, A. M. M. 2012. Kinetic studies on acid hydrolysis of *Meranti* wood sawdust for xylose production. *Chemical Engineering Science.* 71, 431-437.

Rezania, S., Oryani, B.,Cho, J., Talaiekhozani, A., Sabbagh, F., Hashemi, B., Rupani, P. F., Mohammadi, A. A. 2020. Different pretreatment technologies of lignocellulosic biomass for bioethanol production: An overview. *Energy.* 199, 117457.

Roberto, I. C., Mussatto, S. I., Rodrigues, R. C. L. B. 2003. Dilute-acid hydrolysis for optimization of xylose recovery from rice straw in a semi-pilot reactor. *Industrial Crops and Products.* 17, 171-176.

Rodrigues, R. C. L. B., Rocha, G. J. M., Rodrigues Jr., D., Filho, H. J. I., Felipe, M. G. A., Pessoa Jr., A. 2010. Scale-up of diluted sulfuric acid hydrolysis for producing sugarcane bagasse hemicellulosic hydrolysate (SBHH). *Bioresource Technology.* 101, 1247-1253.

Sabliov, C. M., Salvi, D. A., Boldor, D. 2006. High frequency electromagnetism, heat transfer and fluid flow coupling in ANSYS multiphysics. *Journal of Microwave Power and Electromagnetic Energy*. 41, 5-17.

Sarkar, S., Thummar, K., Shah, N., Vagrecha, V. 2019. A review paper on aerodynamic drag reduction and CFD analysis of vehicles. *International Research Journal of Engineering and Technology.* 6, 1.

Selvakumar, P., Adane, A. A., Zelalem, T., Hunegnaw, B. M., Karthik, V., Kavitha, S., Jayakumar, M., Karmegam, N., Govarthanan, M., Kim, W. 2022. Optimization of binary acids pretreatment of corncob biomass for enhanced recovery of cellulose to produce bioethanol. *Fuel.* 321, 124060.

Solarte-Toro, J. C., Romero-García, J. M., Martínez-Patiño, J. C., Ruíz-Ramos, E., Castro-Galiano, E., Cardona-Alzate, C. A. 2019. Acid pretreatment of lignocellulosic biomass for energy vectors production: A review focused on operational conditions and techno-economic assessment for bioethanol production. *Renewable and Sustainable Energy Reviews.* 107, 587-601.

Torget, R. W., Kim, J. S., Lee, Y. Y. 2000. Fundamental aspects of dilute acid hydrolysis/fractionation kinetics of hardwood carbohydrates. *Cellulose hydrolysis. Industrial and Engineering Chemistry.* 39, 2817-2825.

Wang, Z., He, X., Yan, L., Wang, J., Hu, X., Sun, Q., Zhang, H. 2020. Enhancing enzymatic hydrolysis of corn stover by twin-screw extrusion pretreatment. *Industrial Crops and Products*. 143, 111960.

Wolfaardt, F. J., Leite Fernandes, L. G., Cangussu Oliveira, S. K., Duret, X., Görgens, J. F., Lavoie, J. M. 2021. Recovery approaches for sulfuric acid from the concentrated acid hydrolysis of lignocellulosic feedstocks: A mini review. *Energy Conversion and Management: X*. 10, 100074.

Wright, J. D., Bergeron, P. W., Werdene, P. J. 1987. Progressing batch hydrolysis reactor. *Industrial and Engineering Chemistry.* 26, 699-705.

Yong, K. J., Wu, T. Y., Loong Lee, C. B. T., Lee, Z. J., Liu, Q., Jahim, J. M., Zhou, Q., Zhang, L. 2022. Furfural production from biomass residues: Current technologies, challenges and future prospects. *Biomass and Bioenergy*. 161, 106458.

Zawawi, M. H., Saleha, A., Salwa, A., Hassan, N. H., Zahari, N. M., Ramli, M. Z., Muda, Z. C. 2018. A review: Fundamentals of computational fluid dynamics (CFD). *AIP Conference Proceedings.* 2030, 020252.

Zhou, Z., Liu D., Zhao, X. 2021. Conversion of lignocellulose to biofuels and chemicals via sugar patform: An updated review on chemistry and mechanisms of acid hydrolysis of lignocellulose. *Renewable and Sustainable Energy Reviews.* 146, 111169.

Vol. 24, No. 2(2025) IA25486
Revista Mexicana de Ingeniería Química

Preparation and characterization of a biocomposite for Cr(VI) adsorption by evaluating the useful life of the biomaterial

Preparación y caracterización de un biocompuesto para la adsorción de Cr(VI) evaluando la vida útil del biomaterial

C. Tejada-Tovar[1]*, Á. Villabona-Ortiz [1], R. Ortega-Toro [2], N. Beleño-Garrido [3], L. Sierra-Payares [3]
[1] Full Professor, Universidad de Cartagena, Faculty of Engineering, Department of Chemical Engineering, Cartagena, Colombia. Process Design, and Biomass Utilization Research Group (IDAB). Avenida del Consulado St. 30. Cartagena de Indias, Colombia, 130015
[2] Full Professor, Universidad de Cartagena, Faculty of Engineering, Department of Food Engineering, Cartagena, Colombia. Food Engineering Department, Food Packaging and Shelf-Life Research Group (FP&SL). Avenida del Consulado St. 30. Cartagena de Indias 130015, Colombia
[3] Chemical Engineering, Universidad de Cartagena, Faculty of Engineering, Department of Chemical Engineering, Cartagena, Colombia. Process Design, and Biomass Utilization Research Group (IDAB). Avenida del Consulado St. 30. Cartagena de Indias, Colombia, 130015
Received: December 14, 2024; Accepted: April 25, 2025

Abstract
The objective of this work was to prepare and characterize a biocomposite made from plantain pseudo stem (PSP), agro-industrial waste and polylactic acid (PLA) for potential use in removing Cr(VI) from solution. Cellulose (CL) was extracted from the plantain pseudo stem waste and modified with PLA. The effect of adsorbent dosage on adsorption efficiency at different concentrations was evaluated, and an adsorption-desorption study was conducted to determine the biocomposite's lifetime. FTIR, SEM and TGA-DSC analyses were performed. The results showed that the plant fiber was successfully modified with PLA, resulting in the formation of the PSP/PLA biocomposite. It was observed that the adsorbent dosage affected the adsorption process, with the best removal efficiencies being 51.74% at 65 mg/L and 49.74% at 30 mg/L at an optimal pH of 2. Adsorption-desorption cycles showed that the biocomposite can be reused up to twice. The inherent properties of the plant fiber were critical, and the crosslinking agent enhanced the biomaterial's performance. This biocomposite shows potential for removing metal contaminants from the solution, thereby contributing to the increased utilization of waste biomass.
Keywords: Polylactic acid, Biocomposite, Cellulose, plantain pseudo stem, Agricultural waste.

Resumen
El objetivo de este trabajo fue la preparación y caracterización de un biocompuesto a partir de residuos agroindustriales de pseudotallo de plátano (PSP) y ácido poliláctico (PLA) con potencial uso en la remoción de Cr (VI) en solución. Se realizó un proceso de extracción y modificación de celulosa con PLA. Se evaluó el efecto de la dosis de adsorbente sobre la eficiencia de adsorción a distintas concentraciones, y se realizó un estudio de adsorción-desorción para determinar la vida útil del biocompuesto. Se realizaron análisis de caracterización FTIR, SEM y TGA-DSC. Los resultados mostraron la exitosa modificación de la fibra vegetal con PLA, dando lugar a la formación del biocompuesto PSP/PLA. Se observó que la dosis de adsorbente afecta el proceso de adsorción, siendo las mejores eficiencias del 51.74% para 65 mg/L y del 49.74% para 30 mg/L a un pH óptimo de 2. Los ciclos de adsorción-desorción determinaron que el biocompuesto posee una reutilización máxima de 2 veces. Las propiedades inherentes de la fibra vegetal fueron fundamentales, y el agente entrecruzante mejoró el desempeño del biomaterial. Este biocompuesto muestra potencial para la eliminación de contaminantes metálicos en solución, contribuyendo a reducir la brecha en el uso de biomasas residuales.
Palabras clave: Ácido poliláctico, Biocompuesto, Celulosa, Pseudotallo de plátano, Residuos agrícolas.

* *Corresponding author. E-mail*: ctejadat@unicartagena.edu.co ;
https://doi.org/10.24275/rmiq/IA25486
ISSN:1665-2738, *issn-e*: 2395-8472

1 Introduction

In recent years, suitable solutions have been sought for the utilization of agro-industrial waste generated by various industries worldwide to reduce their environmental impact. Collectively, the United States, India, and China generate approximately 1,550 million tons of agricultural waste annually, with China being the largest producer (Kumar Sarangi *et al*., 2023; McNeill *et al*., 2024). Much of this waste represents a valuable source of biomass for the production of value-added products, contributing to environmental sustainability and the circular economy by reducing the accumulation of agricultural residues and offering an alternative to fossil-based materials (Kumar Sarangi *et al*., 2023). The waste generated includes sugarcane bagasse, coconut shells, wheat husks, jute fibers, peanut shells, plantain peels, cassava peels, yam peels, and oil palm residues (Nata *et al*., 2024; Saifullah *et al*., 2024; Tejada-Tovar *et al*., 2019). To take advantage of these biomasses, the synthesis of composite materials has been proposed as an alternative that contributes to environmental protection, with potential applications in the development of biodegradable packaging and wastewater treatment due to their biological origin (Saifullah *et al*., 2024; Sherugar *et al*., 2022). For use in treating contaminated water, waste biomasses are transformed into porous surface-active adsorbent biocomposites capable of retaining both organic and inorganic contaminants. However, the use of residual fiber alone is not sufficient to produce highly efficient materials; therefore, natural fibers are combined with a polymeric matrix to enhance their physicochemical properties and increase the adsorption capacity of the materials. This positions them as a promising alternative due to their low cost, environmental friendliness, and high efficiency (Zarna *et al*., 2021; Zheng *et al*., 2024).

Plantain pseudo stem (PSP) is a lignocellulosic natural fiber commonly used in the preparation of biocomposites due to the presence of hydroxyl and carboxyl functional groups that facilitate the removal of contaminants from solutions (Selimin *et al*., 2022). An effective method for preparing PSP-based biocomposites involves crosslinking the vegetable fiber with a modifying agent such as polylactic acid (PLA). PLA provides good thermal and mechanical resistance, which enhances the adhesion characteristics of the biomaterial, modifies its hydrophilic properties to hydrophobic ones, and improves its efficiency in adsorbing pollutants from solutions (Kadea *et al*., 2024; Vatanpour *et al*., 2022).

Chromium is a heavy metal that has been widely studied due to its classification as one of the most toxic pollutants and its high prevalence in various industrial processes. Chromium in its hexavalent form, Cr(VI), is among the most common and hazardous species found in the environment (Diaz-Rodriguez *et al*., 2025). Its level of toxicity poses a serious threat to all living organisms, causing conditions such as stomach ulcers, anemia, and disorders of the lungs, kidneys, liver, and even the reproductive system. In addition to its mutagenic and teratogenic effects, Cr(VI) exhibits high environmental mobility due to its strong oxidizing potential and high solubility (Islam *et al*., 2020; Zhao *et al*., 2023). Exposure to this chemical increases the risk of developing various types of cancer, including stomach, colon, and lung cancer. As a result, environmental protection agencies have established permissible concentration limits for Cr(VI) in water. According to the U.S. EPA, the maximum allowable concentration of chromium is 0.05 mg/L in drinking water and 0.1 mg/L in surface water (Khan *et al*., 2016; Zhao *et al*., 2023).

The literature does not report many applications of converting waste biomass into PLA-modified materials for use in metal removal. For example, Luqman. *et al*., 2020 developed a biocomposite film using cellulose derived from banana fiber, and PLA, and characterized their morphological and crystalline properties by SEM and XRD respectively. Analyzing the results obtained, PLA/plantain cellulose seemed to increase the thermal stability of the biocomposite film. Similarly, Yang *et al*., 2024 developed a biocomposite from a mixture of starch, cellulose, and PLA. The prepared biocomposite showed good hydrophobic properties and excellent mechanical properties, improving the tensile strength from 2.09 MPa to 3.53 MPa. On the other hand, Madenli *et al*., 2023 prepared a biocomposite based on fungal hyphae (*Aspergillus oryzae* and *Penicillium roqueforti*) for the removal of Cr(VI). The results showed a removal efficiency of 98.9% of the contaminant within 11 hours and Moreno-Rubio *et al*., 2025, used Luffa as a bioadsorbent material to remove Cr(VI) from synthetic waters. The prepared material was characterized by SEM and FTIR analysis. The results obtained showed the presence of mainly C and O, while FTIR identified hydroxyl, carbonyl and carboxyl functional groups. It was also obtained that Luffa is composed of 14% lignin, 76% cellulose and 10% hemicellulose. Finally, the adsorption process obtained an efficiency of 100% of Cr(VI) in a period of 1416 hours.

Considering the importance of developing new materials using waste biomass generated by various anthropogenic activities, this research aims to prepare and characterize a biocomposite based on PSP and PLA for the removal of Cr(VI) from solution, positioning it as an adsorbent material that contributes to closing the existing gap in the utilization of agro-industrial waste for potential applications in pollutant adsorption processes.

2 Methodology

2.1 *Materials and reagents*

Plantain pseudo stem from agro-industrial waste collected in the city of Cartagena, Colombia, and PLA $(C_3H_4O_2)_n$ purchased from Nature Works were used as raw materials in the preparation of the biocomposite. PLA served as the modifying agent. Sodium hydroxide (NaOH), supplied by EMSURE, was used for alkaline extraction; sodium chlorite ($NaClO_2$) and glacial acetic acid (CH_3COOH) were employed for cellulose purification; and sulfuric acid (H_2SO_4), also from EMSURE, was used to obtain cellulose acetate (CA). Additional materials used included hydrochloric acid, acetic anhydride, dichloromethane, acetone, a heating plate with magnetic stirrer, analytical balance, oven, sieve shaker, and electric mill.

2.2 *Obtaining cellulose acetate*

To obtain cellulose acetate, a pre-treatment of the plantain pseudo stem fiber was first carried out. The fiber was sourced from a plantation in the city of Cartagena. It underwent a process of peeling, washing, and air-drying for three days. After drying, the fiber was milled to reduce its size and then sieved to obtain the desired particle size. Cellulose extraction was performed through a double alkaline treatment using 2 wt.% NaOH for 45 minutes at a temperature of 75 °C to remove lignin, hemicellulose, and other impurities. Considering the solid-to-liquid ratio, 20 g of NaOH and 20 g of pretreated fiber were added to one liter of solution. This process was carried out in duplicate. The fibers were then thoroughly washed with water until a neutral pH of 7 was reached and subsequently dried at 60 °C for 24 hours (Joshi *et al*., 2024; Melikoğlu *et al*., 2019).

Subsequently, 500 mL of distilled water were used to prepare a bleaching solution by adding 50 mL of glacial acetic acid (CH_3COOH) and 50 g of sodium chlorite ($NaClO_2$), with magnetic stirring at 200 rpm for 24 hours to carry out the bleaching of the cellulose. The recovered material was filtered, washed to a neutral pH (7), and dried for 24 hours at 50 °C (González-Delgado *et al*., 2022; Melikoğlu *et al*., 2019).

Finally, to obtain CA, 10 g of CL were mixed with 25 mL of CH_3COOH and stirred at 160 rpm for 30 minutes at 35 °C. To the resulting mixture, 40 mL of CH_3COOH and 0.08 mL of sulfuric acid (H_2SO_4) at 95% concentration were added, followed by an additional 45 minutes of stirring. Then, a solution of 40 mL of acetic anhydride and 0.6 mL of H_2SO_4 was added to the mixture, which was maintained under stirring for 1.5 hours. Afterward, 10 mL of distilled water and 20 mL of CH_3COOH were added, and the mixture was kept under agitation for 20 hours. The final material obtained from this entire process was filtered under vacuum, washed with distilled water, and dried at 35 °C for 48 hours (Ortega & Rodríguez, 2018). This methodology is illustrated in Figure 1.

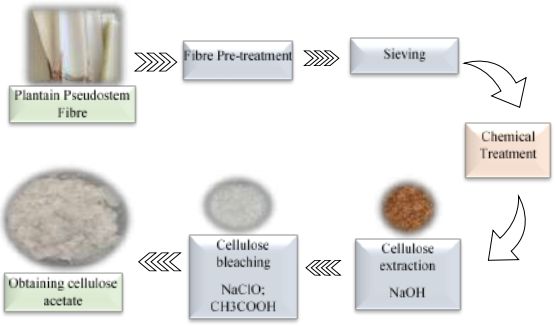

Figure 1. Methodology for obtaining CA.

Once the CA was obtained, it was washed with plenty of distilled water until a neutral pH (7) was obtained and then dried at room temperature for 48 hours.

2.3 *Preparation of the biocomposite*

Two solutions were prepared: the first containing 50 mL of dichloromethane and 1.8 g of PLA, and the second containing 50 mL of acetone and 5 g of the obtained CA. Each solution was poured into a glass container with a lid and subsequently subjected to ultrasound treatment for 45 minutes at 60 °C. After the designated time, 17 mL of the first solution and 50 mL of the second were taken and evenly combined in a Petri dish. Finally, the mixture was left to stand at room temperature for 24 hours to allow for solvent evaporation (Abu Aldam *et al*., 2020).

2.4 *Parametric study*

A parametrization study was carried out, evaluating two factors: the initial concentration of the pollutant (C_i) and the amount of adsorbent (X_i). The operating ranges evaluated are shown in Table 1.

Table 1. Study parameters and ranges.

Parameter	Range	Unit
C_i	30 65 100	(mg/L)
X_i	10 20 30	(mg)

2.5 Characterization of the biocomposite

The biocomposite surface charges were studied by means of pHpzc Fourier Transform Infrared Spectroscopy (FTIR) analysis was also carried out to identify the functional groups involved in the materials, using the IRAffinity-1 FTIR Shimadzu equipment, serial number A213749. The morphology and surface composition of the biocomposite were studied by SEM analysis using a TESCAN MIRA3 model. Thermogravimetric analysis and DSC were performed to determine thermal stability, using a TA Instruments thermogravimetric analyzer, serial number 0600-11099, model SDT Q600, with a heating ramp of 10 °C/min, alumina crucibles, and a flow rate of 20 cm^3/min.

2.6 Point of zero charge (pHpzc)

The point of zero charge of the synthesized PSP/PLA biocomposite was determined to establish the pH at which it has the greatest capacity to retain contaminants on the surface. Eighteen test tubes were used, including replicates, each containing 0.01 g of biocomposite, to which 10 mL of $K_2Cr_2O_7$ solution at 100 ppm was added. The pH of each solution in the test tubes was adjusted with 0.1 M HCl and 0.1 M NaOH over a range from pH 2 to pH 10, and the samples were shaken for 24 hours in a shaker (Iheanacho *et al*., 2023). After the set time, the pH of each sample, both original and replicate, was measured.

2.7 Biocomposite reuse study

A study was carried out to evaluate the reusability and regeneration of the synthesized Cr(VI)-loaded biocomposite using an adsorption–desorption cycling process with NaOH and HCl solutions. For this purpose, 30 mL solutions of 0.2 M HCl and NaOH (separately) were prepared, and each of these solutions was placed in contact with 0.5 g of residual biomaterial recovered from the adsorption tests for 2 hours under stirring at 140 rpm. The material was then washed and dried in an oven at 100 °C for 20 minutes. The resulting biomaterial was tested with Cr(VI) solutions at 100 mg/L under agitation at 140 rpm for 2 hours. To measure the reuse efficiency, the absorbance was measured using a UV-Vis spectrophotometer by the diphenyl carbazide method (Badawy *et al*., 2023). This process was performed in triplicate.

3 Results and discussion

3.1 Synthesis of PSP/PLA composite biomaterial

According to the proposed methodology, Figure 2 shows the synthesized PSP/PLA biocomposite. During the synthesis process, the alkaline extraction of CL showed a brown color attributable to lignin and impurities remaining in the plantain stem fiber, which were subsequently removed through the alkaline process. With the bleaching process, the lignin present was eliminated by oxidation, resulting in purified CL. The alkaline extraction technique and the formation of CA were used to successfully modify PSP/PLA from 20 g of plantain pseudo stem fiber, obtaining 18 g of CL in the extraction process and 6 g of PSP/PLA biocomposite.

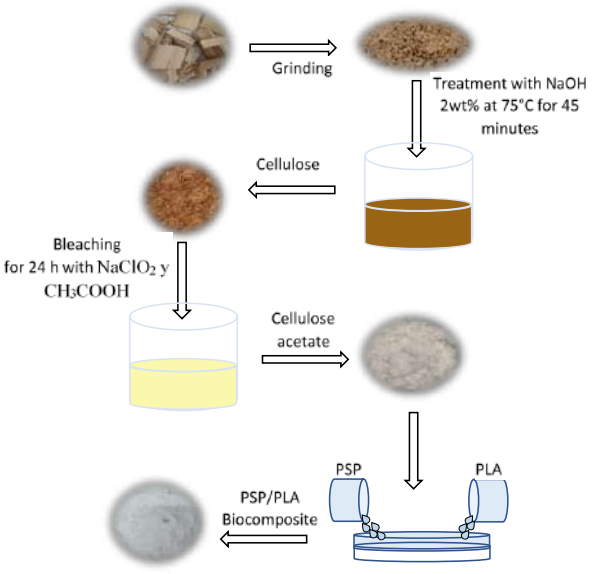

Figure 2. Synthesized PSP/PLA Biocomposite.

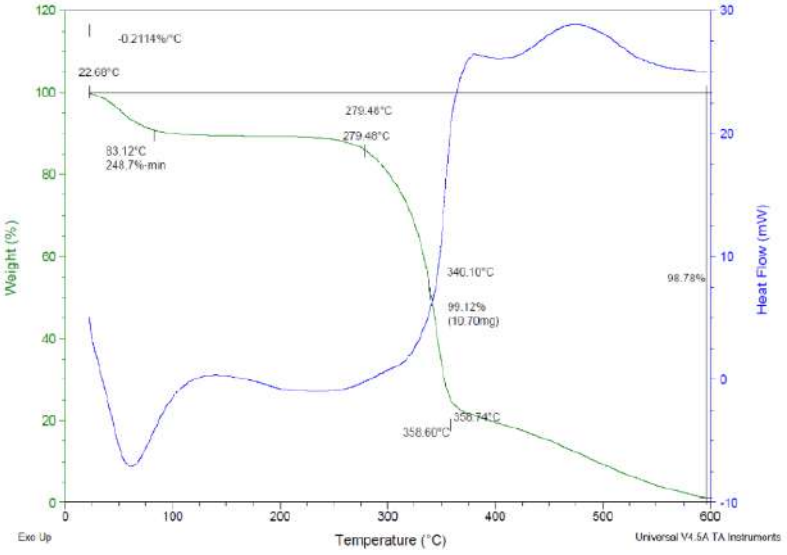

Figure 3. TGA-DSC analysis of CL extracted from plantain pseudo stem

The results showed good yield throughout the fiber utilization process, achieving 90% for the extraction of CL and 100% for the synthesis of the biocomposite. These results are consistent with those reported in previous studies on the CL fraction obtained from the plantain stem, where Thi Thuy Van *et al*., 2022 and Meng *et al*., 2019, obtained efficiencies of 82.136% and 91.33%, respectively. Regarding the mixture of CA with PLA, recent research shows that a higher content of CL improves the mechanical properties of the material, such as tensile strength and elasticity. Additionally, it improves its hydrophobic properties and its amorphous nature, as specified in the study conducted by Abu Aldam *et al*., 2020.

3.2 Thermogravimetric analysis - TGA

In order to analyze the purity, thermal, and stability properties of the CL extracted from plantain stem fiber, a TGA-DSC analysis was carried out over a temperature range from 0 °C to 600 °C with a heating ramp of 10 °C/min and a flow rate of 20 cm^3/min. The results obtained from the analysis are shown in Figure 3, where it is observed that the thermal stability of the plantain stem CL is reached at 22 °C, with a slight mass loss between 23–83 °C, which can be attributed to the evaporation of contained water and adsorbed moisture from the environment (Mi & Wang, 2024). The onset of decomposition occurs between 279.48 °C and 358.74 °C, with a significant mass loss, reaching 99.12% at 340.10 °C, which can be attributed to the degradation of lignin, CL, and hemicellulose still present in the sample (Satha *et al*., 2020). These results are consistent with those reported by Gupta & Raghav, 2020, who observed similar behavior in terms of weight loss and degradation of CL obtained from *Citrus limetta*, recording a degradation temperature between 165 °C and 390 °C. Similarly, Shrestha *et al*., 2021, obtained comparable results for weight loss and degradation of CL extracted from plantain stem, reporting a degradation temperature range of 228 °C to 384 °C.

3.3 Point of charge pHpzc

Figure 4 presents the results obtained in the determination of pHpzc for the synthesized PSP/PLA biocomposite. The determination of the point of zero charge is of great importance, as it helps to understand the electrical charges of the biomaterial, which are dependent on the pH of the solution and related to the ionization of functional groups on the surface of the adsorbent (Aigbe & Osibote, 2021; Rodríguez *et al*., 2010). The results showed that for PSP/PLA, the pHpzc exhibited a value of 8, indicating that at this value the surface charge of the adsorbent is zero (Tejada-Tovar *et al*., 2023). It is important to mention that electrostatic interaction favors the adsorption of anionic species when the pH of a solution is lower than the point of zero charge (pHpzc), while covalent interactions facilitate the adsorption of cationic compounds when the pH of the solution is higher than the pHpzc (Labied *et al*., 2018). Studies reported in the literature have highlighted the importance of pH in the adsorption of heavy metals. For example, Yadav *et al*., 2024, showed that the optimum pH for the removal of Ni(II) ions is 8. Similarly, in the study by Nurdin *et al*., 2015, cited in Aigbe & Osibote, 2021, they found that the optimum removal of Cd(II), Ni(II), and Cu(II) ions occurs at pH 8. Considering that in aqueous solutions, chromium is generally present as $Cr_2O_7^{2-}$ and $HCrO^{4-}$, carrying out the adsorption at low pH will favor the PSP/PLA biocomposite to have a positively charged surface,

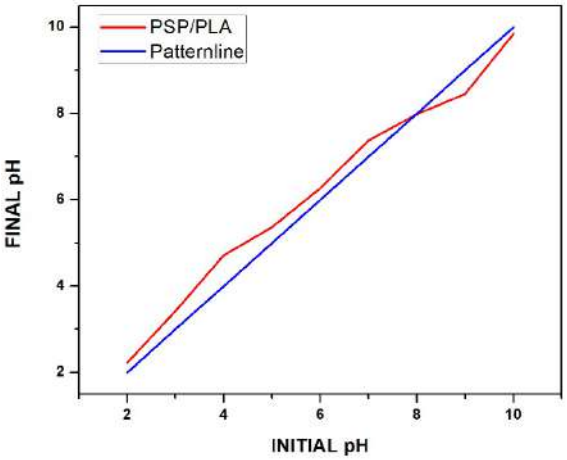

Figure 4. Data obtained from pHpzc.

which will facilitate the adsorption of chromium (Tejada-Tovar *et al*., 2023)**.** Due to this, a pH of 2 was chosen, considering that most related studies are conducted at pH 2–3. For instance, Liang *et al*., 2023, successfully removed Cr(VI) ions using sodium alginate/phosphorus tetramethyl sulfate beads at an optimum pH of 3.

3.4 Fourier Transform Infrared Analysis – FTIR

Fourier Transform Infrared Spectroscopy (FTIR) is a technique used to characterize different types of samples, whether in solutions, pastes, films, powders, fibers, liquids, or gases. Figure 5 shows the FTIR spectra of the plantain pseudo stem vegetable fiber and the synthesized PSP/PLA biocomposite, both before and after the Cr(VI) adsorption test. It is observed that the plantain pseudo stem fiber (Figure 5a) shows peaks between 3300–3500 cm^{-1}, indicating the presence of amines (N–H), and between 3500–3750 cm^{-1}, indicating O–H, which could be due to residual water present in the sample. On the other hand, peaks with strong intensity appear, indicating the presence of a carbonyl group (C=O) between 1690–1760 cm^{-1}, and alkenes (C–H) at lower frequencies (Rahim & Mas Haris, 2022).

On the other hand, the synthesized biocomposite with PLA, presented in Figure 5b, displays more frequent and characteristic peaks. The presence of amines (N-H) is maintained, and a strong absorption band appears between 2850-2970 cm^{-1}, indicating the presence of alkanes (C-H), which consecutively generate other bands that extend down to 1470 cm^{-1}, indicating the stability of the formed molecule. Likewise, aromatic rings (C-H) are observed at lower frequencies, 690-900 cm^{-1}, indicating greater stability and confirming that a homogeneous mixture of the PSP and PLA materials was obtained (Luqman *et al*., 2020; Villabona-Ortíz *et al*., 2024).

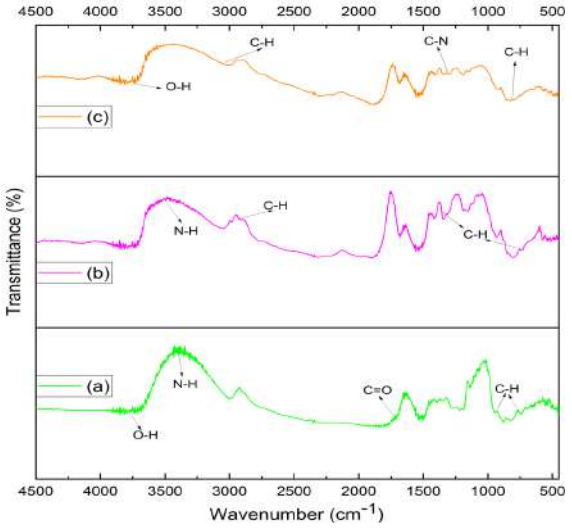

Figure 5. IR Spectra of (a) Plantain pseudo stem fiber, (b) PSP/PLA before adsorption, (c) PSP/PLA after adsorption.

Analysis of the biocomposite after adsorption (Figure 5c) reveals a clear decrease in the characteristic peaks of the functional groups; however, stretching vibrations are still present: a stretching vibration belonging to hydroxyl groups (O-H) is observed between the wavelengths of 3800-3900 cm^{-1}, and peaks characteristic of C-H groups (alkanes) appear between 2890-2940 cm^{-1}. Peaks indicating the presence of amines (C-N) are also evident between 1250-1500 cm^{-1}, which help maintain pH balance by counteracting the acidity of the adsorbed Cr(VI) solutions. Additionally, the presence of aromatic rings (C-H) is observed between 750-1000 cm^{-1}, confirming the stability of the synthesized biocomposite (Hsini *et al*., 2020; Nandiyanto *et al*., 2019). The notable decrease in the intensity of the bands is due to the fact that the pollutant is captured by the active sites of the biocomposite, generating interactions with the functional groups of the adsorbent that cause these changes, which confirms the functionality of the material in the adsorption process (Villabona-Ortíz *et al*., 2024).

3.5 Scanning Electron Microscopy – SEM Analysis

SEM analysis was carried out on the biocomposite prepared before and after the Cr(VI) adsorption test to study its morphological characteristics and understand the effect of the PLA matrix on its behavior. Figure 6 shows the SEM micrographs of the biocomposite before (Figure 6a) and after the adsorption test (Figure 6b). Figure 6a shows the general structure of the biocomposite with more visible fibers, along with a clear distribution and organization of the PSP materials within the PLA matrix. The homogenization

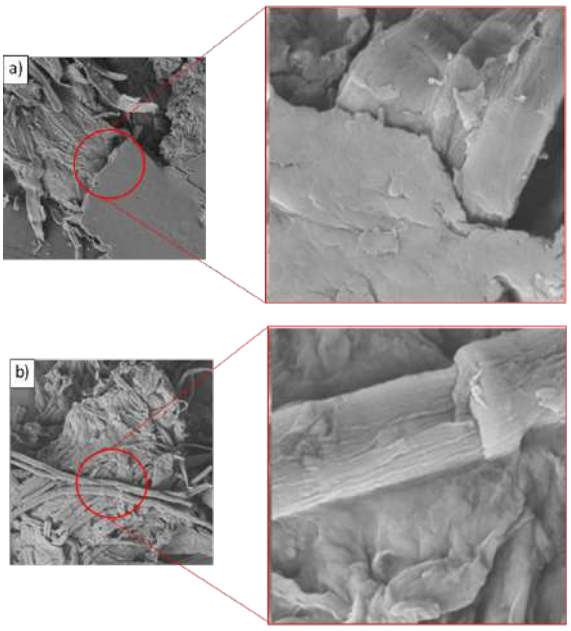

Figure 6. SEM micrographs of PSP/PLA at magnifications of ×500 and ×10,000: (a) before adsorption, (b) after Cr(VI) adsorption.

of the mixture and adhesion between the components can also be observed, resulting in a composite with a rough and fibrous surface in parts, which may confer hydrophobic characteristics and greater tensile strength (Wang *et al*., 2020). These results are similar to those presented by Wan Ishak *et al*., 2020, who synthesized a cellulose–PLA-based biocomposite, and SEM analysis showed a homogeneous mixture of the components with a rough surface. Similarly, Singh *et al*., 2020, developed a biocomposite based on cellulosic fibers and PLA, obtaining similar results in the homogenization of the material mixture and surface roughness of the biocomposite.

After the Cr(VI) adsorption test (Figure 6b), it is observed that the biocomposite presents a more compact surface, with fewer visible pores and brighter areas, suggesting the adhesion of the contaminant to the biocomposite surface, highlighting its capacity for Cr(VI) removal from solution (Fijoł *et al*., 2021).

3.6 Effect of adsorbent dosage on adsorption

The adsorption processes are affected by different parameters, such as temperature, contact time, pH, initial concentration, and stirring speed (Ishtiaq *et al*., 2020). In this study, the adsorption capacity of the synthesized biocomposite was evaluated by varying the adsorbent dose and the initial concentration of the pollutant at pH 2. The adsorbent doses used were 30 mg, 20 mg, and 10 mg. Figure 7 shows the results obtained for the efficiency of the adsorption process (%) as a function of the amount of adsorbent used for the removal of Cr(VI) at initial concentrations

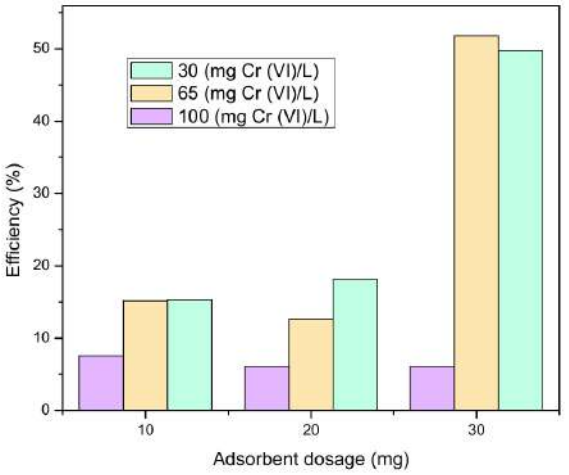

Figure 7. Variation of adsorbent dose at different initial concentrations. a) 30 mg/L, b) 65 mg/L, c) 100 mg/L.

of 30 mg/L, 65 mg/L, and 100 mg/L. It can be observed that, for an initial concentration of 30 mg/L, an efficiency of 49.74% was obtained with a dose of 30 mg of adsorbent, 18.15% with a dose of 20 mg, and 15.29% with a dose of 10 mg. For an initial concentration of 65 mg/L, an efficiency of 51.77% was obtained with a dose of 30 mg of adsorbent, 12.62% with 20 mg, and 15.15% with 10 mg. Finally, for an initial concentration of the pollutant (Cr(VI)) of 100 mg/L, an efficiency of about 6% was obtained with a dose of 30 mg and 20 mg, and an efficiency of 7.57% with a dose of 10 mg. The results showed a trend in which increasing the dose of the synthesized biocomposite led to greater adsorption efficiency, with the best adsorption yield obtained at a contaminant concentration of 65 mg/L and an adsorbent dose of 30 mg. This is due to the fact that a greater presence of adsorbent enhances the removal of a greater amount of contaminant (Shekhawat *et al*., 2023).

3.7 Biomaterial reuse tests

The recovery and reuse of the synthesized biocomposite were evaluated using two Cr(VI) elution agents (0.2 M HCl and 0.2 M NaOH). As shown in Figure 8, the capacity of the biocomposite for efficient Cr(VI) removal was assessed over three adsorption–desorption cycles. It was observed that HCl has the advantage of recovering the surface of the adsorbent more effectively than NaOH. This is due to the fact that HCl reduces the electrostatic interactions generated between the adsorbent and Cr(VI), allowing the release of the metal ions and the recovery of the adsorbent surface for reuse. It is also evident that, with each cycle, the biocomposite significantly reduces its adsorption capacity, especially when using NaOH (Prasad *et al*., 2022).

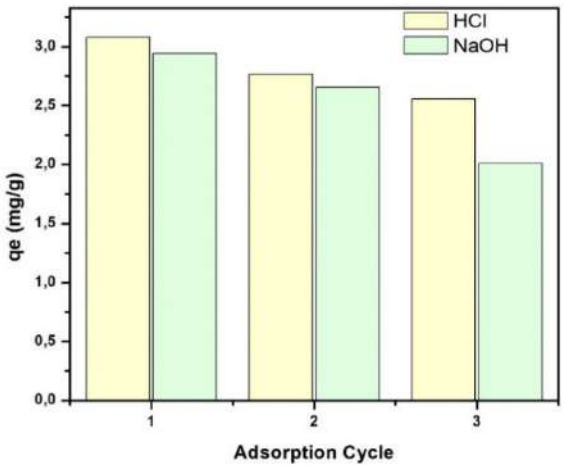

Figure 8. Metal removal in three adsorption cycles.

The results obtained throughout the study suggest that the biocomposite synthesized and modified with PLA represents a promising alternative for the treatment of contaminated water due to its characteristics, including excellent homogeneity in the material mixture, water resistance, thermal stability, good adhesion of the polymeric matrix to the fiber, as well as excellent yield in the synthesis process. In order to provide a broader and more versatile perspective on the PSP/PLA biocomposite, a comparative table (Table 2) is presented, including other studies reported in the literature on the synthesis and characterization of materials derived from agricultural waste. The data presented show consistency between the synthesis and characterization results obtained in this study and those reported by other researchers.

Table 2. Comparison with other studies.

Biomass	Modifying agent	Contaminant removed	Characterization	Reference
Bamboo	Glycidyl methacrylate (GMA)	Cr (VI)	**SEM:** Showed a rough surface on the synthesized material. **FTIR:** 1697–1706 cm^{-1} (C=O stretching vibration), a peak at 1173 cm^{-1} attributed to C–O group stretching, and 814 cm^{-1} (epoxy ring group); peaks between 2929 and 3380 cm^{-1} are due to aliphatic C–H, N–H, and O–H stretching vibrations. The peaks at 2900–3000 cm^{-1} were weakened, which was attributed to the impact of amine, hydroxyl, and aliphatic C–H groups on adsorption. **pH: 2**	(Zhang *et al*., 2022)
Coconut shell	PHB	Methylene blue	**SEM:** The biocomposite presented effective homogenization; it was observed that the biopolymer layers are thin due to increased water resistance in the presence of PHB. **FTIR:** It showed peaks between 3200–3500 cm^{-1}, attributed to single bonds indicating the presence of hydrogen bonds and the vibration of O–H, COOH, and NHx functional groups. Peaks at 2860 cm^{-1} and 2935 cm^{-1} are attributed to aliphatic compounds; peaks between 1650 cm^{-1} and 1850 cm^{-1} suggest the presence of carbonyl groups and aromatic rings; 1490 cm^{-1} and 829 cm^{-1} correspond to C–H, O–H, and C–O bonds. **TGA:** The highest mass loss of coconut cellulose occurs between 250 °C and 350 °C, with a loss of 49.4%, corresponding to the degradation of hemicellulose, lignin, extractives, and lignocellulosic derivatives. **pH:** 8	(Villabona-Ortíz *et al*., 2024)
Passion fruit peels Orange peels	NaOH y $Ca(CH_3CO)_2$	Zinc (II)	**TGA:** 390 °C to 400 °C represents the degradation of cellulose. **FTIR:** Peaks between 3600–3000 cm^{-1} correspond to the hydroxyl group (O–H); 3000–2800 cm^{-1} belong to the stretching of C–H groups; 1744 cm^{-1} and 1638 cm^{-1} correspond to the stretching of COO^- and C=O; peaks between 1430–1455 cm^{-1} indicate C–H groups, and peaks between 1422–1420 cm^{-1} indicate the presence of N–H.	(Castro *et al*., 2021)
Plantain peels			**SEM:** It showed a porous structure due to the removal of soluble substances during treatment with alkaline solutions.	
Potato pulp (PP)	PHBV	-	**SEM:** This indicates that the interfacial adhesion between the PHBV matrix and the PP powder is relatively poor. **TGA:** Thermal degradation occurs in the temperature range of 200 °C to 600 °C and is due to the degradation of hemicellulose, cellulose, and lignin.	(Righetti *et al*., 2019)
Plantain pseudo stem	PLA	-	**FTIR:** A peak between 3300–3500 cm^{-1} indicates the presence of amines (N–H); 2850–2970 cm^{-1} corresponds to C–H stretching; and peaks between 690–900 cm^{-1} indicate greater stability. **SEM:** Homogenization of the mixture and adhesion between the components, resulting in a composite with a rough and partially fibrous surface. **TGA:** The onset of decomposition occurs between 279.48 °C and 358.74 °C, with greater mass loss due to the degradation of lignin, cellulose, and hemicellulose present in the sample. **pH:** 2	Present study

Conclusions

The process of preparation and modification of the PSP/PLA biocomposite was successful, showing that the PLA biopolymer confers hydrophobic properties to the cellulose acetate extracted from the plantain stem, demonstrating that it is possible to cross-link vegetable fibers with biopolymers to produce biocomposites with potential use in the removal of pollutants.

Similarly, the TGA-DSC analysis of the cellulose showed that its decomposition occurs between 279.48 °C and 358.74 °C, with a mass loss of 99%, primarily due to the evaporation of water and moisture content and the degradation of lignin, cellulose, and hemicellulose present in the sample. Additionally, the point of zero charge (pHpzc) for the biocomposite was determined to be 8, indicating that at this pH value, the surface charge of the adsorbent is neutral, which may favor the adsorption of metals when treating solutions with a higher pH.

The results obtained in the adsorption test showed that at a concentration of 65 mg/L and a dose of 30 mg of adsorbent, an efficiency of 51.77% and an adsorption capacity of 3.72 mg/g were achieved. Finally, the characterization of the material revealed that the biocomposite possesses high stability. SEM analysis showed that the biocomposite has a fibrous and compact surface, confirming the presence of the biomass used. Additionally, it was observed that after the adsorption process, Cr(VI) adhered to the surface of the biocomposite, confirming its capacity to remove this contaminant. FTIR analysis also revealed the presence of O–H, C–H, amine (C–N) groups, and aromatic rings (C–N).

Acknowledgements

The authors would like to thank the University of Cartagena for supporting the development of this work.

References

Abu Aldam, S., Dey, M., Javaid, S., Ji, Y., & Gupta, S. (2020). On the synthesis and characterization of polylactic acid, polyhydroxyalkanoate, cellulose acetate, and their engineered blends by solvent casting. *Journal of Materials Engineering and Performance*, *29*(9), 5542–5556. https://doi.org/10.1007/s11665-020-04594-3

Aigbe, U. O., & Osibote, O. A. (2021). Carbon derived nanomaterials for the sorption of heavy metals from aqueous solution: A review. *Environmental Nanotechnology, Monitoring & Management*, *16*, 100578. https://doi.org/10.1016/j.enmm.2021.100578

Badawy, A. M., Farghali, A. A., Bonilla-Petriciolet, A., Selim, A. Q., & Seliem, M. K. (2023). Effective removal of Cr(VI) and methyl orange by nano magnetite loaded starch/muscovite biocomposite: Characterization, experiments, advanced modeling, and physicochemical parameters interpretation. *International Journal of Biological Macromolecules*, *224*, 1052–1064. https://doi.org/10.1016/j.ijbiomac.2022.10.190

Castro, D., Rosas-Laverde, N., Belén Aldás, M., Almeida-Naranjo, C., Guerrero, V. H., & Pruna, A. (2021). Chemical modification of agro-industrial waste-based bioadsorbents for enhanced removal of Zn (II) ions from aqueous solutions. *Materials*, *14*(9), 2134. https://doi.org/10.3390/ma14092134

Diaz-Rodriguez, K. F., Salazar-Pinto, B. M., Flores-Calla, S. S., & Gonzales-Condori, E. G. (2025). Potential use of artichoke (*Cynara cardunculus* L.) waste packed in filter bags for the removal of hexavalent chromium from water. *Revista Mexicana de Ingeniería Química*, *24*(1), 1–21. https://doi.org/10.24275/RMIQ/ia25426

Fijoł, N., Abdelhamid, H. N., Pillai, B., Hall, S. A., Thomas, N., & Mathew, A. P. (2021). 3D-printed monolithic biofilters based on a polylactic acid (PLA) – hydroxyapatite (HAp) composite for heavy metal removal from an aqueous medium. *RSC Advances*, *11*(51), 32408–32418. https://doi.org/10.1039/d1ra05202k

González-Delgado, A., Villabona-Ortíz, A., & Tejada-Tovar, C. (2022). Evaluation of three biomaterials from coconut mesocarp for use in water treatments polluted with an anionic dye. *Water*, *14*(3), 408. https://doi.org/10.3390/w14030408

Gupta, R. D., & Raghav, N. (2020). Nano-crystalline cellulose: Preparation, modification and usage as sustained release drug delivery excipient for some non-steroidal anti-inflammatory drugs. *International Journal of Biological Macromolecules*, *147*, 921–930. https://doi.org/10.1016/j.ijbiomac.2019.10.057

Hsini, A., Essekri, A., Aarab, N., Laabd, M., Ait Addi, A., Lakhmiri, R., & Albourine, A. (2020).

Elaboration of novel polyaniline@Almond shell biocomposite for effective removal of hexavalent chromium ions and Orange G dye from aqueous solutions. *Environmental Science and Pollution Research*, *27*(13), 15245–15258. https://doi.org/10.1007/s11356-020-08039-1

Iheanacho, O. C., Nwabanne, J. T., Obi, C. C., Igwegbe, C. A., Onu, C. E., & Dahlan, I. (2023). Adsorptive dephenolization of aqueous solutions using thermally modified corn cob: mechanisms, point of zero charge, and isosteric heat studies. *Adsorption Science and Technology*, *2023*. https://doi.org/10.1155/2023/2813663

Ishtiaq, F., Bhatti, H. N., Khan, A., Iqbal, M., & Kausar, A. (2020). Polypyrole, polyaniline and sodium alginate biocomposites and adsorption-desorption efficiency for imidacloprid insecticide. *International Journal of Biological Macromolecules*, *147*, 217–232. https://doi.org/10.1016/j.ijbiomac.2020.01.022

Islam, M. A., Angove, M. J., Morton, D. W., Pramanik, B. K., & Awual, M. R. (2020). A mechanistic approach of chromium (VI) adsorption onto manganese oxides and boehmite. *Journal of Environmental Chemical Engineering*, *8*(2), 103515. https://doi.org/10.1016/j.jece.2019.103515

Joshi, M., Dwivedi, C., & Manjare, S. (2024). A renewable cellulose-rich biofiller material extracted from waste banana stem fibers for reinforcing natural rubber composites. *Journal of Materials Science*, *59*(2), 519–534. https://doi.org/10.1007/s10853-023-09230-8

Kadea, S., Kittikorn, T., & Hedthong, R. (2024). Sustainable laminate biocomposite of wood pulp/PLA with modified PVA-MFC compatibilizer: Weathering resistance and biodegradation in soil. *Industrial Crops and Products*, *218*, 118913. https://doi.org/10.1016/j.indcrop.2024.118913

Khan, T., Isa, M. H., Mustafa, M. R., Yeek-Chia, H., Baloo, L., Abd Manan, T. S. B., & Saeed, M. O. (2016). Cr(VI) adsorption from aqueous solution by an agricultural waste based carbon. *RSC Advances*, *6*(61), 56365–56374. https://doi.org/10.1039/c6ra05618k

Kumar Sarangi, P., Subudhi, S., Bhatia, L., Saha, K., Mudgil, D., Prasad Shadangi, K., Srivastava, R. K., Pattnaik, B., & Arya, R. K. (2023). Utilization of agricultural waste biomass and recycling toward circular bioeconomy. *Environmental Science and Pollution Research*, *30*(4), 8526–8539. https://doi.org/10.1007/s11356-022-20669-1

Labied, R., Benturki, O., Eddine Hamitouche, A. Y., & Donnot, A. (2018). Adsorption of hexavalent chromium by activated carbon obtained from a waste lignocellulosic material (*Ziziphus jujuba* cores): Kinetic, equilibrium, and thermodynamic study. *Adsorption Science & Technology*, *36*(4), 1066–1099. https://doi.org/10.1177/0263617417750739

Liang, S., Cai, W., Dang, C., Peng, X., Luo, Z., & Wei, X. (2023). Synthesis of sodium alginate/phosphorus tetramethylmethyl sulfate biocomposite beads with exceptional adsorption rate for Cr(VI) removal. *Journal of Environmental Chemical Engineering*, *11*(2), 109317. https://doi.org/10.1016/j.jece.2023.109317

Luqman., M., Vesuanathan, T. A., & Salleh, M. N. (2020). Isolation and characterization of microcrystalline cellulose extracted from banana fiber in poly(lactic acid) biocomposite produced from solvent casting technique. *IOP Conference Series: Materials Science and Engineering*, *957*(1), 012005. https://doi.org/10.1088/1757-899x/957/1/012005

Madenli, Ö., Akarsu, C., & Deveci, E. Ü. (2023). Effective removal of hexavalent chromium by novel modified alginate-based biocomposites: Characterization, kinetics and equilibrium studies. *Ceramics International*, *49*(10), 16440–16450. https://doi.org/10.1016/j.ceramint.2023.02.005

McNeill, D. C., Pal, A. K., Nath, D., Rodriguez-Uribe, A., Mohanty, A. K., Pilla, S., Gregori, S., Dick, P., & Misra, M. (2024). Upcycling of ligno-cellulosic nutshells waste biomass in biodegradable plastic-based biocomposites uses-a comprehensive review. *Composites Part C: Open Access*, 100478. https://doi.org/10.1016/j.jcomc.2024.100478

Melikoğlu, A. Y., Bilek, S. E., & Cesur, S. (2019). Optimum alkaline treatment parameters for the extraction of cellulose and production of cellulose nanocrystals from apple pomace. *Carbohydrate Polymers*, *215*, 330–337. https://doi.org/10.1016/j.carbpol.2019.03.103

Meng, F., Wang, G., Du, X., Wang, Z., Xu, S., & Zhang, Y. (2019). Extraction and characterization of cellulose nanofibers and

nanocrystals from liquefied banana pseudo-stem residue. *Composites Part B: Engineering*, *160*, 341–347. https://doi.org/10.1016/j.compositesb.2018.08.048

Mi, B., & Wang, Y. (2024). Performance and mechanism of porous carbons derived from biomass as adsorbent for removal of Cr(VI). *Processes*, *12*(10), 2229. https://doi.org/10.3390/pr12102229

Moreno-Rubio, J. G., Osornio-Rubio, N. R., Jiménez-Islas, H., Barrera-Calva, E., Ramírez-Yañez, A. Y., & Martínez-González, G. M. (2025). Characterization and efficiency of Luffa cylindrica as bioadsorbent in Cr (VI) remotion from synthetic wastewater. *Revista Mexicana de Ingeniera Quimica*, *24*(2), 1–14. https://doi.org/10.24275/rmiq/Mat25443

Nandiyanto, A., Oktiani, R., & Ragadhita, R. (2019). How to read and interpret FTIR spectroscope of organic material. *Indonesian Journal of Science and Technology*, *4*(1), 97–118. https://doi.org/10.17509/ijost.v4i1.15806

Nata, I., Irawan, C., Hudha, M. I., Lesti, A., Syarkani, M. H., & Naufal, A. (2024). Enhanced copper ion adsorption by rice husk and sugarcane bagasse-based magnetic nanoparticles biocomposites. *ASEAN Journal of Chemical Engineering*, *24*(1), 79–89. https://doi.org/10.22146/ajche.12236

Nurdin, S., Roslan, A., Abbakar, M. S. A., Khairuddin, S. A., & Sukri, H. A. M. (2015). Rock melon activated carbon (RMAC) for removal of Cd(II), Ni(II) and Cu(II) from wastewater: kinetics and adsorption equilibrium. *International Journal of Chemical Engineering and Applications*, *6*(2), 105–110. https://doi.org/10.7763/ijcea.2015.v6.461

Ortega, G. S., & Rodríguez, A. E. (2018). Síntesis de acetato de celulosa y rayón a partir de residuos agroindustriales del cultivo y procesamiento de piña. *Revista Teinnova*, *3*, 22–28.

Prasad, P. S., Gomathi, T., Sudha, P. N., Deepa, M., Rambabu, K., & Banat, F. (2022). Biosilica/Silk Fibroin/Polyurethane biocomposite for toxic heavy metals removal from aqueous streams. *Environmental Technology and Innovation*, *28*, 102741. https://doi.org/10.1016/j.eti.2022.102741

Rahim, M., & Mas Haris, M. R. H. (2022). Banana trunk fibers-infused acidified chitosan-based biocomposite for Cadmium(II) sorption. *Journal of Natural Fibers*, *19*(13), 4908–4922. https://doi.org/10.1080/15440478.2020.1870636

Righetti, M. C., Cinelli, P., Mallegni, N., Stäbler, A., & Lazzeri, A. (2019). Thermal and mechanical properties of biocomposites made of poly(3-hydroxybutyrate-co-3-hydroxyvalerate) and potato pulp powder. *Polymers*, *11*(2), 308. https://doi.org/10.3390/polym11020308

Rodríguez, A., Ovejero, G., Sotelo, J. L., Mestanza, M., & García, J. (2010). Adsorption of dyes on carbon nanomaterials from aqueous solutions. *Journal of Environmental Science and Health, Part A* , *45*(12), 1642–1653. https://doi.org/10.1080/10934529.2010.506137

Saifullah, A., Chacko, N. G., Dhakal, H. N., Khan, S. H., Sarker, F., & Zhang, Z. (2024). Valorisation of agricultural residue bio-mass date palm fibre in dry-blended polycaprolactone (PCL) bio-composites for sustainable packaging applications. *Waste and Biomass Valorization*, 1–13. https://doi.org/10.1007/S12649-024-02550-z

Satha, H., Kouadri, I., & Benachour, D. (2020). Thermal, structural and morphological studies of cellulose and cellulose nanofibers extracted from bitter watermelon of the cucurbitaceae family. *Journal of Polymers and the Environment*, *28*(7), 1914–1920. https://doi.org/10.1007/S10924-020-01735-6

Selimin, M. A., Latif, A. F. A., Er, Y. C., Muhamad, M. S., Basri, H., & Lee, T. C. (2022). Adsorption efficiency of banana blossom peels (*musa acuminata colla*) adsorbent for chromium (VI) removal. *Materials Today: Proceedings*, *57*, 1262–1268. https://doi.org/10.1016/j.matpr.2021.10.502

Shekhawat, A., Jugade, R., Gomase, V., Kahu, S., Dhandayutham, S., & Pandey, S. (2023). Adsorptive removal of As (III) by cellulose-Sn (IV) biocomposite. *Journal of Composites Science*, *7*(1), 19. https://doi.org/10.3390/jcs7010019

Sherugar, P., Padaki, M., Naik, N. S., George, S. D., & Murthy, D. H. (2022). Biomass-derived versatile activated carbon removes both heavy metals and dye molecules from wastewater with near-unity efficiency: Mechanism and kinetics. *Chemosphere*, *287*, 132085. https://doi.org/10.1016/j.chemosphere.2021.132085

Shrestha, P., Sadiq, M. B., & Anal, A. K. (2021). Development of antibacterial biocomposites reinforced with cellulose nanocrystals derived from banana pseudostem. *Carbohydrate Polymer Technologies and Applications*, *2*, 100112. https://doi.org/10.1016/j.carpta.2021.100112

Singh, A. A., Genovese, M. E., Mancini, G., Marini, L., & Athanassiou, A. (2020). Green processing route for polylactic acid–cellulose fiber biocomposites. *ACS Sustainable Chemistry and Engineering*, *8*(10), 4128–4136. https://doi.org/10.1021/acssuschemeng.9b06760

Tejada-Tovar, C., Gonzalez-Delgado, A. D., & Villabona-Ortiz, A. (2019). Characterization of residual biomasses and its application for the removal of lead ions from aqueous solution. *Applied Sciences*, *9*(21), 4486. https://doi.org/10.3390/app9214486

Tejada-Tovar, C., Villabona-Ortíz, Á., & Ortega-Toro, R. (2023). Removal of metals and dyes in water using low-cost agro-industrial waste materials. *Applied Sciences*, *13*(14), 8481. https://doi.org/10.3390/app13148481

Van, T. T., Gaspillo, P., Thanh, H. G. T., Nhi, N. H. T., Long, H. N., Tri, N., Van, T. T. N., Nguyen, T. T., & Huynh, K. P. H. (2022). Cellulose from the banana stem: optimization of extraction by response surface methodology (RSM) and charaterization. *Heliyon*, *8*(12), e11845. https://doi.org/10.1016/j.heliyon.2022.e11845

Vatanpour, V., Dehqan, A., Paziresh, S., Zinadini, S., Zinatizadeh, A. A., & Koyuncu, I. (2022). Polylactic acid in the fabrication of separation membranes: A review. *Separation and Purification Technology*, *296*, 121433. https://doi.org/10.1016/j.seppur.2022.121433

Villabona-Ortíz, Á., Ortega-Toro, R., & Pedroza-Hernández, J. (2024). Biocomposite based on polyhydroxybutyrate and cellulose acetate for the adsorption of methylene blue. *Journal of Composites Science*, *8*(7), 234. https://doi.org/10.3390/jcs8070234

Wan-Ishak, W. H., Rosli, N. A., & Ahmad, I. (2020). Influence of amorphous cellulose on mechanical, thermal, and hydrolytic degradation of poly(lactic acid) biocomposites. *Scientific Reports*, *10*(1), 1–13. https://doi.org/10.1038/s41598-020-68274-x

Wang, Q., Ji, C., Sun, J., Zhu, Q., & Liu, J. (2020). Structure and properties of polylactic acid biocomposite films reinforced with cellulose nanofibrils. *Molecules*, *25*(14), 3306. https://doi.org/10.3390/molecules25143306

Yadav, N., Saini, O., Debnath, N., Singh, S., Thakur, T. K., Rajendra, K., Meena, R., Thakur, I. S., & Srivastava, S. (2024). Optimizing enhanced heavy metal detoxification by novel hybrid fungal hyphae-nano-biocomposite functionalized with graphene oxide: Unravelling process parameters & adsorption modelling. *Process Safety and Environmental Protection*, *188*, 917–928. https://doi.org/10.1016/j.psep.2024.05.086

Yang, J., Li, Y., Li, X., Ji, M., Peng, S., Man, J., Zhou, L., Li, F., & Zhang, C. (2024). Starch-fiber foaming biodegradable composites with polylactic acid hydrophobic surface. *International Journal of Biological Macromolecules*, *267*, 131406. https://doi.org/10.1016/j.ijbiomac.2024.131406

Zarna, C., Opedal, M. T., Echtermeyer, A. T., & Chinga-Carrasco, G. (2021). Reinforcement ability of lignocellulosic components in biocomposites and their 3D printed applications–a review. *Composites Part C: Open Access*, *6*, 100171. https://doi.org/10.1016/j.jcomc.2021.100171

Zhang, Y. N., Guo, J. Z., Wu, C., Huan, W. W., Chen, L., & Li, B. (2022). Enhanced removal of Cr(VI) by cation functionalized bamboo hydrochar. *Bioresource Technology*, *347*, 126703. https://doi.org/10.1016/j.biortech.2022.126703

Zhao, M. L., Wang, J. X., Bian, X. K., Zhang, J., Han, Y. W., Xu, S. X., Lee, S. C., & Zhao, J. Z. (2023). Hexavalent chromium causes centrosome amplification by inhibiting the binding between TMOD2 and NPM2. *Toxicology Letters*, *380*, 12–22. https://doi.org/10.1016/j.toxlet.2023.03.008

Zheng, G., Kang, X., Ye, H., Fan, W., Sonne, C., Lam, S. S., Liew, R. K., Xia, C., Shi, Y., & Ge, S. (2024). Recent advances in functional utilisation of environmentally friendly and recyclable high-performance green biocomposites: A review. *Chinese Chemical Letters*, *35*(4), 108817. https://doi.org/10.1016/j.cclet.2023.108817

Vol. 24, No. 2(2025) IA25488
Revista Mexicana de Ingeniería Química

Changes in microbial diversity and methane yield caused by overloading in systems of chicken litter, microalgae oil-free and glycerol in co-digestion

Cambios en la diversidad microbiana y producción de metano causados por sobrecarga en sistemas de gallinaza, microalgas libres de aceite y glicerol en codigestión

G. Hernández-Eugenio[1], T. Espinosa-Solares[2,3], C. López-Ortiz[4], J. C. Meneses-Reyes[2], T. G. Ochoa-Bernal[1]*
[1]*Departamento de Ingeniería Agrícola y Uso Integral del Agua, Universidad Autónoma Chapingo, Chapingo 56230, Estado de México 56230, MÉXICO*
[2]*Departamento de Ingeniería Agroindustrial, Universidad Autónoma Chapingo, Chapingo 56230, Estado de México 56230, MÉXICO*
[3]*Agricultural Research and Extension Center, Southern University, Baton Rouge, LA 70813, USA*
[4] *Biology Department, West Virginia State University, Dunbar, WV 25112-1000, USA*
Received: December 16, 2024; Accepted: March 25, 2025

Abstract
The objective of this study was to observe the response of chicken litter (CL), oil-free microalgae (M), and glycerol (G) in disturbed systems with organic loading rate (OLR) in mono, and co-digestion. To elucidate the impact of the OLR on the methane yield, Volatile Fatty Acids (VFAs), and microbial communities. In this study, 3 treatments were performed CL, CL-M, CL-M-G, in different ratios 100: 0: 0 (CL), 70:30:0 (CL-M) y 67:30:3 (CL-M-G) which were based on the best substrates with the highest Biochemical Methane Potential (BMP) reported in our previous research. Our results indicated that the CL-M system had the highest methane yield (12,481.16 mL CH_4 $g_{vs\ added}^{-1}$) and a lower production of VFAs (70,842.07 mg L^{-1}) compared with the CL and CL-M-G systems. In addition, the microbial analysis revealed that each methanogen was more related to a system, *Methanoculleus* to the CL system, *Methanosarcina* to the CL-M system, and *Methanothrix* to the CL-M-G system. Although the systems were disturbed, did not inhibit the anaerobic digestion (AD). These findings have shown that disturbances acidify the environment, reduce the abundance of bacteria, and promote methane production in the hydrogenotrophic pathway.
Keywords: Disturbances; Organic loading rate; Mesophilic; Chicken litter; Microbial diversity; Methane yield.

Resumen
El objetivo de este estudio fue observar la respuesta que tuvo pollinaza (CL), microalga libre de aceite (M), y glicerol en sistemas perturbados con sobre carga de materia orgánica (OLR) en mono- y co-digestión. Para elucidar el impacto de la OLR sobre el rendimiento de metano, en los ácidos grasos volátiles (AGVs) y en las comunidades microbianas. En este estudio, se realizaron 3 tratamientos CL, CL-M, CL-M-G, en diferentes proporciones 100: 0: 0 (CL), 70:30:0 (CL-M) y 67:30:3 (CL-M-G) que se basaron en los mejores sustratos con el mayor Potencial Bioquímico de Metano (PBM) reportado en nuestra investigación anterior. Nuestros resultados indicaron que CL-M tuvo el mejor rendimiento de metano (12,481.16 mL CH_4 $g_{svalimentados}^{-1}$) y la más baja producción de AGVs (70,842.07 mg L^{-1}) comparado con CL y CL-M-G. En adición, el análisis microbiano reveló que cada metanógeno fue más a fin a cada sistema, *Methanoculleus* para el sistema CL, *Methanosarcina* para CL-M y *Methanothrix* para CL-M-G. A pesar de que los sistemas se encontraban perturbados no se inhibió la DA. Estos hallazgos han demostrado que las perturbaciones acidifican el medio, reducen la abundancia de bacterias y promueven la producción de metano por la vía hidrógenotrófica.
Palabras clave: Perturbaciones; Sobrecarga de materia orgánica; Mesofílico; Pollinaza; Diversidad microbiana; Rendimiento de metano.

* *Corresponding author. E-mail*: thaliagpeochoabernal@gmail.com ;
https://doi.org/10.24275/rmiq/IA25488
ISSN:1665-2738, *issn-e*: 2395-8472

1 Introduction

Anaerobic digestion (AD) is one of the alternatives to produce clean energy, either in the form of heat, electricity, and/or biofuels (methane and hydrogen) (Kabeyi & Olanrewaju, 2022). AD can also contribute to reduce the greenhouse gas (GHG) emissions (Malet *et al*., 2023) through the use of digestate produced rich in carbon (C) and nitrogen (N), which, when used as fertilizer, helps to capture organic carbon in the soils, thus contributing to the elimination of atmospheric carbon dioxide (CO_2) and by replacing synthetic nitrogen fertilizers helps to avoid the emission of gases from of these synthetic fertilizers (Malet *et al*., 2023). Another use of digestate from AD is the phytoregulators; for instance, Castro-Sierra *et al*. (2024) reported that dairy cattle and swine manure digestates produce gibberellic acid, indoleacetic acid, and kinetin. The residuals are from diverse sources, such as food (Mahmudul *et al*., 2022) and algae (Rivera-Hernández *et al*., 2022) wastes. Each residual has its own characteristics and biodegradability, which can be used as a mono-substrate or by the co-digestion method, using municipal (Sanaye *et al*., 2022) to food waste (Oduor *et al*., 2022). Among several substrates, *Chlorella* sp microalgae have been used in the co-digestion with effluents from wastewaters (Solé-Bundó *et al*., 2019), cooking oil, maize silage (Wirth *et al*., 2019), cow manure (Alharbi, 2024), and chicken litter and glycerol (Meneses-Reyes *et al*., 2018).

Chlorella sp microalga biomass is rich in protein; it has been reported that its carbon-nitrogen ratio (C/N) ranges from 4.3 (Zhu et al., 2019), 4.86 (Ruirui Li *et al*., 2017) to 5.35 (Meneses-Reyes *et al*., 2017), which is less than the optimal range for AD (20 to 30) (Gil et al., 2019). Microalgae have been reported to be efficiently digested in co-digestion with carbon-rich raw materials, rebalancing the C/N and increasing methane production. The optimal C/N for co-digestion varies depending on the co-digestion material. Thus, for chicken manure was 6.75 C/N (Ruirui Li *et al*., 2017), for triple co-digestion with glycerol and chicken litter was 6.94 C/N (Meneses-Reyes *et al*., 2017), and for used cooking oil was 4.77 C/N (Rétfalvi *et al*., 2016).

It has also been reported that high loads of Organic Loading Rate (OLR) can cause a drop in pH due to the rapid generation of volatile fatty acids (VFA) (Magdalena *et al*., 2019). Slezak *et al*. (2017) studied the effect of OLR on VFA production in dark fermentation and identified the VFA concentration increases only up to the initial OLR of 48.2 g_{VS} L^{-1}. Increasing the OLR also effects the VFAs composition in the product stream. Wijekoon *et al*. (2011) identified that the predominant VFAs component changed from acetic acid to n-butyric acid with an overall increase in VFAs concentration when OLR was increased from 5 to 12 kg COD $m^{-3}d^{-1}$ in a two-stage thermophilic anaerobic membrane bioreactor. In a study by Babaee and Shayegan (2011) in a 70 L digester with vegetable wastes, when reaching OLR of 2.75 kg VS $m^{3\text{-}1}d^{-1}$, the degradation of volatile solids and biogas production decreased. Musa et al. (2018) reports a decrease in chemical oxygen demand (COD) from 50 % to an OLR of 15 g $L^{-1}d^{-1}$ of cattle slaughterhouse wastewater.

In fact, changes in OLR affect the AD process in terms of population dynamics and organic matter availability and, therefore, methane production yields (Li *et al*., 2022). The OLR is a critical operating parameter of AD that must be controlled to avoid disturbances in the process (Nkuna *et al*., 2022). An OLR shock generally causes an imbalance between the hydrolysis / acidogenesis and methanogenesis steps (Wu et al., 2021). The behavior of bacterial communities during disturbances due to organic overload is more complex due to the high number of species and their functional redundancy (Nguyen *et al*., 2019). Even when the overload is caused by the same co-substrate, the results of different studies are contradictory, so the response of the microbial community is not predictable by the raw material or the inoculum used in the reactors (Braz *et al*., 2019).

Most mono-substrate AD practices have poor digestion performance due to inherent substrate defects (Vivekanand *et al*., 2018) leading to different conversion rates and lower production efficiency methane (Wei *et al*., 2019). Anaerobic co-digestion of two or more organic wastes (Zhang *et al*., 2020) can overcome the inherent limitations associated with mono-digestion of an individual substrate by synergistic effect, resulting in increased biomethane yield specific or an increase in digestion kinetics (Kim *et al*., 2019). For example, Serna-García *et al*. (2020) evaluated the performance of biogas production and reported a methane production of 130 mL CH_4 $d^{-1}L^{-1}_{reactor}$, with microalgae (*Scenedesmus* and *Chlorella*) and primary sludge. With an increase in biodegradability of around 73 % compared to the mono-digestion of pristine algae. Another study conducted by Zhang et al. (2020) showed that microalgae *Chlorella vulgaris* in co-digestion with potato processing waste and glycerol (G) to an average OLR of 0.30 g COD per L per d improved the volumetric production of methane with an average production of 0.59 ± 0.08 L CH_4 per L per d. An additional study by R. Li *et al*. (2017) microalgae *Chlorella* 1067 was cultivated in chicken manure (CM) based digestate, and then algae biomass was used as co-substrate for AD with CM. They showed that co-digestion achieved the highest methane production of 238.71 mL g_{VS}^{-1} and the most

significant synergistic effect.

The synergistic effect of co-digestion generally demonstrates higher biomethane yields, accelerated biodegradation processes, higher hydrolysis rate, or a combination of these (Karki *et al*., 2021). In this sense, co-digestion is a strategy that consists of mixing a substrate with another carbon source, in order to improve operational parameters such as the C / N ratio, buffer disturbances and / or dilute inhibitors. As a result, higher process performance can be achieved. Furthermore, co-digestion allows the treatment of different wastes using the same facilities, and biofertilizers can also be generated (Pan *et al*., 2021), in fact, co-digestion has been proposed as a promising approach to improve the performance of methane and the general performance of digestion (Lv *et al*., 2021). To our knowledge, various substrates have been used in co-digestion. Our research team has worked with chicken litter (CL) -oil-free microalgae (M) - glycerol (G) as substrates, where Meneses-Reyes *et al*. (2018) proved that the Biochemical Methane Potential (BMP) and the Specific Methanogenic Activity (SMA) increased in CL-M-G, which shows that these systems improved AD. In the present study we introduce an additional level of complexity, that is, disturbing systems with OLR. Therefore, the objectives of this study were to observe the response that the systems had to the overloading and to elucidate the impact of the influence of OLR on microbial communities and the methane yield in mono, and co-digestion of three substrates from the CL, M, and G. For a better understanding of how this complex process is affected, including microbial interactions and methane production. So far, the response of how the microbiomes in the digesters respond to overloading is imperative both from the point of view of microbial ecology and the performance of biogas production.

2 Material and methods

2.1 Experimental procedure

The feedstock used in this work were chicken litter (CL, provided by a commercial poultry farm located in the municipality of Tepetlaoxtoc, State of Mexico, Mexico); oil-free microalgae biomass from Chlorella vulgaris powder (M, Future Foods Company, México); and glycerol (G, grade United States Pharmacopeial Convention, USP). Our research team reported the physical and chemical characteristics of these feedstocks in a previous report (Meneses-Reyes *et al*., 2017). Three different treatments were tested based on different ratios of CL, M, and G as shown: 100:0:0 (CL), 70:30:0 (CL-M), and 67:30:3 (CL-M-G), which were based on the best feedstocks ratios with highest BMP reported in our previous research (Meneses-Reyes *et al*., 2017). The digestion process was performed in a stainless-steel digester with a working volume of 10 L and a headspace of 3 L each. To achieve a steady state condition, two hydraulic retention times (HRT=30 d), 60 d, were used, and the end of this period was considered time 0. The disturbances were induced with two OLR shocks of 49.3 g_{VS} L^{-1} d^{-1} and 35.7 g_{VS} L^{-1} d^{-1} starting on day 0 and 301, respectively, and both were maintained for 11 consecutive days, the other day's food with 3 % TS. On days 297 and 360, samples from the digester were taken for the DNA for microbial communities' analysis, as shown in Figure 1.

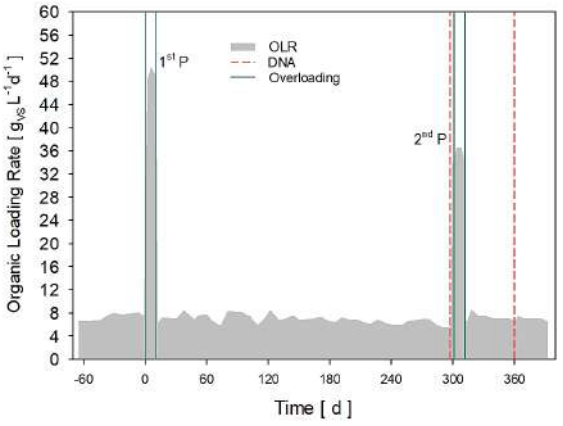

Figure 1. Organic loading rate and sample collection points for DNA analysis during the experiment. The green line ( ) indicated the first overloading period 49.3 g_{VS} L^{-1} d^{-1} (1st P), and the second overloading period 35.7 g_{VS} L^{-1} d^{-1} (2nd P); Red short dashed line (----) indicated dates of sampling DNA; Gray box indicates stable feeding of the 3 % TS system.

2.2 Analytical methods

The analytical methods employed in this study were previously described by our research group in Meneses-Reyes *et al*. (2017). To evaluate the profiles of volatile fatty acids (VFAs), including acetate, propionate, butyrate, iso-butyrate, valerate, iso-valerate, caproate, and iso-caproate, we followed the detailed procedure outlined by Meneses-Reyes *et al*. (2017) using gas chromatography (GC). Initially, VFAs were determined from a sample of effluent that had been acidified with HCl to achieve a pH of three after centrifugation at 14,500 rpm for 10 minutes to obtain the supernatant. The acidified samples were then injected into a gas chromatograph system (Clarus 500, Perkin Elmer, USA) equipped with a flame ionization detector (FID) and a capillary column (Elite-FFAP; 30 m x 0.32 mm; Perkin Elmer, USA). For analysis, we used the Volatile Free Acid Mix analytical standard (Supelco 46975-U, Sigma-Aldrich, USA). A potentiometer (Thermo Scientific

Orion 5 Star, Singapore) was employed to determine the pH. Biogas production was measured using a saline water displacement method in conjunction with a digital counter (LA8N-BN, Autonics, Korea). The methane content in the biogas was estimated using the same gas chromatograph (Clarus 500, Perkin Elmer, USA) based on a calibration curve established with a pure methane standard (HDSP No. P-4618-F, Praxair, México).

2.3 *Total DNA isolation and sequencing*

Total DNA was isolated using the MoBio Power Soil DNA isolation kit (MoBio Laboratories, Carlsbad, CA, United States), following the manufacturer's protocol. The DNA integrity was checked by electrophoresis on agarose gel (1 % w/v), and the quantification of the extracted DNA samples was performed by using LabChip GX Touch Nucleic Acid Analyzer (Perkin Elmer).

For the preparation of libraries, the GenXpro (Frankfurt am Main, Germany) protocol was used, which consisted of after the fragmentation with directed ultrasound (Diagenode Bioruptor Pico), barcoding adapters included in UMIs - TrueQuant Adapters (patented by GenXpro) were added. All samples were sequenced by duplicate from the ends (2 × 150 bp) using the Illumina NextSeq500 platform (Illumina, USA).

2.4 *Metagenomic analysis*

Raw reds were quality checked by using FASTQC (Brown *et al*., 2017) and adapter-and low-quality-filtered (Q value ≤ 30) by using Trimmomatic (Bolger *et al*., 2014). Clean reads were used to perform the metagenomics assembly using MEGAHIT v1.0 (Li *et al*., 2016), and Kraken2 (Wood *et al*., 2019) on the Omics box platform (https://www.biobam.com/omicsbox). Subsequently, taxonomy classification and microbial abundance was assigned by MetaPhlAn v3.0 software through blasting marker genes with effective reads (Beghini *et al*., 2021).

The raw sequence data obtained from this study have been deposited into the NCBI sequence read archive (SRA) under the BioProject ID: PRJNA1183444.

3 Results and discussion

3.1 *Methane yield*

Figure 2 illustrates the effects of the overloading Organic Loading Rate (OLR) at 49.3 g_{VS} $L^{-1}d^{-1}$ and 35.7 g_{VS} $L^{-1}d^{-1}$ on the methane yield. Prior to the first disturbance, the three systems were in a quasi-study state. The average initial methane yield recorded was 218.17, 260.90, and 264.44 mL CH_4 $g_{vsadded}^{-1}$ for CL, CL-M, and CL-M-G systems, respectively.

During the first overloading of OLR (49.3 g_{VS} $L^{-1}d^{-1}$) phase, the impact on the methane yield was significant. The reductions observed were 59 %, 44 %, and 26 % for the CL, CL-M, and CL-M-G systems, respectively.

After the first disturbance, when the overloading of OLR pressure was alleviated, the systems exhibited partial recovery, displaying high methane yield values of 500 mL CH_4 $g_{vsadded}^{-1}$ for CL, 490 mL CH_4 $g_{vsadded}^{-1}$ for CL-M, and 700 mL CH_4 $g_{vsadded}^{-1}$ for CL-M-G. This recovery can be attributed to the residual organic matter available for methane processing after removing the OLR pressure overloading. The initial methane yield levels recovered to 164, 109, and 250, respectively.

Between the two disturbances, the CL-M system showed the most stability, suggesting that co-digestion aided in mitigating the impacts of organic matter overload.

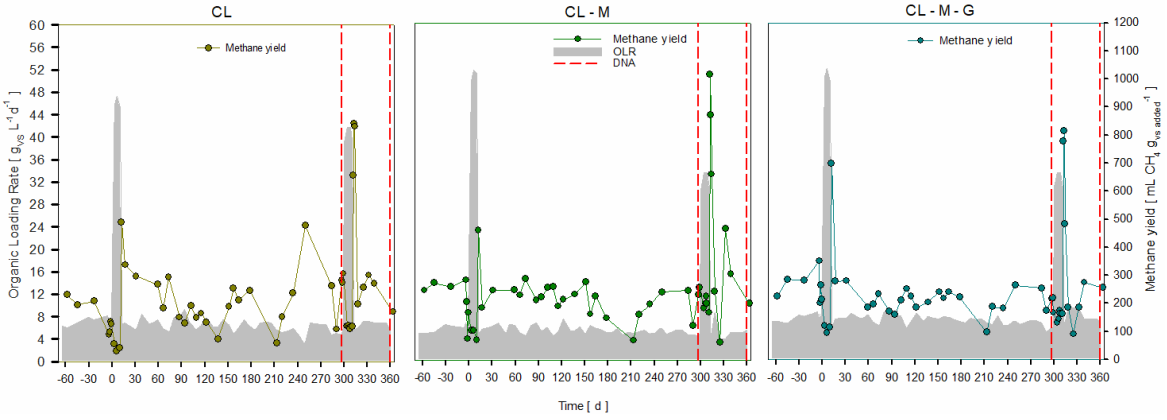

Figure 2. Changes observed in the methane yield and organic loading rate (OLR) during the experiment. CL: Chicken litter; M: Microalgae oil-free; G: Glycerol. The red short dashline (----) indicated DNA sample. Gray area ( ) indicated the organic loading rate.

During the second disturbance (35.7 g_{VS} $L^{-1}d^{-1}$), the decline in the methane yield was less severe than during the first disturbance, with the reductions being 44 %, 25 %, and 41 % for the CL, CL-M, and CL-M-G systems, respectively. The systems regained stability in 14, 7, and 28 days. This response may indicate that the systems were learning how to recover from disturbances, a phenomenon noted by other researchers who suggest that disturbed systems may have some degree of memory, allowing the microbiome to adapt to changes (Spirito *et al*., 2018).

After the second disturbance, upon stopping the OLR pressure overloading, the methane yield peaks were more pronounced in the systems. This could be due to the rapid degradation of substrates by resilient microorganisms that had been adapted following the first disturbance. In the CL and CL-M-G systems, the maximum peak in activity doubled, reaching around 800 mL CH_4 $g_{vsadded}^{-1}$, while in the CL-M system, it approached nearly 1000 mL CH_4 $g_{vsadded}^{-1}$. Although these measures are instantaneous reflections of methane production, they also indicate the potential development of specific microbial communities capable of efficiently processing acetate and propionate produced after the disturbances.

At the final observation point, all systems were in recovery, with the CL-M system demonstrating the best recovery. This success may be attributed to its higher abundance of microorganisms. The increased diversity has likely allowed for various microorganisms to fulfill different roles, adapting to the changed conditions.

In all cases, despite the disturbances, no process inhibition was observed. This suggests that there were microorganisms adapted to stressful overload conditions with rapid recovery, especially in the CL-M system, strengthening that co-digestion favors anaerobic digestion for biogas production.

3.2 Volatile fatty acid

fFigure 3 shows the volatile fatty acids (VFAs) in the order from greater to lower concentration as follows: acetate, propionate, iso-valerate, butyrate, iso-butyrate, caproate, valerate, and iso-caproate. In the 430-day study period, the highest total of the VFAs was obtained in the CL system with 214,591.11 mg L^{-1}, as observed in **Table 1**. In the VFAs generation, the opposite behavior was observed contrary to the methane yield (Figure 2). As expected in the first impact (49.3 g_{VS} $L^{-1}d^{-1}$), more significant concentrations of VFAs were generated concerning the second impact (35.7 g_{VS} $L^{-1}d^{-1}$).

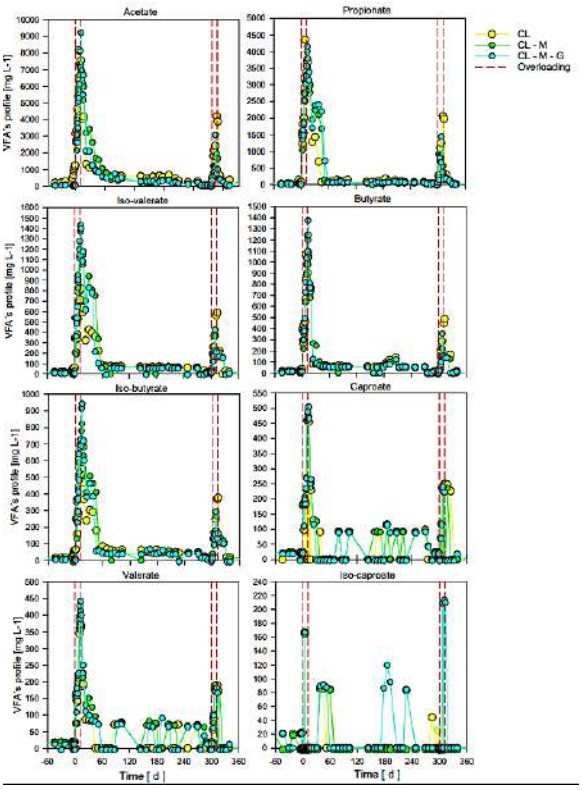

Figure 3. Volatile Fatty Acids profile during the experiment (VFAs). CL: Chicken litter; M: Microalgae oil-free; G: Glycerol. The red short dash line (----) indicated overloading periods.

This indicates that the CL system remained acidified, which explains why it had the slightest methane yield compared to the CL-M system. These high levels of VFAs found in our systems could inhibit the process of methanogenesis (Serrano-Meza *et al*., 2020). However, these systems remained stable, and it is inferred that the microbiome adapts to these stress conditions. Braz *et al*. (2019) researched anaerobic reactors using sewage sludge, which produced 2,500 mg L^{-1} of VFAs. Basak *et al*. (2021) studied the effects of overloading digesters with food waste leachate, resulting in 11300 mg L^{-1} of VFAs. Both studies found that these conditions led to the acidification of the systems. It is well known that acidified environments inhibit biogas production because methanogens are sensitive to acidic conditions.

Table 1. Volatile Fatty Acids (VFAs) concentrations produced by each system.

System	Acetate [mg L^{-1}]	Propionate [mg L^{-1}]	Iso-valerate [mg L^{-1}]	Butyrate [mg L^{-1}]	Iso-butyrate [mg L^{-1}]	Caproate [mg L^{-1}]	Valerate [mg L^{-1}]	Iso-Caproate [mg L^{-1}]
CL	112,927.40	52,661.75	13,901.43	13,997.48	10,000.58	5,249.15	4,896.41	956.92
CL-M	103,575.49	49,677.13	19,149.85	12,295.13	11,853.58	6,211.71	5,998.41	546.34
CLM-G	98,259.82	52,560.35	18,672.62	13,726.77	11,900.30	6,350.18	5,961.98	1,516.77

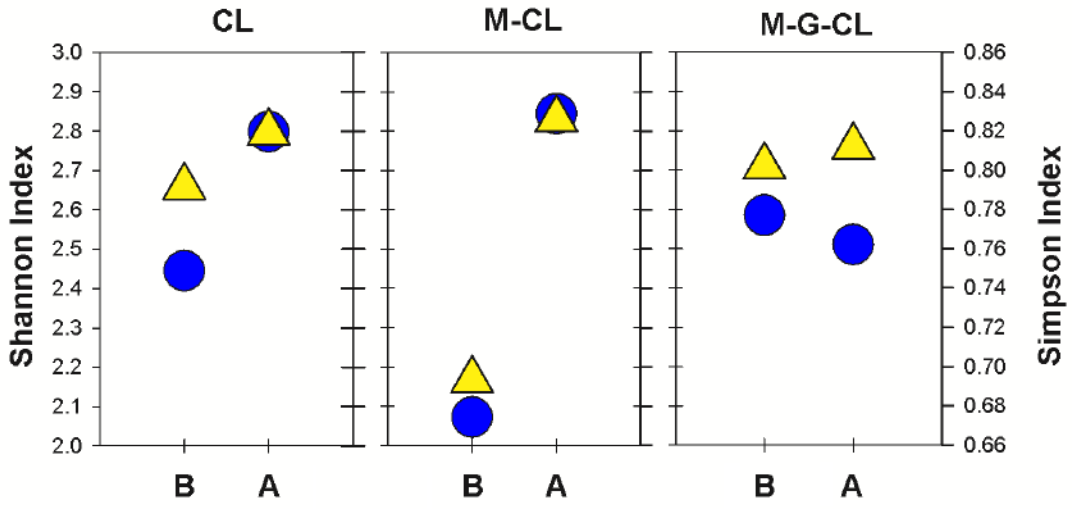

Figure 4. Shannon (●) and Simpson (△) index for each treatment. Letters B and A mean before and after the overloading period for each treatment, respectively.

3.3 Diversity index

Before the second disturbance, the Shannon and Simpson indices (Figure 4) for the CL, CL-M, and CL-M-G systems were recorded as follows: 2.44 and 0.79 for CL, 2.07 and 0.69 for CL-M, and 2.58 and 0.80 for CL-M-G. After the disturbance, the CL and CL-M systems showed an increase in diversity of 14.4 % and 37.3 %, respectively. In contrast, the CL-M-G system experienced a decrease in abundance of 2.9 %. The disturbances caused an increase in the diversity of microbial communities in the CL and CL-M systems, indicating that the CL-M system exhibited higher methane yield due to its greater species diversity. Cortez-Cervantes *et al*. (2024) and Rahman *et al*. (2021) reported that higher methane yields were associated with increases in microbial diversity.

3.4 Microbial community

The most representative microbial community in this study is shown in Figure 5, composed of 2 kingdoms, 8 phyla, and 32 genera. Regarding the archaea, the genus *Methanosarcina,* the disturbances did not affect their abundance in the three systems. Otherwise, Methanothrix was affected. However, the CL-M-G system increased significantly. *Methanoculleus* was only favored in the CL system; it is worth mentioning that this archea increased its abundance in CL and CL-M systems after the system was disturbed, except in the CL-M system. Regarding bacteria, 3 genera were not affected by the disturbances; these were, *Fermentimonas, Petrimonas, Proteiniphilum, Erysipelothrix, Jeotgalicoccus,* and *Aminobacterium*, from higher to lower abundance, respectively. In the remaining 26 genera, their abundance is relatively low compared to the previous ones.

The Heatmap (Figure 6) showed us four separations: the most abundant bacteria, the medium ones, the low ones, and the methanogens. In the high abundance at *Fermentimonas,* disturbances increased its abundance, and *Proteiniphilum* was affected along with *Erysipelothrix*. *Petrimonas* only remained in the CL system. In the medium abundance, the disturbances favored the CL-MG system since it promoted the appearance of 15 genera (as shown in figure 6), otherwise to the CL system that disappeared, the CL-M system the disturbances promoted the increase and decrease of what already contained apart the appearance of 6 genera. Regarding the low abundance, the CL-M system was the only one favored with the disturbances activating *Acetomicrobium,* and *Bacteroidales*. *Methanosarcina mazei*, *Methanothrix soehngenii*, and *Methanoculleus bourgensis* were the representative methanogens in this study.

The CL-M System had the highest methane yield because the microorganisms involved allowed degradation of the VFAs, avoiding the medium's acidification. Each methanogen has a substrate to grow and tolerate disturbances. The microorganisms in AD systems change according to the fed substrate and the environmental conditions under which the digester operates (Karki *et al*., 2021). However, *Bacteroidetes*, *Firmicutes*, and *Proteobacteria* are usually present in most cases (Pei *et al*., 2022); this may be because they are hydrolytic fermentative bacteria responsible for decomposing macromolecules (Menzel *et al*., 2020).

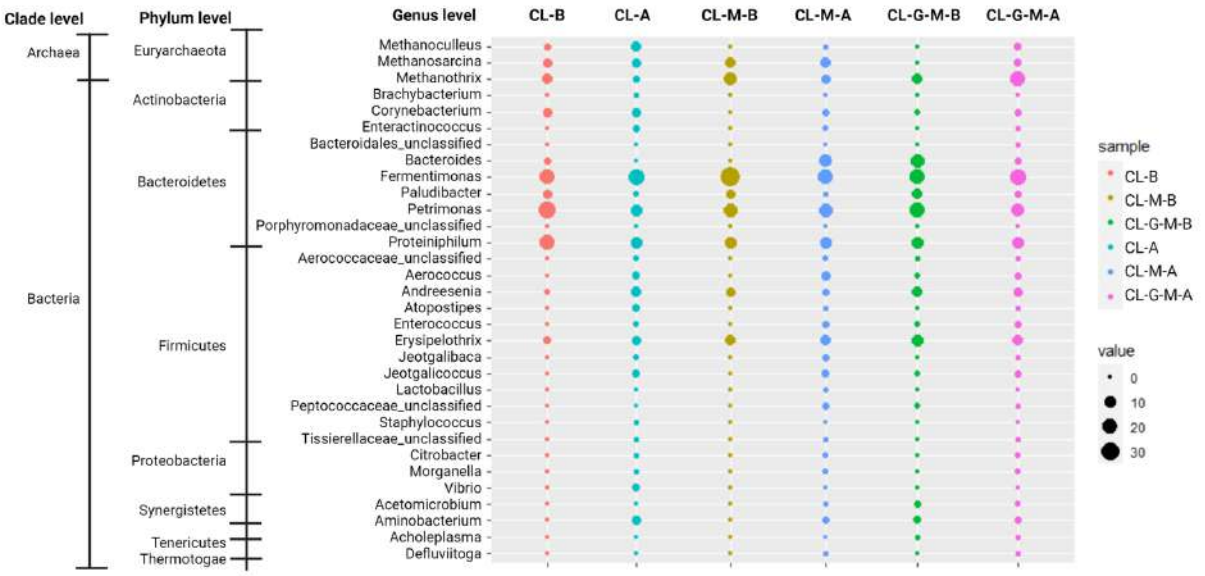

Figure 5. Relative abundance of main genera in CL-B: chicken litter before disturbance. CL-A: chicken litter after disturbance. CL-M-B: chicken litter-microalga before disturbance. CL-M-A: chicken litter-microalga after disturbance. CL-G-M-B: chicken litter-microalga-glycerol before disturbance. CL-G-M-A: chicken litter-microalga-glycerol after disturbance.

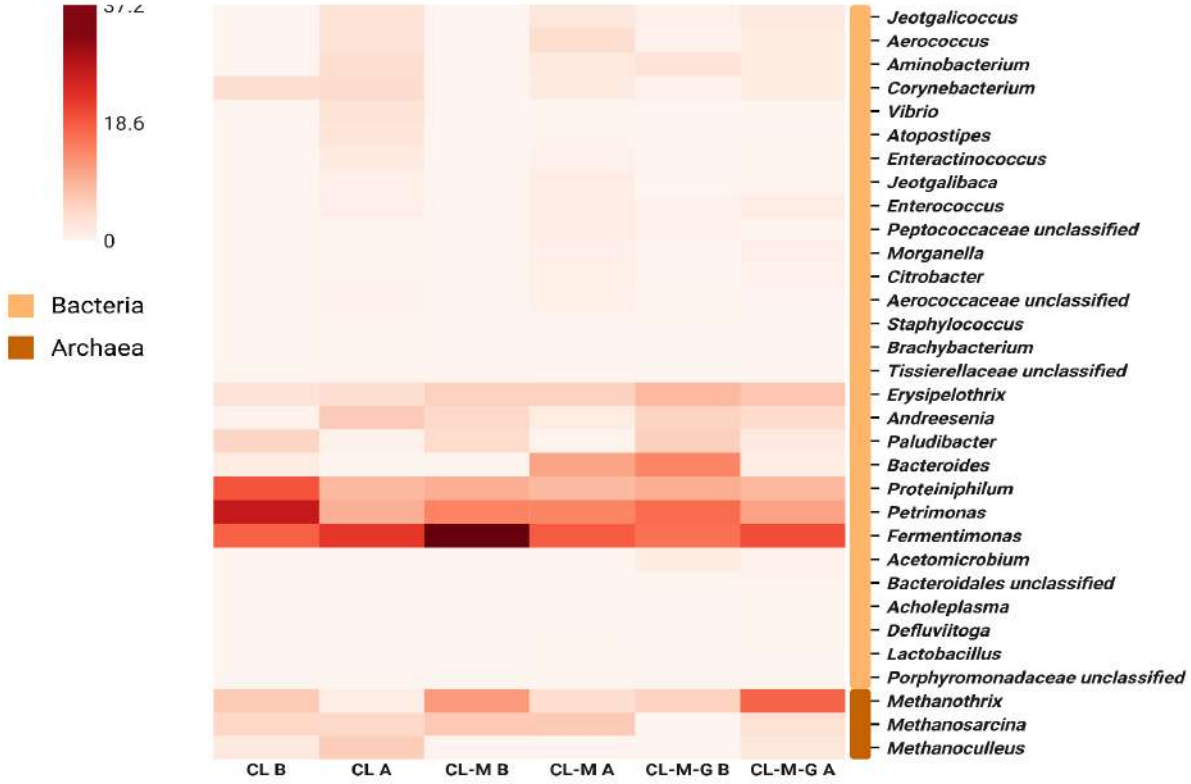

Figure 6. Heatmap of taxonomic abundance genus level found in systems.

Conclusions

The CL-M system exhibited the highest methane yield due to the buffering effect of co-digestion, which mitigated disturbances caused by fluctuations in organic loading rates. This environment allowed for the rapid degradation of volatile fatty acids by bacteria such as *Jeotgalicoccus, Aerococcus, Aminobacterium, Corynebacterium, Enterococcus, Acetomicrobium, Erysipelothrix, Proteiniphilum, Petrimonas,* and *Fermentimonas*. As a result, the medium remained non-acidic, enabling *Methanosarcina* and *Methanothrix* to carry out the methanogenesis process without being inhibited.

Methanoculleus was linked to the CL substrate, *Methanosarcina* was found in both the CL-M and CL-M-G substrates, and *Methanothrix* was predominantly associated with the CL-M-G substrate. Notably, *Methanosarcina* was generally resilient to disturbances caused by organic matter overload across all three systems.

The disturbances negatively affected the bacterial populations, leading to a decrease in their abundance. Despite the overload of organic matter, the anaerobic digestion process remained stable across all three systems, as they continued to demonstrate specific methanogenic activity even after the disturbances.

Acknowledgements

The present work was supported by Consejo Nacional de Ciencia y Tecnología (Mexico) and the Universidad Autónoma Chapingo (Mexico) through the projects CB-2016-01(288716) and 24020-EI, respectively. The authors would like to thank the Consejo Nacional de Ciencia, Humanidades y Tecnología (CONACHYT) (México) for the scholarship (number 862782) granted to Thalia Guadalupe Ochoa-Bernal and the Bioprocesses Laboratory Team of the Universidad Autónoma Chapingo (UACH) for their comments concerning this manuscript.

Data availability

The datasets generated and/or analyzed during the current study are available in the sequence read archive (SRA, https://ncbi.nlm.nih.gov/bioproject/?term=PRJNA1183444).

References

Alharbi, R. M. (2024). Anaerobic co-digestion of cow manure and microalgae to increase biogas production: A sustainable bioenergy source. *Journal of King Saud University - Science*, *36*(9), 103380. https://doi.org/https://doi.org/10.1016/j.jksus.2024.103380

Babaee, A., & Shayegan, J. (2011). Effect of organic loading rates (OLR) on production of methane from anaerobic digestion of vegetables waste. Proceedings of the world renewable energy congress, Linköping, Sweden.

Basak, B., Patil, S. M., Saha, S., Kurade, M. B., Ha, G.-S., Govindwar, S. P., Lee, S. S., Chang, S. W., Chung, W. J., & Jeon, B.-H. (2021). Rapid recovery of methane yield in organic overloaded-failed anaerobic digesters through bioaugmentation with acclimatized microbial consortium. *Science of The Total Environment*, *764*, 144219. https://doi.org/https://doi.org/10.1016/j.scitotenv.2020.144219

Beghini, F., McIver, L. J., Blanco-Míguez, A., Dubois, L., Asnicar, F., Maharjan, S., Mailyan, A., Manghi, P., Scholz, M., Thomas, A. M., Valles-Colomer, M., Weingart, G., Zhang, Y., Zolfo, M., Huttenhower, C., Franzosa, E. A., & Segata, N. (2021). Integrating taxonomic, functional, and strain-level profiling of diverse microbial communities with bioBakery 3. *eLife*, *10*, e65088. https://doi.org/10.7554/eLife.65088

Bolger, A. M., Lohse, M., & Usadel, B. (2014). Trimmomatic: a flexible trimmer for Illumina sequence data. *Bioinformatics*, *30*(15), 2114-2120. https://doi.org/10.1093/bioinformatics/btu170

Braz, G. H. R., Fernandez-Gonzalez, N., Lema, J. M., & Carballa, M. (2019). Organic overloading affects the microbial interactions during anaerobic digestion in sewage sludge reactors. *Chemosphere*, *222*, 323-332. https://doi.org/https://doi.org/10.1016/j.chemosphere.2019.01.124

Brown, J., Pirrung, M., & McCue, L. A. (2017). FQC Dashboard: integrates FastQC results into a web-based, interactive, and extensible FASTQ quality control tool. *Bioinformatics*, *33*(19), 3137-3139. https://doi.org/10.1093/bioinformatics/btx373

Castro-Sierra, A., Espinosa-Solares, T., Houbron, E., Castro-Rivera, R., Azcárraga-Salinas, B., Pacheco-Ortíz, J., & Solís-Oba, M. (2024). Production of phytoregulators during anaerobic digestion of bovine and swine manures Producción de fitorreguladores durante las digestiones anaerobias de estiércoles bovinos

y porcinos. *Revista Mexicana de Ingeniería Química*, *23*(Bio24289). https://doi.org/doi.org/10.24275/rmiq/Bio24289

Cortez-Cervantes, J., Moreno-Andrade, I., Escalante, A. E., de los Cobos-Vasconcelos, D., & Carrillo-Reyes, J. (2024). Identifying reliable microbial indicators in anaerobic digestion of organic solid waste: Insights from a meta-analysis. *Journal of Environmental Chemical Engineering*, *12*(5), 113392. https://doi.org/https://doi.org/10.1016/j.jece.2024.113392

Gil, A., Siles, J. A., Serrano, A., Chica, A. F., & Martín, M. A. (2019). Effect of variation in the C/[N+P] ratio on anaerobic digestion. *Environmental Progress & Sustainable Energy*, *38*(1), 228-236. https://doi.org/https://doi.org/10.1002/ep.12922

Kabeyi, M. J. B., & Olanrewaju, O. A. (2022). Biogas Production and Applications in the Sustainable Energy Transition. *Journal of Energy*, *2022*(1), 8750221. https://doi.org/https://doi.org/10.1155/2022/8750221

Karki, R., Chuenchart, W., Surendra, K. C., Shrestha, S., Raskin, L., Sung, S., Hashimoto, A., & Kumar Khanal, S. (2021). Anaerobic co-digestion: Current status and perspectives. *Bioresource Technology*, *330*, 125001. https://doi.org/https://doi.org/10.1016/j.biortech.2021.125001

Kim, J., Baek, G., Kim, J., & Lee, C. (2019). Energy production from different organic wastes by anaerobic co-digestion: Maximizing methane yield versus maximizing synergistic effect. *Renewable Energy*, *136*, 683-690.

Li, B.-Y., Xia, Z.-Y., Gou, M., Sun, Z.-Y., Huang, Y.-L., Jiao, S.-B., Dai, W.-Y., & Tang, Y.-Q. (2022). Production of volatile fatty acid from fruit waste by anaerobic digestion at high organic loading rates: Performance and microbial community characteristics. *Bioresource Technology*, *346*, 126648. https://doi.org/https://doi.org/10.1016/j.biortech.2021.126648

Li, D., Luo, R., Liu, C.-M., Leung, C.-M., Ting, H.-F., Sadakane, K., Yamashita, H., & Lam, T.-W. (2016). MEGAHIT v1.0: A fast and scalable metagenome assembler driven by advanced methodologies and community practices. *Methods*, *102*, 3-11. https://doi.org/https://doi.org/10.1016/j.ymeth.2016.02.020

Li, R., Duan, N., Zhang, Y., Liu, Z., Li, B., Zhang, D., & Dong, T. (2017). Anaerobic co-digestion of chicken manure and microalgae Chlorella sp.: Methane potential, microbial diversity and synergistic impact evaluation. *Waste Management*, *68*, 120-127. https://doi.org/https://doi.org/10.1016/j.wasman.2017.06.028

Li, R., Duan, N., Zhang, Y., Liu, Z., Li, B., Zhang, D., Lu, H., & Dong, T. (2017). Co-digestion of chicken manure and microalgae Chlorella 1067 grown in the recycled digestate: Nutrients reuse and biogas enhancement. *Waste Management*, *70*, 247-254. https://doi.org/10.1016/j.wasman.2017.09.016

Lv, Y., Chang, N., Li, Y.-Y., & Liu, J. (2021). Anaerobic co-digestion of food waste with municipal solid waste leachate: A review and prospective application with more benefits. *Resources, Conservation and Recycling*, *174*, 105832. https://doi.org/https://doi.org/10.1016/j.resconrec.2021.105832

Magdalena, J. A., Greses, S., & González-Fernández, C. (2019). Impact of Organic Loading Rate in Volatile Fatty Acids Production and Population Dynamics Using Microalgae Biomass as Substrate. *Scientific Reports*, *9*(1), 18374. https://doi.org/10.1038/s41598-019-54914-4

Mahmudul, H. M., Akbar, D., Rasul, M. G., Narayanan, R., & Mofijur, M. (2022). Estimation of the sustainable production of gaseous biofuels, generation of electricity, and reduction of greenhouse gas emissions using food waste in anaerobic digesters. *Fuel*, *310*, 122346. https://doi.org/https://doi.org/10.1016/j.fuel.2021.122346

Malet, N., Pellerin, S., Girault, R., & Nesme, T. (2023). Does anaerobic digestion really help to reduce greenhouse gas emissions? A nuanced case study based on 30 cogeneration plants in France. *Journal of Cleaner Production*, *384*, 135578. https://doi.org/https://doi.org/10.1016/j.jclepro.2022.135578

Meneses-Reyes, J. C., Hernández-Eugenio, G., Huber, D. H., Balagurusamy, N., & Espinosa-Solares, T. (2017). Biochemical methane potential of oil-extracted microalgae and glycerol in co-digestion with chicken litter. *Bioresource Technology*, *224*, 373-379. https://doi.org/https://doi.org/10.1016/j.biortech.2016.11.012

Meneses-Reyes, J. C., Hernández-Eugenio, G., Huber, D. H., Balagurusamy, N., & Espinosa-Solares, T. (2018). Oil-extracted Chlorella vulgaris biomass and glycerol bioconversion to methane via continuous anaerobic co-digestion with chicken litter. *Renewable Energy*, *128*, 223-229. https://doi.org/https://doi.org/10.1016/j.renene.2018.05.053

Menzel, T., Neubauer, P., & Junne, S. (2020). Role of Microbial Hydrolysis in Anaerobic Digestion. *Energies*, *13*(21), 5555. https://www.mdpi.com/1996-1073/13/21/5555

Musa, M. A., Idrus, S., Hasfalina, C. M., & Daud, N. N. N. (2018). Effect of Organic Loading Rate on Anaerobic Digestion Performance of Mesophilic (UASB) Reactor Using Cattle Slaughterhouse Wastewater as Substrate. *International Journal of Environmental Research and Public Health*, *15*(10), 2220. https://www.mdpi.com/1660-4601/15/10/2220

Nguyen, A. Q., Nguyen, L. N., Phan, H. V., Galway, B., Bustamante, H., & Nghiem, L. D. (2019). Effects of operational disturbance and subsequent recovery process on microbial community during a pilot-scale anaerobic co-digestion. *International Biodeterioration & Biodegradation*, *138*, 70-77. https://doi.org/https://doi.org/10.1016/j.ibiod.2019.01.002

Nkuna, R., Roopnarain, A., Rashama, C., & Adeleke, R. (2022). Insights into organic loading rates of anaerobic digestion for biogas production: a review. *Critical Reviews in Biotechnology*, *42*(4), 487-507. https://doi.org/10.1080/07388551.2021.1942778

Oduor, W. W., Wandera, S. M., Murunga, S. I., & Raude, J. M. (2022). Enhancement of anaerobic digestion by co-digesting food waste and water hyacinth in improving treatment of organic waste and bio-methane recovery. *Heliyon*, *8*(9). https://doi.org/10.1016/j.heliyon.2022.e10580

Pan, S.-Y., Tsai, C.-Y., Liu, C.-W., Wang, S.-W., Kim, H., & Fan, C. (2021). Anaerobic co-digestion of agricultural wastes toward circular bioeconomy. *iScience*, *24*(7), 102704. https://doi.org/https://doi.org/10.1016/j.isci.2021.102704

Pei, Z., Liu, S., Jing, Z., Zhang, Y., Wang, J., Liu, J., Wang, Y., Guo, W., Li, Y., Feng, L., Zhou, H., Li, G., Han, Y., Liu, D., & Pan, J. (2022). Understanding of the interrelationship between methane production and microorganisms in high-solid anaerobic co-digestion using microbial analysis and machine learning. *Journal of Cleaner Production*, *373*, 133848. https://doi.org/https://doi.org/10.1016/j.jclepro.2022.133848

Rahman, M. S., Hoque, M. N., Puspo, J. A., Islam, M. R., Das, N., Siddique, M. A., Hossain, M. A., & Sultana, M. (2021). Microbiome signature and diversity regulates the level of energy production under anaerobic condition. *Scientific Reports*, *11*(1), 19777.

Rétfalvi, T., Szabó, P., Hájos, A.-T., Albert, L., Kovács, A., Milics, G., Neményi, M., Lakatos, E., & Ördög, V. (2016). Effect of co-substrate feeding on methane yield of anaerobic digestion of Chlorella vulgaris. *Journal of Applied Phycology*, *28*(5), 2741-2752. https://doi.org/10.1007/s10811-016-0796-5

Rivera-Hernández, Y., Hernández-Eugenio, G., Balagurusamy, N., & Espinosa-Solares, T. (2022). Sargassum-pig manure co-digestion: An alternative for bioenergy production and treating a polluting coastal waste. *Renewable Energy*, *199*, 1336-1344. https://doi.org/https://doi.org/10.1016/j.renene.2022.09.068

Sanaye, S., Mohammadi, M. H., Yazdani, M., & Barati Rashvanlou, R. (2022). Bio-gas augmentation and waste minimization by co-digestion process in anaerobic digestion system of a municipal waste water treatment plant. *Energy Conversion and Management*, *268*, 115989. https://doi.org/https://doi.org/10.1016/j.enconman.2022.115989

Serna-García, R., Zamorano-López, N., Seco, A., & Bouzas, A. (2020). Co-digestion of harvested microalgae and primary sludge in a mesophilic anaerobic membrane bioreactor (AnMBR): Methane potential and microbial diversity. *Bioresource Technology*, *298*, 122521.

Serrano-Meza, A., Garzón-Zúñiga, M., Barragán-Huerta, B., Estrada-Arriaga, E., Almaraz-Abarca, N., & García-Olivares, J. (2020). Anaerobic digestion inhibition indicators and control strategies in processes treating industrial wastewater and wastes. *Revista Mexicana de Ingeniería Química*, *19*(Sup. 1), 29-44.

Slezak, R., Grzelak, J., Krzystek, L., & Ledakowicz, S. (2017). The effect of initial organic load of the kitchen waste on the production of VFA and H2 in dark fermentation. *Waste Management*, *68*, 610-617.

Solé-Bundó, M., Passos, F., Romero-Güiza, M. S., Ferrer, I., & Astals, S. (2019). Co-digestion strategies to enhance microalgae anaerobic digestion: A review. *Renewable and Sustainable Energy Reviews*, *112*, 471-482. https://doi.org/https://doi.org/10.1016/j.rser.2019.05.036

Spirito, C. M., Daly, S. E., Werner, J. J., & Angenent, L. T. (2018). Redundancy in Anaerobic Digestion Microbiomes during Disturbances by the Antibiotic Monensin. *Applied and Environmental Microbiology*, *84*(9), e02692-02617. https://doi.org/doi:10.1128/AEM.02692-17

Vivekanand, V., Mulat, D. G., Eijsink, V. G. H., & Horn, S. J. (2018). Synergistic effects of anaerobic co-digestion of whey, manure and fish ensilage. *Bioresource Technology*, *249*, 35-41. https://doi.org/https://doi.org/10.1016/j.biortech.2017.09.169

Wei, Y., Yuan, H., Wachemo, A. C., & Li, X. (2019). Impacts of modification of corn stover on the synergistic effect and microbial community structure of co-digestion with chicken manure. *Energy & Fuels*, *34*(1), 401-411.

Wijekoon, K. C., Visvanathan, C., & Abeynayaka, A. (2011). Effect of organic loading rate on VFA production, organic matter removal and microbial activity of a two-stage thermophilic anaerobic membrane bioreactor. *Bioresource Technology*, *102*(9), 5353-5360.

Wirth, R., Böjti, T., Lakatos, G., Maróti, G., Bagi, Z., Rákhely, G., & Kovács, K. L. (2019). Characterization of Core Microbiomes and Functional Profiles of Mesophilic Anaerobic Digesters Fed With Chlorella vulgaris Green Microalgae and Maize Silage [Original Research]. *Frontiers in Energy Research*, *7*. https://doi.org/10.3389/fenrg.2019.00111

Wood, D. E., Lu, J., & Langmead, B. (2019). Improved metagenomic analysis with Kraken 2. *Genome Biology*, *20*(1), 257. https://doi.org/10.1186/s13059-019-1891-0 Wu, D., Peng, X., Li, L., Yang, P., Peng, Y., Liu, H., & Wang, X. (2021). Commercial biogas plants: Review on operational parameters and guide for performance optimization. *Fuel*, *303*, 121282. https://doi.org/https://doi.org/10.1016/j.fuel.2021.121282

Zhang, Y., Caldwell, G. S., Blythe, P. T., Zealand, A. M., Li, S., Edwards, S., Xing, J., Goodman, P., Whitworth, P., & Sallis, P. J. (2020). Co-digestion of microalgae with potato processing waste and glycerol: effect of glycerol addition on methane production and the microbial community. *RSC advances*, *10*(61), 37391-37408.

Zhu, S., Qin, L., Feng, P., Shang, C., Wang, Z., & Yuan, Z. (2019). Treatment of low C/N ratio wastewater and biomass production using co-culture of Chlorella vulgaris and activated sludge in a batch photobioreactor. *Bioresource Technology*, *274*, 313-320. https://doi.org/https://doi.org/10.1016/j.biortech.2018.10.034

Vol. 24, No. 2(2025) IA25491
Revista Mexicana de Ingeniería Química

Removal of fluoride ions from aqueous solutions and water for human consumption by a surfactant modified zeolite

Eliminación de iones fluoruro de soluciones acuosas y agua para consumo humano mediante una zeolita modificada con un tensioactivo

N. Flores-Alamo[1], J.I. Vázquez-Méndez[1,2], M.J. Solache-Ríos[2], F. Cuellar-Robles[1], M.C. Carreño-de-León[1]*
[1]*División de Estudios de Posgrado e Investigación, Tecnológico Nacional de México/Instituto Tecnológico de Toluca, Av. Tecnológico s/n. Colonia Agrícola Bellavista, Metepec, Estado de México, C.P. 52149, México.*
[2]*Departamento de Química, Instituto Nacional de Investigaciones Nucleares, Carretera México-Toluca S/N, La Marquesa, Ocoyoacac, Estado de México C.P. 52750, México.*
Received: December 27, 2024; Accepted: March 13, 2025

Abstract
Fluoride ions are found in groundwater due to the presence of some minerals like fluorite (CaF_2) and fluorapatite ($Ca_5(PO_4)_3F$). A clinoptilolite type zeolite was modified with hexadecyltrimethylammonium bromide in order to determine its adsorption properties for the removal of fluoride ions from water, the material was characterized by Fourier transform infrared spectroscopy, scanning electron microscopy, X-ray diffraction and the point of zero charge was determined. Sorption experiments were performed by using a solution of sodium fluoride and water from the state of Zacatecas, México. The kinetic data were adequately fitted to the pseudo first-order model, and the isotherms data to the Freundlich model, suggesting that the sorption process is carried out by physisorption on a heterogeneous material, the adsorption was similar between 20 and 50°C and the highest adsorption was between pH 4 and 6. Experiments carried out with water from the state of Zacatecas showed a removal of 86.3 % with 130 mg of modified zeolite and 10 mL of water. The results show that this material is an alternative for removing fluoride ions from water.
Keywords: fluoride ions, adsorption, zeolite, pollution.

Resumen
Los iones de fluoruro se encuentran en el agua subterránea debido a la presencia de algunos minerales como la fluorita (CaF_2) y la fluorapatita ($Ca_5(PO_4)_3F$). Se modificó una zeolita tipo clinoptilolita con bromuro de hexadeciltrimetilamonio con el fin de determinar su capacidad de adsorción para la remoción de iones fluoruro del agua, el material se caracterizó mediante espectroscopia de infrarrojo por transformada de Fourier, microscopía electrónica de barrido, difracción de rayos X y se determinó el punto de carga cero. Los experimentos de sorción se realizaron utilizando una solución de fluoruro de sodio y agua del estado de Zacatecas, México. Los datos cinéticos se ajustaron adecuadamente al modelo de pseudo primer orden, y los datos de isotermas al modelo de Freundlich, sugiriendo que el proceso de sorción se realiza por fisisorción sobre un material heterogéneo, la adsorción fue similar entre 20 y 50°C y la capacidad máxima de adsorción estuvo entre un pH de 4 y 6. Los experimentos realizados con agua del estado de Zacatecas mostraron una remoción del 86.3 % con 130 mg de zeolita modificada y 10 mililitros de agua. Los resultados muestran que este material es una alternativa para la eliminación de iones fluoruro del agua.
Palabras clave: iones fluoruro, adsorción, zeolita, contaminación.

* *Corresponding author. E-mail*: mcarrenod@toluca.tecnm.mx ;
https://doi.org/10.24275/rmiq/IA25491
ISSN:1665-2738, *issn-e*: 2395-8472

1 Introduction

Clean and accessible water for human consumption is one of the greatest challenges (Alarcón-Herrera *et al*. 2020). Due to the increase of population, water demand for irrigation, industrial and domestic uses has increased considerably and turned groundwater into an important source (Chai *et al*. 2022; Serrano-Mesa *et al*. 2024), almost 50 % of the population uses groundwater, however, its quality may be compromised due to the presence of some chemical species like fluoride ions (López-Guzmán *et al*. 2019). An example of this is Zacatecas, a state located in the central north area of the Mexican territory with a dry, semi-dry climate temperate and semi-humid zone (Martínez-Salazar *et al*. 2016). In this region, there are numerous mineral deposits linked to the western Sierra Madre, which are mainly composed of feldspars, limestone, quartz, calcite, cryolite and some clays (Alarcón-Herrera *et al*. 2020).

Fluoride ions are commonly found in minerals that are in contact with groundwater (He *et al*. 2020), their concentrations are generally associated with the geographical regions and the degree of water-minerals interactions (Navarro *et al*. 2017). Fluoride ions are classified among the twelve most dangerous pollutants by the Agency for Toxic Substances and the United States Disease Registry (ATSDR) due to their great reactivity and toxicity (Nizam *et al*. 2022).

Fluoride ions have severe effects on bones and teeth because they displace hydroxide ions from hydroxyapatite, the main mineral component of teeth and bones, to form fluorapatite. Fluorapatite makes teeth and bones more brittle at a high concentration of fluoride ions, a condition known as dental and skeletal fluorosis (Mohapatra *et al*. 2009). Furthermore, fluoride ions may accumulate in soft tissues causing toxic effects in kidneys, heart, reproductive system and brain (Jiang *et al*. 2019).

Currently, more than 25 countries have reported that their water sources have concentrations of fluoride ions above the maximum permissible limit, set at 1.5 mg/L by the World Health Organization (WHO) and more than 300 million people suffer from different types of fluorosis (Alhassan *et al*. 2020).

Multiple technologies have been developed for the removal of fluoride ions, like adsorption, coagulation, precipitation, ion exchange, reverse osmosis, and electrodialysis (Bhatnagar *et al*. 2011). Adsorption has proven to be a simple technology, the nature of the adsorbents is the key for its efficiency, and multiple studies have been carried out to develop high-efficient adsorbents from various materials (Chen *et al*. 2022; Leal-Perez *et al*. 2024).

Zeolites are crystalline aluminosilicates that can be used as adsorbents, they have high cation exchange capacities and high sorption capacities for different types of chemical species, their cation exchange capacities are due to their content of exchangeable cations such as sodium, calcium, potassium and magnesium (Znak *et al*. 2021).

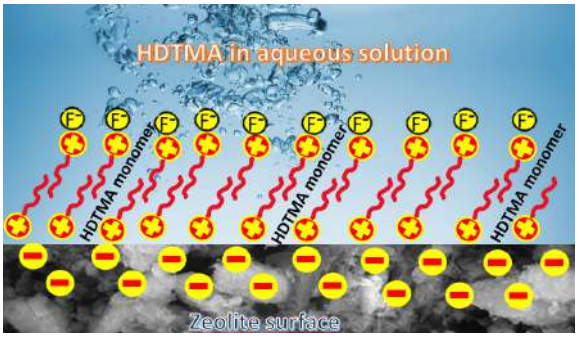

Figure 1 Schematic diagram of zeolite modification by HDTMA and fluoride interaction.

One of the most abundant zeolites is clinoptilolite, which belongs to the heulandite family and has a Si/Al ratio > 4 (Saucedo-Delgado *et al*. 2017). Zeolites have been modified with organic compounds such as hexadecyltrimethylammonium bromide (HDTMA-Br) to remove anions and organic matter from water (Bajda and Kłapyta, 2013). The treatment of zeolite with HDTMA-Br (Figure 1) allows to change the surface charge of the zeolite from negative to positive, the surfactant molecules occupy the cationic exchange sites of the zeolite and form an organic coating, and the positive charge of the surface allows the removal of anions such as fluoride (Barczyk *et al*. 2014).

The objective of this work was to modify and characterize a natural zeolitic material with a surfactant and to determine its behavior in removing fluoride ions from aqueous solutions and drinking water, in order to find a new alternative for the removal of fluoride ions from drinking water.

2 Materials and methods

A natural zeolitic material obtained from Valey of Etla municipality, located about 17 kilometers north of Oaxaca City, Mexico (17°12'22.14" N -96°47'56.04" W) was used, it was ground and sieved to 30 mesh to obtain a particle size of 0.6 mm (Corral-Capulin *et al*. 2018), Jalmek brand analytical grade reagents: hexadecyltrimethylammonium bromide (HDTMA), sodium chloride, sodium fluoride, and silver nitrate, as well as distilled water were used for the preparation of solutions.

2.1 Modification of the zeolitic material

The previously ground and sieved zeolitic material was washed with distilled water and dried at room

temperature for 24 hours. Subsequently, the zeolitic material was put in contact with 500 mL of a 2 M NaCl solution at room temperature (20°C) for 96 hours, then the supernatant was drained and the material was washed with distilled water until the chloride ions were not detected in the washing solutions by the $AgNO_3$ test, then it was dry at room temperature and labeled as ZS. Finally, the zeolite was put in contact with a solution of 60 mmol/L of HDTMA for 120 hours at 30°C (Dávila *et al*. 2016) and it was washed with distilled water to eliminate the excess of surfactant, the zeolitic material was identified as ZM.

2.2 *Characterization of the modified zeolitic material*

A JEOL JSM 6610LV scanning electron microscope was used to observe the morphology of the natural zeolitic material (ZN) and the modified one (ZM), the micrographs were taken at a magnification of 10 000, 5 000 and 3 000 x, subsequently elemental microanalysis was performed by X-ray dispersive spectroscopy (EDS).

The point of zero charge was determined as follows: 10 mL distilled water was placed in beakers and the pH of the solutions was adjusted between two and eleven by adding 0.1 M of HCl or NaOH solutions, samples of 100 mg of zeolitic material were added to each solution and shaken for 24 hours, then the phases were separated and the pH was measured by using a Hanna instruments model HI 2221 potentiometer.

A Fourier transform infrared spectrophotometer was used to obtain the spectra of the zeolitic materials, the equipment worked in transmittance analysis mode in a range from 4000 to 400 cm^{-1}.

The ZS and the ZM were analyzed by X-ray diffraction using the D8 Advance Bruker diffractogram under a range of 5-75 2θ, a step of 0.03 and a voltage of 35 kV, to identify the mineral phases of the zeolitic materials, the patterns of diffraction were compared with those of the Joint Committee of Powder Diffraction Standards cards (JCPDS).

2.3 *Effect of pH*

Samples of 100 mg of zeolitic material (ZM) were put in contact with 10 mL aliquots of a solution with a concentration of 10 mg/L of fluoride ions and pH between 3 and 10. They were left in contact for 9 hours with constant shaking at 20° C (Dávila *et al*. 2016), then, the phases were separated and the final concentrations of fluoride ions in the liquid phase were measured, the experiments were carried out in triplicate.

2.4 *Effect of temperature*

Sorption isotherms were performed at 20, 30, 40 and 50°C, 100 mg of modified zeolitic material were contacted with 10 mL of solutions of fluoride ions with concentrations from 2 to 20 mg/L at a pH of 6 and 100 rpm, the experiments were performed in triplicate.

2.5 *Adsorption kinetics*

100 mg samples of modified zeolitic material were put in contact with 10 mL aliquots of a 10 mg/L of fluoride ions solution at pH 6. They were kept under stirring for different contact times between 0.25 and 72 hours at 20°C and 100 rpm (Naghash and Nezamzadeh-Ejhieh, 2015), the samples were separated and the concentrations of fluoride ions in the liquid phases were analyzed by using a selective electrode. The experimental data were treated with the pseudo first order (Eq. 1), pseudo second order (Eq. 2) and the Elovich models (Eq. 3) using the Origin Lab software (Liu *et al*. 2021).

$$q_t = q_e\left(1 - e^{k_1 t}\right) \tag{1}$$

where q_t (mg/g) is the amount adsorbed at time t, q_e (mg/g) is the amount adsorbed at equilibrium and k_1 (min^{-1}) is the adsorption rate constant.

$$q_t = \frac{t}{\frac{1}{k_2 q_e^2} + \frac{t}{q_e}} \tag{2}$$

where k_2 is the kinetic constant (g/mg*min) and q_e (mg/g) is the amount adsorbed at equilibrium time.

$$q_t = \frac{1}{\beta}\ln(\alpha\beta) + \frac{1}{\beta}\ln(t) \tag{3}$$

where q_t is the amount of adsorbate adsorbed at time t, α is the initial adsorption rate (mg/g min) and β is the desorption constant (g/mg).

2.6 *Adsorption isotherm*

100 mg samples of zeolitic material were put in contact with 10 mL aliquots of fluoride ion solutions with concentrations of fluoride ions from 2 to 20 mg/L at pH 6. The mixtures were kept under constant stirring at 20°C, then, they were separated and the aqueous phases were analyzed to determine the concentration of fluoride ions, the experimental data were treated with the Langmuir (Eq. 4) and Freundlich (Eq. 5) models (Ahamad *et al*. 2018) with the help of the software OriginLab.

$$q_e = \frac{q_m b C_e}{1 + b C_e} \tag{4}$$

where q_e is the amount of fluoride ions absorbed per unit mass (mg/g) and Ce is the equilibrium

concentration of adsorbate in the liquid phase (mg/L) at equilibrium, b (L/mg) is the adsorption equilibrium constant and q_m is the maximum adsorption capacity (mg/g).

$$q_e = K_F C_e^{\frac{1}{n}} \tag{5}$$

where q_e is the amount of fluoride ions absorbed per unit mass (mg/g), C_e is the equilibrium concentration of the adsorbate in the liquid phase (mg/L) and K_F is the Freundlich constant (mg/g) and n is the Freundlich exponent.

2.7 Adsorption of fluoride ions from drinking water

The drinking water sample was from an urban deep well from Ojo Caliente town in the state of Zacatecas, Mexico (22°34'0.00" N -102°15'0.00" W). It was transported in a 5 L polyethylene container at 4ºC as indicated by the NOM-014-SSA1-1993 standard, the sample had a pH of 7.8 and an electrical conductivity of 1532 μmhos/cm. Aliquots of 10 mL of water with adjusted pH of 6 were put in contact with samples (between 10 and 130 mg) of the modified zeolitic material (ZM) for nine hours.

3 Results and discussion

3.1 Adsorbent characterization

Figure 2 shows the micrographs obtained from the natural and the modified zeolitic material, some particles are amorphous and other show the typical morphology of the clinoptilolite zeolite: crystals of monoclinic symmetry of blades and laths and some of them have a coffin shape (Jiménez-Reyes *et al*. 2021) and the morphology of the material was not affected after the modification. The presence of internal cavities of the material is observed as a honeycomb distribution.

The elemental analysis (SEM-EDS) is shown in Table 1, the main elements found were O, Na, Al, Si and C. Oxygen, silicon and aluminum have the highest percentages, they are the main components of the tetrahedrons that make up the zeolite network. The increase of the carbon after modification indicates the presence of the surfactant on the zeolitic material (Wingenfelder *et al*. 2006). The Si/Al ratio of the ZM sample is 5.11, this value corresponds to clinoptilolite-type zeolites.

Figure 3 shows pH *vs.* pH_i-pH_f, the value of the point of zero charge determined for the modified zeolitic material was 7.06. The point where the Y axis is intercepted corresponds to the point where the surface charge is zero, the number of negative and positive charges are the same, the surface charge is negative at a pH higher than the point of zero charge and positive at a pH values lower than the point of zero charge (Ullah *et al*. 2020), the positive charge would attract the fluoride ions.

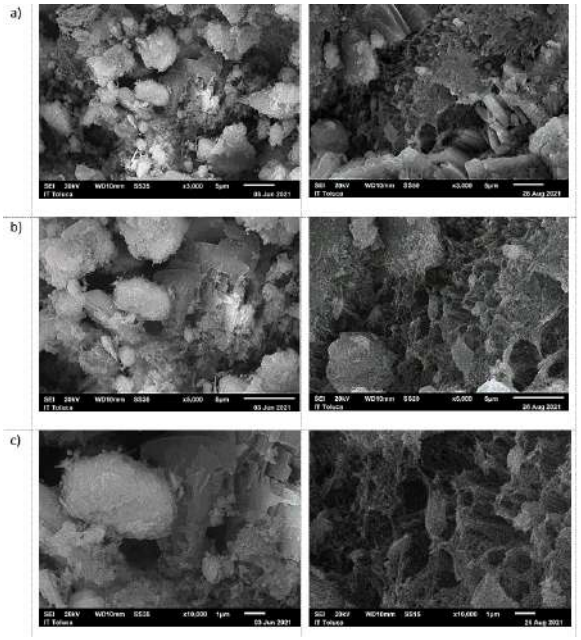

Figure 2 Micrographs of the natural zeolitic material (left) and the modified one (right) with magnifications of a) 3 000, b) 5 000 and c) 10 000 x.

Table 1 Elemental analysis of zeolitic material and modified one.

Element	% Weight	
	ZN	ZM
O	54.44 ± 1.62	50.76 ± 1.13
Na	1.70 ± 0.19	4.08 ± 0.10
Al	6.31 ± 0.57	6.28 ± 0.36
Si	33.55 ± 1.67	32.10 ± 0.65
C	4.00 ± 0.06	6.78 ± 0.31

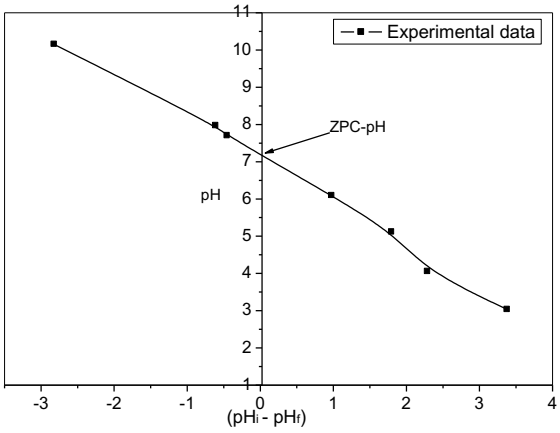

Figure 3. pH vs. pH_i-pH_f for the determination of the point of zero charge of the modified zeolitic material.

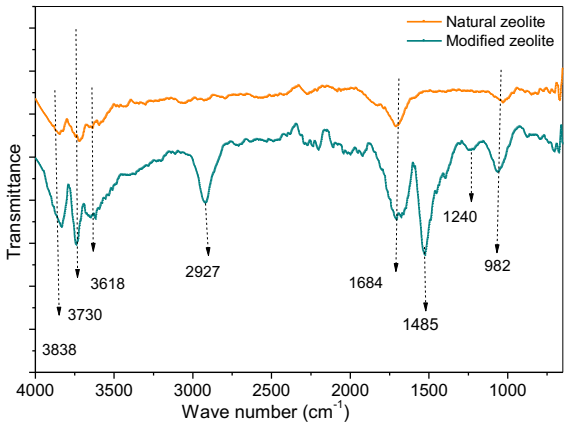

Figure 4 Fourier transform infrared spectra of the natural and modified zeolitic materials.

The Fourier transform infrared spectrum of the natural zeolitic material and the modified one presented in Figure 4, shows the bands at 3838 and 3730 cm^{-1} are related to the O-H bond stretching vibration (Hosseinifard *et al*. 2020). The band at 3618 cm^{-1} corresponds to the Si-OH-Al bond (Dávila *et al*. 2016), the band observed at 1684 cm^{-1} is assigned to the bending vibration of the H-O-H bond due to water (Dimas *et al*. 2021), finally, the band observed at 982 cm^{-1} corresponds to the stretching vibration of the Si-O bond present in the primary structural unit of the SiO_4 tetrahedron (Kabuba and Banza, 2020). On the other hand, a peak is observed at 1240 cm^{-1} in the spectrum of the modified zeolite related to the Al-O bond of the primary structural unit of the zeolite, the peak at 2927 corresponds to the CH_2 stretching vibrations of the aliphatic compounds in the HDTMA surfactant and the peak at 1485 cm^{-1} to the C-H stretching vibrations (Zeng *et al*. 2010), both peaks can confirm the presence of the surfactant in the zeolitic material and coincides with the results obtained by scanning electron microscopy that confirms the modification (Solińska and Bajda, 2022).

Figure 5 shows the diffractogram of the sodium zeolitic material, the main peaks correspond to the diffraction pattern of a clinoptilolite, they are located at 9.8° (0 2 0) and 11.1° (2 0 0) according to the JCPDS card 44-1398 (Saadat and Nezamzadeh- Ejhieh, 2016), the peaks corresponding to quartz are at 20.83° (1 0 0) and 26.644 (1 0 1) according to the JCPDS file 05-0490 (Nezamzadeh-Ejhieh and Tavakoli-Ghinani, 2014), albite has characteristic peaks at 13.76° (0 2 0) and 13.92° (0 0 1) corresponding to the JCPDS card 10-0393 and finally, the characteristic peaks of heulandite are found at 7.45° (1 1 0) and 9.91° (0 2 0) (JCPDS card 75-1712).

Figure 6 shows the diffractogram of the modified zeolitic material, as can be seen, the diffractogram is like the one of the sodium zeolitic material, indicating that after the modification process, the primary structure of the material remains the same and that the modification was carried out superficially (Dimas *et al*. 2021).

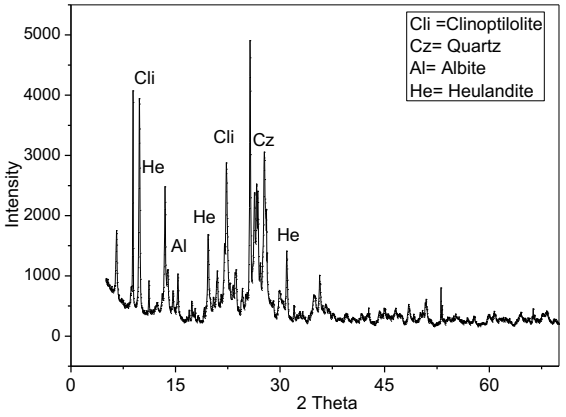

Figure 5. Diffractogram of sodium zeolitic material.

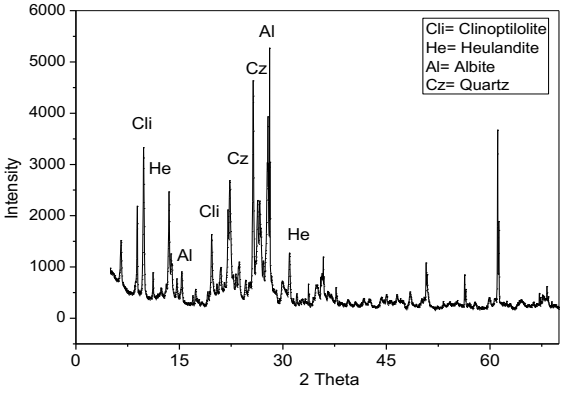

Figure 6. Diffractogram of modified zeolitic material.

Table 2. Main components of zeolitic materials.

Component	JCPDS	Chemical formula
Clinoptilolite-Ca	39-1383	$KNa_2Ca_2(Si_{29}Al_7)\ O_{72}.24H_2O$
Clinoptilolite-Cs	44-1398	$Cs_{5.5}K_{0.4}(Al_7Si_{29})\ O_{72.13}H_2$
Quartz	05-0490	SiO_2
Quartz	65-0466	SiO_2
Albite	19-1184	$NaAlSi_3O_8$
Albite	10-0393	$Na\ (Si_3Al)\ O_8$
Helaudite	13-0196	$CaAl_2Si_7O_{18}.6H_2O$
Helaudite	75-1712	$(Na{\cdot}26K_{0.89}Ca_{3.37}Sr_{0.24}Ba_{0.03})\ Al_{9.48}Si_{26.61}O_{72}(H_2O)_{24.84}H_{1.03}$

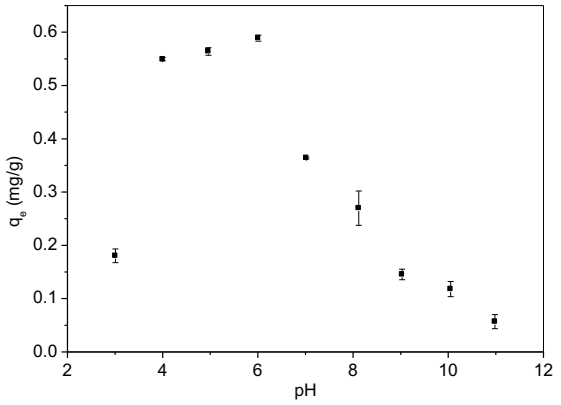

Figure 7 Effect of pH on removal of fluoride ions from solution.

3.2 *Effect of pH*

The effect of pH on the adsorption capacity of the zeolitic material for fluoride ions presented in Figure 7, the highest removal was at pH values between 4 and 6, according to the point of zero charge, below pH 7.06 the surface charge is positive, which favors the removal of fluoride ions and above that the surface charge is negative, which makes removal less probable (Nabbou *et al*. 2019). In addition, at high or low pH values it is possible that the material may suffer structural alterations that would affect its adsorption capacity, at high pH the hydroxyl ions (OH^-) probably compete with the fluoride ions for the adsorption sites, and therefore a decrease in the adsorption capacity of the material occurs (Saucedo-Delgado *et al*. 2017).

3.3 *Isotherms at different temperatures*

Figure 8 shows the isotherms at 20, 30, 40 and 50°C, the isotherms do not show a plateau characteristic of the Langmuir model (Telkapalliwar and Shivankar, 2019), but rather a shape described by the Freundlich model. The lowest removal of fluoride ions was at 20°C and the removal was similar from 30 to 50°C, therefore the thermodynamic parameters could not be calculated in this temperature range.

Table 3 shows the parameters obtained from the fitting of the experimental data to the models of Langmuir and Freundlich, the correlation coefficients are similar for both models, however, the shape of the isotherms suggests a Freundlich type isotherms.

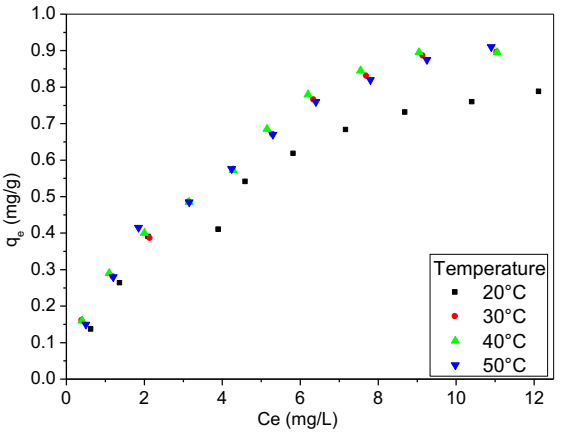

Figure 8 Adsorption isotherms of fluoride ions by the modified zeolitic material at different temperatures.

The results suggest that the adsorption process is carried out through the formation of multilayers on a heterogeneous surface of the adsorbent material (Zhang and Jia, 2018; Zhang *et al*. 2021).

3.4 *Adsorption kinetics*

Figure 9 shows the relationship between the contact time and the adsorption capacity of the modified zeolitic material, the adsorption is fast at the beginning of the adsorption process and then the equilibrium was reached in 9 hours, the experimental adsorption equilibrium capacity (q_{e_exp}) was 0.57 mg/g.

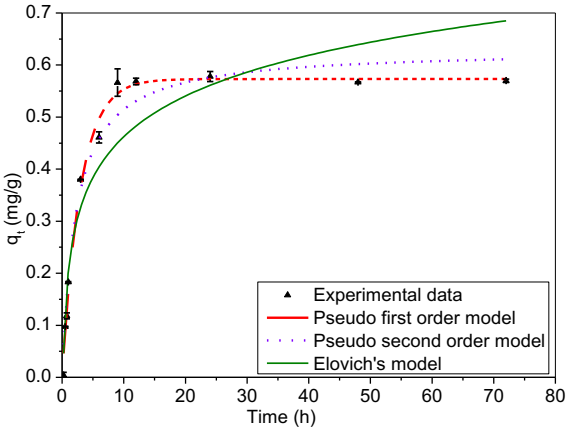

Figure 9. Adsorption kinetics fitted to the models of pseudo first order, pseudo second order and Elovich.

Table 3. Parameters of the isotherms at different temperatures from the experimental data.

T (°C)	Langmuir				Freundlich		
	q_e (mg/g)	q_m (mg/g)	b (L/mg)	R^2	K_F	n	R^2
20	0.78	1.10	0.21	0.97	0.24	1.99	0.96
30	0.86	1.35	0.19	0.98	0.27	1.89	0.98
40	0.86	1.31	0.22	0.97	0.28	1.96	0.97
50	0.91	1.29	0.21	0.99	0.27	1.92	0.99

Table 4 Kinetic parameters for the adsorption of fluoride ions by the modified zeolitic material.

Kinetic model	Parameters	
Pseudo first order	q_{e_exp} (mg/g)	0.56
	q_{e_calc} (mg/g)	0.57
	K_1 (min^{-1})	0.34
	R^2	0.99
Pseudo second order	q_{e_exp} (mg/g)	0.57
	q_{e_calc} (mg/g)	0.63
	K_2 (g/mg·h)	0.11
	R^2	0.97
Elovich	α (mg/g·h)	53.38
	β (mg/g)	0.11
	R^2	0.88

The kinetic parameters were calculated by fitting the experimental data to the pseudo first-order model, the pseudo second-order model, and the Elovich model by using the Origin Lab software and Eq. 1, 2, and 3. The experimental data fit best to the pseudo-first order model.

Table 4 shows the parameters calculated from the experimental data and the models, the results show that the experimental adsorption capacity is similar to the calculated one and the correlation coefficient is the highest for the pseudo first order model, indicating that the mechanism that takes place is physisorption (Flores-Alamo *et al*. 2015). The Elovich model indicates that the adsorption process predominates on the desorption process (α>β).

3.5 Removal of fluoride ions from drinking water

The modified zeolitic material was tested with drinking water from the state of Zacatecas, Mexico, the pH of the sample was 7.88 and its concentration was 5.46 mg/L, the pH of the sample was adjusted to 6 because the highest adsorption was found at this pH. Figure 10 shows adsorption capacity *vs.* the dose, the adsorption capacity increases as the dose increases, this is due to the fact that there are more active sites for the adsorption of fluoride ions, a plateau was observed and the maximum adsorption (86.2 %) was found with 90 mg of modified zeolitic material, later there is no longer a considerable difference in the adsorption capacities (Onyango *et al*. 2010).

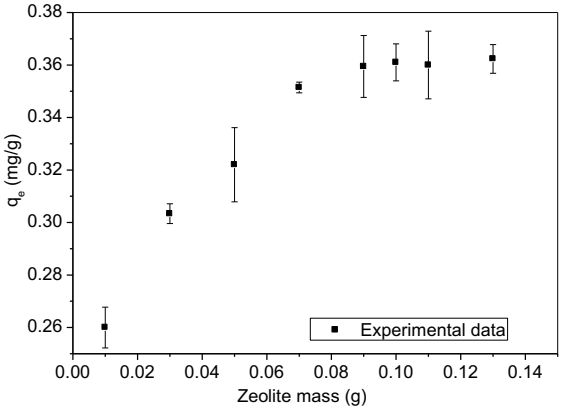

Figure 10. Adsorption capacity vs. dose of adsorbent.

Conclusions

A zeolitic material was modified with a surfactant and characterized, the Si/Al ratio of 5.11 was determined by scanning electron microscopy (EDS), this value has been commonly reported for heulandite-type zeolites. The increase of carbon in the material after modification indicated the presence of the surfactant in the zeolitic material. The point of zero charge was 7.06, then the maximum removal of fluoride ions was expected at pH lower than this value where the zeolitic material surface is positive.

The kinetic data were best adjusted to the pseudo first-order kinetic model, suggesting that the removal of fluoride ions is carried out by physisorption. The adjustment of the experimental data to the Freundlich model indicates that the adsorption process was carried out through the formation of multilayers on the surface of the modified zeolitic material.

The optimum pH for the removal of fluoride ions is between 4 and 6, with a maximum removal of 57.8 %. The removal of fluoride ions is very similar at different temperatures and the data fit best to the Freundlich model with correlation coefficients of 0.96, 0.98, 0.97 and 0.99 for 20, 30, 40, and 50°C respectively. The highest removal percentage of fluoride ions from drinking water was 86.2% with 90 mg of zeolite. The modified material offers an alternative for removing fluoride ions from water.

Acknowledgements

Authors thank Tecnológico Nacional de México/Instituto Tecnológico de Toluca for financial

support and Consejo Nacional de Humanidades, Ciencias y Tecnologías (CONAHCYT) for the scholarship for master's studies of J.I. Vázquez Méndez.

References

Ahamad, K., Singh, R., Baruah, I., Choudhury, H. and Sharma, M. (2018). Equilibrium and kinetics modeling of fluoride adsorption onto activated alumina, alum and brick powder. *Groundwater for Sustainable Development*, 7, 452–458. https://doi.org/10.1016/J.GSD.2018.06.005

Alarcón-Herrera, M, Martin-Alarcon, D., Gutiérrez, M., Reynoso-Cuevas, L., Martín-Domínguez, A., Olmos-Márquez, M. and Bundschuh, J. (2020). Co-occurrence, possible origin, and health-risk assessment of arsenic and fluoride in drinking water sources in Mexico: Geographical data visualization. *Science of The Total Environment*, 698, 134168. https://doi.org/10.1016/J.SCITOTENV.2019.134168

Alhassan, S., He, Y., Huang, L., Wu, B., Yan, L., Deng, H. and Wang, H. (2020). A review on fluoride adsorption using modified bauxite: Surface modification and sorption mechanisms perspectives. *Journal of Environmental Chemical Engineering*, 8(6), 104532. https://doi.org/10.1016/J.JECE.2020.104532

Bajda, T. and Kłapyta, Z. (2013). Adsorption of chromate from aqueous solutions by HDTMA-modified clinoptilolite, glauconite and montmorillonite. Applied Clay Science, 86, 169-173.

Barczyk, K., Mozgawa, W. and Król, M. (2014). Studies of anions sorption on natural zeolites. *Spectrochimica Acta Part A: Molecular and Biomolecular Spectroscopy*, 133, 876–882. https://doi.org/10.1016/J.SAA.2014.06.065

Bhatnagar, A., Kumar, E. and Sillanpää, M. (2011). Fluoride removal from water by adsorption—A review. *Chemical Engineering Journal*, 171(3), 811–840. https://doi.org/10.1016/J.CEJ.2011.05.028

Chai, J., Zhang, W., Liu, D., Li, S., Chen, X., Yang, Y. and Zhang, D. (2022). Decreased levels and ecological risks of disinfection by-product chloroform in a field-scale artificial groundwater recharge project by colloid supplement. *Environment International*, 161, 107130. https://doi.org/10.1016/J.ENVINT.2022.107130

Chen, C., Shih, Y., Su, J., Chen, K. and Huang, C. (2022). Mesoporous zirconium pyrophosphate for the adsorption of fluoride from dilute aqueous solutions. *Chemical Engineering Journal*, 427, 132034. https://doi.org/10.1016/J.CEJ.2021.132034

Corral-Capulin, N., Vilchis-Nestor, A., Gutiérrez-Segura, E. and Solache-Ríos, M. (2018). The influence of chemical and thermal treatments on the fluoride removal from water by three mineral structures and their characterization. *Journal of Fluorine Chemistry*, 213, 42–50. https://doi.org/10.1016/J.JFLUCHEM.2018.07.002

Dávila-Estrada, M., Ramírez-García, J. J., Díaz-Nava, M. C., and Solache-Ríos, M. (2016). Sorption of 17α-ethinylestradiol by surfactant-modified zeolite-rich tuff from aqueous solutions. *Water, Air, & Soil Pollution*, *227*, 1-10. https://doi.org/10.1007/s11270-016-2850-y

Dimas Rivera, G., Martínez Hernández, A., Pérez Cabello, A., Rivas Barragán, E., Liñán Montes, A., Flores Escamilla, G., Sandoval Rangel, L., Suarez Vazquez, S. and de Haro Del Río, D. (2021). Removal of chromate anions and immobilization using surfactant-modified zeolites. *Journal of Water Process Engineering*, 39, 101717. https://doi.org/10.1016/J.JWPE.2020.101717

Flores-Alamo, N., Solache-Ríos, M. J., Gómez-Espinosa, R.M. and García-Gaitán, B. (2015). Estudio de adsorción competitiva de cobre y zinc en solución acuosa utilizando Q/PVA/EGDE. *Revista Mexicana de Ingeniería Química*, 14(3), 801-811. http://www.rmiq.org/ojs311/index.php/rmiq/article/view/995

He, J., Yang, Y., Wu, Z., Xie, C., Zhang, K., Kong, L. and Liu, J. (2020). Review of fluoride removal from water environment by adsorption. *Journal of Environmental Chemical Engineering*, 8(6), 104516. https://doi.org/10.1016/J.JECE.2020.104516

Hosseinifard, S., Aroon, M. and Dahrazma, B. (2020). Application of PVDF/HDTMA-modified clinoptilolite nanocomposite membranes in removal of reactive dye from aqueous solution. *Separation and Purification Technology*, 251, 117294. https://doi.org/10.1016/J.SEPPUR.2020.117294

Jiang, P., Li, G., Zhou, X., Wang, C., Qiao, Y., Liao, D. and Shi, D. (2019). Chronic fluoride exposure induces neuronal apoptosis and impairs neurogenesis and synaptic plasticity: Role of GSK-3β/β-catenin pathway. *Chemosphere*, 214, 430–435. https://doi.org/10.1016/J.CHEMOSPHERE.2018.09.095

Kabuba, J. and Banza, M. (2020). Ion-exchange process for the removal of Ni (II) and Co (II) from wastewater using modified clinoptilolite: Modeling by response surface methodology and artificial neural network. *Results in Engineering*, 8, 100189. https://doi.org/10.1016/J.RINENG.2020.100189

Liu M., Zang, Z., Zhang, S., Ouyang, G. and Han, R. (2021). Enhanced fluoride adsorption from aqueous solution by zirconium (IV)-impregnated magnetic chitosan graphene oxide. *International Journal of Biological Macromolecules*, 182, 1759–1768. https://doi.org/10.1016/J.IJBIOMAC.2021.05.116

Leal-Perez, J. E., Almaral-Sanchez, J. L., Hurtado-Macias, A., Cortez-Valadez, M., Bórquez-Mendívil, A., García-Grajeda, B. A. and Flores-Valenzuela, J. (2024). Structural and chemical analysis of Zn ion exchange in thermally modified zeolite A4. *Revista Mexicana de Ingeniera Química*, *23*(3). https://doi.org/10.24275/rmiq/Mat24264

López-Guzmán, M., Alarcón-Herrera, M., Irigoyen-Campuzano, J., Torres-Castañón, L. and Reynoso-Cuevas, L. (2019). Simultaneous removal of fluoride and arsenic from well water by electrocoagulation. *Science of The Total Environment*, 678, 181–187. https://doi.org/10.1016/J.SCITOTENV.2019.04.400

Martínez-Salazar, E., Flores-Rodríguez, V., Rosas-Valdez, R. and Falcón-Ordaz, J. (2016). Helminth parasites of some rodents (Cricetidae, Heteromyidae, and Sciuridae) from Zacatecas, Mexico. *Revista Mexicana de Biodiversidad*, 87(4), 1203–1211. https://doi.org/10.1016/J.RMB.2016.10.009

Mohapatra, M., Anand, S., Mishra, B., Giles, D, and Singh, P. (2009). Review of fluoride removal from drinking water. *Journal of Environmental Management*, 91(1), 67–77.

https://doi.org/10.1016/J.JENVMAN.2009.08.015

Nabbou, N., Belhachemi, M., Boumelik, M., Merzougui, T., Lahcene, D., Harek, Y., Zorpas, A. and Jeguirim, M. (2019). Removal of fluoride from groundwater using natural clay (kaolinite): Optimization of adsorption conditions. *Comptes Rendus Chimie*, 22(2–3), 105–112. https://doi.org/10.1016/J.CRCI.2018.09.010

Naghash, A. and Nezamzadeh-Ejhieh, A. (2015). Comparison of the efficiency of modified clinoptilolite with HDTMA and HDP surfactants for the removal of phosphate in aqueous solutions. *Journal of Industrial and Engineering Chemistry*, 31, 185–191. https://doi.org/10.1016/J.JIEC.2015.06.022

Navarro, O., González, J., Júnez-Ferreira, H., Bautista, C. and Cardona, A. (2017). Correlation of Arsenic and Fluoride in the Groundwater for Human Consumption in a Semiarid Region of Mexico. *Procedia Engineering*, 186, 333–340. https://doi.org/10.1016/J.PROENG.2017.03.259

Nezamzadeh-Ejhieh, A. and Tavakoli-Ghinani, S. (2014). Effect of a nano-sized natural clinoptilolite modified by the hexadecyltrimethyl ammonium surfactant on cephalexin drug delivery. *Comptes Rendus Chimie*, 17(1), 49–61. https://doi.org/10.1016/J.CRCI.2013.07.009

Nizam, S., Virk, H. S. and Sen, I. (2022). High levels of fluoride in groundwater from Northern parts of Indo-Gangetic plains reveals detrimental fluorosis health risks. *Environmental Advances*, 8, 100200. https://doi.org/10.1016/J.ENVADV.2022.100200

Jiménez-Reyes, M., Almazán-Sánchez, P., and Solache-Ríos M. (2021). Radioactive waste treatments by using zeolites. A short review. *Journal of Environmental Radioactivity*. 233, 106610. https://doi.org/10.1016/j.jenvrad.2021.106610

Onyango, M., Masukume, M., Ochieng, A. and Otieno, F. (2010). Functionalised natural zeolite and its potential for treating drinking water containing excess amount of nitrate. *Water Research Commission*, 36, 655–662. https://doi.org/10.4314/wsa.v36i5.61999

Saadat, M., and Nezamzadeh-Ejhieh, A. (2016). Clinoptilolite nanoparticles containing HDTMA and Arsenazo III as a sensitive carbon paste electrode modifier for indirect voltammetric measurement of Cesium ions. *Electrochimica Acta*, 217, 163–170. https://doi.org/10.1016/J.ELECTACTA.2016.09.084

Saucedo-Delgado, B., Haro, D., González-Rodríguez, L., Reynel-Ávila, H., Mendoza-Castillo, D., Bonilla-Petriciolet, A. and Rivera de la Rosa, J. (2017). Fluoride adsorption from aqueous solution using a protonated clinoptilolite and its modeling with artificial neural network-based model. *Journal of Fluorine Chemistry*, 204, 98–106. https://doi.org/10.1016/J.JFLUCHEM.2017.11.002

Serrano-Meza, A., Vigueras-Cortes, J. M., and Allen, C. D. (2024). Municipal wastewater treatment in a hybrid biofiltration system packed with agave fiber. *Revista Mexicana de Ingeniera Quimica*, *23*(3). https://doi.org/10.24275/rmiq/Mat24264

Solińska, A. and Bajda, T. (2022). Modified zeolite as a sorbent for removal of contaminants from wet flue gas desulphurization wastewater. *Chemosphere*, 286. https://doi.org/10.1016/J.CHEMOSPHERE.2021.131772

Telkapalliwar, N. and Shivankar, V. (2019). Data of characterization and adsorption of fluoride from aqueous solution by using modified Azadirachta indica bark. *Data in Brief*, 26. https://doi.org/10.1016/J.DIB.2019.104509

Ullah, R., Liu, C., Panezai, H., Gul, A., Sun, J. and Wu, X. (2020). Controlled crystal phase and particle size of loaded-TiO2 using clinoptilolite as support via hydrothermal method for degradation of crystal violet dye in aqueous solution. *Arabian Journal of Chemistry*, 13(2), 4092–4101. https://doi.org/10.1016/J.ARABJC.2019.06.011

Wingenfelder, U., Furrer, G. and Schulin, R. (2006). Sorption of antimonate by HDTMA-modified zeolite. *Microporous and Mesoporous Materials*, 95, 265–271.

https://doi.org/10.1016/J.MICROMESO.2006.06.001

Zeng, Y., Woo, H., Lee, G. and Park, J. (2010). Removal of chromate from water using surfactant modified Pohang clinoptilolite and Haruna chabazite. *Desalination*, 257, 102–109. https://doi.org/10.1016/J.DESAL.2010.02.039

Zhang, X., Qi, Y., Chen, Z., Song, N., Li, X., Ren, D., & Zhang, S. (2021). Evaluation of fluoride and cadmium adsorption modification of corn stalk by aluminum trichloride. *Applied Surface Science*, *543*, 148727. https://doi.org/10.1016/j.apsusc.2020.148727

Zhang, Y. and Jia, Y. (2018). Fluoride adsorption on manganese carbonate: Ion-exchange based on the surface carbonate-like groups and hydroxyl groups. *Journal of Colloid and Interface Science*, 510, 407–417. https://doi.org/10.1016/J.JCIS.2017.09.090

Znak, Z., Zin, O., Mashtaler, A., Korniy, S., Sukhatskiy, Y., Gogate, P. R., Mnykh, R. and Thanekar, P. (2021). Improved modification of clinoptilolite with silver using ultrasonic radiation. *Ultrasonics Sonochemistry*, 73, 105496. https://doi.org/10.1016/J.ULTSONCH.2021.105496

Vol. 24, No. 2(2025) IA25505
Revista Mexicana de Ingeniería Química

Enhancement of rheological and filtration properties of water-based drilling fluids through zinc oxide nanoparticles addition

Mejoramiento de las propiedades reológicas y de filtración de un fluido de perforación base agua mediante la adición de nanopartículas de óxido de zinc

L.C. Rodríguez-López[1], H. Pérez-Vidal[1], F.C. Gómez-Torres[2], C. Martínez-Pacheco[2], E.E. Uicab-Córdova[3], S.C. Madrigal-Díaz[4], L.L. Díaz-Flores[4]*

[1]Academic Division of Basic Sciences, Juarez Autonomous University of Tabasco, Tabasco, México.
[2]Division of Industrial Process, Technological University of Tabasco, Tabasco, México.
[3]Division of Chemistry, Technological University of Tabasco, Tabasco, México.
[4]Academic Division of Engineering and Architecture, Juarez Autonomous University of Tabasco, Tabasco, México.

Received: January 17, 2025; Accepted: April 12, 2025

Abstract

Drilling fluids are used in oil well drilling depending on their filtration characteristics and rheological properties. Because of the increase in environmental policies, innovations in water-based drilling fluids (WBDF) have been proposed to convert them into high-performance fluids with stabilizer properties during drilling, avoiding an increase in non-productive time (NPT) and costs. This study proposes the enhancement of WBDF due to the addition of ZnO nanoparticles (ZnO-NPs). After the addition of ZnO-NPs, the results show that the drilling fluid, with a concentration of 0.05 % ZnO-NPs, has improved rheological properties, evaluated at 25, 50, and 70 °C. At room temperature, there is an increase in other parameters such as apparent viscosity (AV) 200 %, the plastic viscosity (PV) 180 %, the yield point (YP) 240 %, compared to the base fluid and furthermore 10-min gel strength elevates by 80 % more. In addition, the amount of filtered fluid reduces from 13.5 to 10.4 mL, even under conditions of 500 psi and 150 °C, there is a 54 % reduction, indicating the formation of a proper filter cake.

Keywords: Filtration control, HPHT conditions, Mechanosynthesis, ZnO nanoparticles, Water-based drilling fluids.

Resumen

Los fluidos de perforación se utilizan en la perforación de pozos petroleros dependiendo de sus características de filtración y propiedades reológicas. Debido al aumento de las políticas ambientales, se han propuesto innovaciones en los fluidos de perforación a base de agua (WBDF) para convertirlos en fluidos de alto rendimiento con propiedades estabilizadoras durante la perforación, evitando un aumento en el tiempo no productivo (NPT) y los costos. Este estudio propone el mejoramiento del WBDF debido a la adición de nanopartículas de ZnO (ZnO-NPs). Después de la adición de las ZnO-NPs, los resultados muestran que el fluido de perforación, con una concentración de 0.05% de ZnO-NPs, tiene propiedades reológicas mejoradas, evaluadas a 25, 50 y 70 °C. A temperatura ambiente, hay un aumento en otros parámetros como la viscosidad aparente (AV) 200 %, la viscosidad plástica (PV) 180 %, el límite elástico (YP) 240 %, en comparación con el fluido base y, además, la fuerza del gel de 10 minutos se eleva en un 80 % más. Además, la cantidad de fluido filtrado se reduce de 13,5 a 10,4 mL, incluso bajo condiciones de 500 psi y 150 °C, hay una reducción del 54%, lo que indica la formación de una torta de filtración adecuada.

Palabras clave: Control de filtración, condiciones HPHT, Mecanosíntesis, Nanopartículas de ZnO, Fluidos de perforación a base de agua.

*Corresponding author. *E-mail*: laura.diaz@ujat.mx ;
https://doi.org/10.24275/rmiq/IA25505
ISSN:1665-2738, *issn-e*: 2395-8472

1 Introduction

The petroleum industry contributes to the energy context due to global oil consumption, increasing since the beginning of this millennium, showing an upward production trend from 3,300 to 4,500 million tons of oil equivalent (toe) (Zheng *et al*., 2022). The growing energy demand and the continuous depletion of conventional oil reserves (Chuck H. *et al*., 2011) have compelled the energy sector to innovate existing technology to locate and drill complex formations (Nwaezeapu *et al*., 2019). Drilling is a decisive process for recovering underground materials such as oil and gas, and drilling fluids are key to achieving this goal (Sadeghalvaad & Sabbaghi, 2015). Furthermore, these fluids are used to suspend cuttings, clean the wellbore (Ofei *et al*., 2021), cool the drill (Yi *et al*., 2024), preserve effective lubrication between the drilling equipment and the well (Lysakova *et al*., 2024), conserve proper weight-on-bit pressure (Reilly *et al*., 2016), and provide wellbore stability (Ma *et al*., 2024). The success of a drilling operation depends on the fluid's composition and properties of the drilling (Aghdam et al., 2020). On the other hand, the selection and quantity of additives in drilling fluids affect the rheology and the desired filtration properties of the fluid (Al-Zubaidi *et al*., 2017). An incorrect formulation of the fluid generates problems during the drilling process, particularly filtrate loss across the formation, resulting in an excessively thick filter cake (Y. Duan *et al*., 2024). This infiltration of the liquid and solid phase of the drilling mud in the reservoir formation affects the hydrocarbon production rate and the liquid phase of the drilling mud could create water-in-oil emulsion (w/o). These problems are avoided when enhancing filtration properties by decreasing the amount of lost volume of the drilling fluid, and by rising rheological properties, such as elastic limit, gel strength and shear rate, drilling mud performance is improved (Ghayedi & Khosravi, 2020). Highly efficient drilling fluids are essential for drilling in challenging zones, such as high-pressure, high-temperature (HPHT) formations (Sulaimon *et al*., 2017).

With recent progress in nanotechnology, Ibrahim *et al*. (2024), Yi *et al*. (2024), and Oseh *et al*. (2024) have studied the possibility of using nanoparticles (NPs) and their integration with natural and synthetic polymers in the petroleum industry. This is because nanomaterials have specific characteristics of surface effect and small-size (Friedheim et al., 2012). These features make them suitable as additives to modify the rheology and filtration properties of WBDF (Rafati *et al*., 2018).

In relation to this topic, Pourkhalil H. and Nakhaee, A. (2019), report the use of different nanoparticles as additives in drilling fluids; they used three Nano-ZnO fluids with different concentrations. These fluids caused a reduction in pore pressure accumulation and proved a desirable effect in blocking pore spaces in the shale samples.

Studies conducted by Ahmad *et al*., (2021), showed the synergistic effect of the polymer and nanoparticles on the hydration of shale and the swelling performance of drilling fluids, confirming that it enhances the inhibition characteristics.

A study of the thermal stability of the fluid, by Medhi *et al*., (2021), found that the addition of ZnO-NP in the water-based drilling nanofluid increase viscosity and reduce fluid loss.

Currently, the formulation of drilling mud has been studied to lower costs, and to reduce the damage caused by the filtration of the mud due to its inefficient stability at high temperatures and pressures (Martin *et al*., 2024), in addition to preserving the environment, without compromising the performance of the fluid and its functions (Ramos et al., 2013).

Therefore, the main objective of this work was to investigate the effect of the addition of ZnO-NPs synthesized by mechanochemical synthesis and incorporating different concentrations to WBDF, to evaluate the behavior of its rheological and filtration properties. In this study it was demonstrated that with short milling times of the inorganic precursors for obtaining ZnO nanoparticles, it is possible to obtain characteristics that contribute to improving the rheological and filtration properties of a WBDF formulation using bentonite and chemical additives.

2 Materials and methods

2.1 Synthesis of ZnO-NPs

Mechanosynthesis method was used to synthesize ZnO, applying as precursors: 3.45 g of J.T. Baker zinc chloride ($ZnCl_2$) at 97% purity, 2.62 g of J.T. Baker sodium carbonate (Na_2CO_3) at 99.5% purity and 11.48 g of sodium chloride (NaCl) or common table salt. These precursors were mixed in a 92.87 mL stainless steel container with stainless steel milling media, which was grinded in a 60 Hz mill (8000M millSpex@), at different milling times: 20, 40 and 60 min, samples were named ZnO 20, ZnO 40 and ZnO 60. The grinding time used to obtain ZnO-NPs was taken from literature reports. (Espitia *et al*., 2012; Sapkota *et al*., 2021), due to its influence on the physical and chemical properties of the nanoparticles. As grinding time increases, the particles tend to reduce their size due to continuous fracture and cold welding, resulting in a higher specific surface area (Abrica G. and Gómez A., 2022). Furthermore, grinding time induce transformations in the crystalline structure of

materials, even long grinding times can lead to the nanoparticles being contaminated by materials from the milling media (such as the grinding balls and the vial), which negatively affect the final material properties (Prieto G. *et al*., 2007).

After milling, the ZnO was separated from the NaCl residue derived from the reaction, with three washing processes with distilled water and vacuum filtration, then ultrasound treatment was conducted for 60 min and washed one more time. Subsequently, the sample was dried in the oven at 120 °C for 2 h and then calcined at 400 °C for 2 h with a ramp rate of 10 °C/min. 3 types of nanoparticles were obtained, labeled depending on the time as ZnO X, where X= 20, 40 and 60.

2.2 *Characterization of ZnO-NPs*

X-ray Diffraction (XRD) was conducted for the analysis of the crystalline phase obtained and the crystal size of the ZnO powders, using an x-ray diffractometer (Bruker D8-Advance) having a CuKα1 radiation with a wavelength of λ=1.54060 Å, 40 Kv and 30 mA. The intensity of the peaks was measured in a range of 20° to 80° in 2θ.

RAMAN spectroscopy was used to identify the structure of the Zn-O bonds, with a WITEC Alpha 300 spectrometer measuring from 50 to 700 cm^{-1}, the laser wavelength was 488 nm, with an integration time of 1s. The ZnO powders were also analyzed by FTIR spectroscopy Shimadzu IRAffinity-1 spectrometer, in the range of 4700 to 370 cm^{-1}.

The morphology of the ZnO powders was determined by Field Emission Scanning Electron Microscopy (FESEM). A JEOL JSM-7600F microscope was employed at 15 kV acceleration voltage, with a field emission gun, with a secondary electron detector.

Particle Size Distribution and Dynamic Light Scattering were carried out Zeta sizer equippment Malvern Panalytical™ model ZS, in solutions at a concentration of 5 mg of material in 10 mL of dispersant in polystyrene disposable cell using Stokes Einstein equation. These techniques were used to characterize stability and surface distribution of ZnO-NPs Water-Based Drilling Fluid.

Finally, the specific area was measured in a Micromeritics™ model TriStar II 320 low-pressure nitrogen adsorption analysis equipment, using the BET method (Brunauer, Emmett and Teller).

2.3 *Preparation of the Water-Based Drilling Fluid (WBDF)*

To compare the effect of the addition of the ZnO-NPs into the fluid, a WBDF, called base fluid, was prepared, mixing sodium bentonite treated with water at 10 % w/v, this mixture was left for 24 h for hydration, and water was added later until an apparent viscosity of 5 cP was obtained. Additives listed in Table 1 were also added. The resulting mixture was stirred at high-speed using a mechanical agitator, considering stirring for 30 min for each additive incorporated. Sonication was performed for 1 h for fluid homogenization.

Table 1. Additives used for the preparation of water-based drilling fluid.

Additives	% w/v
Bentonite ($Al_2O_3 \cdot 4SiO_2 \cdot H_2O$)	10.00
Xanthan gum ($(C_{35}H_{49}O_{29})n$)	0.25
Polyanionic cellulose ($[C_6H_7O_2(OH)_2CH_2COONa]n$)	0.50
Potassium chloride (KCl)	3.00
Sodium hydroxide (NaOH)	0.01
Formaldehyde ($H_2C{=}O$)	0.10

2.4 *Preparation of the modified water-based drilling fluid*

In order to evaluate the effect of ZnO-NPs on the rheological and filtration behavior of WBDF formulation, the modified water-based drilling fluid (MWBDF) was prepared. First, it began a coupling fluid called CF_1, CF_2 and CF_3 (according to the percentage of ZnO-NPs added) was obtained, in 200 mL of a mixture of bentonite with water, diluted to reach 5 cP, xanthan gum was incorporated at 0.25 % w/v stirring for 30 minutes. Afterwards, the synthesized ZnO-NPs were added at 20, 40 and 60 milling minutes, at a concentration of 0.05, 0.10 and 0.15 % w/v (Table 2), concentrations ≥ 0.20 % are not recomended due undesirable effects on water-based drilling fluids (Cardenas A., 2022). These fluids (CF_1, CF_2 and CF_3) were mechanically mixed for 30 min with the WBDF to obtain the MWBDF formulations.

Table 2. Coupling fluids (CF) for the preparation of a modified WBDF.

Nomenclature	% w/v of ZnO-NPs	% w/v of GX
CF_1	0.05	0.25
CF_2	0.10	0.25
CF_3	0.15	0.25

2.5 *Effect of ZnO-NPs on the rheological and filtration properties of water-based drilling fluid*

Each of the samples obtained from the WBDF was evaluated for its rheological and filtration properties. Triplicate tests were carried out, following the procedure and specifications recommended by the American Petroleum Institute (API) (API, 2019), using the appropriate equipment.

2.5.1 Evaluation of rheological properties

The rheological tests of the WBDF and the MWBDF with ZnO-NPs, were carried out with a Fann-35A viscometer; according to the API 13B-1 standard, these tests were tried at temperatures of 25, 50 and 70 °C and readings were recorded at 3, 6, 100, 200, 300 and 600 RPM, to make the measurements, the freshly stirred sample was placed inside a thermal vessel and heated to the test temperature.

2.5.1.1 Apparent viscosity

To calculate the VA, once the temperature was reached, the engine was started by placing the commutator in the high-speed position, with the speed shift lever in the lowest position and when the value was constant the reading at 600 RPM was recorded.

$$\text{Apparent viscosity, cP} = \frac{\text{reading for 600 RPM}}{2}$$

2.5.1.2 Viscosity plastic

To calculate PV, the switch was set to the speed of 300 RPM, when it indicated a constant value, the reading was taken for 300 RPM.

$$\text{Plastic viscosity, cP} = \text{reading at 600 RPM} - \text{reading at 300 RPM}$$

2.5.1.3 Yield point

For the calculation of the yield point, the formula was used:

$$\text{Yield point, lb/100 ft}^2 = \text{reading for 300 RPM} - \text{plastic viscosity}$$

2.5.1.4 Gel strength

For the measurement of the gel strength of 10 seconds and 10 minutes, the sample was stirred at 600 RPM, approximately 15 seconds and the velocity assembly were positioned in neutral; after that time, the engine was shut down, keeping the drilling fluid static for 10 seconds and 10 minutes, respectively. Subsequently, the switch was changed to a low-speed position and the maximum deflection units at 3 rpm were recorded. These readings are taken as values that represent gel strength.

2.5.2 Evaluation of filtration properties

Low-pressure and low-temperature filtration was measured for all samples of the MWBDF and WBDF using an OFITE low-pressure filter press at a pressure of 100 psi and room temperature (API 13B-1, 2019). The volume of fluid passing through the standard filter paper was recorded during 30 minutes within 5-minute intervals.

High-pressure and high-temperature (HPHT) filtration properties were measured at 500 psi and 150 °C using an OFITE HPHT filter press. The test was conducted for 30 minutes, and later the filtered fluid was collected and measured.

2.5.3 Hot-rolling process

400 mL samples of each formulation (WBDF and MWBDF) were poured into cylindrical aging cells and pressurized at 200 psi using CO_2 capsules, maintaining rotation inside the roller oven for 16 hours at 110 °C.

3 Results and discussion

3.1 Characterization of ZnO-NPs added to the WBDF formulation

The ZnO-NPs with milling times of 20, 40 and 60 minutes were analyzed by structural, morphological and textural techniques.

3.1.1 X-ray diffraction

The diffractograms presented in Figure 1 correspond to ZnO-NPs synthesized at three milling duration time: 20, 40, and 60 minutes. No significant differences were observed in the signal of the diffracted peaks, mainly on the (100), (002), and (101) planes. This confirms the successful synthesis of pure and crystalline particles. X-ray diffraction (XRD) analysis also showed the characteristic peaks of a hexagonal wurtzite crystal system, with lattice parameters of a=3.25 Å, b=3.25 Å and c=5.21 Å (Bolarinwa *et al.*, 2017). These results indicate that mechanochemical synthesis produces the crystal structure, consistent with the standard reference card (JCDPS: 00-036-1451).

The most intense peaks were observed at angles of 36.2° and 31.7°, corresponding to the (100) and (101) planes, respectively. Using the Debye–Scherrer equation, the calculated crystal sizes were in the ranges of 42 and 47 nm for ZnO 20; 45 and 48 nm for ZnO 40; and 42 and 47 nm for ZnO 60, corresponding to the main peaks mentioned above.

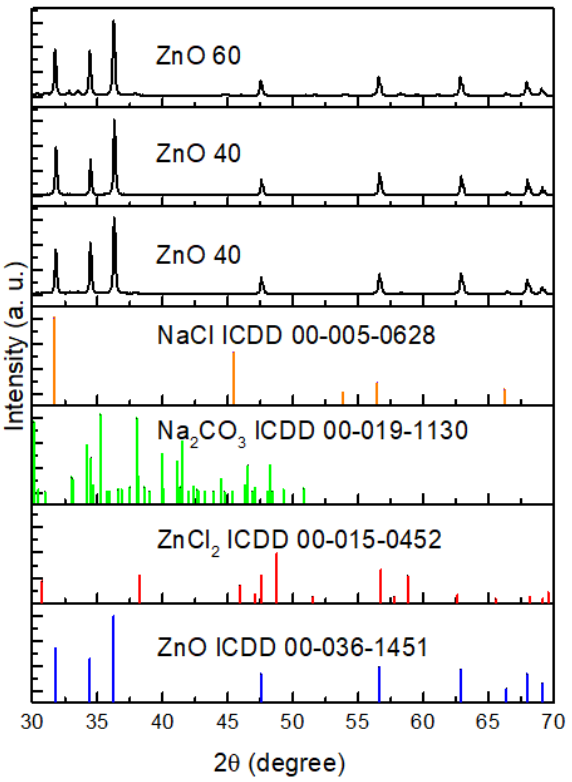

Figure 1. X-ray diffraction patterns of precursors and ZnO powders synthesized by mechanochemical route with varying grinding times of 20 (ZnO 20), 40 (ZnO 40), and 60 (ZnO 60) minutes, and synthesized at 450 °C.

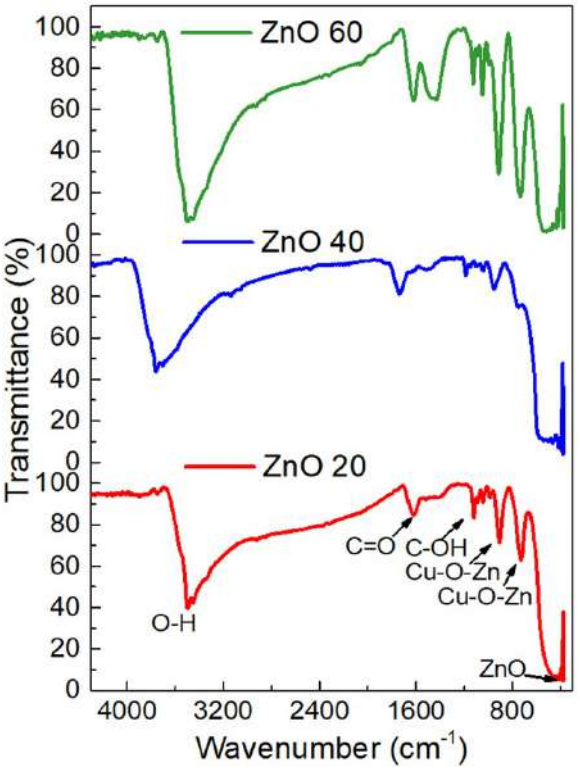

Figure 2. Fourier Transform Infrared (FTIR) spectra of ZnO powders synthesized via mechanochemical route with grinding times of 20, 40, and 60 minutes.

3.1.2 FTIR spectroscopy

As ZnO crystals were obtained by milling techniques, ZnO-NPs powders were analyzed to evaluate the presence of contaminants or residuals from the mechanochemical reaction. Figure 2 presents the FTIR spectra corresponding to the three milling samples. Distinct bands are observed in all three spectra: the band at 3500 cm^{-1} corresponds to the O-H functional group (hydroxyl groups), caused by both molecular and dissociative water absorption, resulting from the synthesis process and moisture absorption from the air (Aquino *et al*., 2018). The band at 1624 cm^{-1} and 1121 cm^{-1} is associated with the C=O functional group linked to symmetric stretching of sodium carbonate, and to the C-OH group resulting from bending, respectively (Senthilkumaar *et al*., 2008). The band at 902 cm^{-1} is associated with the formation of Zn with tetrahedral coordination (García M. *et al*., 2024) and the band at 720 cm^{-1} are attributed to Zn-O stretching (Zargar *et al*., 2014). Additionally, the band located at 380 cm^{-1} corresponds to the ZnO vibration (Aquino *et al*., 2018).

These spectra indicate that the ZnO-NPs samples at 60 min contain the highest amount of reaction residuals, which could potentially influence the rheological properties of the MWBDF formulated in this study.

3.1.3 Raman spectroscopy

Since the bands associated with the precursors appear in the FTIR analysis, the ZnO powders were analyzed by Raman spectroscopy. The peak observed at 100 cm^{-1} in Figure 3 belongs to the low-frequency mode of E_{2L}, related to the vibration of the Zn-sublattice; the peak at 333 cm^{-1} is an E_{2H}-E_{2L} vibrational mode developing from phonons of the boundary zone of wurtzite ZnO. The peak presented at 438 cm^{-1} corresponds to the high-frequency E_{2H} mode; this vibration mode occurs after the movement of oxygen atoms in the ZnO lattice (Tichaona Taziwa *et al*., 2017). Finally, the peak located at 580 cm^{-1} is E_1(LO) mode and originates from oxygen vacancy defects in ZnO (Qi *et al*., 2008). All samples present four vibrational modes characteristic of ZnO, sustaining the obtention of crystalline ZnO, which was observed in the diffractogram in Figure 1. The shift in spectral bands observed around 330 cm^{-1} and 430 cm^{-1} with different grinding times ocurrs due to temperature changes caused by mechanical action (Michael J. Pelletier, 1989) and the stress within the material by grinding time increase, affecting molecular vibrations (Ibáñez *et al*., 2023).

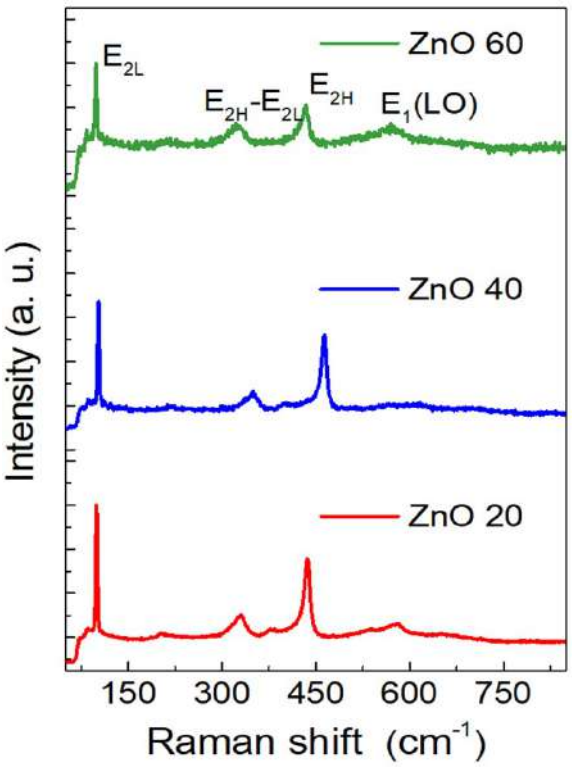

Figure 3. Raman spectra of ZnO powders synthesized via mechanochemical route with varying grinding times of 20, 40, and 60 minutes.

3.1.4 Field emission scanning electron microscopy

Based on the structural analysis, ZnO-NPs were found in crystalline form, but the presence of the remnants could be affecting the agglomeration of the particles. The above is exemplified in the micrographs of Figure 4a, 4b and 4c, which show the ZnO-NPs obtained after 20, 40 and 60 min of milling, respectively. ZnO-NPs of 20 min present an irregular morphology. For the samples of 40 and 60 minutes, a semi-spherical shape is observed, but decreasing in size as the milling time increases. 100 measurements were conducted for the size distribution, and according to the results they have a predominant size of 60 ±8, 40 ±3 and 30 ±2 nm for 20, 40 and 60 minutes, respectively.

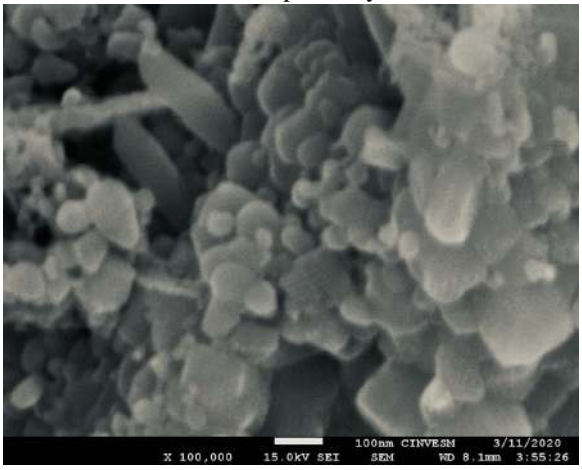

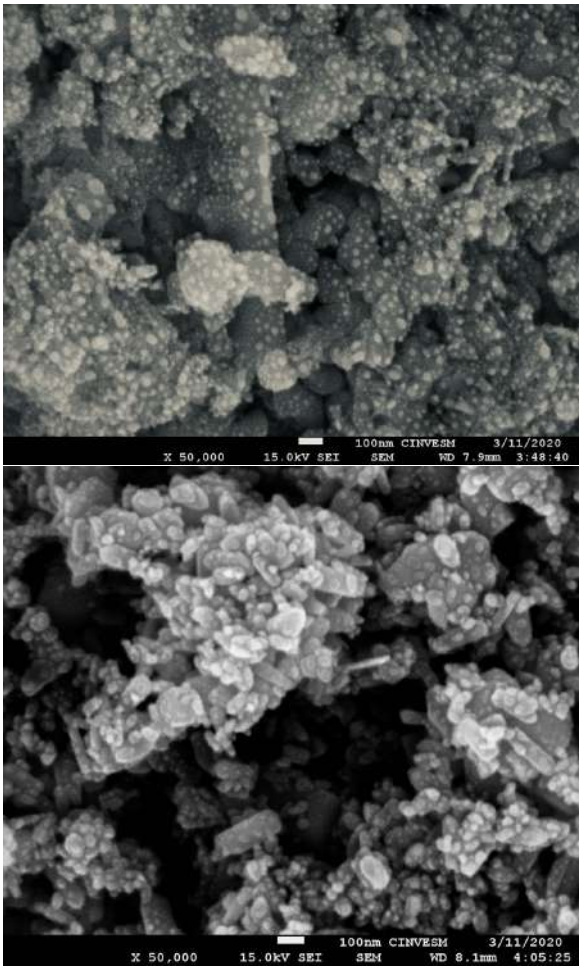

Figure 4. FESEM images of ZnO-NPs synthesized by mechanochemical route, with varying grinding times: a) 20 minutes, b) 40 minutes, and c) 60 minutes.

3.1.5 ZETA potential

Once the shape and size were identified, the size of the ZnO-NPs in suspension was confirmed. Figure 5 exhibits the distribution of particle sizes measured in solution at a concentration of 5 mg of material in 10 mL of dispersant, one for each milling time. The particle size varies for all samples, in the case for ZnO synthesized at 20 minutes the size is 373.7 nm, for ZnO synthesized at 40 minutes the size is 661.5 nm and for ZnO synthesized at 60 minutes the size is 336.2 nm. These results reveal that the nanoparticles synthesized at 60 minutes of milling have a smaller size and could have greater stability in a solution, since larger and heavier particles tend to settle more rapidly (Arenas Gaviria, 2024). The particle size of ZnO determined by this technique differs from FESEM analyses, because in the presence of water, ZnO-NPs could be disperse or aggregate depending on the pH and concentration in suspension; although ZnO does not swell, interaction with water can affect its size and shape due to the adsorption of water molecules on its surface (Salas *et al*., 2016).

Table 3. BET physicochemical characterization of ZnO-NPs, including specific surface area, pore volume, and pore size distribution in agglomerate.

Sample	Specific area (m^2/g)	Pore volume (cm^3/g)	Pore size (nm)
ZnO-20	1.75	5.15 X10^{-3}	25.63
ZnO-40	2.88	7.97 X10^{-3}	24.56
ZnO-60	7.26	21.63 X10^{-3}	15.53

Table 4. Average value and standard deviation of apparent viscosity (cP).

Before hot rolling																		
	25 °C						50 °C						70 °C					
	Zn-60		Zn-40		Zn-20		Zn-60		Zn-40		Zn-20		Zn-60		Zn-40		Zn-20	
C	A	SD	A	SD	A	SD	A	SD	A	SD	A	SD	A	SD	A	SD	A	SD
0	19	1	19	1	19	1	12.5	0	12.5	0	12.5	0	13.8	0.3	13.8	0.3	13.8	0.3
0.05	39	0.5	29.7	0.3	27.3	0.29	35	0.3	27	0.5	24	0	33	0.5	23.2	0.3	21.5	0.5
0.1	33.2	0.7	32	0	28.5	0	29.2	0.3	24.5	0.5	25.8	0.6	26.3	0.8	22.2	0.6	25.3	0.6
0.15	31	0.5	30	0.5	27.7	0.3	26.5	0.5	25.2	0.3	23.8	0.8	24.2	0.3	21.5	0	23.3	0.3
After hot rolling																		
0	21	0.5	21	0.5	21	0.5	18.5	1	18.5	1	18.5	1	13.5	0	13.5	0	13.5	0
0.05	37.7	0.6	36.5	0.6	33	0.3	29.2	0	27	0.6	25	0.3	25.5	0.5	24.5	0.3	23	0
0.1	39.5	0.5	36.5	0.6	36	0.5	31.5	0	31	0.8	27.5	0	28.5	0.5	23	0	25.5	0
0.15	41.2	0.8	34.5	0.3	31.5	0	31.5	0.5	25	0.6	26.5	0	26.5	0	22	0.3	22	0.3

A= Average, SD= Standard deviation, C= Concentration, ZnO-60= ZnO of 60 minutes of grinding, ZnO-40= ZnO of 40 minutes of grinding and ZnO-20= ZnO of 20 minutes of grinding.

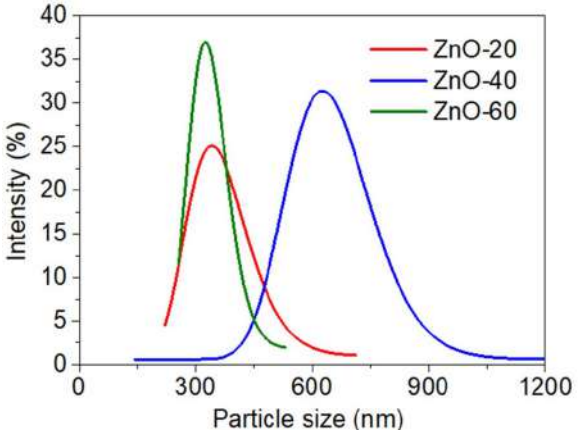

Figure 5. Particle size distribution analysis of ZnO powders synthesized via mechanochemical route, determined by Z potential measurements, using a 10 mL dispersion containing 5 mg of ZnO powder, obtained after 20, 40, and 60 minutes of grinding.

3.1.6 *Textural evaluation of the surface of ZnO-NPs by nitrogen physisorption*

All samples follow typical type IV isotherms, which are characteristic of mesoporous particles (Sing *et al.*, 1985). However, the specific area of ZnO-NPs synthesized at 60 minutes (7.26 m^2/g) is higher than that of ZnO-NPs synthesized at 20 (1.75 m^2/g) and 40 minutes (2.88 m^2/g) of milling (Table 3). This result is expected since the nanoparticles of smaller size are those synthesized at 60 minutes and it can be observed that the smaller the particle size is, the greater the specific area (Ovando, 2018).

3.2 *Evaluation of rheological and filtration properties of drilling fluid*

The results of the evaluation of Rheological properties, Filtration properties and Colloidal stability of drilling fluid for WBDF and MWBDF at 0.05, 0.10 and 0.15 % are shown below.

3.2.1 *Rheological properties*

To evaluate the effect of the ZnO-NPs addition in the WBDF, several tests were performed: apparent viscosity, plastic viscosity, yield point and gel strength at 25, 50 and 70 °C, varying the addition of the ZnO-NPs before and after rolling.

Apparent viscosity (AV) is an important parameter in hydraulic calculations, it must be adequate to lift formation cuttings and to remain between 20 and 60 cP, to ensure adequate hole cleaning capacity and well pressure control. However, these values must be adjusted depending on the specific well conditions.

Figure 6 shows the apparent viscosity (AV) for both the WBDF and the MWBDF with 0.05 %, 0.10 %, and 0.15 % w/v of ZnO-NPs, and at three different evaluated temperatures (Table 4). It is observed that at all three temperatures, the ZnO-NPs-based fluid has higher values than the WBDF. However, the MWBDF with ZnO-NPs synthesized at 60 minutes of milling and a concentration of 0.05 % demonstrates the highest AV of all temperatures. This trend persists after the fluid is submitted to hot rolling, although, in this case, the highest AV is observed at a concentration

of 0.15 %, with a tendency to degrade due to the effects of temperature.

Regarding the impact of ZnO-NPs on AV, an improvement is observed at the NPs concentration compared to the WBDF. This increase is due to the agglomeration of particles in solution (F. Duan *et al*., 2011), while at elevated temperatures it presents an inverse result since the value of AV decreases as temperature increases, this is caused by the deficiency of the intermolecular attractive forces between the nanoparticles and the WBDF (Dejtaradon *et al*., 2019).

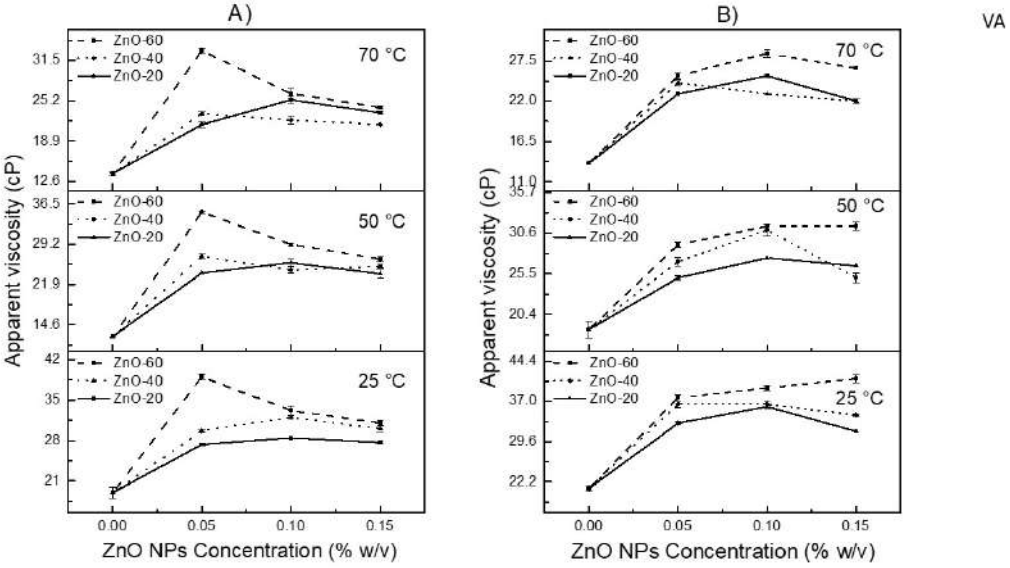

Figure 6. Rheological comparison of the base fluid (WBDF) and ZnO-NPs-based drilling fluid at varying concentrations (0.05, 0.10, and 0.15% w/v) and temperatures (70, 50, and 25 °C), before hot rolling and (A) after hot rolling (B) conditions.

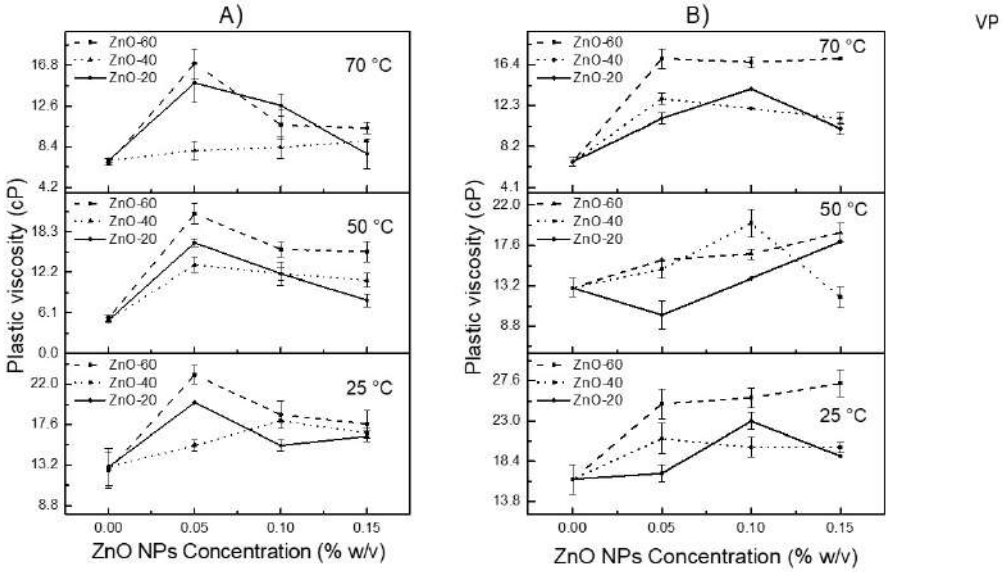

Figure 7. Comparison of the plastic viscosity enhancement of ZnO-NPs-based drilling fluids at varying concentrations (0.05, 0.10, and 0.15 % w/v) and temperatures (70, 50, and 25 °C), relative to the base fluid (BF), before hot rolling and (A) after hot rolling (B) conditions.

The AV of the MWBDF with NPs synthesized at 60 min showed an AV of 20 and 30% higher than the formulations based on NPs synthesized at 40 and 20 min respectively, for all NPs concentrations. This may be because the size of the NPs synthesized at 60 min is smaller compared to the size of those synthesized at 40 and 20 min, and the surface area being larger. This behavior aligns with that reported by Faisal *et al*., in 2024 with the work of uncoated and polymer-coated green magnetite nanoparticles and by Blkor *et al*., in 2021 in their investigation of aqueous mud with polypropylene beads and treated nanosilica treated with sodium carbonate (Blkoor *et al*., 2021; Faisal *et al*., 2024).

Plastic viscosity (PV) represents the flow resistance of drilling fluid caused by mechanical friction within the mud. According to the literature, any increase in solid content of the mud results in higher plastic viscosity (Darley & Gray, 1988). This outcome is evident in Figure 7, where nanoparticle-based fluids reach a significant increase in PV compared to the WBDF, being the highest value observed in the MWBDF with ZnO-NPs synthesized at 60 minutes. For all fluid formulations, PV decreases as the temperature increases (Table 5). At 70 °C, the MWBDF with ZnO-NPs at 40 minutes displays values similar to the WBDF, as the fluid loses thermal stability for this property. After hot rolling Figure 7b, PV values increase compared to PV before rolling. Nonetheless, the MWBDF ZnO-60-NPs fluid generally remains superior to other formulations.

The cationic ZnO-NPs interact with the anionic bentonite plates, causing the formation of larger particles within the drilling fluid. Larger particle sizes result in lower viscosity because mechanical friction is reduced (Guan *et al*., 2020). However, other studies suggest that this formation is limited by the presence of positive potassium ions, which may bind to the anionic bentonite plates (Ahasan *et al*., 2022).

The **yield point** (YP) indicates the initial resistance of the fluid caused by electrochemical forces between particles. Figure 8 shows graphs of this parameter at the three temperatures, showing that the fluid formulations based on ZnO-NPs maintain values above the WBDF (Table 6).

Table 5. Average value and standard deviation of plastic viscosity (cP).

Before hot rolling																		
	25 °C						50 °C						70 °C					
	ZnO-60		ZnO-40		ZnO-20		ZnO-60		ZnO-40		ZnO-20		ZnO-60		ZnO-40		ZnO-20	
C	A	SD	A	SD	A	SD	A	SD	A	SD	A	SD	A	SD	A	SD	A	SD
0	12.7	2	13	2	13	2	5.3	0.5	5	0.5	5	0.5	6.7	0.2	7	0.2	7	0.2
0.05	23	1	15.3	0.6	20	0	21	1.5	13.3	1.2	16.7	0.6	17	1.5	8	1	15	2
0.1	18.7	1.5	18	0	15.3	0.6	15.7	1.2	12	1	12	1.7	10.7	1.5	8.3	1.2	12.7	1.2
0.15	17.7	1.5	16.7	0.6	16.3	0.6	15.3	1.5	11	1	8	1	10.3	0.6	9	0	7.7	1.5
After hot rolling																		
0	16.3	1.7	16.3	1.7	16.3	1.7	13	1	13	1	13	1	6.7	0.5	6.7	0.5	6.7	0.5
0.05	25	1.7	21	1.7	17	1	16	0	15	1	10	1.5	17	1	13	0.6	11	0.6
0.1	25.7	1.2	20	1.2	23	1	16.7	0.6	20	1.5	14	0	16.7	0.6	12	0	14	0
0.15	27.3	1.5	20	0.6	19	0	19	1	12	1.2	18	0	17	0	11	0.6	10	0.6

A= Average, SD= Standard deviation, C= Concentration, ZnO-60= ZnO of 60 minutes of grinding, ZnO-40= ZnO of 40 minutes of grinding and ZnO-20= ZnO of 20 minutes of grinding.

Table 6. Average value and standard deviation of yield point (Pa).

Before hot rolling																		
	25 °C						50 °C						70 °C					
	ZnO-60		ZnO-40		ZnO-20		ZnO-60		ZnO-40		ZnO-20		ZnO-60		ZnO-40		ZnO-20	
C	A	SD	A	SD	A	SD	A	SD	A	SD	A	SD	A	SD	A	SD	A	SD
0	6	1.2	6	1.2	6	1.2	6.8	0.3	6.8	0.3	6.8	0.3	6.8	0.1	6.8	0.1	6.8	0.1
0.05	14.9	0.8	13.8	0.3	7	0.3	13.6	1.2	13.1	0.7	7	0.6	14.6	1	14.6	0.7	6.2	1.4
0.1	13.9	0.8	13.4	0	12.6	0.6	13	0.8	12	0.5	13.3	1.1	15	1	13.3	0.6	12.2	0.6
0.15	12.8	1	12.8	0.3	10.9	0.3	10.7	1	13.6	0.7	15.2	0.3	13.3	0.3	12	0	15	1.2
After hot rolling																		
0	5.4	2.2	5.4	2.2	5.4	2.2	5.3	0.5	5.3	0.5	5.3	0.5	6.6	0.3	6.6	0.3	6.6	0.3
0.05	12.2	1.1	13.6	1.1	15.2	1	12.6	0.3	10.9	0.6	14.9	1.3	8.2	0.5	10.9	0.3	11.8	0.6
0.1	13.3	0.7	15.5	0.6	13	0.5	14.2	0.6	11.4	0.7	13	0	11.4	0.3	10.6	0	11	0
0.15	13.3	0.7	14.2	0.3	12	0	12	0.5	12.8	0.6	8.2	0	9.1	0	10.6	0.5	11.7	0.3

A= Average, SD= Standard deviation, C= Concentration, ZnO-60= ZnO of 60 minutes of grinding, ZnO-40= ZnO of 40 minutes of grinding and ZnO-20= ZnO of 20 minutes of grinding.

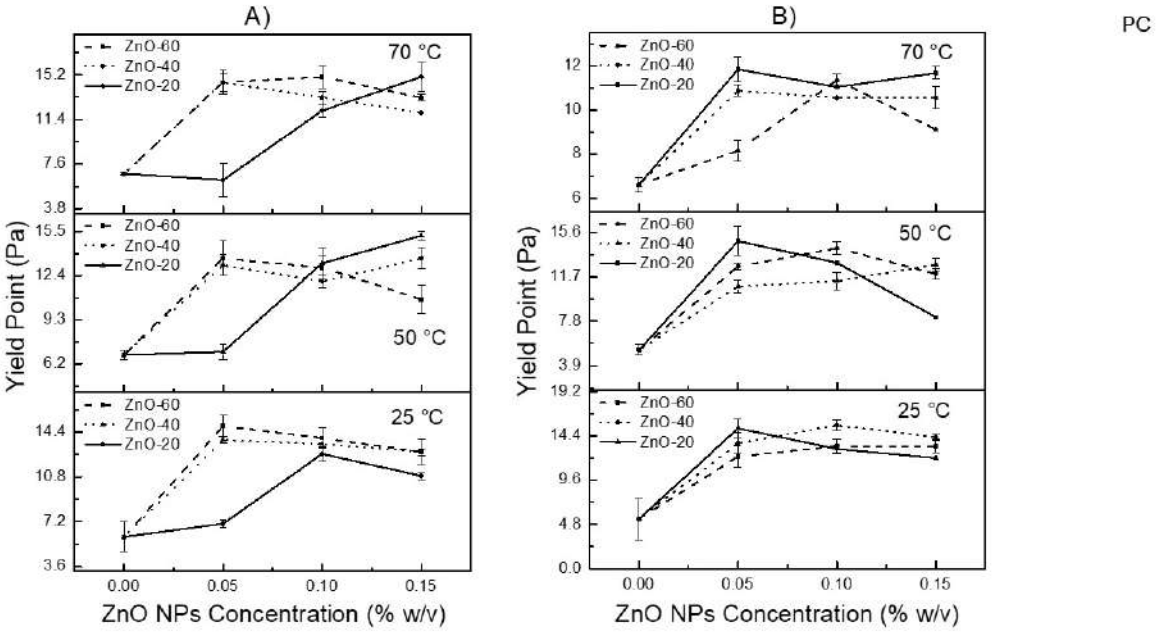

Figure 8. Comparison of the yield point of the base fluid (WBDF) and ZnO-NPs-based drilling fluid at varying concentrations (0.05, 0.10, and 0.15 % w/v) and temperatures (70, 50, and 25 °C), before hot rolling and (A) after hot rolling (B) conditions.

The graphs of the MWBDF with NPs synthesized at 40 and 60 min have similar values to those of 0.05% w/v. With this concentration, the MWBDF with NPs at 20 min and the WBDF do not exhibit a significant difference, there is only an increase in the yield point with a rise in the concentration of ZnO-NPs. After hot rolling, the MWBDF with ZnO-NPs presents an increase in the yield point compared to the WBDF, with a tendency to decrease when temperature rises.

This increase is attributed to the interaction between cationic nanoparticles on the surface and the anionic platelets of bentonite clay, triggering flocculation, which contributes to flow resistance (Baik & Lee, 2010; Barry *et al*., 2015). This means, the viscosity and the internal attraction force of the fluid increase. The surface area of materials expands at the nanoscale, and as a result, the surface energy increases. Therefore, the particles agglomerate together to reduce this energy. In other words, the attraction between the particles grows, thereby increasing the yield point by adding nanocomposites into the fluid (Hyne, 2014). The increase in yield point improves the fluid quality by enhancing the ability to clean drill cuttings from the well, reducing the probability of drillstring sticking, and reducing drillstring torque.

Gel strength is the shear stress of drilling mud that is measured at a low shear rate after the mud remains static for a certain period of time. This property allows the fluid to turn into a gel and maintain the particles and cuts generated during drilling in suspension, when there is no circulation, or the flow is interrupted (Admin, 2022).

A drilling fluid formulation designed with incorrect gel strengths often results in bit balling and settling of the drilled cutting at the bottom of the well (Ahmad *et al*., 2021). This leads to operation problems such as adhesion problems in pipes, excessive pressure and torque, and rise of bit temperature that reduces the lifespan of the tool (Admin, 2022) and causes delayed drilling operations. The main purpose of the gel strength is to suspend the drilled cutting in the wellbore during a small interruption in the drilling process; therefore, drilling formulations that keep the drilled cuttings in suspension are considered optimal (Ahmad *et al*., 2021).

Figure 9 shows the variation of gel forces for 10 minutes and 10 seconds in WBDF and MWBDF samples with the three milling times (20, 40 and 60 min) and concentration variation of the ZnO-NPs in the formulated drilling fluid (C1= C2= and C3=) and the temperature (25, 50 and 70 °C). It is observed that at the different temperatures that were evaluated, the values of this property increase for all concentrations, in contrast to the WBDF, which remains below half the value obtained with the MWBDF samples (Table 7). The fluid with the greatest gel strength is the one formulated at a concentration of 0.05 % with nanoparticles synthesized for 60 minutes of milling time. This is attributed to the fact that the surface area is greater and therefore the number of NPs per unit of weight is higher than that of the NPs synthesized at 20 and 40 minutes of milling, thus increasing the strength

of the gel in comparison with formulations with these latter NPs (Perween *et al*., 2018). After hot rolling, these values decrease due to the degradation of the additives under these temperatures and pressures. Gel strength values decrease as the temperature increases; other studies have reported similar trends (Bayat & Shams, 2019; Dejtaradon *et al*., 2019). Furthermore, progressive behavior of gel strength is observed after time, since gel strength values at 10 minutes are higher than those for the gel strength at 10 seconds; this increase is consequence of the presence of ZnO-NPs and electrostatic forces between particles in the solution (Parizad *et al*., 2018). This effect reveals the ability of the mud to suspend cuttings or drilled solids and any relatively heavy material when circulation is stopped. Although, on the other hand, greater shear force is necessary to break the gel as mud that returns to its liquid state when the drilling operation is resumed, is required.

On the other hand, comparing the rheological behavior as a function of the concentration of nanoparticles, it is observed that when it increases, the values of the rheological properties decrease. Table 8 shows evidence of this and Figure 10 presents the TEM images of ZnO-NPs obtained in the drilling fluid samples at the concentrations studied in this work, it is observed that as the concentration in the fluid sample increases, ZnO-NPs tend to agglomerate. This phenomenon is produced by the specific dynamic interactions of ZnO nanoparticles, which have surface charges that at high concentrations, can generate attraction between opposite particles, facilitating agglomeration (Aquino *et al*., 2018; Abrica and Gómez, 2022).

The enhanced rheological properties resulted from the formulations based on ZnO-NPs with a larger surface area (7.26 m^2/g), which coincides with other reports where a smaller particle size (30 nm) allows

Table 7. Average value and standard deviation of gel strength 10 seconds and 10 minutes (Pa).

		Gel strength 10 Seconds (Pa)						Gel strength 10 minutes (Pa)					
		Before hot rolling			After hot rolling			Before hot rolling			After hot rolling		
	T (°C)	25	50	70	25	50	70	25	50	70	25	50	70
WBDF	A	2.4	1.9	1.9	2.9	1.9	1.9	7	6	5.8	5.5	4.8	5.5
	SD	0.6	0	1	0.6	0.6	0.6	0.7	0.7	1.4	0.7	0	2.1
60-C1	A	6.7	6.2	5.6	6.2	5.9	4.8	10.9	10.2	9.6	9.6	9.1	8.2
	SD	0.6	0	0	0.6	1	0	1.2	1.5	0.6	0.7	0	0.7
60-C2	A	6.5	6.2	5.6	5.3	5.8	4.5	10.8	10.1	9.1	9.1	8.9	8.2
	SD	2.9	0	0.6	0.6	0	0.6	7.8	0.7	1.4	0.7	0.7	2.8
60-C3	A	6.1	5.8	5.3	5.1	4.3	4.3	10.2	9.6	8.6	9.1	8.6	7.2
	SD	0.6	0	0	0	0.6	1	1.2	1.2	0	0.7	1.4	0
40-C1	A	6.2	5.1	5.4	5.9	4.3	4.3	10.1	9.6	9.1	9.1	8.6	7.9
	SD	0	10.8	5.1	4.3	0	0	0	0	3.6	3.1	6.1	3.8
40-C2	A	5.8	5	4.5	5.3	4.3	3.8	9.4	8.9	8.6	8.6	7.7	7.7
	SD	8.3	6.2	6.2	4.7	0	0	3.6	3.8	7.9	0	0	0
40-C3	A	5.4	4.5	4.3	4.8	3.8	3.4	8.4	8.6	8.2	8.2	7	6.7
	SD	5.1	5.6	0	0	0	0	4	3.8	0	0	4.9	0
20-C1	A	6	5.1	5.3	5.4	4.3	4.3	9.6	9.1	8.9	8.9	8.6	7.2
	SD	0.7	1.4	0	1	0.6	0	0.7	1.4	0	1.4	0.7	0.7
20-C2	A	5.8	4.6	5	4.8	4.1	3.8	9.4	9.1	8.6	8.6	7.9	7.2
	SD	0.6	0.6	0	0.6	0	0.6	0	1.4	0	1.4	0.7	1.7
20-C3	A	5.4	4.5	5	4.6	3.8	3.4	9.1	8.9	8.2	8.6	7.2	6.7
	SD	0.6	0.6	0.6	0.6	0	0	0	0	0.7	0	0	1.7

A= Average, SD= Standard deviation, WBDF = water-based drilling fluid, C (1, 2 and 3) = Concentrations (0.05, 0.10, and 0.15 %) and Grinding Times (20, 40, and 60 minutes).

Table 8. Particle size of ZnO-NPs at different concentrations in drilling fluid samples, determined by Dynamic Light Scattering (DLS).

ZnO-NPs	Z-average (d.nm)	St Dev (d.nm)
60-C1	523.1	184.4
60-C2	550.1	272.4
60-C3	641.9	285.2

C1= Concentration de 0.05 %, C1= Concentration de 0.10 %, C1= Concentration de 0.15 % w/v.

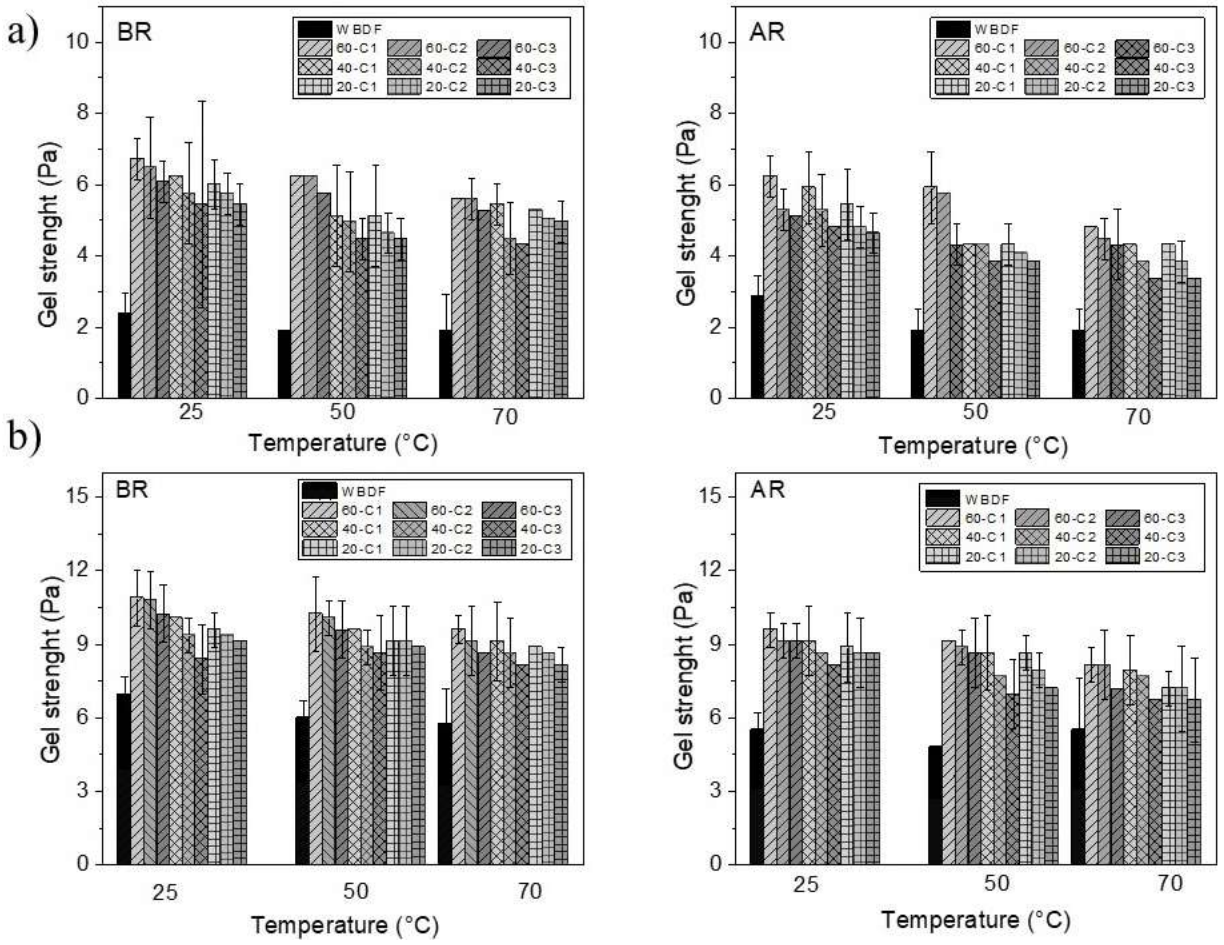

Figure 9. Gel strength behavior of ZnO-NPs-enhanced drilling fluids subjected to various temperatures. Gel strength of a) 10 seconds, b) 10 minutes of the base fluid (WBDF) and the drilling fluid based on ZnO nanoparticles at 0.05, 0.1 and 0.15 % w/v; at 25, 50 and 70 °C.

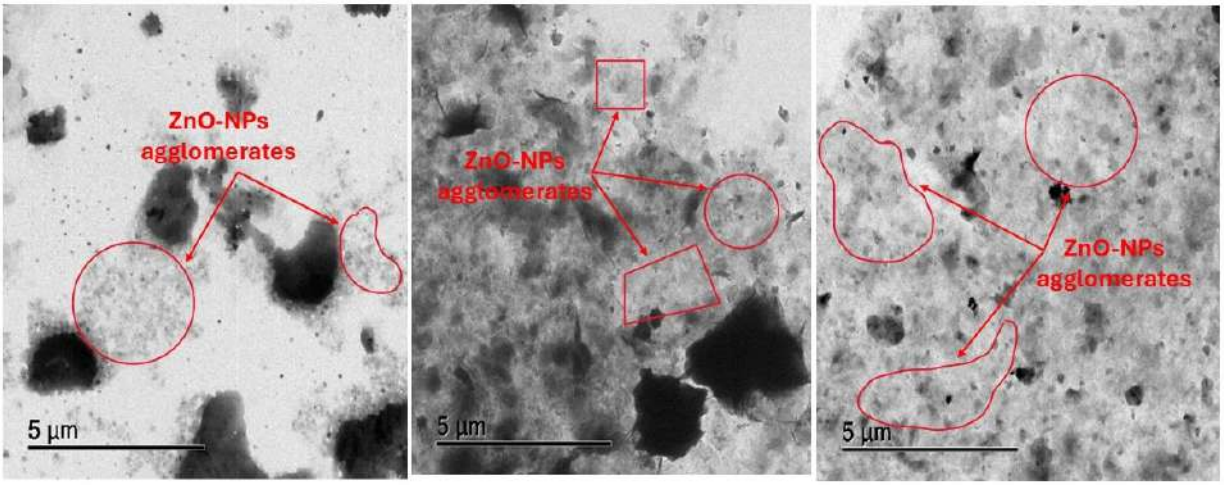

Figure 10. TEM images of ZnO-NPs synthesized by mechanochemical method at 60 minutes of grinding and suspended in drill fluid samples with concentration of (a) 0.05 %, (b) 0.10 %, (c) 0.15 % w/v.

an increase in apparent viscosity and the gel strenght of the drilling fluid (Perween *et al*., 2018), since its interruption in the clay network is less. Additionally, a drilling fluid containing particles smaller than the formation's pore diameters allows for better plugging and forms a thin, impermeable cake, reducing filtrate loss.

Another important characteristic is the specific

area of the nanoparticles that provides thermal stability to the drilling fluid due to the large number of particles per given concentration. According to Dejtaradon *et al*., (2019), the nanoparticles in the drilling fluid are required to remain stable and suspended, so it is crucial that the particle size in suspension is smaller to prevent sedimentation (Dejtaradon *et al*., (2019). These results exhibit a rheological trend similar to previous studies with oxide/polyacrylamide nanosheet nanocomposites evaluated on the properties of a WBDF and the effect of wheat nanobiopolymers on the rheological and filtration properties of the drilling fluid (Ali *et al*., 2024; Gudarzifar *et al*., 2020), Table 9 shows a comparison of rheological enhancement, filtration control, thermal stability and environmental impact of ZnO-NPs obtained in this work with other nanomaterials used in drilling fluids. In conclusion, the results obtained from this research could improve the rheological properties of WBDF more than some materials reported previously for the formulation of drilling fluids.

3.2.2 Filtration properties

Fluid loss is monitored during drilling operation as it causes problems including formation damage, stuck pipes, wellbore instability, etc. Hence, Figure 11 represents the loss of fluid at a pressure of 100 psi and 25 °C. It is observed that with the addition of ZnO-NPs the filtered volume, accumulated during the 30 minutes of the test, decreases from 13.5 to 10.4 mL. After rolling, the same trend is observed, but only with values on the lost volume from 15.2 to 12 mL (Table 10).

Table 9. Comparison of rheological enhancement, filtration control, thermal stability and environmental impact of ZnO-NPs obtained in this work with other commonly used nanomaterials in drilling fluids.

Nanomaterials	Rheological improvement	Filtration control	Thermal stability	Environmental impact
ZnO-NPs	The apparent viscosity (AV) increases by 200 %, the plastic viscosity (PV) by 180 %, and the yield point (YP) by 240% (this work).	The amount of filtered fluid lowers from 13.5 to 10.4 mL. At high pressure and high temperature, the filtered volume is reduced by 54 % (this work).	As the temperature increases, colloidal stability is maintained, although the ZnO-NPs tend to degrade, affecting the properties of the WBDF (this work).	At high concentrations, nanoparticles can pose risks to the environment (this work).
SiO_2	Apparent viscosity and yield point, in a range of 18 % to 47 %(Cardenas, 2022).	Filtration volume at 25 °C and 400 psi decreases by 19 % (Parizad *et al*., 2018)	Destabilization of colloidal dispersion occurs due to increased temperature (Parizad *et al*., 2018).	SiO_2 is considered environmentally safe, especially if used in biodegradable combinations (Cardenas, 2022).
TiO_2	TiO_2-NPs contributes to an increase in the viscosity(Sadeghalvaad & Sabbaghi, 2015).	The volume of filtrate loss decreased by 64 % with the addition of NPs. (Sadeghalvaad & Sabbaghi, 2015).	They have resistance to thermal degradation in the rheological and filtration characteristics of drilling fluids (Beg *et al*., 2020).	TiO_2 nanoparticles can increase the thermal stability of drilling fluid, at high temperature they have little degradation (Mendoza & Rojas, 2021).
Graphene oxide (GO)	The plastic viscosity of the drilling fluid increased reaching 15 and 18 mPa·s, The YP of the drilling fluids increased with NPs (Abdullah *et al*., 2024).	Filtration loss decreased to 38.96 % and 34.36 %, at LPLT and HPHT, respectively (Gudarzifar *et al*., 2020).	The side chains, like the main chains of the nanocomposite, remain stable at high temperaturas (Abdullah *et al*., 2024).	It is thermally more stable with synthesized additives (Gudarzifar *et al*., 2020).
Carbon nanotubes	Plastic viscosity improved by 85.7 % and gel characteristics by more than 160 % (Lysakova *et al*., 2025).	HTHP filtration loss was reduced by 42.86 % 11 % reduction in API filtration loss (Lysakova *et al*., 2025).	The properties of the fluids deteriorated with increasing temperatura (Lysakova *et al*., 2025).	They are more environmentally friendly than their petroleum-based counterparts (Lysakova *et al*., 2025).

Table 10. Average value and standard deviation of volume of filtrate in mL, under Low-Pressure (100 psi) and Low-Temperature (25 °C) Conditions.

Before hot rolling																				
	BF		60-C1		60-C2		60-C3		40-C1		40-C2		40-C3		20-C1		20-C2		20-C3	
Time min	A	SD	A	SD	A	SD	A	SD	A	SD	A	SD	A	SD	A	SD	A	SD	A	SD
0	0	0	0	0	0	0	0	0	0	0	0	0	0	0	0	0	0	0	0	0
5	5	0.2	3.6	0.2	4.8	0.3	4.2	0.6	4.2	0.2	4.4	0.3	4.6	0.4	4.2	0.6	4.6	0.5	4.4	0.6
10	6.8	0.4	5.4	0.4	6.4	0.5	6.6	0.7	6	0.7	6.4	0.6	6.6	0.6	6.4	0.5	6	0.1	6.2	0.2
15	8.5	0.5	7	0.2	7.8	0.4	8	0.3	7.6	0.4	8	0.3	8.2	0.4	7.6	0.3	7.8	0.3	8	0.4
20	10.2	0.3	8.3	0.1	9.2	0.3	9.4	0.4	9	0.3	9.4	0.3	9.4	0.4	8.8	0.4	9	0.1	9.2	0.4
25	11.9	0.4	9.4	0.1	10	0.3	10.6	0.5	10.2	0.3	10.5	0.6	10.2	0.2	10.6	0.5	10	0.4	10.6	0.5
30	13.5	0.5	10.4	0.3	11.2	0.5	11.6	0.2	11.2	0.4	11.6	0.8	11.6	0.5	11.8	0.4	11.2	0.4	11.4	0.2
Before hot rolling																				
0	0	0	0	0	0	0	0	0	0	0	0	0	0	0	0	0	0	0	0	0
5	6	0.4	5	0.2	4.6	0.7	6	0.2	5.6	0.6	4.8	0.4	4.6	0.5	5.4	0.2	5.7	0.2	5.5	1.1
10	8.3	0.5	7	0.7	8.2	0.4	8.6	0.7	7.8	0.3	8.2	0.5	8	0.2	8	0.1	7.6	0.8	7.8	0.6
15	10.8	0.7	8.8	0.7	9.8	0.7	10.6	0.7	9.6	0.6	10	0.5	9.8	0.8	9.8	0.2	10	1.5	9.5	0.5
20	12.5	0.6	9.6	0.2	11.6	0.6	12.2	0.5	10.8	0.6	11.6	0.8	11.6	0.3	11.2	0.5	11.8	1	11	0.6
25	13.6	0.6	10.8	0.4	12.8	0.8	13.4	0.5	12	0.2	12.8	0.2	12.8	0.8	12.6	0.8	12.8	0.2	12.5	0.9
30	15.2	1.2	12	0.4	13.2	0.3	14.8	0.9	13.2	0.4	14.2	0.5	14.5	0.5	13.8	1	14.1	0.5	13.8	0.8

A= Average, SD= Standard deviation, WBDF = Base fluid, C (1, 2 y 3) = Concentrations (0.05, 0.1, and 0.15%) and Grinding Times (20, 40, and 60 minutes).

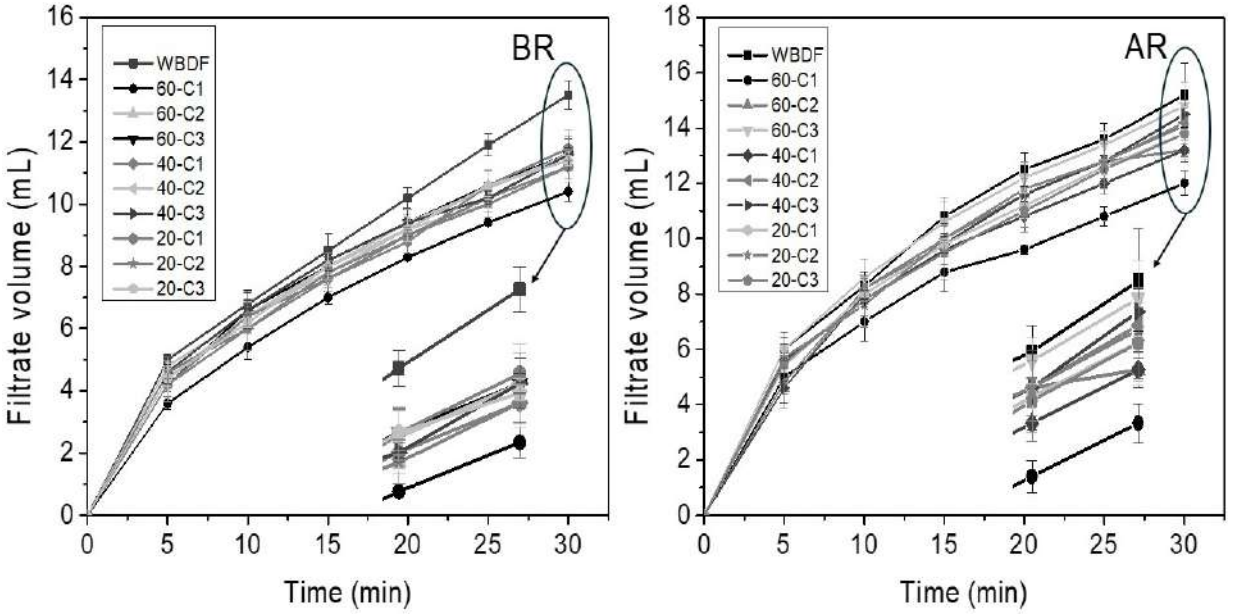

Figure 11. Filtration performance of WBDF and ZnO-NPs-enhanced drilling fluids at various concentrations (0.05, 0.10, and 0.15 % w/v) and grinding times (20, 40, and 60 minutes), Under Low-Pressure (100 psi) and Low-Temperature (25 °C) Conditions.

The formulation of the drilling fluid with the largest volume of filtrate reduction is the fluid with ZnO-NPs of 60 minutes of milling and concentration of 0.05 (60-C1). This is because with this concentration the filter cake that is formed is a thin and impermeable suitable filter cake, in other words, the nanoparticles are filling the pores of the formation, preventing the passage of fluid into the formation (Ahmed *et al*., 2020).

Each cake obtained was measured using an accuracy vernier caliper and Table 11 lists the thicknesses in inches (in) of the cake obtained after the low pressure and temperature filtration test. It can be seen that the thickness is reduced to around 50 % with the addition of the ZnO-NPs compared to the WBDF. Moreover, there is a change in appearance and color as seen in the images in Figure 12.

Regarding the lost filtration test, Figure 13 illustrates the volume filtered at high pressure and high temperature, before and after rolling, for all samples of the WBDF and the drilling fluid with the addition of 0.05, 0.10 and 0.15 % w/v of ZnO-NPs with

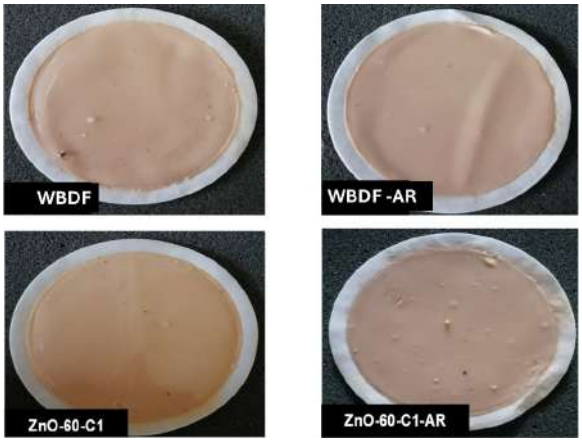

Figure 12. Photograph of filter cakes of the WBDF and with ZnO-NPs, before and after hot rolling.

Table 11. Evaluation of filter cake thickness in ZnO-enhanced drilling fluid formulations: before and after rolling process.

Formulations	Before rolling (mm)	After rolling (mm)
ZnO-20-C1	1.295	1.397
ZnO-20-C2	1.346	1.651
ZnO-20-C3	1.854	2.159
ZnO-40-C1	1.27	1.778
ZnO-40-C2	1.27	1.651
ZnO-40-C3	1.575	2.388
ZnO-60-C1	1.194	1.27
ZnO-60-C2	1.346	1.956
ZnO-60-C3	1.854	2.083

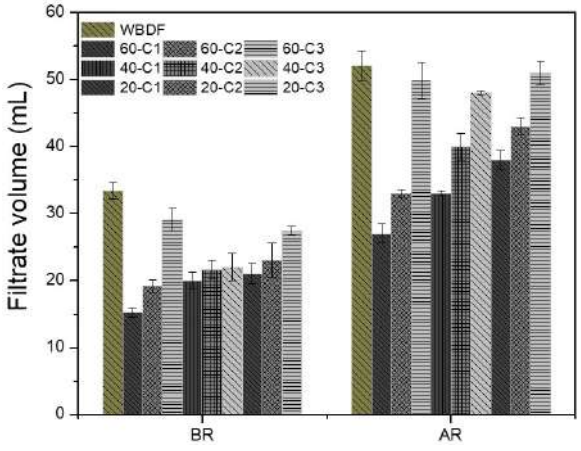

Figure 13. HPHT filtered volume analysis of WBDF and ZnO-NPs-enhanced drilling fluids at various concentrations (0.05, 0.1, and 0.15%) and grinding durations (20, 40, and 60 minutes).

milling times of 20, 40 and 60 min. The filtrate volume lost in the test carried out at 500 psi pressure and 150 °C, a significant reduction in lost volume is observed for the formulations with ZnO-NPs (Table 12). The formulation with ZnO-NPs of 60 minutes of milling was the one that showed the greatest reduction from 54 and 48 % before and after rolling. Therefore, it is assumed that the ZnO-NPs are blocking the pore spaces of the base fluid.

Filtration tests show that ZnO-NPs reduce the volume filtered into the formation; at 100 psi and room temperature, the filtered volume accumulated during the 30 minutes of the test is reduced from 13.5 to 10.4 mL (Tala 12). After hot rolling, the same trend is noticed, with a reduction from 15.2 to 12 mL. For the case of elevated pressure and temperature conditions (500 psi and 100 °C), it is reduced by 54 % (15.2 mL) and 48 % (27 mL), compared to the WBDF (33.4 and 52 mL), before and after rolling, respectively (Table 13). At a temperature of 70 °C and after hot rolling, the rheological properties of the drilling fluid decrease, however, this drop is minor compared to the WBDF.

3.2.3 Colloidal stability of drilling fluid

The colloidal stability study was carried out by visual observation (Li *et al*., 2020; Macías C. *et al*., 2024) , consisting of introducing the samples of the drilling fluid formulations into 15 mL test tubes. They were observed from the beginning and every 24 hours, for 10 days, to show the stability of the samples over time. In Figure 14, it can be seen that samples with different concentrations of ZnO-NPs synthesized at different grinding times showed better stability compared to WBDF. The nine samples of the MWBDF remained stable after 10 days, no sedimentation is observed in the test tubes, however, in the base fluid a separation of the water is observed (Figure 14d). The other formulations based on ZnO-NPs are observed without significant changes in the test tube, evidencing that the addition of these nanoparticles improves colloidal stability.

Conclusion

This study aimed to develop a water-based drilling fluid, MWBDF using ZnO-NPs as additives for this type of drilling fluids. Based on the results, it can be concluded that ZnO-NPs, synthesized by the mechanochemical method, were capable of improving the rheological and filtration properties of water-based drilling fluids. Causing this material to be versatile due to the simplicity of its synthesis and useful due to the characteristics of improvements in rheological properties. Particularly, the MWBDF with ZnO-NPs that had the best performance was the one obtained using the ZnO-NPs for 60 minutes of milling and a concentration of 0.05 in the BF, at room temperature. The other evaluated properties, in comparison to the WBDF, also reported improvements such as an increase in AV to 200 %, PV to 180 %, yield point to

240 % and gel strength increases 80 % more than the WBDF after 10 minutes of being in static condition. It was observed that concentrations of 0.10 and 0.15 % are not recommended since these nanoparticles tend to agglomerate and this deteriorates the properties. In conclusion, this improvement process is viable with only 0.05 % of ZnO-NPs in the BF.

Table 12. Average value and standard deviation of volume of filtrate HPHT.

	WBDF		60-C1		60-C2		60-C3		40-C1		40-C2		40-C3		20-C1		20-C2		20-C3	
	A	SD	A	SD	A	SD	A	SD	A	SD	A	SD	A	SD	A	SD	A	SD	A	SD
BR	33.4	1.2	15.2	0.7	19.2	0.9	29	1.7	20	1.2	21.6	1.4	22	2	21	1.5	23	2.6	27.4	0.7
AR	52	2.3	27	1.4	33	0.5	49.8	2.6	33	0.4	40	2	48	0.3	38	1.4	43	1.2	51	1.7

A= Average, SD= Standar desviation, BR= Before hot rolling, AR= After hot rolling, WBDF = Base fluid, C (1, 2 and 3) = Concentrations (0.05, 0.1, and 0.15%) and Grinding Times (20, 40, and 60 minutes).

Table 13. Comparison of filtered volume reduction in different formulations before and after hot rolling process.

Formulations	Before rolling (%)	After rolling (%)
60-C1	54	48
60-C2	43	37
60-C3	13	4
40-C1	40	37
40-C2	35	23
40-C3	34	8
20-C1	37	27
20-C2	31	17
20-C3	18	2

Figure 14. Samples of ZnO-NPs-based drilling fluid formulations and WBDF: a) day 1, b) day 5, c) day 10 and d) separation of water in the WBDF.

The fluid that gave the best result regarding the filtration property was the WBDF added with 0.05 % of ZnO-NPs synthesized at 60 minutes of milling (60-C1). It was also the one that obtained the best formed filter cake, that is, being permeable and thin, with a lower thickness of the cake formed on the filter paper after the filtration test.

As can be seen, the use of ZnO-NPs can provide significant benefits to the properties of water-based drilling fluids. However, there are also important limitations that must be considered. Obtain ZnO-NPs with controlled properties (such as specific size and morphology) through mechanochemical synthesis could be difficult to scale. Since drilling operations require a large volume of NPs, it is necessary to investigate economical and environmentally friendly synthesis methods to reduce costs. Another limitation is the compatibility of ZnO-NPs with the different conditions and properties of each reservoir and oil well. These NPs are sensitive to factors such as pH, temperature, and the presence of contaminants. In this research, field trials were not possible; it would be important to validate the laboratory results obtained and evaluate their behavior under real-world conditions. Furthermore, it was observed that at high concentrations, nanoparticles tend to agglomerate, reducing the available active surface area and decreasing their effectiveness in functions such as cuttings transport. Therefore, it is important to explore combinations of ZnO with other materials, such as TiO_2 or SiO_2, to create hybrid nanoparticles that further improve the performance of drilling fluid properties. It is also important to investigate methods to coat or functionalize nanoparticles with polymers, organic compounds, or ligands that can improve their stability and compatibility. Another issue is that nanoparticles face specific regulations related to their safe use and handling. Although ZnO is recognized for its antimicrobial capacity, at high concentrations, nanoparticles can pose risks to human health and the environment, especially if released during drilling. Therefore, it is necessary to analyze their biodegradability or ways to recover the nanoparticles after use. The use of ZnO-NPs in drilling fluids remains a promising field, although the implementation of nanoparticles in drilling fluids at the field scale faces several technical, economic and environmental challenges, and research is required to mitigate these limitations.

Acknowledgements

This research was financially supported by the Secretaría de Ciencia, Humanidades, Tecnología e Innovación (SECIHTI) in Universidad Juárez Autónoma de Tabasco.

References

Abdullah, A. H., Ridha, S., Mohshim, D. F., and Maoinser, M. A. (2024). An experimental investigation into the rheological behavior and filtration loss properties of water-based drilling fluid enhanced with a polyethyleneimine-grafted graphene oxide nanocomposite. *RSC Advances* 14(15), 10431–10444. https://doi.org/10.1039/D3RA07874D.

Abrica G., P., and Gómez A., S. (2022). Effects and characterization of airborne nanoparticles (CuO, ZnO-NPs) in plants. *Revista Internacional de Contaminacion Ambiental* 38, 145–164. https://doi.org/10.20937/RICA.54303.

Admin. *Resistencia de gel*. (2022) Available at: Https://Blog.Industriasmorven.Com/Resistencia-de-Gel/. Accessed: November 15, 2023.

Aghdam, S. B., Moslemizadeh, A., Kowsari, E., and Asghari, N. (2020). Synthesis and performance evaluation of a novel polymeric fluid loss controller in water-based drilling fluids: High-temperature and high-salinity conditions. *Journal of Natural Gas Science and Engineering 83*, 103576. https://doi.org/10.1016/j.jngse.2020.103576 .

Ahasan, M. H., Alahi Alvi, M. F., Ahmed, N. and Alam, M. S. (2022). An investigation of the effects of synthesized zinc oxide nanoparticles on the properties of water-based drilling fluid. *Petroleum Research 7*(1), 131–137. https://doi.org/10.1016/j.ptlrs.2021.08.003.

Ahmad, H. M., Iqbal, T., A. Al Harthi, M. and Kamal, M. S. (2021). Synergistic effect of polymer and nanoparticles on shale hydration and swelling performance of drilling fluids. *Journal of Petroleum Science and Engineering 205*. https://doi.org/10.1016/j.petrol.2021.108763.

Ahmed, N., Alam, M. S. and Salam, M. A. (2020). Experimental analysis of drilling fluid prepared by mixing iron (III) oxide nanoparticles with a KCl–Glycol–PHPA polymer-based mud used in drilling operation. *Journal of Petroleum Exploration and Production Technology 10*(8), 3389–3397. https://doi.org/10.1007/s13202-020-00933-1.

Ali, J. A., Abbas, D. Y., Abdalqadir, M., Nevecna, T., Jaf, P. T., Abdullah, A. D. and Rancová, A. (2024). Evaluation the effect of wheat nano-biopolymers on the rheological and

filtration properties of the drilling fluid: Towards sustainable drilling process. *Colloids and Surfaces A: Physicochemical and Engineering Aspects 683*. https://doi.org/10.1016/j.colsurfa.2023.133001.

Al-Zubaidi, N. S., Alwasiti, A. A. and Mahmood, D. (2017). A comparison of nano bentonite and some nano chemical additives to improve drilling fluid using local clay and commercial bentonites. *Egyptian Journal of Petroleum 26*(3), 811–818. https://doi.org/10.1016/j.ejpe.2016.10.015 .

API. (2019). API RP 13B-1 *manual de práctica recomendada para pruebas de campo de fluidos de perforación a base de agua.* 5th edition.

Aquino, P., Osorio, A. M., Ninán, E., and Torres, F. (2018). Characterization of ZnO nanoparticles synthesized by precipitation method and its evaluation in the incorporation in enamel paints. *Rev Soc Quím Perú* 84(1).

Arenas Gaviria, J. A. (2024). *Análisis de las propiedades fisicoquímicas y reológicas que afectan la sedimentación de suspensiones minerales en espesadores en la industria del cemento*. Universidad Nacional de Colombia.

Baik, M. H. and Lee, S. Y. (2010). Colloidal stability of bentonite clay considering surface charge properties as a function of pH and ionic strength. *Journal of Industrial and Engineering Chemistry 16*(5), 837–841. https://doi.org/10.1016/j.jiec.2010.05.002.

Barry, M. M., Jung, Y., Lee, J. K., Phuoc, T. X. and Chyu, M. K. (2015). Fluid filtration and rheological properties of nanoparticle additive and intercalated clay hybrid bentonite drilling fluids. *Journal of Petroleum Science and Engineering 127*, 338–346. https://doi.org/10.1016/j.petrol.2015.01.012.

Bayat, A. E. and Shams, R. (2019). Appraising the impacts of SiO2, ZnO and TiO2 nanoparticles on rheological properties and shale inhibition of water-based drilling muds. *Colloids and Surfaces A: Physicochemical and Engineering Aspects 581*. https://doi.org/10.1016/j.colsurfa.2019.123792.

Beg, M., Kumar, P., Choudhary, P., and Sharma, S. (2020). Effect of high temperature ageing on TiO2 nanoparticles enhanced drilling fluids: A rheological and filtration study. *Upstream Oil and Gas Technology* 5, 100019. https://doi.org/10.1016/j.upstre.2020.100019.

Blkoor, S. O., Ismail, I., Oseh, J. O., Selleyitoreea, S., Norddin, M. N. A. M., Agi, A. and Gbadamosi, A. O. (2021). Influence of polypropylene beads and sodium carbonate treated nanosilica in water-based muds for cuttings transport. *Journal of Petroleum Science and Engineering 200*. https://doi.org/10.1016/j.petrol.2021.108435.

Bolarinwa, H. S., Onuu, M. U., Fasasi, A. Y., Alayande, S. O., Animasahun, L. O., Abdulsalami, I. O., Fadodun, O. G. and Egunjobi, I. A. (2017). Determination of optical parameters of zinc oxide nanofibre deposited by electrospinning technique. *Journal of Taibah University for Science 11*(6), 1245–1258. https://doi.org/10.1016/j.jtusci.2017.01.004.

Cardenas A., W. (2022). Effect of the addition of ZnO and SiO_2 nanoparticles on the rheological properties of a water-based drilling fluid. Degree thesis to obtain the title of Chemist. Universidad industrial de Santander. https://noesis.uis.edu.co/items/0f8b9e94-98b0-442a-9aff-ea275eefdf56 .

Chuck H., C., Pérez C., E., Heredia O., E., and Serna S., S. O. (2011). Sorghum as a multifaceted crop for bioethanol production in Mexico: technologies, advances, and areas of opportunity. *Revista Mexicana de Ingeniería Química* 10 (3).

Darley, H. C. and Gray, G. R. (1988). *Composition and Properties of Drilling and Completion Fluids* (Fifth Edition). Gulf Professional Publishing.

Dejtaradon, P., Hamidi, H., Chuks, M. H., Wilkinson, D. and Rafati, R. (2019). Impact of ZnO and CuO nanoparticles on the rheological and filtration properties of water-based drilling fluid. *Colloids and Surfaces A: Physicochemical and Engineering Aspects 570*, 354–367. https://doi.org/10.1016/j.colsurfa.2019.03.050.

Duan, F., Kwek, D. and Crivoi, A. (2011). Viscosity affected by nanoparticle aggregation in Al2O3-water nanofluids. *Nanoscale Research Letters 6*(1). https://doi.org/10.1186/1556-276X-6-248.

Duan, Y., Dong, X., Yang, H., Fan, Y., Ma, X. and Lin, W. (2024). Study of solid-liquid two-phase flow model of drilling fluids for analyzing mud cake formation. *Geoenergy Science and Engineering 236*, 212761. https://doi.org/10.1016/j.geoen.2024.212761 .

Espitia, P. J. P., Soares, N. de F. F., Coimbra, J. S. dos R., de Andrade, N. J., Cruz, R. S., & Medeiros, E. A. A. (2012). Zinc Oxide Nanoparticles: Synthesis, Antimicrobial Activity and Food Packaging Applications. In Food and Bioprocess Technology (Vol. 5, Issue 5, pp. 1447–1464). https://doi.org/10.1007/s11947-012-0797-6.

Faisal, R., Kamal, I., Salih, N. and Préat, A. (2024). Optimum formulation design and properties of drilling fluids incorporated with green uncoated and polymer-coated magnetite nanoparticles. *Arabian Journal of Chemistry 17*(2). https://doi.org/10.1016/j.arabjc.2023.105492.

Friedheim, J., Young, S., De Stefano, G., Lee, J., Guo, Q. and Swaco, M.-I. (2012). Nanotechnology for Oilfield Applications-Hype or Reality?. *Society of Petroleum Engineers 157032.*

García M., R., Suárez V., G. G., Pech R., W. J., Ordóñez, L. C., Melendez G., P. C., Sánchez P., N. M., and González Q., D. (2024). Soft chemistry synthesis of size-controlled ZnO nanostructures as photoanode for dye-sensitized solar cell. *Revista Mexicana de Ingeniera Química* 23(2). https://doi.org/10.24275/rmiq/IE24235

Ghayedi, A. and Khosravi, A. (2020). Laboratory investigation of the effect of GO-ZnO nanocomposite on drilling fluid properties and its potential on H2S removal in oil reservoirs. *Journal of Petroleum Science and Engineering 184*. https://doi.org/10.1016/j.petrol.2019.106684.

Guan, O. S., Gholami, R., Raza, A., Rabiei, M., Fakhari, N., Rasouli, V. and Nabinezhad, O. (2020). A nano-particle based approach to improve filtration control of water based muds under high pressure high temperature conditions. *Petroleum 6*(1), 43–52. https://doi.org/10.1016/j.petlm.2018.10.006.

Gudarzifar, H., Sabbaghi, S., Rezvani, A. and Saboori R. (2020). Experimental investigation of rheological & filtration properties and thermal conductivity of water-based drilling fluid enhanced. *Powder Technology 368*, 323–341. https://doi.org/10.1016/j.powtec.2020.04.049.

Hyne, N. J. (2014). *Diccionario de exploración, perforación y producción de petróleo* (2nd ed.). PennWell.

Li, S., Ng, Y. H., Lau, H. C., Torsæter, O., and Stubbs, L. P. (2020). Experimental investigation of stability of silica nanoparticles at reservoir conditions for enhanced oil-recovery applications. *Nanomaterials* 10(8), 1–15. https://doi.org/10.3390/nano10081522.

Lysakova, E. I., Skorobogatova, A. D., Neverov, A. L., Pryazhnikov, M. I., Rudyak, V. Ya. and Minakov, A. V. (2024). Physico-chemical studies and development of water-based drilling fluid formulations with carbon nanotube additives. *Journal of Molecular Liquids*, 125448. https://doi.org/10.1016/j.molliq.2024.125448.

Lysakova, E. I., Skorobogatova, A. D., Neverov, A. L., and Minakov, A. V. (2025). Investigation of the effect of spherical nanoparticle additives on the properties of drilling fluids modified by carbon nanotubes. *Nano-Structures & Nano-Objects* 41, 101442. https://doi.org/10.1016/j.nanoso.2025.101442.

Ma, L., Yin, D., Ren, J., Han, B. and Qin, S. (2024). A novel thixotropic structural dynamics model of water-based drilling fluids. *Geoenergy Science and Engineering 234*, 212585. https://doi.org/10.1016/j.geoen.2023.212585.

Macías C., K., Ballesteros R., L. T., Velázquez V., V. W., Frías M., D. M., López G., R., and Alvarez L., M. A. (2024). Effect of chitosan on the electrokinetic, spectroscopic, and textural properties of TiO2 nanoparticles. *Revista Mexicana de Ingeniera Química* 23(1). https://doi.org/10.24275/rmiq/Poly24218

Martin, C., Nourian, A., Babaie, M. and Nasr, G. G. (2024). Innovative drilling fluid containing sand grafted with a cationic surfactant capable of drilling high pressure and high temperature geothermal and petroleum wells. *Geoenergy Science and Engineering 237*. https://doi.org/10.1016/j.geoen.2024.212767.

Mendoza R., M. A., and Rojas P., K. K. (2021). Nanotechnology applied in water-based drilling fluids to inhibit formation damage. Degree project for the title of petroleum engineer. Fundación Universidad de América. Chrome https://repository.uamerica.edu.co/server/api/core/bitstreams/002f5fc5-12e0-496f-8744-1a15a817d893/content .

Nwaezeapu, V. C., Ezenwaka, K. C. and Ede, T. A. (2019). Evaluation of hydrocarbon reserves using integrated petrophysical analysis and seismic interpretation: A case study of

TIM field at southwestern offshore Niger Delta oil Province, Nigeria. *Egyptian Journal of Petroleum 28*(3), 273–280. https://doi.org/10.1016/j.ejpe.2019.06.002.

Ofei, T. N., Lund, B. and Saasen, A. (2021). Effect of particle number density on rheological properties and barite sag in oil-based drilling fluids. *Journal of Petroleum Science and Engineering 206*, 108908. https://doi.org/10.1016/j.petrol.2021.108908 .

Ovando M., V. M. (2018). Facile synthesis of low band gap ZnO microstructures. *Revista Mexicana de Ingeniería Química* 17(2), 455–462. https://doi.org/10.24275/10.24275/uam/izt/dcbi/revmexingquim/2018v17n2/Ovando.

Parizad, A., Shahbazi, K. and Tanha, A. A. (2018). SiO_2 nanoparticle and KCl salt effects on filtration and thixotropical behavior of polymeric water based drilling fluid: With zeta potential and size analysis. *Results in Physics 9*, 1656–1665. https://doi.org/10.1016/j.rinp.2018.04.037 .

Perween, S., Beg, M., Shankar, R., Sharma, S. and Ranjan, A. (2018). Effect of zinc titanate nanoparticles on rheological and filtration properties of water based drilling fluids. *Journal of Petroleum Science and Engineering 170*, 844–857. https://doi.org/10.1016/j.petrol.2018.07.006.

Prieto G., F., Sánchez J., F., Méndez M., M. A., García B., G., and Gordillo M., A. J. (2007). Obtención y caracterización de ferritas ternarias de manganeso por mecanosíntesis. Boletín de La Sociedad Geológica Mexicana 59(1), 125–132. https://doi.org/10.18268/BSGM2007v59n1a10

Qi, Q., Zhang, T., Yu, Q., Wang, R., Zeng, Y., Liu, L. and Yang, H. (2008). Properties of humidity sensing ZnO nanorods-base sensor fabricated by screen-printing. *Sensors and Actuators, B: Chemical 133*(2), 638–643. https://doi.org/10.1016/j.snb.2008.03.035.

Rafati, R., Smith, S. R., Sharifi Haddad, A., Novara, R. and Hamidi, H. (2018). Effect of nanoparticles on the modifications of drilling fluids properties: A review of recent advances. In *Journal of Petroleum Science and Engineering* 161, 61–76. https://doi.org/10.1016/j.petrol.2017.11.067.

Ramos, J., Santamaría Osorio, L., Andrés Mendoza Leiva, C., Uribe, W. and Polanco, L. (2013). Almidón modificado de yuca como aditivo en fluidos de perforación base agua. *Revista Investigacion.indb* 6(1).

Reilly, S. I., Vryzas, Z., Kelessidis, V. C. and Gerogiorgis, D. I. (2016). First-principles Rheological Modelling and Parameter Estimation for Nanoparticle-based Smart Drilling Fluids. In *Computer Aided Chemical Engineering* 38, 1039–1044. https://doi.org/10.1016/B978-0-444-63428-3.50178-8.

Sadeghalvaad, M. and Sabbaghi, S. (2015). The effect of the TiO2/polyacrylamide nanocomposite on water-based drilling fluid properties. *Powder Technology 272*, 113–119. https://doi.org/10.1016/j.powtec.2014.11.032.

Salas, G., Rosas, N., Galeas, S., Guerrero, V., and Debut, A. (2016). Síntesis de Nanopartículas de ZnO por el Método de Pechini. *Revista Politécnica* 38 (1). https://www.redalyc.org/articulo.oa?id=688773643005.

Sapkota, R., Duan, P., Kumar, T., Venkataraman, A., and Papadopoulos, C. (2021). Thin film gas sensors based on planetary ball-milled zinc oxide nanoinks: Effect of milling parameters on sensing performance. *Applied Sciences (Switzerland)* 11(20). https://doi.org/10.3390/app11209676.

Senthilkumaar, S., Rajendran, K., Banerjee, S., Chini, T. K. and Sengodan, V. (2008). Influence of Mn doping on the microstructure and optical property of ZnO. *Materials Science in Semiconductor Processing 11*(1), 6–12. https://doi.org/10.1016/j.mssp.2008.04.005.

Sing, K. S. W., Everett, D. H., Haul, R. A. W., Moscou, L., Pierotti, R. A., Rouquerol, J. and Siemieniewska, T. (1985). *Reporting physisorption data for gas/solid systems-with special reference to the determination of surface area and porosity*. https://doi.org/10.1351/pac198557040603.

Sulaimon, A. A., Adeyemi, B. J., and Rahimi, M. (2017). Performance enhancement of selected vegetable oil as base fluid for drilling HPHT formation. *Journal of Petroleum Science and Engineering* 152, 49–59. https://doi.org/10.1016/j.petrol.2017.02.006.

Tichaona Taziwa, R., Leroy Meyer, E., Taziwa Taziwa, R. and Ntozakhe, L. (2017). Structural, Morphological and Raman Scattering Studies

of Carbon Doped ZnO Nanoparticles Fabricated by PSP Technique. *Journal of Nanoscience and Nanotechnology 1*(1). https://www.researchgate.net/publication/321061464.

Yi, S., Xu, Y., Cao, Y., Mao, H., He, G., Shi, H., Li, X. and Dong, H. (2024). The decisive role of filtration reducers' surface charge in affecting drilling fluid filtration performance. *Journal of Molecular Liquids 409*, 125505. https://doi.org/10.1016/j.molliq.2024.125505.

Zargar, R. A., Khan, S. U. D., Khan, M. S., Arora, M. and Hafiz, A. K. (2014). Synthesis and characterization of screen printed Znu thick film for semiconductor device applications. *Physics Research International 2014*. https://doi.org/10.1155/2014/464809 .

Zheng, X., Wang, R., Liddle, B., Wen, Y., Lin, L. and Wang, L. (2022). Crude oil footprint in the rapidly changing world and implications from their income and price elasticities. *Energy Policy 169*, 113204. https://doi.org/10.1016/j.enpol.2022.113204 .

Vol. 24, No. 2(2025) IA25520
Revista Mexicana de Ingeniería Química

Heterogeneous photo-Fenton treatment in the degradation of indigo carmine (IC) by using ZeoSonFe as a catalyst through an experimental design

Tratamiento foto-Fenton heterogéneo en la degradación de indigo carmín (IC) utilizando ZeoSonFe como catalizador, a través de un diseño experimental

I. Cosme-Torres*, F.J. Illescas-Martinez
Tecnológico Nacional de México/Instituto Tecnológico de Toluca, Av. Tecnológico S/N, Colonia Agrícola Bellavista, C.P. 52149, Metepec, Estado de México, México.
Sent date: February 4, 2025; Accepted: July 1, 2025

Abstract
One of the most important advanced oxidation processes in the treatment of dyes is the photo-Fenton process using heterogeneous catalysts, according to its unique advantages: it allows the complete mineralization of the contaminant and the separation of the catalyst. A clinoptilolite-heulandite zeolite with Fe was conditioned as a catalyst. SEM analysis showed that ZeoSonFe is composed of characteristic cubic and polyhedral shaped crystals. EDS analysis of the ZeoSonFe showed an increase in Fe content in comparison to ZeoSonSod, furthermore it can be mentioned that Na^+ and Ca^{2+} are the cations involved in the cation exchange of Fe^{2+}. The first order rate constant increased with decreasing IC concentration, the k_1 value was given in the following order BAA > BAB > BBA > BBB where three factors were studied: the concentration of IC at a low level (B= 100 mg L^{-1}) and high level (A= 300 mg L^{-1}), the amount of ZeoSonFe (B= 250 mg; A=1000 mg) and the dose of H_2O_2 (B= 3 mmol; A= 9 mmol).
Keywords: Indigo carmine, photo-Fenton, catalyst, experimental design.

Resumen
Uno de los procesos de oxidación avanzada más importantes en el tratamiento de colorantes es el proceso foto-Fenton mediante el uso de catalizadores heterogéneos; de acuerdo a sus ventajas únicas permite la mineralización completa del contaminante y la separación del catalizador. Se acondiciono una zeolita clinoptilolita-heulandita como catalizador. El análisis SEM permitió observar que la ZeoSonFe está compuesta de cristales característicos de forma cúbica y poliédrica. El análisis EDS de la ZeoSonFe mostró un aumento en el contenido de Fe en comparación con la ZeoSonSod, además se puede mencionar que el Na^+ y el Ca^{2+} son los cationes que intervienen en el intercambio catiónico de Fe^{2+}. La constante de velocidad de primer orden aumentó al disminuir la concentración del IC, el valor de k_1 se dio en el siguiente orden BAA > BAB > BBA > BBB, donde se estudiaron tres factores: la concentración de IC a un nivel bajo (B = 100 mg L^{-1}) y nivel alto (A = 300 mg L^{-1}), la cantidad de ZeoSonFe (B = 250 mg; A = 1000 mg) y la dosis de H_2O_2 (B = 3 mmol; A = 9 mmol).
Palabras clave: Indigo carmín, foto-Fenton, catalizador, diseño experimental.

*Corresponding author. *E-mail*: ismael.ct@toluca.tecnm.mx;
https://doi.org/10.24275/rmiq/IA25520
ISSN:1665-2738, *issn-e*: 2395-8472

1 Introduction

The existence of several dyes that are emitted to wastewater from different industries, mainly textile has caused several environmental problems. In most cases, water is returned to the river, lake, or soil without prior treatment due to the difficulty of implementing pollutant removal technologies (Gonzales-Condori *et al*., 2023; Ahmed & Mohamed, 2017). Indigo carmine (IC) dye, also known as acid blue 74 is considered as highly toxic indigo dye whose main component is indigotine, its chemical structure presents two important groups: $NaSO_3$, which attributes the water-soluble property, and the chromophore group (a conjugated system of a C = C bond replaced by two NH groups and two C = O groups), which gives its color (Genázio *et al*., 2017; Mendes *et al*., 2015). IC is released in wastewater from the dyeing of polyester and denim fibers, it is estimated that approximately 5 to 20 % of the 20,000 t/year of dye used in this industry is lost during the dyeing process, it is usually resistant to aerobic biodegradation and is not easily degraded by conventional treatments, it is also used as a redox indicator in analytical chemistry and microscopic staining (Hernández-Gordillo *et al*., 2016; Arenas *et al*., 2017; Hadi *et al*., 2016).

Advanced Oxidation Processes (AOPs), provide an alternative for sustainable water recuperation, are effective chemical, photochemical or electrochemical methods to decompose persistent organic compounds in water (Ganiyu *et al*., 2015; Khataee *et al*., 2016). These have been of great interest for many years through oxidation reactions with highly efficient generation of hydroxyl radicals ($^{\bullet}OH$)(Gagol *et al*., 2018). One of the most important AOPs in the treatment of dyes in effluents is the heterogeneous photo-Fenton process; this classic method is one of the most economical and fastest methodologies within the AOP. Due to its unique advantages of achieving complete mineralization of the pollutant reacting up to (CO_2 and H_2O), as well as relatively easy separation of the heterogeneous catalyst. Solid catalysts must meet a number of requirements such as: high activity in terms of pollutant removal, a leaching margin of active cations, stability over a wide pH and temperature range, high radical generation ($^{\bullet}OH$)(Vázquez-Romero *et al*., 2024; Boczkaj & Fernandes, 2017). Iron (Fe) has emerged as a particularly promising candidate for catalysis, owing to its abundance, low cost, and low toxicity, Fe has undergone a renaissance in catalysis, fueled by advances in heterogeneous catalysis, owing to its several advantages. Heterogeneous Fe-based catalysts offer several advantages availability, cost-effectiveness, and environmental friendliness, they can be easily separated from reaction mixtures, facilitating catalyst recovery and reuse. These catalysts typically exhibit high stability and durability under reaction conditions. They exhibit high thermal and chemical stability, making them suitable for a wide range of reaction conditions. These catalysts often simplify purification processes by reducing product contamination with catalyst residues. Additionally, heterogeneous Fe catalysts can be engineered for high selectivity in specific reactions (Zhu *et al*., 2023; Baruah *et al*., 2024).

Zeolites are microporous crystalline solids formed by tetrahedral structures of aluminate $(AlO_4)^{4-}$ and silicate $(SiO_4)^{5-}$ connected at their vertices by oxygen atoms, with elements from groups I and II as exchange ions and various Si/Al ratios that describe the hydrophobicity of their surface. Due to their crystalline structure, porosity, shape, cavity size and hardness, zeolites present unique characteristics for their application in water treatment, including a high specific surface area associated with their porous structure, biocompatibility, ion exchange capacity, natural abundance and diverse adaptable porous structures (Leal-Perez *et al*., 2024; Ruiz-Baltazar, 2024; Samara *et al*., 2025). The Fenton-based processes involving zeolites also lead to the generation of hydroxyl radicals through the interaction of hydrogen peroxide with diverse iron species incorporated into the zeolites. For instance, iron-exchanged zeolites have been used for organic pollutant degradation through the reaction between the ferric ions in the zeolite and H_2O_2 in the presence of UV light (Serna-Galvis *et al*., 2024). Several parameters influence the photo-Fenton process, in particular the pH of solution, the concentration of ferrous ions, the concentration of hydrogen peroxide, the stirring speed, the initial concentration of the dye, the volume of the solution, temperature, and contact time. For this reason, the factorial design is used to achieve the best overall optimization of a process by determining the effect of each factor on the response, as well as how the effect of each factor varies with the change in the level of the other factors. The interaction effects of different factors could be achieved using only the design of experiments (Elhalil *et al*., 2016; Barka *et al*., 2014). Therefore, the objective of this investigation was to establish a heterogeneous photo-Fenton treatment using a 23 factorial design. The effects analyzed were the amount of iron-conditioned zeolite, IC concentration, and the amount of H_2O_2. This heterogeneous photo- Fenton treatment is an alternative for sustainable water recovery.

2 Materials and methods

2.1 *Conditioning of zeolite with Fe*

Was used a natural zeolite of the clinoptilolite-heulandite type from Guaymas, Sonora, Mexico. The

zeolite was milled and sieved at 60 mesh (0.0098 in). For conditioning of the natural zeolite with NaCl, 100 g were placed in 650 mL of a 0.3 mol L^{-1} NaCl solution (1:6.5), the mixture was kept in a refluxing system for 12 h. Then, the solution was decanted for a second reflux using a new NaCl solution. At the end of the sodium conditioning, the phases were separated and the solids were washed with deionized water before drying at 40 °C for 72 h, this zeolite is named ZeoSonSod. Then it was in contact the ZeoSonSod catalyst with a 0.2 mol L^{-1} $FeSO_4{\cdot}7H_2O$ solution (1:5 relation), the mix was stirred for 6 h at 60 °C. After the solids were washed with deionized water and finally, they were dried at 60 °C for 12 h. The obtained material (ZeoSonFe) was used as heterogeneous catalysts for IC removal tests.

2.2 Characterization

The ZeoSonFe catalyst was characterized by infrared spectroscopy (FTIR), using a spectrophotometer; Varian model 640, equipped with accessory of attenuated total reflection (ATR), in the wavenumber range from 4000 to 400 cm^{-1}. Specific surface area was analyzed by adsorption-desorption processes using nitrogen at a pressure of 72.18 KPa and a temperature of -196.15 °C using BELSORP-MAX equipment. The morphology was analyzed by using a scanning electron microscope; model JEOL JSM7800FEG at 10 Kv, the elemental chemical composition was determined by energy dispersion spectroscopy (EDS) with an Oxford Pentafet cooled, solid - state device.

2.3 Photo-Fenton treatment

The photo-Fenton treatment was performed using a factorial design 2^3, where three factors were studied: the concentration of dye [IC] (100 and 300 mg L^{-1}); the dose of hydrogen peroxide H_2O_2 (3 and 9 mmol); and the ZeoSonFe dosage (250 and 1000 mg), as shown in Tables 1 and 2.

Each experiment was performed in triplicate to reduce experimental error. In the experiments, a 500 ml reactor adapted with an ultraviolet light lamp (250 nm) was used. Subsequently, the IC solution was adjusted to optimum pH, using (HCl 0.1 mol L^{-1}) and maintaining continuous stirring at 300 rpm experiments were carried out according to the combinations of the experimental design. Then samples of the treated solution were taken at different times (0 - 120 min), to evaluate the removal of the IC the samples were filtered using a syringe-type filter (0.45 μm) for the separation of the ZeoSonFe catalyst. After filtration, the residual concentration was determined with an UV-Vis spectrophotometer (Thermo Spectronic Genesy 10 UV) at 612 nm of wavelength. The IC removal efficiency was calculated as follows Eq. (1). Where C_o is the initial IC concentration and C_t is the concentration of IC at time t in solution (mg L^{-1}).

$$\%\text{Removal} = \left(\frac{C_o - C_t}{C_o}\right) \times 100 \tag{1}$$

2.4 Effect of pH and ORP

pH has been identified as a parameter that influences the photo-Fenton treatment, to determine the pH that presents the best IC degradation in aqueous solution, an IC solution (100 mg L^{-1}) was used, this was adjusted to pH 3, 4 and 5 using (HCl 0.1 mol L^{-1}). The pH was measured with a pH-meter (Denver Instrument 250), and then it was subjected to the photo-Fenton treatment heterogeneous using UV radiation (254 nm), 3 mmol H_2O_2 and 250 mg of ZeoSonFe as a catalyst. The residual concentration of IC was determined using a UV-Vis spectrophotometer (Thermo Spectronic Genesy 10 UV) at a wavelength of 612 nm. The oxidation reduction potential (ORP) was monitored in the photo-Fenton treatment at pH 3, 4 and 5, the ORP measurement was performed during the degradation of the IC using an INTELLICAL ORP-REDOX MTC101 sensor.

3 Results and discussion

3.1 FTIR analysis of ZeoSonFe

The FTIR spectrum of the catalyst (ZeoSonFe) is shown in (Figure 1), the vibrational characteristics of the catalyst during Na and Fe conditioning were analyzed. At a wavenumber of 3438 cm^{-1} a broad band related to the hydroxyl groups (OH) of the (Si-OH) bond is observed, deformation of adsorbed water molecules is shown at 1632 cm^{-1} (Pérez-González *et al*., 2024; Paukshtis *et al*., 2019), while at 1060 cm^{-1} they are attributed to internal asymmetric vibrations of the tetrahedra and are susceptible to Si and Al content, the 787 cm^{-1} weak intensity band corresponds to symmetrical stretching vibrations in the external structure of the tetrahedral bonds, at 605 cm^{-1} the asymmetric stretching vibration

Table 1. Factors and levels for three independent variables

Factor	Max. Level (+)	Min. Level (-)
[*IC*] concentration (mg L^{-1})	300	100
ZeoSonFe catalyst dose (mg)	1000	250
[H_2O_2] concentration %(mmol)	9	3

Table 2. Experimentation plan 2^3 for photo-Fenton treatment

Experiment	IC concentration (mg L^{-1})	ZeoSonFe dose (mg)	H_2O_2 concentration (mmol)
1	100	250	3
2	300	250	3
3	100	1000	3
4	300	1000	3
5	100	250	9
6	300	250	9
7	100	1000	9
8	300	1000	9

of the O-Si-O bonds of (SiO_4) is observed, finally the band at 455 cm^{-1} is attributed to internal bending vibrations of the Al-O-Si bond and corresponds to the Si/Al composition of each zeolite, while at 2360 cm^{-1} it is assigned to the symmetric and asymmetric C=O modes that are associated with atmospheric CO_2. It can be observed that the iron-conditioned zeolite does not show a significant change with the sodium-conditioned zeolite (ZeoSonSod) since the transition metal ion exchange does not produce alteration in the zeolitic netting (Abhijith *et al*., 2020; Pérez-González *et al*., 2024).

3.2 Scanning electron microscopy (SEM)

Elemental chemical composition (EDS) of the ZeoSonSod and ZeoSonFe catalyst, is shown in (Table 3). This is mainly composed of silicon (Si) and aluminum (Al), which proves the presence of aluminosilicates; aluminum oxide (Al_2O_3) and silicon oxide (SiO_2) being the main component of the zeolite tetrahedron structure as reported by (Islam & Mohr, 2023; Yordanova *et al*., 2024; Biblioteca *et al*., 2023), and to a lesser percentage potassium (K), sodium (Na), calcium (Ca) and iron (Fe). EDS analysis of the ZeoSonFe catalyst indicated an increase in Fe, this occurs through the cation exchange of Na^+ and Ca^{2+} it can also be observed that their weight percentages decrease due to equivalent substitution. In this work, the Si/Al ratio was 5.35 a value ≥ 5 is typical of zeolites rich in clinoptilolite, the importance of knowing the

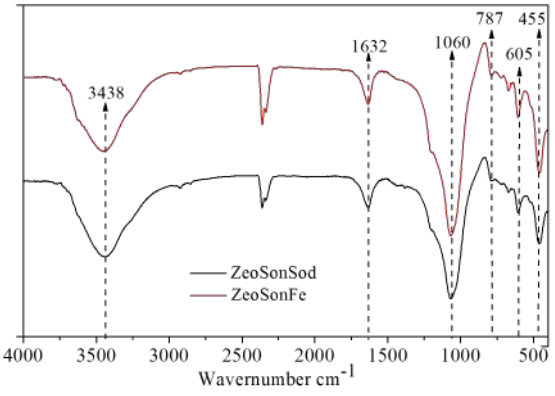

Figure 1. FTIR spectra of the ZeoSonSod and ZeoSonFe.

Si/Al ratio has been stated in terms of the coordination environment of aluminum species because it plays a relevant role in controlling the physical and chemical properties utilized for catalysts, adsorbates and ion-exchange materials, the Si/Al ratio is agreement with previous reports by (Barragán *et al*., 2016). The (Figure 2) shows the micrograph at 20,000× magnifications of the 2a) ZeoSonSod and 2b) ZeoSonFe catalyst, both materials show an irregular morphology and surface, with characteristic crystals of polyhedral and cubic shaped. Finally, the ZeoSonFe catalyst presents a porous structure and agglomerates on the surface (Bhardwaj *et al*., 2012; Barragán *et al*., 2016).

3.3 Surface area BET

It was found that the adsorption isotherms of the ZeoSonSod and ZeoSonFe catalyst belong to type IV, according to the International Union of Pure and Applied Chemistry (IUPAC) allows classifying these materials as mesoporous (between 2 and 50 nm) (Biblioteca *et al*., 2023). The average pore diameter value of the ZeoSonFe catalyst was 15.295 nm (Table 4), this diameter decreased with respect to the ZeoSonSod material due to the diffusion of metal ions that occurs through the macro, meso and microchannels in the zeolite structure, this characteristic is typical in mesoporous materials, with respect to surface area this was 4.970 m^2 g^{-1} and a pore volume of 1.141 cm^3 g^{-1}, the area was favored due to the cation exchange that occurred between the exchangeable cations of sodium zeolite and Fe^{2+}, according to the crystal structure of clinoptilolite, the $[SiO_4]^{4-}$ and $[AlO_4]^{5-}$ tetrahedra are bonded in 0.9 nm wide layers; these layers are linked to each other by oxygen atoms in planar symmetry and form a three-dimensional structure. Sodium and calcium ions predominantly in channels A and B, and potassium preferentially located in channel C. This material is comparable to sodium zeolite since the conditioning process does not modify its anionic structure (Muhammad *et al*., 2024).

Table 3. Elemental chemical composition (EDS)

Composition (% w)	ZeoSonSod	ZeoSonFe
Si	42.8 ± 1.0	42.0 ± 1.0
O	40.1 ± 0.6	40.3 ± 0.6
Al	8.0 ± 0.9	7.8 ± 0.9
K	4.3 ± 0.9	4.4 ± 0.9
Na	2.8 ± 0.8	2.3 ± 0.8
Ca	1.1 ± 0.9	1.0 ± 0.9
Fe	0.6 ± 0.9	1.8 ± 0.9

Table 4. Textural parameters of zeolites

Material	Surface area (m^2g^{-1})	Total pore Volume (cm^3g^{-1})	Average pore diameter (nm)
ZeoSonSod	4.355	1.001	18.829
ZeoSonFe	4.970	1.141	15.295

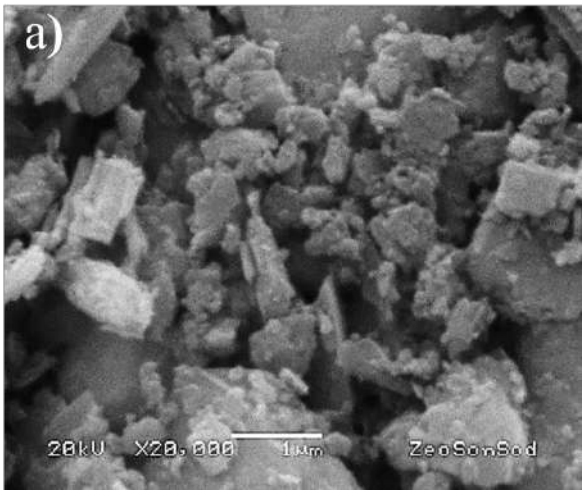

Figure 2a. Micrograph of the ZeoSonSod.

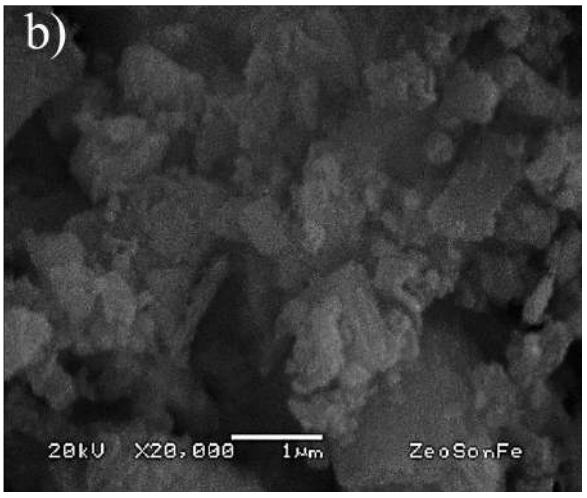

Figure 2b. Micrograph of the ZeoSonFe.

3.4 Oxidation reduction potential (ORP)

ORP values at pH 3 are shown in (Figure 3), there is a rapid increase from 398 ± 5.2 mV to 520 ± 4.3 mV in the first 20 min of treatment, the ORP was positive due to oxidation reactions generated by the ($^{\bullet}$OH) radicals in solution until reaching a maximum value of 542 ± 4.6 mV, however they decrease after 100 min of treatment due to the consumption of the ($^{\bullet}$OH) radicals. The ORP at pH 4 and 5 showed low oxidation reactions reaching maximum values of 508 ± 3.3 mV and 460 ± 3.5 mV at 120 min of treatment. Azizia *et al*., (2020), mentions that ORP can be used as an important parameter to indicate the end of an oxidation reaction. Thus, the optimum pH value in this experimental design was 3, which showed better results since at a pH value ≥ 4 H_2O_2 can decompose into H_2O and O_2 molecules, as shown in Eq. (2) causing the yield of the reaction to decrease, while under very strong acidic conditions pH (2) it is possible that H_2O_2 molecules can carry out a solvation process forming an oxonium ion $[H_3O_2]^+$, these ions make H_2O_2 more stable and reduce its reactivity with ferrous ions (Quadrado & Fajardo, 2017; Babuponnusami & Muthukumar, 2014).

$$2H_2O_2 \rightarrow 2H_2O + O_2 \quad (2)$$

3.5 Effect on pH

The optimum pH was 3 (Figure 4), at this value the greatest degradation of the dye occurred, obtaining 6.00 ± 0.20 mg L^{-1} of residual IC in 120 min of treatment, the acidic condition favors the degradation of the dye. At pH 5 and 4 the residual concentration of the dye was 77.73 ± 2.93 mg L^{-1} and 34.27 ± 1.88 mg L^{-1} respectively. The work carried out on the degradation of dyes treated by heterogeneous photo-Fenton has established an optimal pH value of 3, such as (Quadrado & Fajardo, 2017; Yaman & Gündüz, 2015; Basturk & Karatas, 2015), since a very low pH (pH < 3) is associated with the existence of complex iron $[Fe(H_2O)_6]^{2+}$ and $[Fe(H_2O)_6]^{3+}$ species that react more slowly with H_2O_2 , as stated by (Javaid & Qazi, 2019).

An atomic absorption spectroscopy test was performed to analyze the amount of Fe leached from the ZeoSonFe catalyst in the treated solution after 120 min using a Perkin Elmer Model 31104 spectrophotometer. The results showed that at (pH 3), 0.245 mg L^{-1} of leached Fe was obtained. As a reference, this value is lower than that established by the United States Environmental Protection Agency, since the maximum permitted limit is 0.3 mg L^{-1} in drinking water. leaching of (Fe) cations from the catalyst is

reduced at low pH values, thereby improving catalyst performance ZeoSonFe.

3.6 Experimental design

The degradation kinetics using a high concentration of IC (300 mg L^{-1}) are shown in (Figure 5). The ABB combination corresponding to (300 mg L^{-1} of IC, 250 mg of ZeoSonFe and 3 mmol of H_2O_2) obtained a residual concentration of 115.93 ± 4.6 mg L^{-1} and a removal efficiency of 61.80 ± 1.47 % in 120 min of treatment.

For the AAB (300 mg L^{-1} of IC, 1000 mg of ZeoSonFe and 3 mmol of H_2O_2) combination the residual concentration was 55.74 ± 5.21 mg L^{-1}, the ABA (300 mg L^{-1} of IC, 250 mg of ZeoSonFe and 9 mmol of H_2O_2) and AAA (300 mg L^{-1} of IC, 1000 mg of ZeoSonFe and 9 mmol of H_2O_2) combinations showed favorable results 19.07 ± 1.76 mg L^{-1} and 0.81 ± 0.05 mg L^{-1} of residual IC, being the AAA combination the one that presented the best degradation treatment with a percentage of removal 99.73 ± 0.01 %, the increase in the amount of catalyst generated a greater number of Fe^{2+} catalytic sites which when coming into contact with H_2O_2 molecules, generate a greater amount of ($^{\bullet}$OH) radicals, these are responsible for the degradation of the IC. The low IC removal efficiencies are due to the increase in concentration, since it generates an increase in the internal optical density, this indicates that the higher the number of IC particles in the solution, the more impermeable it becomes to UV radiation. Therefore, H_2O_2 will only be irradiated by a small amount of UV light, which generates less formation of ($^{\bullet}$OH) radicals and less degradation of the IC (Castro-Peña & Durán-Herrera, 2014).

The results of the combinations in which a low concentration of IC (100 mg L^{-1}) is used in the heterogeneous photo-Fenton treatment are shown in (Figure 6). The BAA combination corresponding to (100 mg L^{-1} of IC, 1000 mg of ZeoSonFe and 9 mmol of H_2O_2) showed the best results in 20 min of treatment with a 97.09 ± 0.10 % removal. The BAB (100 mg L^{-1} of IC, 1000 mg of ZeoSonFe and 3 mmol of H_2O_2) combination also showed favorable results by using a greater amount of ZeoSonFe, which accelerated the formation of ($^{\bullet}$OH) radicals, in 40 min a 98.62 ± 0.07 % removal efficiency was obtained, the BBB combination showed a removal efficiency of 94.06 ± 0.22 % in 120 min of treatment. The optimal amount of catalyst is important in photo-Fenton type treatments since an increase in the amount of catalyst generates a higher amount of solid particles in the solution that increasingly obstruct the photons emitted by the UV light due to the turbidity in the solution, consequently, the efficiency in the degradation of the dye decreases as reported by (Huy *et al*., 2020; Phan *et al*., 2018).

The degradation of the dye is initiated by the Fe^{2+} that has formed in the ZeoSonFe catalyst, this accelerates the catalytic decomposition of H_2O_2 in solution, while it is oxidized by H_2O_2 to Fe^{3+} (Fenton reaction). The $^{\bullet}$OH radicals that are generated attack the IC molecule adsorbed on the catalyst surface generating an increase in intermediates. Finally, the intermediates are converted to simpler molecules; as shown in the following reactions.

$$\equiv Fe^{2+} + H_2O_2 \rightarrow \equiv Fe^{3+} + \cdot OH + OH^- \quad (3)$$

$$IC + \cdot OH \rightarrow \text{Intermediates} \quad (4)$$

$$\text{Intermediates} \rightarrow CO_2 + H_2O \quad (5)$$

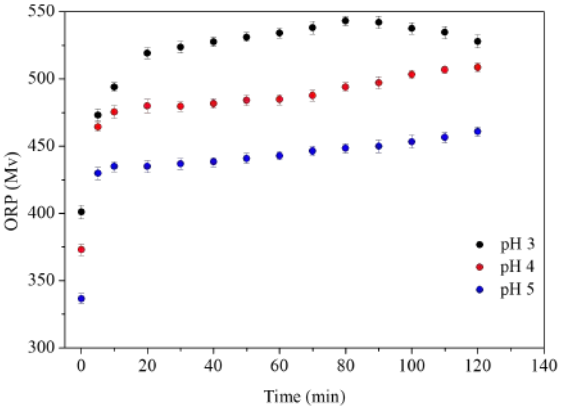

Figure 3. Effect of ORP on photo-Fenton treatment of IC. Conditions: [IC]= 100 mg L^{-1}, Cat.= 250 mg, H_2O_2= 3 mmol, pH (3,4,5), Vol.= 500 mL

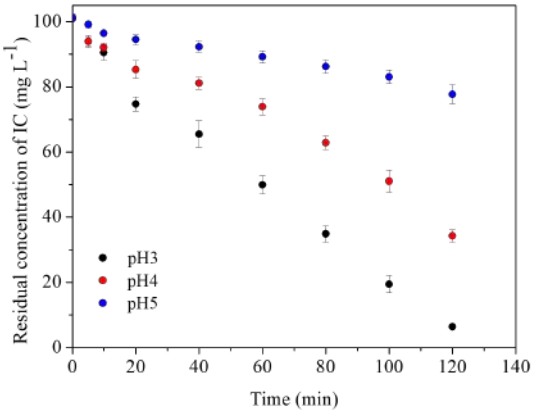

Figure 4. Effect of pH on the photo-Fenton treatment of IC. Conditions: [IC]= 100 mg L^{-1}, Cat.= 250 mg, H_2O_2= 3 mmol, pH (3,4,5), Vol.= 500 mL

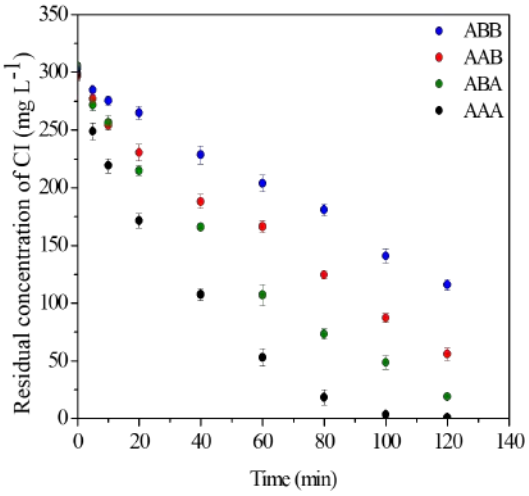

Figure 5. IC degradation kinetics (ABB, AAB, ABA, AAA)

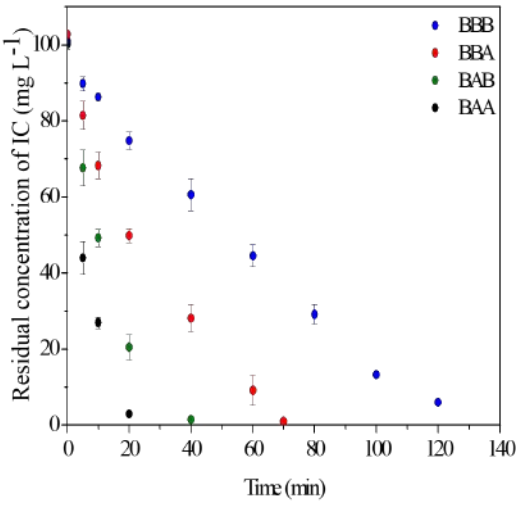

Figure 6. IC degradation kinetics (BBB, BBA, BAB, BAA)

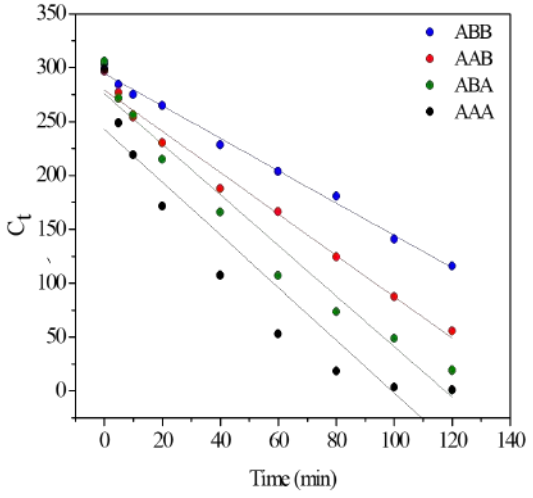

Figura 7. Linear fitting of zero-order kinetics (ABB, AAB, ABA, AAA)

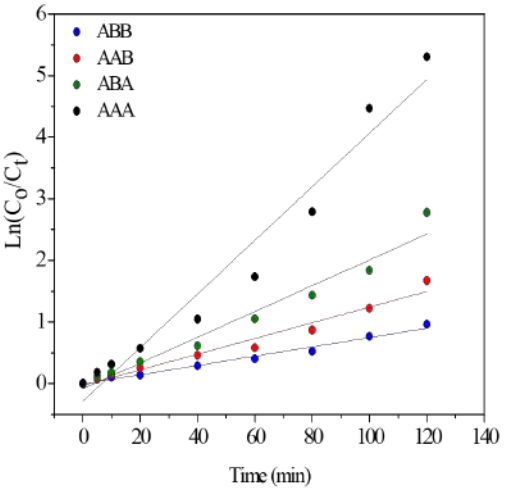

Figura 8. Linear fitting of First-order kinetics (ABB, AAB, ABA, AAA)

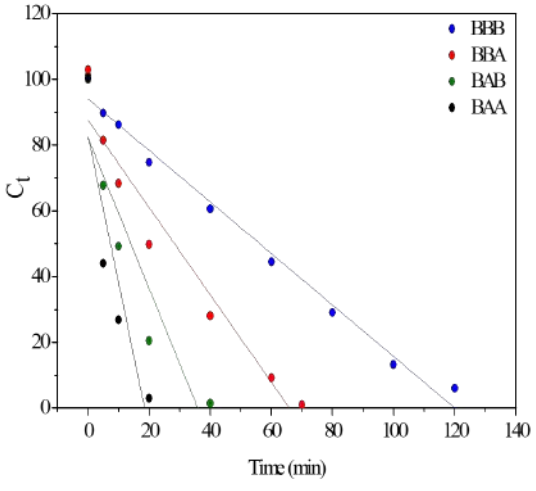

Figura 9. Linear fitting of zero-order kinetics (BBB, BBA, BAB, BAA)

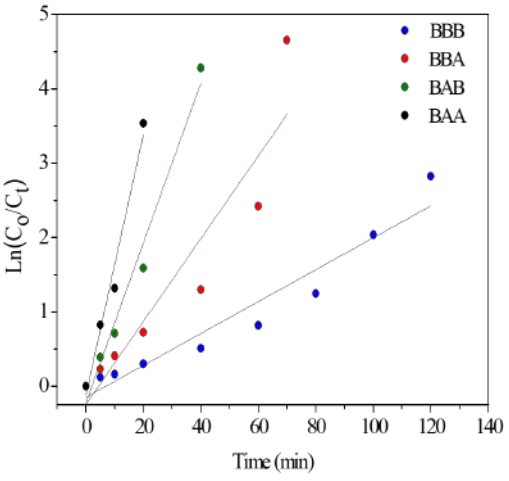

Figura 10. Linear fitting of First-order kinetics (BBB, BBA, BAB, BAA)

In the treatment of degradation, the concentration of H_2O_2 is directly related to the generation of $^{\bullet}OH$ radicals, these can also be generated through the combination of UV light and H_2O_2 by photolysis of H_2O_2 where the UV radiation provides enough energy to break the O-O bond and generate the $^{\bullet}OH$ radicals, in photo-Fenton treatment the UV light significantly accelerates the degradation of the IC (Boczkaj & Fernandes, 2017). To describe the oxidative reaction in the degradation of IC, zero-order and first-order kinetics were used, Origin version 8.0 software was used for linear adjustments of the experimental data, the kinetic models are presented in the following equations:

Zero-order model:

$$C_t = C_0 - k_0 \cdot t \tag{6}$$

First order model:

$$\ln \frac{C_0}{C_t} = k_1 t \tag{7}$$

Where k_0 and k_1 are the rate constants of the kinetics reaction, t is the reaction time, C_0 is the equilibrium concentration of the dye and the concentration of the dye after time t is C_t , to investigate the degradation of IC as a function of time, the degradation rate constant and the half-life of the reaction were calculated. The half-life $t_{1/2}$, indicates the time required for the concentration to decrease to 50 % of its initial concentration. This value is determined according to equation (8), (Sirajudheen & Meenakshi, 2019; Asaduzzaman *et al*., 2024).

half-life time:

$$t_{1/2} = \frac{0.693}{k_1} \tag{8}$$

Where: $t_{1/2}$ = half-life time; k_1= Speed Constant (min^{-1}).

Regarding the degradation kinetics, the experimental data were fitted to the zero-order and first-order kinetic model (Figure 7 and 8), it is observed that the value of the rate constant k_0 is presented according to the following order AAA > ABA > AAB > ABB, this relationship corresponds with the degradation percentages of the IC.

The values of the velocity constant using a low concentration of dye were determined from Figures (9 and 10). The first order rate constant increased with decreasing IC concentration (100 mg L^{-1}), the k_1 value was given in the following order BAA > BAB > BBA > BBB these combinations achieved degradation percentages above 90 %, however, the degradation time was an important parameter since the BAA combination degraded the IC in 20 min with a $t_{1/2}$ of 3.95 min and k_1 of 0.1752 min^{-1}.

3.7 *IC degradation*

To verify the maximum absorbance points of the IC in aqueous solution, a UV-vis absorption spectrum was performed in a range of 200 to 800 nm. The chromophore group is present in the 612 nm band, which gives the IC molecule its characteristic color (blue). The signal at 286 nm is related to the amino group, at 252 nm it is attributed to the carbonyl group, while the signal at 205 nm corresponds to the resonance of the aromatic ring (Ristea & Zarnescu, 2023). The degradation of IC is observed in the UV-vis spectrum (Figure 11). The absorption signals at 286 and 612 nm decrease, causing the break of the C=C double bond. This bond break is associated with the use of $^{\bullet}OH$ radicals to produce isatin 5-sulfonic acid; after 20 minutes of treatment, a new band is observed at an λ of 410 nm. This is attributed to the formation of isatin, as reported by (Bernal *et al*., 2013). Subsequently, the IC molecule continues to be oxidized by $^{\bullet}OH$ radicals to form oxalic acid, which is mineralized into CO_2.

Table 6 presents relevant literature from different studies using heterogeneous photo-Fenton treatment and/or advanced oxidation processes for IC degradation through synthetic solutions. The authors consider the amount of catalyst, dye concentration, H_2O_2, and pH; these parameters have been studied with effective and reproducible results. According to the reports in this work, ZeoSonFe as a heterogeneous catalyst achieves high IC degradation rates. The efficiency of the ZeoSonFe/UV/H_2O_2 treatment is higher than that reported in terms of the initial IC concentration with other research works.

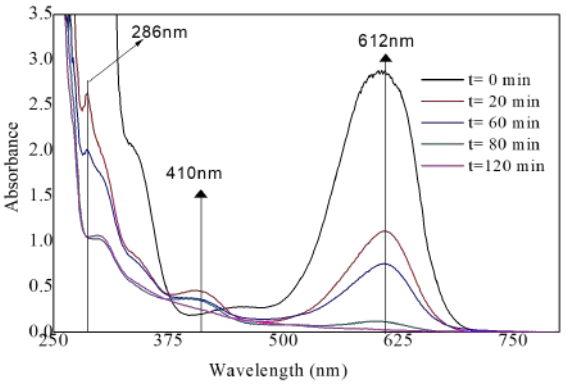

Figure 11. UV-vis spectrum in IC degradation measured at different times.

3.8 *Statistical analysis of the experimental design*

Statistical analysis in the heterogeneous photo-Fenton treatment was performed using the statistical software MINITAB 19. The analysis of variance provides the estimate of the effects of each factor, with a significance value α= 0.05. To know the effect, it is sufficient to

Table 5. Kinetic parameters of the zero-order and first-order model

Kinetic model	Experiment	$_0$ (L^{-1} min^{-1})	R^2
Zero order	ABB	1.501	0.993
	AAB	1.920	0.985
	ABA	2.348	0.959
	AAA	2.447	0.881
	Experiment	$_1$(min^{-1})	R^2
First order	ABB	$7.54x10^{-3}$	0.980
	AAB	$1.27x10^{-2}$	0.966
	ABA	$2.09x10^{-2}$	0.962
	AAA	$4.35x10^{-2}$	0.956
Kinetic model	Experiment	$_0$ (L^{-1} min^{-1})	R^2
Zero order	BBB	0.7835	0.9857
	BBA	1.3294	0.9337
	BAB	2.2865	0.8227
	BAA	4.4629	0.7682
	Experiment	$_1$(min^{-1})	R^2
First order	BBB	$2.14x10^{-2}$	0.9306
	BBA	$5.57x10^{-2}$	0.8492
	BAB	0.1074	0.9738
	BAA	0.1752	0.9691

make it vary between low and high levels, the results presented in (Table 7) show P values lower than the significance level, which indicates a relationship between the factors and the degradation of the IC. Therefore, the concentration of IC, the amount of ZeoSonFe catalyst, the amount of H_2O_2 have an important effect. The ZeoSonFe catalyst with H_2O_2 has less statistical interaction, but it cannot be eliminated because the interaction with the three factors is important, an increase in the amount of catalyst results in a larger surface area improving the degradation of the IC. The coefficient of determination was also determined, which was 99.38 %, this being acceptable in the model, these indicators show how well the mathematical model adjusts to the residual value obtained in the degradation of the IC.

The following equation is based on a transformation of the data to obtain a normality, this equation suggests the control to the model and can indicate what is attributed to the response, which shifts the value of the residual in the heterogeneous photo-Fenton treatment.

$$\text{Residual}^{0.266248} = 1.197 + 0.010436\ \text{IC} - 0.001691\ \text{ZeoSonFe} - 0.1323\ H_2O_2 + 0.0000041\ \text{IC}\cdot\text{ZeoSonFe} - 0.000197\ \text{IC}\cdot H_2O_2 + 0.000356\ \text{ZeoSonFe}\cdot H_2O_2 - 0.0000021\ \text{IC}\cdot\text{ZeoSonFe}\cdot H_2O_2 \quad (9)$$

The effect of the system, represented graphically, is composed of the residual data obtained in the degradation of CI. Figure (12) shows the levels of each factor (concentration of [IC] (100 and 300 mg L^{-1}); dose of hydrogen peroxide (3 and 9 mmol); and the dose of ZeoSonFe (250 and 1000 mg)) at a low and high level, the wider the line, the greater the response of the variable to the degradation treatment. For example, the H_2O_2 line is wider than the ZeoSonFe. In this case, the factor that refers to the amount of H_2O_2 is important for the generation of $^{\bullet}$OH radicals. It also allows to visualize the residual concentration obtained according to the levels of each factor.

The Pareto diagram shown in (Figure 13), establishes the factors involved in the photo-Fenton treatment and the magnitude and importance of their presence can be determined; the graph represents the absolute value of each effect, Additionally, a reference line with a value of 2.31 is presented at the top of the plot (this value is statistically significant at the 0.05 level of significance using the current model terms), indicating that any bar extending beyond this can be considered potentially important in terms of IC degradation. The important factors such as the concentration of the IC, the amount of H_2O_2, followed by the amount of ZeoSonFe catalyst are factors that exceed the baseline which means that they could significantly affect the degradation process, and this can be confirmed with respect to the experimental data, by having a lower concentration of dye (100 mg L^{-1}) the degradation time is much shorter than if a high concentration of dye (300 mg L^{-1}) is used, this degradation time will depend on the amount of H_2O_2 that is being used since it is an important reagent in the generation of $^{\bullet}$OH radicals, by increasing this amount the degradation time decreases.

In Figure 14, specific regions are shown that mark the possible response that can be expected in the presence of a low concentration of IC 100 mg L^{-1} a high amount of catalyst of 1000 mg of ZeoSonFe and 9 mmol of H_2O_2, using these high levels of the factors in the treatment can be seen the areas of operation, if we want to have areas where the residual concentration of the dye is less than 10 mg L^{-1} these parameters allows to have that concentration; both for concentration of 100 mg L^{-1} and an initial concentration of 300 mg L^{-1} of dye see (Figure 15), this residual concentration is guaranteed when the peroxide level is 9 mmol. These residual contour figures can predict the values and levels where visually the residual concentration required in the treatment can be detected and make the availability of resources efficient. The areas in blue color guarantee the degradation of the IC and it is possible to predict the values to work with in order to have low residual values of residual dye, the more intense regions in green color can represent certain affectations in the treatment.

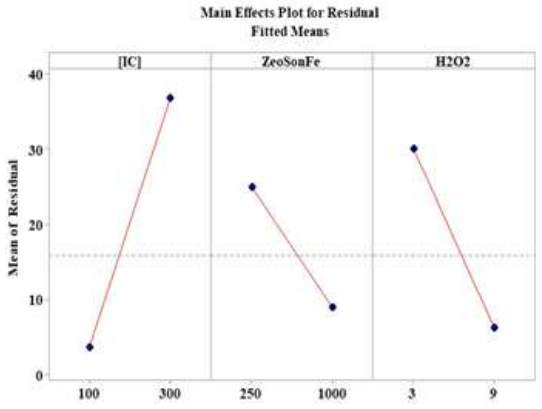

Figure 12. Main effects with ZeoSonFe as catalyst.

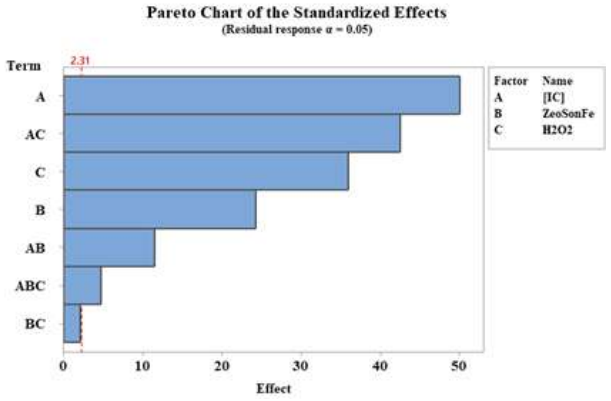

Figure 13. Pareto diagram of standardized effects.

Table 6. Comparison with previous work on the degradation of indigo carmine (IC)

Catalyst	Dye concentration	Decolorization % / Time	Reference
Fe-ZSM5	40 mg L^{-1}	99 % of IC-10 min	Kasiri, *et al*., 2008
HTCMgFe	100 mg L^{-1}	100 % of IC-30 min	Cosme-Torres, *et al*., 2020
FeO/ZnO+SGC	69 mg L^{-1}	95 % of IC-120 min	Reyes-Pérez, *et al*., 2023
FeO/ZnO+SGC	100 mg L^{-1}	88 % of IC-120 min	Reyes-Pérez, *et al*., 2023
$MnFe_2O_4$@BC	30 mg L^{-1}	50 % of IC-100 min	Ajibade & Nnadozie, 2020
$ZnFe_2O_4$@BC	30 mg L^{-1}	65 % of IC-120 min	Ajibade & Nnadozie, 2020
ZnO-Bi_2O_3- xC_3N_4	50 mg L^{-1}	45 % of IC-180 min	Huy, *et al*., 2020
ZeoSonFe	100 mg L^{-1}	96 % of IC-120 min	This Work
	300 mg L^{-1}	99 % of IC-120 min	This Work

Table 7. Coded coefficients for transformed response

Term	Effect	Coef	EE coef.	T-value	p-value	FIV
Constant		1.8274	0.0126	144.53	0.000	
IC	1.1452	0.5726	0.0126	45.29	0.000	1.00
ZeoSonFe	-0.5126	-0.2563	0.0126	-20.27	0.000	1.00
H_2O_2	-0.9262	-0.4631	0.0126	-36.63	0.000	1.00
IC*ZeoSonFe	-0.4234	-0.2117	0.0126	-16.75	0.000	1.00
IC*H_2O_2	-0.7341	-0.3670	0.0126	-29.03	0.000	1.00
ZeoSonFe*H_2O_2	0.0623	0.0311	0.0126	2.46	0.039	1.00
IC*ZeoSonFe*H_2O_2	-0.3696	-0.1848	0.0126	-14.62	0.000	1.00

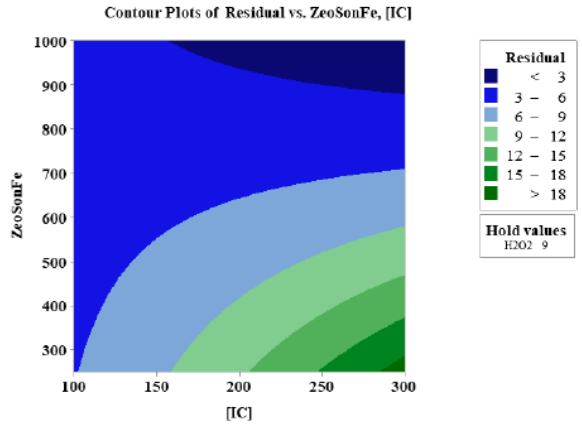

Figure 14. Residual contour Conditions: [IC]= 300 mg L^{-1}, Cat.= 1000 mg, H_2O_2 = 9 mmol

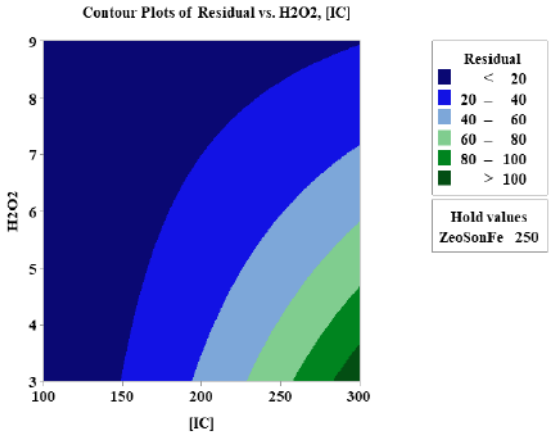

Figure 15. Residual contour Conditions: [IC]= 300 mg L^{-1}, Cat.= 250 mg, H_2O_2 = 9 mmol

4 Conclusions

The EDS analysis of the ZeoSonFe showed an increase in the Fe content compared to the ZeoSonSod, the Na^+ and Ca^{2+} are the cations that intervene in the exchange of Fe^{2+} because their percentage of them decreases (in % w). Oxidation Reduction Potential (ORP) at pH 3 showed a rapid increase in the first 20 min this is due to the generation of ($^{\bullet}$OH) radicals that are carrying out oxidation of IC. The optimum pH was 3, at this value the greatest degradation of the dye occurred, obtaining 6.00 ± 0.20 mg L^{-1} of residual IC in 120 min of treatment, since a very low pH (pH < 3) is associated with the existence of complex iron $[Fe(H_2O)_6]^{2+}$ and $[Fe(H_2O)_6]^{3+}$ species that react more slowly with H_2O_2. The statistical analysis will allow to optimize the materials necessary for the degradation of the IC in different conditions of concentration, on the other hand the synthesized catalyst allowed to obtain good catalytic activity in the generation of hydroxyl radicals; this material will allow its use in later works of advanced oxidation in organic pollutants.

Acknowledgements

To the Technological Institute of Toluca for the facilities and support for the development and dissemination of this research work, to the Mexican Council of Science and Technology (COMECyT) for its support in the program researchers for Mexico.

Nomenclature

SEM	Scanning Electron Microscopy
EDS	Energy Dispersion Spectroscopy
FTIR	Fourier Transform Infrared Spectroscopy
IUPAC	International Union of Pure and Applied Chemistry
IC	Indigo Carmine
AOPs	Advanced Oxidation Processes
ATR	Attenuated Total Reflection
($^{\bullet}$OH)	Hydroxyl Radicals
ORP	Oxide Reduction Potential
EPA	Environmental Protection Agency
$t_{1/2}$	Half-life Reaction Time
k_0, k_1	Constants of the Kinetics Reaction

References

Abhijith, A.R., Srivastava, A.K., Srivastava. (2020). Synthesis and characterization of magnesium doped ZnO using chemical route. *Journal of Physics: Conference Series*, *1*, 1531. http://dx.doi.org/10.1088/1742-6596/1531/1/012005

Ahmed, M.A., & Mohamed, A.A. (2017). An efficient adsorption of indigo carmine dye from aqueous solution on mesoporous Mg/Fe layered double hydroxide nanoparticles prepared by controlled sol-gel route. *Chemosphere*, *174*, 280-288. http://dx.doi.org/10.1016/j.chemosphere.2017.01.147

Ajibade, P.A., & Nnadozie, E.C. (2020). Synthesis and structural studies of manganese ferrite and zinc ferrite nanocomposites and their use as photoadsorbents for indigo carmine and methylene blue dyes. *ACS Omega*, *5*, 32386-32394. https://dx.doi.org/10.1021/

acsomega.0c04404

Arenas, C.N., Vasco, A., Betancur, M., Martínez, J.D. (2017). Removal of indigo carmine (IC) from aqueous solution by adsorption through abrasive spherical materials made of rice husk ash (RHA). *Process Safety and Environmental Protection*, *106*, 224-238. http://dx.doi.org/10.1016/j.psep.2017.01.013

Asaduzzaman, Md, Hasan, N., Begum, K., Hoque, S.M.Z. (2024). Degradation kinetics of lycopene from red amaranth & preparation of winter melon jelly using this lycopene and comparison with commercial jelly. *Heliyon*, *10*, e31135. https://doi.org/10.1016/j.heliyon.2024.e31135

Azizia, E., Darsanja, A., Zakeric, H., Ghayebzadehd, M., Heidaripoure, Z. (2020). A study of the variations of oxidation-reduction potential, pH, and dissolved oxygen during photo-Fenton oxidation of methyl tert-butyl ether in the presence of a nanosized zero-valent iron particle, hydrogen peroxide, and ultraviolet radiation. *Desalination and Water Treatment*, *196*, 238-246. https://doi.org/10.5004/dwt.2020.26044

Babuponnusami, A., & Muthukumar, K. (2014). A review on Fenton and improvements to the Fenton process for wastewater treatment. *Journal of Environmental Chemical Engineering*, *2*, 557-572. https://doi.org/10.1016/j.jece.2013.10.011

Barka, N., Abdennouri, M., Boussaoud, A., Galadi, A., Baâlala, M., Bensitel, M., Sahibed-Dine, A., Nohair, K., Sadiq, M. (2014). Full factorial experimental design applied to oxalic acid photocatalytic degradation in TiO_2 aqueous suspensión. *Arabian Journal of Chemistry*, *7*, 752-757. https://doi.org/10.1016/j.arabjc.2010.12.015

Barragán, P.P., Macedo M.M.G., Olguín, M.T. (2016). Cadmium sorption by sodium and thiourea-modified zeolite-rich tuffs. *Journal of Environmental*, *52*, 39-48. https://doi.org/10.1016/j.jes.2016.03.015

Baruah, M.J., Dutta, R., Zaki, M.E.A., Bania, K.K. (2024). Heterogeneous iron-based catalysts for organic transformation reactions: A brief overview. *Molecules*, *29*, 3177. https://doi.org/10.3390/molecules29133177

Basturk, E., & Karatas, M. (2015). Advanced oxidation of Reactive Blue 181 solution: A comparison between Fenton and Sono-Fenton Process. *Ultrasonics Sonochemistry*, *21*, 1881-1885. http://dx.doi.org/10.1016/j.ultsonch.2014.03.026

Bernal, M., Romero, R., Roa, G., Barrera, C.D., Torres, T.B., Natividad, R. (2013). Ozonation of índigo carmine catalyzed wIth Fe-pillared clay. *International Journal of Photoenergy*, *1*, 1-7. https://dx.doi.org/10.1155/2013/918025

Bhardwaj, D., Sharma, M., Sharma, P., Tomar, R. (2012). Synthesis and surfactant modification of clinoptilolite and montmorillonite for the removal of nitrate and preparation of slow release nitrogen fertilizer. *Journal of Hazardous Materials*, *227-228*, 292-300. https://doi.org/10.1016/j.jhazmat.2012.05.058

Biblioteca, I., Sambuccı, M., Valente, M. (2023). Zeolite-Clinoptilolite conditioning for improved heavy metals ions removal: A preliminary assessment. *Ceramics International*, *49*, 39649-39656. https://doi.org/10.1016/j.ceramint.2023.09.319

Boczkaj, G., & Fernandes, A. (2017). Wastewater treatment by means of advanced oxidation processes at basic pH conditions: A review. *Chemical Engineering Journal*, *320*, 608-633. http://dx.doi.org/10.1016/j.cej.2017.03.084

Castro-Peña, L., & Durán-Herrera, J. (2014). Degradation and decoloration of contaminated water with textile dyes using advanced oxidation processes. *Tecnología en Marcha*, *27*(2), 40-50.

Cosme-Torres, I., Macedo-Miranda, M.G., Martínez-Gallegos, S.M., González-Juárez, J.C., Roa-Morales, G., Illescas-Martínez, F.J., Jiménez-Becerril J. (2020). Synthesis of HTCMgFe for the degradation of indigo carmine through heterogeneous photo-Fenton treatment. *MRS Advances*, *5*, 3273-3282. https://doi.org/10.1557/adv.2020.421

Elhalil, A., Tounsandi, H., Elmoubarki, R., Mahjoubi, F.Z., Farnane, M., Sadiq, M., Abdennouri, M., Qourzal, S., Barka, S. (2016). Factorial experimental design for the optimization of catalytic degradation of malachite green dye in aqueous solution by Fenton process. *Water Resources and Industry*, *15*, 41-48. https://doi.org/10.1016/j.wri.2016.07.002

Gagol, M., Przyjazny, A., Boczkaj, G. (2018). Wastewater treatment by means of advanced oxidation processes based on cavitation - A review. *Chemical Engineering Journal*, *338*, 599-627. https://doi.org/10.1016/j.cej.2018.01.049

Ganiyu, S.O., Hullebusch, E.D., Cretin, M., Esposito, G., Oturan, M.A. (2015). Coupling of membrane filtration and advanced oxidation processes for removal of pharmaceutical residues: A critical review. *Separation and Purification Technology*, *156*, 891-914. https://doi.org/10.1016/j.seppur.2015.09.059

Genázio, P.C., Valoura, R.R., Pavesi, T., Mendes, E.S., Costa, J.M., Veríssimo, F.C. (2017). Lethal and sub-lethal evaluation of Indigo Carmine dye and by products after TiO_2 photocatalysis in the immune system of Eisenia andrei earthworms. *Ecotoxicology and Environmental Safety*, *143*, 275-282. http://dx.doi.org/10.1016/j.ecoenv.2017.05.043

Gonzales-Condori, E.G., Avalos-López, G., Gonzales-Condori, J., Mujica-Guzmán, A., Terán-Hilares, R., Briceño, G., Quispe-Avilés, J.M., Parra-Ocampo, P.J., Villanueva-Salas, J.A. (2023). Avocado seed powder residues as a promising bio-adsorbent for color removal from textile wastewater. *Revista Mexicana de Ingeniería Química*, *22*(3), IA2370. https://doi.org/10.24275/rmiq/IA2370

Hadi, M.D., Karimi, B., Sadege, M.R. (2016). The effect of aeration on advanced coagulation, flotation and advanced oxidation processes for color removal from wastewater. *Journal of Molecular Liquids*, *223*, 75-80. http://dx.doi.org/10.1016/j.molliq.2016.08.019

Hernández-Gordillo, A., Rodríguez-González, V., Oros-Ruiz, S., Gómez, R. (2016). Photodegradation of Indigo Carmine dye by CdS nanostructures under blue-light irradiation emitted by LEDs. *Catalysis Today*, *266*, 27-35. http://dx.doi.org/10.1016/j.cattod.2015.09.001

Huy, B.T., Paeng, D.S., Thao, C.T.B., Phuong, N.T.K., Yong-Ill, L. (2020). ZnO Bi_2O_3/graphitic carbon nitride photocatalytic system with H_2O_2-assisted enhanced degradation of Indigo carmine under visible light. *Arabian Journal of Chemistry*, *13*, 3490-3800. http://dx.doi.org/10.1016/j.arabjc.2019.01.003

Islam, M.S., & Mohr, B.J. (2023). Hydration kinetics of clinoptilolite zeolite blended ternary cementitious materials with fly ash and metakaolin. *Materials Today*. https://doi.org/10.1016/j.matpr.2023.03.468

Javaid. R., & Qazi, U.Y. (2019). Catalytic oxidation process for the degradation of synthetic dyes: An overview. *International Journal of Environmental Research and Public Health*, *16*, 2066. http://dx.doi.org/10.3390/ijerph16112066

Kasiri, M.B., Aleboyeh, H., Aleboyeh, A. (2008). Degradation of acid Blue 74 using Fe-ZSM5 zeolite as a heterogeneous photo-Fenton catalyst. *Applied Catalysis B: Environmental*, *84*, 9-15. http://dx.doi.org/10.1016/j.apcatb.2008.02.024

Khataee, A., Gholami, P., Vahid, B. (2016). Heterogeneous sono-Fenton-like process using nanostructured pyrite prepared by Ar glow discharge plasma for treatment of a textile dye. *Ultrasonics Sonochemistry*, *29*, 213-225. http://dx.doi.org/10.1016/j.ultsonch.2015.09.012

Leal-Perez, J.E., Almaral-Sanchez, J.L., Hurtado-Macias, A., Cortez-Valadez, M., Bórquez-Mendívil, A., García-Grajeda, B.A., Mendivil-Escalante, J.M., Flores-Valenzuela, J. (2024). Structural and chemical analysis of Zn ion exchange in thermally modified zeolite A4. *Revista Mexicana de Ingeniería Química*, *23*(3), Mat24264. https://doi.org/10.24275/rmiq/Mat24264

Mendes, E., Sousa, A., Forsin, D., de Paiva, D., Pavesi, T., Jimenez, M., Maldonado, M., Vieira, L., Costa, J. (2015). Photo-decolorization and ecotoxicological effects of solar compound parabolic collector pilot plant and artificial light photocatalysis of indigo carmine dye. *Dyes and Pigments*, *113*, 571-580. http://dx.doi.org/10.1016/j.dyepig.2014.09.029

Muhammad, R., Al-Muqati, N.S., Schulz, Axel., Alessa, A., Al-Otabi, Raja., Osman, A.I., Al-Fatesh, A.S. (2024). Temperature-induced modifications in natural zeolite clinoptilolite: effects on acidity and catalytic acetalization. *ChemNanoMat*, *10*, e202400041. https://doi.org/10.1002/cnma.202400041

Paukshtis, E.A., Yaranova, M.A., Batueva, I.S., Bal'zhinimaev, B.S. (2019). A FTIR study of silanol nests over mesoporous silicate materials. *Microporous and Mesoporous Materials*, *288*, 109582. https://doi.org/10.1016/j.micromeso.2019.109582

Phan, T.T.N., Nikoloski, A.N., Bahri, P.A., Li, D. (2018). Heterogeneous photo-Fenton degradation of organics using highly efficient Cu-doped $LaFeO_3$ under visible light. *Journal of Industrial and Engineering Chemistry*, *61*, 53-64. http://dx.doi.org/10.1016/j.jiec.2017.11.046

Pérez González N. K., Díaz Guzmán D., Vargas Ramírez M., Legorreta García F., Chávez Urbiola E.A., Trujillo Villanueva L.E., Ramírez Cardona, M. (2024). Interzeolite conversion of a clinoptilolite-rich natural zeolite into merlinoite. *Sociedad española de cerámica y vidrio*, *63*, 279-293. https://doi.org/10.1016/j.bsecv.2024.04.001

Quadrado, R.F.N., & Fajardo, A.R. (2017). Fast decolorization of azo methyl orange via heterogeneous Fenton and Fenton-like reactions using alginate-Fe^{2+}/Fe^{3+} films as catalysts. *Carbohydrate Polymers*, *177*, 443-450. http://dx.doi.org/10.1016/j.carbpol.2017.08.083

Reyes-Pérez, J.A., Roa-Morales, G., De León-Condes, C.A., Balderas-Hernández, P. (2023). Nanocomposites from spent coffee grounds and iron/zinc oxide: green synthesis, characterization, and application in textile wastewater treatment. *Water Science & Technology*, *88*(6), 1547-1563. https://doi.org/10.2166/wst.2023.285

Ristea, M. -E., & Zarnescu, O. (2023). Indigo carmine: between necessity and concern. *ournal of Xenobiotics*, *13*(3), 509-528. https://doi.org/10.3390/jox13030033

Ruíz-Baltazar, A.J. (2024). Advancements in nanoparticle-modified zeolites for sustainable water treatment: An interdisciplinary review. *Science of The Total Environment*, *946*, 174373. https://doi.org/10.1016/j.scitotenv.2024.174373

Samara, F., Hamid, A.A.A., Gopal, V., Dronjak, L., Feghaly, F., Kanan, S. (2025). Modified zeolites for the removal of emerging bio-resistive pollutants in water resources. *Catalysts*, *15*(2),138. https://doi.org/10.3390/catal15020138

Serna-Galvis, E.A., Arboleda-Echavarría, J., Echavarría-Isaza, A., Torres-Palma, R.A. (2024). Removal and elimination of pharmaceuticals in water using zeolites in diverse adsorption processes and catalytic advanced oxidation technologies - a critical review. *Environmental Science and Pollution Research*, *31*, 63427-63457. https://doi.org/10.1007/s11356-024-35204-7

Sirajudheen, P., & Meenakshi, S. (2019). Facile synthesis of chitosan-La^{3+}-graphite composite and its influence in photocatalytic degradation of methylene blue. *International Journal of Biological Macromolecules*, *133*, 253-261. http://dx.doi.org/10.1016/j.ijbiomac.2019.04.073

Yaman, C., & Gündüz, G. (2015). A parametric study on the decolorization and mineralization of C.I. Reactive Red 141 in water by heterogeneous Fenton-like oxidation over FeZSM-5 zeolite. *Journal of Environmental Health Science & Engineering*, *13*(7), 2-12. http://dx.doi.org/10.1186/s40201-015-0162-6

Yordanova, I., Hristov, S., Kolev, H., Todorova, S., Naydenov, A. (2023). Cobalt manganese ion-exchanged clinoptilolite supported catalysts for n-hexane oxidation. *Catalysis Today*, *423*, 114267. https://doi.org/10.1016/j.cattod.2023.114267

Vázquez-Romero, M., Abril-González, M., Pinos-Vélez, V., García-Zumalacarregui, J., Maldonado-Carchi, D., Miranda-Morales, D. (2024). Fenton process by volcanic ash to eliminate aniline of aqueous solution from the dyeing of toquilla straw crafts. *Revista Mexicana de Ingeniería Química*, *23*(2), Cat24238. https://doi.org/10.24275/rmiq/Cat24238

Zhu, F., Lu, G.P., Wang, F., Ren, E., Yu, Y., Lin, Y. (2023). Iron catalyzed organic reactions in water: A "Nature-Like" Synthesis. *Current Opinion in Green and Sustainable Chemistry*, *40*, 100754. https://doi.org/10.1016/j.cogsc.2023.100754

Vol. 24, No. 2(2025) IA25552
Revista Mexicana de Ingeniería Química

Association of pyocyanin and LED red-light irradiation (700 nm) on the biodegradation of waste lube oil

Asociación de la piocianina y la irradiación de luz roja LED (700 nm) en la biodegradación de aceite lubricante usado

H. Borchardt[1], R. Leite[1], A.A.P. Mendes[1], I.P.G. Amaral[2], U. Vasconcelos[3‡]
[1]*Universidade Federal da Paraíba, Centro de Biotecnologia, Campus I, João Pessoa, Paraíba, Brasil.*
[2]*Departamento de Biologia Celular e Molecular, Centro de Biotecnologia, UFPB, Via Ipê Amarelo s/n, Campus I, CEP 58051-900, João Pessoa, Paraíba, Brasil.*
[1]*Departamento de Biotecnologia, Centro de Biotecnologia, UFPB, Via Ipê Amarelo s/n, Campus I, CEP 58051-900, João Pessoa, Paraíba, Brasil.*
Sent date: March 18, 2025; Accepted: June 20, 2025

Abstract
Billions of liters of Waste Lube Oil (WLO) are produced every year and affect the environment. *Pseudomonas aeruginosa* is a versatile bacterium that can be used in processes to remove pollutants from the environment. Its bioactive pyocyanin (PYO) is a blue pigment with multiple cellular functions including a role in the assimilation of hydrocarbons. This study assessed the association of pyocyanin and LED light irradiation (700±10 nm) in the reduction of WLO by *P. aeruginosa* TGC04. Microcosms containing 45 mL of mineral medium combined with 5% WLO (v/v) were added to 5 mL of *P. aeruginosa* TGC04, suspended in 0,9% saline solution, adjusting the turbidity to Optical Density (OD) 0.4 at 600 nm, and different concentrations of PYO (0.1; 1.0 and 10.0 μg/mL). The microcosms were incubated at 29±1°C for 30 days under continuous LED light irradiation (700±10 nm). Control was carried out in the dark. WLO reduction was calculated by gravimetric method. Abiotic losses (≈ 10%) were determined with uninoculated microcosms. Light stimulated the inoculum, reducing the WLO from 17 to 55%. The process was PYO concentration-dependent and significantly influenced by the inoculum. There was an important correlation between PYO and WLO degradation by *P. aeruginosa* TGC04. In contrast, the interactions between light irradiation and PYO, as well as light irradiation alone, were insignificant possibly due to photoinactivation. These results highlight the biotechnological applicability of *P. aeruginosa* metabolites for *ex situ* bioremediation.
Keywords: Bioremediation, Oil hydrocarbons, *Pseudomonas aeruginosa*, Bioactive pigments.

Resumen
Billones de litros de aceite lubricante usado (WLO) se producen anualmente y afectan al medio ambiente. *Pseudomonas aeruginosa* es una bacteria metabólica versátil que puede utilizarse en procesos para eliminar contaminantes del ambiente. Su metabolito bioactivo, la piocianina (PYO), es un pigmento azul con múltiples funciones celulares, incluyendo la asimilación de hidrocarburos. Este estudio evaluó la asociación de la piocianina y la irradiación con luz LED (700±10 nm) en la reducción de WLO por *P. aeruginosa* TGC04. Se añadieron microcosmos con 45 mL de medio mineral combinado con 5 % de aceite lubrificante usado (v/v) a 5 mL de una suspensión de *P. aeruginosa* TGC04 (DO600 = 0,4) y diferentes concentraciones de PYO (0,1; 1,0 y 10,0 μg/mL). Los microcosmos se incubaron a 29±1°C durante 30 días bajo irradiación continua de luz LED (700±10 nm). El control se realizó en oscuridad. La reducción de WLO se calculó mediante un método gravimétrico. Se determinaron pérdidas abióticas (≈ 10 %) con microcosmos sin inocular. La luz estimuló el inóculo y la reducción de WLO fue del 17 al 55%. El proceso fue dependiente de la concentración de PYO y estuvo significativamente influenciado por el inóculo. Se observó una correlación importante entre la degradación de PYO y WLO por *P. aeruginosa* TGC04. Por el contrario, las interacciones entre la irradiación luminosa y PYO, así como la irradiación luminosa por sí sola, fueron insignificantes posiblemente debido a la fotoinactivación. Estos resultados destacan la aplicabilidad biotecnológica de los metabolitos de *P. aeruginosa* para la biorremediación *ex situ*.
Palabras clave: biorremediacíon, hidrocarburos de petróleo, *Pseudomonas aeruginosa*, pigmentos bioactivos.

‡*Corresponding author. E-mail*: u.vasconcelos@cbiotec.ufpb.br;
https://doi.org/10.24275/rmiq/IA25552
ISSN:1665-2738, *issn-e*: 2395-8472

1 Introduction

Lubricant oil plays a role in reducing friction between engine parts and cooling of their components, essential for their proper functioning. During these operations, the lubricant absorbs various contaminants and is subjected to physic-chemical and thermal processes that degrade its structure, ultimately leading to oil breakdown and the formation of waste lube oil (WLO) (Rațiu *et al*., 2021). In the beginning of this decade, more than 30 billion liters were accumulated annually (Ghannam *et al*., 2021). In WLO spills, serious damage is done to the environment, affecting both terrestrial and aquatic ecosystems (Nowak *et al*., 2019). The accumulation of petroleum products in the environment can have far-reaching impacts, including high toxicity to living organisms, compromising water and soil quality, and harm to the physical, chemical, and microbiological conditions of the ecosystem, leading to long-term ecological damage (Peraza-Liñan *et al*., 2025). WLO may be also derived from chemical compounds produced from petroleum, often associated with base oils like mineral oil. Its composition includes aliphatic and aromatic hydrocarbons, such as phenol, naphthalene, benzo[a]pyrene, benzo[a]anthracene, and fluoranthene, which are significant agents in environmental contamination (Taleshpur *et al*., 2025; Ishaya *et al*., 2023; Imam *et al*., 2022).

Pseudomonas aeruginosa is widely distributed in nature and can degrade a wide range of pollutants. Even though *P. aeruginosa* is well known as an opportunistic pathogen related to nosocomial infections (Rodrigues-Recio *et al*., 2025), there are many reports on its capacity to degrade a wide range of hydrocarbons (Hu *et al*., 2023, Muthukumar *et al*., 2023; Ojewumi *et al*., 2018). Given the fact of *P. aeruginosa* dominates oil-contaminated sites, it is renowned as a keystone species in the hydrocarbon degradation processes (Centler *et al*., 2020). Additionally, the non-pathogenic nature of most strains of *P. aeruginosa* recovered from hostile environments has created industrial interest because these strains do not exhibit a serious level of risk to the environment (Jose *et al*., 2018). This has encouraged the use of *P. aeruginosa* in a wide range of biotechnological processes such as bioremediation and production of biosurfactants, biopolymers and pigments (Ruiz-Hernandes *et al*., 2024; Khan, 2022).

P. aeruginosa also synthetizes pyocyanin (PYO), a water-soluble blue phenazine with redox potential (El-Fouly al., 2015). Some studies have suggested that PYO may be useful in hydrocarbon biodegradation by *P. aeruginosa* (Das and Das, 2015; Norman *et al*., 2004). PYO acts as a signaling molecule that modulates multiple functions in the cell, resulting in hydrocarbon metabolization. PYO regulates the synthesis of rhamnolipids (Das and Ma, 2013) as response to the nutritional stress caused by the C:N ratio disbalance caused by an oil spill (Bahari *et al*., 2017). In addition, PYO as an electron acceptor reacts with molecular oxygen forming free radicals that promote nucleophilic attacks on hydrocarbons. Thus, PYO favors transformation and enhances the bioavailability of persistent hydrocarbons (Unglaube *et al*., 2020).

Good results may be achieved using bioremediation associated with abiotic methods such as ultrasound (Zhang and Zhuang, 2024) and phosphate-free mineral detergent (Saucedo-Martínez *et al*., 2023). Photodegradation enhances the kinetics and efficiency of the bioremediation process (Al-Ansari, 2021). Photolysis is an abiotic degradation of molecules either by the absorbed radiant energy of light, or by the reaction initiated by other light absorbing compounds (Kaing *et al*., 2024). Photodegradation methods mainly rely on the use of photons produced from natural sunlight or artificial lights, e.g., ultraviolet and fluorescent lamps. Absorption of radiant energy from photons can trigger physicochemical changes at the molecular level, enhancing their susceptibility to degradation (Sarker and Ahn, 2022).

Photodegradation is also the main abiotic environmental fate of hydrocarbons in nature and two mechanisms of action are addressed. First, a direct transformation based on hydrocarbons absorbs ultraviolet and visible light wavelengths (Frena *et al*., 2014). The second mechanism involves the formation of photosensitizer metabolites that react with hydrocarbons in the vicinity (Bacosa *et al*., 2015a).

By assuming that PYO absorbs light at 690 nm (Parsons *et al*., 2007), we hypothesized that Light Emitting Diode (LED) red-light irradiation could contribute to hydrocarbon degradation by triggering photolysis and increasing the hydrocarbon bioavailability to *P. aeruginosa* TGC04 because light irradiation would also cause PYO to become more reactive. Therefore, this work aimed to assess synergistic interaction of these elements in the reduction of WLO.

2 Material and Methods

2.1 Pseudomonas aeruginosa

The inoculum was prepared with the non-pathogenic wild-type strain *P. aeruginosa* TGC04, recovered from soil samples at a gas station in the city of João Pessoa, Brazil. The strain is registered in the Brazilian registry

of genetic heritage and associated knowledge (SisGen in Portuguese, access number A404D65) and in the UFPEDA culture collection (1063B). The strain was maintained on cetrimide agar.

2.2 *Pyocyanin production*

PYO is a secondary metabolite naturally synthesized by *P. aeruginosa* strains under nutritional stress (Whooley and McLoughlin, 1982). The pre-inoculum of *P. aeruginosa* TGC04 was prepared on cetrimide agar and incubated for 48 h at 29±1°C. Afterwards, the cells from the fresh culture were suspended in 0.9% NaCl saline solution, adjusting the turbidity to Optical Density (OD) 0.4 at 600 nm (Mojsoska *et al.*, 2021). Aliquots of 5 ml of this suspension were transferred to 1000 mL flasks containing 500 ml of King A broth. These flasks were incubated at 29±1°C for 72 h. Then, the aqueous phase was mixed with chloroform (5:1 v/v) and vortexed for 1 min. The blue organic phase was separated and acidified with 0.2 mol/L HCl (2:1 v/v) and vortexed for 1 min. The red acidified phase containing the protonated PYO was neutralized by few drops of 1.5 mol/L Tris-HCl buffer solution, restoring the blue color (Peruzzo *et al.*, 2021). OD was measured at 690 nm (Kasvi, 320-1020 nm, 4NM) and PYO concentration (µg/mL) was determined by using Equation 1, obtained from a standard curve prepared by using different concentrations (0.005-0.035 mg/mL) of PYO 98% HPLC purity (sigma-Aldrich, Saint Louis, USA) hydroalcoholic solutions (1:10) with OD measured at 520 nm (R^2 = 0.999).

$$\text{PYO } (\mu\text{g/mL}) = (8.9968 \times \text{OD}_{690}) + 0.00004 \quad (1)$$

2.3 *Biodegradation tests*

For the biodegradation tests, there were two operational factors: light irradiation, and concentration of PYO. Two and three settings were selected, respectively, for the first and the second factor. A complete experimental design for testing all combinations of the settings and their replicates entailed 48 experiments.

Throughout the experiment, the LED red-light irradiation (700±10 nm) was continuously used. The light irradiation apparatus consisted of a closed cabin measuring 50 x 30 cm with a LED lamp (A60-E27-3-RGB-3B; 100-240 V; 60 Hz; 3 W), 13 cm distant from the microcosm lower side, exposing the system to 160.55±2.30 mW/mm^2. The control group was maintained in the dark.

Transparent polypropylene microcosms with a total capacity of 80 mL (60 × 55 mm) were filled with 45 mL of minimum mineral, composed of (g/L): K_2HPO_4 (0.5), $(NH_4)_2SO_4$ (0.5), $MgSO_4$ (0.5), $FeCl_2$ (0.01), $CaCl_2$ (0.01), $MnCl_2$ (0.0001), $ZnSO_4$ (0.0001), supplemented with 0.1 g of yeast extract and one drop of vitamin B complex solution, pH 7.2 ± 0.2 (Palittapongarnpim *et al.*, 1998). To the medium was added 2.5 mL of a mixture of WLO previously characterized (Table 1), containing 448,000 mg/Kg of the TPH.

Sixteen conditions were tested with three variables: concentration of PYO (0.1; 1.0 and 10.0 µg/mL), and with the presence or absence of LED light irradiation, as summarized in Table 2. Hydrophilic cotton pads were placed (so as not to seal) on the top of the microcosms to provide microbial respiration and avoid oil volatilization. There was no additional oxygen available to microcosms. The systems were incubated statically for 30 days at 29±1ºC. As for the control, four conditions were tested, as follows: with and without inoculum (abiotic), irradiated and unirradiated.

2.4 *Determination of hydrocarbon biodegradation*

The test was carried out using the gravimetric method (Almutairi, 2022). The mass (g) of WLO was calculated by Equation 2:

$$\% = \left(\frac{P_0 - P_1}{P_0}\right) \times 100 \quad (2)$$

Where P_0 = initial mass; and P_1 = final mass (Shimadzu, ATY224).

2.5 *Statistical analysis*

All experiments were carried out in triplicate and results are presented as the average ± standard deviation. All statistics were performed in R (version 4.2.1) in R Studio (2023.06.1 Build 524). First, the data were analyzed for normality and homoscedasticity based on the results of the Shapiro-Wilk and Levene tests respectively. Then, two-way ANOVA followed by Tukey's post-hoc test, with p-value corrected for multiple comparisons using the "false discovery rate" method was carried out. The significance value was 0.05 for all tests.

3 Results, tables and figures

The TPH content reached 448,000 mg/L and, because of the mixed nature of the WLO, the lubricant fraction represented 99.3% of the TPH. The remaining portion contained other hydrocarbon fractions, Polycyclic Aromatic Hydrocarbons (PAHs), water and impurities. Three PHAs from incomplete hydrocarbon combustion were detected, as follows: the majority of two light

Table 1. Settling Time for Hydrogen Production in Different Phases of Digestion.

Parameter	Result	Reference
Density (g/cm^3)	0.8651	ASTM D1298-12b
Total solids (%)	97.4	ASTM D874-23
TPH (mg/Kg)	448,000.0	
Gasoline (C8-C11)	< 10,226.0	
Kerosene (C11-C14)	< 10,226.0	USEPA 8015D
Diesel (C14-C20)	< 10,226.0	
Lubricating oil (C20-C40)	445,000.0	
16 EPA priority PAHs (mg/Kg)	50.1	
Naphthalene (mg/Kg)	45.3	USEPA 8270C
Pyrene (mg/Kg)	2.7	
Phenanthrene (mg/Kg)	2.1	

EPA – US environmental protection agency.

Table 2. Test conditions for biodegradation of WLO by *P. aeruginosa* TGC04

Condition	Pyocyanin(µg/mL)	Light (700±10 nm)	Inoculum (5% v/v)	Biodegradation (%)
1	0.0	+	+	32.27±0.03
2	0.0	–	+	13.34±0.09
3	0.0	+	–	9.86±0.17
4	0.0	–	–	1.79±0.10
5	0.1	+	+	51.32±0.23
6	0.1	–	+	48.00±0.11
7	0.1	+	–	17.43±0.01
8	0.1	–	–	23.94±0.01
9	1.0	+	+	44.05±0.05
10	1.0	–	+	40.12±0.15
11	1.0	+	–	19.73±0.01
12	1.0	–	–	24.53±0.01
13	10.0	+	+	55.23±0.13
14	10.0	–	+	52.40±0.11
15	10.0	+	–	21.64±0.01
16	10.0	–	–	26.08±0.01

PAHs, naphthalene and phenanthrene; and one heavy PAH pyrene (Table 1). *P. aeruginosa* TGC04 grown in the presence of WLO was positive and the strain produced 32 μg/mL of PYO. Additionally, a dense biofilm surrounding the bottom oil layer was observed. The biofilm layer was up to about twice the oily phase in height, as seen in Figure 1.

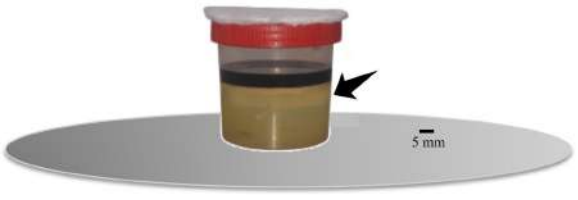

Figure 1. Appearance of the microcosm, highlighting a dense biomass at the oil phase-aqueous phase interface contributing to emulsify the WLO (arrow). The more biofilm formed, the more degradation of the WLO.

Changes in the visual appearance of the WLO were observed during the process, from a dense and dark homogeneous fluid into an emulsified light brownish product. Table 2 shows that after 30 days of incubation, there was a reduction of oil between ≈ 13 and 55% (abiotic loss ≈ 11%). Statistical analysis indicated that the main effect of inoculum size was significant ($p < 0.001$). When evaluated alone, the inoculum achieved a biodegradation rate of 13.34±0.09%. Nevertheless, under LED red-light irradiation (700±10 nm), this rate increased to 32.27±0.03%, demonstrating that the interaction between light and inoculum size was significant ($p = 0.039$). Additionally, the main effect of PYO was significant ($p < 0.001$), with a degradation between ≈ 24 and 26% when tested alone. When combined with the inoculum, however, the degradation rate increased significantly, between ≈ 48 up to 52% in the sample with a higher PYO concentration. Thus, interaction between the variables of inoculum size and pyocyanin was statistically significant when

concentration-dependent (p = 0.010). In contrast, the other evaluated parameters did not yield statistically significant results, i.e., the interactions between light and PYO (p = 0.816); and the interactions between light, inoculum size, and PYO (p = 0.984); as well as the main effect of light alone (p = 0.268) (Figure 2 and Table 3).

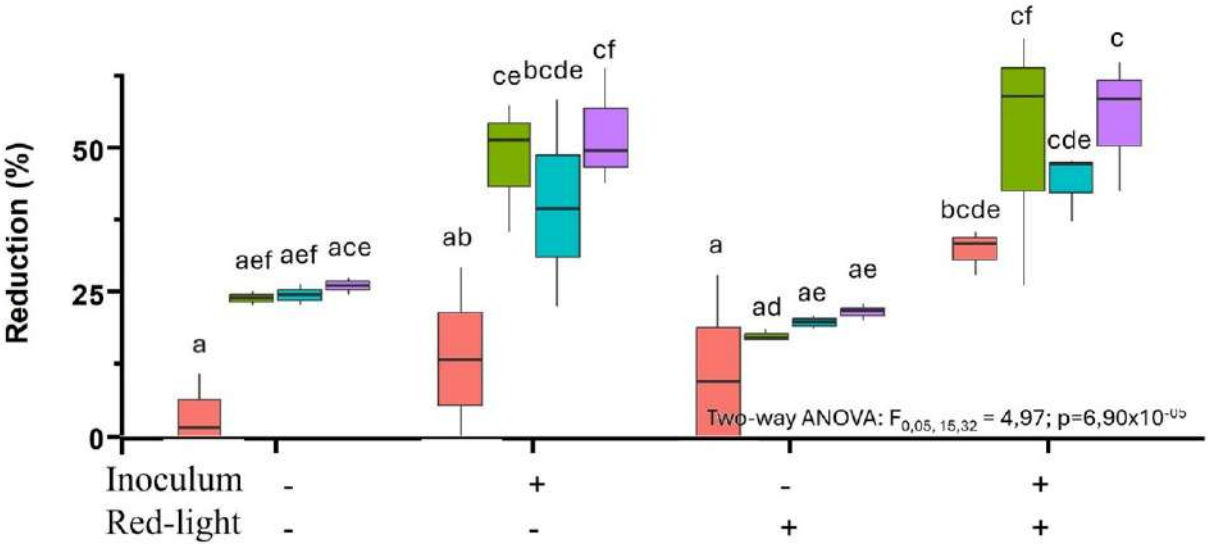

Figure 2. Reduction of WLO in relation to the initial mass after 30 days. The different colors in the graph indicate the different concentrations of pyocyanin (orange = 0.0; green = 0.1; blue = 1.0; and purple = 10.0 μg/mL) tested and the letters indicate the statistical differences obtained. Below is an indication of which test group presents inoculum and/or red-light irradiation (700±10 nm). Abiotic loss = 11.75±0.20%.

Table 3. ANOVA and estimated parameters

Factor	Sum Sq	Df	F value	*p*-value	
LT	28.04	1	1.2686	0.26841	-
Ino	2181.20	1	98.6640	2.67×10^{-11}	***
PYO	1211.49	3	18.2667	4.345×10^{-7}	***
LT:Ino	102.11	1	4.6189	0.03929	*
LT:PYO	20.72	3	0.3124	0,81627	-
Ino:PYO	292.97	3	4.4174	0,01043	*
LT:Ino:PYO	3.44	3	0.0519	0.98410	-

LT: light; Ino: Inoculum; PYO: pyocyanin 0 (***); > 0.01 (*); > 0.1 (-)

4 Discussion

WLO can cause hydrocarbon contamination; its persistent nature and its derivatives poses a severe threat to both human health and environmental safety (Benguenab and Chibani, 2021). This study aimed to evaluate how the association with a physicochemical method may be positive for the biodegradation of WLO by *P. aeruginosa* TGC04. Further, it assessed the impact of visible red-light irradiation (700±10 nm) on the reduction of this pollutant. PYO exhibits two peaks of light absorption, at ultraviolet and visible light bands (Reszka *et al*., 2004). As the study aimed to use reactive PYO in oxidant conditions under safe wavelength irradiation, a LED lamp with an available wavelength close to 690 nm was used. We supposed that phenazine would be integrated into the process since PYO is a redox and bioactive compound important to several functions in *P. aeruginosa*, such as biofilm formation (Pierson and Pierson, 2010), a crucial factor involved in hydrocarbon biodegradation (Dasgupta *et al*., 2013). PYO plays a role in regulating the synthesis of the biosurfactant in *P. aeruginosa*. Moreover, PYO also interacts directly with biosurfactant metabolism since it enhances the emulsification potential of *P. aeruginosa* isolates (Das and Ma, 2013). Previous studies from our group have reported that PYO participates as an inducer of molecules that emulsify different hydrocarbons even in low concentrations (Viana *et al*., 2018). The more PYO produced by the strain, the more polycyclic aromatic hydrocarbons were reduced (Cavalcanti *et al*., 2019). In addition, we

also have observed that exogenous phenazines (PYO and phenazine methosulphate) added to encompassed inoculum of *P. aeruginosa* contributed to the removal of principally 4-6 ring PAHs (Viana *et al*., 2024).

In addition, the redox-active nature of PYO engages in electron transfer reactions, playing a pivotal role in the generation of Reactive Oxygen Species (ROS) such as superoxide and hydrogen peroxide (Saini *et al*., 2025). This could explain the significance of the variable PYO since electrochemical oxidation process increase electron transfer capacity of the organic matter. The result is an increase of WLO bioavailability as reported in previous studies with different redox compounds, e.g., humic-like substances (Deng *et al*., 2020).

Visible light-induced photocatalysis and biodegradation have been used to treat some areas (Sarkar, 2023). Light irradiation in the red spectral range promotes microbial growth (Yeh *et al*., 2014). We assumed that the application of LED red-light irradiation (700±10 nm) would be incorporated into the system as a complementary strategy to stimulate *P. aeruginosa* TGC04 to degrade WLO. This assumption was supported by the fact that variable interaction of red-light irradiation (700±10 nm) and the inoculum size have a subtle statistical significance in the biodegradation of WLO. This is further reinforced by evidence that microbes can perceive differences in light quality and can also perceive differences in light intensity with respect to red and blue light bands (Beattie *et al*., 2018). According to Crugeira *et al*. (2019), LED red-light irradiation significantly enhanced catabolic responses of a microbial consortium in their study on degradation of a textile dye. Differently from this present work, only the consortium was treated by LED red-light-irradiation.

Light may enhance biological treatment as well as abiotic transformation of persistent molecules (Sutar *et al*., 2020; Bacosa *et al*., 2015b). Sensory photoreceptors in microorganisms play a role in converting the absorbed photons into chromophore biological changes, which can include alterations in enzymatic activity or interactions with other macromolecules (Elahi and Matthew, 2024). Crugeira *et al*. (2018) reported that photostimulation by LED red-light promoted a 2.0-2.5-fold increase of cellular proliferation in a thermophilic microbial consortium due to microbial cytochrome absorption in this band. As well, there was an increase in intracellular ATP levels which activated metabolic events involving cellular proliferation. Thus, we presumed that intermittent photostimulation would support the growth of *P. aeruginosa* TGC04 influenced by red-light irradiation, as in the present study.

LED red-light irradiation (700±10 nm) acted in the degradation of the hydrocarbons present in the WLO. This was possibly because during the photocatalytic degradation process, the electrons in the valence band of photocatalysts can be excited to the conduction band and release protons (H+) after collecting photons from a light source such as the LED light used in the experiment. The electrons and protons may react with molecular oxygen and generate ROS which subsequently react with hydrocarbons and increase their bioavailability (Rayaroth *et al*., 2023; Zhang *et al*., 2022). Based on the findings of this present study we speculate that the energy emitted by the LED lamp was not capable of provoking a significant breakdown of the hydrocarbons of the WLO. In contrast, red-light LED was found suitable for the biofilm growth and both inoculum and PYO played a crucial role in the process.

On the other hand, some heavy hydrocarbons exposed to light at ≈ 700 nm may act as photosensitizers and can lead the oxidation of PYO (Reszka *et al*., 2006). This oxidation *per se* is irreversible and effectively inactivates PYO by producing 1-hydroxyphenazine (Mudaliar and Prasad, 2024). Additionally, even though a small fraction of PYO could be oxidized, the stimulation of microbiota by light irradiation compensated for the losses of PYO by inactivation and the amount of abiotic loss reinforced this claim.

In addition, in all concentrations of PYO tested, a dense layer formed by the biofilm was observed. PYO is an important factor for cell aggregation in *P. aeruginosa* (Jabłońska *et al*., 2023). Under stressful nutritional conditions, *P. aeruginosa* may promote auto-poisoning of the planktonic cells and PYO in the reduced state mediate cell lysis and release of eDNA, influencing biofilm structure and stability (Meirelles and Newman, 2018). As well, an approximately 400 μm layer with high gradient of reduced state PYO is maintained close by the upper surface within the biofilm (Koley *et al*., 2011). We hypothesized that this behavior contributed to viable cells degrading the WLO.

Despite a growing interest in the knowledge of photodegradation of organic pollutants in the natural environment, studies using specific visible-light wavelength are still limited (Guo, *et al*. 2023). The level of significance associated with the variables of inoculum size and pyocyanin have indicated their crucial role in the process, confirming that strategies based on these factors can optimize biodegradation of hydrocarbons. Despite the advances in understanding PYO as a molecule, its association with light energy and the use of *P. aeruginosa* in bioremediation remains

poorly explored. Additionally, the environmental agenda required the development of sustainable approaches to solve urgent demands. This present study, for instance, calls for a possible *ex situ* application. Amounts of oily waste transferred from in-shore oil-spilled zones could be treated at industrial plants, replacing common hazardous treatments for these cases, such as incineration.

Conclusions

Under the experimental conditions carried out in this study, both variables, inoculum size and pyocyanin, alone or associated, were pivotal for optimizing the biodegradation of WLO by *P. aeruginosa* TGC04. The effect of PYO on the process was concentration-dependent under the assumption that part of PYO may be inactivated by light. In contrast, variable light irradiation (700±10 nm) exhibited some effect when combined with the inoculum and did not show a significant impact when used alone. Our findings highlight the potential for the use of microbial bioactive metabolite and renewable energy combined to provide *ex situ* bioremediation substituting treatments that negatively impact the environment. Further studies may elucidate all the mechanisms involved.

Acknowledgements

The authors want to thank to CNPq and Federal University of Paraíba for the financial support (project ID: PVI16295-2023; PIBIC/UFPB/CNPq - EDITAL 01/2023/PROPESQ). The English text of this paper has been revised by Sidney Pratt, Canadian, MAT (The Johns Hopkins University), RSAdip - TESL (Cambridge University).

Nomenclature

LED	Light Emitting Diode
OD	Optical Density
PAHs	Polycyclic Aromatic Hydrocarbons
PYO	Pyocyanin
ROS	Reactive Oxygen Species
TPH	Total Petroleum Hydrocarbons
UFPEDA	UFPE Department of Antibiotics
WLO	Waste Lube Oil

References

Al-Ansari, M. (2022). Influence of blue light on effective removal of arsenic by photosynthetic bacterium Rhodobacter sp. BT18. *Chemosphere*, *292*, 133399. https://doi.org/10.1016/j.chemosphere.2021.133399

Almutairi, M. S. (2022). Determination of total petroleum hydrocarbons (TPHs) in weathered oil contaminated soil. *Environmental Engineering Research*, *27*(5). https://doi.org/10.4491/eer.2021.324

ASTM. (2017). *D1298-12b. Standard test method for density, relative density, or API gravity of crude petroleum and liquid petroleum products by hydrometer method*. New York, USA.

ASTM. (2023). *D874-23. Standard test method for sulfated ash from lubricating oils and additives*. New York, USA.

Bacosa, H. P., Erdner, D. L., & Liu, Z. (2015a). Differentiating the roles of photooxidation and biodegradation in the weathering of Light Louisiana Sweet crude oil in surface water from the Deepwater Horizon site. *Marine Pollution Bulletin*, *95*, 265-272. https://doi.org/10.1016/j.marpolbul.2015.04.005

Bacosa, H. P., Liu, Z., & Erdner, D. L. (2015b). Natural sunlight shapes crude oil-degrading bacteria communities in northern Gulf of Mexico surface waters. *Frontiers in Microbiology*, *6*, 1325. https://doi.org/10.3389/fmicb.2015.01325

Bahari, S., Zeighami, H., Mirshahabi, H., Roudashti, S., & Haghi, F. (2017). Inhibition of Pseudomonas aeruginosa quorum sensing by subinhibitory concentrations of curcumin with gentamicin and azithromycin. *Journal of Global Antimicrobial Resistance*, *10*, 21-28. https://doi.org/10.1016/j.jgar.2017.03.006

Beattie, G. A., Hatfield, B. M., Dong, H., & McGrane, R. S. (2018). Seeing the light: The roles of red-and blue-light sensing in plant microbes. *Annual Review of Phytopathology*, *56*, 41-66. https://doi.org/10.1146/annurev-phyto-080417-045931

Benguenab, A., & Chibani, A. (2021). Biodegradation of petroleum hydrocarbons by filamentous fungi (Aspergillus ustus and Purpureocillium lilacinum) isolated from used engine oil contaminated soil. *Acta Ecologica Sinica*, *41*, 416-423. https://doi.org/10.1016/j.chnaes.2020.10.008

Cavalcanti, T. G., Souza, A. F., Ferreira, G. F., Dias, D. S. B., Severino, L. S., Morais, J. P. S., Sousa, K. A., & Vasconcelos, U. (2019). Use of agroindustrial waste in the removal of phenanthrene and pyrene by

microbial consortia in soil. *Waste & Biomass Valorization*, *10*, 205-214. https://doi.org/10.1007/s12649-017-0041-8

Centler, F., Günnigmann, S., Fetzer, I., & Wendeberg, A. (2020). Keystone species and modularity in microbial hydrocarbon degradation uncovered by network analysis and association rule mining. *Microorganisms*, *8*(2), 190. https://doi.org/10.3390/microorganisms8020190

Crugeira, P. J. L., Santos, G. M. P., Oliveira, S. C. P. S., Sampaio, F. J. P., Correia, N. A., Fagnani, S. R. C. A., Chinalia, F. A., Almeida, P. F., & Pinheiro, A. L. B. (2018). Photobiological effect of Laser or LED light in a thermophilic microbial consortium. *Journal of Photochemistry and Photobiology B: Biology*, *181*, 115-121. https://doi.org/10.1016/j.jphotobiol.2018.03.006

Crugeira, P. J. L., Santos, G. M. P., Oliveira, S. C. P. S., Sampaio, F. J. P., Fagnani, S. R. C. A., Sampaio, I. C. F., Ferreira, E. S., Chinalia, F. A., & Pinheiro, A. L. B. (2019). Effects of photostimulation on the catabolic process of xenobiotics. *Journal of Photochemistry and Photobiology B: Biology*, *191*, 38-43. https://doi.org/10.1016/j.jphotobiol.2018.12.004

Das, S., & Das, P. (2015). Effects of cultivation media components on biosurfactant and pigment production from Pseudomonas aeruginosa. *Brazilian Journal of Chemical Engineering*, *32*, 317–324. https://doi.org/10.1590/0104-6632.20150322s00003262

Das, P., & Ma, L. Z. (2013). Pyocyanin pigment assisting biosurfactant-mediated hydrocarbon emulsification. *International Biodeterioration & Biodegradation*, *85*, 278-283. https://doi.org/10.1016/j.ibiod.2013.07.013

Dasgupta, D., Ghosh, R., & Sengupta, T. K. (2013). Biofilm-mediated enhanced crude oil degradation by newly isolated Pseudomonas species. *International Scholarly Research Notices*, *2013*, 250749. https://doi.org/10.5402/2013/250749

Deng, Y., Wen, J., Zhu, X., Chen, N., Feng, C., Zheng, Y., Wang, H., Chen, F., & Guo, Y. (2020). Research on the redox behavior changes of humic-like substances wastewater during electrochemical oxidation process and using the treated effluent to improve the heavily contaminated soil: Taking petroleum hydrocarbon contaminated soil as example. *Journal of Cleaner Production*, *263*, 121398. https://doi.org/10.1016/j.jclepro.2020.121398

El-Fouly, M. Z., Sharaf, A. M., Shahin, A. A. M., El-Bialy, H. A., & Omara, A. M. A. (2015). Biosynthesis of pyocyanin pigment by Pseudomonas aeruginosa. *Journal of Radiation Research and Applied Sciences*, *8*(1), 36–48. https://doi.org/10.1016/j.jrras.2014.10.007

Elahi, Y., & Baker, M. A. B. (2024). Light control in microbial systems. *International Journal of Molecular Sciences*, *25*(7), 4001. https://doi.org/10.3390/ijms25074001

Frena, M., Oliveira, C. R., Silva, C. A., Madureira, L. A. S., & Azevedo, D. A. (2014). Photochemical degradation of diesel oil in water: a comparative study of different photochemical oxidation processes and their degradation by-products. *Journal of the Brazilian Chemical Society*, *25*(7), 1372-1379. https://doi.org/10.5935/0103-5053.20140119

Ghannam, M. T., Selim, M. Y. E., Khedr, M. A. M., Bin Taleb, N. A. G., & Kaalan, N. R. (2021). Investigation of the rheological properties of waste and pure lube oil. *Fuel*, *298*, 120774. https://doi.org/10.1016/j.fuel.2021.120774

Guo, Z., Kodikara, D., Albi, L. S., Hatano, Y., Chen, G., Yoshimura, C., & Wang, J. (2023). Photodegradation of organic micropollutants in aquatic environment: Importance, factors and processes. *Water Research*, *231*, 118236. https://doi.org/10.1016/j.watres.2022.118236

Hu, F., Wang, P., Li, Y., Ling, J., Ruan, Y., Yu, J., & Zhang, L. (2023). Bioremediation of environmental organic pollutants by Pseudomonas aeruginosa: Mechanisms, methods and challenges. *Environmental Research*, *15*, 117211. https://doi.org/10.1016/j.envres.2023.117211

Imam, A., Suman, S. K., Kanaujia, P. K., & Ray, A. (2022). Biological machinery for polycyclic aromatic hydrocarbons degradation: A review. *Bioresource Technology*, *343*, 126121. https://doi.org/10.1016/j.biortech.2021.126121

Ishaya, S., Usman, S., Nweke, O. D., Adams, N. H., Umar, R., Ilyasu, N. S., Jagaba, A. H., Atangwho, I. J., & Yakasai, H. M. (2023). Degradation of used engine oil by Alcaligenes sp. strain isolated from oil contaminated site: Isolation, identification, and optimization of the growth parameters. *Case Studies in Chemical and Environmental*

Engineering, *8*, 100516. https://doi.org/10.1016/j.cscee.2023.100516

Jabłońska, J., Augustyniak, A., Dubrowska, K., & Rakoczy, R. (2023). The two faces of pyocyanin – why and how to steer its production? *World Journal of Microbiology and Biotechnology*, *39*(4), 103. https://doi.org/10.1007/s11274-023-03548-w

Jose, D., Mohandas, A., & Singh, I. S. B. (2018). A non-pathogenic environmental isolate of Pseudomonas aeruginosa MCCB 123 with biotechnological potential. *International Journal of Current Microbiology and Applied Sciences*, *7*(1), 3060-3071. https://doi.org/10.20546/ijcmas.2018.701.363

Kaing, V., Guo, Z., Sok, T., Kodikara, D., Breider, F., & Yoshimura, C. (2024). Photodegradation of biodegradable plastics in aquatic environments: Current understanding and challenges. *Science of the Total Environment*, *911*, 168539. https://doi.org/10.1016/j.scitotenv.2023.168539

Khan, N. T. (2022). Pseudomonas aeruginosa in industries. *Journal of Pharmaceutical Sciences and Drug Development*, *4*(2), 1-2. https://doi.org/10.37532/jpsdd.22.4.2.1-2

Koley, D., Ramsey, M. M., Bard, A. J., & Whiteley, M. (2011). Discovery of biofilm electrocline using real-time 3D metabolite analysis. *Proceedings of the National Academy of Sciences*, *108*(50), 19996-20001. https://doi.org/10.1073/pnas.1117298108

Meirelles, L. A., & Newman, D. K. (2018). Both toxic and beneficial effects of pyocyanin contribute to the lifecycle of Pseudomonas aeruginosa. *Molecular Microbiology*, *110*(6), 995-1010. https://doi.org/10.1111/mmi.14132

Mojsoska, B., Ghoul, M., Perron, G. G., Jenssen, H., & Alatraktchi, F. A. A. (2021). Changes in toxin production of environmental Pseudomonas aeruginosa isolates exposed to sub-inhibitory concentrations of three common antibiotics. *PLoS One*, *16*(3), e0248014. https://doi.org/10.1371/journal.pone.0248014

Mudaliar, S. B., & Prasad, A. S. B. (2024). A biomedical perspective of pyocyanin from Pseudomonas aeruginosa: its applications and challenges. *World Journal of Microbiology and Biotechnology*, *40*(3), 90. https://doi.org/10.1007/s11274-023-03889-0

Muthukumar, B., Surya, S., Sivakumar, K., Alsalhi, M. S., Rao, T. N., Devanesan, S., Arunkumar, P., & Rajasekar, A. (2023). Influence of bioaugmentation in crude oil contaminated soil by Pseudomonas species on the removal of total petroleum hydrocarbon. *Chemosphere*, *310*, 136826. https://doi.org/10.1016/j.chemosphere.2022.136826

Norman, R. S., Moeller, P., McDonald, T. J., & Morris, P. J. (2004). Effect of pyocyanin on a crude-oil-degrading microbial community. *Applied and Environmental Microbiology*, *70*(7), 4004-4011. https://doi.org/10.1128/AEM.70.7.4004-4011.2004

Nowak, P., Kucharska, K., & Kamiński, M. (2019). Ecological and health effects of lubricant oils emitted into the environment. *International Journal of Environmental Research and Public Health*, *16*(16), 3002. https://doi.org/10.3390/ijerph16163002

Ojewumi, M. E., Anenih, E. V., Taiwo, O. S., Adekeye, B. T., Awolu, O. O., & Ojewumi, E. O. (2018). A bioremediation study of raw and treated crude petroleum oil polluted soil with Aspergillus niger and Pseudomonas aeruginosa. *Journal of Ecological Engineering*, *19*(3), 226-235. https://doi.org/10.12911/22998993/83564

Palittapongarnpim, M., Pokethitiyook, P., Upatham, E. S., & Tangbanluekal, L. (1998). Biodegradation of crude oil by soil microorganisms in the tropic. *Biodegradation*, *9*(2), 83-90. https://doi.org/10.1023/a:1008272303740

Parsons, J. F., Greenhagen, B. T., Shi, K., Calabrese, K., Robinson, H., & Ladner, J. E. (2007). Structural and functional analysis of the pyocyanin biosynthetic protein PhzM from Pseudomonas aeruginosa. *Biochemistry*, *46*(7), 1821-1828. https://doi.org/10.1021/bi6024403

Peraza-Liñan, D. L., Ayíl-Gutiérrez, B. A., Urías-Salazar, A. A., López-Santillán, J. A., Estrada-Drouaillet, B., Segura-Martínez, M. T. J., & Poot-Poot, W. A. (2025). Biodegradation of crude oil by Aspergillus tubingensis: biosurfactant-producing strain. *Revista Mexicana de Ingeniería Química*, *24*(1), 1-11. https://doi.org/10.24275/rmiq/Bio24332

Peruzzo, R., Corrà, S., Costa, R., Brischigliaro, M., Varanita, T., Biasutto, L., & Szabò, I. (2021). Exploiting pyocyanin to treat mitochondrial disease due to respiratory complex III dysfunction. *Nature Communications*, *12*(1), 2103. https://doi.org/10.1038/s41467-021-22062-x

Pierson, L. S., & Pierson, E. A. (2010). Metabolism and function of phenazines in bacteria: impacts on the behavior of bacteria in the environment and biotechnological processes. *Applied Microbiology and Biotechnology*, *86*(6), 1659-1670. https://doi.org/10.1007/s00253-010-2509-3

Raţiu, S., Josan, A., Alexa, V., Cioată, V. G., & Kiss, I. (2021). Impact of contaminants on engine oil: A review. *Journal of Physics: Conference Series*, *1781*(1), 012051. https://doi.org/10.1088/1742-6596/1781/1/012051

Rayaroth, M. P., Marchel, M., & Boczkaj, G. (2023). Advanced oxidation processes for the removal of mono and polycyclic aromatic hydrocarbons–A review. *Science of The Total Environment*, *857*, 159043. https://doi.org/10.1016/j.scitotenv.2022.159043

Reszka, K. J., O'Malley, Y., McCormick, M. L., Denning, G. M., & Britigan, B. E. (2004). Oxidation of pyocyanin, a cytotoxic product from Pseudomonas aeruginosa, by microperoxidase 11 and hydrogen peroxide. *Free Radical Biology & Medicine*, *36*(11), 1448-1459. https://doi.org/10.1016/j.freeradbiomed.2004.03.011

Reszka, K. J., Denning, G. M., & Britigan, B. E. (2006). Photosensitized oxidation and inactivation of pyocyanin, a virulence factor of Pseudomonas aeruginosa. *Photochemistry and Photobiology*, *82*(2), 466-473. https://doi.org/10.1562/2005-07-29-RA-626

Rodríguez-Recio, F. R., Garza-Cervantes, J. A., Balderas-Cisneros, F. J., & Morones-Ramírez, J. R. (2025). Genomic insights into and lytic potential of native bacteriophages M8-2 and M8-3 against clinically relevant multidrug-resistant Pseudomonas aeruginosa. *Antibiotics*, *14*(2), 110. https://doi.org/10.3390/antibiotics14020110

Ruiz-Hernandez, I. H., Madrigal-Perez, L. A., & González-Hernández, J. C. (2024). The potential use of Pseudomonas aeruginosa in terrestrial and space agriculture. *Brazilian Journal of Biology*, *84*, e282664. https://doi.org/10.1590/1519-6984.282664

Saini, M., Das, S. K., Kumar, D., Dutt, G., Singh, K. K., & Prakash, D. (2025). The correlation between redox activity and antimicrobial properties of pyocyanin from Pseudomonas aeruginosa. *bioRxiv*. https://doi.org/10.1101/2025.02.17.638708

Sarkar, M. (2023). Light-responsive biodegradation of wastewater pollutants: New developments and potential perspectives. *Journal of Hazardous Materials Advances*, *10*, 100281. https://doi.org/10.1016/j.hazadv.2023.100281

Sarker, M. A. R., & Ahn, Y.-H. (2022). Green phytoextracts as natural photosensitizers in LED-based photodynamic disinfection of multidrug-resistant bacteria in wastewater effluent. *Chemosphere*, *297*, 134157. https://doi.org/10.1016/j.chemosphere.2022.134157

Saucedo-Martínez, B. C., Benavides, L. M., & Sánchez-Yañez, J. M. (2023). In the biostimulation of soil impacted by hydrocarbons the detergent emulsifies them the elimination depends on microorganisms induced by mineral solution. *Novel Aspects on Chemistry and Biochemistry*, *7*, 1-12. https://doi.org/10.9734/bpi/nacb/v7/7258A

Sutar, R. S., Barkul, R. P., Delekar, S. D., & Patil, M. K. (2020). Sunlight assisted photocatalytic degradation of organic pollutants using g-C3N4-TiO2 nanocomposites. *Arabian Journal of Chemistry*, *13*(1), 4966-4977. https://doi.org/10.1016/j.arabjc.2020.01.019

Taleshpur, S., Taghavi, L., Farahani, H. F., Rasekh, B., & Bazgir, S. (2025). Oil pollution removal using g-C3N4/PEG nanocomposite in the presence of bacterial consortium isolated from contaminated areas: optimization Study. *International Journal of Environmental Science and Technology*, *2025*, 1-8. https://doi.org/10.1007/s13762-024-06307-y

Unglaube, F., Hünemörder, P., Guo, X., Chen, Z., Wang, D., & Mejía, E. (2020). Phenazine radical cations as efficient homogeneous and heterogeneous catalysts for the crossdehydrogenative aza-henry reaction. *Helvetica Chimica Acta*, *103*(7), e2000184. https://doi.org/10.1002/hlca.202000184

USEPA. (2007). *Method 8015D. Nonhalogenated organics by gas chromatography/flame ionization detector*. Washington, USA.

USEPA. (2007). *Method 8270D. Semivolatile organic compounds by gas chromatography/mass spectrometry*. Washington, USA.

Viana, A. A. G., Borchardt, H., Dantas, J. V., Bernardes-Dias, D. S., Gurgel-Amaral, I. P., & Vasconcelos, U. (2024). Effect of exogenous phenazine addition on crude heavy oil

degradation by Pseudomonas aeruginosa TGC04. *Revista Mexicana de Ingeniería Química*, *23*, 1-15. https://doi.org/10.24275/rmiq/IA24251

Viana, A. A. G., Oliveira, B. T. M., Cavalcanti, T. G., Sousa, K. A., Mendonça, E. A. M., Amaral, I. P. G., & Vasconcelos, U. (2018). Correlation between pyocyanin production and hydrocarbonoclastic activity in nine strains of Pseudomonas aeruginosa. *International Journal of Advanced Engineering Research and Science*, *5*(7), 212-223. https://doi.org/10.22161/ijaers.5.7.28

Whooley, M. A., & McLoughlin, A. J. (1982). The regulation of pyocyanin production in Pseudomonas aeruginosa. *European Journal of Applied Microbiology and Biotechnology*, *15*(3), 161-166. https://doi.org/10.1007/BF00511241

Yeh, N., Yeh, P., Shih, N., Byadgi, O., & Cheng, T. C. (2014). Applications of light-emitting diodes in researches conducted in aquatic environment. *Renewable and Sustainable Energy Reviews*, *32*, 611–618. https://doi.org/10.1016/j.rser.2014.01.047

Zhang, H., Lu, Y., Li, Y., Wang, C., Yu, Y., Zhang, W., Wang, L., Niu, L., & Zhang, C. (2022). Propelling the practical application of the intimate coupling of photocatalysis and biodegradation system: System amelioration, environmental influences and analytical strategies. *Chemosphere*, *287*, 132196. https://doi.org/10.1016/j.chemosphere.2021.132196

Zhang, Y., & Zhuang, H. (2024). Effectiveness of low-intensity ultrasound on anaerobic bioaugmentation of phenolic wastewater: Model optimization and system stabilization. *Bioresource Technology*, *406*,30980.https://doi.org/10.1016/j.biortech.2024.130980

Vol. 24, No. 2(2025) IE25411
Revista Mexicana de Ingeniería Química

Numerical and experimental study of air heating solar collector constructed of aluminum tube pipes

Estudio numérico y experimental de un colector solar de calentamiento de aire construido con tubos de aluminio

A. López-López[1], I. A. García-Montalvo[2], S. Sandoval-Torres[3], E. Hernández-Bautista[1]*
[1]Departamento de ingeniería química y bioquímica, Tecnológico Nacional de México/ Instituto Tecnológico de Oaxaca, Oaxaca 68033, México.
[2]División de Estudios de Posgrado e Investigación Tecnológico Nacional de México/ Instituto Tecnológico de Oaxaca, Oaxaca 68033, México.
[3]Instituto Politécnico Nacional, CIIDIR Unidad Oaxaca, Santa Cruz Xoxocotlán 71230, México
Received: September 3, 2024; Accepted: March 3, 2025

Abstract
A model was developed to simulate an air heating solar collector. A 3D geometry was proposed, consisting of nine rectangular aluminum tubes and a rectangular space between the glass cover (GC) where air flows. The spatial distribution of air velocity was simulated using a Reynolds-Averaged Navier-Stokes $\kappa - \varepsilon$ model, in steady state, to calculate the heat transfer coefficients. The energy balances in transient state were performed in the GC, aluminum absorber plate (AP) and in the fluid. The energy balance considers the heat transfer in the fluid by convection, conduction and surface radiation between the AP-GC. The energy balance in the AP used a lumped analysis and considered the heat loss due to convection between the AP and fluid and heat source due to solar radiation considering transmissivity and absorptivity. The model was used to simulate different inlet velocities. The transfer coefficients in the tubes were higher and therefore the temperature, compared to the space between GC and AP. Besides, it was found that there is an increase in outlet temperature with increasing air velocity.
Keywords: Heat transfer coefficient; Interior no slip condition; Transient analysis; Turbulent flow; Surface to surface radiation.

Resumen
Se desarrolló un modelo para simular un colector solar para calentamiento de aire. Se propuso una geometría 3D, compuesta por nueve tubos rectangulares de aluminio y un espacio rectangular entre la cubierta de vidrio (GC) por donde fluye el aire. La distribución espacial de la velocidad del aire se simuló utilizando un modelo $\kappa - \varepsilon$ de Reynolds-Averaged Navier-Stokes, en estado estacionario, para calcular los coeficientes de transferencia de calor. Los balances de energía en estado transitorio se realizaron en el GC, placa absorbente de aluminio (AP) y en el fluido. El balance de energía considera la transferencia de calor en el fluido por convección, conducción y la radiación superficial entre la AP-GC. El balance de energía en la AP utilizó un análisis agrupado y consideró la pérdida de calor por convección entre la AP y el fluido y la fuente de calor por radiación solar considerando transmisividad y absortividad. El modelo se utilizó para simular diferentes velocidades de entrada. Los coeficientes de transferencia y la temperatura en los tubos fueron más altos, en comparación con el espacio entre GC y AP. Además, se encontró que hay un aumento en la temperatura de salida con el aumento de la velocidad del aire.
Palabras clave: Coeficiente de transferencia de calor; Condición interior no deslizamiento; Estado transitorio; Flujo turbulento; Radiación superficie a superficie.

* *Corresponding author. E-mail*: Bautistahe@gmail.com ;
https://doi.org/10.24275/rmiq/IE25411
ISSN:1665-2738, *issn-e*: 2395-8472

1 Introduction

The rapid population growth and increasing demand for energy in developing countries exposes concerns such as poverty, pollution, health, and environmental problems (Ndukwu *et al*. 2023). For this reason, these countries need modern energy to increase production, generate income and promote social development, as well as to address the health problems caused by the use of fossil fuels (Shahsavari y Akbari 2018). Currently, sustainable alternatives are being developed, such as biofuel production for energy-intensive processes (Mota et al. 2025; Romero-Bonilla et al. 2025), which generate an average energy output of 37 MJ/kg. In contrast, for low-temperature processes, solar drying plays a crucial role in achieving sustainable development goals in rural Mexican communities, as it is the most viable preservation technology for certain agricultural products (Messina *et al*. 2022).

Drying is a highly energy-intensive operation, consuming 6 to 30 times more energy than cooling and freezing depending on temperature conditions, which requires a large amount of fossil fuel consumption that generates carbon emissions into the atmosphere (Ndukwu *et al*. 2023). The use of renewable energy has the benefit of reducing dependence on these fuels and reducing carbon emissions into the atmosphere.

Global warming has increased the demand for renewable energy sources, making solar radiation the most abundant and cleanest energy source available today. In recent years, solar collector technology has developed rapidly and has been widely applied. However, solar energy is intermittent with low energy density and easy to be affected by climatic factors, which has an impact on the low solar energy use efficiency of the collector (Xiao *et al*. 2022). Therefore, technological improvements are required, such as: 1)The incorporation of thermochemical energy storage and phase change storage (AZEEZ *et al*. 2023; Mahroug *et al*. 2021). 2) The improved spatial distribution of air within the collector and the integration of ventilation systems that help to increase the heat transfer coefficients in the absorber plate (Bolaji 2012). As well as 3) the sizing and improvements in collector geometry based on computational and CFD simulations (Rajarajeswari, Alok, and Sreekumar 2018).

The development of mathematical models describing the CFD and the heat transfer in the fluid aims to describe the process to maximize the heat transfer between the absorber plate and the air, that means that more energy as heat is transported into the fluid and consequently the outlet air temperature will be higher. In this work the fluid in the collector is air, which is commonly used for drying operations.

The $\kappa-\varepsilon$ model is one of the most used turbulence models in CFD for flat plate solar collectors (AZEEZ *et al*. 2023; Rouissi *et al*. 2021; Vivekanandan *et al*. 2020). This is relatively simple compared to other more complex turbulence models. This simplicity enhances computational, enabling quicker simulations with reduced demand on computational resources. Moreover, it effectively predicts turbulence within the fluid and vortex effects in the flow.

The collector is connected to a drying chamber (Kumar y Singh 2020; Mohana *et al*. 2020), where the air at room temperature enters the collector and leaves it at a higher temperature to enter the drying chamber. The hot air leaving the collector enters the drying chamber and passes through the material to be dried, in order to yield its sensible heat and remove the water from the material.

The solar tube collector for air heating consists of a GC, an AP and wood insulation on the bottom. Solar radiation crosses the glass cover which allows the radiation to pass through (Bakari 2018; Bakari, Minja and Njau 2014), but minimizes heat loss. This is absorbed by a flat plate inside the collector, which transfers it to the fluid. This heat is transferred to the air circulating through the collector while the insulation on the sides and bottom helps to reduce thermal losses (Lingayat *et al*. 2020), retaining the heat effectively (Tiwari 2011).

In an energy balance, the AP gains energy from solar radiation and loses it by transferring heat to the air. Due to the previously mentioned and to the thermal conductivity of the AP, we can obtain a homogeneous spatial distribution of temperatures on the AP, changing only as a function of time due to solar radiation throughout the day from 500 Wm^{-2} to 1100 Wm^{-2} (Matsumoto *et al*. 2014).

The process of heat transfer between the AP and the fluid is described by the use of energy balances between these two domains, where the concept of thermal boundary layer is involved, that is described through the convective coefficients of heat transfer between the plate and the fluid. Another phenomenon is radiation between surfaces (Alleyne and Milczarek 2015) a phenomenon in parallel with the convective mechanism.

The incoming light passes through the GC because it allows passage mainly into the short infrared. The GC is a selective barrier for different wavelengths of electromagnetic radiation. In particular, it allows the shorter wavelengths of the infrared (IR) spectrum to pass through. These short IR have higher energies and are able to easily pass through materials such as GC. This light heats the AP through which the air flows; when this material is heated, it emits longer IR radiation. When the short IR passes through the glass and reaches the aluminum within the thermal system, it absorbs this energy and increases its temperature.

As the AP is heated, it begins to emit its own thermal radiation according to Planck's law. This emission is typically at longer wavelengths known as far or long IR. The long wavelengths cannot easily pass through the same material that allowed the short IR to enter initially. So. some of this energy is trapped within the system due to the greenhouse effect created by this phenomenon: heat enters but does not leave as easily due to the selective blocking exerted by the optical properties of the transparent material. This contributes significantly to the total energy losses within the collector system.

Furthermore, the air inlet temperature varies throughout the day. Early in the day, the inlet temperature and energy flux are low, resulting in a lower outlet temperature. By midday, however, with an energy flux of 1100 Wm^{-2} and a higher inlet temperature, the outlet temperature also increases.

Some studies have been developed that consider a steady state, which takes into account that the fluid temperature remains constant at the inlet and that the energy flux absorbed by the plate also remains constant (Gopi *et al*. 2020; Jallut, Jemni, y Lallemand 1988). Consequently, a state is reached in which an equilibrium is achieved in which the amount of heat entering is the same as the amount of heat leaving It is considered to be a solution that helps to understand the problem (Bensaci *et al*. 2020) but it is distant from reality.

Because of the processes mentioned above, what is proposed in this work are a series of fundamental assumptions that help us to develop a set of equations based on energy balances that can be used to simulate the process in a non-steady state. The objective of this work is to analyze the effect of the geometry of the flat plate solar collector on the heat transfer coefficients and its effect on the temporal temperature distribution.

The first part of the work presents the development of the model, which includes considerations for geometry, conservation equations, flow equations, initial conditions, and boundary conditions. It also discusses the parameters utilized to solve these equations using finite element methods. Additionally, this section outlines the experimental procedure used to obtain temperature profiles, solar radiation data, and air velocity measurements in a solar collector.

The final section presents the experimental results, primarily focusing on simulated numerical outcomes. First, it discusses the velocity distribution within the solar collector, along with the calculation of heat transfer coefficients based on this distribution. Second, it provides a comparison between experimental and simulated results. Finally, the section presents temperature distributions within the solar collector throughout the day under various velocity conditions.

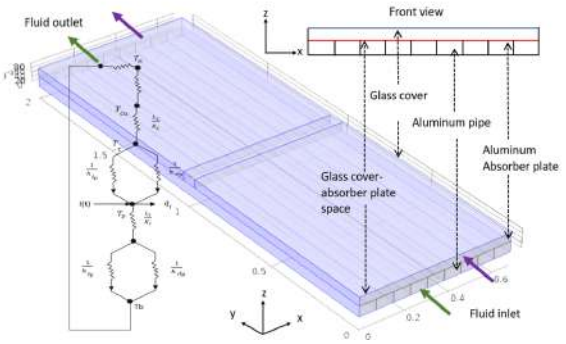

Figure 1 Geometry of flat plate solar collector for air heating and equivalent diagram of thermal resistances 1d z-direction.

2 Mathematical model

2.1 Geometry

The simulated solar collector has the dimensions of 2 m long and 0.684 m wide and consists of 9 aluminum tubes located at the bottom of the collector with dimensions of 0.076 m wide by 0.045 m high each, through which air flows. There is a space between the GCs and the AP, which is 0.684 m wide and 0.037 m high, where air also flows. The absorber plate (AP) is the upper area of the tubes exposed to solar irradiation (2mx0.684m).

The geometry does not consider the thickness of the glass cover, nor the thickness of the insulating wood on the sides of the collector and at the bottom, as these are considered as a boundary condition for thermal insulation and convective heat loss on the outer surface of the glass. Also, the thickness of the tubes is not taken into account since aluminum has a high thermal conductivity of 237 Wm^{-2} K^{-1} and a very thin thickness of less than 1 mm. In addition, these considerations reduce the solution time, since by using FEM, the mesh refinement at thin thicknesses generates many more nodes, so that the geometry of the flat plate collector is considered only as separate air sections with outer and inner boundaries. The energy transport is represented with thermal resistances separating the domains as shown in Figure 1. This diagram illustrates the heat flow in the z-direction. The environment and glass cover present a thermal resistance defined by an overall heat transfer coefficient, ho. Between the glass cover and the absorber (AP), there are resistances due to convection within the fluid (h_{fp}) and radiation (h_{rpf}) between the surfaces. Additionally, within the tubes, there is resistance due to fluid convection (h_{fp}). In this diagram, solar radiation affects the temperature T_p, modulated by the absorptivity and transmissivity of the materials.

2.2 Model assumptions

In order to reduce the complexity of the model and focus on the phenomena of interest, the following major assumptions were considered, some other assumptions will be considered during model development.

- Air is considered as an incompressible fluid
- The air fluid presents a fully developed turbulent flow distribution pattern.
- There is no temperature gradient in the thickness and length of the glass cover and absorber plate (Al-Tabbakh 2022).
- The temperature of the absorber plate varies as a function of time, but not of space, so a global analysis of heat transfer is possible.
- The heat lost at the side boundaries is negligible.
- The absorptivity of solar radiation on the glass cover is negligible.
- Forced convection is present, therefore the velocity distribution remains steady state during operation.

2.3 Conservation equations

2.3.1 Air velocity distribution in the solar collector

The working fluid is considered as air, as an incompressible fluid with 11 % relative humidity. Air was introduced into the collector (Figure 1) with an average velocity at the inlet in the y-direction of 1.5 m s^{-1}, 2 m s^{-1} and 2.5 m s^{-1}. All these conditions start from zero, these velocities generate a turbulent distribution pattern, with Reynolds number greater than 4000, as will be shown below.

Equation 1 is the modified Navier Stokes equation for Reynolds average Reynolds number (RANS) and the turbulent distribution parameters are $\kappa-\varepsilon$. Because in the assumptions we have that the distribution does not change with temperature, this equation is solved in steady state. Besides, the continuity equation (1) accompanies this equation. It expresses that the amount air mass in is the same as the air mass out.

$$\rho_f(\mathbf{u}\cdot\nabla\mathbf{u}) = \nabla\cdot\left[-p\mathbf{I}+(\mu+\mu_T)\left(\nabla\mathbf{u}+(\nabla\mathbf{u})^T\right)-\frac{2}{3}\rho_f\kappa\mathbf{I}\right]$$
$$\rho_f\nabla\cdot\mathbf{u}=\mathbf{0} \quad (1)$$

This equation models the behavior of a turbulent flow considering both viscous effects and the additional effects of turbulence. The boundary conditions at the walls of the tubes and the walls of the space between the glass and the absorber plate are non-slip conditions for the air. These are classified into inner and outer boundaries. Equation 2 shows the conditions applied to these boundaries.

$$\mathbf{u}\cdot\mathbf{n}=\mathbf{0} \quad (2)$$

2.3.2 Heat transfer coefficients

The Reynolds number was calculated once the velocity distribution generated by equation 1 was obtained. This considers an equivalent hydraulic diameter for rectangular ducts (equation 3)

$$D_h=\frac{4b_1b_2}{2(b_1+b_2)} \quad (3)$$

Where b_1 and b_2 are the height and width of the tubes and the height and width in the space between the glass cover and the absorber plate. Therefore, there will be two different equivalent diameters, one for the tubes and one for the space between AP and GC.

The Reynolds and Prandtl number are calculated at an average temperature of the fluid air in the collector, initially proposed. This will be modified when the energy balance will be solved, until the value will be obtained by successive approximations. These values are used in the following expression to calculate the Nusselt number (Bensaci *et al*. 2020).

$$Nu=\frac{h\cdot D_h}{k}=0.023Re^{0.8}Pr^{0.4} \quad (4)$$

This expression is used to calculate the heat transfer coefficients inside the tubes and in the space between the glass cover and the absorber plate.

The radiation transfer coefficient (Tiwari 2011) between the absorber plate and the glass cover in °C, uses the average temperatures of T_p and T_c, also proposed initially and obtained by successive approximations as well.

$$h_{rpc}=\varepsilon_{eff}\sigma\frac{\left[T_p{}^4-T_c{}^4\right]}{T_p-T_c} \quad (5)$$

Where σ value 5.67x10^{-8} W$m^{-2}K^{-4}$ is the Stefan-Boltzmann constant and ?$_{eff}$ is the effective emissivity of the glass-plate system and is given as follows.

$$\varepsilon_{eff}=\left[\frac{1}{\varepsilon_p}+\frac{1}{\varepsilon_c}-1\right]^{-1} \quad (6)$$

2.3.3 Kinetics of temperature on the absorber plate

Because aluminum is a material with a high thermal conductivity (237 W$m^{-1}K^{-1}$) and very thin thickness (1 mm). Also, the convective heat transfer coefficients range from 8 to 18 W$m^{-2}K^{-1}$, giving us a Biot number « 1(Ranmode, Singh, Bhattacharya 2019). Furthermore, the absorber plate is subjected to an energy flux during operation that goes from 550 to 1100 Wm^{2-2}, it can be considered that the absorber plate has a uniform temperature distribution profile that only varies as a function of time. Therefore, a lumped analysis can be performed(Al-Tabbakh 2022). The system is divided into a number of discrete "lumps" and assumes that the temperature difference within each lump is negligible. This approximation is

useful for simplifying otherwise complex differential heat equation.

$$\rho_p C_{p_p} d_p \frac{\partial T_p}{\partial t} = \alpha\tau I(t) - h_{fp}\left(T_p - T_f\right) - h_{rpc}\left(T_p - T_c\right) \quad (7)$$

The energy balance in the absorber plate (equation 7) considers that the temperature variation as a function of time depends on an energy flux due to solar radiation, multiplied by the absorbance and transmissivity of the glass plate, minus the amount of energy lost by the plate due to convection from the two sides of the plate, plus the surface-to-surface radiation between the absorber plate and the glass cover, considered in the heat transfer coefficient in equation 5. These are shown in the equivalent thermal resistance diagram.

The solar radiation I(t) is a function of time, and the data were taken experimentally, they are required by the model. Besides, equation 3 being an ODE requires initial conditions, the initial value for the temperature is 18.7 °C.

2.3.4 *Transient-state temperature distribution in the fluid*

The energy balance in the fluid considers variations in time and space of the fluid domain. Therefore, a PDE as energy conservation equation is used for the description of this phenomenon. The conservation equation considers the mechanism of heat transfer due to conduction and convection considering the velocity distribution of equation 1.

$$\rho_f C_{p_f} \frac{\partial T_f}{\partial t} + \rho_f C_{p_f} \mathbf{u} \cdot \nabla T_f = \nabla \cdot \left(\mathbf{k_f} \nabla T_f\right) \quad (8)$$

However, to take into account, the heat transfer between the fluid and the absorber plate. As well as the fluid and the glass cover, the following boundary conditions in the fluid were considered.

2.3.4.1 Boundary condition of the energy conservation equation in the fluid

The fluid space of the glass cover and absorber plate (Figure 1) is subjected to two sources of heat. The first term represents convective heat transfer between the fluid and the GC within the space between the GC and AP. The second is due to heat gain by the fluid through the absorber plate due to convection, shown in equation 9.

$$\mathbf{n_z} q_z = h_{cf}\left(T_c - T_f\right) + h_{fp}\left(T_p - T_f\right) \quad (9)$$

The boundary condition inside the tubes is due to convection using a different heat transfer coefficient h_{fp} inside the tubes, as the equivalent diameter is modified. This energy flux depends on the fluid temperature and the plate temperature, shown in equation 10.

$$\mathbf{n_z} q_z = h_{fp}\left(T_p - T_f\right) \quad (10)$$

Furthermore, the convective boundary condition on the outer glass cover depends on the external velocity, and the ambient temperature (T_0). This was considered as the input to the solar collector at each time. This temperature is used in equation 11.

$$\mathbf{n_z} q_z = h_0\left(T_c - T_0\right) \quad (11)$$

The collector base (bottom) as well as the side faces are considered insulated, thermal insulation boundaries.

2.4 *Numerical simulation*

Figure 2 show the flowchart of the model solution. The model operates as follows: initially, input parameters such as solar radiation and ambient temperature are introduced. Next, the steady-state Navier-Stokes equation is solved, assuming a proposed average fluid temperature. After the velocity distribution in the collector is obtained, the transfer coefficients based on Reynolds and Nusselt numbers are calculated.

These coefficients are used to perform the transient state energy balance in the absorber plate and the fluid. If the average temperature of the fluid does not coincide with that proposed, the Navier-Stokes equation is solved again with the calculated temperature, repeating the process by successive approximations. Finally, the temperature in the plate, in the fluid and in the glass, cover is determined.

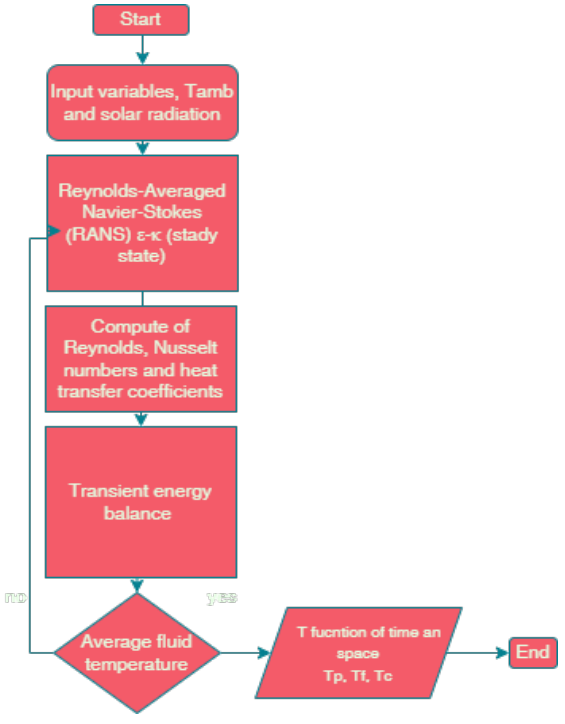

Figure 2 Flowchart of the model solution.

The model was solved using Comsol Multiphysics 4.3b, using a computer with a 3. 30 GHz and 16 Gb in Ram, equation 1 was solved for 295806 degrees of freedom, in a total time of 699s, in steady state and for equation 3 and 4, coupled transient state equations were used, using the velocity distribution of equation 1, for 45968 degrees of freedom plus 21357 internal degrees of freedom, with a time step of 60s, which gives a solution time of 589s. A mesh was created with 10269 tetrahedral elements, with mesh refinement at the corners. The size of the elements varies from 0.0513m to 0.0128m.

For the solution of the model, solar radiation, ambient temperature, and air velocity at the collector inlet are input. The output variables are the velocity distribution in the solar collector, the plate temperature as a function of time, the fluid temperature as a function of time and space, and the glass cover temperature.

2.5 Experimental data for model validation

For the data collection in the solar collector described in the previous section, a Vaisala Veritec logger and type K thermocouples of the same brand were used, with an accuracy of 0.01°C. The thermocouples were positioned as follows: one before the inlet of the solar collector (T0) to measure the ambient temperature, another in contact with the tubes (Tp) in the area exposed to solar radiation, a third at the outlet of the solar collector, measuring the air temperature in the space between the glass cover and the absorber plate (T C-P space), and the last one the outlet temperature of the tubes (Tpipe). The nomenclature in parentheses will be referenced in subsequent figures under different conditions.

Solar radiation (Sol_rad) at the collector was measured using a Fluke FLK-IRR1-SOL pyranometer, positioned at the same angle of incidence as the solar collector, which is 40°. The air velocity at the inlet was maintained at 2 m/s and measured at the outlet of the collector using an anemometer. Data acquisition spanned 6 hours, from 10 am to 4 pm in Oaxaca, Mexico.

In this operation, the controllable variables are limited. These include the air velocity and the angle of inclination of the collector. For this study, an air velocity of 2 m/s was chosen. This was because the calculation of the Reynolds number resulted in a fully developed turbulent flow distribution. On the other hand, a tilt angle of 40° was used to compensate for the lower solar radiation during winter or months with low irradiation. In addition, the steeper angle facilitates rainwater runoff and reduces the need for cleaning during the rainy season (Kramer *et al.*, 2017).

3 Results and discussion

Figure 3 shows the velocity distribution in the flat plate collector in the tubes and the space between the absorber plate and the glass cover. The inlet air velocity was uniformly distributed average initial velocity. This figure shows that the velocity variation was mainly in the longitudinal direction of the collector, y-direction. This profile shows a slightly higher velocity in the tubes than in the space between the glass cover and the absorber plate. This modified the heat transfer coefficients to the fluid in each of these spaces.

Figure 3 presents the steady-state velocity distribution. In the yz-plane, it is observed that the velocity at the tube inlets corresponds to the initial values (1.5, 2, and 2.5 m/s) but increases along the y-direction due to the thermal expansion of the fluid as it is heated. This behavior was experimentally confirmed using an anemometer, which showed higher velocities at the tube outlets. Thermal expansion occurs more rapidly at higher velocities, as demonstrated in Figures 3b and 3c, where the velocity profile becomes uniform in the y-direction more quickly. Additionally, the xz-plane visualizations emphasize the no-slip condition at the tube walls and the presence of higher velocities at the center of the tube.

Higher Reynolds numbers were generated in the part of the glass cover and absorber plate (Figure 4), than in the tubes. Contrary to the fluid velocity, because the Reynolds numbers were proportional to the equivalent diameter, calculated with equation 3. The equivalent diameter of the space between the glass cover and the absorber plate was larger. This when multiplied by the properties of the fluid generates higher Reynolds numbers than in the tubes. These Reynolds numbers had values above 4000 for all cases, which confirms a fully developed turbulent flow. This is shown in Figure 4 for all velocities.

Once the Reynolds number was obtained, the Nusselt Number was calculated (equation 4). Also using the equivalent diameter, the heat transfer coefficients were calculated. However, in this case the transfer coefficients resulted proportionally inverse to this diameter, so we will have higher transfer coefficients in the tubes compared to the space between the glass cover and the absorber plate. This is also shown in Figure 4, for all simulated air velocities.

Figure 4 is consistent with the findings in Figure 3, showing that the initial inlet velocity provided by the fan increases due to thermal expansion. This velocity is accounted for in the Reynolds number and Equation 4, implying that any changes in velocity directly influence these coefficients and, consequently, the heat transfer process. Although convection coefficients are relatively low compared to other heat transfer process,

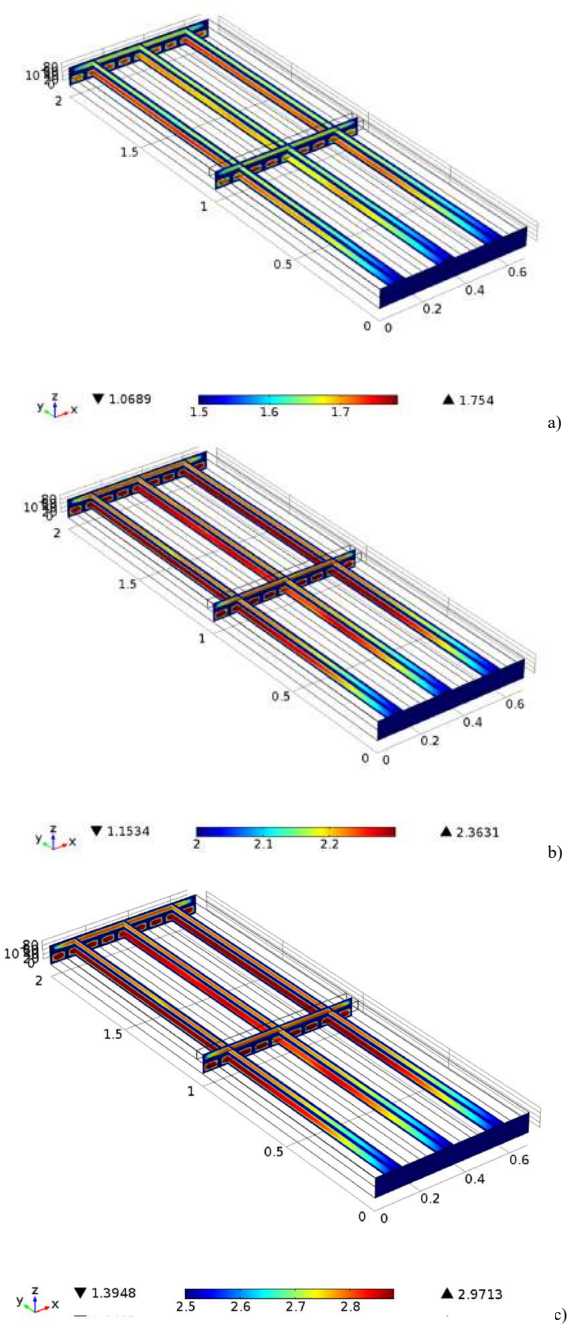

Figure 3 Velocity distribution in the flat plate solar collector a) 1.5 m s^{-1}, b)2 m s^{-1} and c)2.5 m s^{-1}.

Tiwari *et al*. (2011) report even smaller values for natural convection, such as 2.847 $Wm^{-2}K^{-1}$. In this study, the maximum forced convection coefficient reaches 15 $Wm^{-2}K^{-1}$, with variations observed along the longitudinal axis of the solar collector.

Bensaci *et al*. (2020) calculated heat transfer coefficients for Reynolds numbers in the range of 2300 to 8300, using standard Dittus-Boelter correlations. The values obtained for the heat transfer coefficients ranged from 10 to 20 $Wm^{-2}K^{-1}$. These coefficients were observed to vary along the length of the collector, decreasing due to the presence of baffles on the absorber plate.

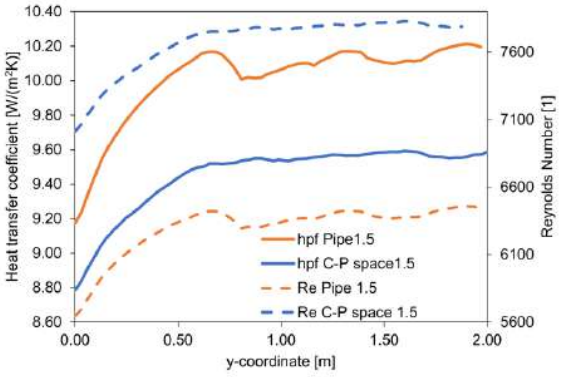

a)

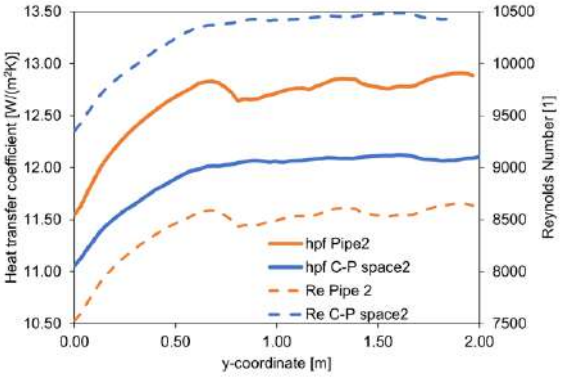

b)

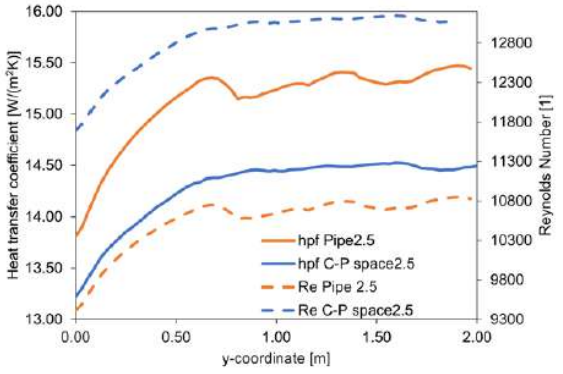

c)

Figure 4 Reynolds number computed with velocity distribution and heat transfer coefficient between the fluid and the absorber plate at a) 1.5 m s^{-1}, b) 2 m s^{-1} and c) 2.5 m s^{-1}.

Figure 5 shows the temperature distribution in the solar collector at different velocities and times, the first profile is shown at 3600s, where the heating of air in the collector began, where it is shown that the heating of the air was greater in the tubes than in the space between the absorber plate and the glass cover, this behavior was the same at all velocities. As time progresses, the temperature inside the collector increases as the solar radiation I(t) (equation 9) increases. At 7200 s, the collector

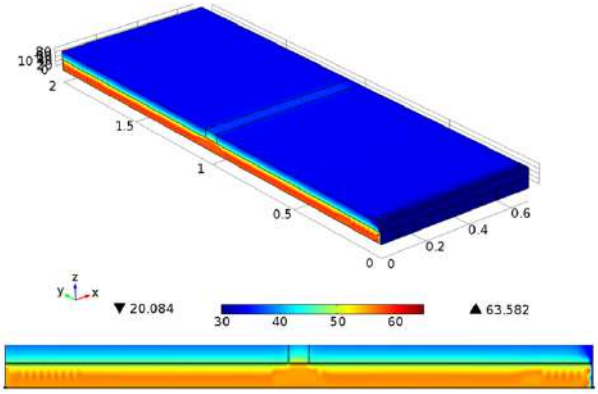
▼ 20.084
30 40 50 60
▲ 63.582

a1)

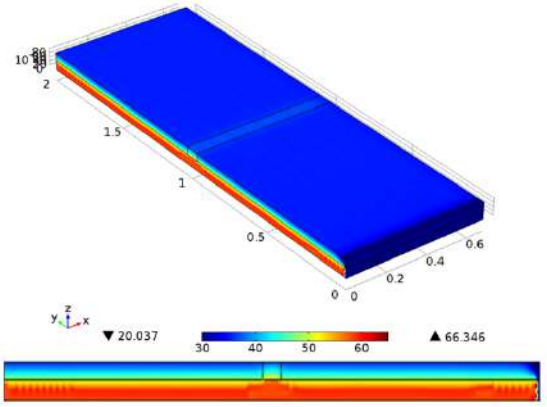
▼ 20.037
30 40 50 60
▲ 66.346

b1)

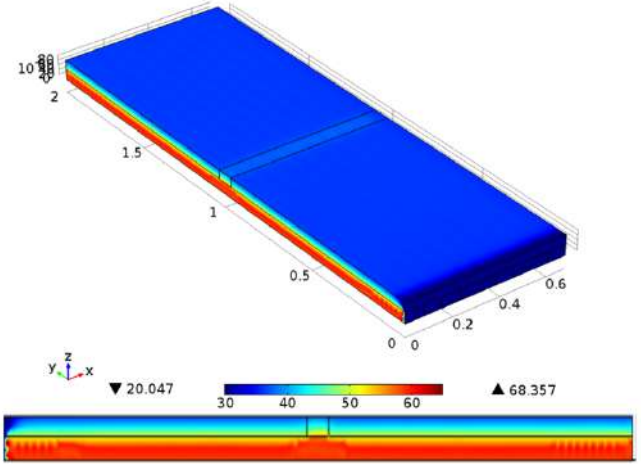
▼ 20.047
30 40 50 60
▲ 68.357

c1)

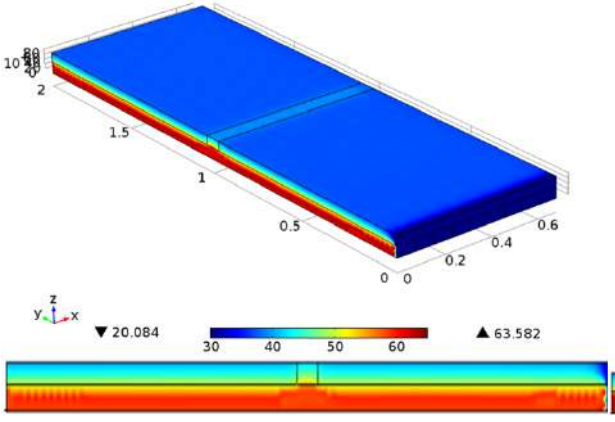
▼ 20.084
30 40 50 60
▲ 63.582

a2)

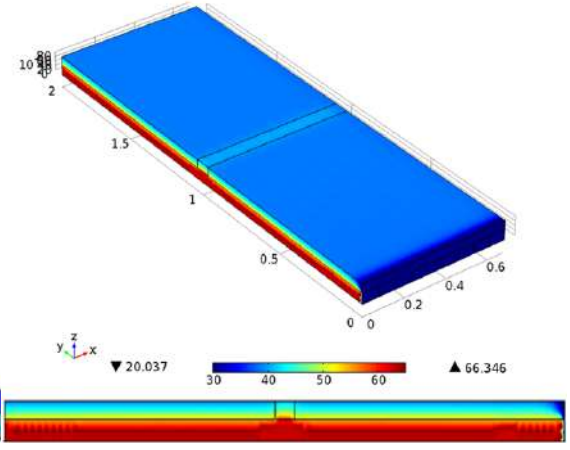
▼ 20.037
30 40 50 60
▲ 66.346

b2)

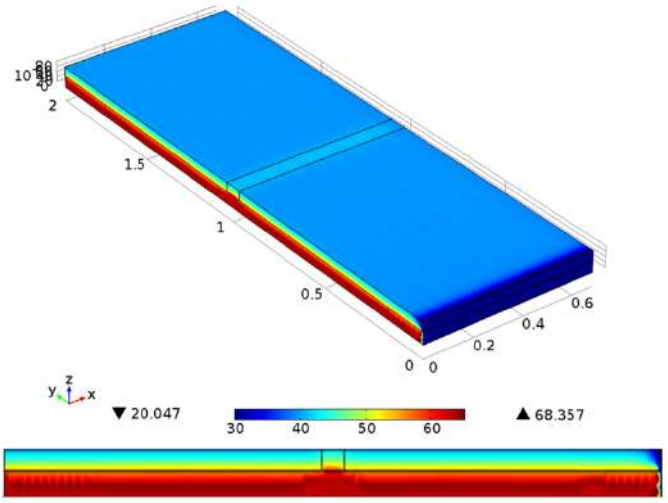
2
1.5
1
0.5
0
0.2
0.4
0.6
▼ 20.047
30
40
50
60
▲ 68.357

c2)

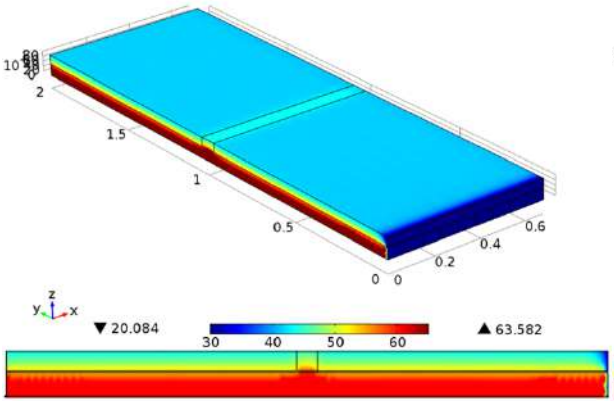
2
1.5
1
0.5
0
0.2
0.4
0.6
▼ 20.084
30
40
50
60
▲ 63.582

a3)

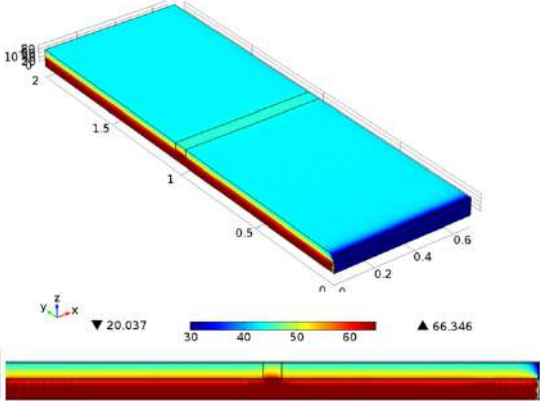
2
1.5
1
0.5
0.2
0.4
0.6
▼ 20.037
30
40
50
60
▲ 66.346

b3)

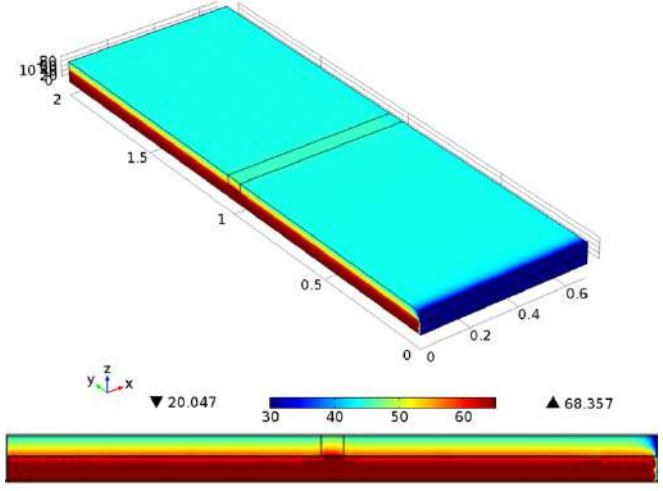
2
1.5
1
0.5
0
0.2
0.4
0.6
▼ 20.047
30
40
50
60
▲ 68.357

c3)

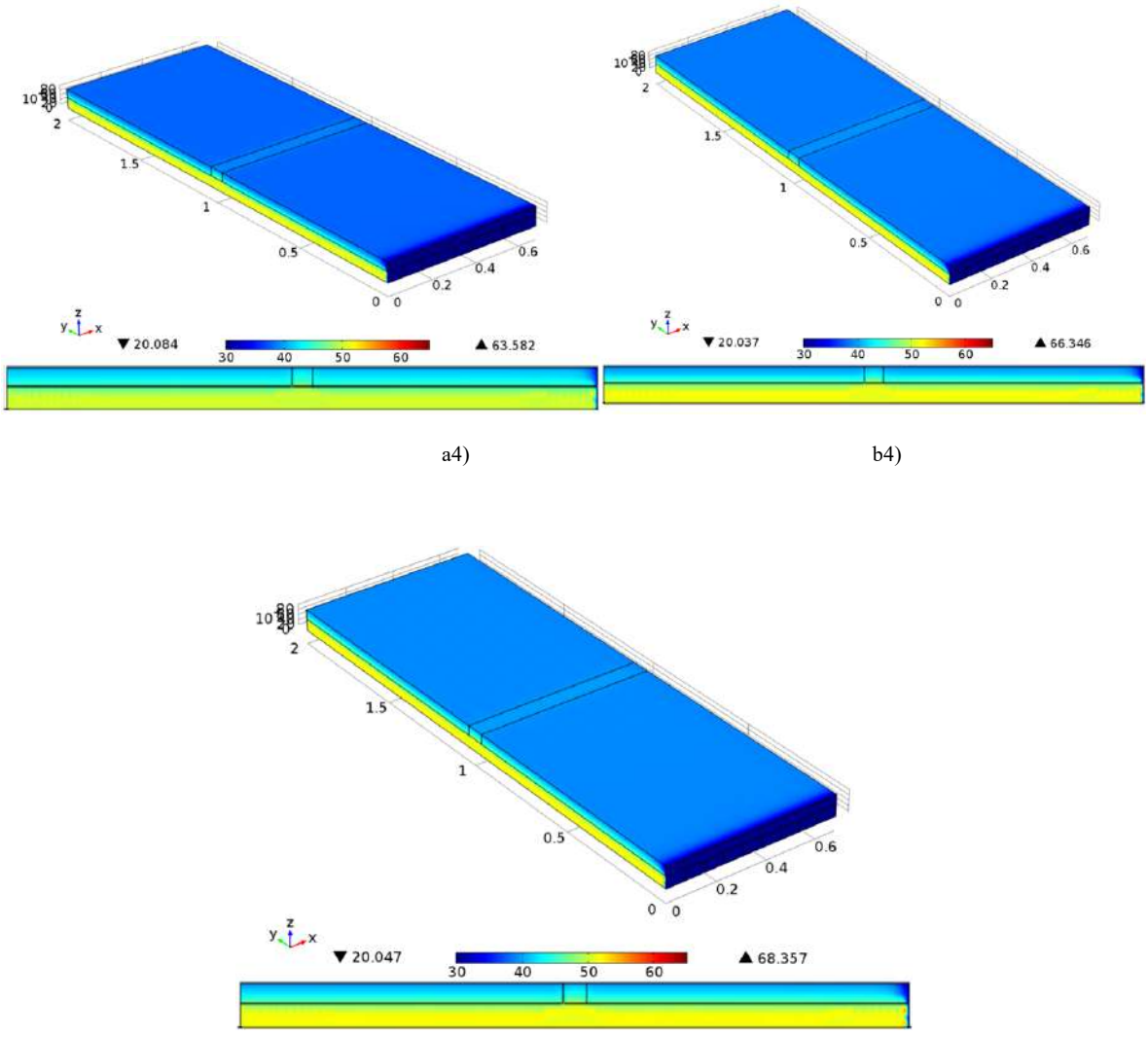

a4) b4)

c4)

Figure 5 Temperature distribution in the flat plate solar collector, for velocities a) 1.5 m s^{-1} b) 2 m s^{-1} and c) 2.5 m s^{-1} at different times 1) 3600 s, 2)7200 s 3)15000 and 4)30600s.

temperature increased maintaining the same behavior as in the previous time, the transfer coefficient increases (Figure 4), so the temperature also increased, one of the advantages of this model is that it is possible to use the same function of solar radiation with respect to time and vary only the air velocity, keeping the other conditions constant. This is very complicated experimentally, since the solar radiation varies a lot due to the weather conditions each day.

The time of 15000 s was chosen because it was when the highest solar radiation occurs and it was at that time when the highest temperature inside the collector was obtained (Figure 5 a3,b3,c3). We can also observe that the higher the air velocity, the higher the transfer coefficients since the temperature profile was much higher. Finally, Figure 5 a4, b4 and c4 show the temperature distribution when the solar radiation decreases. Therefore, the temperature also decreases, and the model was able to capture these variations.

Figure 5 illustrates the temperature distribution in the yz-plane, showing that the temperature is higher inside the tubes compared to the space between the glass cover and the absorber plate. Due to the small variation in the coefficients, the temperature variation along the y-direction is much smaller than that along the z-direction. This indicates that the dependence of the coefficients on velocity is minimal. The temperature variation along the z-axis is more pronounced, with the highest temperatures observed at the absorber plate, represented by the horizontal line in the yz-plane that separates the space between the glass cover (C-P) and the tubes. The average temperatures of the glass cover, the air space between the glass cover and the absorber plate, the air inside the tubes, and the absorber plate were calculated and plotted as a function of time, as shown in Figure 6.

Figure 6 depicts the temperature kinetics of the absorber plate (Tp), the air within the tubes (Tpipe),

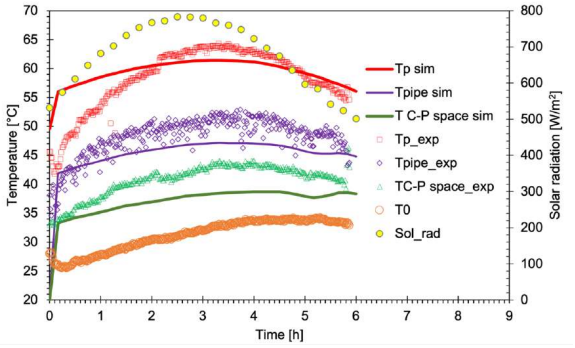

Figure 6 Experimental and simulated comparison of temperature kinetics in various sections of the solar collector operating with an inlet velocity of 2 m/s.

and the space between the glass cover and the absorber plate (T C-P space). Both experimental and simulated curves are displayed at 2 m/s. Additionally, ambient temperature and solar radiation are shown on the secondary axis; these were used as input data for the model. It is evident that the model consistently underestimates the temperature values over time, except for the temperature at the plate, where the simulated temperature is initially higher in the first few hours. These findings are attributed to the calculation of the transfer coefficients based on empirical correlations.

Figure 6 demonstrates a good agreement between the experimental and simulated data after the first hour, with a maximum discrepancy of 6 °C. The fit improves further after 2.2 hours, with the maximum difference reaching 10 °C, except for the AP temperature. The energy balance on the AP incorporates two coefficients: one for radiation (hprf) and one for convection (hpf). The convection coefficient is applied both at the top of the AP for the fluid (hpf C-P) and at the bottom (hpf Pipe). However, these coefficients tend to underestimate the energy lost from the plate, necessitating experimental calculation. The model predicts a higher temperature on the plate, which blocks the transfer of heat to the C-P space and the fluid inside the pipes, resulting in a lower simulated temperature in the pipes compared to the experimental data.

Al-Tabbakh (2022) presents a transient state study of a solar air collector with circular tubes, where a constant solar radiation is incident on the absorber plate. The results show that the highest temperature corresponds to the absorber plate, followed by the fluid, the glass cover and finally the ambient temperature. However, the temperatures reach a stationary equilibrium, as the study does not consider daily variations in solar radiation.

Rani and Tripathy (2020) analyze how different mass flow rates affect the performance of a solar air heating collector. Their results plot the temperature variation with time for the absorber plate, the fluid, the glass cover and the ambient temperature, showing similar behavior to that observed by Al-Tabbakh (2022) and this work. In addition, the mass flow, which is directly related to the air velocity, has a significant impact. In this work, it is confirmed that as the velocity increases, the absorber plate and fluid temperatures also increase, as shown in the figure below.

Table 1 presents the average energy losses throughout the day in the collector, calculated experimentally using an energy balance. It is observed that the largest amount of energy is lost at the bottom and sides of the collector, followed by the glass, where losses of 15 % occur due to transmissivity and absorptivity, in addition to a convective loss of 4 %. The table also shows the heat transfer coefficients at the surface and at the sides. It is also indicated that the average heat transfer coefficient used in the fluid and plate is 12 W/m^2 K, a value that coincides with the one used in the model for that velocity (Figure 4c). Overall, the collector achieves an efficiency of 37%, which could be improved by better insulation on the sides and by replacing the glass with polycarbonate.

Finally, in Figure 7 is shown the average temperature of the absorber plate, the fluid, the space between the absorber plate and the glass cover, the glass temperature, and the experimental ambient temperature. The absorber plate was the heat source; therefore, the temperature of the absorber plate will be higher in the solar collector, followed by the fluid temperature in the tubes where the transfer coefficients were higher and then the temperature of the space between the absorber plate and the fluid. Also, this graph also shows the ambient temperature used in these simulations.

Table 1. Efficiency and Energy Loss of Collector (Experimental Data, 2 m/s).

	Convection and radiation on the glass cover surface	Lateral and bottom of the collector	Transmission and absorption glass cover	Efficiency of the collector and heat transfer coefficient in the fluid
Loss of energy	4	44	15	37
Heat transfer coefficient	5 W/m^2 K	10 W/m^2 K		12 W/m^2 K

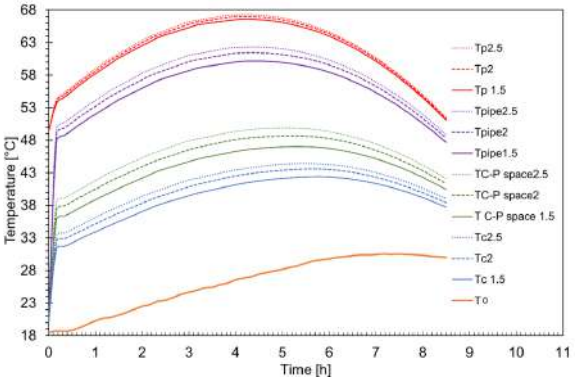

Figure 7 Temperature kinetics of the absorber plate, temperature of the air outlet of the tubes and the space between the glass cover and the absorber plate at different air flows of 1.5 m s^{-1}, 2 m s^{-1} and 2.5 m s^{-1}.

Conclusions

A model was developed to simulate heat transfer in a flat plate solar collector for air. A Reynolds-Averaged Navier-Stokes (RANS) $\kappa-\varepsilon$ model was used to obtain the velocity distribution. The energy balances in the absorber plate were modeled using a Lumped Model and a heat balance in the fluid using an PDE. The model correctly simulates the velocity distribution profile inside the collector and the temperature distribution inside the solar collector in non-steady state, taking into account the geometrical variations of the collector. The velocity distribution profile shows a velocity variation mainly in the longitudinal direction of the solar collector, y-direction.

The Reynolds numbers in the tubes resulted much smaller than in the space of the glass cover and absorber plate, so we have a higher turbulence and mixing in the part of the glass cover and absorber plate. However, the heat transfer coefficients were much lower due to the smaller equivalent diameter of the tubes which is inversely proportional to the Nusselt number.

The experimental temperature data were compared with the simulated data at a velocity of 2 m/s, showing a good fit in the fluid between the two datasets after the first hour, with a maximum difference of 6 °C. However, for the temperature on the plate, the fit improves after 2.16 hours, with a maximum difference of 10 °C.

The energy balance for the plate incorporates two coefficients: one for radiation (hprf) and one for convection. The convection coefficient is applied at the top of the plate for the fluid (hpf C-P) and at the bottom (hpf Pipe). These coefficients, when calculated using a correlation, that tend to underestimate the energy lost by the plate and thus must be experimentally determined to ensure with correlation is the best for the solar collector.

The model tends to estimate a higher temperature on the plate, which reduces the heat transferred to the C-P space and to the fluid in the pipes. Consequently, the simulated temperature in the tubes is lower than that observed experimentally.

Nomenclature

T	Temperature K
p	Pressure, Pa
d	aluminum thickness, m
b_1,b_2	Height and width of the tubes, m
Cp	Specific heat capacity, $Jkg^{-1}K^{-1}$
h_v	Latent heat of evaporation, Jkg^{-1}
I(t)	Solar irradiation, Wm^{-2}
κ	Dilatational viscosity, $kgm^{-1}s^{-1}$
h	Heat transfer coefficient, $Wm^{-2}K^{-1}$
D	Equivalent diameter, m
Greek letters	
α	Absorptivity
σ	Stefan Boltzmann constant, $Wm^{-2}K^{-4}$
ρ	Density, kgm^{-3}
ε	emissivity,m^3m^{-3}
τ	Transmissivity
μ	Viscosity, kg $m^{-1}s^{-1}$
Subscripts	
p	absorbed plate
f	air fluid
c	glass cover
0	ambient
a	Air
r	Radiation
Vectors and matrices	
u	Velocity, m/s
k	Thermal conductivity, $Wm^{-1}K^{-1}$
I	Identity matrix
n	Normal vector

References

Alleyne, F. S., Milczarek R.R. (2015). Design of Solar Thermal Dryers for 24-Hour Food Drying. Pp. 0-3 en *Proceedings of the 2015 COMSOL.*

Al-Tabbakh, A. A. (2022). Numerical Transient Modeling of a Flat Plate Solar Collector. *Results in Engineering* 15:100580. doi: https://doi.org/10.1016/j.rineng.2022.100580.

Azeez, K., Riyadh I. A., Zain A. O., Itimad D. J. A. (2023). Heat transfer enhancement and applications of thermal energy storage techniques on solar air collectors: A review. *Journal of Thermal Engineering* 9(5):1356-71.

doi: https://doi.org/10.18186/thermal.1377246.

Bakari, R. (2018). Heat transfer optimization in air flat plate solar collectors integrated with baffles. *Journal of Power and Energy Engineering* 06(01):70-84. doi: https://doi.org/10.4236/jpee.2018.61006.

Bakari, R., Rwaichi J. A. M., Karoli N. N. (2014). Effect of glass thickness on performance of flat plate solar collectors for fruits drying. *Journal of Energy* 2014:1-8. doi: https://doi.org/10.1155/2014/247287.

Bensaci, C. E., Abdelhafid M., Sánchez de la Flor F.J., Rodríguez Jara E., Rincón-Casado, A., Ruiz-Pardo A. (2020). Numerical and experimental study of the heat transfer and hydraulic performance of solar air heaters with different baffle positions. *Renewable Energy* 155:1231-44. doi: https://doi.org/10.1016/j.renene.2020.04.017.

Bolaji, B. O. (2012). Theoretical and Experimental Analyses of Heat Transfer in a Flat-Plate Solar Collector Design and Performance Evaluation of a Mobile Cooler Refrigerator Retrofitted with R134a View project Evaluation of Water-Extract from Fermented Ground Maize for its Potentials as Coolants for Engine and Machining Operations View project. doi: https://doi.org/10.2004/wjst.v9i3.227.

Gopi, R., Ponnusamy P., Fantin Arokiaraj A., Raji A. (2020). Performance comparison of flat plate collectors in solar air heater by theoretical and computational method. *Materials Today: Proceedings*, 39, 823-826.

Jallut, C., Jemni A., Lallemand M. (1988). Steady-state and dynamic characterization of an array of air flat-plate collectors. *Solar & Wind Technology* 5(5):573-79. doi: https://doi.org/10.1016/0741-983X(88)90049-5.

Kramer, K., Mehnert S., Geimer K., Reinhardt M., Fahr S., Thoma C., Kovacs P., Ollas P. (2017). Guide to standard ISO 9806:2017 a resource for manufacturers, testing laboratories, certification bodies and regulatory agencies. doi: https://doi.org/10.13140/RG.2.2.30241.30562.

Kumar, P., Singh D. (2020). Advanced technologies and performance investigations of solar dryers: A review. *Renewable Energy Focus* 35:148-58. doi: https://doi.org/10.1016/j.ref.2020.10.003.

Lingayat, A. B., Chandramohan V. P., Raju V. R. K., Meda V. (2020). A review on indirect type solar dryers for agricultural crops-Dryer setup, its performance, energy storage and important highlights. *Applied Energy* 258.

Mahroug, I., Doppiu S., Dauvergne J.L., Echeverria M., Toutain J., Palomo del Barrio E. (2021). Study of peritectic compound Li4(OH)3Br for high temperature thermal energy storage in solar power applications. *Solar Energy Materials and Solar Cells* 230. doi: https://doi.org/10.1016/j.solmat.2021.111259.

Matsumoto, Y., Valdés M., Urbano J.A., Kobayashi T., López G., Peña R. (2014). Global solar irradiation in north Mexico city and some comparisons with the south. *Energy Procedia*. Vol. 57. 1179-88.

Messina, S., González F., Saldaña C., Peña-Sandoval G.R., Tadeo H., Juárez-Rosete C.R., Nair P. K. (2022). Solar powered dryers in agricultural produce processing for sustainable rural development worldwide: A case study from Nayarit-Mexico. *Cleaner and Circular Bioeconomy* 3:100027. doi: https://doi.org/10.1016/j.clcb.2022.100027.

Mohana, Y., Mohanapriya R., Anukiruthika T., Yoha K. S., Moses J. A., Anandharamakrishnan C. (2020). Solar dryers for food applications: Concepts, designs, and recent advances. *Solar Energy* 208:321-44.

Mota, F. A. S., Furtado A. S. S., Leitao A. B. V., Medeiros N. C., Pereira G. S., Almeida M. N., Oliveira A., Oliveira M. M., Caselli F. T. R. (2025). Obtention of Methyl Esters Fractions through Distillation and Pour Point Evaluation of the Obtained Fractions. *Revista Mexicana de Ingeniería Química* 24(1). https://doi.org/10.24275/rmiq/IE24221

Ndukwu, M. C., Ibeh M., Okon B.B., Akpan G., Kalu C. A., Ekop I., Nwachukwu C.C., Abam F. I., Lamrani B., Simo-Tagne M., Ben A.E., Mbanasor J., Bennamoun L. (2023). Progressive review of solar drying studies of agricultural products with exergoeconomics and econo-market participation aspect. *Cleaner Environmental Systems* 9.

Rajarajeswari, K., Alok P., Sreekumar A. (2018). Simulation and experimental investigation of fluid flow in porous and non-porous solar air heaters. *Solar Energy* 171:258-70. doi: https://doi.org/10.1016/j.solener.2018.06.079.

Rani, P., Tripathy P. P. (2020). Thermal characteristics of a flat plate solar collector: influence of air mass flow rate and correlation analysis among process parameters. *Solar Energy* 211:464-77. doi: https://doi.org/10.1016/j.solener.2020.08.057.

Ranmode, V., Manmeet S., Bhattacharya J. (2019). Analytical formulation of effective heat transfer coefficient and extension of lumped capacitance method to simplify the analysis of packed bed storage systems. *Solar Energy* 183:606-18. doi: https://doi.org/10.1016/j.solener.2019.03.066.

Romero-Bonilla, H. I.; Jaramillo-Guanolique, A., Zambrano, C., Rios-Hidalgo, M., Solano-Maza, L., Choez-Tobo, C. (2025). Cocoa shell biochars for sustainable biodiesel production in Ecuador. *Revista Mexicana de Ingeniería Química* 24 (1). https://doi.org/10.24275/rmiq/IE24221

Rouissi, W., Naili N., Jarray M., Hazami M. (2021). CFD numerical investigation of a new solar flat air-collector having different obstacles with various configurations and arrangements. *Mathematical Problems in Engineering* 2021. doi: https://doi.org/10.1155/2021/9991808.

Shahsavari, A., Akbari M. (2018). Potential of solar energy in developing countries for reducing energy-related emissions. *Renewable and Sustainable Energy Reviews* 90:275-91.

Tiwari, R., Mishra K., Nath G. (2011). Advanced renewable energy sources. *Advanced Renewable Energy Sources*. Vol. 1. 45-109.

Vivekanandan, M., Jagadeesh D., Natarajan A., Mohan N., Dineshkumar M. (2020). Experimental and CFD investigation of fully developed flow solar air heater. *Materials Today: Proceedings*. Vol. 37. 2158-63.

Xiao, S., Zhang Y., Xia K., Long J. (2022). Influence of operating conditions on solar energy utilization efficiency of flat plate solar collector. *Renewables: Wind, Water, and Solar* 9(1). doi: https://doi.org/10.1186/s40807-022-00070-9.

Vol. 24, No. 2(2025) IA25513
Revista Mexicana de Ingeniería Química

Effect of absorber plate material on the performance of flat plate solar air heater under free convection

Efecto del material de la placa absorbedora en el desempeño de calentadores solares de aire de placa plana (SAH), bajo convección libre

R.C. Salmorán-Salgado[1‡], F. J. Moreno-García[2], J.E. Botello-Álvarez[3], B. Ríos-Fuentes[4], M. Calderón-Ramirez[5], M. C. Pérez-Pérez[6], J. M. Gutiérrez-Villalobos[7], L. Fausto-Castro[8]

[1]*Tecnológico Nacional de México en Celaya, Programa de Doctorado en Ciencias de la Ingeniería. García Cubas 600 Celaya, Gto. 38010, México.*

[2]*Tecnológico Nacional de México en Celaya, Programa de Maestría en Ciencias en Ingeniería Mecatrónica. García Cubas 600 Celaya, Gto. 38010, México.*

[3]*Tecnológico Nacional de México en Celaya, Departamento de Ingeniería Bioquímica y Ambiental. García Cubas 600 Celaya, Gto. 38010, México.*

[4]*Departamento de Ingeniería Agroindustrial, Universidad de Guanajuato, Celaya, 38060, México.*

[5]*Tecnológico Nacional de México CRODE Celaya, Celaya, 38020, México.*

[6]*Tecnológico Nacional de México en Celaya, Departamento de Ingeniería Bioquímica y Ambiental. García Cubas 600 Celaya, Gto. 38010, México.*

[7]*Departamento de Ingeniería Agroindustrial. Universidad de Guanajuato, Celaya, 38060, México.*

[8]*Departmento de Ingeniería Industrial, Universidad del Sabes, Apaseo El Grande, Guanajuato, 38163, México.*

Sent date: January 25, 2025; Accepted: June 23, 2025

Abstract

Solar air heaters (SAH) are an alternative to harness solar energy. In SAH´s, a metal plate absorber retains solar radiation to transfer it to the air. The effect of the plate material: aluminum, galvanized steel and carbon steel and the number of sheets on the thermal efficiency of SAH´s was evaluated, with an experimental design 32. The analysis shows that the material and the number of sheets have no effect on the thermal efficiency of SAH´s. A phenomenological analysis indicates that interfacial heat transport between the black paint film covering the absorber plates, and the air represents the greatest resistance to heat transfer. It is proposed to use covers with better optical properties that increase the surface temperature and the intensity of free convection.

Keywords: Solar energy, absorber plate, coat of paint.

Resumen

Los calentadores solares de aire (SAH) son una alternativa para aprovechar la energía solar. En los SAH´s, un absorbedor de placas metálicas retiene la radiación solar para transferirla al aire. Se evaluó el efecto del material de las placas: aluminio, acero galvanizado y acero al carbón y el número de láminas sobre la eficiencia térmica de los SAH´s, con un diseño experimental 32. El análisis muestra que el material y el número de láminas no tienen efecto sobre la eficiencia térmica de los SAH´s. Un análisis fenomenológico indica que el transporte de calor interfacial entre la película de pintura negra que cubre las placas absorbentes, y el aire representa la mayor resistencia a la transferencia de calor. Se propone utilizar cubiertas con mejores propiedades ópticas que aumenten la temperatura superficial y la intensidad de la convección libre.

Palabras clave: Energía solar, placa absorbedora, cubierta de pintura.

‡*Corresponding author. E-mail*: robertosalgado2329@gmail.com;
https://doi.org/10.24275/rmiq/IA25513
ISSN:1665-2738, *issn-e*: 2395-8472

1 Introduction

The global temperature increase is expected to exceed 2°C in 2050. To avoid this, it is proposed to leave 60% of gas and oil reserves underground and 90% of coal reserves (Welsby *et al*., 2021). Countries and companies whose economies and development are based on the use of fossil fuels will find it challenging to comply with these recommendations, so it is necessary to intensify the use of clean energy and make processes more efficient worldwide. Solar thermal energy systems use solar radiation to heat fluids such as air and water, which is an economical and versatile alternative for integration into industrial applications (Schoeneberger *et al*., 2020).

In 2017, the global food industry consumed 200 EJ (200×10^{18} J); the main forms of energy used are electrical and thermal. Energy consumption per kilogram of finished food product varies from 1.18 to 16.22 MJ. The primary consumption is thermal energy (Ladha-Sabur et al., 2019). Drying consumes between 3.0 and 16 MJ per kg of dried product, and the drying temperature is between 50 and 120 °C (Sanjuán *et al*., 2014). Solar drying is a practice that uses environmentally available energy. It allows for significant energy savings.

Solar thermal energy allows the integration of conventional and renewable energy sources to meet the thermal demands of certain food processing operations. Hybrid solar dryers are designed to combine solar energy with various types of auxiliary energy, including electric, fossil, renewable photovoltaic, wind, and biomass sources (Kong *et al*., 2024). Indirect solar dryers employ air preheating through SAH´s (Mekhilef *et al*., 2011). SAH´s are rectangular prisms comprising a glass cover and a metal plate with a black painted surface, known as the absorber. Air flows between the two plates, with heating occurring via natural or forced convection. The absorber plate receives solar radiation and transforms it into internal energy, enabling the heating of air from 30°C to 80°C (Kalogirou, 2003).

Solar energy, though intermittent, holds immense potential for the future. It is crucial to devise mechanisms that facilitate the accumulation of solar radiation during days with high insolation, its subsequent controlled storage, and regulated discharge, thereby compensating for unpredictable weather patterns. In their 2020 study Das & Akpinar, (2020) developed a solar drying system that employed a tracking mechanism. The SAH´s absorber plate utilized aluminum, which reached temperatures between 51.7°C and 81.7°C. In a study conducted by Mohammed *et al*. (2024), a series of SAH´s absorber surfaces, painted in black and comprising silicon powder, were tested. The surfaces were exposed to solar radiation values of 560 W/m² and temperatures of up to 60°C, demonstrating the promising potential of solar drying technology. Solar radiation impinges upon the absorber plate of the SAH´s, thereby increasing its internal energy and raising its surface temperature. The air entering the SAH´s is subjected to a rise in temperature due to heat transfer through conduction and convection mechanisms. The thermal efficiency of the SAH´s is determined by calculating the ratio between the heat energy gained by the air and the solar energy incident on the absorber plate. It can be seen that a proportion of the energy absorbed by the SAH´s is dissipated into the surrounding environment rather than being transferred to the transfer fluid. The elevated percentage of energy loss in SAH´s can be attributed to the optical properties of the paint layer, the thermal characteristics of the metal plate, hydrodynamic conditions, and the transport properties of the air in contact with the surface (Singh *et al*., 2019, Iglesias-Díaz *et al*. 2011).

The black paint film is the primary active component of an SAH; it is the center of absorption for solar radiation, which is transformed into internal energy and then transferred by conduction to the rear metal plate and into the air through its exposed face. The paint film is formed by a mixture of a polymeric matrix and metal oxides, including copper, cobalt, chromium, and nickel, arranged as dispersed particles or nanoparticles. Techniques have also been used where compounds of the aforementioned metals are electrochemically fixed to the absorber plate, forming dark aggregates with high absorbance (Kumar *et al*., 2022).

Its high thermal conductivity is the primary criterion for selecting an SAH absorber plate material. Using plates with enhanced thermal properties will result in the generation of equipment with superior performance. In a study conducted by Handoyo *et al*., (2014), aluminum-based absorber plates were utilized with a surface treatment referred to as "prismatic obstacles," resulting in efficiency values ranging from 0.15 to 0.85. Srivastava *et al*., (2017) report that implementing fins on aluminum-based absorber plates allows an operating efficiency of approximately 0.338. The selection of absorber plate coatings should be based on their high absorbance and low emissivity coefficients. Kumar *et al*., (2022) describe a coating formed from nanostructured CuO with an absorbance factor of 0.9 and an emissivity of 0.14.

This study aims to ascertain the impact of three SAH absorber plate materials on thermal efficiency when used aluminum, galvanized steel, and carbon

steel in a free convection environment. Three identical SAHs were constructed to ensure that the absorber plates of material different were subjected to identical environmental conditions and equal solar radiation.

2 Methodology

The dimensions of the SAHs are shown in Figure 1a. The prismatic body was constructed of ¾ inch pine wood and was painted with matte black enamel. The bottom was insulated with 1 ½ inch thick pink fiberglass. At the bottom, it has three 2.0 inch diameter holes to allow air inlet; at the top, it has a 4.0 inch diameter hole for air outlet.

The flat absorber plates are made of aluminum, galvanized steel and carbon steel with thicknesses of 1.5, 1.6 and 1.5 mm, respectively. The faces exposed to the sun were coated with matte black enamel. A 5.9 mm thick flat glass was used as a cover. As mentioned before, three identical SAHs were made to expose the absorber plates to the same environmental conditions; for this purpose, a platform was built to support the SAHs, where the dimensions are shown in Figure 1b and 1c. The platform has an inclination of 30º with respect to the horizontal. The experiments were carried out at the facilities of the TecNM in Celaya (20°32'18"N 100°49'09"W), in May and June 2024, exposing the SAHs from 10:00 to 15:00 hours. The environmental conditions during the experiments were: Temperature (25.4ºC - 40.4ºC), Humidity (21% - 57%), and Solar radiation (100 W/m^2-1390 W/m^2).

Air temperatures at the inlet and outlet of the SAHs were measured with J-type thermocouples (Maxim Integrated DS18B20:155 -122°C), where they were recorded on a laptop PC. The air velocity at the inlet of the SAHs was measured with a hot wire anemometer (Hot Wire Traceable Anemometer/Thermometer 4330CC, 0.2-20 m/s). The amount of solar radiation on the SAHs was measured with a solarimeter (TES-1333R, 0-2000 W/m^2). Environmental conditions were recorded through a portable weather station placed at the measurement site (Generic, -40-60ºC, 20%-90% humidity). A portable thermal camera (FLIR TG165, -25ºC-380ºC) was used to measure the temperature profiles on the absorber plates.

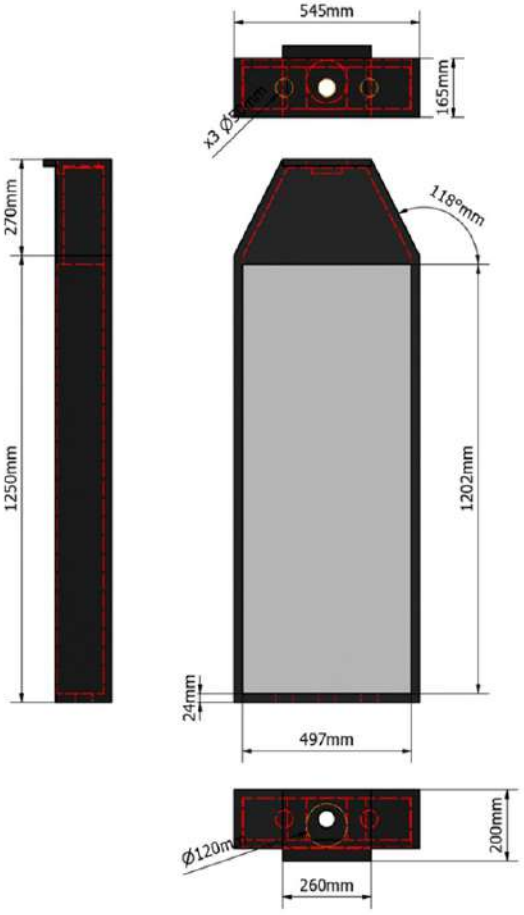

Fig. 1a

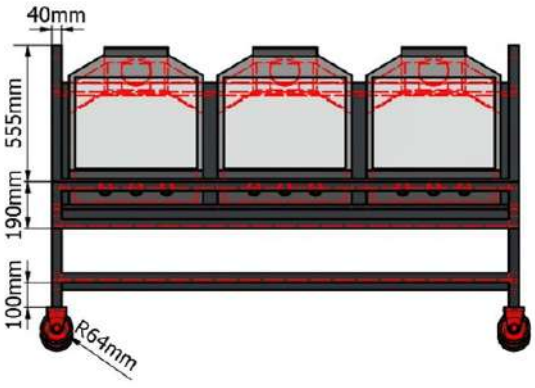

Fig. 1b

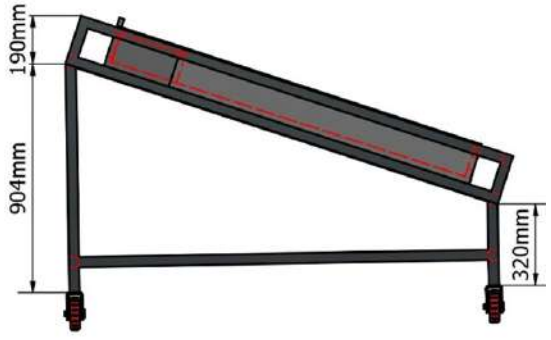

Fig. 1c

A 3^2 experimental design was carried out, where two factors were studied: absorber plate material and number of sheets with three levels, materials: aluminum, galvanized steel, carbon steel and number sheets : 1, 2, 3. In each experiment, absorber plates of different materials were used, placed in each of the SAH´s, in order to reduce the effect of uncontrolled environmental conditions on the thermal performance of the SAH´s, and the experiments were carried out in triplicate for three continuous days.

To estimate the thermal efficiency η according to Equation 1 (Pardeshi *et al*., 2024) it is necessary to estimate the mass flow rate of air circulating through the SAH, driven by buoyancy forces, which depend on the axial and transverse differences in air density associated with the local temperatures between the shell and absorber plate.

$$\eta = \frac{\dot{m}C_p(T_{ao} - T_{ai})}{I_{\text{solar}}A_{\text{plate}}} \quad (1)$$

Where m and Cp are the mass flow rate and heat capacity of the air, T_{ao} and T_{ai} are the air inlet and outlet temperatures to the SAHs, I_{solar} is the solar incidence of the air, and A_{plate} is the area of the absorber plate exposed to solar radiation. The air properties (density and heat capacity) were estimated at the average temperature of Tao and Tai, considering the data reported by Green & Southard (2019). For all experiments, the convective heat transfer coefficients were estimated using Equation 2 (Sidebotham, 2015).

$$Nu_{\text{air}} = 0.54\,Ra^{1/4} \quad (2)$$

This equation is valid for gas mixtures heated on an inclined metal surface. Where Nuair is the Nusselt number for air, using the separation between the absorber plate and the glass cover as the characteristic distance. Ra is the Rayleigh number; this equation is valid for a Ra range of 104–106 10^4-10^6 (Sidebotham, 2015).

The experimental data on air temperatures at the outlet of the SAH´s, as well as the estimated data on thermal efficiency with different absorber plate materials, were statistically analyzed using “t student” tests to evaluate the hypothesis of equality of means. In the case of temperatures, their dispersion was evaluated by estimating confidence intervals for an α of 0.05, using Excel® tools.

In addition, further experiments were performed as described above, with intermittent operation of continuous exposure to radiation for 40 minutes and then for 20 minutes the SAH´s were covered with completely opaque cardboard. During these periods the heating and cooling rates of the air inside the SAH´s were calculated.

3 Results

3.1 Thermal efficiencies

Figure 2 presents the temperatures and solar radiation monitored during an experiment for three solar air heaters (SAHs) with absorber plates made of different materials. The average air temperatures at the SAH outlet are shown for the three experiments using one absorber plate; the bars indicate the maximum and minimum temperatures for each measurement. A comparative Student t-test between the experimental data sets for each absorber plate material indicated no significant differences in the average temperatures for SAHs with absorber plates made of different materials.

Figure 3A presents the thermal efficiencies and average solar radiation, along with their specified ranges between the maximum and minimum values , for SAHs with absorber plates of different materials—case (2 sheets). The estimated efficiencies do not exceed 20% despite a temperature increase of nearly 30°C as the air passes over the absorber plates. The low efficiencies are mainly associated with the low mass air flows driven by free convection phenomena. During some experiments, clouds formed, casting shadows over the SAHs and resulting in a substantial decrease in incident solar radiation, as observed in Figure 3B. Under these circumstances, a significant increase in thermal efficiencies occurs because the air continued to heat up, associated with the energy absorbed by the absorber plates and the rest of the SAH body due to radiation exposure prior to the shadows. Under these circumstances, SAHs with aluminum sheets experience higher thermal efficiencies.

Yadav & Bhagoria (2013) mention that smooth plate SAHs have poor performance; the inclusion of fins, posts, roughness, and baffles improves thermal efficiency but also increases friction, pressure drop, and energy expenditure due to the inclusion of blowers. The thermal efficiency with forced convection for SAHs with smooth and rough plates was 19.78-44.26% and 52.51-72.20%.

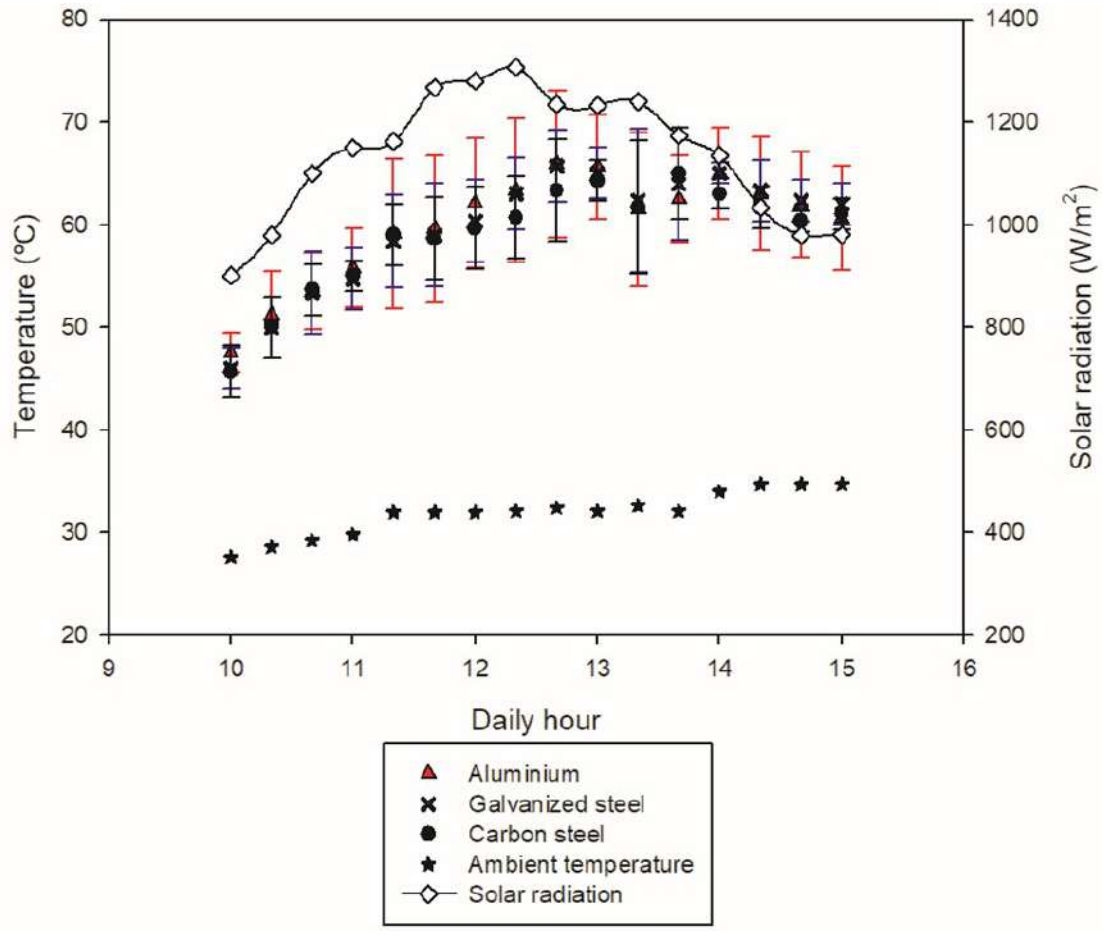

Figure 2. Air temperatures at the inlet and outlet of a SAH and solar radiation.
Use of (1 sheet).

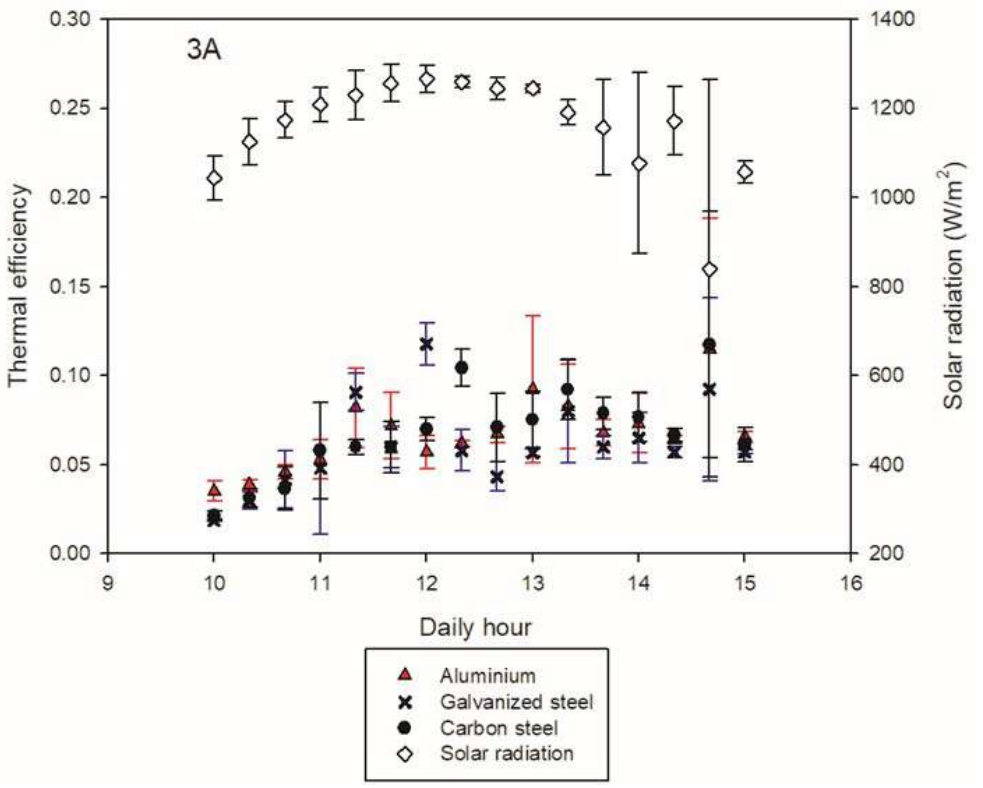

Fig. 3A

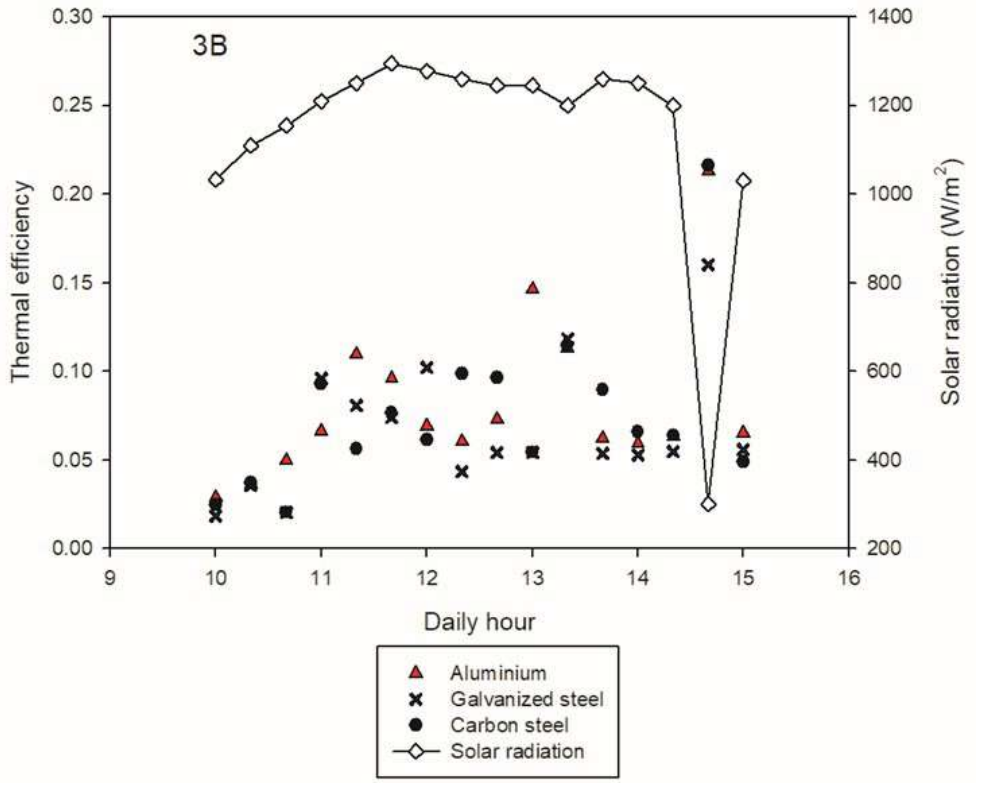

Fig. 3B.

Case II. Use of 2 sheets.

3.2 Statistical analysis

As a response variable in the experimental design, a daily overall efficiency was calculated, represented in Equation 3 (Pardeshi *et al*., 2024). The equation represents the ratio between the total heat given up to the air and the total incident solar radiation on the plate during the experimental time. The subfix i represents the measurement periods (every 20 minutes) performed during the experiment.

$$\eta_{\text{Global}} = \frac{\sum_i \dot{m} C_p (T_{ao} - T_{ai})_i}{\sum_i (I_{\text{solar}} A_{\text{plate}})_i} \tag{3}$$

Table 1 shows the percentages of thermal efficiencies calculated according to equation 4 for the experimental design proposed 32. The efficiency data for the different materials presented in the same row were obtained by exposing the 3 SAH´s to the same environmental conditions in order to reduce the experimental error. Observing the efficiency values per row shows similar values for the different materials, this also occurs when comparing the experiments with different number of sheets.

Table 2 presents the analysis of variance showing that the mean squares associated with the sources of variation of the material and the number of sheets, as well as the interaction of these materials, are lower than the experimental error. The "F" parameter and the confidence interval indicate (P) that the material and the number of sheets does not have a significant effect on the thermal efficiency of the SAH´s. The parameter F is the ratio of the mean squares associated with the sources of variation studied and the mean squares associated with the experimental error; in all cases, the error is significantly greater than the effects of the factors. (Calderón-Ramírez *et al*., 2022) Demonstrated that environmental conditions have a substantial effect on thermal efficiencies; however, since they are considered uncontrollable factors, their effects are included in the experimental error. To avoid this situation, in this work, three identical SAHs were built to expose the different absorber plate materials to identical environmental conditions, as shown in Table 1.

3.3 Phenomenological Analysis

Figure 4 shows the air velocities at the inlet of the SAHs, measured at the center of the lower holes. It can be observed that air velocities vary significantly from their average. In general, air velocities increase with increasing solar radiation and the difference between the SAH air inlet and outlet temperatures (Figure 2). These increases are associated with free or buoyant convection mechanisms due to differences in air density as it heats towards the interior of the SAH, with a transverse contribution from temperature differences between the absorber plate and the air. In general, it is observed that the materials of the absorber plates do not affect the behavior of the air velocities. For these experiments, Grashof and Prandtl numbers were calculated to estimate the Rayleigh number. Under these conditions the Rayleigh number varies in the range of 1.07E+06 - 2.43E+06, which corresponds to a transitional laminar flow regime; to achieve the turbulent regime that satisfactorily enhances the hydrodynamic heat transfer conditions the Rayleigh number must more significant than 1.0E+09 (Sidebotham, 2015). Under these conditions, it is expected that heat transfer in the air-surface interfacial region will be limited to conduction mechanisms.

Table 1. Percentage of thermal efficiencies in SAH´s

	Material		
#sheets	Aluminum	Galvanized steel	Carbon Steel
1	9.02 % 5.45 % 7.05 %	8.08 % 5.60 % 5.98 %	9.07 % 5.59 % 6.59 %
2	5.96 % 7.64 % 5.88 %	5.76 % 6.35 % 5.87 %	6.20 % 7.03 % 6.46 %
3	7.25 % 6.22 % 7.65 %	6.79 % 6.43 % 6.98 %	7.30 % 6.77 % 7.86 %

Table 2. Analysis of variance

Sources of variation	Sum of squares	Degrees of freedom	Mean squares	F	Value - P
A: Material	2.2994	2	1.1449	0.79	0.4675
B: Number of sheets	1.8552	2	0.9276	0.64	0.5389
AB: Interaction	0.1084	4	0.0271	0.02	0.9992
Error	26.0871	18	1.4492	-	-

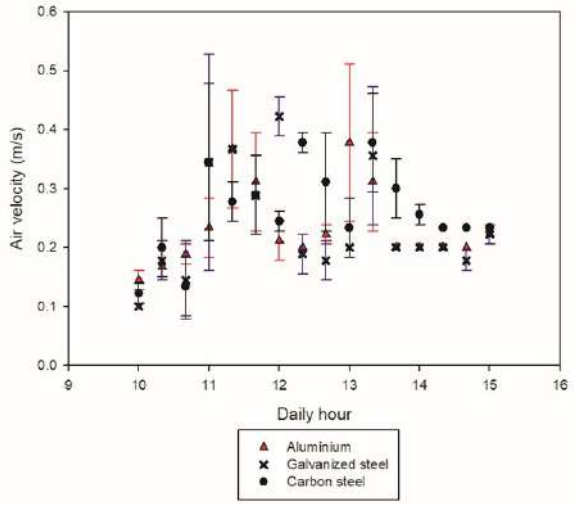

Figure 4. Average air velocities at the SAH´s inlet are measured using a material plate.

Using formula (2), the convective heat coefficients between the absorber plate and the air were estimated in the range of: 4.52 - 5.82 W/m2 ºC, considering the separation between the absorber plate and the glass cover as characteristic distance. Using a thermal camera, the surface temperature of the absorber plate was estimated (67.3ºC - 68ºC). With the temperatures at the inlet and outlet of the SAH, the average logarithmic temperature difference between the absorber plate and the air was calculated, which varied between (14.6 ºC - 47.7 ºC). Considering the best heat transfer conditions, the plate could yield 277.61 W/m2 to the air, while the solar radiation reached up to 1400 W/m^2. Under this phenomenological analysis, the thermal efficiencies will not exceed 20%.

Statistical analysis of thermal efficiencies formally shows that materials and the number of layers do not have a significant effect as sources of variation. However, a deeper understanding of the experimentally observed phenomenology is needed to improve the performance of these devices. It was proposed to study heat transfer between air and the absorber plate in SAH using a composite wall model, whose overall heat transfer coefficient is expressed according to equation 3 (Yadav & Bhagoria, 2013), comprised of the resistances offered by each wall and the fluid media in contact with the external and internal surfaces of the wall.

Figure 5 illustrates a representative schematic of the absorber plate's cross-section, with the insulating material placed on its back. The heat transfer mechanisms involved are also outlined. Solar radiation is primarily absorbed at the surface of the paint film, being absorbed by the related chromophore molecules, as described by Kumar *et al*. (2022). Solar radiation causes a significant increase in molecular vibrations, which translates into an increase in the internal energy and temperature of the paint film. The other portion of solar radiation is reflected or emitted as radiation by the black paint surface to the exterior. "In general, the direct energy interaction of solar radiation is exclusively with the surface of the paint film." Thus, the internal energy received and accumulated in the paint film is transferred to the metal plate by conduction or to the air through conduction and convection mechanisms. The rates of heat transfer to the plate or the air will depend on the local temperature gradients and the resistance offered in each area.

Table 3 presents some properties reported in the literature of the materials used. Panas *et al*., (2021) show characteristic values of paint thicknesses and conductivities. Org (1996), show typical values of thermal conductivity of fiberglass quilts. Using the definition of overall heat transfer coefficient in composite walls shown in Equation 4 (Yadav & Bhagoria, 2013), the resistances offered by each material ($\Delta X_i/K_i$), as well as the heat transfer resistance between the absorber plate and the air ($1/h_{air\text{-}plate}$) were estimated.

$$U = \frac{1}{\frac{1}{h_{air\text{-}plate}} + \sum_i \frac{\Delta X_i}{K_i}} \tag{4}$$

These values indicate that the heat absorbed in the paint film on the surfaces of the plates exposed to solar radiation is transferred more easily to the inside of the plate or overlapping plates than to the air flowing over the surface of the absorber plate. As can be seen, the fiberglass offers great resistance to heat loss through the bottom of the plates, and these should experience temperatures much higher than the observed values. However, it is important to establish that the temperature on the surface is controlled mainly by the heat removal capacity of the circulating air stream. Under these circumstances, it can be hypothesized that a significant portion of the heat is being reflected outward. The paint coating should have a more significant effect than the absorber plate material.

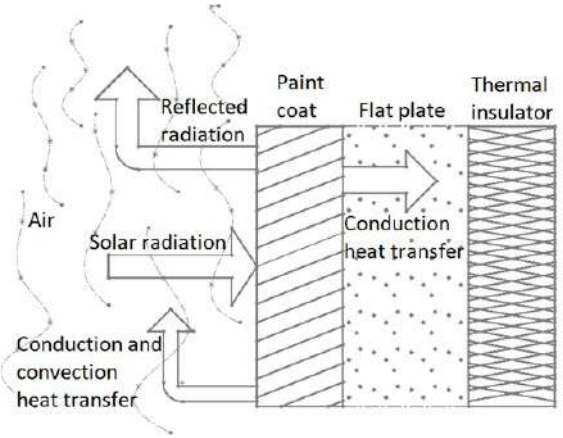

Figure 5. Composite wall model and heat transfer mechanism in the absorber plate.

Figure 3B shows that during the decrease of solar radiation due to some atmospheric effect, the efficiency of the SAH increases significantly, since the air heating does not give way even when the solar radiation decreases drastically, given that the internal energy in the absorber plate and the body of the SAH was accumulated during the time prior to the occurrence of this phenomenon. This graph shows that the aluminum plate has a much higher efficiency than the other materials. To make this phenomenon evident, experiments were carried out with intermittent exposure of the SAH to solar radiation, as described in the methodological section. Air heating rates ($\Delta T/\Delta t$, °C/min) during exposure to solar radiation - heating and shading – cooling, were estimated. The results are presented in Table 4. The results show that the air heating or cooling rates with aluminum absorber plates are higher, mainly for the experiments with 2 and 3 plates. These results are associated with higher thermal conductivity of aluminum. These results appear to be contradictory to the analysis of variance. However, the thermal efficiency during continuous operation of a solar absorber is associated with a continuous and dynamic heat transfer process that can be disturbed circumstantially and temporarily by some uncontrolled event.

Table 3. Thermal properties of the materials and heat transfer resistances

Materials	Specific heat (J/kg °K)	Density (kg/m^3)	Thickness (m)	Thermal conductivity (W/m °K)	Resistance (m^2 °K/W)
Aluminum	903	2702	1.5×10^{-3}	237	6.32×10^{-6}
Carbon steel	434	7854	1.5×10^{-3}	60.5	2.47×10^{-5}
Galvanized steel	444	7822	1.6×10^{-3}	37.7	4.24×10^{-5}
Paint1	–	–	100×10^{-6}	0.58	1.72×10^{-4}
Fiberglass	–	–	3.81×10^{-2}	0.05	0.762
Plate - Air	–	–	–	–	1.71×10^{-1}

Table 4. Heating and cooling rates of air in intermittent operation (°C/min)

Number of plates	Aluminum	Carbon steel	Galvanized steel
Warming up			
1	0.2997	0.2912	0.2103
2	0.2078	0.1688	0.1078
3	0.2131	0.1688	0.1431
Cooling			
1	-0.4656	-0.463	-0.2987
2	-0.3775	-0.2962	-0.1666
3	-0.4031	-0.3132	-0.2405

4 Conclusions

The methodological approach of constructing platforms housing several solar air heaters with different configurations allows for reducing the significant effects of weather conditions on thermal efficiency. Aluminum, galvanized steel, and carbon steel absorber plates did not show a significant difference in the air heating process in the SAH´s under free convection conditions. The paint film has a controlling effect on the plate and air heating. However, experiments varying in thickness, materials, and paint treatment are needed to strengthen this conclusion and to have a better understanding of the transport phenomena occurring at the plate-air interface in solar heaters. We recommend the use of aluminum plates because of their light weight and resistance to environmental effects such as oxidation.

Acknowledgements

This work was supported by the financing of the projects: “Tecnológico Nacional de México Proyect: 20065.24P", and the acknowledgment to CONAHCYT for the scholarship granted Roberto Carlos Salmorán Salgado and Felipe de Jesús Moreno García.

References

Calderón-Ramírez, M., Gomez-Náfate, J. A., Ríos-Fuentes, B., Rico-Martínez, R., Martínez-Nolazco, J. J., & Botello-Álvarez, J. E. (2022). Analysis of the thermal efficiency of flat plate solar air heaters considering environmental conditions using artificial neural networks. *Revista Mexicana de Ingeniería Química*, *21*(3). https://doi.org/10.24275/rmiq/Sim2833

Das, M., & Akpinar, E. K. (2020). Determination of thermal and drying performances of the solar air dryer with solar tracking system: Apple drying test. *Case Studies in Thermal Engineering*, *21*. https://doi.org/10.1016/j.csite.2020.100731

Green, D. W., & Southard, M. Z. (2019). *Perry's Chemical Engineers' Handbook*.

Handoyo, E. A., Ichsani, D., Prabowo, & Sutardi. (2014). Experimental studies on a solar air heater having v-corrugated absorber plate with obstacles bent vertically. *Applied Mechanics and Materials*, *493*, 86–92. https://doi.org/10.4028/www.scientific.net/AMM.493.86

Kalogirou, S. (2003). The potential of solar industrial process heat applications. *Applied Energy*, *76*(4), 337–361. https://doi.org/10.1016/S0306-2619(02)00176-9

Kong, D., Wang, Y., Li, M., & Liang, J. (2024). A comprehensive review of hybrid solar dryers integrated with auxiliary energy and units for agricultural products. *Energy*, *293*. https://doi.org/10.1016/j.energy.2024.130640

Kumar, R., Verma, S. K., Mishra, S. K., Sharma, A., Yadav, A. S., & Sharma, N. (2022). Performance Enhancement of Solar Air Heater using Graphene/Cerium Oxide and Graphene-Black Paint Coating on Roughened Absorber Plate. *International Journal of Vehicle Structures and Systems*, *14*(2), 273–279. https://doi.org/10.4273/IJVSS.14.2.23

Ladha-Sabur, A., Bakalis, S., Fryer, P. J., & Lopez-Quiroga, E. (2019). Mapping energy consumption in food manufacturing. *Trends in Food Science & Technology*, *86*, 270–280. https://doi.org/10.1016/j.tifs.2019.02.034

Iglesias-Díaz, R., Pantoja-Enriquez, J., Moreira-Acosta, J., Farrera, N., & Ibáñez-Duharte, G. (2011). *Diseño de un secador solar con circulación forzada* (Vol. 5, Issue 5).

Mekhilef, S., Saidur, R., & Safari, A. (2011). A review on solar energy use in industries. *Renewable and Sustainable Energy Reviews*, *15*(4), 1777–1790. https://doi.org/10.1016/j.rser.2010.12.018

Mohammed, S. A., Alawee, W. H., Chaichan, M. T., Abdul-Zahra, A. S., Fayad, M. A., & Aljuwaya, T. M. (2024). Optimized solar food dryer with varied air heater designs. *Case Studies in Thermal Engineering*, *53*. https://doi.org/10.1016/j.csite.2023.103961

Org, E. (1996). *Lawrence Berkeley National Laboratory Recent Work Title Impact of the Temperature Dependency of Fiberglass Insulation R-Value of Cooling Energy Use in Building Publication Date*.

Panas, A. J., Szczepaniak, R., Stryczniewicz, W., & Omen, Ł. (2021). Thermophysical properties of temperature-sensitive paint. *Materials*, *14*(8). https://doi.org/10.3390/ma14082035

Pardeshi, P. S., Boulic, M., van Heerden, A. (Hennie), Phipps, R., & Cunningham, C. W. (2024). Review of the thermal efficiency of a tube-type solar air heaters. *Renewable and Sustainable Energy Reviews*, *199*. https://doi.org/10.1016/j.rser.2024.114509

Sanjuán, N., Stoessel, F., & Hellweg, S. (2014). Closing data gaps for LCA of food products: Estimating the energy demand of food processing. *Environmental Science & Technology*, *48*(2), 1132–1140. https://doi.org/10.1021/es4033716

Schoeneberger, C. A., McMillan, C. A., Kurup, P., Akar, S., Margolis, R., & Masanet, E. (2020). Solar for industrial process heat: A review of technologies, analysis approaches, and potential applications in the United States. *Energy*, *206*. https://doi.org/10.1016/j.energy.2020.118083

Sidebotham, G. (2015). Nusselt Number Correlations. In *Heat Transfer Modeling* (pp. 351–375). Springer International Publishing. https://doi.org/10.1007/978-3-319-14514-3_9

Singh, I., Vardhan, S., Singh, S., & Singh, A. (2019). Experimental and CFD analysis of solar air heater duct roughened with multiple broken transverse ribs: A comparative study. *Solar Energy*, *188*, 519–532.

Srivastava, R., Kumar Rai, A., & Kumar Srivastava, R. (2017). A review on solar air heater technology. *International Journal of Mechanical Engineering and Technology*, *8*(7), 1122–1131.

Welsby, D., Price, J., Pye, S., & Ekins, P. (2021). Unextractable fossil fuels in a 1.5 °C world. *Nature*, *597*(7875), 230–234. https://doi.org/10.1038/s41586-021-03821-8

Yadav, A. S., & Bhagoria, J. L. (2013). Heat transfer and fluid flow analysis of solar air heater: A review of CFD approach. *Renewable and Sustainable Energy Reviews*, *23*, 60–79. https://doi.org/10.1016/j.rser.2013.02.035

Vol. 24, No. 2(2025) IE25556
Revista Mexicana de Ingeniería Química

Synergetic control of cascade-configured anaerobic digestion bioreactors for enhanced hydrogen production

Control sinérgetico de biorreactores de digestión anaeróbica configurados en cascada para la producción mejorada de hidrógeno

O. Messili, S. Semcheddine*, A. Chaabna
Laboratory of Power Electronic and Industrial Control (LEPCI), University of Ferhat Abbas Setif 1, Setif 19000 Algeria.
Sent date: March 25, 2025; Accepted: May 27, 2025

Abstract
This work introduces, for the first time, a synergetic control law within a cascade control structure tailored to the dynamics of anaerobic bioreactors for hydrogen generation. This novel integration addresses the challenges of biological system nonlinearities, input saturation, and stability under disturbance, offering a promising alternative to traditional PID-based strategies.

To assess the effectiveness of the proposed approach, simulation studies were conducted in the Matlab/Simulink environment using a validated dynamic model from the literature. A comparative analysis with a classical PID controller optimized via genetic algorithms (GA-PID) was also carried out. The proposed synergetic controller achieved the desired hydrogen outflow rate within 1.1 hours, representing a 78.4 % improvement in response time compared to the GA-PID controller (5.1 hours).

Furthermore, the synergetic controller maintained closed-loop stability under input saturation (D_1), effectively handled external disturbances and sensor noise, and provided consistent tracking performance without biomass washout. These results demonstrate the superior precision, robustness, and convergence speed of the proposed method in regulating hydrogen production under realistic constraints.
Keywords: Cascade bioreactors, Synergetic control, Non linear control, Hydrogen, Methane, Waste recycling.

Resumen
Este trabajo presenta, por primera vez, una ley de control sinergetico integrada dentro de una estructura de control en cascada, adaptada a la dinamica de biorreactores anaerobios para la generacion de hidrogeno. Esta novedosa integracion aborda los desafios inherentes a la no linealidad de los sistemas biologicos, la saturacion de entrada y la estabilidad frente a perturbaciones, constituyendo una alternativa prometedora frente a las estrategias tradicionales basadas en controladores PID.

Para evaluar la eficacia del enfoque propuesto, se realizaron estudios de simulacion en el entorno Matlab/Simulink utilizando un modelo dinamico validado disponible en la literatura. Asimismo, se llevo a cabo un analisis comparativo con un controlador PID clasico optimizado mediante algoritmos geneticos (GA-PID). El controlador sinergetico propuesto alcanzo el caudal de salida de hidrogeno deseado en un tiempo de 1.1 horas, lo que representa una mejora del 78.4% en el tiempo de respuesta en comparacion con el controlador GA-PID (5.1 horas).

Ademas, el controlador sinergetico mantuvo la estabilidad en lazo cerrado bajo condiciones de saturacion de entrada (D_1), gestiono eficazmente perturbaciones externas y ruido en los sensores, y garantizo un seguimiento preciso sin provocar el lavado de biomasa. Estos resultados evidencian la superior precision, robustez y velocidad de convergencia del metodo propuesto en la regulacion de la produccion de hidrogeno bajo restricciones realistas.
Palabras clave: Biorreactores en cascada, control sinérgico, control no lineal, hidrógeno, metano, reciclaje de residuos.

* *Corresponding author. E-mail*: s.semcheddine@ieee.org;
https://doi.org/10.24275/rmiq/IE25556
ISSN:1665-2738, *issn-e*: 2395-8472

1 Introduction

Anaerobic digestion (AD) is a fundamental process to recycle industrial and domestic agricultural waste. The production of energy in the absence of oxygen will allow to valorize them by ensuring their disintegration. Initially, waste recycling focused solely on methane production, but later it was realized that hydrogen (H_2) could also be produced by combining two bioreactors. With a configuration of two bioreactors arranged in cascade, hydrogen can be obtained from the first bioreactor, in addition to methane from the second. The cascade structure allows for a clear separation between the fast and slow dynamics, enabling independent tuning and improved stability (Braguglia *et al*., 2018; Kuang *et al*., 2020). In such cascade systems, a two-stage configuration is typically employed, consisting of separate reactors for hydrogen and methane production, often implemented as two continuous stirred-tank reactors (CSTRs) (Dareioti and Kornaros, 2014; Li and Li, 2019; Borisov *et al*., 2016; Chorukova *et al*., 2021; Borisov *et al*., 2020; Prapinagsorn *et al*., 2018; Arumugam *et al*., 2015).

Hydrogen is one of the most environmentally friendly energy sources, and its energy density per unit of mass is 2.5 times higher than that of fossil fuels (Khan *et al*., 2016). Among various clean alternative energy resources, hydrogen was considered a potential future energy source to replace the progressive depletion of fossil fuels. Hydrogen energy produces more energy than hydrocarbon energy. It plays a key role in the decarbonization of future energy systems, with strong potential as a clean energy carrier, especially in heating and power generation sectors (Ameli *et al*., 2024). Researchers have devoted significant efforts to advancing hydrogen production technologies. For instance, R. García-Amador et al. (2019) assessed the feasibility of bioelectrohydrogen production using microbial electrolysis cells fed with hydrolysate from agave bagasse, demonstrating its potential as a sustainable substrate for renewable energy generation. Additionally, Buitrón *et al*. (2022) demonstrated that key efficiency parameters, such as current density and cathodic efficiency, are strongly correlated with hydrogen production from volatile fatty acids in microbial electrolysis cells. Therefore, biological processes are being identified as a promising technology for hydrogen production (Abdallah *et al*., 2016; Li and Li, 2019; Borisov *et al*., 2020).

Control is crucial for achieving the desired efficiency in the treatment process of AD plants (Serrano-Meza *et al*., 2020). In order to obtain a maximum yield of biogas and biofuels production, a range of control methods are dedicated to the AD process (Bayen and Gajardo, 2019; Simeonov and Queinnec, 2006; Petre *et al*., 2013; Chaabna and Semcheddine, 2025). Control linearization is frequently used as a stable feeding control strategy in anaerobic digestion. E. Petre *et al*. (2013) implemented robust adaptive linearizing controller to control the pollution level in anaerobic digestion process. Intelligent controllers, such as rule-based expert systems (Barnett and Andrews, 1992), fuzzy control (Ghanavati *et al*., 2021), and neural networks (Holubar *et al*., 2003), serve as effective instruments for stabilizing and regulating the anaerobic digestion process. These controllers eliminate the need for precise mathematical models of the anaerobic digestion process. However, their designs heavily depend on fuzzy rules or intricate neural networks, which can increase computational load. The Proportional–Integral–Derivative (PID) control serves as a straightforward and efficient technique for stabilizing the AD process (García-Diéguez *et al*., 2011). It is often implemented for temperature control (Maurya *et al*., 2024). However, PID controller is known for not being robust and might fail to handle the nonlinearities of complex biological systems. In the control of the AD systems, the dilution rate is commonly utilized as the control action (Antonelli *et al*., 2003). Taking into account the practical operation and the need to prevent the decay of microorganisms, there are always minimum and maximum limits to the dilution rate. Therefore, it is both valuable and necessary to develop a controller that operates within these limits (Grognard and Bernard, 2006). Kolesnikov and coauthors in 2000, have developed a nonlinear control method known as synergetic control, which is a recent technique in which the system's nonlinear component is not compensated, but synthesized based on a system model that forces the system to slide onto a manifold. This method is beneficial for reducing the order of the system. It uses a generalized state-space averaged model to maintain stability, even when there are changes in parameters and disturbances (Santi *et al*., 2004). The synergetic control naturally mitigates the impact of nonlinearities, and uncertainties as well (Hagh *et al*., 2021; Belmouhoub *et al*., 2023). This control approach has been effectively utilized in constant power loads such as converters with constant power load (Santi *et al*., 2004), etc.

This work presents a novel application of synergetic nonlinear control approach to perform the hydrogen outflow rate control. The synergetic control shares robustness characteristics with Sliding Mode Control (SMC), yet it successfully eliminates the issue of chattering (Gao *et al*., 2021; Santi *et al*., 2004). This law requires knowledge of the system model in order to solve a tracking problem (Bouchareb *et al*., 2019). It can be implemented for practical use as it is mentioned in Dong *et al*. (2022) for perspective. The novelty of this work resides in the application of a synergetic approach to control hydrogen production for the first time to date. The proposed approach is

further compared to the classical PID controller. The parameters of the PID were meticulously determined and fine-tuned utilizing the heuristic optimization technique known as Genetic Algorithm (GA). The comparison showed that the proposed approach is more effective in term of robustness and noise rejection.
This paper is organized as follows: an overview of the process is briefly outlined, which is then followed by a concise section on synergetic control. The development of the corresponding control law of a biogas plant is then established. The simulation results are presented and discussed in the following sections. Finally a conclusion and perspectives are presented whose can be developed later.

2 Process model

The Cascade AD system is a promising method to solve some energy problems and recycle organic waste. Production of hydrogen via AD is recently one of the most interesting research topics for different reasons. A nonlinear model expresses the biotechnological process, which is characterized by a two-stage reaction. Various mathematical models for cascade AD have been proposed in the specialized literature (Borisov *et al*., 2020; Blumensaat and Keller, 2005).
The model adopted in this study was originally proposed in (Chorukova *et al*., 2021). Hydrogen production takes place in the first bioreactor (BR1) and methane production progress in the second bioreactor (BR2).

The dynamics of a cascade AD system are demonstrated by the following system of first-order differential equations:
BR1:

$$\frac{dS_0}{dt} = -D_1 S_0 - \beta X_1 S_0 + D_1 Y_p S_0^{in} \tag{1}$$

$$\frac{dS_1}{dt} = -D_1 S_1 + \beta X_1 S_0 - \frac{1}{Y_1}\mu_1 X_1 \tag{2}$$

$$\frac{dX_1}{dt} = \mu_1 X_1 - D_1 X_1 \tag{3}$$

$$\frac{dA_{c_1}}{dt} = \frac{1}{Y_2}\mu_1 X_1 - D_1 A_{c_1} \tag{4}$$

$$Q_{H_2} = Y_{H_2}\mu_1 X_1 \tag{5}$$

$$\mu_1 = \frac{\mu_{1max} S_1}{k_{s1} + S_1} \tag{6}$$

BR2:

$$\frac{dX_2}{dt} = \mu_2 X_2 - D_2 X_2 \tag{7}$$

$$\frac{dA_{c_2}}{dt} = -\frac{1}{Y_3}\mu_2 X_2 + D_2(A_{c_1} - A_{c_2}) \tag{8}$$

$$Q_{CH_4} = Y_{CH_4}\mu_2 X_2 \tag{9}$$

$$\mu_2 = \frac{\mu_{2max} A_{c_2}}{k_{s_2} + A_{c_2}} \tag{10}$$

Where the model variables are:

- D_1: Dilution rate for BR1 $[h^{-1}]$;
- D_2: Dilution rate for BR2 $[h^{-1}]$;
- Q_{H_2}: Hydrogen outflow rate [L/h];
- Q_{ch_4}: Methane outflow rate [L/h];
- S_0: Cellulose concentration [g/L];
- S_1: Cellobiose substrate concentration [g/L];
- X_1: Acidogenic bacteria concentration [g/L];
- X_2: Methanogenic bacteria concentration [g/L];
- S_0^{in}: Inlet cellulose concentration in BR1 [g/L];
- A_{c_1}, A_{c_2}: Acetate concentration [g/L];
- μ_1: Specific growth rate for acidogenic bacteria $[h^{-1}]$;
- μ_2: Specific growth rate for methanogenic bacteria $[h^{-1}]$.

And the model parameters:

- μ_{1max}: Maximum specific growth rate for acidogenic bacteria $[h^{-1}]$;
- μ_{2max}: Maximum specific growth rate for methanogenic bacteria $[h^{-1}]$;
- k_{S1}: Saturation coefficient for acidogenic bacteria [g/L];
- k_{S2}:Saturation coefficient for acetogenic bacteria [g/L];
- β: Coefficient of biodegradability [L/(g.h)];
- Y_P: Coefficient [-];
- Y_1: Yield coefficient for acidogenic bacteria [-];
- Y_2: Yield coefficient for acetogenic bacteria [-];
- Y_3: Yield coefficient for methanogenic bacteria [-];
- Y_{H2}: Yield coefficient for hydrogen [L/g];
- Y_{CH4}: Yield coefficient for methane [L/g].

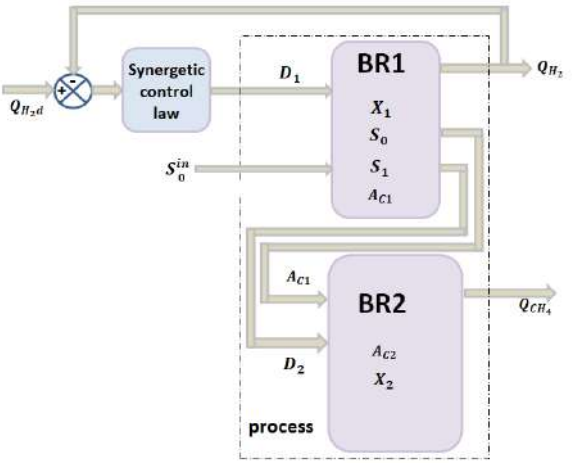

Figure 1. Two-phases process of AD with production of hydrogen and methane under synergetic control law.

3 Synergetic control law design

The concept of synergetic control theory was introduced by Russian researchers in a general manner in the early 2000 (Kolesnikovetal.,2000). The development of synergetic control starts with a judicious choice of macro-variable (Bouchareb *et al.*, 2019). Synergetic control outperforms classical PID by offering inherent robustness to uncertainties and disturbances, ensuring fast convergence with smooth transient responses, and providing a systematic, model-based design suited for complex nonlinear systems. Unlike PID, it guarantees global stability through Lyapunov-based formulations, eliminating the need for frequent gain adjustment.

In a cascade of two interconnected bioreactors, the simplest form of control involves regulating only the first bioreactor (BR1), which produces hydrogen. This control is necessary in the following two cases:

1. To manage disturbances in the influent (inlet organics) of BR1, such as variations in the inlet cellulose concentration, in order to maintain a consistent outflow rate of biohydrogen.
2. To maintain the production of hydrogen and biomethane at a set point level, as required in industrial biogas plants.

Figure 1 presents a cascade system to produce hydrogen and methane under the proposed approach to improve hydrogen production. The process under control appears as a system with two inputs and two outputs where the state vector is: $\begin{pmatrix} S_0 \\ S_1 \\ X_1 \\ A_{c_1} \\ X_2 \\ A_{c_2} \end{pmatrix}$. The input vector is $\begin{pmatrix} D_1 \\ S_0^{in} \end{pmatrix}$ and the output vector is $\begin{pmatrix} Q_{H_2} \\ Q_{CH_4} \end{pmatrix}$ where D_1 is the synergetic control law and D_2 is the input of the second bioreactor (BR2). D_2 evolves optimally based on A_{c1} following eq. 11 as demonstrated in Simeonov etal.(2018):

$$D_2 = \mu_{2max}(1 - \sqrt{\frac{k_{s_2}}{A_{c1} + k_{s_2}}}) \tag{11}$$

The system at hand is a Multi Input Multi Output (MIMO). However, only one output is being controlled; The second is influenced by this control. The hydrogen outflow rate is controlled using D_1 to match practical material use. In this paper and for this process, one have a macro-variable defined by the error between the desired output and the real output of the bioreactor. The closed loop system stability under synergetic control was proven in Bouchareb *et al.*(2019).

For the first bioreactor, the macro-variable is given by Eq. 12:

$$\psi = Q_{H_{2d}} - Q_{H_2} \tag{12}$$

Where $Q_{H_{2d}}$ is the desired hydrogen outflow rate. The macro-variable is then forced to evolve according to a chosen constraint imposing the desired dynamic behavior shown by Eq. 13:

$$T\dot{\psi} + \psi = 0,\ T > 0 \tag{13}$$

T is the forced convergence speed factor. The desired hydrogen outflow rate being constant, its derivative is null $\dot{Q}_{H_{2d}}$. The derivative of Hydrogen outflow rate is given by Eq. 14 :

$$\dot{Q}_{H_2} = Y_{H_2}(\dot{\mu_1} X_1 + \mu_1 \dot{X_1}) \tag{14}$$

The derivative Maximum specific growth rate for acidogenic bacteria is given by Eq. 15:

$$\dot{\mu_1} = \frac{\mu_{1max} k_{s_1} \dot{S}_1}{(k_{s_1} + S_1)^2} \tag{15}$$

Replacing in the chosen constraint Eq. 13, one gets Eq. 16:

$$-TY_{H_2}X_1\left[\frac{\mu_{1max}k_{s_1}\dot{S}_1}{(k_{s_1}+S_1)^2} + \mu_1(\mu_1 - D_1)\right] + \psi = 0 \tag{16}$$

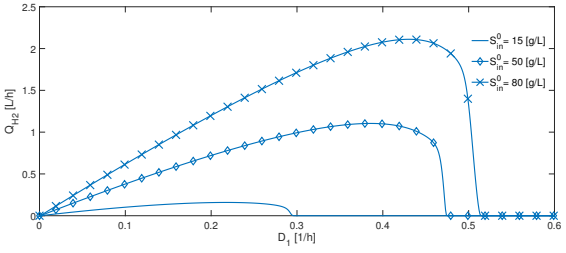

Figure 2. Analysis of the Input-Output response of BR1 Model.

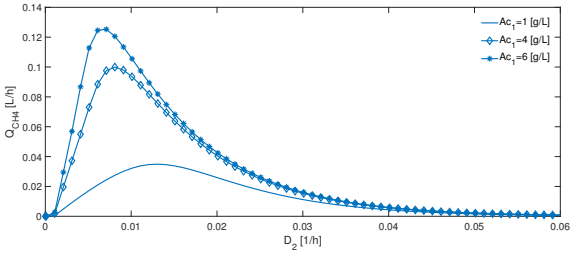

Figure 3. Analysis of the Input-Output response of BR2 Model.

Straightforward steps lead to the controller Eq. 17:

$$D_1 = \frac{k_{s_1}\mu_{1\max}X_1\left(\beta S_0 - \frac{1}{Y_1}\mu_1\right)}{k_{s_1}\mu_{1\max}S_1 + \mu_1(k_{S_1}+S_1)^2} + \frac{\left(\mu_1^2 - \frac{\psi}{X_1 T Y_{H_2}}\right)(k_{s_1}+S_1)^2}{k_{s_1}\mu_{1\max}S_1 + \mu_1(k_{s_1}+S_1)} \quad (17)$$

A major challenge in implementing this approach in real-world plants is the high cost or limited availability of sensors. As a result, unmeasured states can be estimated using software sensors derived from methane or hydrogen measurements (Sbarciog *et al.*, 2020).

4 Introduction of restrictions on the control

Since the practical applicability of the proposed approach is crucial, some static characteristics of both bioreactors need to be defined. Therefore, the authors in (Simeonov *et al.*, 2018) investigate the boundary values of the most important parameters: The boundary value of the dilution rate D_1^{wash} and the optimal value of the dilution rate D_1^{max}. The input-output static characteristic $Q_{H2} = Q_{H2}(D_1)$ for three values of S_0^{in} is shown on Figure 2. D_1^{wash} is approximately 0.28 d^{-1} for S_0^{in}= 15 g/L. If D_1 exceeds the value of 0.28, it leads to biomass washout and complete cessation of biogas production. The input-output static characteristic $Q_{CH4} = Q_{CH4}(D_2)$ for three values of A_{c1} is presented on Figure 3. These figures (2 and 3) were obtained in an open loop. As an optimization objective, it is then natural to consider the maximization of the biogas outflow rate in the first and second bioreactor.

5 Simulation results

The following values of the coefficients of the models in both bioreactors were adopted:

- $S_{\text{in}}^0 = 15$ (g/L);
- $\beta = 1$ $\left(\frac{\text{L}}{\text{g}\cdot\text{h}}\right)$;
- $Y_p = 1$;
- $Y_1 = 0.08$;
- $Y_2 = 1$;
- $Y_3 = 0.24$;
- $k_{s1} = 3.914$ (g/L);
- $k_{s2} = 0.22$ (g/L);
- $Y_{\text{CH}_4} = 18.7$;
- $Y_{\text{H}_2} = 1$;
- $\mu_{1\max} = 0.568$ (1/h);
- $\mu_{2\max} = 0.0083$ (1/h).

The initial conditions were used for simulations as follows:

- $S_0(0) = 0.11$ g/L;
- $S_1(0) = 1$ g/L;
- $X_1(0) = 0.3$ g/L;
- $X_2(0) = 0.9$ g/L;
- $Ac_1(0) = 0.4$ g/L;
- $Ac_2(0) = 0.7$ g/L.

The gains for the PID controller were optimized using a GA, with the Integral Time Absolute Error (ITAE) serving as the objective function: $k_p = 2.2; k_i = 0.31; k_d = 3.2$.

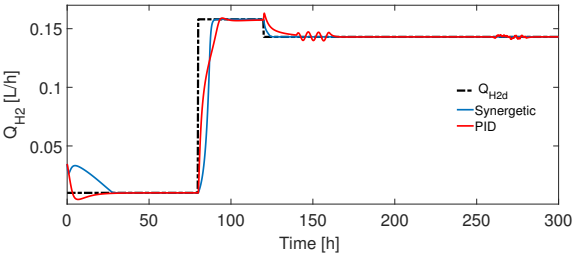

Figure 4. Dynamics of the hydrogen outflow rate Q_{H_2} (BR1) under synergetic and PID.

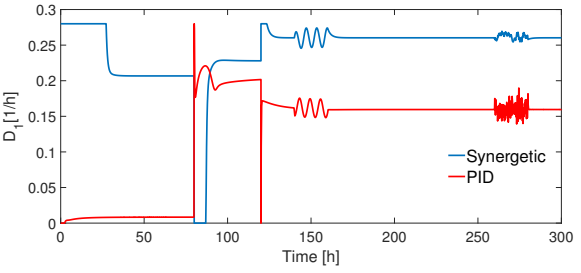

Figure 5. Evolution of the dilution rate (control input D_1) under synergetic and PID.

The GA settings were as follows: Population size: 50 individuals, Number of generations: 100, Selection method: roulette wheel, crossover type and rate: Single-point crossover with rate = 0.8, mutation rate: 0.05, stopping criterion: Maximum number of generations.

In order to evaluate the proposed control law, numerical simulation was carried out under Simulink environment using the block diagram in Figure 1 (ODE45 solver). The solver configuration is as follows: maximum step size: 10^{-2}, minimum step size: 10^{-3}, relative tolerance: 10^{-3}, absolute tolerance: 10^{-3}. The proposed control law is tested by injecting a perturbation between 140h and 160h and a gaussien noise between 260h and 280h in the input S_0^{in} ($S_0^{in} = 15g/L$). The performance of both controller is assessed using three performance indices: ITAE, Integral Squared Error (ISE), Integral Absolute Error (IAE), and the Root Mean Squared Error (RMSE).

- The ITAE is given by the formula :

$$ITAE = \int_0^t t|\psi(t)|dt \tag{18}$$

- The ISE is given by the formula :

$$ISE = \int_0^t \psi(t)^2 dt \tag{19}$$

where t is the simulation time.

- and IAE is calculated as follows:

$$IAE = \int_0^t |\psi|dt \tag{20}$$

- The RMSE could be calculated as follows:

$$RMSE = \sqrt{\sum_{i=1}^{n}[(\psi_i)^2/n]} \tag{21}$$

With n is the total number of samples.

The desired hydrogen outflow rate is shown in Eq. 22:

$$Q_{\mathrm{H2\,d}} = \begin{cases} 0.01 & 0 \le t < 80 \\ 0.148 & 80 \le t \le 120 \\ 0.015 & 120 \le t \le 300 \end{cases} \tag{22}$$

Remark 1. The reaction is assumed to occur under isothermal conditions. Moreover, by assuming hydrogenotrophic methanogenesis as the main hydrogen sink, the conversion of hydrogen and CO_2 to acetate—known as homoacetogenesis—is excluded from the model. Nevertheless, in the experimental setup, homoacetogenesis and other key hydrogen-producing pathways (e.g., lactate-to-acetate) are present, which could significantly affect control performance. However, since the Synergetic controller is designed to be highly robust to uncertainties and nonlinearities, it should, in theory, be capable of mitigating the negative effects caused by these additional hydrogen pathways.

The Synergetic controller has an ITAE value of 74 L/h, while the PID controller has a higher ITAE value of 81.7 L/h. Therefore, the Synergetic controller is more effective at minimizing the product of the absolute error and time, which could indicate faster error correction over time. The ISE value for the Synergetic controller is 0.1 L/h, which is slightly higher than the PID controller's ISE value of 0.05 L/h. Hence, This indicates that the PID controller may be more effective at minimizing large errors, as ISE penalizes larger errors more heavily due to the squaring operation. Figure 4 depicts the dynamics of the output (Q_{H2}) under both controllers. It shows good tracking for both approaches. The convergence of the synergentic controller depends on the parameter T (Bouchareb *et al.*, 2019). The lower T, the faster the convergence is. However, The proposed controller is very robust as it can handle disturbances in the range of 140h and 160h and injected noise of the Inlet cellulose concentration in BR1 between 260h and 280h without losing robustness, which makes it reliable. If the proposed approach is compared with the classical PID, the latter is not robust because the disturbance and the noise (S_0^{in}) appear on the output (Hydrogen outflow rate) as shown in Figure 4 and 5. This interprets the constraint in Eq. 13. The disturbance injected into the input S_0^{in} has been compensated for in the control signal D_1 by the synergetic controller, as shown in the input of the controller in Figure 5.

Table 1. Settling Time for Hydrogen Production in Different Phases of Digestion.

Phase	Synergetic	PID
Phase 1 [0h-80h[	27.5 h	24.6 h
Phase 2 [80h-120h[	8 h	11.4 h
Phase 3 [120h-300h]	1.1 h	5.1 h

Table 2. Comparative Analysis of ITAE, ISE and RMSE Performance Metrics for hydrogen production.

Performance index	Synergetic	PID	PG-ULMPC (He *et al.*,2023)
ITAE	74 L/h	81.7 L/h	-
IAE	1.232 L/h	0.9142 L/h	1.4412 L/h
ISE	0.1 L/h	0.05 L/h	0.2275 L/h
RMSE	7.87e-04 L/h	94 L/h	-

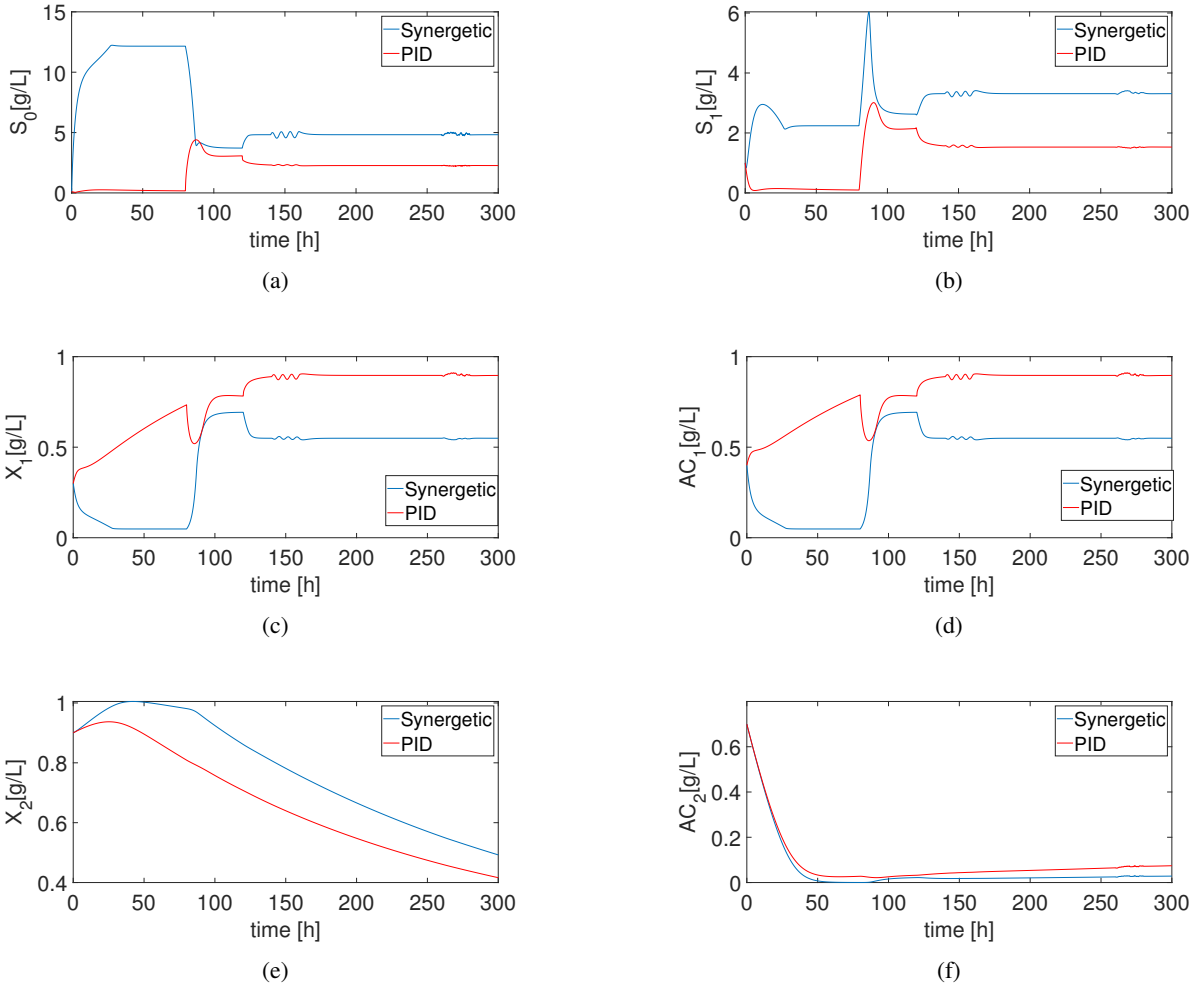

Figure 6. Different concentration of state variables: (a) S_0: Cellulose concentration [g/L], (b) S_1: Cellobiose substrate concentration [g/L], (c) X_1: Acidogenic bacteria concentration [g/L],(d): Ac_1 Acetate concentration [g/L],(e) X_2: Methanogenic bacteria concentration [g/L],(f) Ac_2 :Acetate concentration [g/L]

With this robust control system, the maximum amount of hydrogen Q_{H2} can be extracted, which is 0.16 Liters per day, while staying within the constraint of 0.28 per day for the dilution rate D_1. The results shown in Figure 4 and 5 are consistent with those in Figure 2 and 3, where the limits are well respected.

Figure 6 from a to f show a good evolution of the different concentrations whether with the PID or synergistic controllers. The concentrations always have positive values.

In Figures 6(a) and 6(b), under Synergetic control, S_0 and S_1 reach their steady-state values more rapidly, which demonstrates enhanced disturbance rejection and improved setpoint tracking. In contrast, the PID exhibits slower convergence and notable steady-state deviations, indicating suboptimal substrate utilization efficiency.

In Figures 6(c) and 6(e), the microbial dynamics differ significantly between the two control strategies. Under Synergetic control, X_1 stabilizes efficiently, following a well-defined growth phase, whereas the

PID results in overshoot and prolonged transients. Similarly, X_2 under Synergetic exhibits a more controlled decline, while PID leads to a more abrupt biomass depletion, which may negatively affect system stability and hydrogen yield.

In Figures 6(d) and 6(f), Synergetic ensures a smoother hydrogen accumulation process, effectively minimizing fluctuations and demonstrating superior tracking performance. In contrast, PID introduces oscillations and steady-state discrepancies, which could lead to efficiency losses in practical applications. The improved regulation of AC_1 and AC_2 under Synergetic control contributes to better hydrogen retention and enhanced bioreactor productivity. In Figure 7, it is denoted that the production of methane is greater with the classic PID compared to the proposed controller. However, the objective of the present work is to control the production of hydrogen. Enhancing H_2 production control often compromises CH_4 production due to metabolic competition. Strict control favors hydrogenogenic bacteria but inhibits methanogens, which require low H_2 levels to produce CH_4. Therefore, optimizing H_2 yield typically suppresses CH_4 formation—highlighting a key control conflict in mixed microbial systems.
In other words, the control law is designed to achieve perfect tracking of the desired output, with no deviation from the desired value once the system has reached steady-state. When comparing settling time and ISE, it is observed that the PID controller outperforms during the initial phase, specifically at start-up. However, During the final two phases, the synergetic controller demonstrates superior speed and accuracy.

Table 1 shows the settling times for hydrogen production under different control strategies (Synergetic and PID) across three phases. During the initial phase (0h-80h), the Synergetic controller achieved a settling time of 27.5 h, while the PID controller settled at a slightly faster rate of 24.6 h. In the intermediate phase (80h-120h), the settling times show a notable difference between the two controllers. The Synergetic controller's settling time decreased to 8 h, whereas the PID controller had a higher settling time of 11.4 h. During the final phase (120h-300h), the settling times further diverge. The Synergetic controller demonstrated a significantly lower settling time of 1.1 h compared to the PID controller's 5.1 h. The table 2 presents a comparative analysis of the performance metrics ITAE, IAE, ISE, and RMSE for hydrogen production using different controllers: Synergetic, PID, and another controller from (He *et al.*, 2023) called Performance Guaranteed Ultra Local Model Predictive Controller (PG-ULMPC). The proposed controller outperforms PID and PG-ULMPC in terms of IAE. For the ISE metric, the PID records slightly a lower error than the Synergetic controller with a value of 0.05 L/h compared to 0.1 L/h. The RMSE value for the Synergetic controller is significantly lower (7.87e-04 L/h) than that of the PID controller (94 L/h), suggesting a perfect tracking at the steady state. The PG-ULMPC controller's performance index is only available for the IAE and ISE metrics, where it shows a higher IAE value (1.4412 L/h) and a higher ISE value (0.2275 L/h) compared to both the Synergetic and PID. Overall, the proposed controller achieves superior tracking accuracy, exhibiting minimal error relative to the PID and PG-ULMPC.
Furthermore, the proposed approach enables the controlled system to achieve the target hydrogen outflow rate more rapidly than the PG-ULMPC. Specifically, the system reaches the desired rate in approximately 8 hours with the proposed controller (table 1), compared to around 13 hours with the PG-ULMPC, when a sudden change occurs in the setpoint (He *et al.*, 2023). This rapid response is a critical advantage of the synergetic controller, especially given that abrupt fluctuations in outflow rate frequently occur in industrial bioreactors.
Effective control is essential for optimizing hydrogen production, as it directly impacts both environmental sustainability and energy efficiency. These findings highlight the potential of the proposed controller to enhance hydrogen generation processes, offering a promising solution for improved process stability and performance.

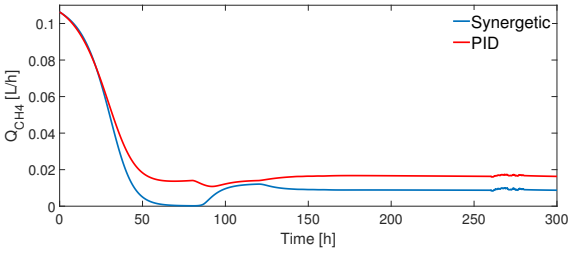

Figure 7. Evolution of methane outflow rate Q_{CH_4}

6 Conclusion

This work has presented a control approach tailored to the nonlinear and highly complex nature of biological hydrogen production via anaerobic digestion. The proposed method has demonstrated its robustness in maintaining system stability and optimizing hydrogen output, even in the presence of dynamic and uncertain process conditions.

A key strength of this approach lies in its simplicity and adaptability, relying on a reduced and well-calibrated model to effectively capture the essential dynamics of the process. Unlike more computationally demanding strategies, this method ensures fast response times and is well-suited for real-time applications.

In comparative analysis, the synergetic controller

outperformed classical PID and recent model predictive strategies by achieving improved tracking precision, enhanced transient behavior, and stronger robustness against disturbances. These advantages make it a promising candidate for complex bioprocess control.

However, the control performance is closely tied to the accuracy of model parameters, which must be clearly identified—a limitation that could affect generalizability under varying biological conditions. Moreover, the inherent variability in microbial behavior introduces uncertainty that can impact control accuracy.

Future work will focus on validating the strategy with experimental or real-time data, and exploring its implementation on embedded systems to assess its practical deployment potential. Integrating adaptive mechanisms to account for biological fluctuations may also further improve performance.

Acknowledgements

This work was supported by the project PRFU A01L08UN190120220002.

References

Abdallah, R., Djelal, H., Amrane, A., Sayed, W., Fourcade, F., Labasque, T., Geneste, F., Taha, S., & Floner, D. (2016). Dark fermentative hydrogen production by anaerobic sludge growing on glucose and ammonium resulting from nitrate electroreduction. *International Journal of Hydrogen Energy*, *41*, 5445–5455. https://doi.org/10.1016/j.ijhydene.2016.02.030

Ameli, H., Strbac, G., Pudjianto, D., & Ameli, M. T. (2024). A review of the role of hydrogen in the heat decarbonization of future energy systems: Insights and perspectives. *Energies*, *17*(7), 1688. https://doi.org/10.3390/en17071688

Antonelli, R., Harmand, J., Steyer, J. P., & Astolfi, A. (2003). Set-point regulation of an anaerobic digestion process with bounded output feedback. *IEEE Transactions on Control Systems Technology*, *11*(4), 495–504.

Arumugam, T., Parthiban, L., & Rangasamy, P. (2015). Two-phase anaerobic digestion model of a tannery solid waste: Experimental investigation and modeling with ANFIS. *Arabian Journal for Science and Engineering*, *40*(2), 279–288. https://doi.org/10.1007/s13369-014-1408-9

Barnett, M. W., & Andrews, J. F. (1992). Expert system for anaerobic-digestion-process operation. *Journal of Environmental Engineering*, *118*(6), 949–963.

Bayen, T., & Gajardo, P. (2019). On the steady state optimization of the biogas production in a two-stage anaerobic digestion model. *Journal of Mathematical Biology*, *78*(4), 1067–1087. https://doi.org/10.1007/s00285-018-1301-3

Belmouhoub, A., Bouzid, Y., Medjmadj, S., Derrouaoui, S. H., Siguerdidjane, H., & Guiatni, M. (2023). Fast terminal synergetic control for morphing quadcopter with time-varying parameters. *Aerospace Science and Technology*, *141*, 108540.

Blumensaat, F., & Keller, J. (2005). Modelling of two-stage anaerobic digestion using the IWA anaerobic digestion model no. 1 (ADM1). *Water Research*, *39*(1), 171–183. https://doi.org/10.1016/j.watres.2004.07.024

Borisov, M., Dimitrova, N., & Simeonov, I. (2016). Mathematical modelling of anaerobic digestion with hydrogen and methane production. *IFAC-PapersOnLine*, *49*(26), 231–238. https://doi.org/10.1016/j.ifacol.2016.12.131

Borisov, M., Dimitrova, N., & Simeonov, I. (2020). Mathematical modeling and stability analysis of a two-phase biosystem. *Processes*, *8*(7), 791. https://doi.org/10.3390/pr8070791

Bouchareb, H., Semcheddine, S., Harmas, M. N., M'sirdi, K. N., & Naamane, A. (2019). Virtual sensors to drive anaerobic digestion under a synergetic controller. *Energies*, *12*(3), 430. https://doi.org/10.3390/en12030430

Braguglia, C. M., Gallipoli, A., Gianico, A., & Pagliaccia, P. (2018). Anaerobic bioconversion of food waste into energy: A critical review. *Bioresource Technology*, *248*, 37–56. https://doi.org/10.1016/j.biortech.2017.06.145

Buitrón, G., Ruiz, V., & Cercado, B. (2022). Efficiency parameters that effectively correspond with hydrogen production from VFAs in microbial electrolysis cells. *Revista Mexicana de Ingeniería Química*, *21*(3), 29–44.

Chaabna, A., & Semcheddine, S. (2025). Robust methane production from anaerobic digestion of maize silage: Feeding control using sliding mode control strategy with anaerobic digestion model N°01. *Bioresource Technology*, *416*, 131749. https://doi.org/10.1016/j.biortech.2024.131749

Chorukova, E., Simeonov, I., & Kabaivanova, L. (2021). Volumes ratio optimization in a cascade anaerobic digestion system producing hydrogen and methane. *Ecological Chemistry and Engineering S*, *28*(2), 183–200. https://doi.org/10.2478/eces-2021-0014

Dareioti, M. A., & Kornaros, M. (2014). Effect of hydraulic retention time (HRT) on the anaerobic co-digestion of agro-industrial wastes in a two-stage CSTR system. *Bioresource Technology*, *167*, 407–415. https://doi.org/10.1016/j.biortech.2014.06.045

Dong, N., Zhao, X., Yan, M., Li, H., & Pan, H. (2022). Synergetic control of hydrogen evolution and ion transport kinetics enabling Zn anodes with high-areal capacity. *Nano Energy*, *104*, 107903. https://doi.org/10.1016/j.nanoen.2022.107903

Gao, S., Lei, X., Ruan, W., & Zhao, M. (2021). Synergetic enhancement of methane production and system resilience during anaerobic digestion of food waste in ammonia-tolerant anaerobic sludge system. *Environmental Science and Pollution Research*, *28*, 21851–21861.

García-Diéguez, C., Molina, F., & Roca, E. (2011). Multi objective cascade controller for an anaerobic digester. *Process Biochemistry*, *46*(4), 900–909.

García-Amador, R., Hernández, S., Ortiz, I., & Cercado, B. (2019). Assessment of microbial electrolysis cells fed hydrolysate from agave bagasse to determine the feasibility of bioelectrohydrogen production. *Revista Mexicana de Ingeniería Química*, *18*(3), 865–874.

Ghanavati, M. A., Vafa, E., & Shahrokhi, M. (2021). Control of an anaerobic bioreactor using a fuzzy supervisory controller. *Journal of Process Control*, *103*, 87–99.

Grognard, F., & Bernard, O. (2006). Stability analysis of a wastewater treatment plant with saturated control. *Water Science and Technology*, *53*(1), 149–157.

Hagh, Y. S., Asl, R. M., Fekih, A., Wu, H., & Handroos, H. (2021). Active fault-tolerant control design for actuator fault mitigation in robotic manipulators. *IEEE Access*, *9*, 47912–47929.

He, D., Wang, H., Tian, Y., Christov, N., & Simeonov, I. (2023). Trajectory tracking of two-stage anaerobic digestion process: A predictive control with guaranteed performance and saturated input, based on ultra-local model. *Journal of Process Control*, *129*, 103039.

Holubar, P., Zani, L., Hager, M., Fröschl, W., Radak, Z., & Braun, R. (2003). Start-up and recovery of a biogas-reactor using a hierarchical neural network based control tool. *Journal of Chemical Technology & Biotechnology: International Research in Process, Environmental & Clean Technology*, *78*(8), 847–854.

Khan, M. A., Ngo, H. H., Guo, W. S., Liu, Y. W., Zhou, J. L., Zhang, J., Liang, S., Ni, B. J., Zhang, X. B., & Wang, J. (2016). Comparing the value of bioproducts from different stages of anaerobic membrane bioreactors. *Bioresource Technology*, *214*, 816–825. https://doi.org/10.1016/j.biortech.2016.05.013

Kolesnikov, A., Veselov, G., Kolesnikov, A., et al. (2000). Modern applied control theory: synergetic approach in control theory. *TRTU, Moscow, Taganrog*, 4477–4479.

Kuang, Y., Zhao, J., Gao, Y., Lu, C., Luo, S., Sun, Y., & Zhang, D. (2020). Enhanced hydrogen production from food waste dark fermentation by potassium ferrate pretreatment. *Environmental Science and Pollution Research*, *27*, 18145–18156.

Li, Q., & Li, Y. (2019). Coproduction of hydrogen and methane in a CSTR-IC two-stage anaerobic digestion system from molasses wastewater. *Water Science and Technology*, *79*(2), 270–277. https://doi.org/10.2166/wst.2019.042

Maurya, P., Paul, N., Prasad, D., & Singh, R. S. (2024). Modified fractional order PID structure for non-integer model bioreactor control. *The Canadian Journal of Chemical Engineering*, *102*(9), 3173–3191. https://doi.org/10.1002/cjce.25254

Petre, E., Selisteanu, D., & Sendrescu, D. (2013). Adaptive and robust-adaptive control strategies for anaerobic wastewater treatment bioprocesses. *Chemical Engineering Journal*, *217*, 363–378. https://doi.org/10.1016/j.cej.2012.11.129

Prapinagsorn, W., Sittijunda, S., & Reungsang, A. (2018). Co-digestion of napier grass and its silage with cow dung for bio-hydrogen and methane production by two-stage anaerobic digestion process. *Energies*, *11*(1), 47. https://doi.org/10.3390/en11010047

Santi, E., Monti, A., Li, D., Proddutur, K., & Dougal, R. (2004). Synergetic control for power electronics applications: A comparison with

the sliding mode approach. *Journal of Circuits, Systems, and Computers*, *13*(4), 737–760.

Sbarciog, M., Vande Wouwer, A., Van Impe, J., & Dewasme, L. (2020). Extremum seeking control of a three-stage anaerobic digestion model. *IFAC-PapersOnLine*, *53*(2), 16773–16778. https://doi.org/10.1016/j.ifacol.2020.12.1142

Serrano-Meza, A., Garzón-Zúñiga, M., Barragán-Huerta, B., Estrada-Arriaga, E., Almaraz-Abarca, N., & García-Olivares, J. (2020). Anaerobic digestion inhibition indicators and control strategies in processes treating industrial wastewater and wastes. *Revista Mexicana de Ingeniería Química*, *19*(Sup. 1), 29–44.

Simeonov, I., & Queinnec, I. (2006). Linearizing control of the anaerobic digestion with addition of acetate (control of the anaerobic digestion). *Control Engineering Practice*, *14*(7), 799–810. https://doi.org/10.1016/j.conengprac.2005.04.011

Simeonov, I. S., Chorukova, E. I., & Lakov, V. T. (2018). Modelling and extremum seeking control of two–stage biotechnological process. *IFAC–PapersOnLine*, *51*(30), 677–682.

Vol. 24, No. 2(2025) Mat25443
Revista Mexicana de Ingeniería Química

Characterization and efficiency of *Luffa cylindrica* as bioadsorbent in Cr (VI) remotion from synthetic wastewater

Caracterización y eficiencia de *Luffa cilíndrica* como bioadsorbente en la remoción de Cr (VI) de aguas residuales sintéticas

J.G. Moreno-Rubio[1], N.R. Osornio-Rubio[1], H. Jiménez-Islas[2], E. Barrera-Calva[3] A.Y. Ramírez-Yañez[1], G.M. Martínez-González[1]*

[1]Departamento de Ingeniería Química, [2]Departamento de Ingeniería Bioquímica y Ambiental, Tecnológico Nacional de México en Celaya. Antonio García Cubas Pte. #600 esq. Av. Tecnológico. Celaya. Gto. México. C.P. 38010.

[3] Universidad Autónoma Metropolitana, Iztapalapa, Área de Ingeniería en Energía, IPH, CBI. Ciudad de México. México.

Received: October 17, 2024; Accepted: March 16, 2025

Abstract

This study investigated luffa as a bioadsorbent for removing Cr (VI) from synthetic wastewater. Luffa was characterized by scanning electron microscopy (SEM) and Fourier-transform infrared spectroscopy (FTIR), which mainly revealed a composition of carbon and oxygen, as identified via SEM. The morphology showed cylindrical fibers arranged in a network, with diameters ranging from 200 to 300 μm and surface fissures between 25 and 100 μm. FTIR analysis detected hydroxyl, carbonyl, and carboxyl functional groups responsible for adsorbing $HCrO_4^{-1}$. The composition of luffa was found to be 14% lignin, 76% cellulose, and 10% hemicellulose. Adsorption kinetics were evaluated at pH 2 using 0.5 g of luffa in 100 mL of synthetic wastewater, with Cr (VI) concentrations varying between 15 and 50 ppm. Sampling followed the NMX-AA-044-SCFI-2014 protocol, and Cr (VI) quantification was performed by UV-Vis spectrophotometry, achieving a removal efficiency of 100%. The adsorption kinetics were adjusted to a pseudo-second-order model using parameter estimation. Luffa demonstrated an adsorption capacity of 10.0 mg Cr (VI)/g, with energy-dispersive X-ray spectroscopy (EDS) revealing 1.21% Cr in dry luffa and 48.23% in calcined luffa, indicating Cr incorporation within the luffa structure. X-ray fluorescence (XRF) analysis detected 8.72% Cr in dry luffa and 75.07% in calcined luffa.

Keywords: Cr (VI), Luffa, Bioadsorption Kinetics, Wastewater.

Resumen

Se estudió la luffa como bioadsorbente para remover Cr (VI) de aguas residuales. La luffa se caracterizó mediante microscopia electrónica de barrido (SEM) y espectroscopia infrarroja (FTIR), encontrando con SEM, C y O principalmente. En la morfología se encontraron fibras cilíndricas en red con diámetros entre 200-300 μm y fisuras superficiales entre 25-100 μm. Con FTIR se encontraron grupos hidroxilo, carbonilo y carboxilo que adsorben $HCrO_4^{-1}$. La composición de la luffa fue 14 % lignina, 76% celulosa y 10% hemicelulosa. También, se determinó la cinética de adsorción a pH 2, con 0.5 gr de luffa en 100 mL de agua residual, empleando concentraciones de 15-50 ppm de Cr (VI). Se muestreó con NMX-AA-044-SCFI-2014 y se determinó el Cr (VI) por Espectrofotometría UV-Vis, obteniéndose una remoción del 100%. La cinética de adsorción se ajustó al modelo de pseudo-segundo orden con estimación de parámetros. La luffa adsorbió 10.0 mg Cr (VI)/ g de luffa, se encontró con EDS, 1.21% de Cr en la luffa seca y 48.23% en la luffa calcinada, indicando que el Cr se encuentra en la estructura de la luffa. Con fluorescencia de rayos X (XRF) en muestra seca de luffa se tiene 8.72% de Cr y 75.07% en luffa calcinada.

Palabras clave: Cr (VI), Luffa, Cinética de Bioadsorbente, Aguas residuales.

*Corresponding author. *E-mail*: gloriam@iqcelaya.itc.mx ;
https://doi.org/10.24275/rmiq/Mat25443
ISSN:1665-2738, *issn-e*: 2395-8472

1 Introduction

A demanding issue in Guanajuato state, Mexico, is wastewater contamination with Cr (VI), primarily from the leather tanning industry associated with shoe production. This industry generates large volumes of wastewater containing significant amounts of Cr (VI). Prolonged exposure to Cr (VI) originates serious health risks, including mutagenic and carcinogenic effects (Vašková and Kolomazník, 2016). Among various methods for removing Cr (VI) from wastewater, adsorption is notable for its cost-effectiveness, particularly when using bioadsorbents made from organic or biological materials, often derived from waste. These bioadsorbents are inexpensive, easily available, and relatively easy to handle as waste management (Hasanzadeha *et al*., 2024). Some examples are the use of artichoke packed in bags as a chromium VI bioadsorbent (Rubio-Campos *et al*., 2022; Diaz-Rodriguez *et al*., 2025), biomass fungus as azo dyes adsorbent (Jiménez-González *et al*., 2024), and the use of avocado seed for the removal of textile dyes (Gonzales-Condori *et al.,* 2023).

During adsorption, atoms, ions, and molecules are retained on the surface of a material until an equilibrium is established between the dissolved solute and the solute bound to the sorbent (Khadir *et al*., 2020). This process can involve three types of interactions: physisorption, chemisorption, and electrostatic sorption (Arroyo and Cervantes, 2018). In this study, bioadsorption focuses on removing heavy metals from wastewater using biological-adsorbent sources. These materials are economically advantageous, as many are byproducts or waste materials. Their effectiveness is due to functional groups within proteins, carbohydrates, and phenolic compounds, such as carboxyl, hydroxyl, sulfate, phosphate, and amino groups (Tejada *et al*., 2018). Bioadsorbents have shown a high capacity to remove trace metals from aqueous solutions. The functional groups on their surfaces, such as hydroxyl and carboxyl, play a crucial role in binding chromium ions. Studies highlight luffa's high surface area, porosity, and eco-friendly nature, making it an efficient and sustainable option for chromium removal compared to conventional methods (Nwosu-Obieogu and Okolo, 2020, Diaz-Rodriguez *et al*., 2025).

Luffa (*Luffa cylindrica*) known as vegetable sponge gourd, is an herbaceous plant with a fibrous vascular network. It has potential as a bioadsorbent due to its lignocellulosic composition, consisting of 50-70% cellulose, 8-22% hemicellulose, and 10-23% lignin (Laidani *et al*., 2020). Luffa contains various functional groups, such as aliphatic hydroxyl, phenolic methoxyl, and carbonyl, which play a significant role in its bioadsorptive properties. These functional groups can be analyzed using Fourier-transform infrared spectroscopy (FTIR), allowing the identification of changes in the characteristic bands of the bonds associated with these groups. Such changes can indicate the occurrence of chemisorption, as they reveal chemical interactions between the Luffa functional groups and the adsorbed substances (Miretzky and Cirelli., 2010; Rahman *et al*., 2014).

The pH of the solution controls the adsorption processes of metals on different adsorbents. The adsorption of metal ions depends on the nature of the surface as well as the distribution of chemical species of the metal in the aqueous solution. The adsorption of cations favors pH values greater than 4 and the adsorption of anions at pH values ranging from 1 to 4 (Kuyucak and Volesky, 1989; Tejada-Tovar *et al*., 2018). Cr (VI) has anionic sorption behavior. Its adsorption decreases with an increasing pH, and when competing dissolved anions are present. Depending on the pH, Cr (VI) in aqueous solutions occurs in anionic form as $HCrO_4^{-1}$ or CrO_4^{-2} (Richard and Bourg, 1991; Tejada-Tovar *et al*., 2019).

The pH also affects the change in the surface area and the groups' protonation degree functionalities of the adsorbent, by having an organic material in contact with an acidic solution the functional groups are protonated, leaving the surface of the bioadsorbent with a positive charge, which favors the adsorption of $HCrO_4^{-1}$ anions which have a negative charge. It has been reported that in the range of 1-2, with increasing pH, the percentage of adsorption of Cr (VI) as an anion increases $HCrO_4^{-1}$, while in the range of 2-8, as the pH increases, the adsorption decreases, and the optimal pH was 2. It is explained that the increase in removal from pH 1 to 2 is due to the conversion of Cr (VI) species in which neutral H_2CrO_4 was formed at pH less than 2. A higher pH causes the degree of protonation of the functional groups to decrease, reducing the adsorption capacity (Sun and Hong, 2011).

When the aqueous solution of Cr (VI) has an alkaline pH, it tends to have a high concentration of -OH ions that compete with $HCrO_4^{-1}$ ions on the active sites of the sorbent's surface, drastically affecting removal.

In this study, we examined the application of luffa as a bioadsorbent for Cr (VI) removal from wastewater. Various characterization techniques were used to analyze the luffa fibers before and after the Cr (VI) adsorption process. Energy Dispersive Spectroscopy (EDS) and X-ray Fluorescence (XRF) were used to identify the elements present and corroborate the adsorption of Cr (VI). The EDS coupled with a scanning electron microscope (SEM), allowed a point analysis of the elemental composition in specific areas and at the micrometer scale. XRF

provided an average sample analysis, confirming the presence of Cr (VI) in a global technique (Komatani *et al*., 2013).

Furthermore, the morphological analysis using SEM allowed us to observe the structural and surface characteristics of the luffa fibers before and after adsorption, highlighting changes in texture and the presence of depositions attributable to Cr (VI). For its part, Fourier Transform Infrared Spectroscopy (FTIR) was used to identify the functional groups present in the fibers and evaluate the chemical interactions between the Cr (VI) species and the adsorbent surface. These coupled techniques provide a comprehensive understanding of the chemical composition and structural characteristics of Luffa fibers, strengthening the interpretation of adsorption processes.

The selection of pH in this study was based on evidence widely documented in the literature, which establishes that the optimal value for Cr (VI) adsorption using *Luffa cylindrica* and other lignocellulosic materials is approximately 2. This value is explained by the interaction between the surface properties of the adsorbent and the chemical speciation of Cr (VI) in aqueous solution. The adsorption kinetic parameters, including the adsorption equilibrium concentration of Cr (VI) on luffa (q_e) and the rate constant (k), were calculated by parameter optimization using Excel^{TM} Solver. A kinetic model was also developed to describe the adsorption of Cr (VI) on Luffa as a function of time.

2 Materials and methods

2.1 Preparation of luffa for use as a bioadsorbent

First, the luffa was washed with tap water and then dried at 90 °C for 24 hours. Subsequently, it was soaked in distilled water at 90 °C for 30 minutes and then soaked in distilled water at 25 °C for 24 hours. Later, the luffa was rinsed again with distilled water and dried to a constant weight. The luffa was cut into cubes approximately 5 mm in size to facilitate grinding and then ground using a blender to obtain luffa filaments ranging from 2 to 7 mm.

2.2 Methodology for the determination of lignin, cellulose, and hemicellulose in luffa

Nine crucibles were weighed using an analytical balance (RADWARD) and dried to a constant weight at 120 °C in an oven (Felisa, Mexico). These crucibles were then used to determine the lignin, cellulose, and hemicellulose content in the luffa samples, following the methodology outlined by Domínguez (2018).

2.2.1 Determination of lignin in luffa

A 0.2 g luffa sample was weighed, and 3 mL of 72% m/v H_2SO_4 solution was added. The mixture was stirred for 2 hours. Then 70 mL of distilled water was added. The sample was then placed in an oven (Felisa, Mexico) at 20 °C for 1 hour. Later the sample was filtered, and the residue was dried to a constant weight. The lignin percentage by weight in the luffa was determined using Equation (1).

$$\% \, Lignin = \frac{P_L \times 100}{W} \tag{1}$$

P_L weight of the lignin, g
W weight of the luffa sample, g

2.2.2 Determination of cellulose and hemicellulose in luffa

Holocellulose, which includes the combined cellulose and hemicellulose content, was first extracted from the luffa. This holocellulose was then used to determine cellulose content directly, with hemicellulose calculated indirectly by weight difference. First, 1 g of luffa (previously extracted from any other components) was weighed and placed into a 300 mL ground-glass stoppered flask. Then, 32 mL of distilled water, 0.4 g of $NaClO_2$, and 0.2 mL of CH_3COOH were added. The mixture was then heated in a Felisa oven at 70 °C for 6 hours, with an additional 0.4 g of $NaClO_2$ and 0.2 mL of CH_3COOH added every hour. After the heating, the sample was vacuum-filtered and dried at 105 °C. The holocellulose content was calculated using Equation (2).

$$\% \, Holocellulose = \frac{P_{Ho} \times 100}{W} \tag{2}$$

P_{Ho} weight of the holocellulose, g

2.2.2.1 Determination of cellulose

To determine cellulose content, 0.3 g of holocellulose was weighed, and 1.5 mL of a 17.5% NaOH solution was added to the sample. The mixture was allowed to stand for 5 minutes, followed by adding another 1.5 mL of NaOH. This process was repeated three times. Afterward, the mixture was left to stand for 30 minutes, and then 5 mL of 17.5% NaOH was added. The mixture was allowed to stand for one hour before being vacuum-filtered. The cellulose retained on the filter paper was then washed with a 17.5% NaOH solution, followed by a rinse with 100 mL of a 5% CH_3COOH solution. Finally, the cellulose was dried, and its percentage was calculated using Equation (3).

$$\% \, Cellulose = \left(\frac{P_C \times 100}{0.3}\right)\left(\frac{100}{\% \, Holocellulose}\right) \tag{3}$$

P_C weight of cellulose, g

2.2.2.2 Determination of hemicellulose

Hemicellulose content was determined by subtracting the cellulose percentage from the holocellulose percentage, as holocellulose represents the combined content of cellulose and hemicellulose. Hemicellulose was calculated using Equation (4).

$$\%\ Hemicellulose = \%\ Holocellulose - \%\ Cellulose \quad (4)$$

2.3 Characterization of luffa

A square luffa sample (1x1 cm) was placed under a Stemi DV4 optical microscope and observed at 32x magnification to analyze the luffa morphology. For elemental composition analysis via energy-dispersive X-ray spectroscopy (EDS), luffa filaments were mounted on a copper pin with carbon tape. Their morphology was examined using a scanning electron microscope (Thermo Fisher Phenom).

For elemental composition analysis after Cr (VI) adsorption, 2.5 g of luffa was added to 100 mL of a 500 ppm Cr (VI) solution, achieving a removal efficiency of 97.45%. Two samples were prepared: one dried at 60 °C to a constant weight and cut manually into cubes, and another calcined at 650 °C in a Thermolyne muffle furnace. The morphology and elemental composition of both samples were subsequently analyzed using SEM.

X-ray fluorescence (XRF)

The luffa beads used in the adsorption of Cr (VI) were rinsed with deionized water adjusted to a pH of 2 to remove unadsorbed residues, dried in a Felisa brand oven at 70 °C until reaching constant weight, and prepared for analysis by X-ray fluorescence (XRF) spectroscopy. For this purpose, they were uniformly distributed on a support designed to form a compact layer and ensure adequate contact with the detector in the window of the XRF equipment. An empty support was used as a blank for the initial calibration, and three measurements were taken at different points of the sample to ensure representative results. The analysis was performed via a portable XRF spectrometer Delta Prof model, configured with specific parameters for detecting heavy metals, such as chromium.

In FT-IR analysis (Thermo Fisher Scientific), luffa samples before Cr (VI) adsorption (LN) and after Cr (VI) adsorption from synthetic wastewater containing 500 ppm Cr (VI) ($LNCr^{6+}$) were placed directly on the diamond ATR crystal. Good contact was ensured by applying pressure. Twenty-five scans were performed within a wavelength range of 650 to 4000 cm^{-1}.

2.4 Experimentation to obtain the kinetics of Cr (VI) adsorption using luffa as a bioadsorbent

According to the NMX-AA-044-SCFI-2014 standard, used for the measurement of Cr (VI) in natural, saline, wastewater, and treated wastewater, the preparation of a stock solution, a calibration curve in the range of 0 to 1 mg/L, and the determination of Cr (VI) in the analyzed samples were carried out.

Preparation of the stock solution (500 ppm of Cr (VI))

A total of 141.4 mg of potassium dichromate $K_2Cr_2O_7$ (Karal S.A. de C.V., Leon, Gto., Mexico) with 99% purity (CAS 7778-50-9, Catalog Number K5081.0500) was weighed and previously dried at 105 °C for 2 hours. Potassium dichromate was dissolved in distilled water, and the final volume was adjusted to 100 ml in a volumetric flask.

This procedure was followed to ensure accurate measurements and compliance with the standards established by the norm. Cr (VI) 15, 20, 30, 40, and 50 ppm solutions were prepared via dilutions from a 500-ppm stock solution. The pH of each Cr (VI) solution was adjusted to 2 by adding 50 μL of a 1:1 HNO_3 solution and diluted to a final volume of 100 mL. These solutions were transferred into 125 mL Erlenmeyer flasks for batch experiments. 0.5 g of previously prepared luffa was added to each volumetric flask, following the methodology described in section 2.1. The mixtures were agitated at 210 rpm in a shaker (IKA model KS 260-C SI).

From each flask, 0.4 mL samples were taken from the initial time until 100% removal was achieved, with sampling intervals of 24 hours. Cr (VI) determination for each sample was performed in triplicate, following the NMX-AA-044-SCFI-2014 standard. A 0.1 mL aliquot from each sample was diluted with 4.9 mL of deionized water to prepare a 2:100 dilution. The pH was adjusted to 9 using 50 μL buffer solution and 30 μL of 1N NaOH solution. Then, a drop of H_3PO_4 was added to adjust the pH below 2, adding 100 μL of diphenyl carbazide. After a 10-minute development period, the absorbance of each sample was measured at 540 nm using a UV-Vis spectrophotometer (VELAB VE-5600UV), and Cr (VI) concentrations in ppm were determined from a previously established calibration curve.

2.5 Kinetic parameters estimation for Cr (VI) adsorption using luffa as a bioadsorbent

To perform nonlinear optimization of the kinetic model parameters for Cr (VI) adsorption, the reaction rate equation (Equation 5) was formulated, incorporating the solution volume and luffa dose, as

described in Equations (6) and (7). This setup allowed for the deduction of the adsorption rate equation (Equation 8), with Cr (VI) considered as the limiting reactive. Initial and boundary conditions were defined for each experiment at $t = 0$ ($C_t = C_i$ and $q_t = 0$) and t = t ($C_t = C_t$ and $q_t = q_t$). These conditions were substituted into Equation (9) to obtain an analytical expression for $q_{t_{est}}$, which was then compared to the experimental values $q_{t_{\exp}}$. (Sahoo and Perlot, 2020)

The method of separation of variables was applied to derive the analytical solution for estimating the Cr (VI) concentration adsorbed by the luffa *versus* time and to solve Equation (8).

$$\frac{dC_A}{dt} = kC_A{}^n \tag{5}$$

$$q_e = \frac{(C_i - C_e)V}{m} \tag{6}$$

$$q_t = \frac{(C_i - C_t)V}{m} \tag{7}$$

$$\frac{dq_t}{(q_e - q_t)^n} = kdt \tag{8}$$

$$\int_0^{q_t} \frac{dq_t}{(q_e - q_t)^n} = \int_0^t kdt \tag{9}$$

To integrate, a variable change was performed, and the initial and final conditions were evaluated (Equation 9). The yielded Equation (10) allows the estimation of the concentration of Cr (VI) adsorbed by the luffa q_t at a given time:

$$q_t = q_e - \left[kt(n-1) + (q_e)^{(1-n)}\right]^{\frac{1}{1-n}} \tag{10}$$

Where

C_A Concentration of the limiting reagent, $\frac{mg\ Cr(VI)}{L}$

C_e Equilibrium concentration, $\frac{mg\ Cr(VI)}{L}$

C_i Initial concentration, $\frac{mg\ Cr(VI)}{L}$

k Adsorption rate constant, g luffa/mg Cr (VI) h

m Luffa mass, mg

n Order of the adsorption reaction

q_e Concentration of Cr (VI) adsorbed by the luffa at equilibrium, $\frac{mg\ Cr(VI)}{g\ de\ luffa}$

q_t Concentration of Cr (VI) adsorbed by the luffa at time t, $\frac{mg\ Cr(VI)}{g\ de\ luffa}$

t Time, h

V Volume of Cr (VI) solution, L

Parameter estimation was performed using the experimental data to obtain the combined model. Given the parabolic behavior observed in the data, it was assumed that the process followed second-order kinetics, n = 2 in equation (10). Using this equation, the initial values of k and q_e were estimated for each experiment. At equilibrium, the time tends to be infinite, to find q_e, a numerical limit of 1×10^6 was used. Subsequently, the calculated values of q_e were plotted against the initial Cr (VI) concentration in solution C, showing linear behavior. Thence, the following linear model is displayed in equation (11).

$$q_e = q_0 + q_1 C \tag{11}$$

Where:

q_0 = Interception on the q_e axis.

q_1 = Slope of the line.

C = Concentration initial of Cr (VI) in the solution (mg/L).

Similarly, the estimated values of k were plotted against C and an exponential behavior was observed. This allowed the following model to be proposed, which is presented in Equation (12).

$$k = k_o e^{k_1 C^{k_2}} \tag{12}$$

Where:

k_0 = First rate constant

k_1 = Second rate constant

k_2 = Solution concentration exponent

Finally, the q_e and k models were combined and a estimation of the parameters q_0, q_1, k_0, k_1 y k_2 was performed. The parameters were optimized using Excel's Solver tool, minimizing the square error (Equation 13), allowing to determination of the optimized parameters for the estimation of q_e and k as functions dependent on the initial concentration of Cr (VI) used in synthetic wastewater.

$$E = \frac{\sum_{i=0}^{p}\left(q_{t\exp_i} - q_{t est_i}\right)^2}{p} \tag{13}$$

Where:

$q_{t_{est}}$ Estimated concentration of Cr (VI) adsorbed by the luffa at time t, $\frac{mg\ Cr(VI)}{g\ de\ luffa}$

$q_{t_{\exp}}$ Experimental concentration of Cr (VI) adsorbed by the luffa at time t, $\frac{mg\ Cr(VI)}{g\ de\ luffa}$

E Mean Square Error

p Number of experiments

3 Results and discussion

3.1 Luffa components

The analyses show that the main components of luffa, in terms of average weight percentage, are 76% cellulose, 10% hemicellulose, and 14% lignin. These values coincide with those reported in previous studies by Tanobe *et al.* (2005), Laidani *et al.* (2020), Adeyanju *et al.* (2020), and Behera *et al.* (2024), which supports the consistency of the data obtained. Furthermore, the results are contrasted with those presented in Table 1 for further comparison and validation.

Table 1. Comparison of the weight percentage of Luffa components.

Author	% Cellulose	% Hemicellulose	% Lignin
Tanobe *et al*., (2005)	63	19.4	11.2
Laidani *et al*., (2020)	60	22	10.6
Adeyanju *et al*. (2020)	57-74	1-22	0-12.8
Behera *et al*., (2024)	57-74	14-30	1-22
This work	76	10	14

Figure 1. Luffa cords under the light microscope at 32x magnification.

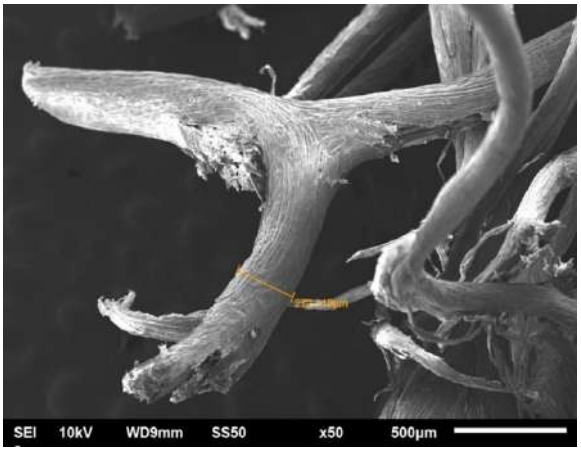

a)

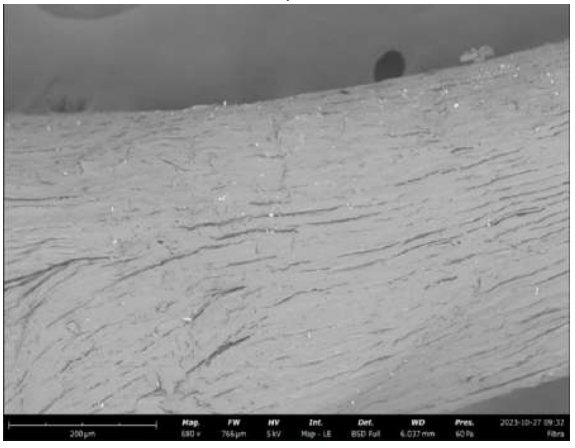

b)

Figure 2. Luffa cord observed in SEM magnification a) x50 and b) x680 (Thermo Fisher Phenom).

3.2 Luffa morphology before Cr (VI) adsorption

Optical microscopy observation at 32x magnification revealed that Luffa has a cylindrical fiber structure with irregular dimensions and rough surfaces. These fibers are interconnected, forming a network with irregular nodes, which facilitates the recovery of the bioadsorbent after the adsorption process (Figure 1).

Scanning electron microscopy (SEM) analysis provided detailed information on the Luffa bead structure, revealing fissures and diameter variations identified as potential adsorption sites for Cr (VI). A micrograph of a luffa bead is presented in Figure 2a at 50x magnification, where an average diameter of 272.119 μm is observed, along with variations in the diameters of the beads. On the other hand, Figure 2b shows the surface structure of the luffa at 680x magnification, highlighting a rough surface with fissures. This morphology is favorable for the adsorption of Cr (VI) in wastewater.

3.3 Elemental composition of luffa before Cr (VI) adsorption

Using the technique of energy dispersive X-ray spectroscopy (EDS) coupled with SEM, the main elements in luffa were determined, the results are found in Table 2. This composition highlights the predominance of organic material in the structure of luffa, which confirms its capacity as a bioadsorbent for the remotion of Cr (VI). Figure 3 shows a scanning electron microscopy (SEM) micrograph of the surface of the cylindrical luffa. The micrograph shows a fibrous structure with irregular and rough surfaces, characteristics of natural materials such as luffa, suggesting high porosity and many potential sites for adsorption. The region delimited by the box (highlighted in magenta) corresponds to the area where the EDS analysis was performed. This analysis allowed the elemental composition of the sample to be determined.

Table 2. Elemental composition of luffa before Cr (VI) adsorption.

Element	Weight %
C	49.31
O	50.69

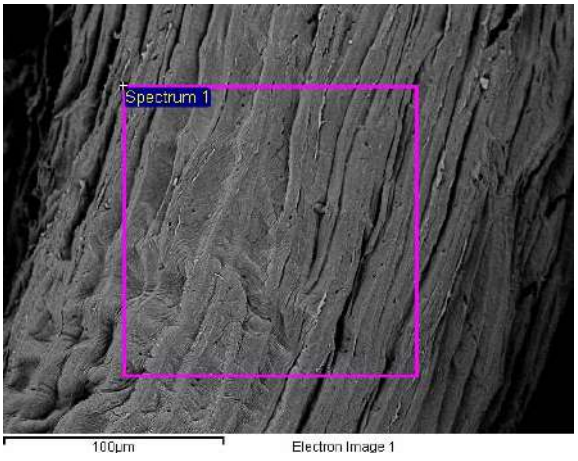

Figure 3. Micrograph for elemental composition determination of luffa.

3.4 Kinetics of Cr (VI) adsorption from wastewater using luffa as a bioadsorbent

Five experiments were conducted with initial Cr (VI) concentrations ranging from 15 to 50 ppm at a pH of 2. This acidic pH level was selected to favor the adsorption process due to the presence of $HCrO_4^{-1}$ ions, which are effectively attracted to the protonated surface of the luffa. In each experiment, 0.5 g of luffa was used as the bioadsorbent to facilitate adsorption, achieve equilibrium, and practically reach 100% Cr (VI) removal. A solution volume of 100 mL was utilized, and complete removal of Cr (VI) was achieved in all cases. The time required to reach 100% removal varied between experiments due to differences in initial concentration, with longer times observed at higher concentrations: 336 hours for 15 ppm, 432 hours for 20 ppm, 864 hours for 30 ppm, 1104 hours for 40 ppm, and 1416 hours for 50 ppm. During the initial 120 hours, a significant increase in removal efficiency was observed, with removal rates of 80%, 68%, 55%, 47%, and 45% for initial concentrations of 15, 20, 30, 40, and 50 ppm, respectively.

The parameters obtained for the equations representing the equilibrium concentration (q_e) and the adsorption rate constant (k) were determined via parameter estimation. These parameters are included in equations (14)-(15).

$$q_e = -0.29044 + 0.2437C \tag{14}$$

With MAE = 0.0261, MSE = 0.00133, RMSE = 0.03642, R^2 = 0.99986, and Error = 0.6167%

$$k = 1.46x10^9 e^{-20.904C^{0.08567}} \tag{15}$$

With MAE = 0.00003, MSE=0.00000, RMSE = 0.00003, R^2 = 0.99965, and Error = 5.6075%

$$Combined\ \ model\ for\ n = 2$$

$$q_t = q_e - \frac{1}{kt + \frac{1}{q_e}} \tag{16}$$

Where:

q_e Concentration at equilibrium of Cr (VI) adsorbed by Luffa, $\frac{mg\ Cr(VI)}{gluffa}$

k Adsorption rate constant

C Initial concentration of Cr (VI) in the solution, mg/L

These equations describe the behavior of the adsorption process and were validated through experimental data, showing their reliability for predicting both the equilibrium capacity and adsorption rate for diverse initial concentrations of Cr (VI). The equilibrium concentrations in luffa (mg Cr (VI)/g luffa) obtained from equation (15) are shown in Table 3, where it can be observed that the equilibrium concentration of Cr (VI) increases as the initial concentration increases. This indicates a good adsorption capacity of the material. However, as the initial concentration of Cr (VI) increases, the adsorption rate obtained with equation (16) decreases. This data was obtained using the pseudo-second-order model through parameter estimation.

Table 3. Optimized parameters for each initial concentration.

Removal time (h)	Legend	Initial Cr (VI) concentration (mg Cr (VI))/L	Final Cr (VI) concentration (mg Cr (VI))/L	Equilibrium concentration of Cr (VI) in luffa. (mg Cr (VI))/(g luffa)	Adsorption rate constant (g luffa)/(mg Cr (VI)*h) k×10^3
336	q_{t1}	15	0	3.365	5.196
432	q_{t2}	20	0	4.583	2.691
840	q_{t3}	30	0	7.019	1.036
1080	q_{t4}	40	0	9.455	0.515
1416	q_{t5}	50	0	11.891	0.296

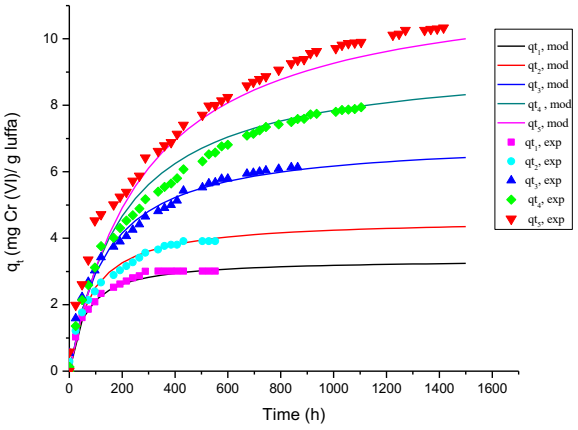

Figure 4. Predictions of combined model versus experimental values in Luffa Cr (VI) adsorption.

Figure 4 shows the evolution of the amount of Cr(VI) adsorbed per unit mass of *Luffa* (q_t, in mg Cr (VI)/g de luffa) as a function of time, for different initial concentrations of Cr(VI): q_{t1} (15 ppm), q_{t2} (20 ppm), q_{t3} (30 ppm), q_{t4} (40 ppm) y q_{t5} (50 ppm). Figure 4 depicts the experimental data (points and symbols) and the estimated values (continuous curves) obtained from the adsorption kinetics model. In general, an increase in the amount of Cr (VI) adsorbed is observed as time progresses, until an equilibrium is reached. This behavior is characteristic of adsorption processes, where, during the initial stage, the adsorption rate is fast due to the high availability of active sites on the adsorbent surface. As these sites become saturated, the adsorption rate gradually decreases until equilibrium is achieved.

The curves estimated by the model generally follow the tendency observed in the experimental data. However, small discrepancies are noted in certain time intervals, suggesting that while the model adequately describes the adsorption kinetics for the initial concentrations studied, additional adjustments may be required to improve its accuracy during the intermediate stages of the process. The results demonstrate that the adsorption capacity of Cr (VI) increases with the initial concentration and aligns well with the proposed kinetic model, validating the performance of Luffa as an effective adsorbent within the evaluated concentration range.

3.5 Luffa morphology after Cr (VI) adsorption

Figure 5a presents a 100x magnification SEM micrograph of luffa cylindrica before the Cr(VI) adsorption process. The image reveals a rough and irregular structure on the bead surface, with evident porosity details and non-uniform textures. These physical features, such as the observed roughness and porosity, are important factors that favor the adsorption capacity of the material by offering a higher

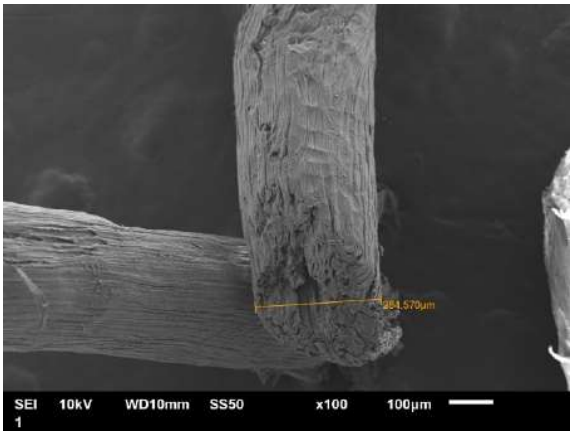

a)

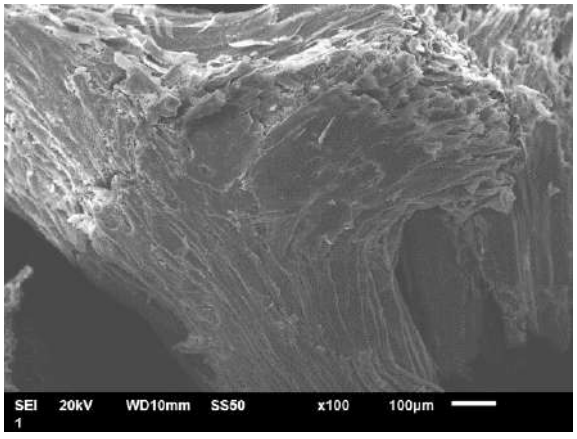

b)

Figure 5. Luffa before a) and after b) Cr(VI) adsorption observed in SEM at 100x magnification.

specific surface area and active sites available for interaction with contaminants in liquid solutions, such as Cr(VI). Figure 5b shows the SEM micrograph at 100x magnification of *Luffa cylindrica* after the Cr (VI) adsorption process. We observed that luffa fibers exhibit an irregular and rough surface, with material accumulations in certain regions. These deposits could correspond to adhered particles resulting from the adsorption, confirming that Cr (VI) was retained on the material's surface.

Figure 6 shows a SEM micrograph at 1000x magnification, providing a more detailed analysis of Luffa fibers after adsorption. In this image, particles are observed to be uniformly distributed over the surface of the fibers, along with an increase in surface irregularities. These particles can be attributed to deposits of Cr (VI) compounds, indicating that the adsorption process was concentrated in these specific regions. This finding suggests an efficient interaction between the $HCrO_4^{-1}$ chemical species in solution and the functional groups on the luffa's surface at pH = 2.

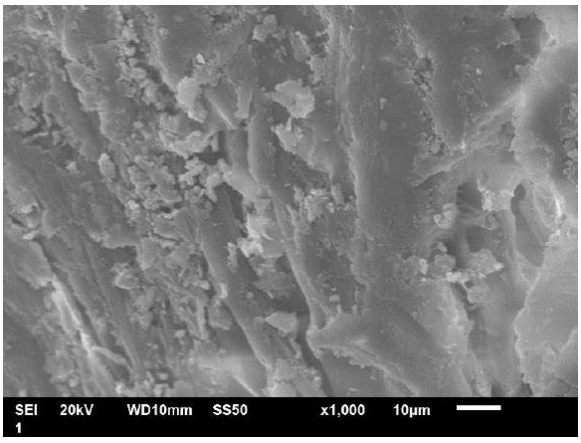

Figure 6. Luffa after Cr (VI) adsorption observed via SEM at 1000x magnification.

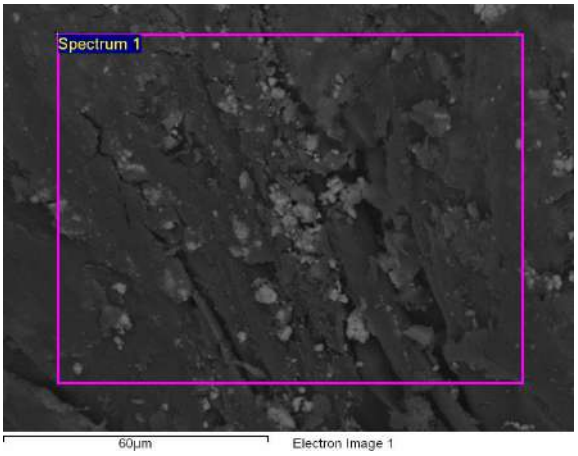

Figure 7. Micrograph for elemental composition determination of luffa after Cr (VI) adsorption.

3.6 Elemental composition of luffa after Cr (VI) adsorption obtained with EDS

The elemental composition of Luffa following Cr (VI) adsorption from wastewater was determined using two different procedures due to the complex structure of luffa. Luffa consists of multiple filaments with external and internal surfaces, which makes it difficult to characterize its morphology and elemental composition completely. Consequently, the analysis focused on the external surface, complemented by an examination of the luffa ash after Cr (VI) adsorption.

3.6.1 Elemental composition of dried luffa after Cr (VI) adsorption obtained with EDS

Figure 7 presents a micrograph obtained by SEM of the luffa after the Cr (VI) adsorption process. The image reveals a heterogeneous surface with elongated textures, where residues are randomly adhered. These residues may have originated during the adsorption process and could correspond to compounds related to the adsorbed Cr (VI) or traces of impurities.

Table 4. Elemental composition of Luffa obtained with EDS after adsorption of Cr (VI) in synthetic wastewater.

Element	Weight %
C	43.73
O	48.51
Al	0.73
Si	2.32
Cr	1.29
Fe	3.43

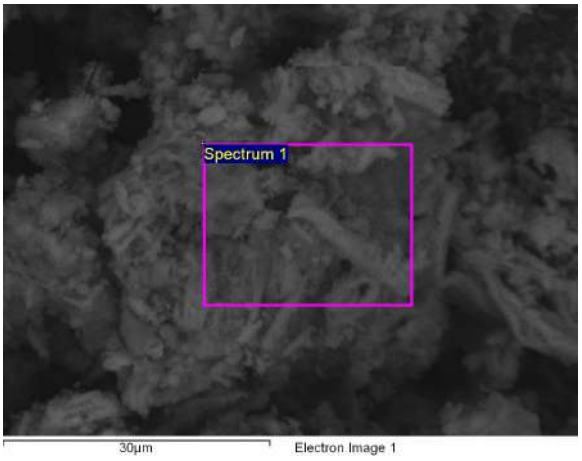

Figure 8. Micrograph for determination of the elemental composition of calcined luffa after Cr (VI) adsorption.

The elemental composition analysis was performed on the region marked as Spectrum 1.

The luffa elemental composition before adsorption consisted primarily of carbon (C) and oxygen (O). Following adsorption, additional elements were detected, including chromium (Cr) at 1.29% by weight, confirming that luffa effectively adsorbed Cr (VI) from the laboratory-prepared wastewater (Table 4).

3.7 Elemental composition of calcined Luffa after Cr (VI) adsorption obtained with EDS

Figure 8 depicts a micrograph obtained by SEM of the luffa calcined at 650 °C after the Cr (VI) adsorption process. The image reveals the sample morphology, featuring a porous and heterogeneous structure with particles of irregular morphology. The region for elemental analysis using EDS is highlighted via a rectangle in the image.

The elemental composition analysis of calcined Luffa after Cr (VI) adsorption revealed a Cr content of 48% weight, confirming luffa's effectiveness as a bioadsorbent for Cr (VI) from wastewater. Additionally, a decrease in oxygen (O) content and the absence of carbon (C) were observed compared

to the uncalcined sample, likely due to the thermal degradation of the bioadsorbent (Table 5).

Table 5. Elemental composition of calcined luffa after adsorption obtained with EDS.

Element	Weight %
O	41.04
Na	1.21
Si	0.65
K	8.86
Cr	48.23

Table 6. Elemental composition by XRF of dried and calcined Luffa after Cr (VI) adsorption in synthetic wastewater.

Element	Dry Luffa	Calcined Luffa
Mg	4.76	3.29
Al	0.79	1.32
Si	3.57	2.04
K	2.06	14.22
Ca	0.81	2.31
Cr	8.73	75.07
Mn	0.08	0.58
Fe	0.12	0.45
Low Energy	78.99	0.00

3.8 Elemental composition of luffa after Cr (VI) adsorption in wastewater by XRF

XRF analysis of Luffa after Cr (VI) adsorption revealed a Cr content of 8.73% by weight, along with 78.99% by weight of low-energy elements. These low-energy elements, which emit X-rays at lower energy levels, typically include light elements such as carbon (C) and oxygen (O), consistent with the organic nature of luffa. In the ash samples of luffa post-adsorption and calcination, a Cr content of 75.07% by weight was observed, with no detectable low-energy elements, attributed to the thermal degradation that occurred during calcination (Table 6).

The Cr content is significantly higher in the luffa ash after Cr (VI) adsorption from wastewater compared to the surface analysis results obtained through EDS and XRF elemental composition determination. This suggests that the entire luffa structure participates in the adsorption of Cr (VI) in the wastewater. The difference in Cr percentages between EDS and XRF is that EDS only analyzes a small region of the luffa sample, whereas XRF provides averaged elemental information over a larger volume of luffa.

FTIR spectra of luffa were obtained to understand its structure. In Figure 9 the normalized FTIR spectra of luffa fibers before adsorption (LN) and after adsorption ($LNCr^{+6}$) can be observed. The normalization criterion used was by maximum intensity (Min-Max Scaling), which scales the

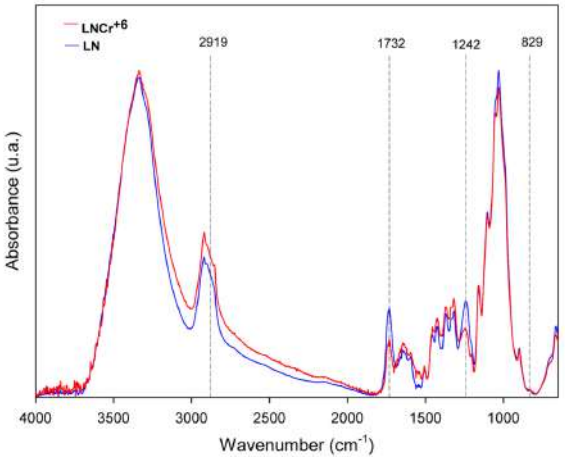

Figure 9. Normalized FTIR spectrum of luffa before and after Cr (VI) adsorption on wastewater at wavenumber 4000-450 cm^{-1}.

absorbance values between 0 and 1, A_{nom}= (A-A_{min})/(A_{max}-A_{min}). A is the original absorbance and the A_{max} value was associated with the band with the highest intensity, which in both spectra corresponded to the C-O vibration at 1030 cm^{-1} and A_{min} was assigned the value of 0 associated with the baseline of the graph.

In the LN spectrum, a broad band between ~3700 cm^{-1} and 3000 cm^{-1} (~3334 cm^{-1}), corresponds to the stretching vibration of hydroxyl groups (-OH). This functional group is present in the three molecules that make up luffa fibers. The peak at ~2919 cm^{-1} corresponds to the asymmetric stretching of CH_2 in cellulose. The sharp peak at ~1732 cm^{-1} is attributed to the C=O stretching in lignin (guaiacyl group). Peaks at ~1646 cm^{-1} and ~1506 cm^{-1} correspond to the stretching of the C=C bond in the aromatic ring of lignin. The peaks at ~1456 cm^{-1}, ~1423 cm^{-1}, and ~1370 cm^{-1} are associated to the deformation of CH_2 and CH_3 bonds (scissoring). The peak at ~1316 cm^{-1} is due to C-H bending vibrations, while the peak at 1242 cm^{-1} corresponds to C-O asymmetric stretching in the guaiacyl ring. The peak at ~1159 cm^{-1} represents C-O symmetric stretching vibrations and the peak at 1103 cm^{-1} for aromatic skeletal vibrations. Also, the peak at 1031 cm^{-1} is due to the C-O stretching in cellulose and hemicellulose, while the peak at 897 cm^{-1} corresponds to the C-O-C stretching in β-(1-4) glycosidic bonds between monosaccharides in cellulose and hemicellulose (NagarajaGanesh and Muralikannan, 2016; Vârban *et al*., 2021).

After Cr (VI) adsorption, several differences were observed in the FTIR spectra. One of these is the peak increasing at 2919 cm^{-1}, inferring that C-H groups are involved in the adsorption of Cr (VI). Additionally, the intensities of the peaks at 1732 cm^{-1} and 1242 cm^{-1} decreased, indicating that C=O and C-O bonds are affected in the adsorption of Cr (VI). In the FTIR spectrum, no new peak was observed at 829 cm^{-1} after

the adsorption process, which typically corresponds to the Cr–O bond. This suggests that the adsorption of Cr (VI) on cylindrical luffa does not directly involve the formation of a covalent bond with chromium, but that the process may be dominated by electrostatic interactions, hydrogen bonds, or surface complexation between the functional groups present in the surface of luffa and Cr (VI) chemical species. (Perry *et al*., 1999).

3.9 Comparison of the adsorption capacity of Luffa with other materials

In this section, the results obtained for the adsorption capacity of Luffa are compared with other lignocellulosic materials reported in the literature. Table 7 describes the maximum adsorption capacities (mg/g) and the composition of cellulose, hemicellulose, and lignin for each reported material.

As can be seen in Table 7, the adsorption capacity is variable and depends on various factors such as pH, temperature, internal structure, and functional groups present in the biomaterial studied. The low adsorption capacity of Cr (VI) in *Luffa cylindrica* can be explained by its chemical composition, the nature of its functional groups, and its morphology. Luffa has a relatively low lignin content (14%), whereas other lignocellulosic materials, such as walnut hull (48.3% lignin) and coconut husk (43% lignin), have demonstrated higher adsorption capacities. Lignin contains functional groups such as phenols, carboxyls, and methoxyls, which facilitate both adsorption and Cr (VI) reduction to Cr (III), enhancing removal efficiency. Additionally, although pH 2 favors Cr (VI) adsorption in the form of $HCrO_4^{-1}$, the positive surface charge of luffa may not be sufficiently high to attract efficiently these anions. This suggests that electrostatic interaction plays a limited role in the adsorption process.

The morphology of luffa, as observed by SEM, reveals a fibrous structure with relatively large pores, which reduces the available specific surface area for adsorption compared to microporous materials. The lower density of active sites limits Cr (VI) retention on the bioadsorbent's surface. Finally, competition with other anions present in the solution may affect the material's selectivity for Cr (VI) adsorption. To improve removal efficiency, chemical modifications such as controlled oxidation or functionalization with amino and carboxyl groups, as well as physical treatments to increase porosity, could be explored. These combined factors explain the lower Cr (VI) adsorption capacity of luffa compared to other bioadsorbents and suggest that its performance can be optimized through appropriate pretreatment strategies.

Table 7. Comparison of different lignocellulosic materials on Cr (VI) adsorption and its elemental composition.

Adsorbent material	Maximum Capacity (mg/g)	% Cellulose	% Hemicellulose	% Lignin	Reference
Luffa	10	76	10	14	This work
Ground Luffa	29.98	60	22	10.6	(Laidani *et al*.,2020)
Coconut husk	29	40	0.2	43	(Tan *et al*., 1993)
Sugarcane bagasse	23	32-48	19-24	23-32	(Krishnani *et al*., 2009)
Rice husk	52.1	35	25	20	(Krishnani *et al*., 2007)
Walnut hull	98.3	33.2	9.6	48.3	(Wang *et al*., 2008)
Orange peels	16.66	13.08	6.47	6.5	(Tejeda-Tovar *et al*., 2015)
coffee waste biomass	0.827	**	**	**	(Rubio-Campos *et al*., 2022)
Activated Carbon Fiber	2.5-13	**	**	**	(Leyva-Ramos *et al*., 2008)

** Not applicable or not reported

Conclusions

This research achieved the removal of 100% Cr (VI) from laboratory-prepared wastewater using Luffa as a bioadsorbent which had an adsorption capacity of 10 mg/g luffa. The characterization of dried luffa revealed a composition of 76% cellulose, 14% lignin, and 10% hemicellulose by weight, highlighting its high cellulose content, a key component in the adsorption of contaminants. Lignin, with its carboxyl, methoxyl, and carbonyl functional groups, plays a crucial role in Cr (VI) reduction to Cr (III), which contributes significantly to the effectiveness of the material in heavy metal adsorption processes. This agrees with previous studies, such as those of Dupont and Guillon (2003), who demonstrated that, under acidic pH conditions, lignin is more effective than cellulose in the adsorption and reduction of Cr (VI). In this sense, the lignocellulosic composition of dried luffa, with a significant proportion of lignin, is decisive in its ability to adsorb and reduce Cr (VI) in aqueous solutions, since the largest amount of lignin is found in the outer surface of Luffa fibers. Scanning electron microscopy (SEM) with energy-dispersive X-ray spectroscopy (EDS) confirmed an elemental makeup primarily of carbon (56% by weight) and oxygen (38% by weight), consistent with its structural components. Fourier-transform infrared spectroscopy (FTIR) analysis identified functional groups on the luffa surface, including carbonyl, carboxyl, hydroxyl, and methoxyl groups. At a pH of 2, these groups become protonated, enhancing the chemisorption of Cr (VI) ions. Microscopy analysis revealed a rough, fissured surface structure, facilitating the physisorption of Cr (VI) onto the luffa.

An essential preparatory step involved boiling the luffa for 30 minutes, as omitting this step significantly reduced its adsorption efficiency. In experiments with synthetic wastewater containing initial Cr (VI) concentrations between 15 and 50 ppm, and using 0.5 g of luffa, complete removal of Cr (VI) was achieved. Specifically, up to 10 mg of Cr (VI) were adsorbed per gram of luffa at 50 ppm initial concentration. Adsorption time was increased with higher Cr (VI) initial concentrations, highlighting a dependence on concentration. The kinetic models indicate that Cr (VI) adsorption follows a pseudo-second-order model, with a rate constant inversely related to the initial concentration.

Finally, this study demonstrates that luffa is an effective and sustainable bioadsorbent for removing Cr (VI) from synthetic wastewater at concentrations of up to 50 ppm, achieving a 100% removal rate using 0.5 g of Luffa fibers. These findings highlight the potential for further research to assess its performance at higher concentrations, aiming to expand its application in contaminated water treatment. The findings suggest that the adsorption process involves chemisorption (as indicated by FTIR) and physisorption (as observed through SEM).

As observed in the micrographs obtained by SEM and optical microscopy, the three-dimensional structure of the luffa, formed by intertwined fibers, presents an important advantage for the recovery of the adsorbent material. Its morphology facilitates the manipulation of luffa after the adsorption process, allowing a simple separation of the aqueous medium. Additionally, the Luffa firmness prevents collapse or compaction of the fibers during the adsorption process, ensuring that the material maintains its original structure. This is especially relevant in recycling the luffa after chemical or thermal regeneration. Compared to other adsorbent materials, such as nanoparticles or fine powders, the fibrous form of luffa offers an additional advantage: it significantly reduces material loss during its recovery, making it a practical and sustainable option for water treatment applications.

These insights are the basis for future research and assessment of potential industrial applications of Luffa in wastewater treatment, contributing to the sustainable removal of heavy metals from water and addressing a significant environmental issue.

Acknowledgements

The authors thank Tecnológico Nacional de México (TecNM) for the financial support to perform the research project **"***Removal of hexavalent chromium in wastewater using luffa as a bioadsorbent*", grant 19749.24-P. We also thank CONAHCYT for the scholarship granted, which was important for finishing this work.

References

Adeyanju, C. A., Ogunniyi, S., Ighalo, J. O., Adeniyi, A. G., & Abdulkareem, S. A. (2020). A review on Luffa fibres and their polymer composites. *Journal of Materials Science*, *56*(4), 2797-2813. https://doi.org/10.1007/s10853-020-05432-6

Arroyo, I. J., & Cervantes, G. (2018). Huella hídrica de un producto industrial: una metodología (*In Spanish*). *Tecnología y Ciencias del Agua, 9*(6), 70-90. https://doi.org/10.24850/j-tyca-2018-06-03

Behera, D., Pattnaik, S. S., Mishra, P. P., Sahu, R., Manna, S., Das, N., Misra, M., Mohanty, A. K., & Behera, A. K. (2024). Fabrication

and characterization of industrial biocomposite from cellulosic fibers of *Luffa cylindrica* in a protein based natural matrix. *Industrial Crops and Products*, *212*, 118328. https://doi.org/10.1016/j.indcrop.2024.118328

Diaz-Rodríguez, K. F., Salazar-Pinto, B. M., Flores-Calla, S. S., & Gonzales-Condori, E.G. (2025). Potential use of artichoke (*Cynara cardunculus L.*) waste packed in filter bags for the removal of hexavalent chromium from water. *Revista Mexicana de Ingeniería Química, 24*(1), IA25426. https://doi.org/10.24275/rmiq/IA25426

Domínguez, J. (2018). Obtención de Materiales carbonosos y furanos a partir de bagazo de agave por carbonización hidrotérmica *(Spanish)*. Tesis de Maestría en Ciencia y Tecnología Ambiental, Centro de Investigación en Materiales Avanzados (CIMAV), Chihuahua, México.

Dupont, L., & Guillon, E. (2003). Removal of hexavalent chromium with a lignocellulosic substrate extracted from wheat bran. *Environmental Science & Technology, 37*(18), 4235–4241. https://pubs.acs.org/doi/10.1021/es0342345

Gonzales-Condori, E., Avalos-López, G., Mujica-Guzman, A., Terán-Hilares, R., Briceño, G., Quispe-Avilés, J., Parra, P., & Villanueva-Salas, J. (2023). Avocado seed powder residues as a promising bio-adsorbent for color removal from textile wastewater. Revista *Mexicana de Ingeniería Química*, *22*(3), IA2370. https://doi.org/10.24275/rmiq/IA2370

Hasanzadeha, S., Mortazavi-Derazkolab, S., & Khosravi, R. (2024). Green synthesis of iron nanoparticles using *Pistacia-atlantica* leaf extract for enhanced removal of Cr (VI) from aqueous solution. *Desalination and Water Treatment, 318*, 100347. https://doi.org/10.1016/j.dwt.2024.100347

Jiménez-González, A., Tec-Caamal, E. N., & Medina-Moreno, S. A. (2024). Biosorption performance evaluation of azo dyes Reactive Red 2 and Reactive Blue 4 on thermally sterilized biomass of *Cladosporium tenuissimum* fungus. *Revista Mexicana de Ingeniería Química*, *23*(1), IA24161. https://doi.org/10.24275/rmiq/IA24161

Khadir, A., Motamedi, M., Pakzad, E., Sillanpää, M., & Mahajan, S. (2020). The prospective utilization of Luffa fibres as a lignocellulosic bio-material for environmental remediation of aqueous media: A review. *Journal of Environmental Chemical Engineering*, *9*(1), 104691. https://doi.org/10.1016/j.jece.2020.104691

Komatani, S., Aoyama, T., Nakazawa, T., & Tsuji, K. (2013). Comparison of SEM-EDS, Micro-XRF and Confocal Micro-XRF for Electric Device Analysis. *e-Journal of Surface Science and Nanotechnology*, *11*, 133-137. https://doi.org/10.1380/ejssnt.2013.133

Krishnani, K., Meng, X., Christodoulatos, C., & Boddu, V. (2007). Biosorption mechanism of nine different heavy metals onto biomatrix from rice husk. *Journal of Hazardous Materials*, *153*(3), 1222-1234. https://doi.org/10.1016/j.jhazmat.2007.09.113

Krishnani, K., Meng, X., & Dupont, L. (2009). Metal ions binding onto lignocellulosic biosorbent. *Journal of Environmental Science and Health Part A*, *44*(7), 688-699. https://doi.org/10.1080/10934520902847810

Kuyucak, N., & Volesky, B. (1989). Accumulation of cobalt by marine alga. *Biotechnology and Bioengineering*, *33*(7), 809-814. https://doi.org/10.1002/bit.260330703

Laidani, Y., Henini, G., Hanini, S., & Fekaouni, A. (2020). Study of the kinetics and thermodynamics of adsorption of hexavalent chromium on the *Luffa Cylindrica* cords. *Iranian Journal of Chemistry and Chemical Engineering-International English Edition, 39*(4), 137-151. https://doi.org/10.30492/ijcce.2020.39755

Leyva-Ramos, R., Flores, J. V, Díaz, P. E., & Berber, M. S. (2008). Adsorción de cromo (VI) en solución acuosa sobre fibra de carbón activado. *Información Tecnológica*, *19*(5), 27-36. https://dx.doi.org/10.4067/S0718-07642008000500005

Miretzky, P., & Cirelli, A. F. (2010). Cr (VI) and Cr (III) removal from aqueous solution by raw and modified lignocellulosic materials: a review. *Journal of Hazardous Materials*, *180*(1-3), 1-19. https://doi.org/10.1016/j.jhazmat.2010.04.060

NagarajaGanesh, B., & Muralikannan, R. (2016). Extraction and characterization of lignocellulosic fibers from *Luffa cylindrica* fruit. *International Journal of Polymer Analysis and Characterization/IJPAC*, *21*(3), 259-266. https://doi.org/10.1080/1023666x.2016.1146849

Nwosu-Obieogu, K., & Okolo, B. I. (2020). Biosorption of chromium (VI) from textile wastewater using luffa cylindrica activated carbon. *Environmental Quality Management*, *29*(4), 23-31. https://doi.org/10.1002/tqem.21687

Perry, D. L., Hoi-Ying, & Dale L. (1999). Real-Time characterization of biogeochemical reduction of Cr (VI) on basalt surfaces by SR-FTIR imaging. *Geomicrobiology Journal*, *16*(4), 307-324. https://doi.org/10.1080/014904599270569

Rahman, N. N. N. A., Shahadat, M., Won, C. A., & Omar, F. M. (2014). FTIR study and bioadsorption kinetics of bioadsorbent for the analysis of metal pollutants. *RSC Advances*, *4*(102), 58156-58163. https://doi.org/10.1039/c4ra05931j

Richard, F. C., & Bourg, A. C. (1991). Aqueous Geochemistry of Chromium: a review. *Water Research, 25*(7), 807-816. https://doi.org/10.1016/0043-1354(91)90160-r

Rubio Campos, B. E., Gamiño Arroyo, Z., Murrieta Escoto, S., Méndez Segoviano, P. A., Ibarra Rivera, B. M., Jiménez Verver y Vargas, P., López Chávez, F. Y., & Álvarez Torres, X. (2022). Remoción de Cromo VI de soluciones acuosas empleando biomasa de residuos de café, *JÓVENES EN LA CIENCIA*, *16*, 1–8 https://www.jovenesenlaciencia.ugto.mx/index.php/jovenesenlaciencia/article/view/3798

Secretaría de Economía. (2014). Norma Mexicana NMX-AA-044-SCFI-2014 Análisis de agua. - medición de cromo hexavalente en aguas naturales, salinas, residuales y residuales tratadas-método de prueba (*In Spanish*). Publicado en el Diario Oficial de la Federación el 13 de enero de 2015, México. *www.gob.mx/cms/uploads/attachment/file/166148/nmx-aa-044-scfi-2014.pdf*

Sahoo, T. R., & Prelot, B. (2020) Adsorption processes for removal of contaminants from wastewater. *Nanomaterials for the detection and removal of wastewater pollutants, Chapter 7,* 161-222. https://doi.org/10.1016b978-0-12-818489-9.00007-4

Sun, M., & Hong, L. (2011). Impacts of the pendant functional groups of cellulose precursors on the generation of pore structures of activated carbons. *Carbon*, *49*(7), 2173-2180. https://doi.org/10.1016/j.carbon.2011.01.031

Tan, W., Ooi, S., & Lee, C. (1993). Removal of chromium (VI) from solution by coconut husk and palm pressed fibres. *Environmental Technology*, *14*(3), 277-282. https://doi.org/10.1080/09593339309385290

Tanobe, V. O., Sydenstricker, T. H., Munaro, M., & Amico, S. C. (2005). A comprehensive characterization of chemically treated Brazilian sponge-gourds (Luffa). *Polymer Testing*, *24*(4), 474-482. https://doi.org/10.1016/j.polymertesting.2004.12.004

Tejada-Tovar, C., Quiñones-Bolaños, E., Tejeda-Benitez, L., & Marimon-Bolivar, W. (2015). Absorción de cromo hexavalente en soluciones acuosas por cascaras de naranja (*Citrus sinensis). Rev. P+L*, *10*(1), 9-21. http://www.scielo.org.co/scielo.php?script=sci_arttext&pid=S1909-04552015000100002

Tejada-Tovar, C., González-Delgado, A., & Villabona-Ortiz, A. (2018). Adsorption kinetics of orange peel biosorbents for Cr (VI) uptake from water. *Contemporary Engineering Sciences*, *11*(24), 1185-1193. https://doi.org/10.12988/ces.2018.83105

Tejada-Tovar, C., Herrera-Barros, A., & Villabona-Ortíz, A. (2019). Assessment of chemically modified lignocellulose Waste for the Adsorption of Cr (VI). *Revista Facultad de Ingeniería*, *29*(54), e10298. https://doi.org/10.19053/01211129.v29.n54.2020.10298

Vârban, R., Crisan, I., Vârban, D., Ona, A., Olar, L., Stoie, A., & Stefan, R. (2021). Comparative FT-IR prospecting for cellulose in stems of some fiber plants: Flax, Velvet Leaf, Hemp and Jute. *Applied Science, 11* (18), 8570. https://doi.org/10.3390/app11188570

Vašková, H., & Kolomaznik, K. (2016). Spectroscopic measurement of trivalent and hexavalent chromium. *2006 17th International Carpathian Control Conference (ICCC)*, 775-778. https://doi.org/10.1109/carpathiancc.2016.7501200

Wang, X. S., Li, Z. Z., & Tao, S. R. (2008). Removal of chromium (VI) from aqueous solution using walnut hull. *Journal of Environmental Management*, *90*(2), 721-729. https://doi.org/10.1016/j.jenvman.2008.01.011

Vol. 24, No. 2(2025) Mat25444
Revista Mexicana de Ingeniería Química

Molecular dynamics of SDS-coated gold nanoparticles in aqueous medium with Coarse-grained model and MARTINI force field

Dinámica molecular de nanopartículas de oro recubiertas con SDS en medio acuoso con modelo Coarse-grained y campo de fuerza MARTINI

D.E. Altamirano-Bulnes*, E.D. Estrada-López
Departamento de Ingeniería Química. Universidad Nacional Autónoma de Honduras, Tegucigalpa, Francisco Morazán, Honduras.
Received: October 17, 2024; Accepted: April 8, 2025

Abstract
Gold nanoparticles have garnered significant interest in recent years across various fields of study, including materials science, biomedicine, drug delivery design, electronics, and optics, among others. Numerous studies have aimed to visualize their properties by coating them with polymers, proteins, surfactants, and genes to observe and analyze variations in their functioning. With advances in computing, these nanoparticles have been examined using molecular dynamics methodologies to simulate their interactions with different solvents and particles, thereby predicting their behavior in diverse applications. In this research, spherical gold nanoparticle systems with a radius of 1.5 nm, coated with the surfactant sodium dodecyl sulfate (SDS), are investigated in an aqueous medium with varying concentrations utilizing molecular dynamics with a coarse-grained approach and the MARTINI force field to examine energy, structural, transport, and stability aspects properties.
Keywords: metal nanoparticles, active agent, interface, computer simulation, nanomaterials.

Resumen
Las nanopartículas de oro han cobrado en los últimos años un gran interés en diversos campos de estudio, entre ellos: la ciencia de materiales, la biomedicina, el diseño de transporte de fármacos, la electrónica, la óptica, entre otros. Diversos estudios han buscado visualizar sus propiedades al recubrirlas con polímeros, proteínas, surfactantes y genes con el fin de observar y estudiar las variaciones en su funcionamiento. Debido a los avances en el área de la computación, este tipo de nanopartículas se han estudiado a través de la metodología de dinámica molecular con el fin de simular sus interacciones con diversos disolventes y otras partículas, para predecir su comportamiento en diferentes aplicaciones. En esta investigación se estudian sistemas de nanopartícula de oro esférica con un radio de 1.5 nm recubiertas del surfactante dodecilsulfato sódico (SDS) en un medio acuoso a través de la dinámica molecular con enfoque de coarse-grained y campo de fuerza MARTINI para analizar propiedades de energía, estructurales, de transporte y de estabilidad.
Palabras clave: nanopartículas de metal, agente activo, interfase, simulaciones computacionales, nanomateriales.

*Corresponding author. *E-mail*: d.bulnes97.db@gmail.com ;
https://doi.org/10.24275/rmiq/Mat25444
ISSN:1665-2738, *issn-e*: 2395-8472

1 Introduction

Nanomaterials are defined as particles that form crystals, with structures depending on the synthesis method, the surface area of the nanoparticle, and the intended final application. Their dimensions range from 1 nm to 100 nm (Khan *et al*., 2019). These versatile materials can create structural systems in materials science, enabling the characterization of electronic, photochemical, electrochemical, optical, magnetic, catalytic, and mechanical properties that differ significantly from those of macro systems. (Khan *et al*., 2019). This difference has led to a growing interest in nanomaterials in recent years, particularly in metals that interact with various electronic, photochemical, electrochemical, catalytic, and mechanical systems. One metal that has attracted attention due to technological advances in materials science at both macro and nano scales is gold. Gold nanoparticles (AuNPs) have numerous applications in the medical field, especially in the transport of drugs, genes, and proteins; treatments for tumors and cancer cells through photothermal therapy (PTT), photodynamic therapy (PDT), radiative therapy (RT), and imaging via X-ray and computed tomography (Hu *et al*., 2020; Ramalingam, 2019). Moreover, due to their diverse characteristics and modifications, AuNPs are significantly interesting in various multidisciplinary fields, such as chemical and biological labeling, gaseous labeling, CO_2 capture, and other important applications (Barrak *et al*., 2016; Ganesh *et al*., 2013; I. Khan *et al*., 2017; Lee *et al*., 2011; Mansha *et al*., 2017; Montoya-Villegas *et al*., 2020; Nuñez-Delgado *et al*., 2023; Ramacharyuly, P. V. R. K.; Muhammad, Raeesh; Kumar, Praveen J.; Prasad, 2015; Rawal & Kaur, 2013; Shaalan et al., 2016; Velasco-Rodriguez *et al*., 2012).

For decades, ligands like oligonucleotides, drugs, peptides, and conjugated polymers have been used to bind to AuNPs via thiol group bonds, aiming to support and protect these structures (Asish, Pal; Aasheesh & Bhattacharya, 2009; Lu *et al*., 2014; Si *et al*., 2018). The AuNPs are anchored to the ligands of interest through covalent and non-covalent interactions, which, under specific pH or salt conditions, facilitate the release of these particles in targeted areas via in-solution injection (Applications, 2017). Notably, one of the most frequently used ligands is sodium dodecyl sulfate (SDS), a surfactant that transforms the properties of interfaces. Its characteristics have been extensively studied, making it a suitable candidate for various applications in materials science in conjunction with gold nanoparticles.

Molecular dynamics studies have been conducted using various coatings for AuNPs. (Elahi *et al*., 2018). Due to the high computational cost of all-atom simulations, the coarse-grained approach, which involves packing individual chemical structures into larger assemblies, offers an appealing method for mesoscale modeling. This is because it significantly extends simulation times and the average size of study systems from nanometers to micrometers. Coarse-grained molecular dynamics (CGMD) uses a mapping technique that groups together functional groups of three to five atoms, along with their hydrogens, into beads or spheres that interact with each other. (Marrink *et al*., 2007). These beads indicate the degree of polarity and affinity between chemical groups, excluding specific interactions like hydrogen bonds. The greatest advantage of this approach is that it allows for longer simulation times by mapping atoms as beads, which reduces computational costs. (Marrink *et al*., 2007).

Additionally, the coarse-grained methodology in molecular dynamics has established itself as an essential tool for studying complex biological systems and complex materials in the field of nanomaterials (Joshi & Deshmukh, 2021; Kmiecik *et al*., 2016). The methodology has allowed the modeling of systems such as pulmonary surfactant, lipid membranes, surfactant self-assembly, or membrane characterization with favorable results for the research of biomolecules or potential uses in industry (Baoukina *et al*., 2017; Estrada-López *et al*., 2017; Joshi & Deshmukh, 2021; Owen, 2014; Pizzirusso *et al*., 2016 Souza *et al*., 2018). Similarly, the methodology has been used during the simulation of polymers in solution and in the study of their mechanical properties, as in the case of poly(n-isopropylacrylamide) (PNIPAM) or polyacrylic acid (PAA); models that, through CGMD, allowed the study of their complex structures and sensitivity to temperature changes (Abu Samah & Heard, 2014; Baranowska-Korczyc *et al*., 2019; Deshmukh *et al*., 2009).

In this research, the interactions of AuNPs coated with SDS in an aqueous medium will be studied using CGMD and Newtonian dynamics in two separate systems: one with a single nanoparticle and the other with three nanoparticles, aiming to examine their energy, structural, transport, and stability properties.

2 Methodology

2.1 General conditions

In this work, a coarse-grained model utilizing the MARTINI force field version 2.1 (Marrink *et al*., 2007; Marrink & Tieleman, 2013) was employed to simulate the interactions of gold nanoparticles coated with SDS in an aqueous system. This enables

longer simulation times with extended time steps, ranging from 10 to 50 fs, in contrast to the time steps used in all-atom molecular dynamics, which simulate each atom-atom interaction, ranging from 1 to 2 fs (Fitzgerald *et al*. al., 2015). The GROMACS computational package version 2021.4 was utilized (Abraham et al., 2015; Pronk *et al*., 2013) for system construction, molecular dynamics simulations, and analysis. The minimization of energy for the relaxation of the molecules was done using the steepest descent method (Alexander, 1986). at 100 kJ/mol. Molecular dynamics simulations were performed using the leap-frog algorithm (Hockney *et al*., 1974; Taylor et al., 2007). For temperature balance, an NVT assembly was used using the V-rescale thermostat (Bussi *et al*., 2007). The integration time for all simulations was 20 fs. A cutoff radius of 1.2 nm was used for all nonbonding, van der Waals, and electrostatic interactions. The Lennard-Jones potential was gently delocalized from 0.9 to 1.2 nm to reduce noise at the cutoff radius. The Coulomb potential was smoothly delocalized from 0 to 1.2 nm. A dielectric constant of 15 was used for water, and a value of 4.5×10^{-5} bar was used for isothermal compressibility. The cutoff radius performs an update every 10 steps of each simulation (Marrink *et al*., 2007). All snapshots were prepared using the VMD program.

2.2 *Parametrization*

The AuNPs-SDS model was generated by the Nano Modeler program (Franco-ulloa *et al*., 2022). A summary of the atomistic and coarse-grained structures of all the structures in this investigation is provided in Table 1.

Table 1. Coarse-grained schemes and chemical structures.

Name	Chemical structure	Coarse grained representation
AuNP	Au X5	Au
SDS	SO_4, C1A, C2A, C3A, Na^+	Qa (A3), C1A (A2), C2A (A1), C3A (A0)

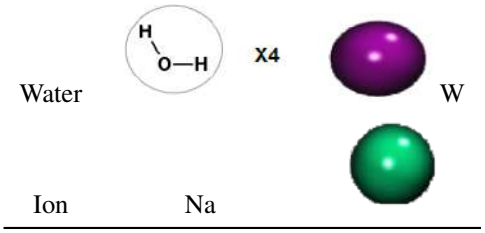

2.3 *AuNPs-SDS systems in aqueous medium*

The AuNPs were constructed in a spherical shape, with a radius of 1.5 nm, density of 19.3 g/cm^3, area density per ligand of 0.5 nm^2 /ligand, with bead type C5, bead radius of 0.166 nm and a force constant of 32,500 kJ/(mol-nm^2) for the C5-C5 interaction. Coating the AuNPs, with SDS (Wassenaar et al., 2015), parameterized with 3 C1 bead type with a charge of 0 and one Qa bead type with a charge of -1, using the Nano Modeler program (Franco-ulloa *et al*., 2022). This system can be visualized in Illustration 1. The system of a single AuNP-SDS in aqueous medium is depicted in Illustration 2, while the system of three AuNPs-SDS in aqueous medium is shown in the subsequent illustration 3.

For creating both systems, the gmx editconf program was used to establish a 12x12x12 nm box by introducing, with the gmx insert-molecules program, 10,000 water beads with a radius of 0.21 nm, which corresponds to 4 water molecules. Temperature equilibration was performed using the NVT ensemble at 298 K with a simulation time of 100 ns. Subsequently, an NPT molecular dynamic at 1 bar pressure with a simulation time of 200 ns was done using isotropic coupling and a Berendsen barostat (Berendsen, 1991). Analyses of the radial distribution function, the radius of gyration, and the mean square distance (MSD) were conducted. The latter provides information on the lateral diffusion coefficient of the nanoparticle in the aqueous medium, while thermodynamic studies offer insights into the stability of the system based on temperature, pressure, and density parameters.

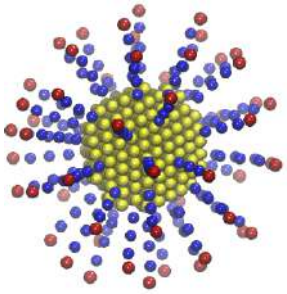

Illustration 1. Coarse-grained model of AuNP coated with SDS (AuNP-SDS). Gold nanoparticle (yellow), carbon chains of the SDS ligand (C1A-C3A) (blue) and polar head (Qa) (red).

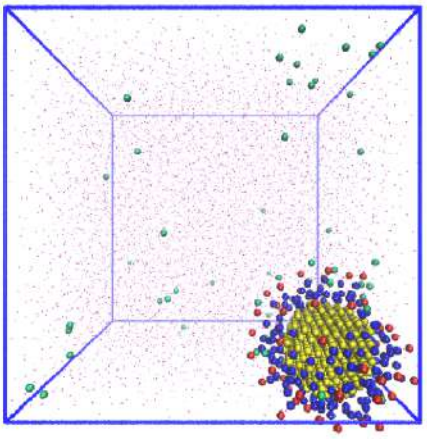

Illustration 2. Coarse-grained model of AuNP-SDS solvated in water (purple) and counterbalanced by sodium ions (green) in a 12x12x12 nm box.

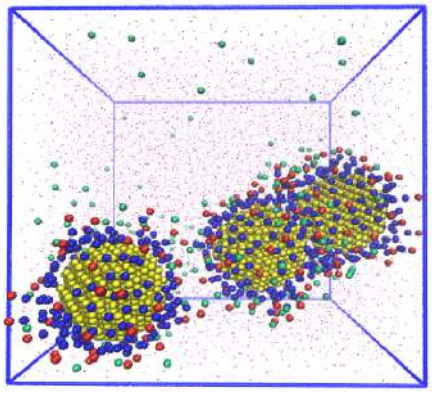

Illustration 3. Coarse-grained model of a 3 AuNPs-SDS system solvated in water (purple) and counterbalanced by sodium ions (green) in a 12x12x12nm box.

3 Results and discussion

3.1 Thermodynamics parameters

The results of a single gold nanoparticle in an aqueous medium system (AuNP-SDS-H_2O) demonstrate temperature stability of (298 ± 2)K, indicating that the thermostat employed effectively maintains a consistent temperature in the system. This illustrates that the V-rescale thermostat is a well-known approximation for temperature control in the CGMD system. The experimental density of water at room temperature (25 °C) is 997.05 kg/m^3. Considering that the coarse-grained model overestimates the parameterization for water, the expected density at this temperature is 1000 kg/m^3. The AuNP-SDS-H_2O system exhibits an increase in density from 1000 kg/m^3 to 1233 kg/m^3, with an uncertainty of 5 kg/m^3 (1233 ± 5) kg/m^3, thus demonstrating an increase of approximately 233 kg/m^3 resulting from the addition of the SDS-coated gold nanoparticle, which remains relatively constant throughout the simulation.

For the three gold nanoparticles in the aqueous medium system (AuNP-SDS-H_2O), the temperature remained constant at a value of (298 ± 2)K like that observed for the simulation of a single AuNP. The three AuNP-SDS-H_2O systems show a density increase from 1000 kg/m^3 to 1609 kg/m^3, with an associated uncertainty of 3 kg/m^3 (1609 ± 3)kg/m^3; this shows an increase of approximately 609 kg/m^3 from the addition of three gold nanoparticles coated with SDS. When performing a simple subtraction, compared to the single AuNP-SDS-H_2O system, the density difference is 376 kg/m^3. This suggests that each gold nanoparticle coated with the surfactant contributes to an increase of approximately 200 kg/m^3 in the system's density, assuming the system's density is the sum of its individual contributors.

3.2 Coulomb and van der Waals interaction energy

Table 2 shows the average Coulomb (E_C) and van der Waals (E_{LJ}) interaction energies for the entire system, including AuNP-SDS-ions and AuNP-SDS-AuNP-SDS, for one and three AuNPs, measured in kJ/mol. The values presented in this table are strongly dependent on the field used, so they may vary from those of other studies. This emphasizes the importance of properly using force fields for simulations conducted with coarse-grained methodologies. Therefore, the objective of this discussion is to illustrate the trends of the simulated systems. Both the E_C and E_{LJ} interaction energies show an increase in energy for both whole systems; however, the E_C interactions exhibit an increase of more than three times for the entire system. Conducting a more detailed analysis of the interactions between the two systems and AuNP-SDS-ions, we observe that the E_C and E_{LJ} energies exhibit the same trend as the whole systems, showing an increase of more than three times in their energies when transitioning from one to three AuNPs. This increase indicates a stronger attraction of the AuNP-SDS to the Na^+ ions as their concentration rises from one to three AuNP-SDS. In the case of the E_C and E_{LJ} analyses of the AuNP-SDS-AuNP-SDS interaction, it can be observed that the electrical interactions between the Au-NP-SDS are repulsive as the concentration increases and attracts through van der Waals intermolecular forces. However, the sum of E_C and E_{LJ} is negative, indicating a consistent tendency for AuNPs-SDS clusters to form as the concentration increases. Similar findings are presented in the following work (Bordoni & Colherinhas, 2022).

Table 2. The average interaction energy calculated for Coulomb (EC) and van der Waals (ELJ) for one and three AuNP in the whole system, including AuNP-SDS-ions and AuNP-SDS-AuNP-SDS, is presented in kJ/mol. The latter two measurements are provided per number of AuNP in an aqueous solution. RMSD values are shown for all average interactions.

Components	1 AuNP	3 AuNP
	E_C	
Whole system	-870.79 ± 36.63	$-2,971.33 \pm 56.89$
AuNP-SDS-ions	-659.09 ± 45.84	$-2,621.94 \pm 77.99$
AuNP-SDS-AuNP-SDS	-	31.14 ± 30.36
	E_{LJ}	
Whole system	$-316,540 \pm 499$	$-374,201 \pm 540$
AuNP-SDS-ions	-406.90 ± 46.23	$-1,565.79 \pm 78.50$
AuNP-SDS-AuNP-SDS	-	$-76,039.5 \pm 145.61$

Nonetheless, this also suggests that if the electrical force increases significantly, the AuNPs-SDS could experience repulsion.

3.3 Lateral diffusion

Lateral diffusion is an important dynamic property that measures a system's ability to move through a medium. The lateral diffusion coefficient can be calculated using Einstein's relation through the calculation of the mean square distance (MSD) of a set of atoms at specific positions. The MSD quantifies the deviation between a particle's position and its reference position. The lateral diffusion coefficient can be derived through linear regression by the least squares method, as represented by the equation:

$$\langle \|r(t) - r(t=0)\|^2 \rangle = 2Dt \tag{1}$$

Where $r(t)$is the position of the center of mass in the xy plane at a time t, $r(t = 0)$ is the position of the center of mass at an initial time 0, and D is the lateral diffusion coefficient.

In the lateral diffusion study, all data was collected from start to finish. To compare with experimental values or atomistic simulations, a conversion factor of 4 must be applied to the diffusion coefficient obtained from a simulation conducted in coarse-grained. The objective of this factor is to compensate for the faster diffusion in the coarse-grained model (Marrink *et al*., 2004)

The lateral diffusion coefficient is influenced by factors such as molecular size, shape, and interactions with the environment, including the solvent and other molecules present in the system. In the simulation of the single AuNP-SDS-H_2O system, the MSD was examined in relation to the simulation time, revealing consistently increasing and linear behavior throughout the duration of the simulation. By performing a linear fit $MSD = 4Dt + b$, as shown in Figure 1 for both systems, it was found that the lateral diffusion coefficient in the xy plane in the z direction of the nanoparticle for the single AuNP-SDS-H_2O system is $(5.559 \pm 0.004) \times 10^{-7} cm^2/s$. This value is greater than that reported by Giorgio of $1 \times 10^{-8} cm^2/s$ for uncoated gold nanoparticles sized at 50 nm using atomistic molecular dynamics. In another study of gold nanoparticles measuring 5 nm, the experimentally reported value is $1.5 \times 10^{-9} cm^2/s$; this nanoparticle size would be in greater agreement with this study (Vaisey *et al*., 2022). Wong and collaborators studied the translational diffusion of gold nanoparticles in toluene and water using the dynamic light scattering technique at different temperatures. They found that for a nanoparticle with a hydrodynamic radius of 16 nm at 298 K in an aqueous medium, its diffusion coefficient is $(1.53 \pm 0.035) x 10^{-7} cm^2/s$, which is of the same order of magnitude as the value calculated by the simulation. Other values have been reported experimentally in various sizes, yielding comparable results. (Albaladejo *et al*., 2009; Zimbone *et al*., 2011). It is important to note that even the experimental values for the diffusion of gold nanoparticles vary depending on the technique and the objectives of the study. The variations in values may be directly attributed to the coating of the gold nanoparticle with SDS, which significantly enhances its diffusion throughout the system by lowering the surface tension of water. Furthermore, the CGMD restricts the particle's degrees of freedom. Another factor that may explain the variations is the particle size used (Wong *et al*., 2015). In a CGMD study, a diffusion coefficient of approximately value $4.0 \times 10^{-7} cm^2/s$ for a size of 2 nm is reported. As the radius of the discovered nanoparticle increases, the diffusion coefficient decreases from 4.0×10^{-7} cm^2/s to $2.0 \times 10^{-7} cm^2/s$. Therefore, there is a dependence on the size of the nanoparticle on its diffusion in an aqueous medium (Gupta & Rai, 2017). Regarding the three AuNPs-SDS-H_2O system, it has been found that the lateral diffusion coefficient is $(7.300 \pm 0.015) x 10^{-7} cm^2/s$. This value is higher than that calculated for a gold nanoparticle in an

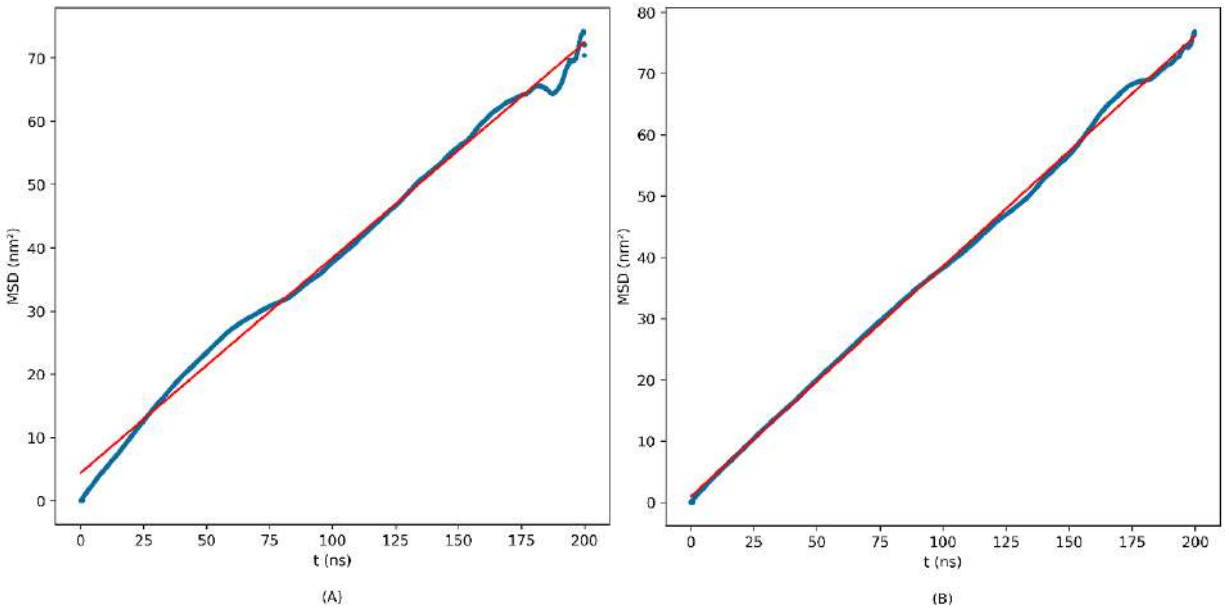

Figure 1. Comparison of linear regression for the variation of the mean square distance (MSD) throughout the simulation for one (A) and three (B) AuNPs-SDS systems in an aqueous medium. Simulated data (turquoise) and linear fit (red).

aqueous medium. This suggests that a greater number of coated nanoparticles may result in enhanced diffusion throughout the aqueous system. Subsequent simulations are needed to consider a larger number of AuNPs, which can form a bigger cluster to achieve increased diffusion.

3.4 Radial distribution function

In statistical mechanics, the Radial Distribution Function (RDF) describes the spatial distribution of particles in condensed phase systems, such as liquids or solids. The RDF indicates the probability of locating a particle at a specific point in space relative to another reference particle (Harding & Harding, 2007).

Mathematically, RDF is defined as the conditional probability density of finding a particle at a distance r with respect to a reference particle located at the origin within a system of particles. The RDF, denoted as $g(r)$ is defined as:

$$g(r) = \frac{1}{\langle \rho_B \rangle_{local}} \left(\frac{1}{N_A} \right) \sum_{i \in A}^{N_A} \sum_{j \in B}^{N_B} \frac{\delta\left(r_{ij} - r\right)}{4\pi r^2} \qquad (2)$$

Where $\langle \rho_B \rangle_{local}$ is the particle density of type B averaged over all spheres around particles A with radius $r_{\max}$, r is the distance between the particles, r_{ij} is the distance between the reference particle and neighboring particle i, N_A is the density of the particles A, N_B is the density of the particles B, and $\delta\left(r - r_{ij}\right)$ is the Dirac delta function which represents the probability of finding a particle at the distance r relative to the particle reference r_{ij}. The sum is calculated over all neighboring particles in the system. This provides insight into the structure and organization of the particles system.

The RDF analysis referenced the water particles of the system for both the one and three AuNP-SDS systems in an aqueous medium. As shown in Figure 2, the different RDFs for the A0 to A3 beads of the single AuNP-SDS are displayed. It is visualized that the A0 bead, which is the carbon atom linked to the gold nanoparticle by disulfide bonds, has a lower probability of being closer to water particles at shorter distances, which increases as the radial distance increases. The A1, A2, and A3 beads demonstrate an increase in RDF as the radius expands. This behavior, as illustrated in the figure, indicates that the polar head (A3) of the surfactant is near the water particles, varying throughout the simulation due to the folding of the ligand. At an approximate radial distance of 0.5 nm, this indicates a probability value of approximately 2.2. In the three AuNPs-SDS-H_2O systems, a similar behavior is observed for all beads, with only a smaller increase in the probability for the A3 bead, which is around 2.4 at 0.5 nm. We can see that both RDFs are remarkably similar, indicating that the cluster of three AuNPs-SDS behaves like a system of one AuNP-SDS. This can be useful because systems with more AuNPs-SDS can be treated as just one AuNP-SDS for this analysis. Regarding the folding of the tails on the nanoparticles, we observe that they attempt to stay together throughout the simulation. This approach would be beneficial for maintaining a cluster of gold nanoparticles that wish to remain united in an aqueous medium.

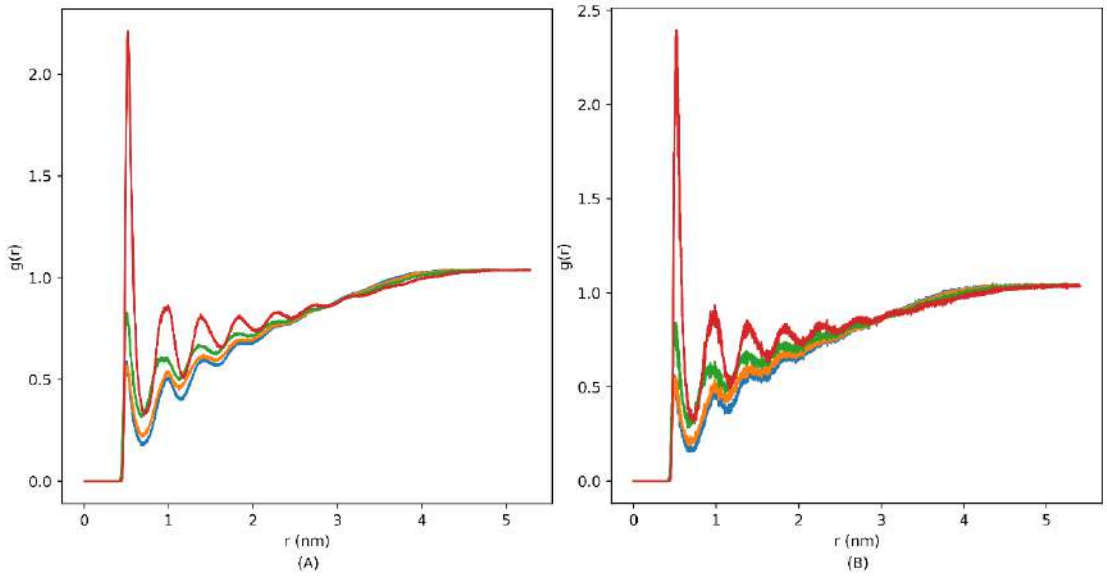

Figure 2. Comparison of RDF g(r) as a function of the nucleus radius with reference to water particles for one (A) and three (B) AuNPs-SDS systems in aqueous medium. *Bead A0* is carbon (blue), *Bead A1* is carbon (orange), *Bead A2* is carbon (green), and *Bead A3,* is polar head (red).

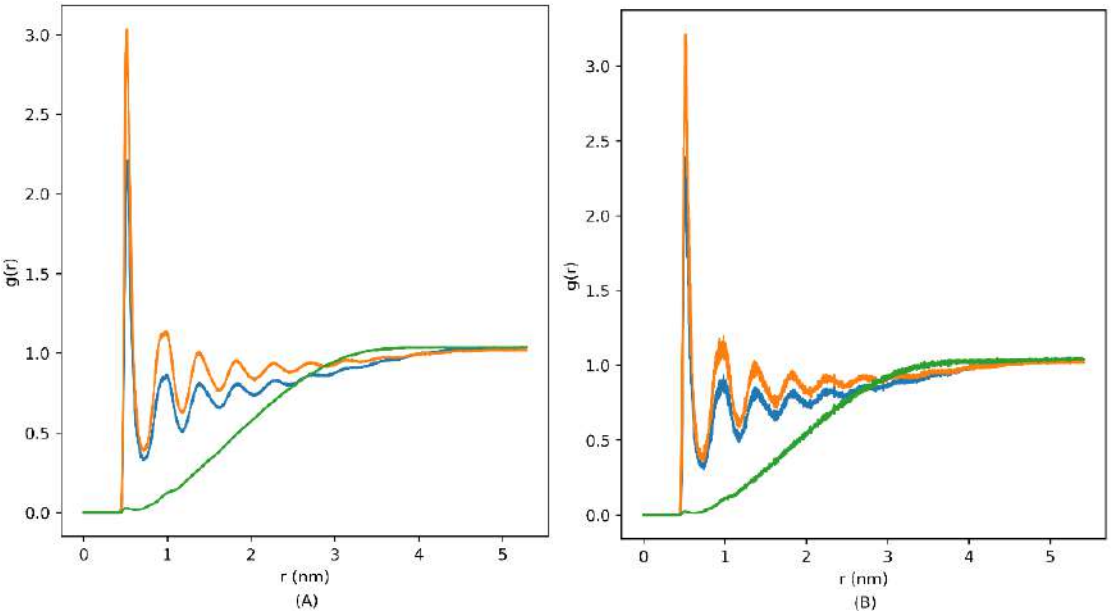

Figure 3. Comparison of the RDF g(r) for one (A) and three (B) AuNP-SDS systems with water particles as the reference. Nucleus (green), polar head (blue), and ion (orange).

Figure 3 compares the RDF of the nucleus, polar head, and ion for both AuNPs-SDS systems, using water as the reference. The ions are more likely to be near water particles than the nucleus and the polar head in both systems. Additionally, in the three AuNP-SDS systems, the slight increase in probability persists among the three references of the nucleus, the polar head, and the ion. As the concentration of AuNP-SDS increases, as seen in the energy analysis, the attraction of the sodium ions grows, imparting a polar behavior to the AuNP-SDS system compared to the uncoated AuNP, which exhibits nonpolar characteristics in the coarse-grained approach. (Marrink *et al*., 2007).

3.5 Gyration radius

The radius of gyration is defined as the radial distance to a point that would possess a moment of inertia equal to that of the actual mass distribution of the body at its center of mass. This measure provides information

about the spatial distribution of mass or charge within the system, thus serving as a metric for studying the structural properties of motion objects. Formally, this is defined as the average distance of the particles in the system from their center of mass and is commonly denoted by the letter R_g. Mathematically, the radius of gyration can be calculated through the equation:

$$R_g = \sqrt{\frac{1}{N}\sum_{i=1}^{N}(r_i - R_{cm})^2} \tag{3}$$

where N is the total number of particles in the system, r_i is the coordinate of the individual particles in the system, typically represented in Cartesian coordinates, and R_{cm} is the center of mass of the system, calculated as the weighted average of the particle coordinates in the system. The radius of gyration provides information about the spatial extent and shape of the entity under study. A larger value R_g indicates an extended entity, while a smaller value R_g indicates a more compact entity.

When performing the radius of gyration analysis on the single AuNP-SDS-H_2O system, stable behavior is observed throughout the simulation time. For the nucleus, Figure 4 (A) displays an average value of (1.1172 ± 0.0006) nm. This value indicates that the nucleus of the nanoparticle does not experience a sudden conformational change during its interaction with the aqueous medium. For the ligands, the reported average value is (2.01 ± 0.01) nm, which is greater than that of the nucleus. This indicates that the SDS surfactant is spread throughout the simulation when compared to the nucleus.

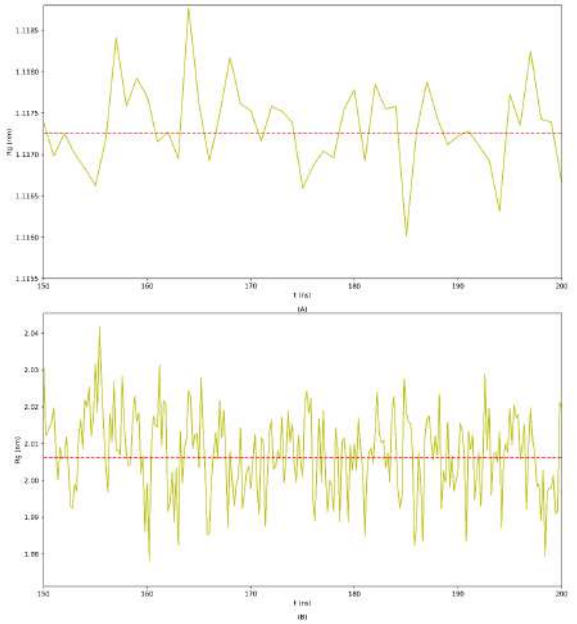

Figure 4. Values of the Rg for the nanoparticle nucleus (A) and ligands (B) throughout the simulation of the single AuNP-SDS in aqueous medium. The variation of the Rg is depicted in yellow, along with the average value of Rg shown in red.

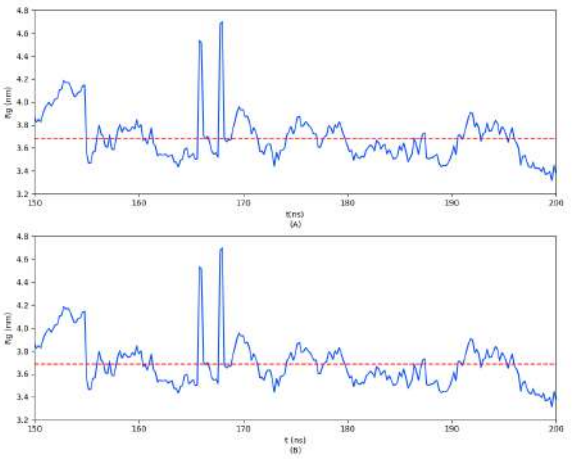

Figure 5. Values of Rg for the nanoparticle nucleus (A) and ligands (B) throughout the simulation of the three AuNPs-SDS in an aqueous medium. The variation of the Rg is depicted in blue, along with the average value of Rg shown in red.

Figure 5 displays the radius of gyration values for the nucleus and ligands in the three AuNPs-SDS systems. An average value of (3.7 ± 0.2) nm for the nucleus of the three AuNPs-SDS- H_2O systems is reported. In comparison to the overall simulation duration, a decreasing trend is evident in the last nanoseconds of the simulation. This is explained by observing the trajectory of the simulation, where, initially, the three nanoparticles are randomly positioned within the box. As the simulation progresses, they become compacted and draw closer to one another, ultimately resulting in a value below 3.4 nm. Comparing this result to the single AuNP nucleus, we observe an increase in the average value that exceeds even the Rg SDS analysis. However, stability is observable in the aqueous medium with low variability. This can be interpreted to mean that nanoparticles in an aqueous medium prefer to form conglomerates rather than remain separate from one another. This behavior could be useful for agglomerating a certain number of nanoparticles that facilitate the transport of particles in various context systems. For the SDS in the tree AuNPs system, the average value reported is (3.7 ± 0.2)nm. It is observed that, similar to the nucleus, the radius of gyration of the ligands for the three AuNPs-SDS systems decreases as the three nanoparticles come closer together throughout the simulation. No differences were observed in the Rg value when we compared the nucleus and SDS in the three AuNPs-SDS systems. Indicating that the three AuNP-SDS systems offer more flexibility compared to the single one.

3.6 Density profile

The density profile informs us about the local distribution of structures within the simulation

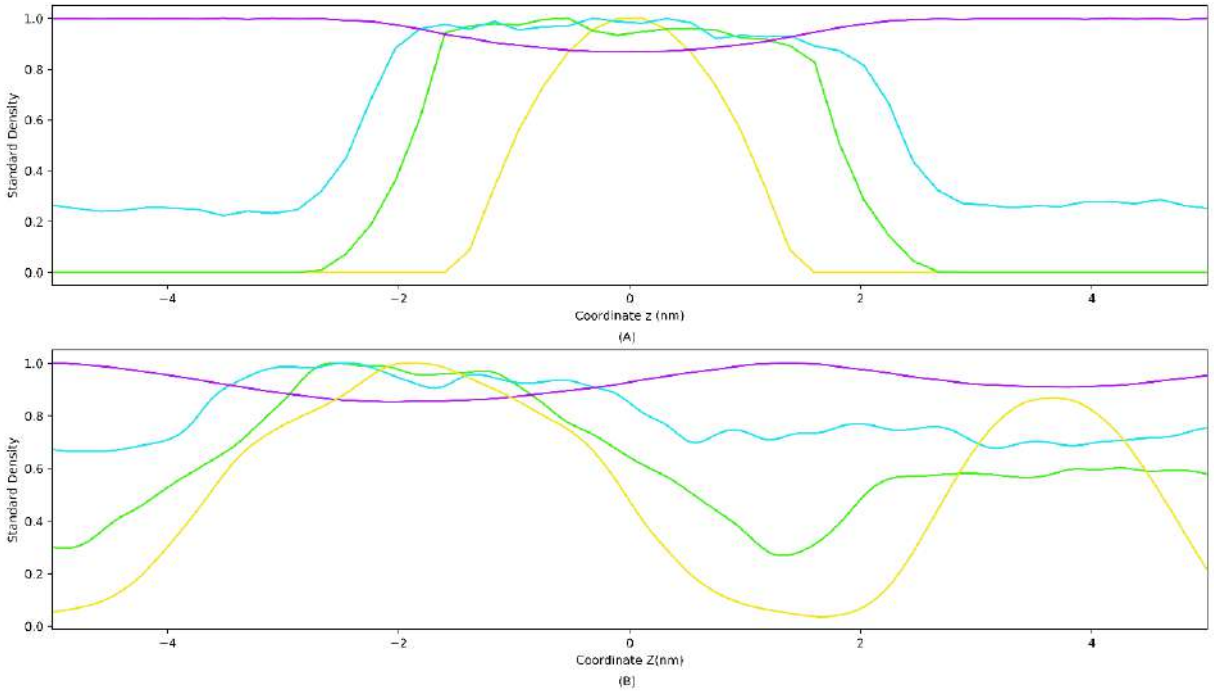

Figure 6. Density profile for one (A) and three (B) AuNPs-SDS systems in aqueous medium. Nucleus (yellow), water (purple), ion (blue), and SDS (green).

system. When analyzing the density profile for one AuNP-SDS-H_2O system and three AuNPs-SDS-H_2O systems, a distinction in the distribution of the components is visualized. The analysis involved standardizing all density values using the maximum value calculated in the simulation for each element: gold nucleus, SDS, ion, and water. Figure 6 shows that in the single AuNP-SDS-H_2O system, the ligands are located far from the nucleus, while the ion remains within the ligands, thus supporting the neutralization of the polar head. On the other hand, in the system with three AuNP-SDS, when three gold nuclei are present, there is a higher concentration of gold nanoparticle nuclei at distances between -4 and 0 nm. This indicates that two AuNPs-SDS are present on this side of the box, compared to the other AuNP-SDS located between 2 and 4 nm, where the presence of the SDS and ions has a slight separation. This suggests that the presence of more than two AuNPs-SDS in the same system modifies the interactions of ions, SDS, and water. The AuNP-SDS on the right side of the box is deeper in water than the others.

On the other hand, in the sections without AuNPs, we observe that sodium ions are dissolved in the water at a level comparable to that of the AuNP-SDS, which is situated slightly further away.

Conclusions

Through the study, CGMD was performed for a single and three AuNPs-SDS in an aqueous medium using MARTINI for 300 ns. Conducting analysis on Coulomb and van der Waals energy, diffusion, and structure. In the energy analysis, both systems showed an increase in energy with the rise in concentration, always accompanied by an attractive force. In the case of the Coulomb interaction between AuNPs and AuNPs, the concentrated system exhibited repulsion, which could be a factor to consider if the AuNP concentration increases considerably. These results indicate a trend that the AuNP-SDS CG model provides an acceptable framework for CG simulations alongside other structures. The diffusion analysis shows an increase in the diffusion coefficient with an increase in the AuNP-SDS numbers. The three AuNPs-SDS system display better diffusion in an aqueous medium than the single one, suggesting that introducing more nanoparticles forms a larger and more diffuse cluster. This property is desirable for substrates used to transport active ingredients. In the structural analysis, the RDF indicates that the ions, SDS, and AuNPs display the same structural order as the concentration increases. This suggests that the increase in concentration does not influence the organization of the beads in the SDS and that the AuNPs-SDS remain neutralized by sodium ions. The

Rg demonstrated a difference when we conducted the nucleus and the SDS for the single AuNP. As we anticipated, the Rg increased due to the flexibility of the ligands. However, no differences were observed among the three AuNPs regarding the nucleus and SDS; these last two exhibited the same Rg value. Therefore, regarding the stability of AuNPs, we conclude that both uncoated and coated particles interacting in an aqueous medium are stable and remain compact, highlighting their usefulness for particle transport in various study systems. The standard density reinforces the RDF analyses, where we can see the ions, SDS, and AuNP in a structural order. However, for the tree AuNPs system, we observe that one AuNP is slightly separated from the others. In this AuNP, the ion and the SDS were observed to be more separated from each other, suggesting that increasing concentration can change the way ions, SDS, and water interact in the same system. However, in this study, we can conclude that the three AuNP-SDS remain relatively close together instead of staying dispersed in the aqueous medium. The above opens a range of opportunities to design larger, organized structures that interact with one another or with other materials relevant to materials science.

Acknowledgements

The authors thank Diana J. Velásquez-Tinoco and Oscar V. Ortiz-Hernández for their time spent reading and offering comments on this work. Additionally, we would like to thank Alejandro J. Cuevas-Martínez for translating the draft article from Spanish to English.

References

Abraham, M. J., Murtola, T., Schulz, R., Páll, S., Smith, J. C., Hess, B., & Lindah, E. (2015). Gromacs: High performance molecular simulations through multi-level parallelism from laptops to supercomputers. *SoftwareX*, *1–2*, 19–25. https://doi.org/10.1016/j.softx.2015.06.001

Abu Samah, N. H., & Heard, C. M. (2014). The effects of topically applied polyNIPAM-based nanogels and their monomers on skin cyclooxygenase expression, ex vivo. *Nanotoxicology*, *8*(1), 100–106. https://doi.org/10.3109/17435390.2012.754511

Albaladejo, S., Marqués, M. I., Scheffold, F., & Sáenz, J. J. (2009). Giant enhanced diffusion of gold nanoparticles in optical vortex fields. *Nano Letters*, *9*(10), 3527–3531. https://doi.org/10.1021/nl901745a

Alexander, S. T. (1986). The Method of Steepest Descent. *Adaptive Signal Processing*, 46–67. https://doi.org/10.1007/978-1-4612-4978-8_4

Applications, I. (2017). *Unique Roles of Gold Nanoparticles in Drug Delivery, Targeting and Imaging Applications*. https://doi.org/10.3390/molecules22091445

Asish, Pal; Aasheesh, S. S., & Bhattacharya. (2009). Role of Capping Ligands on the Nanoparticles in the Modulation of Properties of a Hybrid Matrix of Nanoparticles in a 2D Film and in a. 9169–9182. https://doi.org/10.1002/chem.200900304

Baranowska-Korczyc, A., Stelmach, E., Paterczyk, B., Maksymiuk, K., & Michalska, A. (2019). Ultrasmall self-assembly poly (N-isopropylacrylamide-butyl acrylate) (polyNIPAM-BA) thermoresponsive nanoparticles. Journal of Colloid and Interface Science, 542, 317–324. https://doi.org/10.1016/j.jcis.2019.02.004

Barrak, H., Saied, T., Chevallier, P., Laroche, G., Mnif, A., & Hamzaoui, A. H. (2016). Synthesis, characterization, and functionalization of ZnO nanoparticles by N-(trimethoxysilylpropyl) ethylenediamine triacetic acid (TMSEDTA): Investigation of the interactions between Phloroglucinol and ZnO@TMSEDTA. Arabian Journal of Chemistry. https://doi.org/10.1016/j.arabjc.2016.04.019

Baoukina, S., Rozmanov, D., & Tieleman, D. P. (2017). Composition Fluctuations in Lipid Bilayers. *Biophysical Journal*, *113*(12), 2750–2761. https://doi.org/10.1016/j.bpj.2017.10.009

Berendsen, H. J. C. (1991). Transport Properties Computed by Linear Response through Weak Coupling to a Bath. *Computer Simulation in Materials Science*, 139–155. https://doi.org/10.1007/978-94-011-3546-7_7

Bordoni, G. P., & Colherinhas, G. (2022). On the influence of increasing the concentration of Au144(SRCOO1-)60 nanoparticles in water/Na1+ solution using molecular dynamics simulations. *Journal of Molecular Liquids*, *368*, 120776. https://doi.org/10.1016/J.MOLLIQ.2022.120776

Bussi, G., Donadio, D., & Parrinello, M. (2007). Canonical sampling through velocity rescaling. *Journal of Chemical Physics*, *126*(1). https://doi.org/10.1063/1.2408420

Deshmukh, S., Mooney, D. A., McDermott, T., Kulkarni, S., & Don MacElroy, J. M. (2009). Molecular modeling of thermo-responsive hydrogels: Observation of lower critical solution temperature. *Soft Matter*, *5*(7), 1514–1521. https://doi.org/10.1039/b816443f

Elahi, N., Kamali, M., & Baghersad, M. H. (2018). Recent biomedical applications of gold nanoparticles: A review. *Talanta*, *184*(February), 537–556. https://doi.org/10.1016/j.talanta.2018.02.088

Estrada-López, E. D., Murce, E., Franca, M. P. P., & Pimentel, A. S. (2017). Prednisolone adsorption on lung surfactant models: Insights on the formation of nanoaggregates, monolayer collapse and prednisolone spreading. *RSC Advances*, *7*(9), 5272–5281. https://doi.org/10.1039/c6ra28422a

Fitzgerald, G., Dejoannis, J., & Meunier, M. (2015). Multiscale modeling of nanomaterials. In *Modeling, Characterization and Production of Nanomaterials: Electronics, Photonics and Energy Applications*. Elsevier Ltd. https://doi.org/10.1016/B978-1-78242-228-0.00001-6

Franco-ulloa, S., Riccardi, L., Rimembrana, F., Grottin, E., Pini, M., & Vivo, M. De. (2022). *NanoModeler CG: A Tool for Modeling and Engineering Functional Nanoparticles at a Coarse-Grained Resolution*. https://doi.org/10.1021/acs.jctc.2c01029

Ganesh, M., Hemalatha, P., Peng, M. M., & Jang, H. T. (2013). One pot synthesized Li, Zr doped porous silica nanoparticles for low temperature CO 2 adsorption. ARABIAN JOURNAL OF CHEMISTRY, 2–6. https://doi.org/10.1016/j.arabjc.2013.04.031

Gupta, R., & Rai, B. (2017). Effect of Size and Surface Charge of Gold Nanoparticles on their Skin Permeability: A Molecular Dynamics Study. *Scientific Reports*, *7*(February), 1–13. https://doi.org/10.1038/srep45292

Harding, G., & Harding, A. (2007). *X-ray Diffraction Imaging for Explosives Detection*. *October 2006*, 199–235.

Hockney, R. W., Goel, S. P., & Eastwood, J. W. (1974). Quite high-resolution computer models of plasma. *Journal of Computational Physics*, *14*(2), 148–158. https://doi.org/10.1016/0021-9991(74)90010-2

Hu, X., Zhang, Y., Ding, T., Liu, J., & Zhao, H. (2020). *Multifunctional Gold Nanoparticles: A Novel Nanomaterial for Various Medical Applications and Biological Activities*. *8*(August), 1–17. https://doi.org/10.3389/fbioe.2020.00990

Joshi, S. Y., & Deshmukh, S. A. (2021). A review of advancements in coarse-grained molecular dynamics simulations. *Molecular Simulation*, *47*(10–11), 786–803. https://doi.org/10.1080/08927022.2020.1828583

Khan, I., Saeed, K., & Khan, I. (2019). Nanoparticles: Properties, applications, and toxicities. *Arabian Journal of Chemistry*, *12*(7), 908–931. https://doi.org/10.1016/j.arabjc.2017.05.011

Khan, I., Yamani, Z. H., & Qurashi, A. (2017). Ultrasonics Sonochemistry Sonochemical-driven ultrafast facile synthesis of SnO_2 nanoparticles: Growth mechanism structural electrical and hydrogen gas sensing properties. Ultrasonics - Sonochemistry, 34, 484–490. https://doi.org/10.1016/j.ultsonch.2016.06.025

Kmiecik, S., Gront, D., Kolinski, M., Wieteska, L., Dawid, A. E., & Kolinski, A. (2016). Coarse-Grained Protein Models and Their Applications. Chemical Reviews, 116(14), 7898–7936. https://doi.org/10.1021/acs.chemrev.6b00163

Lee, J. I. E. U. N., Lee, N., Kim, T., Kim, J., & Hyeon, T. (2011). Multifunctional Mesoporous Silica Nanocomposite Nanoparticles for Theranostic Applications. 44(10), 893–902

Lu, X., Zhu, T., Chen, C., & Liu, Y. (2014). Right or Left: The Role of Nanoparticles in Pulmonary Diseases. 17577–17600. https://doi.org/10.3390/ijms151017577

Mansha, M., Khan, I., Ullah, N., & Qurashi, A. (2017). Synthesis, characterization, and hydrogen evolution reaction of carbazole-containing conjugated polymers. International Journal of Hydrogen Energy, 1–10. https://doi.org/10.1016/j.ijhydene.2017.02.053

Marrink, S. J., Risselada, H. J., Yefimov, S., Tieleman, D. P., & De Vries, A. H. (2007). The MARTINI force field: Coarse grained model for biomolecular simulations. *Journal of Physical Chemistry B*, *111*(27), 7812–7824. https://doi.org/10.1021/jp071097f

Marrink, S. J., & Tieleman, D. P. (2013). Perspective on the martini model. *Chemical Society Reviews*, *42*(16), 6801–6822. https://doi.org/10.1039/c3cs60093a

Marrink, S. J., Vries, A. H. De, & Mark, A. E. (2004). *Coarse Grained Model for Semiquantitative Lipid Simulations*. 750–760.

Montoya-Villegas, K., Navarro-Félix, R. ., Rejón-Garcia, L., Silva-Carillo, C., Trujillo-Navarrete, B., Lin-Ho, S. ., & Reynoso-Soto, E. . (2020). Synthesis of Au-TiO_2 nanoparticles as sensors of 3-mercaptopropionic acid. *Revista Mexicana De Ingenieria Quimica*, *19*(941–952), 97–104.

Núñez-Delgado, C., Luna-Flores, A., Conde-Hernández, L. A., Flores-Aquino, E., Romero-López, A., & Tepale, N. (2023). Biosynthesis of gold nanoparticles using the aqueous extract of *Hippocratea excelsa* root bark. Antioxidant and photocatalytic evaluation. Revista Mexicana De Ingeniería Química, 22(IA2367).

Owen, D. M. (2014). Methods in membrane lipids: Second edition. *Methods in Membrane Lipids: Second Edition*, *1232*, 1–327. https://doi.org/10.1007/978-1-4939-1752-5

Pizzirusso, A., De Nicola, A., & Milano, G. (2016). MARTINI Coarse-Grained Model of Triton TX-100 in Pure DPPC Monolayer and Bilayer Interfaces. *Journal of Physical Chemistry B*, *120*(16), 3821–3832. https://doi.org/10.1021/acs.jpcb.6b00646

Pronk, S., Páll, S., Schulz, R., Larsson, P., Bjelkmar, P., Apostolov, R., Shirts, M. R., Smith, J. C., Kasson, P. M., Van Der Spoel, D., Hess, B., & Lindahl, E. (2013). GROMACS 4.5: A high-throughput and highly parallel open-source molecular simulation toolkit. *Bioinformatics*, *29*(7), 845–854. https://doi.org/10.1093/bioinformatics/btt055

Ramacharyuly, P.V.R.K; Muhammad, Raeesh; Kumar, Praveen J.; Prasad, G. K. (2015). Iron Phthalocyanine Modified Mesoporous Titania Nanoparticles for Photocatalytic Activity and CO_2 Capture Applications. https://doi.org/10.1039/C5CP03576G

Ramalingam, V. (2019). Multifunctionality of gold nanoparticles: Plausible and convincing properties. *Advances in Colloid and Interface Science*, *271*, 101989. https://doi.org/10.1016/j.cis.2019.101989

Rawal, I., & Kaur, A. (2013). Sensors and Actuators A: Physical Synthesis of mesoporous polypyrrole nanowires / nanoparticles for ammonia gas sensing application. Sensors & Actuators: A. Physical, 203, 92–102. https://doi.org/10.1016/j.sna.2013.08.023

Shaalan, M., Saleh, M., & El-mahdy, M. (2016). Recent progress in applications of nanoparticles in fish medicine: A review. Nanomedicine: Nanotechnology, Biology, and Medicine, 12(3), 701–710. https://doi.org/10.1016/j.nano.2015.11.005

Si, K. J., Chen, Y., Shi, Q., & Cheng, W. (2018). Nanoparticle Superlattices: The Roles of Soft Ligands. https://doi.org/10.1002/advs.201700179

Souza, L. M. P., Nascimento, J. B., Romeu, A. L., Estrada-López, E. D., & Pimentel, A. S. (2018). Penetration of antimicrobial peptides in a lung surfactant model. *Colloids and Surfaces B: Biointerfaces*, *167*, 345–353. https://doi.org/10.1016/J.COLSURFB.2018.04.030

Taylor, P., Gunsteren, W. F. Van, & Berendsen, H. J. C. (2007). *A Leap-frog Algorithm for Stochastic Dynamics A LEAP-FROG ALGORITHM FOR STOCHASTIC DYNAMICS*. *May 2013*, 37–41.

Vaisey, G., Banerjee, P., North, A. J., Haselwandter, C. A., & Mackinnon, R. (2022). Piezo1 as a force-through-membrane sensor in red blood cells. *ELife*, *11*, 1–21. https://doi.org/10.7554/ELIFE.82621

Velasco-Rodríguez, V., Cornejo-Mazon, M., Flores-Flores, J. O., Gutierrez-Lopez, G. F., & Hernandez-Sanchez, H. (2012). Preparation and properties of alpha-lipoic acid-loaded chitosan nanoparticles. Revista Mexicana De Ingenieria Química, 11(1), 155–161.

Wassenaar, T. A., Ingólfsson, H. I., Böckmann, R. A., Tieleman, D. P., & Marrink, S. J. (2015). *Computational lipidomics with insane: a versatile tool for generating custom membranes for molecular simulations*. https://doi.org/10.1021/acs.jctc.5b00209

Wong, K., Chen, C., Wei, K., Roy, V. A. L., & Chathoth, S. M. (2015). Diffusion of gold nanoparticles in toluene and water as seen by dynamic light scattering. *Journal of Nanoparticle Research*, *17*(3). https://doi.org/10.1007/s11051-015-2965-x

Zimbone, M., Calcagno, L., Messina, G., Baeri, P., & Compagnini, G. (2011). Dynamic light scattering and UV-vis spectroscopy of gold nanoparticles solution. *Materials Letters*, *65*(19–20), 2906–2909. https://doi.org/10.1016/j.matlet.2011.06.054

Vol. 24, No. 2(2025) Mat25509
Revista Mexicana de Ingeniería Química

Synthesis of zinc ferrite ($ZnFe_2O_4$) by mechanical grinding and calcination with a magnetite/maghemite precursor obtained by coprecipitation, its influence on crystalline, morphological and thermal properties, for its potential use at high temperatures.

Síntesis de ferrita de zinc ($ZnFe_2O_4$) mediante molienda mecánica y calcinación con un precursor de magnetita/maghemita obtenido por coprecipitación, su influencia en las propiedades cristalinas, morfológicas y térmicas, para su potencial uso a altas temperaturas.

E.M. García-Rosales[1], M. G. Rosales-Sosa[2]*,I. A. Facundo-Arzola[2], M. García-Yregoi[2], C. V. Reyes-Guzmán[2], Y.M. Rangel-Hernández[2], B. I. Rosales-Sosa[2]

[1]*Facultad de Ciencias Químicas, Universidad Autónoma de Coahuila, Boulevard Venustiano Carranza 935, República, Saltillo, C.P. 25280, México.*

[2]*Facultad de Metalurgia, Universidad Autónoma de Coahuila, Boulevard Pape km. 4.5, zona universitaria, C.P. 25750, Monclova Coahuila, México.*

Sent date: January 21, 2025; Accepted: May 15, 2025

Abstract

Magnetite/maghemite produced by chemical coprecipitation at different temperatures was reacted with reagent-grade zinc oxide to produce zinc ferrite ($ZnFe_2O_4$) by mechanical grinding. After grinding, calcination was applied at 400 °C for 3 hours. The obtained samples were characterized by X-ray diffraction (XRD), scanning electron microscopy (SEM), thermogravimetric analysis (TGA), and differential scanning calorimetry (DSC). After grinding treatment, three-phase combinations were observed of the same ferrite, which had not been reported previously and which were stabilized by the application of a calcination treatment. The crystallite sizes of the zinc ferrite ($ZnFe_2O_4$) compound ranged from 10.602 nm to 11.602 nm. Particle agglomerations were found by SEM, while TGA analysis shows possible moisture loss, in addition to stability at high temperatures. DSC analysis shows endothermic and exothermic reactions. The best results were obtained with magnetite/maghemite stabilized at 300 °C.

Keywords: mechanical milling, zinc ferrite, coprecipitation, magnetite/maghemite, calcination.

Resumen

La magnetita/maghemita producida por coprecipitación química a diferentes temperaturas, se hizo reaccionar con óxido de zinc grado reactivo para producir ferrita de zinc ($ZnFe_2O_4$) mediante molienda mecánica. Luego de la molienda, se aplicó calcinación a 400 °C durante 3 horas. Las muestras obtenidas se caracterizaron por difracción de rayos X (DRX), microscopía electrónica de barrido (MEB), análisis termogravimétrico (TGA) y calorimetría diferencial de barrido (DSC). Luego del tratamiento de molienda, se observaron combinaciones trifásicas de la misma ferrita, lo cual no había sido reportado previamente y que se estabilizaron con la aplicación de un tratamiento de calcinación. Los tamaños de cristalita del compuesto de ferrita de zinc ($ZnFe_2O_4$) variaron de 10.602 nm a 11.602 nm. Se encontraron aglomeraciones de partículas por medio de MEB, mientras que el análisis TGA muestra una posible pérdida de humedad, además de estabilidad a altas temperaturas. DSC muestra reacciones endotérmicas y exotérmicas. Los mejores resultados se obtuvieron con magnetita/maghemita estabilizada a 300 °C.

Palabras clave: molienda mecánica, ferrita de zinc, coprecipitación, magnetita/maghemita, calcinación.

*Corresponding author. *E-mail*: mrosales@uadec.edu.mx ;
https://doi.org/10.24275/rmiq/Mat25509
ISSN:1665-2738, *issn-e*: 2395-8472

1 Introduction

Zinc ferrite ($ZnFe_2O_4$) is a magnetic ceramic material that has been studied since the 1950s. Its magnetic properties are of great research interest because of their potential multiple applications. The uses of zinc ferrite are highly varied and include microwave devices, recording media, devices used at high frequencies, biomedical devices, and permanent and temporary magnets (Baena *et al*., 2011).

Iron oxide with the oxides of one or more other metals combine to form ferrite, not all ferrites develop spinel structure, but many do. While bulk zinc ferrites are paramagnetic at ambient temperature, nano-crystalline zinc ferrites can be ferrimagnetic at the same temperature. Its structural formula is $(ZnFe)_x[ZnFe]_{2-x}O_4$, in which the coordination sites marked by the parentheses represent Tetrahedron A, the brackets represent Octahedron B, and x represents the degree of inversion, which is defined as the fraction of the A sites occupied by Fe^{3+}. One of the precursors of the zinc ferrite compound may be Fe_2O_3 (maghemite), which can be obtained by chemical coprecipitation, which, as an easily scalable process, enables the industrial use of zinc ferrite for the manufacture of iron oxide nanoparticles. Chemical coprecipitation consists of adding Fe^{2+} salt and Fe^{3+} solutions to an excess basic medium. The advantages of this method are its simplicity and low cost, while the disadvantage is the high number of uncontrolled variables and the wide distribution of particle sizes (Baena *et al*., 2011). Various methods are used to obtain zinc ferrite, such as the ceramic method, sol-gel synthesis, chemical coprecipitation, the hydrothermal method, and microemulsion. In recent times, alternative synthesis methods have been explored in search of a more economical, faster, and purer process, one of which alternatives is mechanical milling, which presents the above-described advantages.

Synthesis by mechanical milling is defined as the chemical reaction induced by the direct absorption of mechanical energy (James *et al*., 2012). Mechanical energy is produced by the combination of impact, shear, and friction forces that activate the surface and produce defects in the network, radicals on the surface, and even break bonds, causing the activation and chemical reaction of the mixed powders (Fuentes *et al*., 2013). The interaction of forces during milling generates local temperatures and pressures at the points where collisions occur, which are believed to reach up to 10,000 K and 17 GPa. This, in turn, promotes a local fusion phenomenon that induces the dissolution of chemical species of immiscible elements, consequently inducing the formation of alloys that cannot be synthesized by other techniques (Baláž *et al*., 2009). Over the last few decades, mechanical milling has developed from an elementary method used primarily for particle size reduction in mineral processes to a potent technique for the preparation of materials with improved mechanical and physical properties, and new phases and engineering materials (El-Eskandarany *et al*., 2021).

Koch (1983) observed that mechanical milling induces the amorphization of the material when he subjected Ni and Nb powders to high-energy grinding. Since then, research has continued, with the combination of coprecipitation and mechanical milling reported by various authors for the preparation of both ferrites and nanoferrites. Ding *et al*. (1999) used a combination of both methods to produce $BaFe_{12}O_{19}$, $CoFeO_4$, and $NiFeO_4$, while Shi *et al*. (1999) produced $NiFe_2O_4$ and Shenoy *et al*. (2004) manufactured $ZnFe_2O_4$ via similar processes. Sheikhi *et al*. (2006) produced $BaFe_{12}O_{19}$. All of the authors mentioned above emphasize the possibility of obtaining ferrites by combining coprecipitation and mechanical milling. Sani *et al*. (2007) synthesized $CoFe_2O_4$ using only mechanical milling and in the same year, Rao *et al*. (2007), compared the separate use of coprecipitation and mechanical milling to obtain various ferrites of (Ni-Zn-In-Ti), (Ni-Zn), and (Mn-Zn). Zhigang *et al*. (2015) synthesized nickel ferrite nanoparticles ($NiFe_2O_4$) achieving a solid-state reaction through milling. The technique is considered a simple and effective synthesis method for $NiFe_2O_4$ and other nanomaterials. Pedrosa *et al*. (2016) reported the use of mechanical grinding for the synthesis of the ferrite $CoFe_2O_4$, while Sarkar *et al*. (2019) prepared the $Co_{0.5}Zn_{0.5}O_4$ nanoferrite by applying a combination of coprecipitation and various thermal treatments in addition to mechanical milling.

Mahdikhah *et al*. (2019) produced the ferrite $CoFe_2O_4$ via mechanical milling and Cobos *et al*. (2020) compared various ferrite synthesis methods, including mechanical grinding, for manufacturing $ZnFe_2O_4$. Navipour *et al*. (2020) investigated the sole use of mechanical grinding to manufacture $ZnFe_2O_4$, while Sukmarani *et al*. (2020) synthesized $MnFe_2O_4$ and Moravvej-Farshi *et al*. (2020) manufactured Ni-Zn ferrites, both using the same technique. Younes *et al*., (2021) synthesized $CuFeO_4$ via mechanical milling and Tomiczek *et al*., (2021) produced the ferrite $CoFe_2O_4$. Hejazi *et al*. (2024) produced $ZnFe_2O_4$ ferrites using the separate application of coprecipitation and mechanical milling, investigating the effects of each method on crystallinity, purity, and particle size distribution. A recent study, reported by Leal *et al*. (2024) investigated the production of ZnO, which can be a precursor to zinc ferrite. The study sought to produce ZnO nanoparticles using ion exchange and thermal treatments, which, although at different temperatures, were also used in the present study. According to a review by Bhattu *et al*. (2024), zinc ferrites have a variety of production methods

and intriguing applications. Characteristics such as crystallite size, doping, and manufacturing process influence their use in biological applications, sensors, magnetic data storage, and catalysis. Garg *et al.* (2024) mentioned, zinc ferrite ($ZnFe_2O_4$) nanoparticles are considered to be non-toxic and to have better drug delivery properties than other nanoparticles. Wider uses of $ZnFe_2O_4$ nanoparticles for the treatment of infectious illnesses and cancer have been documented in several research. The reduction of both organic and inorganic environmental contaminants is another advantage of these nanoparticles. Additionally, their environmental and biological uses have been extensively studied. Similarly, studies of ZnO (ferrite precursor) and its nanostructures have received recent attention for potential use in environmental applications such as solar cells (Garcia *et al*., 2024).

The present study sought to combine mechanical milling and the chemical coprecipitation of magnetite to synthesize a $ZnFe_2O_4$ ferrite, aiming to ascertain the behavior of ferrite synthesis when applied with both one precursor obtained via coprecipitation and another that was reagent grade. All this is done in the interest of the various potential applications discussed in the introduction.

2 Materials and methods

The methodology reported by previous studies was used for the present study. The technique reported by Zhang *et al*. (2009) was used for the synthesis of magnetite, wherein $FeCl_3{\cdot}6H_2O$ and $FeCl_2{\cdot}4H_2O$ (2:1 ratio) were mixed in 50 mL of deionized water, while 150 ml of deionized water was placed in a ball flask and heated to 50 ºC with constant stirring. 50 ml of concentrated ammonium hydroxide was then added in order to provide a basic medium for the solution. The precursors were used to obtain the highest possible purity of the desired compound.

The iron chloride mixture was added drop by drop to the basic solution and subjected to constant stirring for 30 minutes, after the elapse of which, the precipitate was washed with 2 liters of deionized water to eliminate excess chlorides and left to dry at room temperature for three days. Finally, the product obtained was washed with 1 liter deionized water and 250 ml ethanol and left to dry at room temperature. The quantity of magnetite obtained was divided into five parts and heated at 100 °C (T1), 200 °C (T2), 250 °C(T3), 300 °C(T4), and 350 °C (T5), with a residence time of 3 hours. Once heating had been completed, the samples were left to slowly cool inside the oven, to ensure greater crystallinity.

2.1 Mechanical milling and calcination

The preparation of zinc ferrite used two powders obtained from the precursor oxides ZnO (reagent grade 99.8% pure, SkySpring Nanomaterials) nanometric zinc oxide (9–20 nm) and magnetite obtained via chemical coprecipitation.

At a 1:1 ratio, the powders were mixed, placed in a 25-ml stainless steel vial, and then placed in a RETSCH mill to apply the milling process. A 2:1 ball-material ratio was used for the milling, which was conducted at a frequency of 20 cycles per second (1200 rpm) for five hours for all samples. Dry grinding was used, without any type of additive or binder. Once the milling treatment had been completed, calcination was conducted in a Witeg brand muffle (capacity of 1200 °C) on all samples at 400 °C for three hours to stabilize the metastable phases that had formed during the mechanical milling process. The smallest crystallite sample was then characterized via scanning electron microscopy (SEM), thermogravimetric analysis (TGA), and differential scanning calorimetry (DSC).

2.2 X-ray diffraction (XRD)

This technique was applied to identify the ferrite phases and determine crystallite size, using a Bruker D8 Advance X-ray diffractometer, with a scanning range of 10 to 80° on the 2θ scale and a scanning speed of 0.01°/s. For Co-Kα type radiation, the conditions of operation were 40 mA and 40 kV, while the Match 1.1 diffraction software was used to achieve sample identification.

2.2.1 Crystallite size (Debye Scherrer equation)

To achieve correct measurements of the crystallite size, the results of the XRD analyses were used with the help of the Origin 2019 (b) software together with the peak analyzer (using the longest peak as a reference) and the Gauss mathematical function included in the software. Based on the data obtained, the Debye Scherrer equation (Eq.1) was used, where each variable means the following:

$$L = \frac{0.9 \times \lambda_{a1}}{\beta_{2\theta} \times \cos\theta_{\max}} \tag{1}$$

- L: the crystallite size
- λ_{a1}: the wavelength of the X-ray source implemented using Co-Kα (λ_{a1} = 1.54056 Å)
- $\theta_{\max}$: the value of the angle at 2θ for reflection (311)
- $\beta_{2\theta}$: the amplitude, at half the height of the peak, for this reflection

2.3 Scanning electron microscopy (SEM)

The measurement of the magnetite level after chemical coprecipitation used a JEOL 6010 Plus scanning electron microscope with a resolution of up to 4.0 nm (at 20 kV), magnification from 8X to 300,000X, acceleration voltages from 500V to 20kV, and the secondary and backscattered electron imaging mode.

The SEM technique was used to determine the morphology, structure, and particle size. A microscope with the Hitachi cold cathode technique, model SU8230, was used. The sample was fastened to the sample holder using carbon tape. The images were taken by applying a 6 kV and 5 μA energy level at a working distance of 2.2 nm.

2.3.1 Particle size measurement using SEM image

The public domain ImageJ 1.54g software was used to measure particle size distribution. An area of the image was selected, and particle quantification and size measurements were performed using the software's measurement functions, taking 500 nm as the standard. The particles were measured according to the researchers' interpretation, taking into account their feasible delimitation.

2.4 Thermogravimetric analysis (TGA)

Thermogravimetric analysis was used to ascertain both how the samples behave at high temperatures and their thermal stability, using, for the gas, atmospheric air with a temperature range of 30°C to 800°C at a heating rate of 10°C/min. The equipment used was a DISCOVERY Series model manufactured by the TA Instruments.

2.5 Differential scanning calorimetry analysis (DSC)

The gas used for the DSC analysis was atmospheric air, while heating, cooling and heating cycles were applied in a temperature range of 30 to 500 °C, with a heating rate of 5 °C/min. The equipment used was a DISCOVERY Series model manufactured by the TA Instruments.

3 Results and discussion

3.1 Chemical coprecipitation of magnetite and crystallography

Based on previous studies (Park *et al*., 2001; Gnanaprakash *et al*., 2007) the following chemical equations are adapted according to the possible growth and nucleation of the ferrites in the present study. The iron II and III salts were mixed in an aqueous medium, immediately taking on an orange-yellowish hue, and then poured drop by drop into the basic medium, which was kept at a constant temperature of 70 °C and a pH of 14 and was subject to constant stirring. The Fe^{3+}/Fe^{2+} iron salt solution changed color when added to ammonium hydroxide, along with the formation of a black precipitate, which is the characteristic color of magnetite. This precipitate (iron oxide) is sensitive to magnetic fields (magnetite phase). Ammonium hydroxide was used as a precipitating agent due to its high solubility and alkaline conditions (pH > 11), presenting due to the formation of OH^- (Eq. 2):

$$NH_3 + H_2O \longrightarrow NH^+ + OH^- \quad (2)$$

This base generates OH^- ions slowly, enabling homogeneous nucleation with the formation of iron oxo-hydroxides, thus preventing the aggregation of disordered clusters and, therefore, controlling the reaction rate. With a pH of between 8 and 14, the reaction given in Equation 3 could have occurred during this process:

$$Fe^{2+} + 2Fe^{3+} + OH^- \longrightarrow Fe_3O_4 + 4H_2O \quad (3)$$

Three regimes of particle generation are applied during the precipitation process: the induction period, in which solid building units are formed (still in solution); the nucleation period, in which nucleation occurs when the concentration of building units reaches the saturation level; and the growth phase, which occurs after the nucleation period and until the reacting species in the solution reach equilibrium.

Once the nucleus generated attains the critical radius (R), it remains stable and continues with its subsequent growth, while particles with a radius of less than R will dissolve in the reaction medium. It can be said that, given a certain concentration of reactants, a maximum number of nuclei will be formed if the reaction is given sufficient time for stable nuclei to form.

At short reaction times, a low number of stable nuclei are generated, as the residence time of the nuclei in the mother liquor is likely to be very short, meaning that, at low reaction times, the particle yield will be low. Increasing the reaction time should have a positive effect on the yield, as more stable nanoparticles may be generated. However, this may not be true if a range of reaction times is applied, as secondary processes, such as Ostwald ripening, may dominate, causing larger particles to grow at the expense of smaller particles, which could adversely affect the reaction yield (Thanh *et al*., 2014).

According to stoichiometry, the reaction yield is that for every 2 moles of Fe^{+3}, one mole of magnetite Fe_3O_4 is produced. The theoretical amount of magnetite produced was 10.59 g, and an actual 9.4 g was obtained at the time of synthesis, giving a

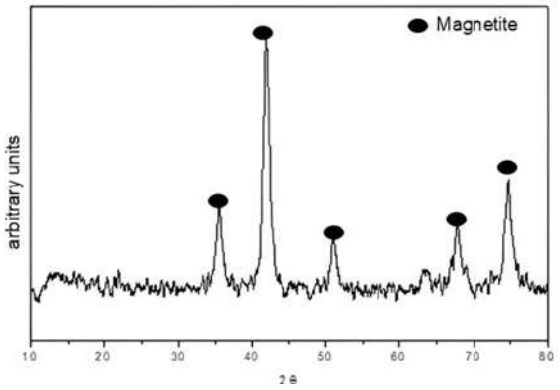

Figure 1. Diffractogram of the magnetite sample obtained via coprecipitation.

reaction yield of 88.79%. The diffractogram for the synthesis of magnetite, reveals that the highest peak corresponds to the magnetite phase (Figure 1).

The phase obtained is consistent with the findings of Aliramajia *et al*. (2015), who synthesized magnetite by means of the sonochemical method. This phase was found at 2θ angles of 21, 35, 41, 50, 63, 67, and 75, with their corresponding reflection planes of (111), (220), (311), (400), (422), (511), (440), thus indicating that it is a magnetite compound with a cubic spinel crystalline structure. Measured with the Debye-Scherrer formula, the particle size of the magnetite phase was 9.790 nm.

3.2 Calcination of magnetite and crystallography

After thermal treatments of 100, 200, 250, 300, and 350 °C were applied to the maghemite samples, they presented a change in color from black (magnetite) to different shades of red-brown (maghemite). Further evidence of the aforementioned color change is observed in Figure 2, section a) where after synthesis by coprecipitation, a black color is obtained, and after the application of heat treatment it changes to a red-brown color (section b) (Castaño *et al*., 1998). According to the literature (Teja *et al*., 2009), the magnetic behavior of the iron oxide structure varies from hematite (α-Fe_2O_3), maghemite (γ-Fe_2O_3), and magnetite (Fe_3O_4) and depends on the synthesis conditions. This, therefore, confirms that the magnetite changes to the maghemite structure, as observed in the present study, occur due to the thermal treatments applied.

The diffractograms of the maghemite samples, when heated to 100, 200, 250, 300, and 350 °C, were compared to the diffraction patterns and found to be of the crystallographic phases of maghemite (Figure 3).

Table 1 shows variations ranging from 21.077-9.751 nm. A correlation is observed, in which increasing the temperature results in a reduction in particle size, behavior which could be explained by an increase in crystallinity during calcination treatment. It is un-known whether increasing the temperature further would result in a greater reduction in particle size. Contrary to what was expected, the crystallite size decreases as the temperature increases, but this is possible and already reported by Méndez and collaborators in 2019, when an increase in the calcination temperature led to a smaller crystallite size.

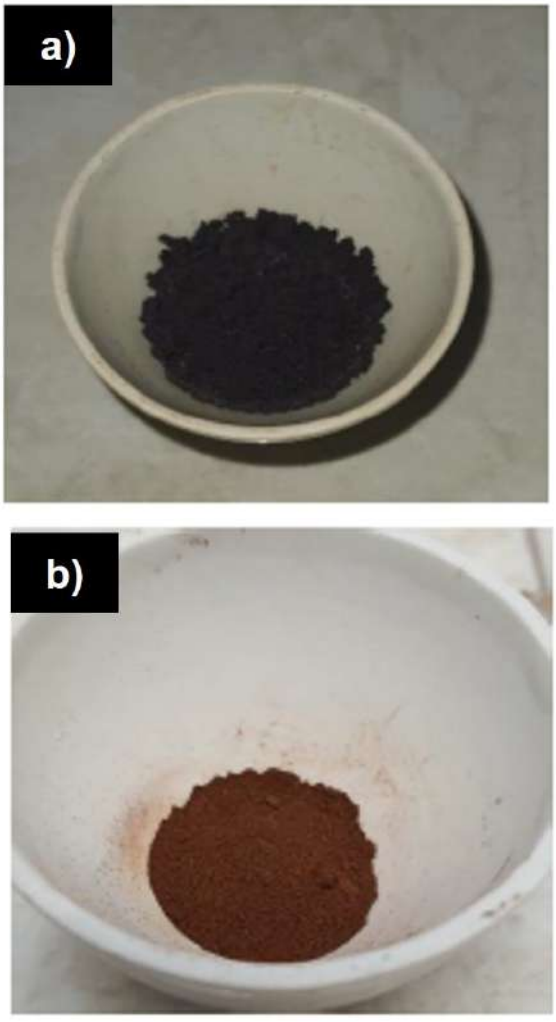

Figure 2. Change from a) magnetite to b) maghemite after calcination.

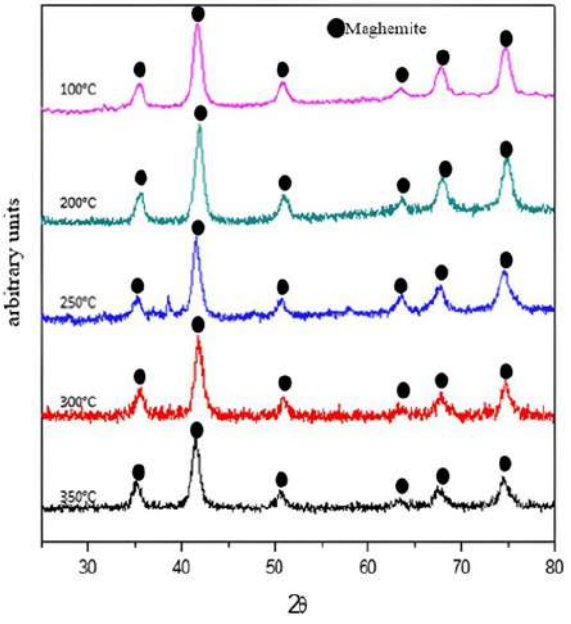

Figure 3. Diffractogram of maghemite samples heat treated at 100, 200, 250, 300, and 350 °C.

Table 1. Particle size variation of maghemite

Maghemite Sample	Heat treatment (°C)	Particle size (nm)
T1	100	21.077
T2	200	10.954
T3	250	10.7448
T4	300	10.433
T5	350	9.751

3.3 Crystallography of ferrite synthesis via mechanical milling

Figure 4 shows the diffractograms corresponding to the reactions observed after five hours of the mechanical grinding of maghemite and reagent grade zinc oxide, with the corresponding powders prepared in stoichiometric proportions, in accordance with Equation 4

$$Fe_2O_3 + ZnO \longrightarrow ZnFe_2O_4 \quad (4)$$

The presence of three phases is observed at the highest intensity peaks, which are very close to each other. The first peak, located at angle 41.71 in scale 2θ, indicates the presence of the franklinite phase (Zhang *et al*., 2008). The zincite phase is identified at angle 42 in scale 2θ (Verwey *et al*., 1947) while the last in this combination of phases, the maghemite phase, is identified at angle 42.5 2θ (Wyckoff, 1963). At this point, the measurement of particle size using the Debye-Scherrer equation and the Origin 2019 (b) software became difficult because a main peak could not be defined, due to the three-phase combination. This triphasic combination, about which abundant information is not available in the literature, was not expected. A possible explanation is that, as the franklinite crystalline phase is just beginning to form and the zinc oxide and oxide phases still contain iron (maghemite), the phase in question cannot be identified with certainty because the phases are mixed.

From the foregoing findings, it can also be considered that, as occurs in solid systems, the equilibrium state has not been completely reached and that additional energy is required to reach the equilibrium phases as, in this case, there are mixed phase peaks. The compounds could be considered, at this point in the mixing of the phases, to be in a state of non-equilibrium and, thus, corresponding to intermediate phases. While this combination of phases may also indicate the presence of crystallinity, inclusions of different elements in a semi-defined crystalline network were observed. It would be expected that more milling time could rearrange the atoms completely to achieve a totally defined phase or structure. As the coexistence of the zincite, maghemite, and franklinite phases is observed at the most intense peaks, a thermal treatment was conducted at 400 °C, giving a residence time of three hours. The result of the thermal treatment is shown in the diffractograms presented in Figure 5. The samples were left to cool inside the oven to achieve greater crystallinity. The temperature applied, 400 °C, was able to generate sufficient activation energy to transform the maghemite and zinc oxide into the crystalline $ZnFe_2O_4$ structure, and to obtain a completely defined crystalline structure, as some had already been transformed during the mechanical grinding process. The atoms are able to migrate to the equilibrium positions corresponding to the zinc-ferrite phase. The crystal structure corresponds to space group number Fd3m (Oh7), indicating that they present the spinel phase crystal structure. The lattice parameters observed were a = 8.4411Å (Tehranian *et al*., 2019).

In contrast to other authors, who used a combination of coprecipitation and mechanical milling (Ding *et al*., 2000; Shi *et al*., 1999; Shenoy *et al*., 2004) the present study did not use a combination of two types of precursors, namely one obtained via coprecipitation and one reactive grade. The type of synthesis applied could give rise to different results, such as the interphases reported previously.

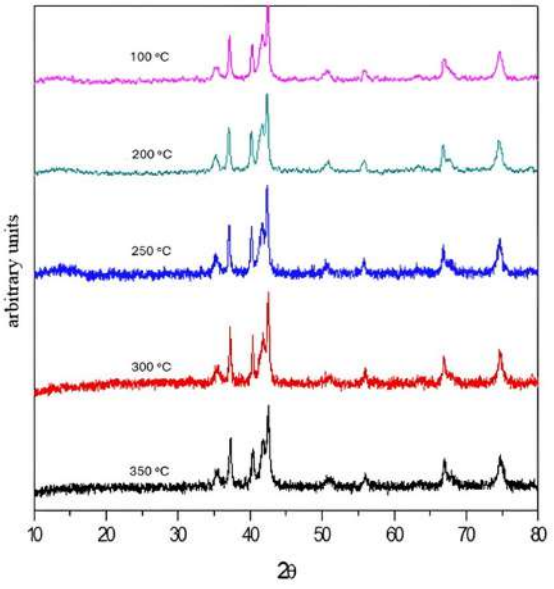

Figure 4. Diffractogram obtained for the maghemite Fe_2O_3 samples (obtained from magnetite at 100, 200, 250, 300, and 350 °C) with ZnO reacted by mechanical grinding for five hours.

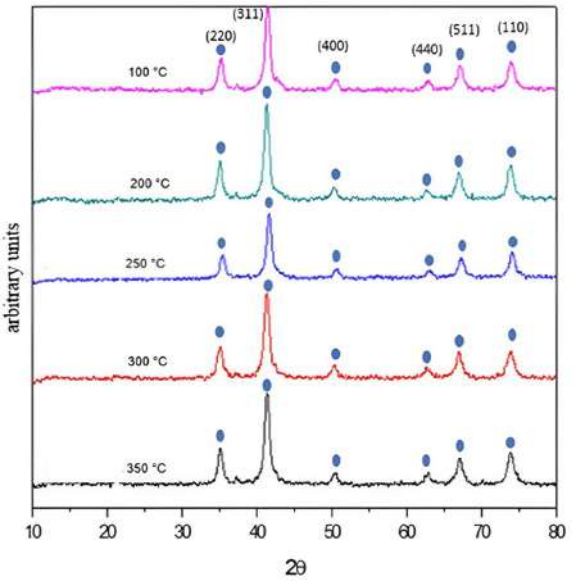

Figure 5. Diffractogram of the maghemite plus zinc oxide samples, subjected to mechanical grinding for five hours and a heat treatment at 400ºC for three hours.

Table 2. Particle size variation.

Maghemite (Fe_2O_3) obtained at:	Time, in hours, of maghemite grinding treatment (Fe_2O_3) + ZnO.	Heat treatment of maghemite (Fe_2O_3) at 400 ºC + ZnO grinding mixture	Particle size (nm)
No treatment	No treatment	No treatment	9.790
100 °C	5	3	11.602
200 °C	5	3	11.421
250 °C	5	3	11.544
300°C	5	3	10.602
350°C	5	3	11.473

Those other authors who have synthesized the $ZnFe_2O_4$ ferrite via milling only (Shenoy *et al*., 2004; Cobos *et al*., 2020; Navidpour *et al*., 2020) also did not report metaphase formation, which could be attributable to the precursors, but also confirmed that calcination treatments can be effective for the stabilization of the phases described here. Table 2 shows that the particle size of the ferrite ranges from 10.602 nm to 11.602 nm, while the maghemite particle obtained at 300 °C was found to be the smallest. However, no considerable variation in particle sizes was observed among all the samples synthesized.

The present study found that mechanical milling had a great influence on the formation of zinc ferrite after the mixtures had been milled for five hours. The mechano-chemical activation occurring during the grinding stage provided sufficient mechanical energy to initiate the solid-state reaction, which can accumulate during the plastic deformation of the crystals and the generation of their surfaces, thus producing regions of special chemical reactivity that facilitate the development of the solid phase processes. According to Takacs (1998), under the system and activation conditions of interest, solid phase reaction can occur during mechanical treatment at room temperature. However, as the grinding times applied during the present study were insufficient to complete the reaction, a heat treatment must be applied at relatively low temperatures to complete the reaction and form the zinc ferrite.

In many reactions, depending on the nature of the precursors involved, the temperature increases and results in the decomposition of both the reactants and the products themselves, requiring long reaction times that reduce the advantages of the method, thus leading studies to resort to synthesis techniques which use a solvent. No solvent was used in the present study, which is considered an advantage because it makes the process more efficient without affecting the quality of the compound obtained.

In general, these mechanical milling processes can be said to change the structure according to the movement of the cations, which, when displaced, distorts the cubic structure of the initial oxides, giving rise to new compounds. In the present study, this dynamic gave rise, albeit partially, to an arrangement corresponding to the $ZnFe_2O_4$ spinel-type structure.

3.4 Morphological analysis of maghemite obtained by chemical coprecipitation and calcination

The 150,000 X micrograph of maghemite calcined at 300 °C (T4) (Figure 6) enables better observation of the spherical shape of the particles that tend to form branched agglomerations, the sizes of which range from 10.2, 13.8, and 14.6 nm. These agglomerations may occur due to the method of chemical coprecipitation applied and any potential magnetic tendency of the synthesized compounds.

3.5 Morphological analysis of zinc ferrite obtained by mechanical milling

The micrograph of sample T4 shows agglomerates with irregular zinc ferrite particle shapes, an agglomeration that may be due to the mechanical grinding and/or the magnetic nature of the material. In other regions, agglomerates with diffuse sharpness are observed (Figure 7).

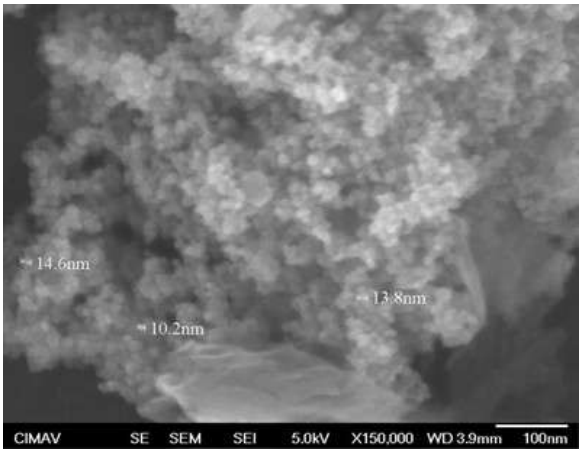

Figure 6. Morphology, at 150,000 X, of maghemite, as obtained by coprecipitation and thermal treatment at 300ºC for three hours (T4).

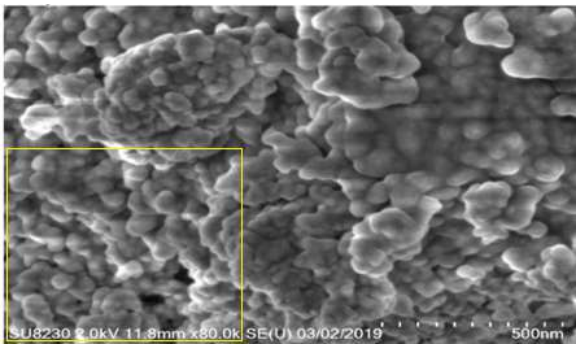

Figure 7. T4 morphological mapping (yellow rectangle area analyzed).

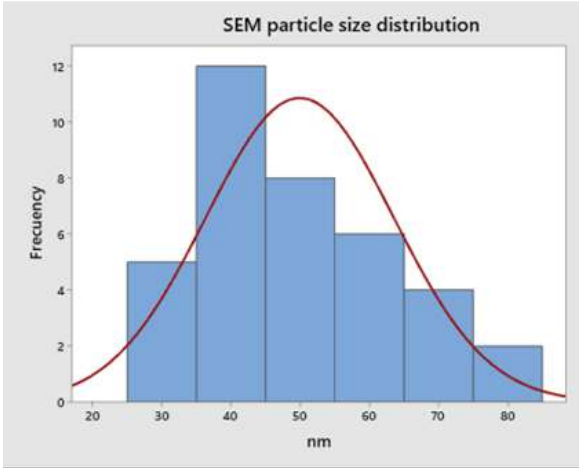

Figure 8. SEM particle size histogram.

Figure 8 shows a histogram of the particle size analyzed based on the image obtained by SEM. The yellow rectangle (Figure 7) was analyzed, and various particle sizes were found, ranging from 30 nm, 40 nm, 50 nm, 60 nm, 70 nm and 80 nm, with an average particle size of 49.93 nm, following an almost standard distribution.

Differences in particle size were found between the maghemite obtained by chemical coprecipitation and calcination and the zinc ferrite obtained by mechanical milling. This difference could be due to a greater agglomeration of particles and the methods used for their synthesis.

3.6 Thermal analyses (TGA and DSC)

As shown in Figure 9, the TGA analysis conducted on T4 shows a high level of physical and thermal stability because the material only lost 4.5% of mass, presenting small losses at 150 °C and 600 °C-700 °C. In other studies, such as that of Vidales *et al*. (1999), their materials lost around 20% of mass in some TGA tests under relatively similar conditions. The effects of the loss of mass could have occurred due to a certain degree of potential humidity in a precursor especially maghemite, as it had undergone coprecipitation in an aqueous solution.

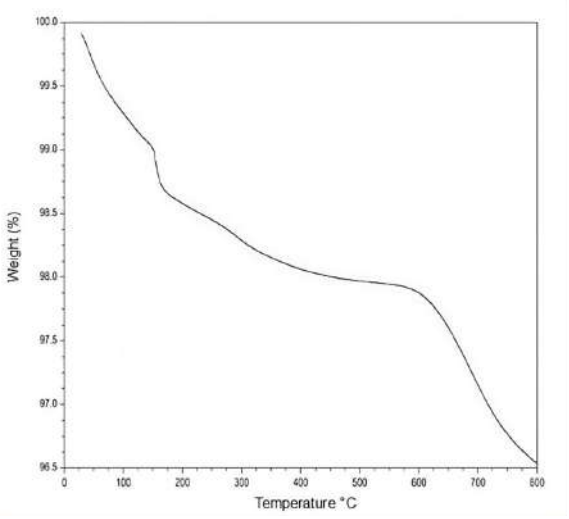

Figure 9. TGA analysis of T4.

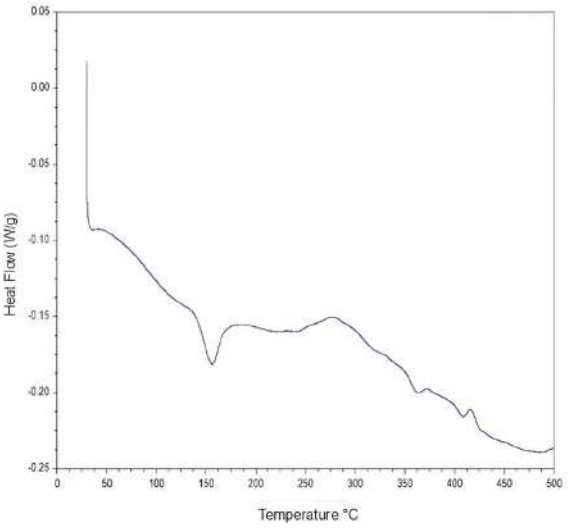

Figure 10. DSC analysis of T4.

The thermal stability observed enables the synthesized ferrites to be used in applications where they must be brought to high temperatures without losing their properties or becoming degraded. An example of the above could be its possible use in high-temperature piezoelectrics (Wang *et al*., 2024).

Endothermic and exothermic reactions may help us understand material trends. Glass transition temperature, melting and crystallization temperatures, heat of fusion, heat of reaction, purity, heat capacity, and liquid crystal transition measurements are a few examples (Prime *et al*.,2009). The DSC conducted on the T4, shown in Figure 10, revealed three little endothermic reactions at 75°C, 150°C, and 360°C, the most significant of which being the second. Another small exothermic reaction, crystallization, is observed at 410°C, at which point, a sudden and pronounced decrease in energy is observed, wherein the heat being released proves an exothermic reaction.

When the sample undergoes exothermic processes, such as crystallization, the precursor molecules of

the zinc ferrite compound gain sufficient freedom of movement to arrange themselves into a crystalline form. All these changes could be correlated with the arrangement of the final crystalline structure and the thermal stability achieved in the material, as its structure and properties may have been completely different had these energy changes not occurred (TIP, 2023).

4 Conclusions

In the present study, chemical coprecipitation proved to be a good method of preparing magnetite, which, upon calcination, is converted into maghemite, which exhibits a reduction in particle size as its temperature increases. Mechanical milling is a useful tool for the preparation of ferrites. The reactions observed between ZnO and maghemite after five hours of grinding presented different phases, with the coexistence of the zincite (ZnO), maghemite, and franklinite phases observed, which is a hitherto unreported behavior that requires further research. This triphasic effect may be explained by the failure of the grinding conditions to provide sufficient energy to complete the reaction between zinc oxide and iron oxide, achieving only partial reactions, thus explaining the three phases observed.

The mechanochemical activation occurring during the milling stage provided sufficient mechanical energy to initiate the solid-state reaction, which can accumulate during the plastic deformation of the crystals and the generation of their surfaces, thus producing regions of special chemical reactivity that facilitate the development of the solid phase processes.

The results observed for calcination at 400 °C show that this temperature was able to generate sufficient activation energy to completely transform maghemite and zinc oxide into zinc ferrite and obtain a completely defined crystalline structure, thus eliminating the three phases and leaving only the formation of the phase of interest, zinc ferrite. The crystallite size found for this phase was 10.602-11.602 nm, with sample T4 presenting the smallest crystallite size. The spinel phase crystal structure corresponds to space group number Fd3m (Oh7). The lattice parameters were observed as a=8.4411 Å, can be concluded from the findings of the present study that thermal treatments are capable of stabilizing phases.

The scanning electron microscopy analysis shows agglomeration at various levels, even allowing for the conclusion that there may be a systematization of the agglomerations. The maghemite obtained by chemical coprecipitation and calcination had particle size variations between 10.2 and 14.6 nm. Moreover, the zinc ferrite obtained by mechanical milling had particle sizes of 30–80 nm. Differences in particle size were found that could be due to greater particle agglomeration and the methods used for their synthesis.

The thermogravimetric analysis showed physical and thermal stability due to the low level of losses of mass (4.5%), which may have occurred due to moisture loss. These characteristics could be good in high temperature applications such as piezoelectric. The differential scanning calorimetry analysis showed endothermic and exothermic reactions at different temperature points.

Acknowledgements

The present study is supported and financed by the metallurgy and materials science academic body (UACOAH-CA-95) of the Metallurgy Faculty of the AUTONOMOUS UNIVERSITY OF COAHUILA.

References

Aliramaji, S., Zamanian, A., & Sohrabijam, Z. (2015). Characterization and synthesis of magnetite nanoparticles by innovative sonochemical method. *Procedia Materials Science*, *11*, 265–269. https://doi.org/10.1016/j.mspro.2015.11.022

Baena, J., & Marulanda, J. (2011). Análisis de procesos químicos para la síntesis de magnetita en aplicaciones biomédicas. In *Proceedings of XVIII Congreso Argentino de Bioingeniería*, Argentina.

Baláž, P., & Dutková, E. (2009). Fine milling in applied mechanochemistry. *Minerals Engineering*, *22*(7–8), 681–694. https://doi.org/10.1016/j.mineng.2009.01.014

Bhattu, M., Acevedo, R., & Shnain, A. (2024). A comprehensive review on the synthesis routes, properties and potential applications of $ZnFe_2O_4$ ferrites. *E3S Web of Conferences*, *588*, 02014. https://doi.org/10.1051/e3sconf/202458802014

Castaño, J., & Arroyave, C. (1998). La funcionalidad de los óxidos de hierro. *Revista de Metalurgia*, *34*(3), 274–280. https://doi.org/10.3989/revmetalm.1998.v34.i3.794

Cobos, M., de la Presa, P., Llorente, I., García-Escorial, A., Hernando, A., & Jiménez, J. (2020). Effect of preparation methods on magnetic properties of stoichiometric zinc ferrite. *Journal of Alloys and Compounds*, *849*, 156353. https://doi.org/10.1016/j.jallcom.2020.156353

De Vidales, J., López, A., Vila, E., & López, F. (1999). The effect of the starting solution on the physico-chemical properties of zinc ferrite synthesized at low temperature. *Journal of Alloys and Compounds*, *287*(1–2), 276–283. https://doi.org/10.1016/S0925-8388(99)00069-9

Ding, J., Liu, X., Wang, J., & Shi, Y. (2000). Ultrafine ferrite particles prepared by coprecipitation/mechanical milling. *Materials Letters*, *44*(1), 19–22. https://doi.org/10.1016/S0167-577X(99)00290-6

El-Eskandarany, M., Al-Hazza, A., Al-Hajji, L., Ali, N., Al-Duweesh, A., Banyan, M., & Al-Ajmi, F. (2021). Mechanical milling: a superior nanotechnological tool for fabrication of nanocrystalline and nanocomposite materials. *Nanomaterials*, *11*(10), 2484. https://doi.org/10.3390/nano11102484

Fuentes, A., & Takacs, L. (2013). Preparation of multicomponent oxides by mechanochemical methods. *Journal of Materials Science*, *48*(2), 598–611. https://doi.org/10.1007/s10853-012-6909-x

Garg, J., Chiu, M., Krishnan, S., Kumar, R., Rifah, M., Ahlawat, P., & Gupta, P. (2024). Emerging trends in zinc ferrite nanoparticles for biomedical and environmental applications. *Applied Biochemistry and Biotechnology*, *196*(2), 1008–1043. https://doi.org/10.1007/s12010-023-04570-2

García, R., Suarez, G., Pech, W., Ordonez, L., Melendez, P., Sanchez, N., & González, D. (2024). Soft chemistry synthesis of size-controlled ZnO nanostructures as photoanode for dye-sensitized solar cell. *Revista Mexicana de Ingeniería Química*, *23*(2). https://doi.org/10.24275/rmiq/IE24235

Gnanaprakash, G., Mahadevan, S., Jayakumar, T., Kalyanasundaram, P., Philip, J., & Raj, B. (2007). Effect of initial pH and temperature of iron salt solutions on formation of magnetite nanoparticles. *Materials Chemistry and Physics*, *103*(1), 168–175. https://doi.org/10.1016/j.matchemphys.2007.02.011

Hejazi, A., Al-Hunaiti, A., Bsoul, I., Mohaidat, Q., & Mahmood, S. (2024). Optimizing the synthesis of $ZnFe_2O_4$ through chemical and physical methods: effects of the synthesis route on the phase purity, inversion, and magnetic properties of spinel zinc ferrite. *Physica Scripta*, *99*(6), 065029. https://doi.org/10.1088/1402-4896/ad4746

James, S., Adams, C., Bolm, C., Braga, D., Collier, P., Friščić, T., & Waddell, D. (2012). Mechanochemistry: opportunities for new and cleaner synthesis. *Chemical Society Reviews*, *41*(1), 413–447. https://doi.org/10.1039/C1CS15171A

Koch, C. (1993). The synthesis and structure of nanocrystalline materials produced by mechanical attrition: A review. *Nanostructured Materials*, *2*(2), 109–129. https://doi.org/10.1016/0965-9773(93)90016-5

Leal, J., Almaral, J., Hurtado, A., Cortez, M., Bórquez, A., García, B., & Flores, J. (2024). Structural and chemical analysis of Zn ion exchange in thermally modified zeolite A4. *Revista Mexicana de Ingeniera Química*, *23*(3), Mat24264. https://doi.org/10.24275/rmiq/Mat24264

Mahdikhah, V., Ataie, A., Babaei, A., Sheibani, S., Ow-Yang, C., & Abkenar, S. (2019). Control of structural and magnetic characteristics of cobalt ferrite by post-calcination mechanical milling. *Journal of Physics and Chemistry of Solids*, *134*, 286–294. https://doi.org/10.1016/j.jpcs.2019.06.018

Méndez, N., Apátiga, L., Rivera, E., Manzano, A., Gonzalez, C., & Zamora, M. (2019). Crystal growth of hydroxyapatite microplates synthesised by Sol–Gel method. *Micro & Nano Letters*, *14*(14), 1414–1417. https://doi.org/10.1049/mnl.2019.0402

Moghaddam, K., & Ataie, A. (2006). Role of intermediate milling in the processing of nano-size particles of barium hexaferrite via co-precipitation method. *Journal of Alloys and Compounds*, *426*(1–2), 415–419. https://doi.org/10.1016/j.jallcom.2006.02.038

Moravvej-Farshi, F., Amishi, M., & Nekouee, K. (2020). Influence of different milling time on synthesized Ni–Zn ferrite properties by mechanical alloying method. *Journal of Materials Science: Materials in Electronics*, *31*, 13610–13619. https://doi.org/10.1007/s10854-020-03917-3

Navidpour, A., & Fakhrzad, M. (2020). Photocatalytic and magnetic properties of $ZnFe_2O_4$ nanoparticles synthesised by mechanical alloying. *International Journal of Environmental Analytical Chemistry*, *102*(3), 690-706. https://doi.org/10.1080/03067319.2020.1726331

Pedrosa, F., Rial, J., Golasinski, K., Guzik, M., Quesada, A., Fernández, J., & Bollero, A. (2016).

Towards high performance $CoFe_2O_4$ isotropic nanocrystalline powder for permanent magnet applications. *Applied Physics Letters*, *109*(22). https://doi.org/10.1063/1.4969064

Park, J., Oh, S., & Ha, B. (2001). Characterization of iron (III) oxide nanoparticles prepared by using ammonium acetate as precipitating agent. *Korean Journal of Chemical Engineering*, *18*, 215-219. https://doi.org/10.1007/BF02698462

Prime, R. B., Bair, H. E., Vyazovkin, S., Gallagher, P. K., & Riga, A. (2009). Thermogravimetric analysis (TGA). *Thermal Analysis of Polymers: Fundamentals and Applications*, 241-317.

Rao, B., Caltun, O., Cho, W., & Kim, C. (2007). Synthesis and characterization of mixed ferrite nanoparticles. *Journal of Magnetism and Magnetic Materials*, *310*(2), 812-814. https://doi.org/10.1016/j.jmmm.2006.10.771

Sani, R., Beitollahi, A., Maksimov, Y., & Suzdalev, I. (2007). Synthesis, phase formation study and magnetic properties of $CoFe_2O_4$ nanopowder prepared by mechanical milling. *Journal of Materials Science*, *42*, 2126-2131. https://doi.org/10.1007/s10853-006-1235-9

Sarkar, K., Mondal, R., Dey, S., Majumder, S., & Kumar, S. (2019). Presence of mixed magnetic phase in mechanically milled nanosized $Co_{0.5}Zn_{0.5}Fe_2O_4$: A study on structural, magnetic and hyperfine properties. *Journal of Magnetism and Magnetic Materials*, *487*, 165303. https://doi.org/10.1016/j.jmmm.2019.165303

Shenoy, S., Joy, P., & Anantharaman, M. (2004). Effect of mechanical milling on the structural, magnetic and dielectric properties of coprecipitated ultrafine zinc ferrite. *Journal of Magnetism and Magnetic Materials*, *269*(2), 217-226. https://doi.org/10.1016/S0304-8853(03)00596-1

Shi, Y., Ding, J., Liu, X., & Wang, J. (1999). $NiFe_2O_4$ ultrafine particles prepared by co-precipitation/mechanical alloying. *Journal of Magnetism and Magnetic Materials*, *205*(2-3), 249-254. https://doi.org/10.1016/S0304-8853(99)00504-1

Sukmarani, G., Kusumaningrum, R., Noviyanto, A., Fauzi, F., Habieb, A., Amal, M., & Rochman, N. (2020). Synthesis of manganese ferrite from manganese ore prepared by mechanical milling and its application as an inorganic heat-resistant pigment. *Journal of Materials Research and Technology*, *9*(4), 8497-8506. https://doi.org/10.1016/j.jmrt.2020.05.122

Takacs, L. (1998). Combustion phenomena induced by ball milling. *Materials Science Forum*, *269*, 513-522. https://doi.org/10.4028/www.scientific.net/MSF.269-272.513

Teja, A., & Koh, P. (2009). Synthesis, properties, and applications of magnetic iron oxide nanoparticles. *Progress in Crystal Growth and Characterization of Materials*, *55*(1-2), 22-45. https://doi.org/10.1016/j.pcrysgrow.2008.08.003

Thanh, N., Maclean, N., & Mahiddine, S. (2014). Mechanisms of nucleation and growth of nanoparticles in solution. *Chemical Reviews*, *114*(15), 7610-7630. https://doi.org/10.1021/cr400544s

Tomiczek, A. (2021). Effect of milling time on microstructure of cobalt ferrites synthesized by mechanical alloying. *Archives of Materials Science and Engineering*, *111*(1). https://doi.org/10.5604/01.3001.0015.5561

TIP, T. (2023). Interpreting DSC curves Part 1: Dynamic measurements.

Tehranian, P., Shokuhfar, A., & Bakhshi, H. (2019). Tuning the magnetic properties of $ZnFe_2O_4$ nanoparticles through partial doping and annealing. *Journal of Superconductivity and Novel Magnetism*, *32*, 1013-1025. https://doi.org/10.1007/s10948-018-4785-6

Verwey, E., & Heilmann, E. (1947). Physical properties and cation arrangement of oxides with spinel structures. *Journal of Chemical Physics*, *15*, 174-180. https://doi.org/10.1063/1.1746464

Wang, Q., Liang, E., & Wang, C. (2024). High performance bismuth titanate-ferrite piezoelectric ceramics for high-temperature applications. *Journal of the European Ceramic Society*, *44*(8), 5080-5087. https://doi.org/10.1016/j.jeurceramsoc.2024.02.017

Wyckoff, R. (1963). *Crystal Structures* (Vol. 1). Interscience Publishers.

Younes, A., Kherrouba, N., & Bouamer, A. (2021). Magnetic, optical, structural and thermal properties of copper ferrite nanostructured synthesized by mechanical alloying. *Micro & Nano Letters*, *16*(4), 251-256. https://doi.org/10.1049/mna2.12040

Zhang, C., Zhong, X., Yu, H., Liu, Z., & Zeng, D. C. (2009). Effects of cobalt doping on the microstructure and magnetic properties of Mn-Zn ferrites prepared by the co-precipitation method. *Physica B: Condensed Matter*, *404*(16), 2327-2331. https://doi.org/10.1016/j.physb.2008.12.044

Zhang, F., Su, Z., Wen, F., & Li, F. (2008). Synthesis and characterization of polystyrene-grafted magnetite nanoparticles. *Colloid and Polymer Science*, *286*, 837-841. https://doi.org/10.1007/s00396-008-1854-6

Zhang, Z., Yao, G., Zhang, X., Ma, J., & Lin, H. (2015). Synthesis and characterization of nickel ferrite nanoparticles via planetary ball milling assisted solid-state reaction. *Ceramics International*, *41*(3), 4523-4530. https://doi.org/10.1016/j.ceramint.2014.11.147

Appendix

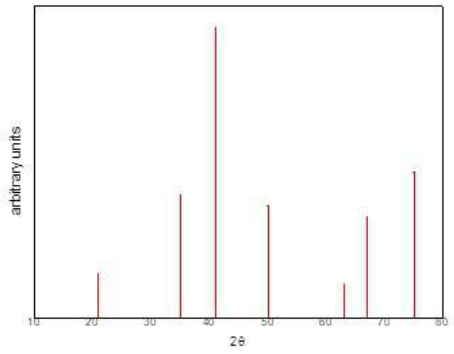

Fig. A.1. X-ray diffraction pattern of magnetite according to Aliramaji *et al*. (2015).

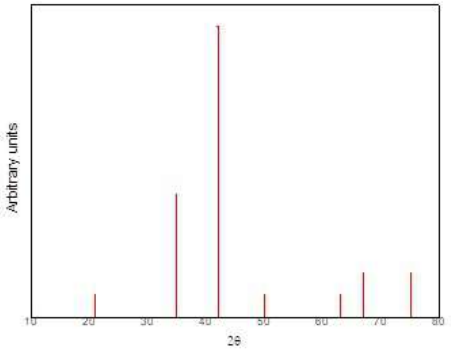

Fig. A.2. X-ray diffraction pattern of $ZnFe_2O_4$ according to Tehranian *et al*. (2019).

Vol. 24, No. 2(2025) Mat25518
Revista Mexicana de Ingeniería Química

3D printing of microchannels with MSLA technology for microfluidic devices: From design to manufacturing

Impresión 3D de microcanales con tecnología MSLA para dispositivos microfluídicos: del diseño a la fabricación

E.G. Rivera-Medellin[1,2], I. Pereyra-Laguna[3], L.E. Lugo-Uribe[4], M.A. González-López[3*], J. Mayen-Chaires[3*]
[1]*Posgrado CIATEQ, A.C., Eje 126 No. 225, Zona Industrial San Luis C.P. 78395 San Luis Potosí, SLP, México.*
[2]*Universidad Tecnológica de San Luis Potosí, Prol. Av. Dr. Arturo Nava Jaimes, Rancho Nuevo, Soledad de Graciano Sánchez, SLP.*
[3]*CIATEQ, A.C., Centro de Tecnología Avanzada, Eje 126 No. 225, Zona Industrial, 78395, San Luis Potosí, SLP, México.*
[4]*CIATEQ, A.C., Centro de Tecnología Avanzada. 52004, Estado de México, Lerma, México.*
Received: January 30, 2025; Accepted: March 27, 2025

Abstract
Microfluidics has gained prominence in recent decades due to its ability to manipulate fluids through micrometric channels and perform analyses comparable to those of a full laboratory. Applications span fields such as chemistry and neuroscience. However, one of the main challenges is the fabrication process, which is often expensive and requires specialized facilities. This study aims to design and fabricate microfluidic devices with microchannels that achieve high concordance between the design and the final product, using a low-cost MSLA 3D printer. Variables such as microchannel width and height, along with printing parameters like exposed layer height and exposure time, were evaluated. The fabricated samples were analyzed using a KEYENCE microscope equipped with a VH-20R RZ x20–x200 lens. A design of experiments was conducted to optimize the variable levels, resulting in ideal printing parameters. The findings demonstrate that this technology enables the fabrication of functional microchannels for microfluidic devices, offering an affordable and efficient alternative to traditional methods. This approach has the potential to broaden access to microfluidic technology.
Keywords: microfluidics, microchannels, MSLA 3D printing, area compliance, design of experiments.

Resumen
La microfluídica ha cobrado relevancia en las últimas décadas por su capacidad de manipular fluidos a través de canales micrométricos y realizar análisis similares a los de un laboratorio. Sus aplicaciones abarcan campos tan diversos como la química y la neurociencia. Sin embargo, uno de los mayores retos es su fabricación, que suele ser costosa y requerir instalaciones especializadas. Este estudio tiene como objetivo diseñar y fabricar dispositivos microfluídicos con microcanales que logren alta concordancia entre el diseño y el producto final, empleando una impresora 3D de tecnología MSLA de bajo costo. Se evaluaron variables como el ancho y la altura de los microcanales, junto con parámetros de impresión como la altura de capa expuesta y el tiempo de exposición. Las muestras fabricadas fueron analizadas con un microscopio KEYENCE equipado con un lente VH-20R RZ x20–x200. Mediante un diseño de experimentos, se optimizaron los niveles de las variables, obteniendo parámetros de impresión ideales. Los resultados muestran que esta tecnología permite fabricar microcanales funcionales para dispositivos microfluídicos, ofreciendo una alternativa económica y eficiente frente a los métodos tradicionales, con el potencial de ampliar el acceso a esta tecnología.
Palabras clave: microfluídica, microcanales, impresión 3D MSLA, cumplimiento del área, diseño de experimentos.

*Corresponding author. *E-mail*: dcmiguelgl@gmail.com; dr.jmayen@gmail.com ;
https://doi.org/10.24275/rmiq/Mat25518
ISSN:1665-2738, *issn-e*: 2395-8472

1 Introduction

Microfluidics is a technology designed to manipulate fluids in channels with dimensions in the range of tens of micrometers (Whitesides, 2006). Due to its applicability in diverse research areas such as chemistry, medicine, and physics, this technology has evolved rapidly (Bragheri *et al*., 2019). It enables the processing of extremely small fluid volumes (10^{-9} to 10^{-18} L) using channels at the micrometer scale (Niculescu *et al*., 2021; Ren *et al*., 2013). This technology is succinctly described by the term "lab-on-a-chip" (Dietzel Andreas, 2016), which illustrates how a small device, considered a chip, can encompass the analytical functions, capabilities, and applications of a complete laboratory (Dittrich & Manz, 2006). Additional research highlights the growing importance of microfluidics in bioseparations, emphasizing its ability to enhance analytical processes by reducing reagent consumption and processing times (Lapizco-Encinas, 2008). Microfluidics is also employed for culturing neuronal populations, acting as a guide for neurites and providing tools to dissect the spatiotemporal complexity of normal development and the establishment of brain circuits in vitro. This has popularized the use of such tools as neuronal microenvironments (Kajtez *et al*., 2020; Taylor *et al*., 2003).

However, this technology faces significant challenges, particularly in the manufacturing of microfluidic devices. Some of these devices are fabricated through photolithography, a process that involves harmful chemicals and requires expensive facilities meeting Class 10/ISO4 cleanliness standards (US FED STD 209E Cleanroom Standards) (Mukherjee *et al*., 2019). Additionally, the high production costs associated with substrate materials and material removal techniques contribute to significant waste generation. Scalability also remains a critical issue. Recent studies have explored alternative fabrication approaches, including dielectrophoresis-based techniques, which offer potential advantages in manipulating biological samples and improving separation efficiency at the microscale (Garza-García & Lapizco-Encinas, 2010).

The fabrication processes for these devices can be classified into material removal techniques and material addition techniques, as shown in Figure 1. Material removal techniques, such as electrical discharge machining (EDM), direct laser machining, engraving techniques, CNC machining, and soft lithography, create structures by eliminating material from a bulk substrate. While these approaches offer precision and versatility, they inherently generate material waste, require specialized equipment, and involve multi-step processes that increase costs.

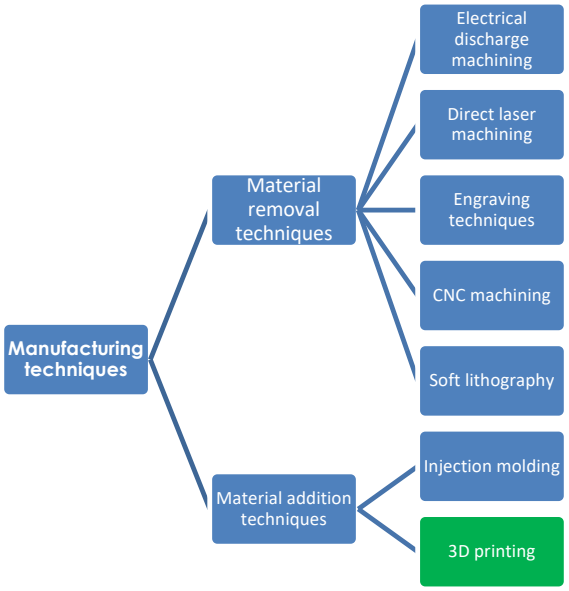

Figure 1.Microfluidic device fabrication process.

Conversely, material deposition techniques, such as stereolithography (SLA), inkjet 3D printing, and direct writing, construct structures by adding material layer by layer. These methods are generally more material-efficient, allow for rapid prototyping, and enable complex geometries, but may also present surface roughness challenges and limitations in fabricating fully enclosed channels (Waldbaur *et al*., 2011).

Among material deposition methods, MSLA 3D printing has emerged as a promising alternative for microfluidic device fabrication. Unlike soft lithography, which requires cleanroom environments, elastomeric molding, and multi-step fabrication (Talam *et al*., 2025), or CNC machining, which often struggles with high-resolution enclosed microchannels, MSLA enables the direct fabrication of custom-designed microchannels with high reproducibility and significantly reduced material waste (Garza-García & Lapizco-Encinas, 2010). While soft lithography remains ideal for applications requiring highly flexible substrates, and CNC machining excels in rigid open-channel designs, MSLA provides a balance between cost efficiency, precision, and accessibility. Recent studies have demonstrated that, with proper optimization, MSLA 3D printing can achieve dimensional compliance close to 100%, making it a viable alternative for rapid prototyping and scalable microfluidic applications (Liu *et al*., 2024).

In recent years, additive manufacturing has made significant advancements, enabling high-resolution fabrication of microparts. Some of these technologies include selective laser sintering (SLS) (Wei & Li, 2021) and two-photon polymerization (TPP) (Zhou *et al*., 2015). These systems offer exceptional resolution, but their high cost and limited scalability restrict their broader implementation (Gibson *et al*., 2010).

MSLA 3D printing, on the other hand, provides a low-cost, scalable solution that bridges the gap between traditional and modern fabrication techniques, making it an ideal choice for microfluidic research and prototyping.

Conversely, material addition techniques, such as injection molding, rely on the deposition or formation of material to construct the required components. Among these approaches, 3D printing emerges as a pivotal technology due to its versatility, customization capabilities, and potential to reduce both costs and material waste.

In recent years, additive manufacturing has made significant advancements, enabling high-resolution fabrication of microparts. Some of these technologies include selective laser sintering (SLS) and two-photon polymerization (TPP) (Zhou *et al*., 2015). These systems are ideal for device fabrication due to their high resolutions; however, their high cost limits their scalability for mass production. In addition, the integration of microscale cell analysis techniques in microfluidic platforms has been widely studied, providing insights into their application in fields such as biotechnology and biomedical research (Sósol-Fernández *et al*., 2012).

Recently, desktop 3D printers have emerged, now widely used for product customization (Shahrubudin *et al*., 2019). These printers offer great flexibility and good resolution at low cost (Leong *et al*., 2024). Examples of 3D printing technologies include SLA (stereolithography) (Manapat *et al*., 2017) , DLP (digital light processing) (Zhang *et al*., 2020), MSLA (masked stereolithography) (Borra & Neigapula, 2023), and CLIP (continuous liquid interface projection) (Tumbleston *et al*., 2015). The principle behind these technologies involves slicing the 3D model into 2D layers, which are then solidified layer by layer, typically along the z-axis, through a resin photopolymerization process until the entire piece is formed.

To fully leverage the advantages of 3D printing in microfluidic device fabrication, the design process plays a crucial role, requiring the integration of advanced software tools and precise modeling techniques. Computer-aided design (CAD) software has been widely used for 3D modeling in various fields such as engineering, mechanics, technology, electronics, and architecture. More recently, it has been applied to the development of 3D-printed components (Junk & Kuen, 2016). These tools allow precise design of models with ideal dimensional parameters, enabling the creation of microchannels with scales smaller than 100 μm (Autodesk.com, n.d.).

Once the design is complete, it must be exported to the STL format (STereoLithography), which is considered the standard for data exchange in additive manufacturing. This conversion involves running a surface triangulation algorithm commonly used in finite element methods. Process planning includes steps such as dividing the part's surfaces into triangles, generating trajectories for each layer. This data conversion produces a standardized language known as G-code, used in additive manufacturing and CNC machining to control machine movements and operations (Topcu & Unver, 2011).

This research aims to establish manufacturing principles for fabricating microfluidic devices capable of fluid transport and analysis using MSLA 3D printing technology. This approach leverages its high commercial availability and flexibility for low-cost prototyping. Variables such as layer height, exposure time, channel width, and channel depth are analyzed using a full factorial experimental design.

2 Material and methods

For this study, a commercial standard (brand: e-sun, transparent standard) with a liquid density of 1.08–1.13 g/cm^3 was used. The 3D resin printer utilized was an Elegoo Saturn 3 12K, with a resolution of 19 × 24 μm, equipped with a 10-inch monochrome 12K LCD screen operating at a wavelength of 405 nm and a build volume of 218.88 mm (length) × 122.88 mm (width) × 250 mm (height). The cleaning of the printed parts was performed using a Solv 3D washer with isopropyl alcohol. The characterization of the printed samples was conducted using a KEYENCE VHX-970F digital optical microscope, equipped with a VH-20R lens (magnification range: x20 - x200). The general method used is depicted in Figure 2.

Initially, the geometry of the channels was defined, and the design was created using Autodesk Fusion. The printing parameters were then configured in the slicing software. Test specimens were subsequently printed and washed with isopropyl alcohol. Excess alcohol was removed using compressed air. Each specimen was labelled and individually packed. Finally, the printed parts were characterized using the microscope, and the data were analyzed statistically.

2.1 Microchannel design

The experimental test specimen designed for this study measured 50 mm in length, 21 mm in width, and 5 mm in height. It contained 12 open microchannels. This design choice was informed by previous studies reporting that closed channels fabricated at dimensions <300 μm often become clogged with resin(Ahmed *et al*., 2022)**.** The microchannels were grouped into four clusters with varying dimensions and characteristics, as described below.

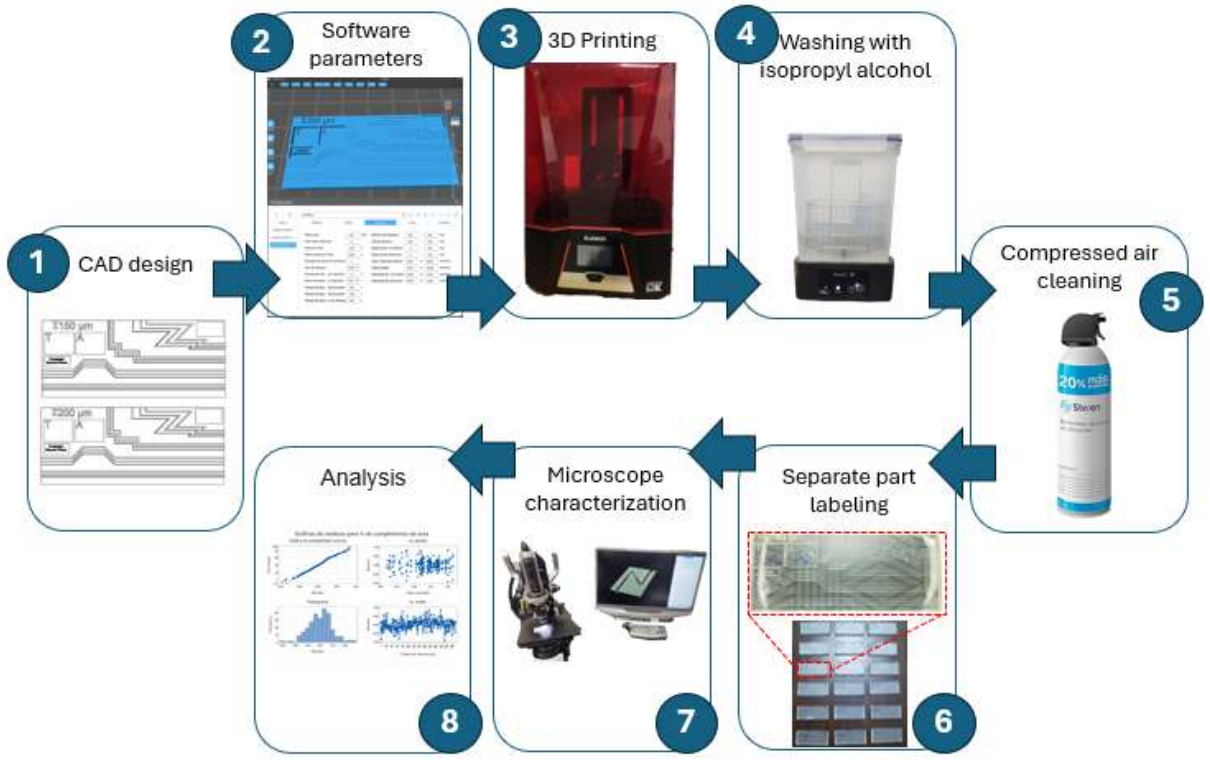

Figure 2. Method for printing microchannel samples.

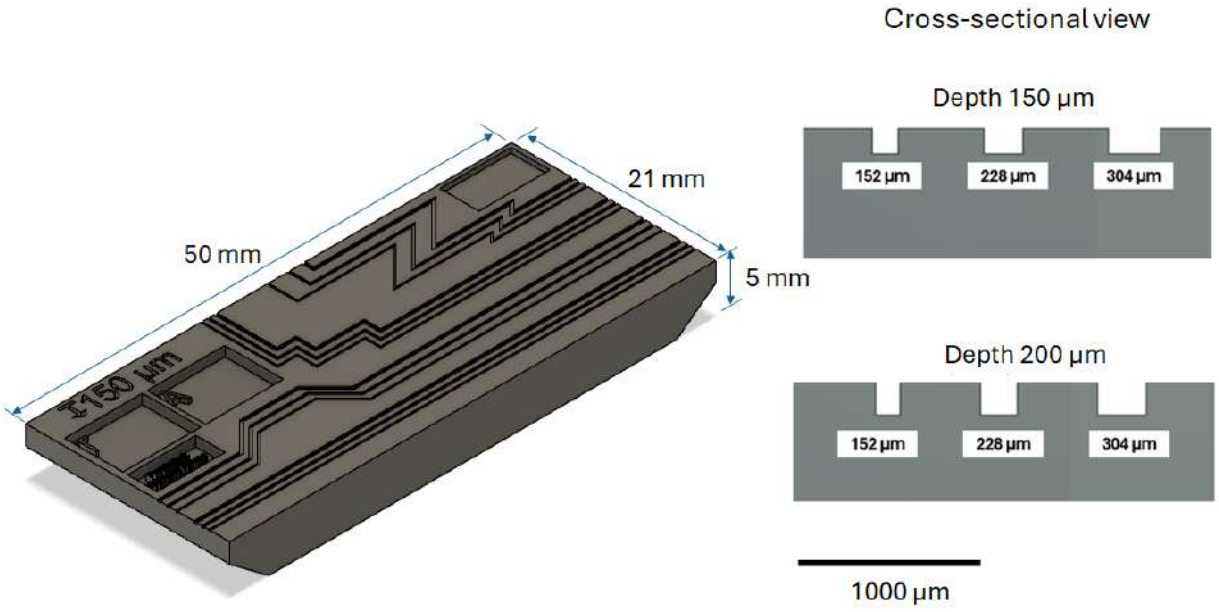

Figure 3. Dimensions of channel cross-sectional area.

The cross-sectional geometry of the channels as seen in Figure 3 was defined as a rectangular shape pattern, given the nature of the MSLA 3D printing process. In this method, the pixels of the LCD screen define the shape of the layer being photopolymerized, making additive manufacturing a viable microfabrication process (J. F. Blinn, 2005; Gao *et al*., 2023; Mishra, 2020; Tabeling, 2023)

The channel dimensions were determined based on the advancement of the build plate along the z-axis for depth and along the x- and y-axes for width. These dimensions were referenced from pixel multiples as established by Leong *et al*. (2024) in their experiments. For the printer used in this study, the pixel dimensions were 19 μm in the x-axis, 24 μm in the y-axis, and a minimum step of 10 μm in the z-axis. Consequently, channels with two different depths (150 μm and 200 μm) and three different widths (152 μm,

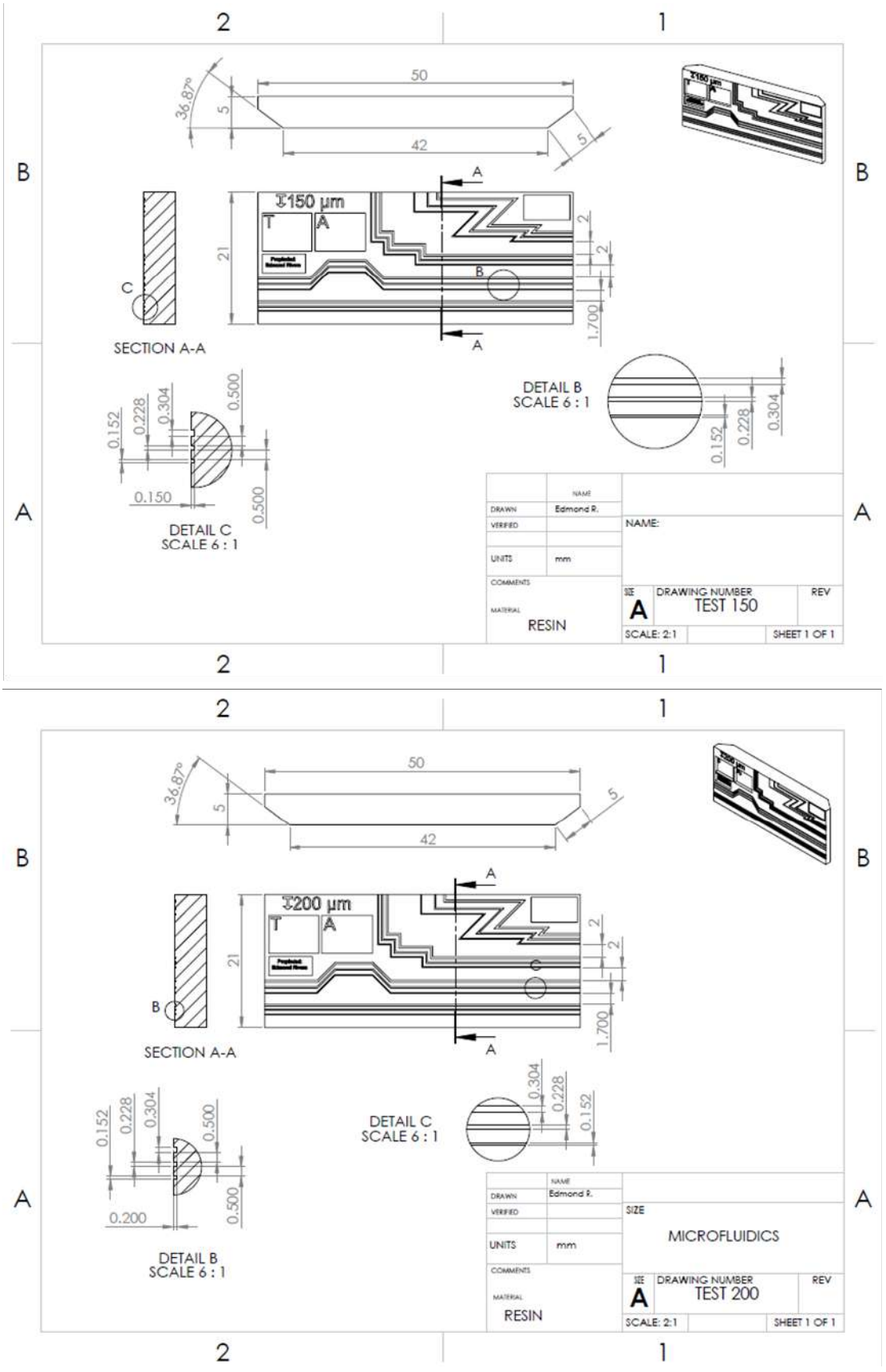

Figure 4. Microchannel sample diagrams according to ISO standard.

228 μm, and 304 μm) were evaluated, corresponding to pixel counts of 8, 12, and 16 along the x-axis, respectively, as shown in Figure 3. These dimensions align with the ranges reported in prior studies by Leong *et al*. (2024)(34.4 to 309.6 nm) and Razavi Bazaz *et al*. (2020) (40 to 300 μm).

The details of the test samples are presented in the schematics under the ISO standard shown in Figure 4.

2.2 Printing parameters

The printing parameters were based on the specifications provided by the slicing software, as shown in Table 1. However, two parameters identified in the study by Leong *et al*. (2024), were found to influence the resolution of the microchannel significantly. These variables were layer height, where the minimum height allowed by the printer is 10 μm. Based on this, three levels were selected: 20 μm, 30 μm, and 50 μm, taking 50 μm as a reference from the study by Orzeł& Stecuła (2022). The second variable was the UV exposure time for each layer to solidify, with the levels set at 1.5 s, 1.8 s, and 2 s (Leong *et al*., 2024; Valizadeh *et al*., 2023).

Table 1. Parameters for printing.

Parameter	Value	Unit
Layer height	0.02 & 0.03 & 0.05	mm
Total lower layers	10	
Exposure Time	1.5 & 1.8 & 2	s
Bottom Exposure Time	20	s
Transition Layer Count	8	
Machine type	Linear	
Transition Decrement	2	s
Printing standby mode	Time	
Ascend descent time	0	s
Retreat descent time	0.5	s
Bottom Lift Distance	3 + 4	mm
Lifting Distance	3	mm
Bottom lift distance	5.5	mm
Retraction distance	5.5	mm
Lower lifting speed	65 & 180	mm/min
Lifting Speed	65	mm/min
Retraction speed	180 & 65	mm/min

2.3 Printing process

The first step involved calibrating the build plate as specified by the manufacturer. The resin was poured to the specified level, and the printer's cover was closed. The preloaded program was selected from the printer's memory, and printing commenced. The process was conducted within a temperature range of 23 and 26°C (+/- 0.3°C), (Ahmed *et al*., 2022; Kaufmann *et al*., 2024; Milovanović *et al*., 2024).

2.4 Post-processing: Washing procedure

Each specimen took between 40 and 90 minutes to print. After detaching the printed part from the building plate, it was placed in a washing station containing isopropyl alcohol. The washing process lasted 5 minutes and involved the rotation of internal blades, which stirred the isopropyl alcohol to ensure thorough cleaning of the printed structures.

Following the washing process, compressed air was applied for 30 seconds to remove any residual isopropyl alcohol from the surface of the printed parts (Collingwood *et al*., 2023), ensuring proper post-processing before characterization. Each specimen was labelled and accompanied by a registration sheet for individual storage.

2.5 Experimental design

The experimental design employed was a full factorial design with multiple levels to evaluate the influence of various variables and their interactions. Table 2 summarizes the Design of Experiments (DOE) approach (Niedz & Evens, 2016), based on the described variables.

The first factor was the UV exposure time, which had three levels: 1.5, 1.75, and 2 s. The second factor was the layer height, also with three levels: 20 μm, 30 μm, and 50 μm. The third factor was the channel width, with three levels: 152 μm, 228 μm, and 304 μm. The final factor was the channel depth, with two levels: 150 μm and 200 μm. Five samples were taken for each combination of factors.

Table 2. Summary of DOE.

Element	Value
Factors	4
Replicas	5
Base runs	54
Total runs	270
Base blocks	1
Total blocks	1
Number of levels	3, 3, 3, 2

The direct output variables measured using the microscope included the cross-sectional area, maximum channel depth, and roughness. These output variables were used to calculate the average channel width, the percentage compliance of the designed cross-sectional area compared to the fabricated area, and the percentage compliance of the designed depth compared to the fabricated depth. This indicator was calculated using Equation 1, as described in the literature (Torres-Alvarez *et al*., 2024).

$$\%\ Cross-sectional\ area\ compliance = \left(\frac{Fabricated\ cross-sectional\ area}{Designed\ cross-sectional\ area}\right)\times 100 \quad (1)$$

This indicator is essential as it provides a value reflecting the degree of compliance between the

fabricated and designed cross-sectional areas. Since this is expressed as a percentage, the response and optimization of the variables and their levels are consistent across all designed cross-sectional sizes.

Similarly, the percentage compliance of the designed depth compared to the fabricated depth was also considered, using Equation 2.

$$\%\ Depth\ Compliance = \left(\frac{Fabricated\ depth}{Designed\ depth}\right) \quad (2)$$

3 Results

The specimens appeared to have permeable channels. In Figure 5a, a complete image of the specimen is shown, highlighting well-defined channels. Figure 5b presents a magnified view of the channels, while Figure 5c provides a 3D reconstruction of a segment selected for measurement.

The specimens were measured using a microscope in the areas indicated in Figure 6a. Random sampling was performed in the specified zones, and the images obtained were from the straight sections of the channels. The microscope allowed for the acquisition of three-dimensional images of the segments to be measured, as shown in Figures 5c and 6a. This 3D reconstruction made it possible to section the image and obtain measurements of the cross-sectional dimensions. Five measurements were taken for each segment of every channel.

The cross-sectional height and area were measured in these sections, with the cross-sectional area highlighted in pink in Figure 6b.

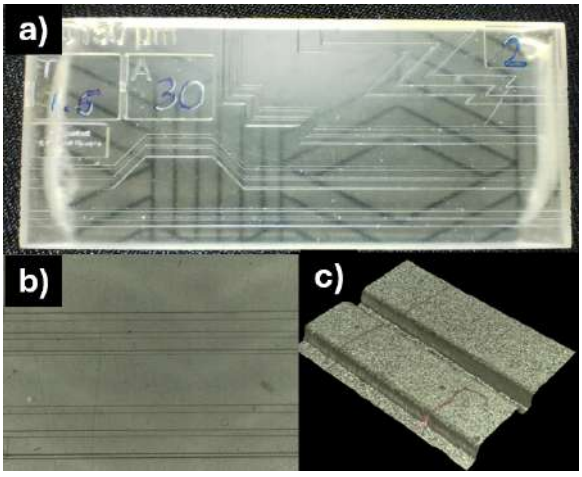

Figure 5. a) Test device image, b) expansion of a segment, and c) reconstruction of a segment of a microchannel.

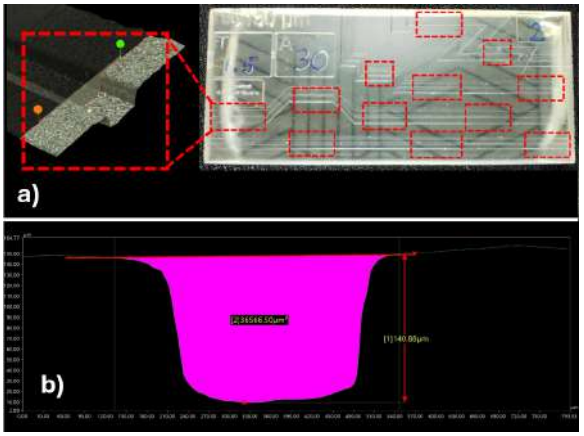

Figure 6. a) Indicated areas where characterization is carried out in a test device microchannels and 3D reconstruction of the microchannel, and b) cross-sectional area of the channel.

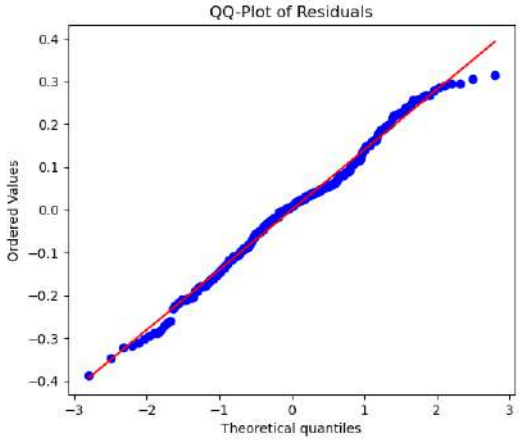

Figure 7. Normal probability plot.

3.1 *Factorial design analysis*

The data obtained from the microscope were statistically analyzed using a full factorial design. Figure 7 presents the normal probability plot for the cross-sectional area compliance percentage, showing a linear correlation and normal behavior.

An analysis of variance (ANOVA) was conducted for the main factors, with results presented in Table 3. It was observed that the most significant contributors to the variation in the microchannel's cross-sectional area were layer height and channel width (X-axis), as indicated by their F-values.

The model summary indicates a standard error (S) of 0.129233. The R-squared value is 72.93%. The adjusted R-squared is slightly lower, at 72.20%, accounting for the number of predictors in the model. Finally, the predicted R-squared value is 71.25%.

Given that the p-value obtained is less than 0.001, with a confidence level of 90%, it can be assumed that there is a relationship between the variables: exposure time, layer height, channel width, and depth,

Table 3. Analysis of variance.

Source	DF	Adj SS	Adj MS	F-Value	P-Value
Model	7	11.7876	1.68394	100.83	0
Linear	7	11.7876	1.68394	100.83	0
Exposure Time	2	1.0577	0.52885	31.67	0
Layer height	2	6.6199	3.30996	198.19	0
Chaneel width (X)	2	4.0466	2.02329	121.15	0
Depth (Z)	1	0.0634	0.06336	3.79	0.053
Error	262	4.3757	0.0167		
Lack-of-Fit	46	4.1555	0.09034	88.62	0
Pure Error	216	0.2202	0.00102		
Total	269	16.1633			

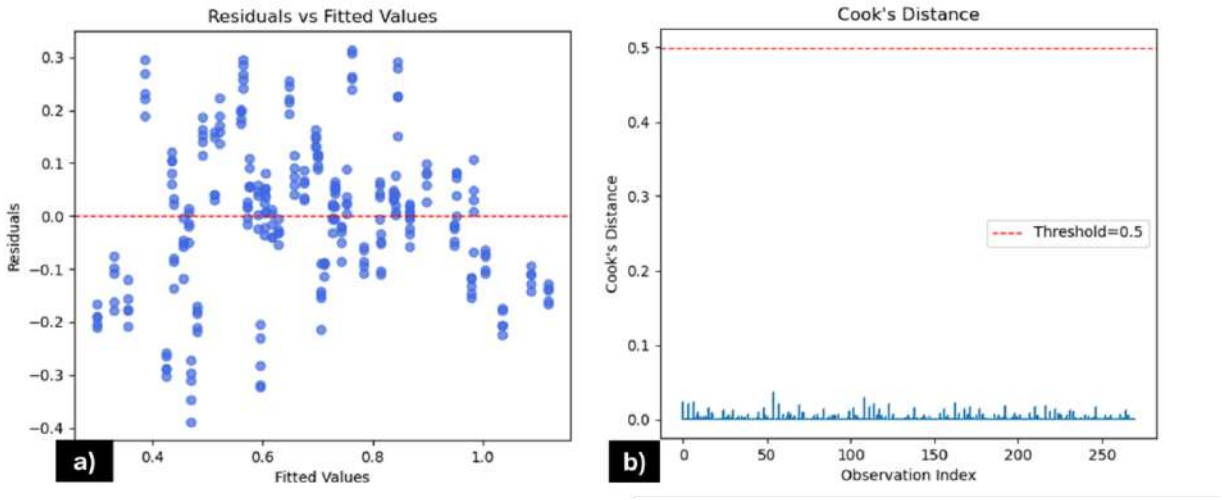

Figure 8. a) Residuals vs Fitted Values for area compliance percentage. b) Cook's distance plot.

according to the statistical study. Derived from the multiple regression analysis for cross-sectional area compliance, an R-squared value of 78.49% was achieved, indicating that a significant proportion of the variation in compliance is explained by the input variables (layer height, exposure time, channel width, and depth). A higher percentage indicates a better fit of the regression model to the observed data.

The 270 samples obtained from the experiment are sufficient to achieve an accurate estimation of the relationship between the variables. As shown in the scatter plot in Figure 8a, the values appear to be randomly distributed. Furthermore, using Cook's Distance (Figure 8b), no point exceeds the threshold (indicated by the red dashed line), meaning there are no outliers that could negatively impact the model.

According to the Shapiro-Wilk test, where:

- H_0: The distribution is normal
- H_1: The distribution is not normal,

With a significance level of 0.5, the resulting p-value is 0.0662. Therefore, the normality of the data is accepted.

3.2 *Main effects and trends*

In the main effects plot (Figure 10) for the adjusted mean compliance percentage of the cross-sectional area, the factor with the greatest influence on this variable is layer height. A positive trend is observed, indicating that increasing layer height results in higher compliance percentages. Similarly, channel width exhibits a positive correlation, suggesting that wider channels yield higher compliance percentages for the cross-sectional area.

Conversely, exposure time per layer shows a negative correlation, meaning that shorter exposure times result in higher compliance percentages. Finally, channel depth exhibits a slight negative trend.

3.3 *Interactions and optimization analysis*

Figure 10a presents an interaction plot for the factors affecting the percentage compliance of the cross-sectional area in adjusted means. For the interaction between exposure time and layer height, the condition yielding the highest compliance percentage is a combination of an exposure time of 1.5 seconds and a layer height of 50 μm.

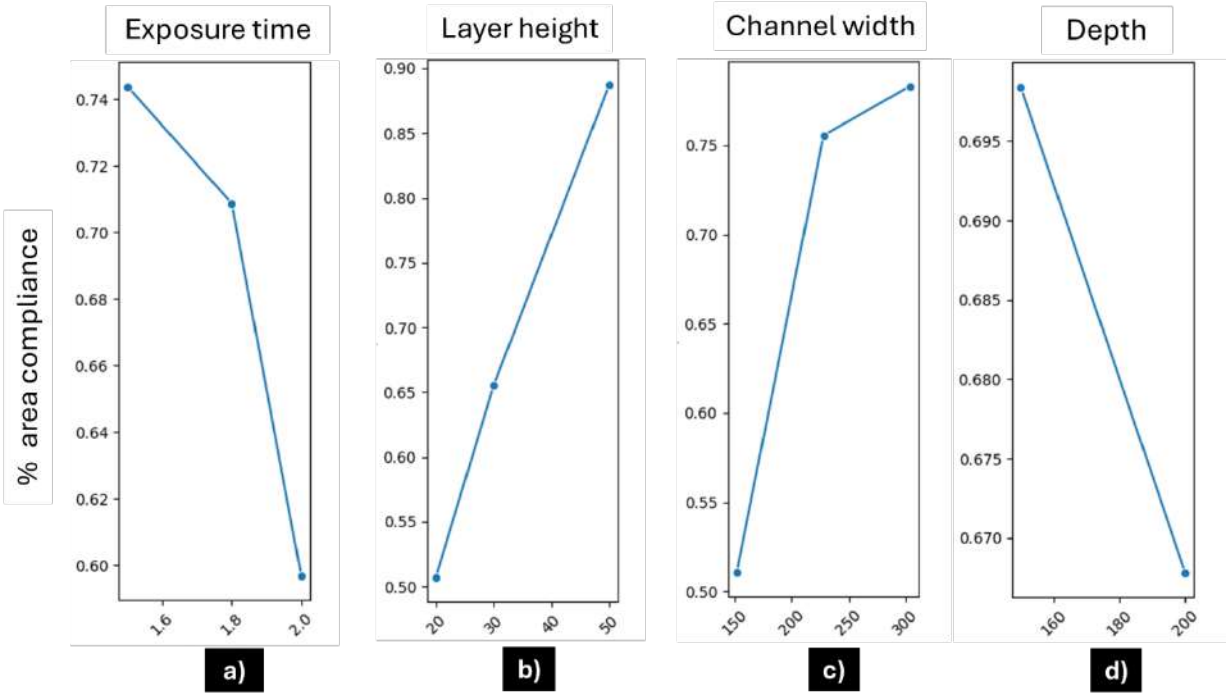

Figure 9. Main effects graph of area compliance with input variables.

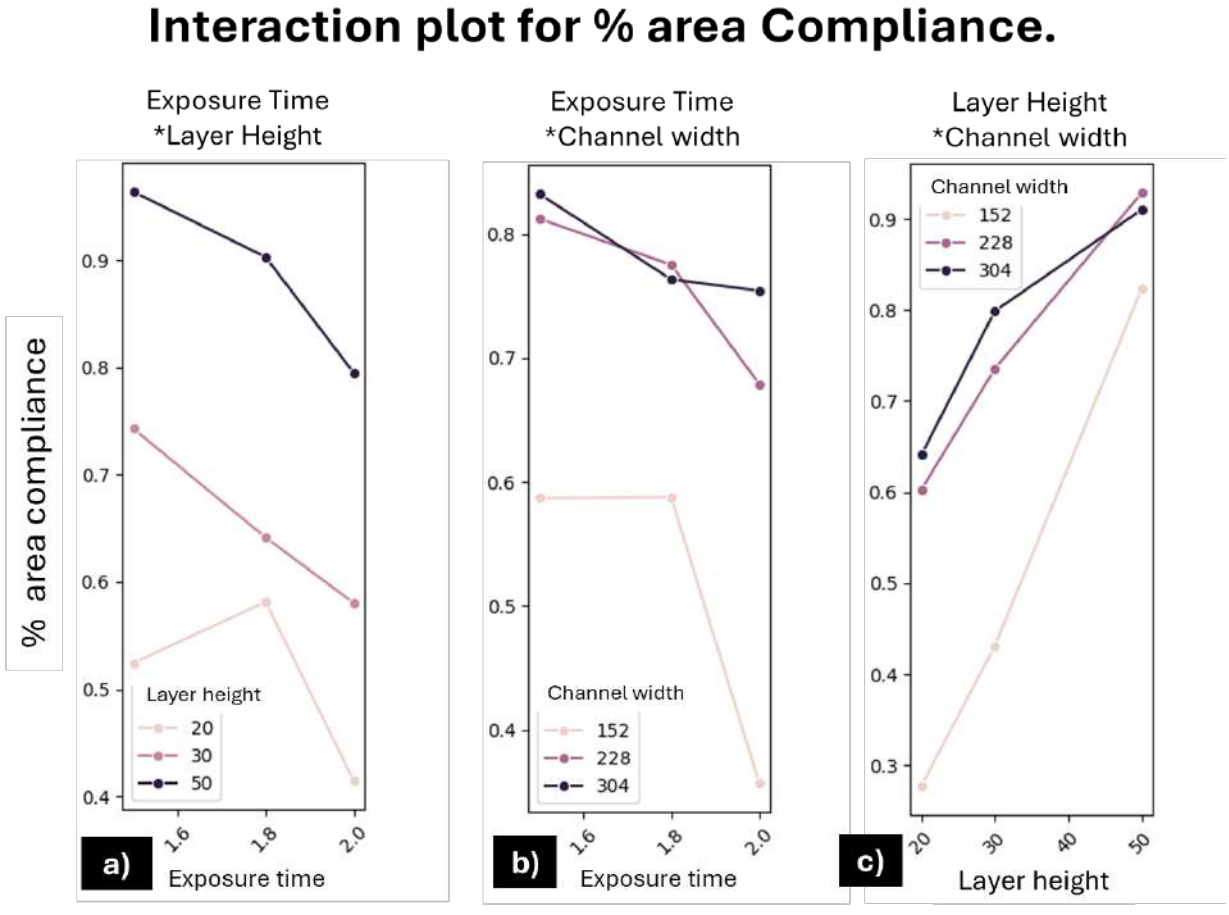

Figure 10. Interactions of input variables against printed area compliance.

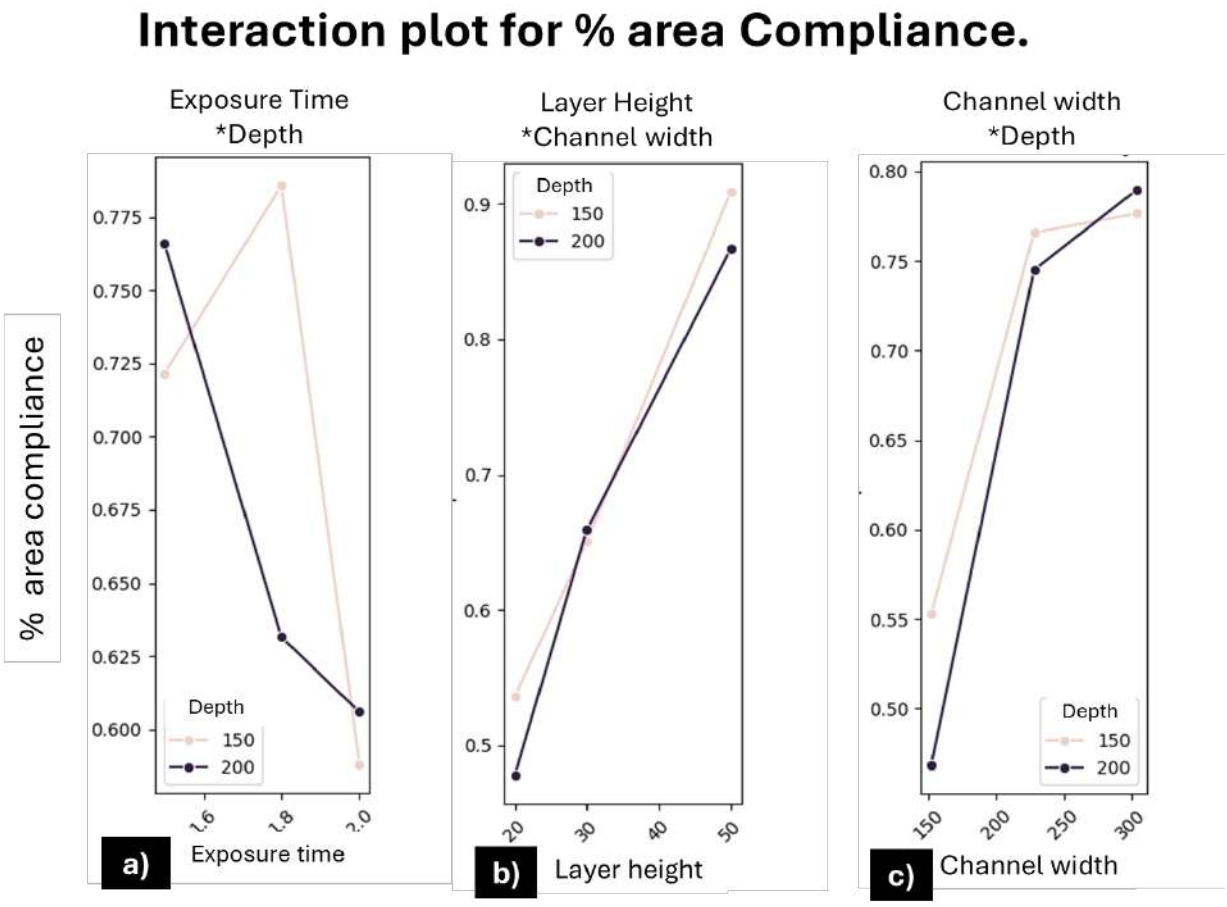

Figure 11. Interactions of input variables against printed area compliance.

In the interaction between exposure time and channel width Figure 10b, the behavior is similar for channel widths of 228 μm and 304 μm. However, the exposure time of 1.5 seconds still provides the highest area compliance in this interaction.

For the interaction between layer height and channel width Figure 10c, a similar trend is observed for channels with widths of 228 μm and 304 μm. However, higher layer heights lead to better compliance percentages for the cross-sectional area.

In the interaction between exposure time and depth 11a, the behavior is consistent at 1.5 and 2 seconds, with a slight variation observed for the 1.8-second exposure time at a depth of 150 μm.

For the interaction between layer height and depth Figure 11b and 11c, both depths exhibit similar trends, as does the interaction between channel width and depth, which shows a positive trend.

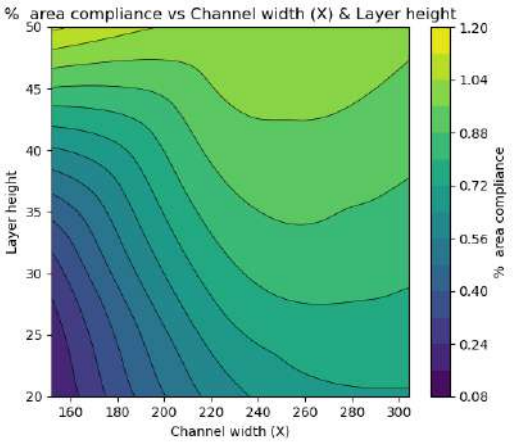

Figure 12. Area contour plot for percentage compliance of cross-sectional area vs layer height and channel width.

3.4 Contour plot and prediction

The contour plot in Figure 12 shows that when variables are set to a layer height of 50 μm and a channel width exceeding 300 μm, the probability of achieving nearly 100% compliance in the cross-sectional area increases significantly.

Using optimization and prediction statistics, the predictor "Y" achieved a maximized compliance value of 1.11805, exceeding 100%, indicating an area larger than the specified design. This optimal solution, suggested by the software, is achieved with the following parameters:

- **X1 (Exposure time):** 1.5 s
- **X2 (Layer height):** 50 μm
- **X3 (Channel width):** 304 μm
- **X4 (Depth):** 150 μm

Other possible solutions according to statistical optimization, closer to 100% compliance are shown below

Solution 1: X1 = 1.8 s, X2 = 50 μm, X3 = 304 μm, X4 = 200 μm

Solution 2: X1 = 1.5 s, X2 = 50 μm, X3 = 228 μm, X4 = 150 μm

These two solutions encompass a range where 100% optimization of the microchannel's cross-sectional area is achieved. Based on these predictions, future experiments with a larger sample size are planned to validate these results.

Conclusions

This study demonstrates the feasibility of fabricating microchannels for microfluidic devices using MSLA 3D printing technology. The experimental results validate the effectiveness of this approach in achieving high-resolution microfabrication, highlighting its potential for broader applications beyond specific printer models.

As discussed throughout this work, the input factors—layer height, exposure time, and the channel dimensions (width and depth)—have a significant impact on the compliance of the cross-sectional area of the channels. Among these, layer height and channel width were identified as the most influential parameters, with a positive correlation to cross-sectional area compliance.

Moreover, it was observed that optimizing these factors can yield microchannels with cross-sectional areas achieving compliance levels very close to 100% of the designed specifications. The ability to reach such high accuracy underscores the potential of MSLA 3D printing technology in the precise manufacturing of microfluidic devices at a considerable low cost.

The findings also highlight the importance of using systematic experimental approaches, such as factorial designs, to identify optimal manufacturing conditions. This approach not only enables precise tuning of input parameters but also facilitates the identification of interactions between variables, which is critical in achieving optimal outcomes.

The successful fabrication of microchannels using a commercially available, cost-effective desktop 3D printer opens new possibilities for the democratization of microfluidic technology. However, future work should explore additional factors such as resin composition, post-processing techniques, and the mechanical properties of the printed devices. Furthermore, scaling up the sample size and conducting long-term reliability tests will be essential for establishing the robustness of the proposed manufacturing process.

Finally, this work demonstrates that additive manufacturing, particularly MSLA 3D printing, holds great promise in advancing the field of microfluidics at a very low cost, promoting a paradigm shift for sensing solutions in different specialized sectors such as medicine and environmental applications by democratization of these technologies. By enabling the fabrication of complex geometries with precision and repeatability, this technology can significantly contribute to the development of innovative solutions for fluid manipulation at the microscale.

References

Ahmed, I., Sullivan, K., & Priye, A. (2022). Multi-resin masked stereolithography (MSLA) 3D printing for rapid and inexpensive prototyping of microfluidic chips with integrated functional components. *Biosensors (Basel)*, *12*(8), 652. https://doi.org/10.3390/bios12080652

Autodesk.com. (n.d.). Presición de autodesk. In *Autodesk.com*. Retrieved December 28, 2024, from https://www.autodesk.com/mx/solutions/cad-software#:~:text=%C2%BFQu%C3%A9%20es%20el%20software%20de,y%20simular%20el%20rendimiento%20real

Blinn, J. F. (2005). What Is a Pixel? *IEEE Computer Graphics and Applications*, *25*(5), 82–87. https://doi.org/10.1109/MCG.2005.119

Borra, N. D., & Neigapula, V. S. N. (2023). Parametric optimization for dimensional correctness of 3D printed part using masked stereolithography: Taguchi method. *Rapid Prototyping Journal*, *29*(1), 166–184. https://doi.org/10.1108/RPJ-03-2022-0080

Bragheri, F., Vázquez, R. M., & Osellame, R. (2019). Microfluidics. In *Three-Dimensional Microfabrication Using Two-Photon Polymerization* (pp. 493–526). Elsevier. https://doi.org/10.1016/B978-0-12-817827-0.00057-6

Collingwood, J., De Silva, K., & Arif, K. (2023). High-speed 3D printing for microfluidics: Opportunities and challenges. *Materials Today:*

Proceedings. https://doi.org/10.1016/j.matpr.2023.05.683

Dietzel Andreas. (2016). *Microsystems for Pharmatechnology Manipulation of Fluids, Particles, Droplets, and Cells*.

Dittrich, P. S., & Manz, A. (2006). Lab-on-a-chip: Microfluidics in drug discovery. In *Nature Reviews Drug Discovery* (Vol. 5, Issue 3, pp. 210–218). https://doi.org/10.1038/nrd1985

Gao, H., An, J., Chua, C. K., Bourell, D., Kuo, C. N., & Tan, D. T. H. (2023). 3D printed optics and photonics: Processes, materials and applications. In *Materials Today* (Vol. 69, pp. 107–132). Elsevier B.V. https://doi.org/10.1016/j.mattod.2023.06.019

Garza-García, L. D., & Lapizco-Encinas, B. H. (2010). STATE OF THE ART ON PROTEIN MANIPULATION EMPLOYING DIELECTROPHORESIS. *Revista Mexicana de Ingeniería Química*, *2*(2), 1156–1741. https://rmiq.org/iqfvp/Pdfs/Vol9%20no%202/RMIQVol9No2_1.pdf

Gibson, I., Rosen, D. W., & Stucker, B. (2010). *Additive manufacturing technologies: Rapid prototyping to direct digital manufacturing*. Springer US. https://doi.org/10.1007/978-1-4419-1120-9

Junk, S., & Kuen, C. (2016). Review of Open Source and Freeware CAD Systems for Use with 3D-Printing. *Procedia CIRP*, *50*, 430–435. https://doi.org/10.1016/j.procir.2016.04.174

Kajtez, J., Buchmann, S., Vasudevan, S., Birtele, M., Rocchetti, S., Pless, C. J., Heiskanen, A., Barker, R. A., Martínez-Serrano, A., Parmar, M., Lind, J. U., & Emnéus, J. (2020). 3D-Printed Soft Lithography for Complex Compartmentalized Microfluidic Neural Devices. *Advanced Science*, *7*(16). https://doi.org/10.1002/advs.202001150

Kaufmann, B. K., Rudolph, M., Pechtl, M., Wildenburg, G., Hayden, O., Clausen-Schaumann, H., & Sudhop, S. (2024). mSLAb – An open-source masked stereolithography (mSLA) bioprinter. *HardwareX*, *19*. https://doi.org/10.1016/j.ohx.2024.e00543

Lapizco-Encinas, B. H. (2008). APLICACIONES DE MICROFLUÍDICA EN BIOSEPARACIONES MICROFLUIDICS APPLICATIONS IN BIOSEPARATIONS. *Revista Mexicana de Ingeniería Química*, *7*(3), 205–214. https://rmiq.org/iqfvp/Pdfs/Vol%207%20no%203/3_RMIQ_Vol7No3_290508.pdf

Leong, K. M., Sun, A. Y., Quach, M. L., Lin, C. H., Craig, C. A., Guo, F., Robinson, T. R., Chang, M. M., & Olanrewaju, A. O. (2024). Democratizing Access to Microfluidics: Rapid Prototyping of Open Microchannels with Low-Cost LCD 3D Printers. *ACS Omega*. https://doi.org/10.1021/acsomega.4c07776

Liu, X., Sun, A., Brodský, J., Gablech, I., Lednický, T., Vopařilová, P., Zítka, O., Zeng, W., & Neužil, P. (2024). Microfluidics chips fabrication techniques comparison. *Scientific Reports*, *14*(1). https://doi.org/10.1038/s41598-024-80332-2

Manapat, J. Z., Chen, Q., Ye, P., & Advincula, R. C. (2017). 3D Printing of Polymer Nanocomposites via Stereolithography. In *Macromolecular Materials and Engineering* (Vol. 302, Issue 9). Wiley-VCH Verlag. https://doi.org/10.1002/mame.201600553

Milovanović, A., Montanari, M., Golubović, Z., Mărghitaş, M. P., Spagnoli, A., Brighenti, R., & Sedmak, A. (2024). Compressive and flexural mechanical responses of components obtained through mSLA vat photopolymerization technology. *Theoretical and Applied Fracture Mechanics*, *131*. https://doi.org/10.1016/j.tafmec.2024.104406

Mishra, P. (2020). Additive Manufacturing (3D Printing): A Review on the Micro fabrication Methods. *International Journal for Research in Applied Science and Engineering Technology*, *8*(4), 956–975. https://doi.org/10.22214/ijraset.2020.4160

Mukherjee, P., Nebuloni, F., Gao, H., Zhou, J., & Papautsky, I. (2019). Rapid prototyping of soft lithography masters for microfluidic devices using dry film photoresist in a non-cleanroom setting. *Micromachines*, *10*(3). https://doi.org/10.3390/mi10030192

Niculescu, A.-G., Chircov, C., Bîrcă, A. C., & Grumezescu, A. M. (2021). Fabrication and Applications of Microfluidic Devices: A Review. *International Journal of Molecular Sciences*, *22*(4), 1–26. https://doi.org/10.3390/ijms22042011

Niedz, R. P., & Evens, T. J. (2016). Design of experiments (DOE)—history, concepts, and relevance to in vitro culture. In *In Vitro Cellular and Developmental Biology - Plant* (Vol. 52, Issue 6, pp. 547–562). Springer New York

LLC. https://doi.org/10.1007/s11627-016-9786-1

Orzeł, B., & Stecuła, K. (2022). Comparison of 3D Printout Quality from FDM and MSLA Technology in Unit Production. *Symmetry*, *14*(5). https://doi.org/10.3390/sym14050910

Razavi Bazaz, S., Rouhi, O., Raoufi, M. A., Ejeian, F., Asadnia, M., Jin, D., & Ebrahimi Warkiani, M. (2020). 3D Printing of Inertial Microfluidic Devices. *Scientific Reports*, *10*(1). https://doi.org/10.1038/s41598-020-62569-9

Ren, K., Zhou, J., & Wu, H. (2013). Materials for microfluidic chip fabrication. *Accounts of Chemical Research*, *46*(11), 2396–2406.

Shahrubudin, N., Lee, T. C., & Ramlan, R. (2019). An overview on 3D printing technology: Technological, materials, and applications. *Procedia Manufacturing*, *35*, 1286–1296. https://doi.org/10.1016/j.promfg.2019.06.089

Sósol-Fernández, R. E., Marín-Lizárraga, V. M., Rosales-Cruzaley, E., & Lapizco-Encinas, B. H. (2012). ANÁLISIS DE CÉLULAS EN DISPOSITIVOS MICROFLUÍDICOS. *Revista Mexicana de Ingeniería Química*. https://rmiq.org/iqfvp/Pdfs/Vol.%2011,%20No.%202/Bio2/Bio2.pdf

Tabeling, P. (2023). *Introduction to Microfluidics*. Oxford University Press.

Talam, S., Avula, K. P., Syed, S., & Battula, S. (2025). Fabrication techniques for microfluidics devices. In *Utilizing Microfluidics in the Food Industry* (pp. 69–96). Elsevier. https://doi.org/10.1016/B978-0-443-13453-1.00004-8

Taylor, A. M., Rhee, S. W., Tu, C. H., Cribbs, D. H., Cotman, C. W., & Jeon, N. L. (2003). Microfluidic multicompartment device for neuroscience research. *Langmuir*, *19*(5), 1551–1556. https://doi.org/10.1021/la026417v

Topcu, O., & Unver, H. O. (2011). *A method for slicing CAD models in binary STL format*. https://www.researchgate.net/publication/259843304

Torres-Alvarez, D., Bosques-Palomo, B., Martínez-Dibildox, A., Marcos-Abdala, A., Jiménez-Nuñéz, R., Morones-Ramírez, J. R., Aeinehvand, M. M., & Aguirre-Soto, A. (2024). Introduction of the lowest printable (channel) characteristic length (LPCL) as a geometrical metric for the SLA 3D printing of embedded negative micro-structures. *Progress in Additive Manufacturing*. https://doi.org/10.1007/s40964-024-00788-6

Tumbleston, J. R., Shirvanyants, D., Ermoshkin, N., Janusziewicz, R., Johnson, A. R., Kelly, D., Chen, K., Pinschmidt, R., Rolland, J. P., & Ermoshkin, A. (2015). Continuous liquid interface production of 3D objects. *Science*, *347*(6228), 1349–1352.

Valizadeh, I., Tayyarian, T., & Weeger, O. (2023). Influence of process parameters on geometric and elasto-visco-plastic material properties in vat photopolymerization. *Additive Manufacturing*, *72*. https://doi.org/10.1016/j.addma.2023.103641

Waldbaur, A., Rapp, H., Länge, K., & Rapp, B. E. (2011). Let there be chip - Towards rapid prototyping of microfluidic devices: One-step manufacturing processes. In *Analytical Methods* (Vol. 3, Issue 12, pp. 2681–2716). https://doi.org/10.1039/c1ay05253e

Wei, C., & Li, L. (2021). Recent progress and scientific challenges in multi-material additive manufacturing via laser-based powder bed fusion. *Virtual and Physical Prototyping*, *16*(3), 347–371.

Whitesides, G. M. (2006). The origins and the future of microfluidics. *Nature*, *442*(7101), 368–373. https://doi.org/10.1038/nature05058

Zhang, J., Hu, Q., Wang, S., Tao, J., & Gou, M. (2020). Digital light processing based three-dimensional printing for medical applications. *International Journal of Bioprinting*, *6*(1), 12–27. https://doi.org/10.18063/ijb.v6i1.242

Zhou, X., Hou, Y., & Lin, J. (2015). A review on the processing accuracy of two-photon polymerization. *AIP Advances*, *5*(3). https://doi.org/10.1063/1.4916886

Vol. 24, No. 2(2025) Proc25524

Revista Mexicana de Ingeniería Química

Evaluation of the presence of metallic cations (Cu^{2+}, Zn^{2+}, Fe^{2+}, Pb^{2+}) in silver sulfide leaching with thiosulfate: Thermodynamic and experimental study

Evaluación de la presencia de cationes metálicos (Cu^{2+}, Zn^{2+}, Fe^{2+}, Pb^{2+}) en la lixiviación de sulfuro de plata con tiosulfato: Estudio termodinámico y experimental

G. Cisneros-Flores[1], J. C. Juárez-Tapia[1], I. A. Reyes-Domínguez[2], N. Toro[3], G. Urbano-Reyes[1], E. J. Muñoz-Hernández[1], J. I. Martínez-Soto[1], A. M. Teja-Ruíz[4]*

[1] Área Académica de Ciencias de la Tierra y Materiales, Universidad Autónoma del Estado de Hidalgo (UAEH), Pachuca de Soto 42184, México

[2] Catedrático CONACYT-Instituto de Metalurgia, Universidad Autónoma de San Luis Potosí, San Luis Potosí 78210, México

[3]Faculty of Engineering and Architecture, Universidad Arturo Prat, Iquique 1110939, Chile

[4] *Dirección* de Laboratorios, Universidad Autónoma del Estado de Hidalgo (UAEH), Pachuca de Soto 42184, México

Received: February 8, 2025; Accepted: April 20, 2025

Abstract

This study evaluates the effect of Cu^{2+}, Zn^{2+}, Pb^{2+}, and Fe^{2+} on the selective leaching of Ag_2S with thiosulfate. Pourbaix diagrams were used to identify the stability and predominance regions of the species formed as a function of ORP and pH, providing a theoretical framework to predict the influence of each ion. Experimental tests were conducted with high-purity reagents (≥ 99.5%) to isolate the individual effect of each ion without interference from complex matrices. The results showed that Cu^{2+} at low concentrations and Zn^{2+} enhance Ag_2S leaching, while Fe^{2+}, Pb^{2+}, and higher concentrations of Cu^{2+} inhibit the process, exhibiting behavior similar to cyanicide metals. X-ray Diffraction (XRD) analysis allowed the identification of byproducts formed in the solid residues. The correlation between thermodynamic, experimental, and XRD results led to the proposal of reaction mechanisms in the S_2O_3 – Ag_2S – M^{2+} systems, where M represents the analyzed cations. These findings provide fundamental insights into Ag_2S leaching with thiosulfate and its potential application in polymetallic sulfides and precious metal-containing waste.

Keywords: Silver leaching with thiosulfate, Leaching chemistry, Thiosulfate decomposition.

Resumen

Este estudio evalúa el efecto de los cationes Cu^{2+}, Zn^{2+}, Pb^{2+} y Fe^{2+} en la lixiviación selectiva de un sulfuro de plata con tiosulfato. A través del modelado termodinámico mediante diagramas de Pourbaix, se identificaron las zonas de estabilidad y predominio de las especies formadas en función del ORP y pH, proporcionando un marco teórico para predecir la influencia de cada ion en el sistema de lixiviación. Se realizaron pruebas experimentales con reactivos de alta pureza (≥ 99.5%) para aislar el efecto individual de cada ion sin interferencias de matrices complejas. Los resultados revelaron que Cu^{2+} en bajas concentraciones y Zn^{2+} favorecen la lixiviación de Ag_2S, mientras que Fe^{2+}, Pb^{2+} y concentraciones elevadas de Cu^{2+} la inhiben, exhibiendo un comportamiento similar al de los metales cianicidas. Mediante Difracción de Rayos X (DRX), se identificaron los subproductos formados en el residuo sólido. La correlación entre los resultados termodinámicos, experimentales y los difractogramas permitió proponer los mecanismos de reacción en los sistemas S_2O_3 – Ag_2S – M^{2+}, donde M representa los cationes analizados. Estos hallazgos no solo contribuyen a la comprensión fundamental de la lixiviación de Ag_2S con tiosulfato, sino que también proporcionan información relevante para su aplicación en sistemas más complejos, como sulfuros polimetálicos y residuos de metales preciosos.

Palabras clave: Lixiviación de plata con tiosulfato, química de lixiviación, descomposición de tiosulfato.

* *Corresponding author. E-mail*: aislinn_ teja@uaeh.edu.mx ;
https://doi.org/10.24275/rmiq/Proc25524
ISSN:1665-2738, *issn-e*: 2395-8472

1 Introduction

Cyanide has been widely used in the leaching process of precious metals such as gold (Au) and silver (Ag), but it is not without areas for improvement. Cyanide is selective for metals such as copper, zinc, iron, and nickel, among others, significantly increasing its consumption. On the other hand, it is incapable of dissolving refractory minerals, making it ineffective for processing complex ores (Alarcon *et al*., 2018; Liu *et al*., 2023; Soto *et al*., 2023). In addition to these technical limitations, its high toxicity and the associated risks of its use have been the subject of study, as cyanide-related incidents have led to environmental disasters, regulatory restrictions, and increasing public opposition in mining communities (Dwivedi *et al*., 2021; Mitra, 2019). Moreover, the growing demand for Ag and Au, driven by their implementation in a wide variety of everyday products, has caused the overexploitation of primary extraction sources, resulting in their depletion and forcing the min ing industry to face the challenge of processing increasingly complex ores. This has generated growing interest in the processing of alternative sources, such as electronic waste, and mining byproducts, including tailings and concentrates, which contain valuable metals that can be recovered through hydrometallurgical processes (Erust *et al*., 2023; Serga *et al*., 2022). Given these challenges, exploring more sustainable and environmentally friendly leaching agents has become essential. Conventional lixiviants not only exhibit technical limitations but also pose significant environmental and economic concerns, reinforcing the need for alternative approaches not only in leaching agents but also in complementary remediation strategies, such as biosorption and the use of metal-resistant microorganisms (Asencios *et al*., 2022; Cos & Fuentes, 2023; Meléndez *et al*., 2022). Among the alternatives to cyanide, thiosulfate has stood out as one of the most promising leaching agents for precious metals due to its low toxicity and reduced environmental impact. Thiosulfate acts as a bifunctional ligand, coordinating with metals through two types of donor atoms: sulfur (S) and oxygen (O). This characteristic allows it to form stable complexes with various metals following the hard and soft acids and bases theory. Sulfur, being a soft donor, tends to have an affinity for metals such as Au(I) and Ag(I), while oxygen, being a hard donor, binds to metals such as copper and iron (Pearson, 1997; Trachevskii *et al*., 2008). However, one of the main areas of opportunity for the effective use of thiosulfate lies in its excessive oxidative degradation and the complexity of its reaction chemistry (Urzúa *et al*., 2018; Puente *et al*., 2021; Xu *et al*., 2017; Yae *et al*., 2023). Because of this, there is great interest in finding oxidizing agents that promote an optimal ORP, including the use of air and O_2, as well as the implementation of metallic ions such as Cu^{2+}, Zn^{2+}, Co^{3+}, and Fe^{3+} (Juárez-Tapia *et al*., 2012; Puente *et al*., 2017; Zhang *et al*., 2022a, 2022b). However, the use of these oxidizing agents may increase thiosulfate consumption due to their reactivity with these ions, generating undesirable secondary reactions. This behavior is similar to that observed with the so-called cyanicide metals, which also form stable complexes with cyanide and increase its consumption during leaching (Larrabure & Rodríguez, 2021). This study examines the effect of metallic ions (Cu^{2+}, Zn^{2+}, Pb^{2+}, and Fe^{2+}) at various concentrations on the dissolution behavior of silver sulfide in a thiosulfate medium. The objective is to determine whether these ions enhance silver dissolution or, conversely, trigger secondary reactions that compromise thiosulfate stability. Based on this analysis, we aim to establish a classification analogous to cyanicide metals, identifying as *thiosulfacide metals* those that negatively impact the thiosulfate leaching process. Additionally, this study provides insights into reaction mechanisms involved in the leaching of silver sulfide with thiosulfate in the presence of these cations, facilitating the identification of metallic species that may interfere with the recovery of the target metal. This information allows for the design or adjustment of multi-stage leaching processes, where problematic cations are selectively dissolved in an initial phase before implementing thiosulfate leaching (Segura & Lapidus, 2023). This approach optimizes the recovery of the target metal while minimizing adverse effects on the lixiviant. Although the experiments were conducted using synthetic samples to ensure controlled conditions and isolate the specific influence of each metallic ion, the findings provide fundamental insights into the mechanisms governing thiosulfate leaching. This study serves as a valuable reference for future research involving more complex matrices, such as polymetallic ores or secondary metal sources, including electronic waste, where additional interactions may further influence the leaching process.

2 Methods and materials

For this investigation, high-purity reagents were used: silver sulfide (Ag_2S, Sigma-Aldrich ≥99.5%), copper sulfate ($CuSO_4 \cdot 5H_2O$, M&B ≥99.5%), zinc sulfate ($ZnSO_4 \cdot 7H_2O$, J.T. Baker 99.9%), lead sulfate ($PbSO_4$, Analytyka ≥99.5%), ferrous sulfate ($FeSO_4 \cdot 7H_2O$, J.T. Baker 99.9%), and sodium thiosulfate ($Na_2S_2O_3 \cdot 5H_2O$, MEYER ≥99.5%). Deionized water was used in all the experiments.

The thermodynamic analysis was performed prior to the experimental phase to predict the stability of silver-thiosulfate complexes and the potential interactions with Cu^{2+}, Zn^{2+}, Pb^{2+}, and Fe^{2+}. This was achieved through the construction of Eh-pH diagrams using the Hydra MEDUSA Chemistry software, while the thermodynamic constant database was updated with the assistance of HSC Chemistry 6 software. The insights from this analysis guided the selection of key experimental conditions, particularly the pH range (~8), which was chosen to maintain thiosulfate stability while minimizing the formation of undesirable species. Additionally, the thermodynamic predictions regarding the formation of solid phases were later verified through X-Ray Diffraction (XRD) analysis of the leaching residues. Silver sulfide leaching tests were conducted with 0.5 L of an alkaline solution (pH ≈ 8) in a PYREX glass reactor placed on a Thermo Scientific heating plate, which was used to monitor temperature and applied stirring speed. Air was injected through a diffuser and regulated with a flowmeter. During the process, 10 mL aliquots were extracted at predetermined time intervals: 0, 0.5, 1.0, 1.5, 2, 3, 4, 6, 8, 10, 12, and 24 hours. The aliquots were subsequently analyzed by Inductively Coupled Plasma Emission Spectrometry (ICP) using a Perkin Elmer 3000 spectrometer to determine the concentration of Ag in solution. The experimental parameters used in the leaching tests are presented in Table 1. Finally, the solid residues from the leaching process were analyzed by X-Ray Diffraction (XRD) using an INEL EQUINOX 2000 X-ray diffractometer (Thermo Fisher Scientific, Ecublens, Switzerland) with Co-Kα1 radiation (1.789010 Å). The radiation settings were 30 mA, 20 kV, and 220 V, with a resolution of 0.095 FWHM. Phase identification was carried out using Match 3 software with the COD-Inorg REV140301 database.

Table 1 Experimental conditions of the leaching tests.

Parameter	Value
$[CuSO_4 \cdot 5H_2O]$ (g/L)	0.062, 0.187, 0.25, 0.5, 0.75, 1.0
$[PbSO_4]$ (g/L)	0.045, 0.11, 0.22, 0.33, 0.44, 0.55
$[Na_2S_2O_3 \cdot 5H_2O]$ (g/L)	30
$[Ag_2S]$ (g/L)	0.4
$ZnSO_4 \cdot 7H_2O$ (g/L)	0.33, 0.44, 0.55, 1.1, 2.2. 3.3
$FeSO_4 \cdot 7H_2O$ (g/L)	0.25, 0.5, 0.75, 1.0, 1.5, 2.0
Temperature (K)	298
Agitation Speed (RPM)	700
pH	≈ 8
Solution volume (L)	0.5

The experimental pH and temperature conditions were selected based on the literature, which indicates that thiosulfate remains stable at ambient temperature, preventing unnecessary degradation (Alvarado *et al*., 2015). Additionally, it has been reported that pH values exceeding the 8–9 range negatively impact the process by promoting the formation of undesirable species (Deutsch, 2012; Xu *et al*., 2017).

3 Results

3.1 Eh - pH diagrams

The following section presents the thermodynamic analysis of the systems examined in this research by constructing Eh–pH diagrams. In addition, Table 2 shows the reactions involved in the thermodynamic analysis along with their log(K) values, where log(K) represents the logarithm of the equilibrium constant associated with each reaction. These values, determined using HSC Chemistry 6 software, indicate the thermodynamic favorability of the reactions, with higher log(K) values suggesting more spontaneous processes under the studied conditions.

The Pourbaix diagram in Figure 1 illustrates the species present in the thiosulfate–silver medium at different potential and pH values. On one hand, Figure (1a) shows the different by products generated from the oxidative process of thiosulfate, including tetrathionate ($S_4O_6^{2-}$), dithionate ($S_2O_6^{2-}$), and persulfate ($S_2O_8^{2-}$), while Figure (1b) presents the formation of thiosulfate–silver complexes such as $AgS_2O_3^-$ and $Ag(S_2O_3)_2^{3-}$. Additionally, the formation of silver sulfites is observed, including $AgSO_3^-$, $Ag(SO_3)_2^{3-}$, and $Ag(SO_3)_3^{5-}$. Likewise, according to the studies by Melashvili *et al*., 2015, and Ou *et al*., 2023, the oxidation of thiosulfate in the presence of oxygen and in an alkaline medium favors the formation of trithionate and tetrathionate. Both compounds can regenerate thiosulfate molecules, as shown in Eq (2). However, as observed in Eq (3), trithionate leads to the formation of sulfite ions (SO_3^{2-}), which, upon oxidation, are transformed into sulfate (SO_4^{2-}), as described in Eq (4). The latter represents the final product of thiosulfate oxidation.

The Eh–pH diagrams in Figure 2 present the stability regions of the aqueous species in the systems S_2O_3–Ag–Cu^{2+}, S_2O_3–Ag–Zn^{2+}, S_2O_3–Ag–Fe^{2+}, and S_2O_3–Ag–Pb^{2+}. In the S_2O_3–Ag - Cu^{2+} system (Figure 2a), three thiosulfate–silver complexes ($AgS_2O_3^{2-}$, $Ag(S_2O_3)_2^{3-}$, and $Ag(S_2O_3)_3^{5-}$) are identified, with $Ag(S_2O_3)_3^{5-}$ being the predominant species at pH ≈ 8 and under oxidizing potentials, which requires a higher concentration of thiosulfate (Eq 7). As the system's ORP increases, the oxidative degradation of thiosulfate is favored, leading to the formation of species such

Table 2 Equilibrium constants and associated equations of the reactions in the thiosulfate system.

Equation	log (K)	Eq.
$2S_2O_3^{2-} + 0.5O_2 + H_2O \rightarrow S_4O_6^{2-} + 2OH^-$	28.171	(1)
$4S_4O_6^{2-} + 6OH^- \rightarrow 5S_2O_3^{2-} + 2S_3O_6^{2-} + 3H_2O$	10.044	(2)
$2S_3O_6^{2-} + 6OH^- \rightarrow S_2O_3^{2-} + 4SO_3^{2-} + 3H_2O$	55.685	(3)
$SO_3^{2-} + 0.5O_2 \rightarrow SO_4^{2-}$	90.344	(4)
$2S_2O_3^{2-} + Ag^+ \rightarrow Ag(S_2O_3)_2^{3-}$	10.997	(5)
$S_2O_3^{2-} + Ag^+ \rightarrow AgS_2O_3^-$	8.5	(6)
$3S_2O_3^{2-} + Ag^+ \rightarrow Ag(S_2O_3)_3^{5-}$	14.2	(7)
$S_2O_3^{2-} + Ag^+ + 3H_2O \rightarrow 6H^+ + 4e^- + Ag(SO_3)_2^{3-}$	-36.2	(8)
$S_2O_3^{2-} + 2Ag^+ + 3H_2O \rightarrow 6H^+ + 4e^- + 2Ag(SO_3)^-$	-17.09	(9)
$S_2O_3^{2-} + Cu^+ + e^- \rightarrow CuS_2O_3^-$	12.93	(10)
$Cu^{2+} + 2H_2O \rightarrow 2H^+ + Cu(OH)_2$	-6.401	(11)
$Cu^{2+} + 3H_2O \rightarrow 3H^+ + Cu(OH)_3^-$	-25.38	(12)
$S_2O_3^{2-} + 2Cu^{2+} + 3H_2O \rightarrow 6H^+ + 2e^- + 2CuSO_3^-$	-12.06	(13)
$S_2O_3^{2-} + Cu^{2+} + 3H_2O \rightarrow 6H^+ + 3e^- + 2Cu(SO_3)_2^{3-}$	-33.95	(14)
$S_2O_3^{2-} + Zn^{2+} \rightarrow ZnS_2O_3$	2.3	(15)
$S_2O_3^{2-} + Fe^{2+} \rightarrow FeS_2O_3^+ + e^-$	-11.04	(16)
$S_2O_3^{2-} + Pb^{2+} \rightarrow PbS_2O_3$	5.634	(17)

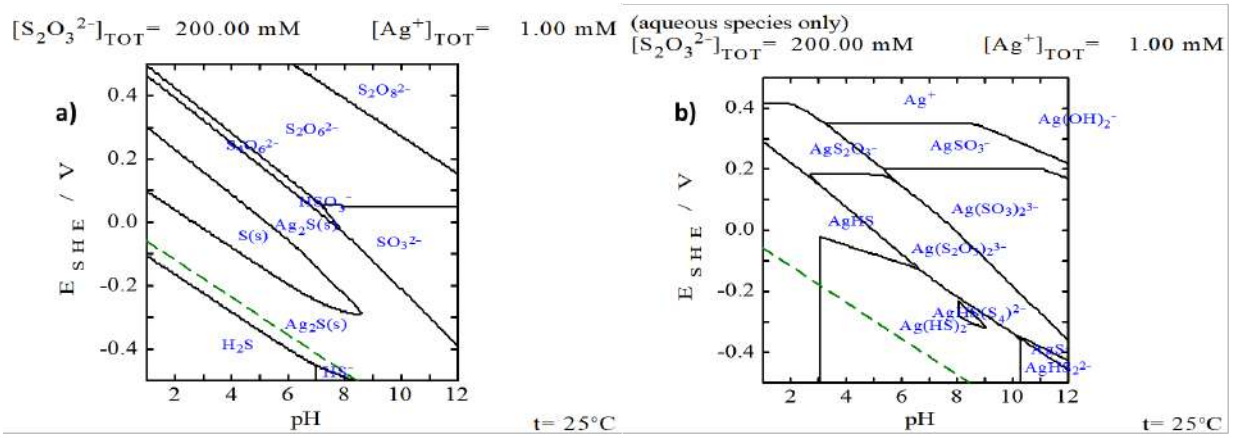

Figure 1 Eh–pH Diagram of the $S_2O_3^{2-}$–Ag system.

as silver sulfite. Similarly, the Pourbaix diagram in Figure (3a) shows the formation of the $CuS_2O_3^-$ complex, which is stable under the same Eh and pH conditions as the thiosulfate–silver complexes, highlighting the competition between Cu^{2+} and Ag^+ ions for the complexing agent. At reducing potentials and neutral to alkaline pH, solids such as CuS and Cu_2S are formed, evidencing copper precipitation. Previous studies indicate that Cu^{2+} ions act as catalysts in silver leaching with thiosulfate; however, chelating agents such as NH_3 (ammonia), EDTA (ethylenediaminetetraacetic acid), and MEA (monoethanolamine) have been used. These agents stabilize copper ions and prevent their precipitation, optimizing the efficiency of the process (Bruez *et al*., 2024; Puente *et al*., 2013; 2017; 2021; Xiang *et al*., 2020; Rezaee *et al*., 2023). Finally, thiosulfate decomposition produces S^0 (elemental sulfur), which can passivate the mineral surface.

In the Zn^{2+}–S_2O_3–Ag system (Figure 2b), the $Ag(S_2O_3)_2^{3-}$ complex predominates at pH ≈ 8 and moderately oxidizing potentials, but a lower concentration of thiosulfate is required compared to the system in the presence of Cu^{2+}. Although the formation of the ZnS_2O_3 complex is observed (Figure 3b), its stability zone is limited due to its lower equilibrium constant (log K = 2.33, Eq. 15) compared to $CuS_2O_3^-$ (log K = 12.93, Eq. 10). Furthermore, under reducing conditions and neutral to alkaline pH, ZnS precipitates are observed, while in more oxidizing environments, ZnO may form.

In the S_2O_3–Ag–Fe^{2+} system (Figure 2c), the stability of the $Ag(S_2O_3)_3^{5-}$ complex is more limited compared to the Cu^{2+} system, due to a greater tendency for thiosulfate oxidation, which favors the formation of $Ag(SO_3)_2^{3-}$ and reduces the stability of the thiosulfate–silver complex. On the other hand, the formation of the FeS_2O_3 complex is not thermodynamically favored (log K = -11.04, Eq. 16),

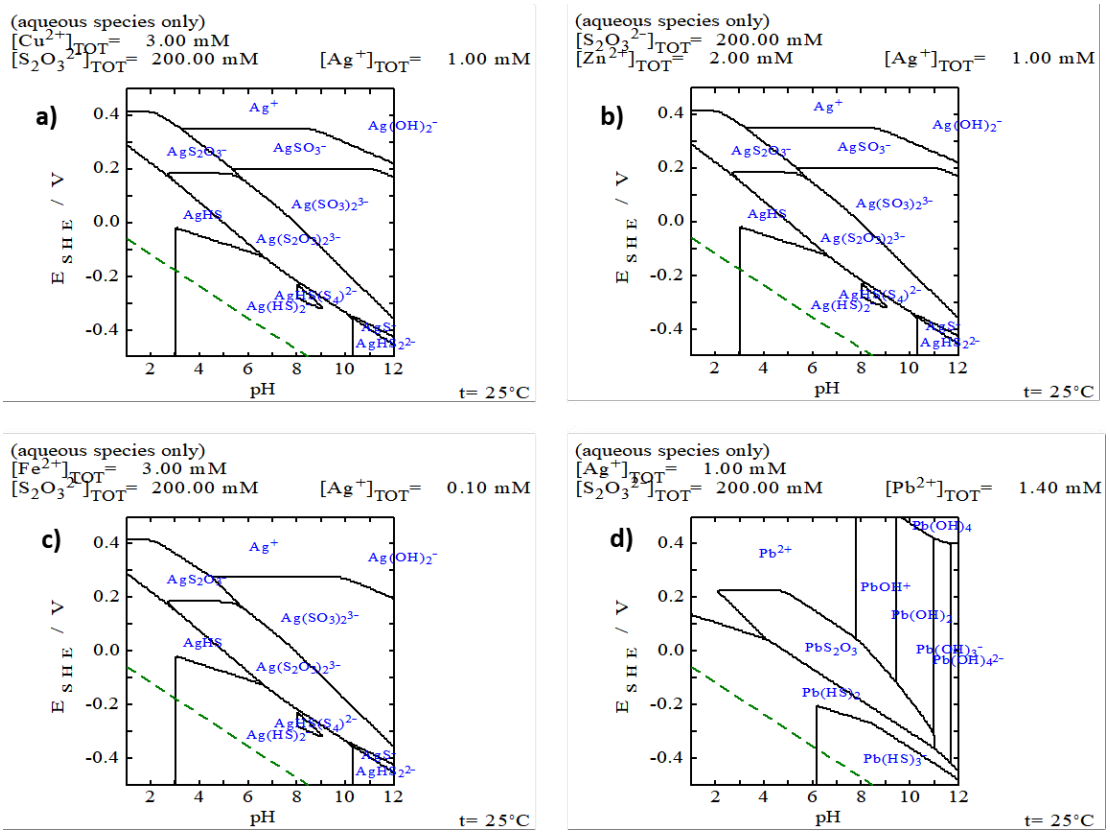

Figure 2. Eh-pH diagrams (aqueous species) of the systems: a) S_2O_3-Ag-Cu^{2+}, b) S_2O_3-Ag-Zn^{2+}, c) S_2O_3-Ag-Fe^{2+}, d) S_2O_3-Ag-Pb^{2+}.

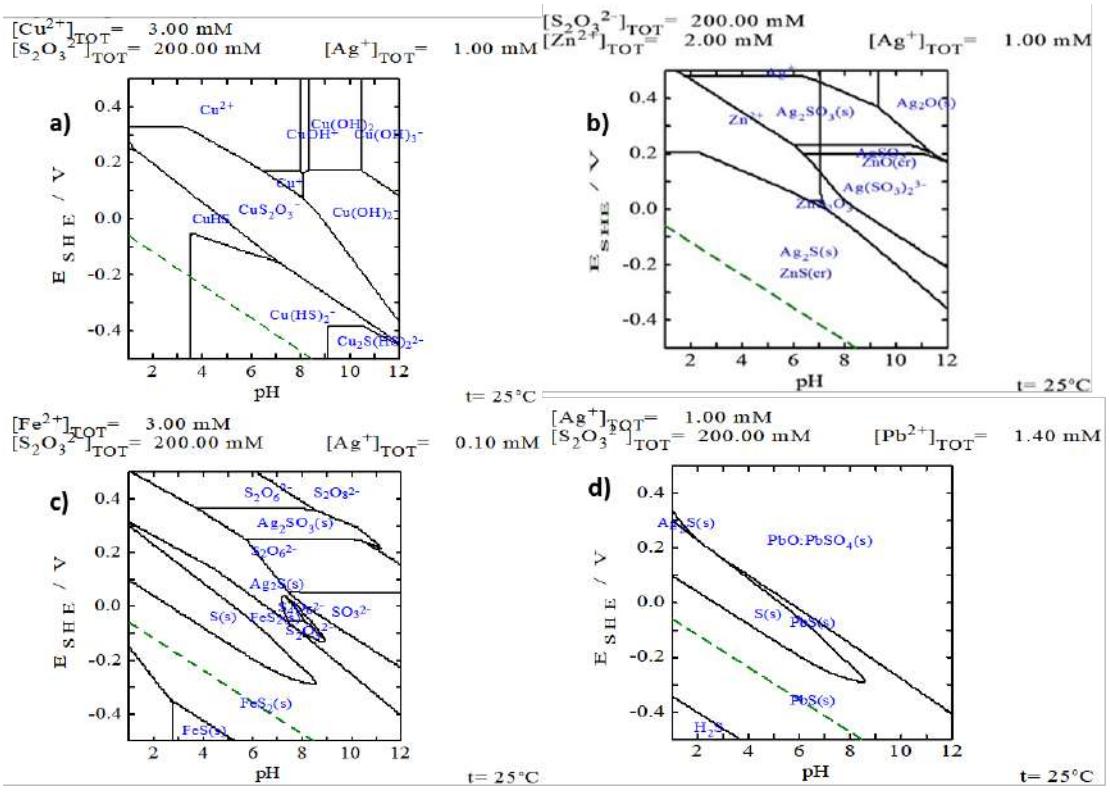

Figure 3 Eh–pH Diagrams of the Systems: a) S_2O_3–Ag–Cu^{2+}, b) S_2O_3–Ag–Zn^{2+}, c) S_2O_3–Ag–Fe^{2+}, d) S_2O_3–Ag–Pb^{2+}.

indicating an unlikely reaction. Instead, species such as HSO_3^- and SO_3^{2-} predominate (Figure 3c). The formation of HSO_3^- is significant, as its acidic nature can reduce the system's pH, altering the experimental conditions and accelerating the decomposition of thiosulfate in the presence of Fe^{2+}.

Finally, the predominant phases of the S_2O_3–Ag–Pb^{2+} system are shown (Figures 2 and 3d). The $AgS_2O_3^-$ and $Ag(S_2O_3)_3^{5-}$ complexes are stable in the presence of Pb^{2+}; however, the PbS_2O_3 complex (Eq. 17) is also formed under similar Eh and pH conditions, suggesting competition between Ag^+ and Pb^{2+} ions for the complexing agent, potentially decreasing the efficiency of Ag leaching. Additionally, under reducing conditions, PbS precipitates are formed, while in oxidizing environments, $PbO \cdot PbSO_4$ is observed (Figure 3d).

3.2 *Leaching tests*

The following section presents the analysis of the effect of different metallic ions (Cu^{2+}, Zn^{2+}, Fe^{2+}, Pb^{2+}) on silver sulfide leaching in the S_2O_3–air–OH system.

3.2.1 *Effect of Cu^{2+} concentration*

Figure 4 shows the performance of AgS dissolution in the presence of Cu^{2+} ions at different concentrations. It is observed that lower concentrations of $CuSO_4$ (0.062 and 0.187 g/L) allow achieving the highest silver leaching percentages, reaching 45.63% at 12 hours and 41.33% at 24 hours, respectively. In contrast, increasing the concentration in the range of 0.25 to 1.0 g/L results in a decrease in silver dissolution, with percentages lower than those obtained in the absence of Cu^{2+}. Concentrations of 0.75 and 1.0 g/L led to the lowest recovery values, reaching only 16.17% and 18.10%, respectively. Additionally, the slopes of the curves corresponding to the lower $CuSO_4$ concentrations are steeper, reflecting a higher dissolution rate.

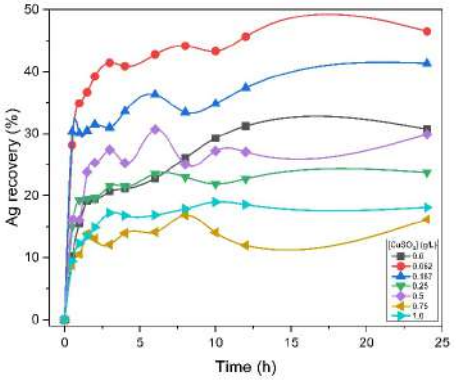

Figure 4 Silver sulfide leaching in the presence of Cu^{2+} ions.

The limitation in the maximum dissolution percentage of silver sulfide can be attributed to the partial decomposition of the complexing agent, followed by undesirable reactions that reduce the contact between the leaching solution and the Ag_2S surface, preventing the complete reaction and dissolution of the sample (eq 23-24).

3.2.2 *Effect of Zn^{2+} concentration*

Figure 5 illustrates the silver sulfide leaching behavior in the presence of different concentrations of zinc sulfate. During the first hour, the percentages of leached silver range between 27% and 33%, reflecting a rapid response of the system to the presence of Zn^{2+} and suggesting a very short or non-existent induction period. This allows the process to progress directly toward the conversion and stability phases. Specifically, concentrations of 0.33 g/L and 0.55 g/L of $ZnSO_4$ showed a sustained increase in silver sulfide dissolution between 12 and 24 hours, reaching a maximum value of 37.83% with 0.33 g/L. This behavior aligns with the findings of Juárez *et al.* (2012), who reported that the presence of Zn^{2+} enhances the silver dissolution rate with thiosulfate. Although the other concentrations analyzed show dissolution percentages similar to the system without Zn^{2+}, none resulted in a value lower than the 30.72% observed in the absence of this ion. Overall, Ag dissolution values remained between 30.8% and 33.76%. These results suggest that, while the increase in silver leaching is not significant, the process rate is notably higher, which implies a reduction in the resources required during experimentation.

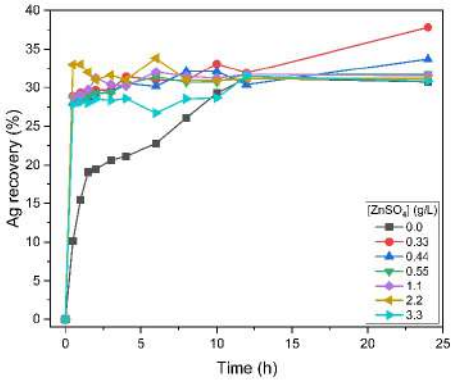

Figure 5 Silver sulfide leaching in the presence of Zn^{2+} ions.

3.2.3 *Effect of Fe^{2+} concentration*

Figure 6 shows the effect of different $FeSO_4$ concentrations (0.0 to 2.0 g/L) on silver sulfide leaching. In the absence of Fe^{2+} (0.0 g/L), a leaching percentage of approximately 35% was achieved after 12 hours of reaction, maintaining good stability

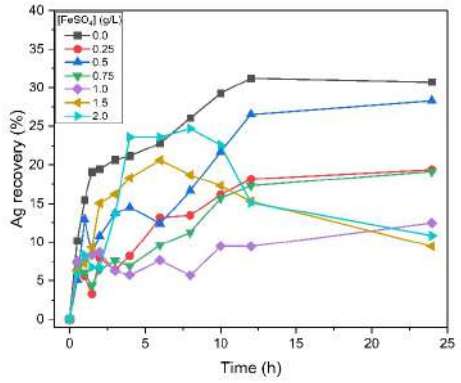

Figure 6 Silver sulfide leaching in the presence of Fe^{2+} ions.

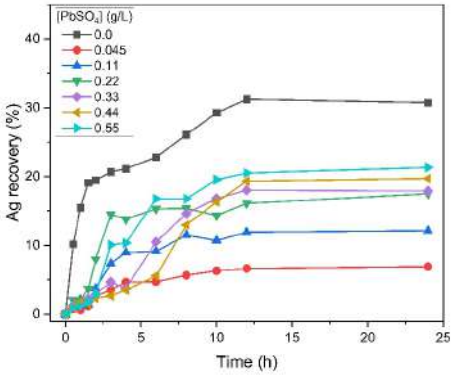

Figure 7 Silver sulfide leaching in the Presence of Pb^{2+} ions.

over time. However, the addition of Fe^{2+} negatively impacted both silver recovery and process stability (pH < 6), with effects varying according to the concentration used. At $FeSO_4$ concentrations between 1.0 and 2.0 g/L, a decrease in process efficiency was observed. At 1.0 g/L, the maximum recovery was 12.4%, while concentrations of 1.5 and 2.0 g/L resulted in values decreasing to 10% and 9%, respectively, after 5 hours. The presence of Fe^{2+} resulted in lower silver leaching efficiencies compared to its absence. This effect is attributed to the thiosulfacide behavior of Fe^{2+} ions, which alter the experimental conditions by increasing the oxidation-reduction potential (ORP) and promoting iron hydrolysis, leading to a gradual decrease in pH. According to Xu *et al*. (2017), the reduction in pH accelerates thiosulfate decomposition, forming elemental sulfur and other sulfur species, thereby reducing the availability of the leaching agent. This phenomenon explains the lower silver recovery observed under these conditions.

3.2.4 *Effect of Pb^{2+} concentration*

Figure 7 shows the effect of different $PbSO_4$ concentrations on silver sulfide dissolution with thiosulfate. In all cases, Ag_2S dissolution in the presence of Pb^{2+} was lower compared to the system without this ion. The maximum silver leaching percentage, 21.3%, was achieved after 24 hours of reaction with a $PbSO_4$ concentration of 0.55 g/L. At lower concentrations, such as 0.045 g/L of $PbSO_4$, silver recovery decreased significantly, reaching only 6.89% over the same period. This behavior suggests that the presence of lead has a significant inhibitory effect on silver sulfide leaching. Overall, the presence of Pb^{2+} not only limits silver sulfide dissolution but also slows down the process, acting as a thiosulfacide cation.

Given that the presence of certain ions in thiosulfate-based leaching systems can negatively affect silver extraction, the implementation of a staged leaching process is suggested. This approach would allow for the selective removal of species that may act as thiosulfate consuming agents, either by decomposing thiosulfate, generating undesirable reactions, or increasing its consumption (Ruíz & Lapidus, 2017). Table 3 presents several systems that have been studied with the aim of selectively extracting some of these cations.

3.3 *Characterization of solid residues by XRD*

The solid residues analyzed correspond to the precipitates obtained directly from the leaching experiments, which were subsequently filtered and dried before characterization.

3.3.1 *$Ag_2S - S_2O_3 - Cu$ system*

Figure 8 shows the diffractogram of the solid residues obtained during the silver sulfide leaching process with thiosulfate in the presence of Cu^{2+} ions. Characteristic peaks of silver sulfide (Ag_2S), copper(II) sulfide (CuS), copper(II) oxide (CuO), and elemental sulfur (S) are observed.

The reaction mechanism for silver sulfide leaching in the Ag_2S–$S_2O_3^{2-}$–Cu^{2+} system is based on the species identified through XRD, thermodynamic analysis, and experimental results. This mechanism is described as follows:

Silver sulfide dissociates (Eq. 18), releasing silver ions (Ag^+) and sulfide S^{2-}, which can subsequently be converted to elemental sulfur either by oxidation (Eq. 19) or through thiosulfate decomposition.

$$Ag_2S \rightarrow 2Ag^+ + S^{2-} \quad (18)$$

$$S^{2-} \rightarrow S^0 + 2e^- \quad (19)$$

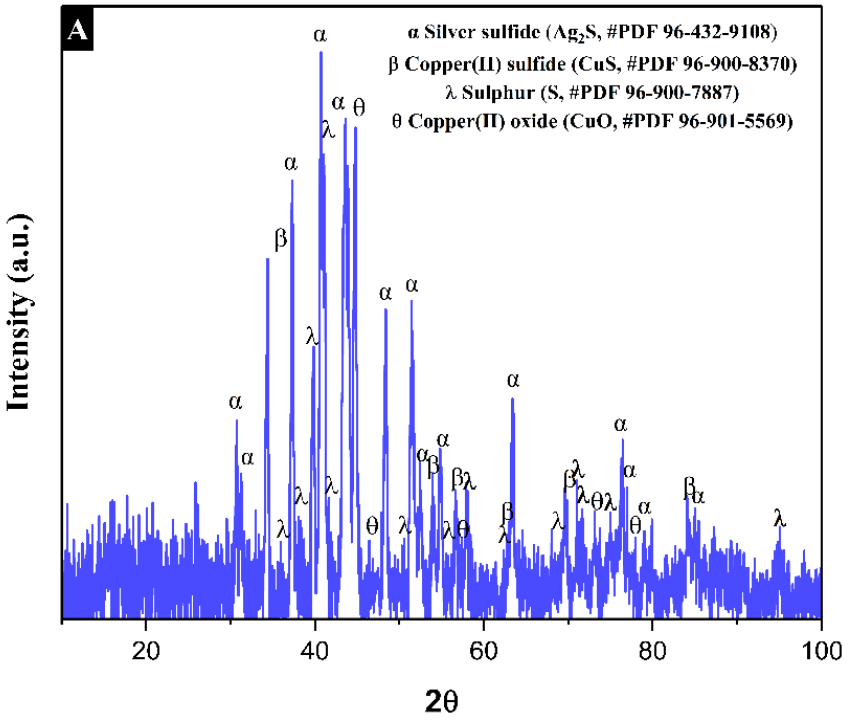

Figure 8 Diffractogram of the Leaching Residues from the Ag_2S–$S_2O_3^{2-}$–Cu System.

Table 3 Comparative Analysis of Selective Leaching Systems for Iron, Copper, Zinc, and Lead from Different Mineral Phases.

Element	Phase	System used	Reference
Iron (Fe) and Copper (Cu)	Chalcopyrite ($CuFeS_2$)	Two-stage leaching: (1) Oxalic acid + H_2O_2 to selectively dissolve iron, leaving copper in the matrix; (2) H_2SO_4 + H_2O_2 + ethylene glycol to extract copper without iron interference.	Ruiz-Sánchez & Lapidus, 2022
Copper (Cu)	Cuprite (Cu_2O) and Tenorite (CuO)	Advanced oxidation with sulfate radicals ($Na_2S_2O_8$) + acidic leaching.	Zuo *et al.*, 2023
Iron (Fe) and Lead (Pb)	Galena (PbS) and Pyrite (FeS_2)	Sodium citrate + H_2O_2 at pH 8 to selectively dissolve lead, followed by (2) pH adjustment to 5 to dissolve iron.	Torres & Lapidus, 2020; Calla *et al.*, 2024
Zinc (Zn)	Sphalerite, Wurtzite, and ZnO	H_2SO_4 at 90°C (a), at 30 °C (b)	(a) Xin *et al.*, 2022, (b) Borda *et al.*, 2021
Iron (Fe)	Goethite (FeOOH), Hematite (Fe_2O_3), Magnetite (Fe_3O_4)	H_2SO_4 + SO_2 / Organic acids (citric, oxalic)	Senanayake *et al.*, 2011
Zinc (Zn)	Sphalerite	Citrate – $Fe(NO_3)_3$ at 90°C	Nikkhou *et al.*, 2019
Lead (Pb)	Cerrusite ($PbCO_3$), Anglesite ($PbSO_4$)	EDTA at 25°C	Fin-gar & Letan, 2007
Zinc (Zn)	ZnO	Ultrasound-Enhanced NH_3-NH_4Cl-H_2O	Ma *et al.*, 2024

The available Ag ions (Eq. 18) can form complexes with thiosulfate in solution, as shown in Eq. 20. The $Ag(S_2O_3)_3^{5-}$ complex is the predominant phase indicated in Figure 2, considering the process described in Eq. 19:

$$2Ag^+ + 6S_2O_3^{2-} \rightarrow 2Ag(S_2O_3)_3^{5-} + S^0 + 2e^- \quad (20)$$

In parallel, dissolved oxygen is reduced to partially produce hydrogen peroxide (Eq. 21), which is subsequently reduced to produce OH^- ions (Eq. 22):

$$O_{2(ac)} + 2H_2O + 2e^- \rightarrow H_2O_2 + 2OH^- \quad (21)$$

$$H_2O_2 + 2e^- \rightarrow 2OH^- \quad (22)$$

On the other hand, Cu^{2+} ions in solution react with thiosulfate to form the $CuS_2O_3^-$ complex, as shown in Eq. 23. Additionally, these ions can react with the generated products to form copper(II) oxide (CuO) and copper(II) sulfide (CuS), as reported by Senanayake (2005), which are the result of thiosulfate decomposition into elemental sulfur (S^0) and sulfate (SO_4^{2-}), as described in Eqs. 24 and 25.

$$Cu^{2+} + S_2O_3^{2-} + e^- \rightarrow CuS_2O_3^- \quad (23)$$

$$Cu^{2+} + S_2O_3^{2-} + 2OH^- \rightarrow CuS_{(s)} + SO_4^{2-} + H_2O \quad (24)$$

$$Cu^{2+} + 2OH^- \rightarrow CuO + H_2O \quad (25)$$

Considering Eqs. 20 to 25, the following overall equation is proposed to describe the thiosulfate–silver sulfide–copper system (Eq. 26):

$$5Ag_2S + 33S_2O_3^{2-} + 4Cu^{2+} + 2O_2 + 2H_2O \rightarrow 10Ag(S_2O_3)_3^{5-} + 2CuS_2O_3^- + CuO + CuS_{(s)} + 5S + SO_4^{2-} + 4OH^- \quad (26)$$

Numerous studies support the use of Cu^{2+} ions as catalysts in silver leaching, highlighting their ability to enhance precious metal dissolution (Benijamali *et al*., 2021). However, the effectiveness of this catalyst critically depends on its concentration in the leaching solution. At elevated concentrations, undesirable reactions occur, including the formation of copper–thiosulfate complexes and precipitates such as CuS, CuO, and elemental sulfur (S^0), which may deposit on the Ag_2S surface and form passivating layers that hinder reactivity—thereby limiting process efficiency even in the presence of excess lixiviant. Furthermore, in continuous or closed systems, CuO accumulation within the leaching circuit can alter process dynamics and compromise both chemical stability and silver recovery. The findings of this study provide key insights into the dual role of Cu^{2+} in these systems and inform strategies to mitigate its adverse effects. For instance, the use of chelating agents such as EDTA can prevent precipitate formation, while sequential copper removal or the addition of stabilizing agents like ammonia or glycine may enhance overall system performance (Barrios *et al*., 2024; Bruez *et al*., 2024; Hao *et al*., 2023).

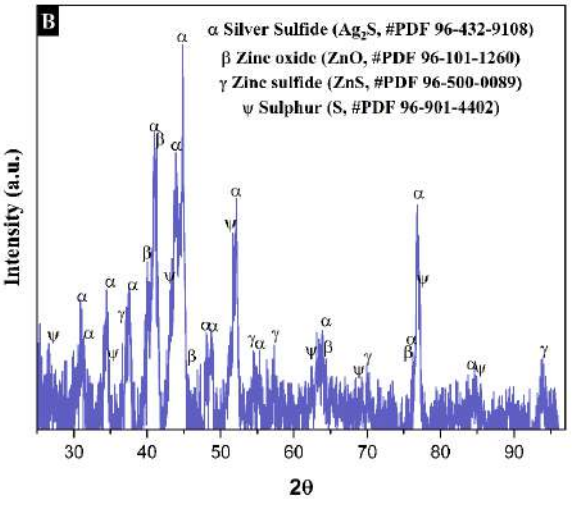

Figure 9 Diffractogram of the Leaching Residues from the Ag_2S–$S_2O_3^{2-}$– Zn System.

3.3.2 $Ag_2S - S_2O_3 - Zn$ system

The diffractogram corresponding to the solid residues of the $S_2O_3^{2-}$–Ag_2S–Zn^{2+} system, presented in Figure 9, reveals characteristic peaks of silver sulfide (Ag_2S), which did not react with the leaching agent, zinc oxide (ZnO), zinc sulfide (ZnS), and elemental sulfur (S).

The dissociation process proceeds as shown in Eqs. 18 and 19. According to the thermodynamic study, Ag^+ ions form complexes with thiosulfate in solution in the presence of Zn^{2+} ions (Figure 2b), as shown in Eq. (27). In parallel, Zn^{2+} ions and thiosulfate react according to Eq. (28) (Figure 3b):

$$2Ag^+ + 4S_2O_3^{2-} \rightarrow 2Ag(S_2O_3)_2^{3-} + S^0 + 2e^- \quad (27)$$

$$Zn^{2+} + S_2O_3^{2-} + 2OH^- \rightarrow ZnS + SO_4^{2-} + H_2O \quad (28)$$

In turn, zinc in solution reacts with hydroxide ions (OH^-) to form zinc hydroxides ($Zn(OH)_4^{2-}$), as described in Eqs. 29 and 30. However, Eq. 31 outlines how the reaction in Eq. 30 leads to the formation of zinc oxide (ZnO) (Ismail *et al*., 2016):

$$O_2 + 2H_2O + 4e^- \rightarrow 4OH^- \quad (29)$$

$$Zn + 4OH^- \rightarrow Zn(OH)_4^{2-} + 2e^- \quad (30)$$

$$Zn(OH)_4^{2-} \leftrightarrow ZnO + H_2O + 2OH^- \quad (31)$$

From Eqs. 27 to 31, the overall equation for the S_2O_3–Ag_2S–Zn system in solution is established (Eq. 32). It is noteworthy that the required S_2O_3:Ag_2S ratio in this case is 5:1, which is lower than that of the copper system (6.6:1). This finding explains the higher initial reaction rate, as the consumption of the complexing agent is lower. Consequently, the concentration of thiosulfate becomes particularly relevant as a critical

factor in the leaching of precious metals (Godigamuwa & Okibe, 2023).

$$Ag_2S + 2ZnSO_4 + 5S_2O_3^{2-} + O_2 \rightarrow 2Ag(S_2O_3)_2^{3-} + ZnS + ZnO + S + 3SO_4^{2-} \quad (32)$$

Unlike Cu^{2+}, Zn^{2+} ions exhibit low thermodynamic affinity for thiosulfate, which limits its degradation and enhances the stability of the complexing agent. This creates a more favorable chemical environment, allowing for a faster initial leaching rate compared to other systems, such as that involving copper. However, despite this favorable kinetics, silver extraction stabilizes at moderate levels. This behavior suggests that the limiting factor is not thiosulfate availability, but the gradual formation of products such as ZnS and elemental sulfur (S^0), which deposit into the Ag_2S surface. These species may form passivating layers that hinder the lixiviant's access to the mineral, acting as kinetic barriers that restrict further leaching. As a result, even in chemically active conditions, the surface reactivity of Ag_2S becomes compromised, leading to a self-limiting process. At the industrial level, controlling parameters such as Zn^{2+} concentration, pH, and redox potential is critical to minimizing the precipitation of interfering species. If these effects are significant, strategies like the HNO_3–Fe^{3+}–citrate system (Nikkhou *et al*., 2019) can be applied for selective zinc removal prior to silver leaching.

3.3.3 $Ag_2S - S_2O_3 - Fe$ system

In Figure 10, corresponding to the diffractogram of the leaching residues of Ag_2S in the presence of Fe, phases corresponding to Ag_2S, FeO_2H, and S were identified.

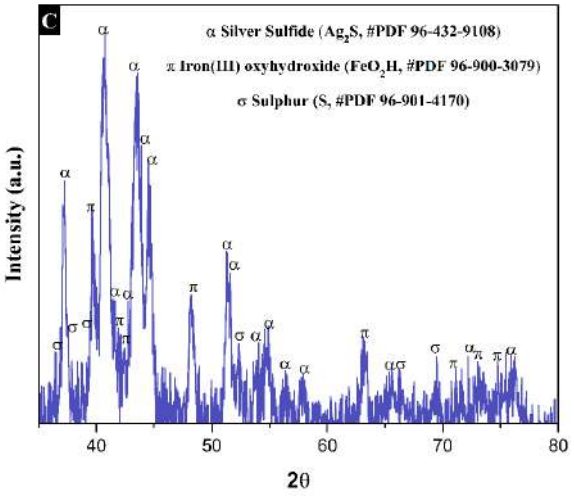

Figure 10 Diffractogram of the Leaching Residues from the S_2O_3–Ag_2S–Fe System.

In this case, the dissociation of Ag_2S proceeds as described in Eqs. 18 and 19. Furthermore, as observed in the results of Figure 2c, the formation of the $Ag(S_2O_3)_3^{5-}$ complex is represented by Eq. 20. On the other hand, the oxidation of Fe(II) to Fe(III) occurs through a coupled hydrolysis and precipitation process, represented by Equation 33. This mechanism generates cationic species that explain the pH decrease observed during the experimental process (Tabakova *et al*., 1996). Additionally, as this is a redox process in the presence of dissolved oxygen—directly injected into the system—the conversion of Fe^{2+} to Fe^{3+} contributes to the increase in the oxidation-reduction potential (ORP), by removing a reducing agent (Fe^{2+}) and forming more oxidizing species. This reaction is considered the predominant pathway in the system, as X-ray diffraction (XRD) analysis confirmed the presence of FeOOH as the stable solid product.

$$FeSO_4 + 2H_2O \rightarrow FeOOH + 3H^+ + SO_4^{2-} + e^- \quad (33)$$

Although ferric iron tends to hydrolyze and contribute to acidification of the medium, the system was not maintained under acidic conditions. On the contrary, periodic pH adjustments were made to keep it within a neutral to slightly alkaline range, favoring the formation of FeOOH over less stable phases. This explains the absence of Fe(OH)- in the solid residues and the prevalence of FeOOH as the dominant precipitate under buffered conditions. Nonetheless, under transient, locally acidic conditions, additional reactive pathways may occur, such as the hydrolysis equilibria of Fe^{2+}:

$$Fe^{2+} + H_2O \rightarrow Fe(OH)^+ + H^+ \quad (34)$$

$$Fe(OH)^+ + H_2O \rightarrow Fe(OH)_2 \quad (35)$$

$$8Fe^{2+} + 5O_2 + 14H_2O \rightarrow 8Fe(OH)_{3(s)} + 4H^+ \quad (36)$$

With the increase in acidity in the leaching system, the decomposition of the complexing agent is favored, as described in Eqs. 37 to 40. Simultaneously, Eq. 40 represents the reduction process of dissolved O_2 under the specific conditions of the system:

$$0.5S_2O_3^{2-} \rightarrow 2H^+ + HSO_3^- + 2e^- \quad (37)$$

$$3H^+ + 2e^- + 0.5S_2O_3^{2-} \rightarrow S_{(s)} \quad (38)$$

$$S_2O_3^{2-} + H^+ \rightarrow HSO_3^- + S_{(s)} \quad (39)$$

$$O_2 + 4H^+ + 4e^- \rightarrow 2H_2O \quad (40)$$

Considering the redox processes involved in the system, along with the degradation of the complexing agent due to the pH decrease, the overall equation for Ag leaching with thiosulfate in the presence of Fe^{2+} ions is proposed in Eq. 41:

$$4Ag_2S + 25S_2O_3^{2-} + 4Fe^{2+} + 2H_2O + 3O_2 + H^+ \rightarrow 8Ag(S_2O_3)_3^{5-} + 4FeOOH + HSO_3^- + 5S \quad (41)$$

Taken together, these processes, whether through direct oxidation of Fe^{2+} or partial hydrolysis, lead to localized acidification of the medium, which significantly compromises thiosulfate stability. The decomposition of the complexing agent under these conditions results in the generation of elemental sulfur (S^0), which may accumulate on the Ag_2S surface and form passivating layers that hinder further reaction. This dual effect, the loss of the active lixiviant and surface blockage, provides a compelling explanation for the low silver extraction observed in the presence of Fe^{2+}, which was the least efficient system despite the controlled pH conditions. At larger scales, Fe^{2+} presents substantial operational challenges due to its high reactivity in thiosulfate media. It disrupts the chemical equilibrium of the solution, accelerates lixiviant degradation, and promotes the formation of solid precipitates. These solids not only increase reagent consumption but also hinder silver recovery, complicate waste handling, and interfere with the control of key parameters such as pH and ORP. For this reason, strategies such as the oxalic acid–H_2O_2–ethyleneglycol system (Ruíz & Lapidus, 2020) are essential for selectively dissolving iron compounds, minimizing precipitate accumulation, and enhancing overall process stability in industrial applications.

3.3.4 $S_2O_3 - Ag_2S - Pb$ system

In the S_2O_3–Ag_2S–Pb^{2+} system, the analysis of solid residues by XRD (Figure 11) reveals the presence of phases such as silver sulfide (Ag_2S), lead oxide (PbO), lead sulfide (PbS), and elemental sulfur (S^0).

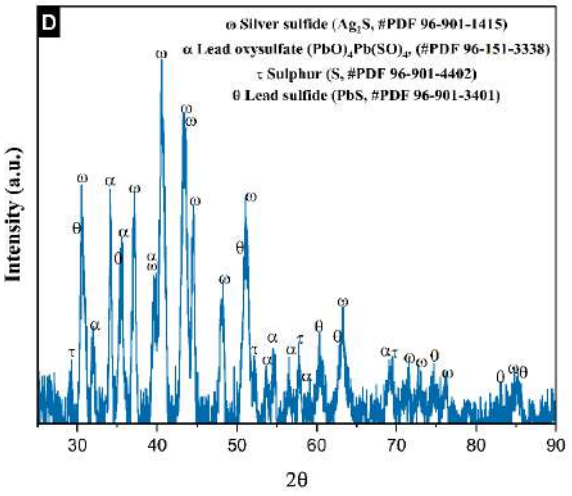

Figure 11 Diffractogram of the Leaching Residues from the S_2O_3–Ag_2S–Pb System.

These results suggest that the leaching process is strongly affected by secondary reactions that promote the formation of passivating layers. According to the thermodynamic analysis and the results in Figure 2d, silver ions form thiosulfate complexes as described in Eq. 20. Simultaneously, Pb^{2+} ions interact with thiosulfate to produce $PbO \cdot PbSO_4$, as shown in Eq. 42, contributing to the accumulation of stable solid phases.

$$S_2O_3^{2-} + 4Pb^{2+} + 7H_2O \rightarrow 2PbO \bullet PbSO_4 + 14H^+ + 8e^- \quad (42)$$

Considering the reduction of dissolved oxygen (Eq. 29), the net redox process is proposed in Eq. 43:

$$Ag_2S + 7S_2O_3^{2-} + 4PbSO_4 + 2.5O_2 + 2H_2O \rightarrow 2Ag(S_2O_3)_3^{5-} + 2PbO \bullet PbSO_4 + 4SO_4^{2-} + S + 4H^+ \quad (43)$$

On the other hand, thiosulfate decomposition in alkaline conditions, as reported by Melashvili *et al.* (2015), leads to the formation of sulfide ions (S^{2-}) and the oxidation of sulfite to sulfate (Eqs. 44 and 45). These species react with Pb^{2+}, precipitating as lead sulfide (PbS), as supported by Chen *et al.* (2014):

$$2S_2O_3^{2-} + 6OH^- \rightarrow 4SO_3^{2-} + 2S^{2-} + 3H_2O \quad (44)$$

$$SO_3^{2-} + 0.5O_2 \rightarrow SO_4^{2-} \quad (45)$$

$$S^{2-} + Pb^{2+} \rightarrow PbS \quad (46)$$

These reactions are consolidated in Eq. 47, which describes the mechanism of Ag_2S leaching in the presence of Pb^{2+}:

$$4Ag_2S + 10S_2O_3^{2-} + 6PbSO_4 + 4.5O_2 + 6OH^- \rightarrow 2Ag(S_2O_3)_3^{5-} + 2PbS + 2PbO \bullet PbSO_4 + 10SO_4^{2-} + S + 4H^+ + H_2O \quad (47)$$

The formation of PbS, $PbO.PbSO_4$, and elemental sulfur (S^0) indicates the development of passivating layers on the mineral surface that inhibit silver dissolution and reduce process efficiency. This is consistent with the results in Figure 7, where silver recovery appears limited despite the presence of excess thiosulfate. These passivating phases restrict the accessibility of the lixiviant to reactive sites, representing a major kinetic limitation.

In industrial applications, the presence of Pb^{2+} presents multiple challenges. It increases thiosulfate consumption through side reactions, complicates silver recovery due to co-precipitation, and reduces the purity of the final product. Furthermore, the persistence of Pb in leaching tailings raises environmental and regulatory concerns due to its toxicity. To mitigate these effects, Alonso & Lapidus (2009) proposed the addition of phosphate, which decreases Pb^{2+} solubility during leaching. Additionally, citrate-based leaching systems combined with hydrogen peroxide have been shown to selectively extract Pb while minimizing its interference in silver recovery, as demonstrated by Torres *et al.* (2018). Implementing such strategies

improves process efficiency and product quality while reducing environmental liabilities and treatment costs.

The results obtained in this study confirm the predictions made through the thermodynamic analysis. The Eh-pH diagrams (Section 3.1) provided insight into the stability regions of the silver-thiosulfate complexes and the potential interactions of Cu^{2+}, Zn^{2+}, Fe^{2+}, and Pb^{2+} in the system. These predictions were validated by the leaching experiments (Section 3.2), which demonstrated that Cu^{2+} at low concentrations and Zn^{2+} favor silver dissolution, while Fe^{2+} and Pb^{2+} negatively affect the process by promoting thiosulfate decomposition or forming passivating layers. The XRD analysis (Section 3.3) further confirmed these findings, identifying the formation of solid phases such as CuS, ZnO, FeOOH, and $PbO \cdot PbSO_4$, which were consistent with the species predicted in the thermodynamic modeling. These results highlight the importance of considering both thermodynamic stability and experimental validation when designing leaching processes for complex systems. Additionally, the information presented in Table 3 reinforces the relevance of selective dissolution approaches for problematic cations, providing a framework for optimizing multi-stage leaching strategies.

Conclusions

In this research, the effect of different metallic ions on the silver sulfide leaching process with thiosulfate was analyzed, yielding the following findings:

(1) The dual influence of Cu^{2+} in thiosulfate leaching was confirmed, acting as a catalyst at low concentrations and as a thiosulfacide species at higher concentrations. Its control is key to optimizing silver recovery.

(2) Zn^{2+} ions enhance the dissolution kinetics of Ag_2S without significantly affecting the final silver recovery, representing an advantage in terms of lixiviant stability and process efficiency.

(3) Fe^{2+} and Pb^{2+} exhibited negative effects on Ag leaching, promoting thiosulfate degradation and the formation of passivating layers, thereby reducing process efficiency.

(4) The efficiency of the silver sulfide leaching process is closely linked to the chemical stability of thiosulfate and the surface reactivity of the mineral. The generation of decomposition products such as elemental sulfur, as well as the precipitation of metal sulfides or oxides, can lead to passivating layers that inhibit the lixiviant–mineral interaction. This behavior, observed in systems containing Fe^{2+} and Pb^{2+}, is also evident with Cu^{2+} and Zn^{2+} at higher concentrations, where they contribute to thiosulfate degradation or surface passivation. These effects are analogous to the action of cyanide-consuming metals (cyanicides) in conventional leaching systems. Therefore, it is proposed that these interfering species be conceptually classified as "thiosulfacide metals," given their capacity to reduce silver recovery and their importance for guiding pre-treatment strategies in polymetallic ores.

Acknowledgements

The authors of this article extend their gratitude to the Universidad Autónoma del Estado de Hidalgo for providing the facilities required to conduct the experimentation. Additionally, they thank the Secretaría de Ciencia, Tecnología, Humanidades e Innovación (SeCiTHI)for the financial support provided.

References

Alarcon, A., Segura, C., Gamarra, C., & Rodriguez-Reyes, J. C. F. (2018). Green chemistry in mineral processing: chemical and physical methods to enhance the leaching of silver and the efficiency in cyanide consumption. Pure and Applied Chemistry, 90(7), 1109-1120. https://doi.org/10.1515/pac-2017-0904

Alonso, A. R., & Lapidus, G. T. (2009). Inhibition of lead solubilization during the leaching of gold and silver in ammoniacal thiosulfate solutions (effect of phosphate addition). Hydrometallurgy, 99(1-2), 89-96. https://doi.org/10.1016/j.hydromet.2009.07.010

Alvarado, G., Fuentes-Aceituno, J. C., & Nava-Alonso, F. (2015). Silver leaching with the thiosulfate–nitrite–sulfite–copper alternative system. Hydrometallurgy, 152, 120-128. https://doi.org/10.1016/j.hydromet.2014.12.017

Asencios, Y. J., Martínez, J. C., & Rodríguez, A. (2022). Biosorción de metales pesados utilizando algas marinas modificadas químicamente. Revista Mexicana de Ingeniería Química, 21(1), 157–170. https://rmiq.org/iqfvp/Numbers/V21/No1/IA2600.pdf

Barrios, J. M. H., Flores, G. C., Tapia, J. C. J., Ruíz, A. M. T., Ortiz, O. J. H., & García, F. L. (2024).

Efecto sinérgico de tiosulfato de sodio y glicina en la lixiviación de plata, utilizando peróxido de hidrógeno como oxidante y etilenglicol, en una muestra polimetálica de Zimapán: influencia de la temperatura. Tópicos de Investigación en Ciencias de la Tierra y Materiales, 11(11), 46-52. https://doi.org/10.29057/aactm.v11i11.13140

Borda, J., Torres, R., & Lapidus, G. Selective leaching of zinc and lead from electric arc furnace dust using citrate and H2SO4 solutions. A kinetic perspective Lixiviación selectiva de zinc y plomo del polvo de un horno de arco eléctrico utilizando soluciones de citrato y H2SO4. Una perspectiva cinética. https://doi.org/10.24275/rmiq/Cat2606

Bruez, C., Rousseau, A., Lefèvre, G., & Monteux, C. (2024). Investigation of the use of foams for silver leaching using the thiosulfate-copper (II)-ammonia system in the context of e-waste recycling. Hydrometallurgy, 225. https://doi.org/10.1016/j.hydromet.2024.106279

Calla, D., Pantaleón, D. M., & Lapidus, G. T. (2024). The fate of the sulfide ion in galena leaching with neutral citrate media. Revista Mexicana de Ingeniería Química, 23(3), Artículo IA24304. https://doi.org/10.24275/rmiq/IA24304

Chen, J. H., Li, Y. Q., Lan, L. H., & Guo, J. (2014). Interactions of xanthate with pyrite and galena surfaces in the presence and absence of oxygen. Journal of Industrial and Engineering Chemistry, 20(1), 268-273. https://doi.org/10.1016/j.jiec.2013.03.039

Cos, C. E., & Fuentes, J. C. (2023). Comprehensive Analysis of the Dissolution of Precious Metals with Innovative Amine-Based Leaching Systems. Epistemus (Sonora), 17(34), 32-40. https://doi.org/10.36790/epistemus.v17i34.267

Deutsch, J. L. (2012). Fundamental aspects of thiosulfate leaching of silver sulfide in the presence of additives (Doctoral dissertation, University of British Columbia). https://dx.doi.org/10.14288/1.0072556

Dwivedi, N., & Dwivedi, S. (2021). Sustainable biological approach for removal of cyanide from wastewater of a metal-finishing industry. In Membrane-Based Hybrid Processes for Wastewater Treatment (pp. 463-479). Elsevier. https://doi.org/10.1016/B978-0-12-823804-2.00010-0

Erust, C., Karacahan, M. K., & Uysal, T. (2023). Hydrometallurgical roadmaps and future strategies for recovery of rare earth elements. Mineral Processing and Extractive Metallurgy Review, 44(6), 436-450. https://doi.org/10.1080/08827508.2022.2073591

Godigamuwa, K., & Okibe, N. (2023). Gold leaching from printed circuit boards using a Novel Synergistic Effect of Glycine and Thiosulfate. Minerals, 13(10). https://doi.org/10.3390/min13101270

H.Y., Li., Elsayed, Oraby., Jacques, Eksteen. (2022). Development of an integrated glycine-based process for base and precious metals recovery from waste printed circuit boards. Resources Conservation and Recycling. https://doi.org/10.1016/j.resconrec.2022.106631

Hao, J., Wang, X., Wang, Y., Guo, F., & Wu, Y. (2023). Study of gold leaching from pre-treated waste printed circuit boards by thiosulfate-cobalt-glycine system and separation by solvent extraction. Hydrometallurgy, 221. https://doi.org/10.1016/j.hydromet.2023.106141

Hou, L., Valdivieso, A. L., Robledo-Cabrera, A., Zainiddinovich, N. Z., Wu, C., Song, S., & Jia, F. (2024). Stepwise oxidation of refractory pyrite using persulfate for efficient leaching of gold and silver by an eco-friendly copper (II)-glycine-thiosulfate system. Powder Technology, 448. https://doi.org/10.1016/j.powtec.2024.120323

Ismail, W. M. I. W., Zulkefeli, N. S. W., & Masri, M. N. (2016). A sight of zinc corrosion in various alkaline media. Journal of Tropical Resources and Sustainable Science (JTRSS), 4(2), 95-97. https://doi.org/10.47253/jtrss.v4i2.614

Juárez, Julio C, Rivera, Isauro, Patiño, Francisco, & Reyes, María I. (2012). Efecto de la Temperatura y Concentración de Tiosulfatos sobre la Velocidad de Disolución de Plata contenida en Desechos Mineros usando Soluciones S2O32--O2-Zn2+. Información tecnológica, 23(4), 133-138. https://dx.doi.org/10.4067/S0718-07642012000400015

Larrabure, G., & Rodríguez-Reyes, J. C. F. (2021). A review on the negative impact of different elements during cyanidation of gold and silver from refractory ores and strategies to optimize the leaching process. Minerals

Engineering, 173. https://doi.org/10.1016/j.mineng.2021.107194

Li, K., Li, Q., Zhang, Y., Liu, X., Yang, Y., & Jiang, T. (2023). Improved thiourea leaching of gold from a gold ore using additives. Hydrometallurgy, 222. https://doi.org/10.1016/j.hydromet.2023.106204

Liu, W., Li, W., Liu, W., Shen, Y., Zhou, S., & Cui, B. (2023). A new strategy for extraction of copper cyanide complex ions from cyanide leach solutions by ionic liquids. Journal of Molecular Liquids, 383. https://doi.org/10.1016/j.molliq.2023.122108

Ma, A., Li, J., Chang, J., & Zheng, X. (2024). Mechanism Analysis and Experimental Research on Leaching Zn from Zinc Oxide Dust with an Ultrasound-Enhanced NH3-NH4Cl-H2O System. Sustainability, 16(7). https://doi.org/10.3390/su16072901

Melashvili, M., Fleming, C., Dymov, I., Matthews, D., & Dreisinger, D. (2015). Equation for thiosulphate yield during pyrite oxidation. Minerals Engineering, 74, 105-111. https://doi.org/10.1016/j.mineng.2015.02.004

Meléndez-Sánchez, A. C., Hernández-Carmona, G., & López-Maldonado, E. A. (2022). Aislamiento y caracterización de microorganismos resistentes a metales pesados en jales mineros. Revista Mexicana de Ingeniería Química, 21(1), 191–204. https://rmiq.org/iqfvp/Numbers/V21/No1/Bio2700.pdf

Mitra, S. (2019). Depletion, technology, and productivity growth in the metallic minerals industry. Mineral economics, 32(1), 19-37. https://doi.org/10.1007/s13563-018-0165-8

Mystrioti, C., Kousta, K., Papassiopi, N., Adam, K., Taxiarchou, M., & Paspaliaris, I. (2024). Evaluation of Thiosulfate for Gold Recovery from Pressure Oxidation Residues. Materials Proceedings, 15(1). https://doi.org/10.3390/materproc2023015087

Nikkhou, F., Xia, F., & Deditius, A. P. (2019). Variable surface passivation during direct leaching of sphalerite by ferric sulfate, ferric chloride, and ferric nitrate in a citrate medium. Hydrometallurgy, 188, 201-215. https://doi.org/10.1016/j.hydromet.2019.06.017

Ou, Y., Yang, Y., Li, K., Gao, W., Wang, L., Li, Q., & Jiang, T. (2023). Eco-friendly and low-energy innovative scheme of self-generated thiosulfate by atmospheric oxidation for green gold extraction. Journal of Cleaner Production, 387. https://doi.org/10.1016/j.jclepro.2022.135818

Pearson, R. G. (1997). Ácidos y bases duros y blandos. Primera parte: principios fundamentales. Educación Química, 8(4), 208-215. https://doi.org/10.22201/fq.18708404e.1997.4.66600

Puente, D. M., Fuente, J. C., Nava, F., Uribe, A., Pérez, R., & Martínez, V. J. (2021). A phenomenological study of the silver sulfide passivation and oxidative degradation of thiosulfate in the thiosulfate-ammonia-copper-citrate leaching system. Hydrometallurgy, 200. https://doi.org/10.1016/j.hydromet.2020.105547

Puente, D. M., Fuentes, J. C., & Nava, F. (2013). A kinetic–thermodynamic study of silver leaching in thiosulfate–copper–ammonia–EDTA solutions. Hydrometallurgy, 134, 124-131. https://doi.org/10.1016/j.hydromet.2013.02.010

Puente, D. M., Fuentes, J. C., & Nava, F. (2017). An analysis of the efficiency and sustainability of the thiosulfate-copper-ammonia-monoethanolamine system for the recovery of silver as an alternative to cyanidation. Hydrometallurgy, 169, 16-25. https://doi.org/10.1016/j.hydromet.2016.12.003

Rezaee, M., Shafaei, S. Z., Abdollahi, H., Mohammadnejad, S., & Mabudi, A. (2023). An Experimental and DFT Study on Using the Thiosulfate–Glycine Complex as an Alternative Agent of Cyanide in the Gold Leaching Process. Journal of Sustainable Metallurgy, 9(3), 1239-1252. https://doi.org/10.1007/s40831-023-00726-w

Ruiz, Á., & Lapidus, G. T. (2017). Study of chalcopyrite leaching from a copper concentrate with hydrogen peroxide in aqueous ethylene glycol media. Hydrometallurgy, 169, 192-200. https://doi.org/10.1016/j.hydromet.2017.01.014

Ruiz, Á., & Lapidus, G. T. (2018). Improved process for leaching refractory copper sulfides with hydrogen peroxide in aqueous ethylene glycol solutions. In Extraction 2018: Proceedings of the First Global Conference on Extractive Metallurgy (pp. 1289-1298). Springer International Publishing. https://doi.org/10.1007/978-3-319-95022-8_105

Ruiz, A., & Lapidus, G. T. (2022). A study to understand the role of ethylene glycol in the oxidative acid dissolution of chalcopyrite. Minerals Engineering, 180. https://doi.org/10.1016/j.mineng.2022.107502

Ruiz, A., Lázaro, I., & Lapidus, G. T. (2020). Improvement effect of organic ligands on chalcopyrite leaching in the aqueous medium of sulfuric acid-hydrogen peroxide-ethylene glycol. Hydrometallurgy, 193. https://doi.org/10.1016/j.hydromet.2020.105293

Segura, B. & Lapidus, G. (2023). Importance of chemical pretreatment for base metals remotion and its effect on the selective extraction of gold from Printed Circuits Boards (PCBs). Revista Mexicana de Ingeniería Química, 22(2), 563–578. https://doi.org/10.24275/rmiq/IA2335

Senanayake, G. (2005). Gold leaching by thiosulphate solutions: a critical review on copper (II)–thiosulphate–oxygen interactions. Minerals Engineering, 18(10), 995-1009. https://doi.org/10.1016/j.mineng.2005.01.006

Senanayake, G., Childs, J., Akerstrom, B. D., & Pugaev, D. (2011). Reductive acid leaching of laterite and metal oxides—A review with new data for Fe (Ni, Co) OOH and a limonitic ore. Hydrometallurgy, 110(1-4), 13-32. https://doi.org/10.1016/j.hydromet.2011.07.011

Serap, Ubiç., Rasoul, Khayyam, Nekouei., V., Sahajwalla. (2024). A Two-Step Leaching Process Using Thiourea for the Recovery of Precious Metals from Waste Printed Circuit Boards. https://doi.org/10.3390/waste2030018

Serga, V., Zarkov, A., Blumbergs, E., Shishkin, A., Baronins, J., Elsts, E., & Pankratov, V. (2022). Leaching of gold and copper from printed circuit boards under the alternating current action in hydrochloric acid electrolytes. Metals, 12(11). https://doi.org/10.3390/met12111953

Soto-Uribe, J. C., Valenzuela-Garcia, J. L., Salazar-Campoy, M. M., Parga-Torres, J. R., Vazquez-Vazquez, V. M., Encinas-Romero, M. A., & Martinez-Ballesteros, G. (2023). Electrocoagulation process for recovery of precious metals from cyanide leachates using a low voltage. ACS Engineering Au, 4(1), 139-144. https://doi.org/10.1021/acsengineeringau.3c00041

Tabakova, T., & Andreeva, D. (1996). Mechanism of the oxidative hydrolysis of Iron (II) sulphate. Bulgarian chemical communications, 29(2), 172-187. https://doi.org/10.1007/BF00703026

Torres, R., & Lapidus, G. T. (2020). Base metal citrate pretreatment of complex ores to improve gold and silver leaching with thiourea. Hydrometallurgy, 197. https://doi.org/10.1016/j.hydromet.2020.105461

Torres, R., Segura, B., & Lapidus, G. T. (2018). Effect of temperature on copper, iron and lead leaching from e-waste using citrate solutions. Waste management, 71, 420-425. https://doi.org/10.1016/j.wasman.2017.10.029

Trachevskii, V. V., Zimina, S. V., & Rodina, E. P. (2008). Thiosulfate metal complexes. Russian Journal of Coordination Chemistry, 34, 664-669. https://doi.org/10.1134/S1070328408090066

Urzúa, D. A., Fuentes, J. C., Uribe, A., & Lee, J. C. (2018). An electrochemical study of silver recovery in thiosulfate solutions. A window towards the development of a simultaneous electroleaching-electrodeposition process. Hydrometallurgy, 176, 104-117. https://doi.org/10.1016/j.hydromet.2018.01.017

Xiang, P. Z., Deng, C., Yao, H., Liu, L. J., & Mogdal, S. (2020, August). Leaching Kinetics of Gold Involved in the System S2O32--EDTA-Cu2+. In Materials Science Forum (Vol. 1001, pp. 212-218). Trans Tech Publications Ltd. https://doi.org/10.4028/www.scientific.net/MSF.1001.212

Xin, C., Xia, H., Jiang, G., Zhang, Q., Zhang, L., & Xu, Y. (2022). Studies on Recovery of Valuable Metals by Leaching Lead–Zinc Smelting Waste with Sulfuric Acid. Minerals, 12(10). https://doi.org/10.3390/min12101200

Xu, B., Kong, W., Li, Q., Yang, Y., Jiang, T., & Liu, X. (2017). A review of thiosulfate leaching of gold: Focus on thiosulfate consumption and gold recovery from pregnant solution. Metals, 7(6). https://doi.org/10.3390/met7060222

Yae, S., Iwai, Y., Takashima, Y., Osaka, T., & Matsumoto, A. (2023, December). Gold Recovery from Thiosulfate Leaching Solution Using Silicon Powder and Electrochemical Monitoring of Its Process. In Electrochemical Society Meeting Abstracts 244 (No. 25, pp.

1363-1363). The Electrochemical Society, Inc. https://doi.org/10.1149/MA2023-02251363mtgabs

Zhang, Y., Li, Q., Liu, X., & Jiang, T. (2022). A thermodynamic analysis on thiosulfate leaching of gold under the catalysis of Fe^{3+}/Fe^{2+} complexes. Minerals Engineering, 180. https://doi.org/10.1016/j.mineng.2022.107511

Zhang, Z. Y., Wu, L., He, K., & Zhang, F. S. (2022). A sequential leaching procedure for efficient recovery of gold and silver from waste mobile phone printed circuit boards. Waste Management, 153, 13-19. https://doi.org/10.1016/j.wasman.2022.08.011

Zuo, Q., Wu, D., Wen, S., Cao, J., Wang, Z., & Chen, H. (2023). Advanced oxidation using sulfate radicals for the surface oxidation of Cu_2O and the separation of copper via acid leaching. Journal of Molecular Liquids, 390. https://doi.org/10.1016/j.molliq.2023.123195

Vol. 24, No. 2(2025) Sim25480

Revista Mexicana de Ingeniería Química

Numerical analysis of ilmenite particle diameter on thermal and fluid dynamic behavior in a chemical looping combustion system

Análisis numérico del diámetro de partículas de ilmenita sobre el comportamiento térmico y fluidodinámico en un sistema de combustión en ciclos químicos

F.A. Ocampo-Vaca[1], C. A. Hernández-Bocanegra[2*], R. Maya-Yescas[1] and J. A. Ramos-Banderas [2]

[1]Faculty of Chemical Engineering, Universidad Michoacana de San Nicolás de Hidalgo, Morelia, Michoacán, México.

[2]National Technological Institute of Mexico, Morelia Campus, Morelia, Michoacá, México.

Received: November 29, 2024; Accepted: March 5, 2025

Abstract

This study utilized numerical simulation to analyze the effect of particle diameter on the fluid dynamics within a chemical looping combustion (CLC) system consisting of two interconnected fluidized bed reactors. The non-isothermal multiphase Eulerian model was employed to simulate ilmenite particles as the granular phase in the CLC system, aiming to investigate the impact of particle diameters of 80 μm, 120 μm, 150 μm, 180 μm, 220 μm, and 270 μm on their distribution within the reactor system. The results demonstrated that particle diameter is a critical variable, significantly influencing their distribution. For particles measuring 80 μm and 120 μm, the drag force generated by the airflow predominates, resulting in complete entrainment of the granular phase in the air reactor. In the cases of particles with diameters between 150 μm and 180 μm, the drag force is counterbalanced by gravitational force and for particles with diameters of 220 μm and larger gravitational force exceeds drag force for particles with diameters of 220 μm and larger, rendering them unsuitable for use within this system. Finally, regarding temperature the results showed less cooling of the system when 150 μm particles were used.

Keywords: Chemical looping combustion, CO_2 emissions, particle flow, numerical simulation.

Resumen

Este estudio utilizó simulación numérica para analizar el efecto del diámetro de partículas sobre la fluidodinámica dentro de un sistema de combustión en ciclos químicos (CLC, por sus siglas en inglés) compuesto por dos reactores de lecho fluidizado interconectados. Mediante un modelo euleriano multifásico no isotérmico, se simularon partículas de ilmenita como fase granular, evaluando diámetros de 80 μm, 120 μm, 150 μm, 180 μm, 220 μm y 270 μm para analizar su distribución en el sistema. Los resultados mostraron que el diámetro de las partículas es crítico, afectando significativamente su comportamiento. Las partículas de 80 μm y 120 μm fueron completamente arrastradas por el flujo de aire en el regenerador, mientras que para diámetros entre 150 μm y 180 μm, la fuerza de arrastre fue equilibrada por la gravedad. En partículas de 220 μm o mayores, la fuerza gravitacional superó la de arrastre, haciéndolas inadecuadas para este sistema. Respecto a la temperatura, las partículas de 150 μm resultaron en un menor enfriamiento del sistema, mostrando un comportamiento óptimo en comparación con los otros diámetros evaluados.

Palabras clave: Combustión en ciclos químicos, emisiones de CO_2, flujo de partículas, simulación numérica.

*Corresponding author. *E-mail*: constantin.hb@morelia.tecnm.mx ;

https://doi.org/10.24275/rmiq/Sim25480

ISSN:1665-2738, *issn-e*: 2395-8472

1 Introduction

It is well known that since the Industrial Revolution, humanity's energy consumption has grown exponentially. Fossil fuels have been the primary energy sources used since then, primarily due to their low cost and ease of handling. Fossil fuels account for approximately 85% of global energy consumption (Kumar & Muhuri, 2019). Since the mid-20th century, this widespread use of fossil fuels, along with the resulting carbon dioxide (CO_2) emissions, has been considered one of the primary causes of climate change (Kumar & Muhuri, 2019) (Stocker, *et al*., 2013). Greenhouse gases are classified as direct and indirect based on their induction of radiative forcing. Direct greenhouse gases are those that induce global warming and are responsible for the increase in planetary temperature as well as regional climate variability. These include carbon dioxide (CO_2), methane (CH_4), nitrous oxide (N_2O), hydrofluorocarbons, perfluorocarbons, and sulfur hexafluoride (SF_6). On the other hand, indirect greenhouse gases impact atmospheric chemistry by altering the lifespan of direct greenhouse gases in the atmosphere (Martínez-Prado, M. A., 2016). CO_2 accounts for nearly 75% of anthropogenic gas emissions (Adanez, Abad, Garcia-Labiano, Gayan, & De Diego, 2012), with an estimated atmospheric lifespan of approximately 12 years (Archer & Jacobson, 2005). Climate change is a recognized phenomenon, and its most detrimental impact is the potential alteration of the biodiversity of Earth (Gitay, 2002). By 2017, human-induced global warming had reached approximately 1°C above pre-industrial levels, with the planet's temperature increasing at 0.2°C per decade (Masson-Delmotte, *et al*., 2018). It is estimated that by 2045, fossil fuels will remain a significant energy source (Pugazhendhi, *et al*., 2019), meaning that energy generation and climate change are closely connected and require a holistic solution (Höök & Tang, 2013). One alternative that combines the necessity of using fossil fuels with the urgency of reducing CO_2 emissions to the atmosphere is Chemical Looping Combustion (CLC) systems. This process involves two interconnected fluidized bed reactors. In the first reactor, called the fuel reactor, syngas ($CO + H_2$) is fully oxidized in the absence of air, using oxygen carried by the natural metal oxide known as ilmenite ($Fe^{2+}Ti^{4+}O_2$), which is simultaneously reduced. In the second air reactor, the carrier is oxidized again through contact with air. The fuel reactor operates in a bubbling regime, while the air reactor operates in a particle entrainment or riser regime.

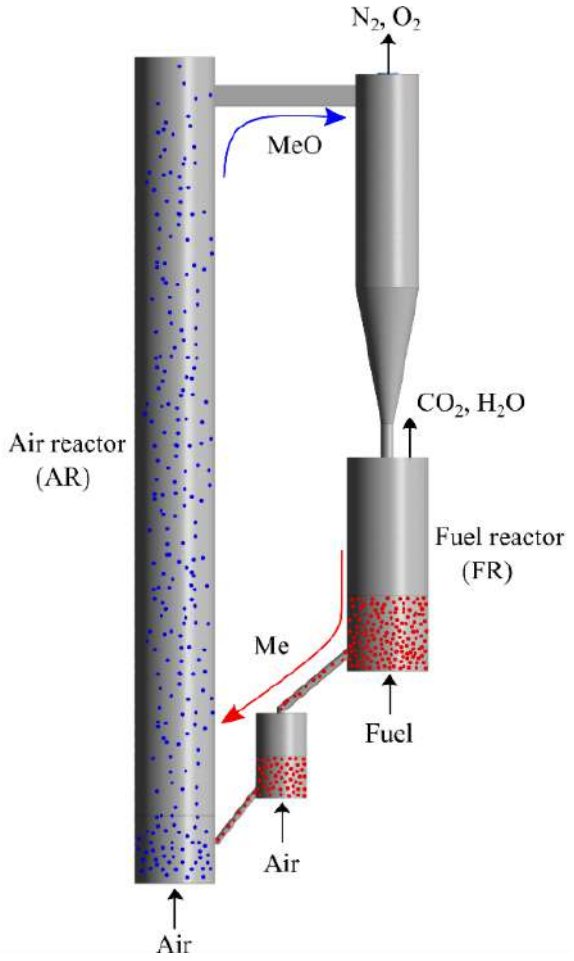

Figure 1. Scheme of the CLC process.

For this reason, these processes do not involve high economic costs for CO_2 capture. Figure 1 shows a diagram of the CLC process. In its special report on carbon dioxide capture and storage (2005), the IPCC identified chemical looping combustion as one of the cheapest technologies for CO_2 capture, especially when complementing power generation plants (Kerr, 2005) (Deng Z., Xiao, Jin, Song, & Huang, 2008). The main drawback of CLC is the low confidence level due to the lack of technological maturity, which presents a significant opportunity to study chemical looping combustion.

Various mathematical simulation studies of particle flow have been developed to study the CLC process, some of them focusing solely on the fuel reactor (Deng *et al*., 2009; Jin *et al*., 2009; Jung & Gamwo, 2008; Mahalatkar *et al*., 2011; Shuai *et al*., 2011). In other studies, the complete CLC system has been examined, that is, both the fuel reactor and the air reactor (Kruggel-Emden *et al*., 2010; Nguyen *et al*., 2012; Seo *et al*., 2011; Shuai *et al*., 2011; Shuai *et al*., 2014). This work stands out from previous research because it analyzes an aspect that has been relatively underexplored in the existing literature: the variation in the diameter of oxygen-carrying particles

Table 1. Summary of studies related to particle size in CLC.

Reference	Year	System	Particle diameter (μm)
Peirano *et al*. [21]	2001	Fluidized bed	283
Jung & Gamwo [11]	2008	FR	120
Deng *et al*. [12]	2009	FR	275
Kruggel-Emden *et al*. [16]	2010	FR + AR	150
Shuai *et al*. [22]	2011	FR + AR	150
Shuai *et al*. [18]	2011	FR	120
Mahalatkar *et al*. [15]	2011	FR	128
Kruggel-Emden *et al*. [23]	2011	FR	150
Seo *et al*. [19]	2011	FR	250
Nguyen *et al*. [20]	2012	FR + AR	250
Shuai *et al*. [18]	2014	FR + AR	135
Guan *et al*. [24]	2014	FR + AR	150
Bougamra *et al*. [25]	2014	FR + AR	200
Alobaid *et al*. [26]	2015	FR	120
Porrazzo *et al*. [27]	2016	FR	200
Zhang *et al*. [28]	2017	FR + AR	135
Sornumpol *et al*. [29]	2017	FR	150 and 175
May *et al*. [30]	2018	FR + AR	300
Lin *et al*. [31]	2019	FR	200
Li and Shen [32]	2021	AR	140

and its impact on the fluid dynamic distribution of both the granular phase and the continuous phase, as well as on the distribution and thermal profiles within chemical looping combustion systems. In many prior studies, a single diameter value has been employed (Table 1), which limits understanding how variations in this parameter can influence system behavior. By analyzing multiple particle diameters, this research expands knowledge about fluidization dynamics and provides a more realistic and applicable approach to practical situations. Examining how the variation in particle diameter affects their distribution can help optimize the performance of chemical looping combustion systems, promoting a more effective and sustainable operation. This work enhances the current knowledge in chemical looping combustion and contributes to improving cleaner and more efficient technologies.

2 Methodology

2.1 *Domain dimensions, boundary conditions and assumptions*

The simulation was conducted considering the geometry of a chemical looping combustion process at scale, taken from the work of Guan *et al*. (Guan, Chang, Zhang, Wang, & Sun, 2014). Figure 2(a) shows the model's dimensions, and Figure 2 (b) shows the phases and boundary conditions.

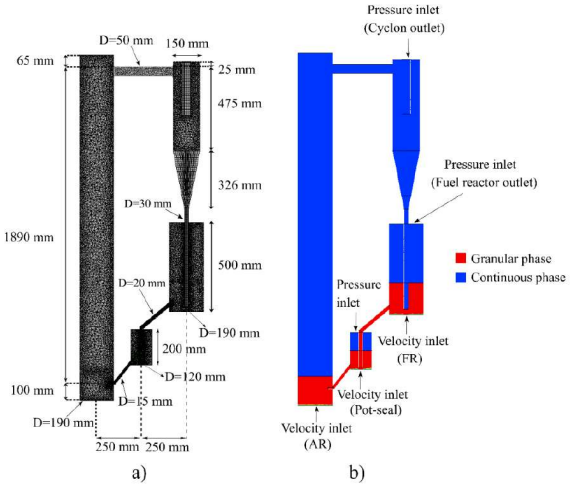

Figure 2. a) Mesh and dimensions of the model and b) Boundary conditions.

The mesh of the computational domain consisted of 697,584 elements. This mesh was determined through a mesh sensitivity analysis, shown in Figure 3, where the fluid velocity in the air reactor was analyzed for four different meshes. Based on this analysis, mesh 3, corresponding to 697,584 elements, was used since, as shown in Figure 3, the velocity profiles of meshes 3 and 4 are practically superimposed on one another. This analysis allowed us to conclude that the results are no longer affected by the number of elements in the mesh, and there is no point in using meshes with a more significant number of elements. Tables 2 and 3 show the properties of the materials used in the numerical simulation of the multiphase system, as well

Table 2. Thermo-physical properties of materials.

Property	Value	Units
Fluid phase density	1.225	$kg \cdot m^{-3}$
Granular phase density	2600	$kg \cdot m^{-3}$
Fluid phase viscosity	1.7894×10^{-5}	$kg \cdot m^{-1} \cdot s^{-1}$
Granular phase viscosity	Kinetic theory	$kg \cdot m^{-1} \cdot s^{-1}$
Fluid phase specific heat	1006.43	$J \cdot kg^{-1} \cdot K^{-1}$
Granular phase specific heat	Kinetic theory	$J \cdot kg^{-1} \cdot K^{-1}$
Fluid phase thermal conductivity	0.0242	$W \cdot m^{-1} \cdot K^{-1}$
Granular phase thermal conductivity	Kinetic theory	$W \cdot m^{-1} \cdot K^{-1}$

Table 3. Operation parameters and boundary conditions.

Parameter	Value	Units
Inventory of solids in the system	17.5	kg
Velocity inlet in AR	0.9	$m \cdot s^{-1}$
Velocity inlet in FR	0.08	$m \cdot s^{-1}$
Velocity inlet in pot-seal	0.002	$m \cdot s^{-1}$
Pressure inlet	1	atm
Initial temperature of granular phase	1273	K

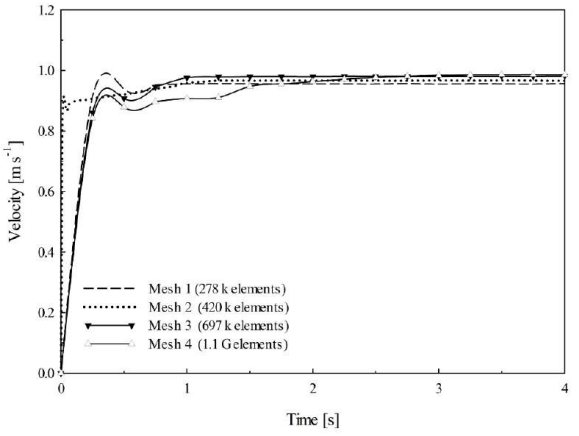

Figure 3. Mesh sensitivity analysis study.

as the system's operating parameters and boundary conditions.

2.2 *Governing equations*

The Eulerian model is the most complex and robust of the multiphase models. In this model, the volume fractions represent the space occupied by each phase (gas phase and solid phase). The principles of mass and momentum conservation are solved individually for each phase. Coupling is achieved through pressure and exchange coefficients at the interface; for granular flows (fluid-solid), the properties are obtained through the application of kinetic theory.

2.2.1 *Continuity equations*

The mass conservation equation is described by equation 2.1 (ANSYS, 2013):

$$\frac{\partial}{\partial t}\left(\alpha_q \rho_q\right) + \nabla \cdot \left(\alpha_q \rho_q \vec{v}_q\right) = \sum_{p=1}^{n} \left(\dot{m}_{pq} - \dot{m}_{qp}\right) + S_q \quad (1)$$

Here ρ_q is the density, $\vec{v}_q$ is the velocity vector, and α_q is the volume fraction, with the subscript q representing phase q, m_{pq} characterizes the mass transfer from the p^{th} to q^{th} phase, and $\dot{m}_{qp}$ characterizes the mass transfer from the q^{th} to p^{th}. The term S_q is a mass source term for cases where chemical reactions are present.

2.2.2 *Conservation equations of momentum for both phases*

The balance of forces for phase q is described by equation 2.2 (ANSYS, 2013):

$$\frac{\partial}{\partial t}\left(\alpha_q \rho_q \vec{v}_q\right) + \nabla \cdot \left(\alpha_q \rho_q \vec{v}_q \vec{v}_q\right) = -\alpha_q \nabla P + \nabla \cdot \bar{\bar{\tau}}_q + \alpha_q \rho_q \vec{g} + \sum_{p=1}^{n} \left(R_{pq}\left(\vec{v}_p - \vec{v}_q\right) + \dot{m}_{pq}\vec{v}_{pq} - \dot{m}_{qp}\vec{v}_{qp}\right) + \left(\vec{F}_q + \vec{F}_{lift,q} + \vec{F}_{wl,q} + \vec{F}_{vm,q} + \vec{F}_{td,q}\right) \quad (2)$$

Here $\bar{\bar{\tau}}_q$ is the q^{th} phase stress-strain tensor:

$$\bar{\bar{\tau}}_q = \alpha_q \mu_q \left(\nabla \vec{v}_q + \nabla \vec{v}_q^{\,T}\right) + \alpha_q \left(\lambda_q - \frac{2}{3}\mu_q\right) \nabla \cdot \vec{v}_q \bar{\bar{I}} \quad (3)$$

Here μ_q and λ_q are the shear and bulk viscosity of phase q, $\vec{F}_q$ is an external body force, $\vec{F}_{lift,q}$ is a lift force, $\vec{F}_{wl,q}$ is a wall lubrication force, $\vec{F}_{vm,q}$ is a virtual mass force and $\vec{F}_{td,q}$ is a turbulent dispersion force. R_{pq} is an interaction force between phases, and P is the pressure shared by all phases. $\vec{v}_{pq}$ is the interphase velocity, defined as follow, If $\dot{m}_{pq} > 0$ (that is, phase p mass is being transferred to phase q), $\vec{v}_{pq} = \vec{v}_p$; if $\dot{m}_{pq} < 0$ (that is, phase q mass is being transferred to phase p) $\vec{v}_{pq} = \vec{v}_q$. Likewise, if $\dot{m}_{qp} > 0$ then $\vec{v}_{qp} = \vec{v}_q$; if $\dot{m}_{qp} < 0$ then $\vec{v}_{qp} = \vec{v}_p$.

2.2.3 Energy equations

$$\frac{\partial}{\partial t}\left(\alpha_q \rho_q \bar{h}_q\right) + \nabla \cdot \left(\alpha_q \rho_q \bar{u}_q h_q\right) = \alpha_q \frac{\partial p_q}{\partial t} + \bar{\bar{\tau}}_q + \nabla \bar{u}_q - \nabla \cdot \bar{q}_q + S_q + \sum_{p=1}^{n} (Q_{pq} + \dot{m}_{pq} h_{pq} - \dot{m}_{qp} h_{qp}) \quad (4)$$

here, h_q is the specific enthalpy of the phase q, $\bar{q}_q$ is the heat flux, S_q is the source term, Q_{pq} represents the intensity of heat exchange between the phases and h_{pq} is the interfacial enthalpy.

2.2.4 Standard $\kappa - \varepsilon$ turbulence model (Launder & Spalding, 1983)

The robustness, economy, and reasonable accuracy for many turbulent flows explain the popularity of this model in fluid flow simulations (5) (6).

$$\frac{\partial}{\partial t}(\rho k) + \frac{\partial}{\partial x_i}(\rho k u_i) = \frac{\partial}{\partial x_j}\left[\left(\mu + \frac{\mu_t}{\sigma_k}\right)\frac{\partial k}{\partial x_j}\right] + G_k + G_b - \rho\varepsilon - Y_M + S_k \quad (5)$$

$$\frac{\partial}{\partial t}(\rho \varepsilon) + \frac{\partial}{\partial x_i}(\rho \varepsilon u_i) = \frac{\partial}{\partial x_j}\left[\left(\mu + \frac{\mu_t}{\sigma_\varepsilon}\right)\frac{\partial \varepsilon}{\partial x_j}\right] + C_{1\varepsilon}\frac{\varepsilon}{k}(G_k + C_{3\varepsilon}G_b) - C_{2\varepsilon}\rho\frac{\varepsilon^2}{k} + S_\varepsilon \quad (6)$$

where G_k is the generation of turbulent kinetic energy, G_b is the generation of turbulent kinetic energy, Y_M is the contribution of the fluctuating dilatation. $C_{1\epsilon}$, $C_{2\epsilon}$ and $C_{3\epsilon}$ are model constants. σ_k *y* σ_ε are the turbulent Prandtl numbers for k and for ε, respectively. S_k and S_ε are the source terms.

2.3 Models for granular properties

It is necessary to calculate granular properties when using the Eulerian multiphase model for a granular phase. The employed software provides various models that can be employed for each of these properties.

2.3.1 Granular viscosity

Syamlal *et al* (ANSYS, 2013):

$$\mu_s = \frac{\alpha_s d_s \rho_s \sqrt{\theta_s \pi}}{6(3 - e_{ss})}\left[1 + \frac{2}{5}(1 + e_{ss})(3e_{ss} - 1) g_0 \alpha_s\right] \quad (7)$$

2.3.2 Bulk viscosity

The solids bulk viscosity considers the resistance of the granular phase to compression and expansion (Lun, Savage, Jeffrey , & Chepurniy, 1984):

$$\lambda_s = \frac{4}{3}\alpha_s^2 \rho_s d_s g_0 (1 + e_{ss})\left(\frac{\theta_s}{\pi}\right)^{1/2} \quad (8)$$

2.3.3 Solids pressure

The total solids pressure is calculated and included in the momentum conservation equations. The total solids pressure is the sum of the solids pressure for each solid phase:

$$P_{s,total} = \sum_{q=1}^{n} p_q \quad (9)$$

The solids pressure formulation consists of a kinetic term and a second term corresponding to particle collisions:

$$P_s = \alpha_s \rho_s \theta_s + 2\rho_s (1 + e_{ss}) \alpha_s^2 g_{0,ss} \theta_s \quad (10)$$

Here, e_{ss} is the coefficient of restitution for particle collisions, $g_{0,ss}$ is the radial distribution function, and θ_s is the granular temperature.

2.3.4 Granular temperature

The granular temperature of the solid phase is proportional to the kinetic energy of the particles' random motion.

$$\theta_s = \frac{1}{3} u_s, i u_{s,i} \quad (11)$$

Here, $iu_{s,i}$ represents the component of the fluctuating velocity of the solids in the Cartesian coordinate system. This is defined as an ensemble average of the random velocity of particles within a finite volume over a period of time.

The transport equation derived from kinetic theory takes the form:

$$\frac{2}{3}\left[\frac{\partial}{\partial t}(\rho_s \alpha_s \theta_s) + \nabla \cdot (\rho_s \alpha_s v_s \theta_s)\right] = \left(-p_s \bar{\bar{I}} + \bar{\bar{\tau}}_s\right) : \nabla \bar{v}_s + \nabla \cdot (k_{\theta_s} \nabla \theta_s) - \gamma_{\theta_s} + \varphi_{ls} \quad (12)$$

Here, $\left(-p_s \bar{\bar{I}} + \bar{\bar{\tau}}_s\right) : \nabla \bar{v}_s$ is the generation of energy by the solid stress tensor, $k_{\theta_s} \nabla \theta_s$ is the energy diffusion term, γ_{θ_s} represents energy dissipation due to collisions and φ_{ls} represents energy exchange between the continuous and granular phases.

Equation (13) contains the term $k_{\theta_s} \nabla \theta_s$, which describes the diffusion of the granular flow. When using the default Syamlal *et al*. model (Syamlal, Rogers, & O'Brien, 1993), the diffusion coefficient is given by:

$$k\theta_s = \frac{15 d_s \rho_s \alpha_s \sqrt{\theta_s \pi}}{4(41 - 33\eta)}\left[1 + \frac{12\eta^2}{5}(4\eta - 3)\alpha_s g_0 + \frac{16}{15\pi}(41 - 33\eta)\eta \alpha_s g_0\right] \quad (13)$$

2.3.5 Radial distribution function

The radial distribution function is a correction factor that modifies the probability of collisions between grains when the granular solid phase becomes dense.

$$g_0 = \frac{s + d_p}{s} \tag{14}$$

Here, s is the distance between grains.

2.3.6 Frictional viscosity

In dense flows where the volume fraction of the secondary phase approaches the packing limit, stress generation is mainly due to friction between particles. Frictional viscosity is included through the Schaeffer expression (Scheaffer, 1987):

$$\mu_{s,fr} = \frac{p_s \sin\Phi}{2\sqrt{I_{2D}}} \tag{15}$$

where p_s is the solids pressure, Φ is the angle of internal friction, I_{2D} and is the second invariant of the deviatoric stress tensor.

2.3.7 Limit packing fraction

The maximum value for the volume fraction of the granular phase is specified. For monodisperse spheres, the packing limit is approximately 0.63.

2.3.8 Elastic modulus

It is defined as:

$$G = \frac{\partial P_s}{\partial \alpha_s} \tag{16}$$

for $G \geq 0$.

2.3.9 Models for interactions between phases

2.3.9.1 Drag coefficient

The Gidaspow model is a combination of the Wen and Yu model (Wen & Yu, 1966) and the Ergun equation (Ergun, 1949). When $\alpha_l > 0.8$, the exchange coefficient between the solid and liquid phase, K_{ls}, is defined as follows:

$$K_{sl} = \frac{3}{4} C_D \frac{\alpha_s \alpha_l \rho_l |\overline{v}_s - \overline{v}_l|}{d_s} \alpha_l^{-2.65} \tag{17}$$

Here, the drag coefficient is given by:

$$C_D = \frac{24}{\alpha_l Re_s}\left[1 + 0.15\,(\alpha_l Re_s)^{0.687}\right] \tag{18}$$

2.3.9.2 Turbulent dispersion

For turbulent multiphase flows using the Eulerian model, the effects of turbulent dispersion forces, which explain the transfer of momentum between phases, can be taken into account. The turbulent dispersion force acts as turbulent diffusion in dispersed flows.

2.3.9.3 Simonin model

$$\overline{F}_{td,q} = -\overline{F}_{td,p} = C_{TD} K_{pq} \frac{D_{t,pq}}{\sigma_{pq}} \left(\frac{\nabla \alpha_p}{\alpha_p} - \frac{\nabla \alpha_q}{\alpha_q} \right) \tag{19}$$

Here, σ_{pq} is the default dispersion Prandtl number 0.75. K_{pq} is the interaction coefficient between the phases, $\nabla\alpha_p$ and $\nabla\alpha_q$ are the gradients of the volume fraction of the discrete phase and the continuous phase, respectively. C_{TD} is a constant equal to 1 by default.

3 Results and discussion

3.1 Volume fraction contours and fluidization regimes for particles of different diameters

Figure 4 shows the axial contours of the ilmenite volume fraction in a vertical plane that cuts through the middle of the mathematical domain, using different particle sizes. If 80 μm particles are used (Figure 4a), it can be observed that the granular phase is carried out of the system by the gas phase, both in the air reactor and the fuel reactor; in regions (1) and (2), it can be seen that the flow lines for the granular phase at the cyclone separator and fuel reactor outlets, respectively, show that the particles leave the system through the cyclone and fuel reactor outlets. Therefore, using this particle size for the given operating and boundary conditions is not feasible. In the case of particles with a diameter of 120 μm (Figure 4b), the volume fraction contour reveals an absence of the granular phase in the air reactor, as the granular phase is wholly carried away. However, in region (3)., the flow lines show that not all granular phase leaves the system through the air reactor outlet.

On the other hand, in the fuel reactor, the volume fraction contour shows a higher level of the granular phase, confirming that a large portion of the granular phase from the air reactor passed into the fuel reactor. At the same time, the flow lines in region (4) also show that most of the granular phase is not leaving the system through the air reactor. When using 150 μm particles (Figure 4c), the volume fraction contour shows a turbulent fluidization regime with pneumatic transport of particles throughout the air reactor. In contrast, a bubbling fluidization regime is observed in the fuel reactor and the pot-seal. In regions (5) and (6), the flow lines indicate that the gas carries the granular phase in the air reactor. Subsequently, in the cyclone, most of the particles fall into the fuel reactor, indicating that this particle size is suitable for the CLC system, as it allows particles to pass from

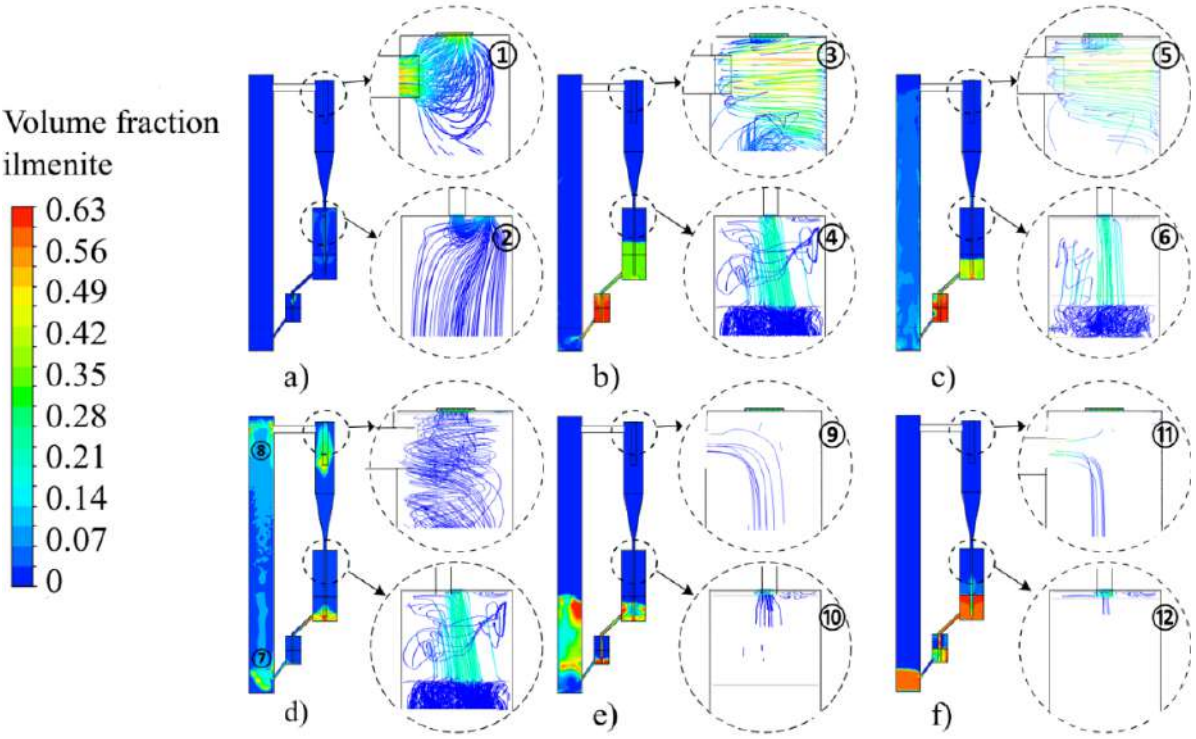

Figure 4. Axial volume fraction contours of ilmenite at 30 s after the start of the simulation and close-ups of particle path lines colored by velocity. a) 80 μm, b) 120 μm, c) 150 μm, d) 180 μm, e) 220 μm, f) 270 μm.

one reactor to another through pneumatic transport. On the other hand, in the fuel reactor, a bubbling fluidized bed regime is maintained, facilitating contact between the granular and gas phases. In the case of using 180 μm particles (Figure 4d), in regions (7) and (8), a behavior similar to the 'flat slugging' regime is observed, with particles forming agglomerations that hinder pneumatic transport.

Meanwhile, in the fuel reactor and the sealing bed, a low level of the granular phase is noted, as gravity causes the particles to move downward. The flow lines indicate behavior similar to that observed for 150 μm diameter particles. Finally, when using 220 μm particles (Figure 4e) or 270 μm (Figure 4f), it can be seen that the granular phase is in a minimum fluidization regime throughout the CLC system, which prevents the transport and exchange of particles between the air reactor and the fuel reactor. This can be confirmed by the volume fraction contour and the flow lines shown in regions (9), (10), (11), and (12), as a minimal granular phase is observed in the cyclone separator. Similarly, there is very little presence of granular phase entering the fuel reactor through the cyclone separator.

The fluidization regime that most favors the oxidation reactions of ilmenite in the air reactor is the turbulent fluidization regime with pneumatic drag, as it allows for better interaction between both phases. Meanwhile, the bubbling fluidization regime in the fuel reactor is the most suitable for reducing ilmenite particles. This regime allows for contact between the phases but prevents the drag of the granular phase. The behavior described above corresponds to particles with a diameter of 150 μm. In Figure 5, the cross-sectional volume fraction contours are analyzed. When using particles of 80 μm (Figure 5a) or 120 μm (Figure 5b), a low presence of the granular phase is observed, similar to what is seen in the axial contours (Figures 4a and 4b). When the particles in the system are 150 μm, a better distribution of particles is also noted, as seen in the axial contour profiles (Figure 4c). Suppose 180 μm particles are used (Figure 5d). In that case, a considerable presence of the granular phase is observed in the cross-section, and this concentration of particles corresponds to what is shown in the axial profiles (Figure 4d); however, this high concentration of the granular phase is not maintained throughout the air reactor, as can be seen in the axial contour of the vertical plane in Figure 4d, which shows regions with low particle concentration. When using 220 μm particles (Figure 5e), a central region is observed with no presence of the granular phase, and around it, a region with low particle concentration, clearly indicating no good fluidization regime. Finally, in Figure 5(f), it can be seen that the granular phase occupies the space shown in the contour of the plane

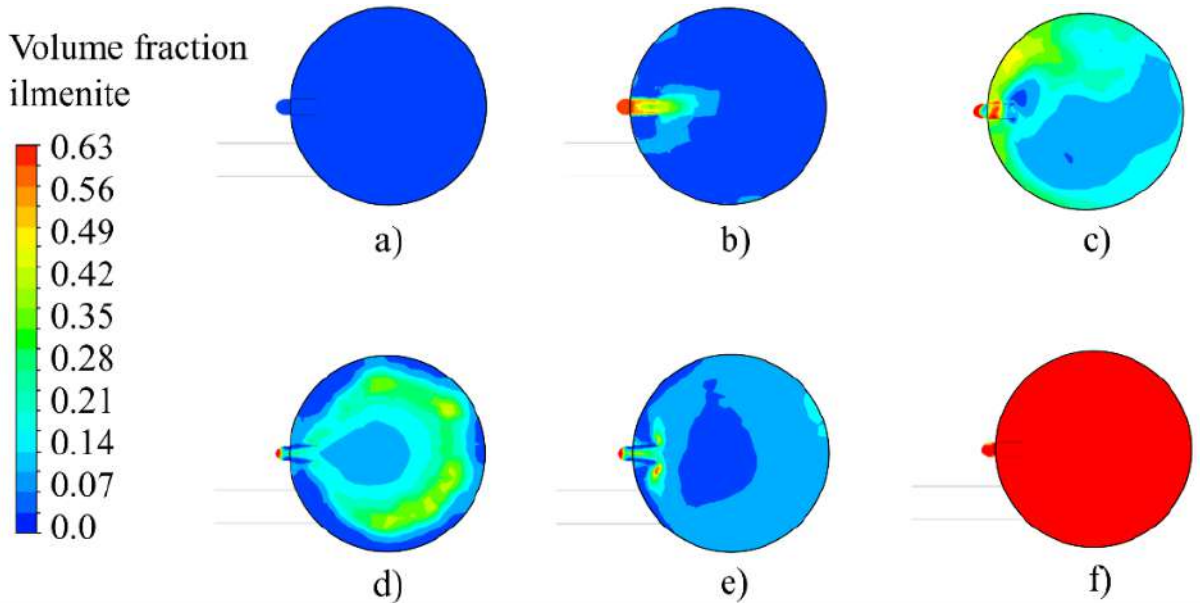

Figure 5. Cross-sectional volume fraction contours of ilmenite at 30 seconds after startup, in the cross-section at 0.1 m from the bottom of the air reactor a) 80 μm, b) 120 μm, c) 150 μm, d) 180 μm, e) 220 μm, f) 270 μm.

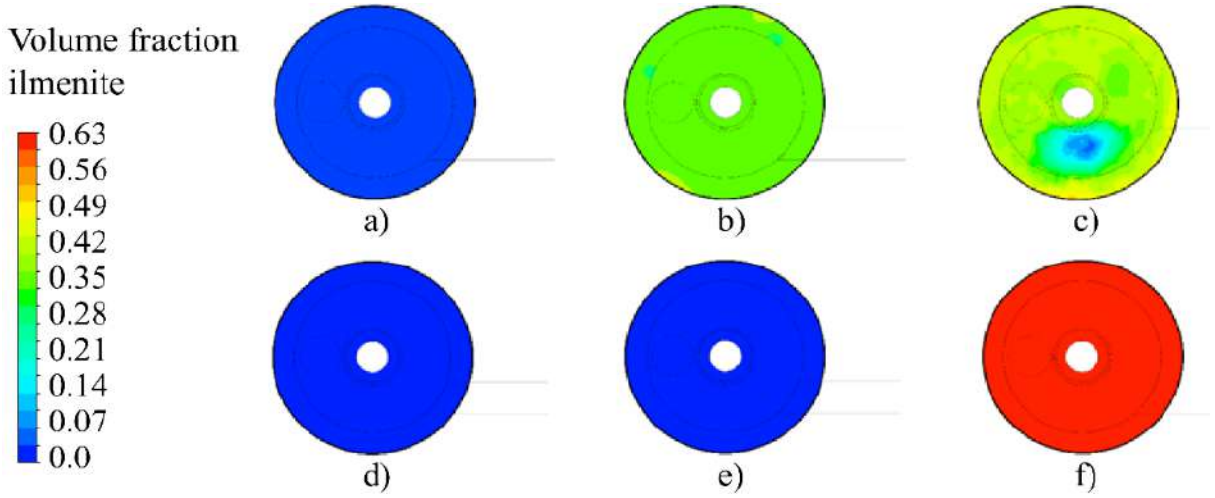

Figure 6. Volume fraction contours of ilmenite at 30 seconds, in cross-section at 0.1 m from the bottom of the fuel reactor. a) 80 μm, b) 120 μm, c) 150 μm, d) 180 μm, e) 220 μm, f) 270 μm.

due to gravitational forces exceeding drag forces, leaving the granular phase at the bottom of the air reactor.

The cross-sectional volume fraction contours of ilmenite in the fuel reactor show that when using 80 μm particles (Figure 6a), there is no concentration of the granular phase due to the strong drag caused by the gas phase. When using larger diameter particles, such as 120 μm (Figure 6b) or 150 μm (Figure 6c), the presence of the granular phase is observed, confirming that the fluidized bed regime is achieved. However, when attempting to use larger diameter particles, such as 180 μm (Figure 6d) or 220 μm (Figure 6e), there is no granular phase, as the particles have mainly moved toward the sealing bed. In the case of using 270 μm particles (Figure 6f), the behavior of the minimum fluidization regime is reaffirmed.

3.2 Particle distribution and average axial velocity profile for particles of different diameters

In Figure 7, the particle distribution profiles are analyzed at three different heights: 0.5 meters, 0.8 meters, and 1.5 meters. At 0.5 meters in height (Figure

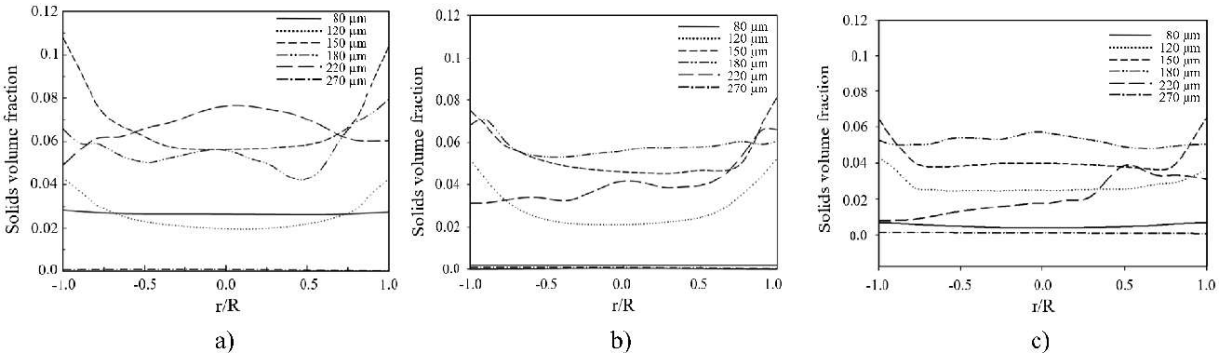

Figure 7. Particle distribution at different heights in the air reactor. a) 0.5 m, b) 0.8 m and c) 1.5 m.

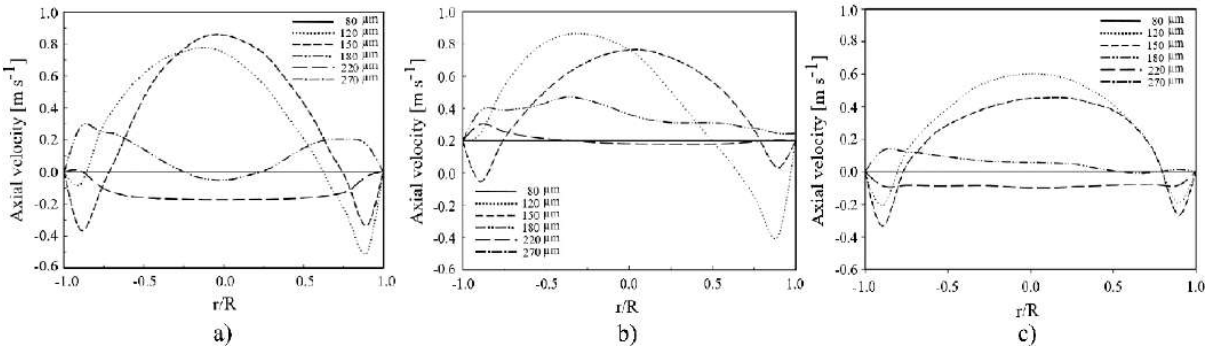

Figure 8. Velocity profiles at different heights in the air reactor. a) 0.5 m, b) 0.8 m and c) 1.5 m.

7a), the profile varies for each size. The curve for 80 μm particles is nearly horizontal with a low volume fraction. The distribution of 120 μm particles shows a volume fraction similar to that of 80 μm particles; however, the profile is not horizontal but concave, indicating a higher concentration of the granular phase near the walls. The 150 μm particles also exhibit a concave profile but with a greater concentration than the 120 μm particles. This particle distribution profile is similar to that obtained in previous studies for diameters of 150 μm (Guan, Chang, Zhang, Wang, & Sun, 2014; Shuai W. *et al*., 2011). The distribution observed for the 180 μm particles is similar to that of the 150 μm curve. In the 220 μm particle distribution curve, a slight increase in the concentration of the granular phase is observed in the central region of the air reactor; however, the profile is slightly convex. The volume fraction curve for 270 μm particles is zero, as the airflow does not carry these particles. At 0.8 meters height (Figure 7b), the particle distribution is similar to that observed in the graph at 0.5 meters (Figure 7a). The particles with diameters of 120 μm and 150 μm exhibit concave profiles, being more significant with a solid fraction of the 150 μm curve. At 1.5 meters height, the same trend is observed for the granular phase concentration profiles as those shown at 0.8 meters, as seen in Figure 7c; however, they differ in the concentration of the granular phase, as at 1.5 meters height, the volume fraction of solids decreases slightly.

On the other hand, Figure 8 shows the axial velocity profiles, which, at a height of 0.5 m (Figure 8a), exhibit convex curves for the 120 μm and 150 μm particles. These curves reveal an upward behavior in the central region of the air reactor, while negative velocities are observed near the walls, indicating a downward movement. These profiles correspond to those reported in the work of Guan *et al*. (Guan, Chang, Zhang, Wang, & Sun, 2014). The profiles for the other diameters are close to zero. The axial velocity profile at 0.8 m height (Figure 8b) is similar to that shown for 0.5 m height. It can be seen that, again, the curves for the 120 μm and 150 μm particles maintain a convex profile; however, a decrease in the maximum velocity achieved by the granular phase is observed. The axial velocity profiles at 1.5 m height (Figure 8c) remain unchanged from the previous heights; however, a decrease in the axial velocity of the particles is noticeable, and again, the profile shown by the 120 μm and 150 μm particles is similar to those reported in previous studies (Guan, Chang, Zhang, Wang, & Sun, 2014; Shuai W. *et al*., 2011). Such a profile can also be observed in the results presented by Lin et al. (2019), where negative velocities are shown near the walls, while the maximum velocity is observed in the central region, as demonstrated in this study for 150 and 120–micron particles.

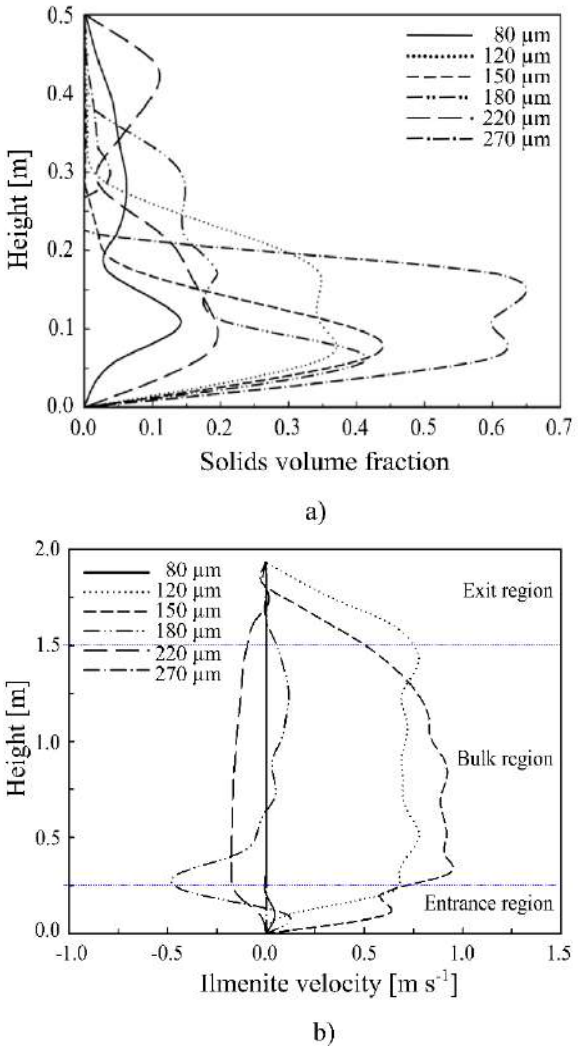

Figure 9. a) Particle distribution profiles in the fuel reactor, b) Velocity profiles of the granular phase throughout the air reactor.

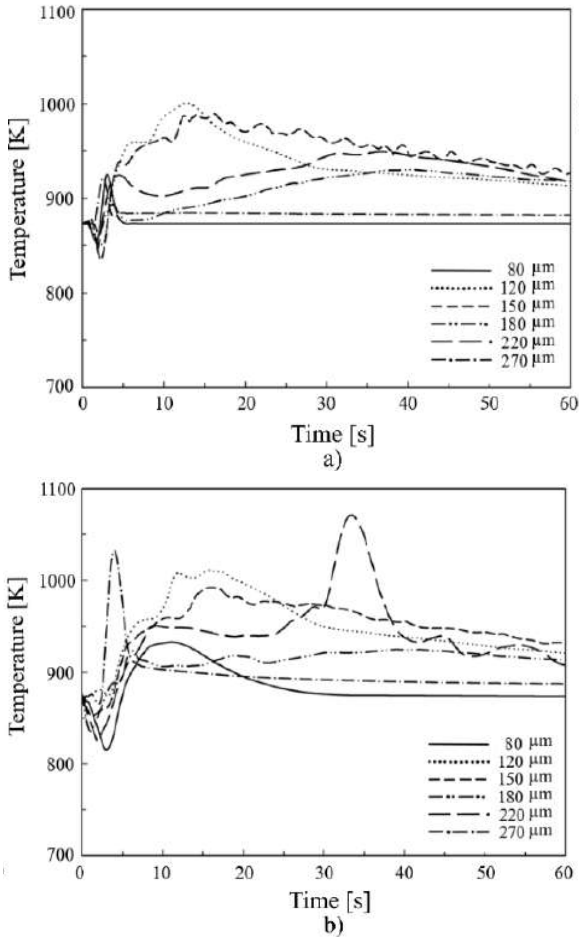

Figure 10. Temperature profiles. a) cyclone outlet, b) fuel reactor outlet.

These studies help validate the velocity profiles found in this numerical simulation.

In Figure 9a), the distribution of particles in the fuel reactor can be observed. The graph shows that, in general, for all particle diameters, the fluidized bed is located below 0.22 meters in height. However, there are apparent differences in the distribution of particles of different diameters. The 270 μm particles show a high concentration below 0.2 meters due to the fact that the airflow hardly fluidizes the bed. The 120 μm, 150 μm, and 180 μm particles show similar distributions below 0.2 meters, with maximum volume fractions of 0.44. This behavior is advantageous as it allows for a more significant volume fraction for the gas phase, leading to better conditions for the combustion reaction. However, having high volume fraction values in higher regions of the fuel reactor is undesirable, as this could cause particles to be dragged out of the system. In this regard, the 150 μm particles have the lowest volume fraction above 0.2 m in height. Regarding the 80 μm and 220 μm particles, a maximum volume fraction of 0.2 is observed, which is not ideal as it may affect the combustion reaction. The results in the fuel reactor shown by the profiles in Figure 9a) again indicate that the 150 μm diameter particles exhibit the most suitable behavior within the fuel reactor. This particle size aligns with what Sornumpol *et al*. reported (Sornumpol, Uraisakul, Kuchonthara, Chalermsinsuwan, & Piumsomboon, 2017), who concluded through an experimental design that the best particle size corresponds to 150 μm. On the other hand, the velocity profiles of the granular phase throughout the air reactor are shown in Figure 9b), where it is evident that the 120 μm and 150 μm particles are satisfactorily fluidized. These profiles are similar to those obtained in the work of Guan *et al*. (Guan, Chang, Zhang, Wang, & Sun, 2014). As in that study, the 120 μm and 150 μm profiles exhibit three regions: an inlet region, a bulk region, and an outlet region, as can be seen in Figure 9b).

3.3 Analysis of thermal results within the CLC system

Figures 10a) and 10b) show temperature profiles at the outlets of the cyclone separator and the fuel

reactor, respectively, for different particle diameters. In both figures, it can be observed that the system that best conserves heat corresponds to the 150 μm diameter particles. The cases that show the greatest cooling correspond to the 80 μm and 270 μm diameter particles. The 120 μm, 180 μm, and 220 μm particles show final temperatures that are very close to each other; however, all are below the final temperature of the 150 μm particle system. These temperature profiles suggest that the appropriate fluidization regimes for the granular phase, both in the air and fuel reactors, help reduce heat losses through the system outlets. In contrast, systems with poorer fluidization regimes exhibit temperature profiles with more significant cooling. Including chemical reactions in the system would affect these temperature profiles by introducing heat generation or absorption depending on the nature of the reactions. Exothermic reactions could generate higher temperatures in the fuel reactor, especially in systems with efficient fluidization. At the same time, endothermic reactions in the air reactor could lower the temperature, particularly in systems with poor fluidization, where heat transfer is less effective. Including these reactions would also affect heat distribution and the dynamics of the flows within the reactors, possibly altering the fluidization behavior and the temperature profiles observed in this simulation. Therefore, the role of chemical reactions could be significant in optimizing the thermal balance and improving the overall system efficiency. However, this work determined the analysis of particle sizes suitable for fluid dynamic phenomena within reactors; that is, to obtain a homogeneous dispersion of particle-gas flow. This study lays the foundation for future work involving chemical reactions since, being a surface phenomenon, the results obtained in this work determine the optimal gas-particle contact areas.

3.4 Modelling perspectives

As shown, momentum, mass, and energy balances are possible to solve using CFD software for different particle sizes and feedstocks. Nevertheless, the system's actual behavior could be better known because this model inferred the movement of the particles inside the reactor using supported correlations instead of experimental data. Due to their advantages in high mass and heat transfer rates and the vigorous mixing of solids that provokes good gas-solids contact, both reactors were considered solid-gas fluidized beds. However, any problem related to poor solid mixing, undesirable gas flow patterns, or physical operating problems will provoke a decrease in reactor performance (Shafiq, Azam, & Hussain, 2021). The hydrodynamic behavior of gas-solid fluidized beds varies with scale. When scaling up fluidized bed reactors, the behavior of large-scale fluidized beds usually differs significantly from the lab-scale behavior (Efhaima & Al-Dahhan, 2017) and, more severely, from the CSTR model (Levesnpiel, 1999). Therefore, it is essential to identify the experimental conditions that can provide similar and non-similar radial profiles of the gas holdup in the used beds to properly assess the new mechanistic scale-up of gas-solid fluidized beds (Efhaima & Al-Dahhan, 2021). In order to solve these uncertainties intrinsic to the scale-up procedure, Zaid and Al-Dahan (Zaid, Al-Rubaye, Aljuwaya, & Al-Dahhan, 2023) have recently proposed to group all the important parameters related to mechanical and thermal energy as well as to the geometry of particles and reactors into dimensionless numbers. This group completes the previous proposition of dimensionless groups (Glicksman, Hyre, & Woloshun, 1993). This approach seems very promising because mass and energy balances can be derived from the momentum balances, once the particle movement inside the reactor is known (Whitaker, 2009).

Conclusions

A 3D model of a combustion process in chemical cycles was developed using CFD, incorporating the kinetic theory of granular flow to study the effect of particle diameter on its behavior within the system. The results of this study showed the following:

1. Particle diameter significantly influences particle distribution in the fuel and air reactors, as different fluidization regimes develop depending on the particle diameter.

2. The distribution of particles and the velocity profile in the air reactor at different heights demonstrate that, according to previous reports, diameters of 120 μm and 150 μm achieve the most suitable profiles.

3. The velocity profiles throughout the air reactor are most suitable for the 120 μm and 150 μm particles. These profiles exhibit three defined regions: an inlet region, a bulk region, and an outlet region; this behavior has also been reported in previous studies.

4. In the fuel reactor, for the six different diameters, most of the particles are located below 0.2 m in height; however, the best distribution was obtained for the 120 μm, 150 μm, and 180 μm particles.

5. Regarding the temperature profiles, the results show less cooling in the combustion system in chemical cycles with 150 μm diameter particles.

Based on the evaluation of fluidization regimes, particle distribution, and thermal conservation, the use of 150 μm diameter particles in CLC systems is recommended, as they ensure a balance between pneumatic transport, phase contact, and thermal efficiency, improving the performance of the system in terms of conversion and operational stability. Generally, it can be concluded that, for the conditions of velocity, pressure, and temperature (shown in Table 3), particles with diameters of 150 μm exhibit better performance in particle distribution, velocity, and temperature profiles.

Acknowledgements

The authors thank the support of project 20.20-CIC-UMSNH, TecNM for the use of facilities, FAOV thanks for the CONACYT scholarship 956195, and CAHB, GJG, JARB, and RMY thank for the CONACYT-SNI scholarships. The authors would like to extend their thanks to Dr. Gildardo Solorio Díaz for his support in using ANSYS software.

Nomenclature

α_q	Volume fraction of phase q
ρ_q	Density of phase q, kg/m^3
$\vec{v}_q$	Velocity vector of phase q, m/s
m_{pq}	Mass transfer rate from phase p to phase q, kg/s
S_q	Mass source term, kg/s
P	Pressure shared between phases, Pa
τ_q	Stress tensor of phase q, Pa
μ_q	Stress tensor of phase q, Pa ·s
λ_q	Bulk viscosity of phase q. Pa·s
g	Gravitational acceleration, m/s^2
h_q	Specific enthalpy of phase q, J/kg
$\overline{q}$	Heat flux, W/m^2
G_k	Generation of turbulent kinetic energy, m^2/s^3
G_b	Generation of turbulent kinetic energy by buoyancy, m^2/s^3
e_{ss}	Coefficient of restitution in particle collisions
θ_s	Granular temperature of the solid phase, m^2/s^2
g_0	Radial distribution function
d_s	Particle diameter of the solid phase, m
$F_{td,q}$	Turbulent dispersion force for phase q, N
C_D	Drag coefficient
$\mathrm{Re_s}$	Reynolds number of the solid phase
σ_{pq}	Dispersion Prandtl number
C_{TD}	Turbulent dispersion constant
Φ	Angle of internal friction, degrees
I_{2D}	Second invariant of the deviatoric stress tensor
G	Elastic modulus of the granular material, Pa

References

Adanez , J., Abad, A., Garcia-Labiano, F., Gayan, P., & De Diego, L. (2012). Progress in chemical-looping combustion and reforming technologies. *Progress in energy and combustion science, 38*(2), 215-282. doi: https://doi.org/10.1016/j.pecs.2011.09.001

ANSYS. (2013). Ansys Fluent Theory Guide. *Theory Guide*. Retrieved from Retrieved from https://www.ansys.com

Archer, C., & Jacobson, M. (2005). *Journal of Geophysical Research: Atmospheres*, 110(D12). doi: https://doi.org/10.1029/2004JD005462

Deng, Z., Xiao, R., Jin, B., & Song, Q. (2009). Numerical simulation of chemical looping combustion process with $CaSO_4$ oxygen carrier. *International Journal of Greenhouse Gas Control, 3*(4), 368-375. doi: https://doi.org/10.1016/j.ijggc.2008.11.004

Deng, Z., Xiao, R., Jin, B., Song, Q., & Huang, H. (2008). Multiphase CFD modeling for a chemical looping combustion process (fuel reactor). *Chemical Engineering & Technology, 31*(12), 1754-1766. doi: https://doi.org/10.1002/ceat.200800341

Efhaima, A., & Al-Dahhan, M. (2017). Assessment of scale-up dimensionless groups methodology of gas-solid fluidized beds using advanced non-invasive measurement techniques (CT and RPT). *The Canadian Journal of Chemical Engineering, 95*(4), 656-669. doi: https://doi.org/10.1002/cjce.22745

Efhaima, A., & Al-Dahhan, M. (2021). Validation of the new mechanistic scale-up of gas-solid fluidized beds using advanced non-invasive measurement techniques. *The Canadian Journal of Chemical Engineering, 99*(9), 1984-2002. doi: https://doi.org/10.1002/cjce.23938

Ergun, S. (1949). Fluid Flow through Randomly Packed Columns and Fluidized Beds. *Industrial & Engineering Chemistry, 41*(6), 1179-1184. doi: https://doi.org/10.1021/ie50474a011

Gitay, H. (2002). Biodiversity IPCC Technical Paper. *Change Climate*.Glicksman, L., Hyre, M., & Woloshun, K. (1993). Simplified scaling relationships for fluidized beds. *Power*

Technology, 77, 177-199. doi: https://doi.org/10.1016/0032-5910(93)80055-F

Guan, Y., Chang, J., Zhang, K., Wang, B., & Sun, Q. (2014). Three dimensional CFD simulation of hydrodynamics in an interconnected fluidized bed for chemical looping combustion. *Powder technology 268*, 316-328. doi: https://doi.org/10.1016/j.powtec.2014.08.046

Höök, M., & Tang, X. (2013). Depletion of fossil fuels and anthropogenic climate change—A review. Energy policy. *Energy policy, 52*, 797-809. doi: https://doi.org/10.1016/j.enpol.2012.10.046

Jin, B., Xiao, R., Deng, Z., & Song, Q. (2009). Computational fluid dynamics modeling of chemical looping combustion process with calcium sulphate oxygen carrier. *International Journal of Chemical Reactor Engineering, 7*(1). doi: https://doi.org/10.2202/1542-6580.1786

Jung, J., & Gamwo, I. (2008). Multiphase CFD-based models for chemical looping combustion process: Fuel reactor modeling. *Powder Technology, 183*(3), 401-409. doi: https://doi.org/10.1016/j.powtec.2008.01.019

Kerr, H. (2005). Capture and separation technologies gaps and priority research needs. *Elsevier Ltd. Oxford, UK, 1*, 655-660.

Kruggel-Emden, H., Rickelt, S., Stepanek, F., & Munjiza, A. (2010). Development and testing of an interconnected multiphase CFD-model for chemical looping combustion. *Chemical engineering science, 65*(16), 4732-4745. doi: https://doi.org/10.1016/j.ces.2010.05.

Kumar, S., & Muhuri, P. (2019). A novel GDP prediction technique based on transfer learning using CO_2 emission dataset. *Applied Energy, 253*, 113476. doi: https://doi.org/10.1016/j.apenergy.2019.113476

Launder, B., & Spalding, D. (1983). The numerical computation of turbulent flows. *Numerical prediction of flow, heat transfer, turbulence and combustion*, 96-116. doi: https://doi.org/10.1016/B978-0-08-030937-8.50016-7

Levesnpiel, O. (1999). COMMENTARIES: Chemical Reaction Engineering. *Industrial and Engineering Chemistry Research, 38*, 4140-4143.

Lin, J., Luo, K., Sun, L., Wang, S., Hu, C., & Fan, J. (2019). Numerical investigation of nickel–copper oxygen carriers in chemical-looping combustion process with zero emission of CO and H_2. *Energy & Fuels*, *33*(11), 12096-12105.

Lun, C., Savage, S., Jeffrey , D., & Chepurniy, N. (1984). Kinetic theories for granular flow: inelastic particles in Couette flow and slightly inelastic particles in a general flowfield. *Journal of fluid mechanics, 140*, 223-256. doi: https://doi.org/10.1017/S0022112084000586

Mahalatkar, K., Kuhlman, J., Huckaby, E., & O'Brien, T. (2011). Computational fluid dynamic simulations of chemical looping fuel reactors utilizing gaseous fuels. *Chemical engineering science, 66*(3), 469-479. doi: https://doi.org/10.1016/j.ces.2010.11.003

Martínez-Prado, M. A. (2016). Estimación de las emisiones de gases de efecto invernadero para el estado de Durango, México. *Revista Mexicana de Ingeniería Química*, *15*(2), 575-601. https://rmiq.org/iqfvp/Pdfs/Vol.%2015,%20No.%202/IA3/RMIQTemplate.pdf

Masson-Delmotte, V., Zhai, P., Pörtner, H., Roberts, D., Skea, J., Shukla, P., . . . Pidcock, R. (2018). *Global Warming of 1.5 OC: An IPCC Special Report on the Impacts of Global Warming of 1.5° C Above Pre-industrial Levels and Related Global Greenhouse Gas Emission Pathways, in the Context of Strengthening the Global Response to the Threat of Climate Chang.* Geneva, Switzerland: World Meteorological Organization.

Nguyen, T., Seo, M., Lim, Y., Song, B., & Kim, S. (2012). CFD simulation with experiments in a dual circulating fluidized bed gasifier. *Computers & chemical engineering, 36*, 48-56. doi: https://doi.org/10.1016/j.compchemeng.2011.07.005

Pugazhendhi, A., Mathimani, T., Varjani, S., Rene, E., Kumar, G., Kim, S., & Yoon, J. (2019). Biobutanol as a promising liquid fuel for the future-recent updates and perspectives. *Fuel, 253*, 637-646. doi: https://doi.org/10.1016/j.fuel.2019.04.139

Scheaffer, D. (1987). Instability in the evolution equations describing incompressible granular flow. *Journal of differential equations, 66*(1), 19-50. doi: https://doi.org/10.1016/0022-0396(87)90038-6

Seo, M., Nguyen, T., Lim, Y., Kim, S., Park, S., Song, B., & Kim, Y. (2011). Solid circulation and loop-seal characteristics of a

dual circulating fluidized bed: experiments and CFD simulation. *Chemical engineering journal, 168*(2), 803-811. doi: https://doi.org/10.1016/j.cej.2011.01.041

Shafiq, H., Azam, S., & Hussain, A. (2021). Steam gasification of municipal solid waste for hydrogen production using Aspen Plus Simulation. *Discover Chemical Engineering, 1*(4), 1-16. doi: https://doi.org/10.1007/s43938-021-00004-9

Shuai, W., Guodong, L., Huilin, L., Juhui, C., Yurong, H., & Jiaxing, W. (2011). Fluid dynamic simulation in a chemical looping combustion with two interconnected fluidized beds. *Fuel Processing Technology, 92*(3), 385-393. doi: https://doi.org/10.1016/j.fuproc.2010.09.032

Shuai, W., Huilin, L., Feixiang, Z., & Guodong, L. (2014). CFD studies of dual circulating fluidized bed reactors for chemical looping combustion processes. *Chemical Engineering Journal, 236*, 121-130. doi: https://doi.org/10.1016/j.cej.2013.09.033

Shuai, W., Yunchao, Y., Huilin, L., Jiaxing, W., Pengfei, X., & Guodong, L. (2011). Hydrodynamic simulation of fuel-reactor in chemical looping combustion process. *Chemical Engineering Research and Design, 89*(9), 1501-1510. doi: https://doi.org/10.1016/j.cherd.2010.11.002

Sornumpol, R., Uraisakul, W., Kuchonthara, P., Chalermsinsuwan, B., & Piumsomboon, P. (2017). CFD simulation of fuel reactor in chemical looping combustion. *Energy Procedia, 138*, 979-984. doi: https://doi.org/10.1016/j.egypro.2017.10.096

Stocker, T., Qin, D., Plattner, G., Alexander, L., Allen, S., Bindoff, N., & Xie, S. (2013). Technical summary. In Climate change 2013: the physical science basis. Contribution of Working Group I to the Fifth Assessment Report of the Intergovernmental Panel on Climate Change. *Cambridge University Press*, 1535.

Syamlal, M., Rogers, W., & O'Brien, T. (1993). MFIX documentation theory guide. USA: USDOE Morgantown Energy Technology Center. doi: https://doi.org/10.2172/10145548

Wen, & Yu, C. (1966). Mechanics of fluidization., *62*, pp. p. 100-111.

Whitaker, S. (2009). Chemical Engineering Education: Making Connections at Interfaces. *Revista Mexicana de Ingeniería Química, 8*, 1-33. Retrieved from https://rmiq.org/iqfvp/Pdfs/Vol%208%20no%201/RMIQ_Vol_8_No_1_1.pdf

Zaid, F., Al-Rubaye, H., Aljuwaya, T., & Al-Dahhan, M. (2023). Assessment of the Dimensionless Groups-Based Scale-Up of Gas-Solid Fluidized Beds. *Processes, 11*(1). doi: https://doi.org/10.3390/pr11010168

Casa abierta al tiempo

UNIVERSIDAD AUTÓNOMA METROPOLITANA

Coordinador del Posgrado

Dr. Guadalupe Ramos Sánchez

piq@xanum.uam.mx; pdiv@xanum.uam.mx

http://piq.izt.uam.mx

Ejemplos de algunos temas de investigación actuales y trascendentes en el escenario nacional e internacional:

- Ciencia de datos aplicadas al diseño de procesos químicos.
- Síntesis de productos de alto valor agregado mediante catalizadores heterogéneos, biocatalizadores y microorganismos.
- Potabilización de agua mediante tratamientos fisicoquímicos.
- Materiales, prototipos y análisis de Baterías Ion-Li con aplicaciones en autos eléctricos y almacenamiento de energía a gran escala.
- Hidrotratamiento de combustibles convencionales y provenientes de energías renovables.
- Captura de CO_2 y valorización mediante catálisis para la producción de combustibles sintéticos y otros productos de alto valor agregado.
- Cultivo y utilización de micro algas para la producción de biocombustibles
- Eliminación de contaminantes orgánicos e inorgánicos en el tratamiento de agua.
- Ciencia de alimentos aplicada a la estabilización de sistemas

Doctorado: ingreso cada trimestre
Próxima convocatoria: julio 2024
Recepción de Documentos: agosto-septiembre 2024
Inicio de Clases: octubre 2024

Maestría: ingreso a inicios de cada año
Próxima convocatoria: octubre 2024
Propedéutico: noviembre-diciembre 2024
Ingreso: febrero 2025

Universidad Autónoma Metropolitana Unidad Iztapalapa, Av. Ferrocarril San Rafael Atlixco 186, Colonia Leyes de Reforma 1a. Sección Iztapalapa, C. P. 09310 Ciudad de México. Tel. 5804 4600

investigación y docencia

Posgrados

ciencia tecnología arte humanismo

uam

Maestría y Doctorado en Ciencias (Ingeniería Química)

CBI Unidad Iztapalapa

División de Ciencias Básicas e Ingeniería

Líneas de Investigación:

- *Ingeniería de reactores catalíticos*
- *Fenómenos de transporte en sistemas multifásicos*
- *Ingeniería de sistemas en procesos químicos*
- *Catálisis y nuevos materiales*
- *Bioprocesos y tecnología de alimentos*

Casa abierta al tiempo
UNIVERSIDAD AUTÓNOMA METROPOLITANA